NOVEL STRATEGIES TO IMPROVE THE EFFICIENCY AND STABILITY OF BINARY-BASED ORGANIC PHOTOVOLTAIC DEVICES

Enas Moustafa Mohamed Abdelghafar

UNIVERSITAT ROVIRA i VIRGILI

Novel Strategies to Improve the Efficiency and Stability of Binary-Based Organic Photovoltaic Devices

ENAS MOUSTAFA MOHAMED ABD ELGHAFAR

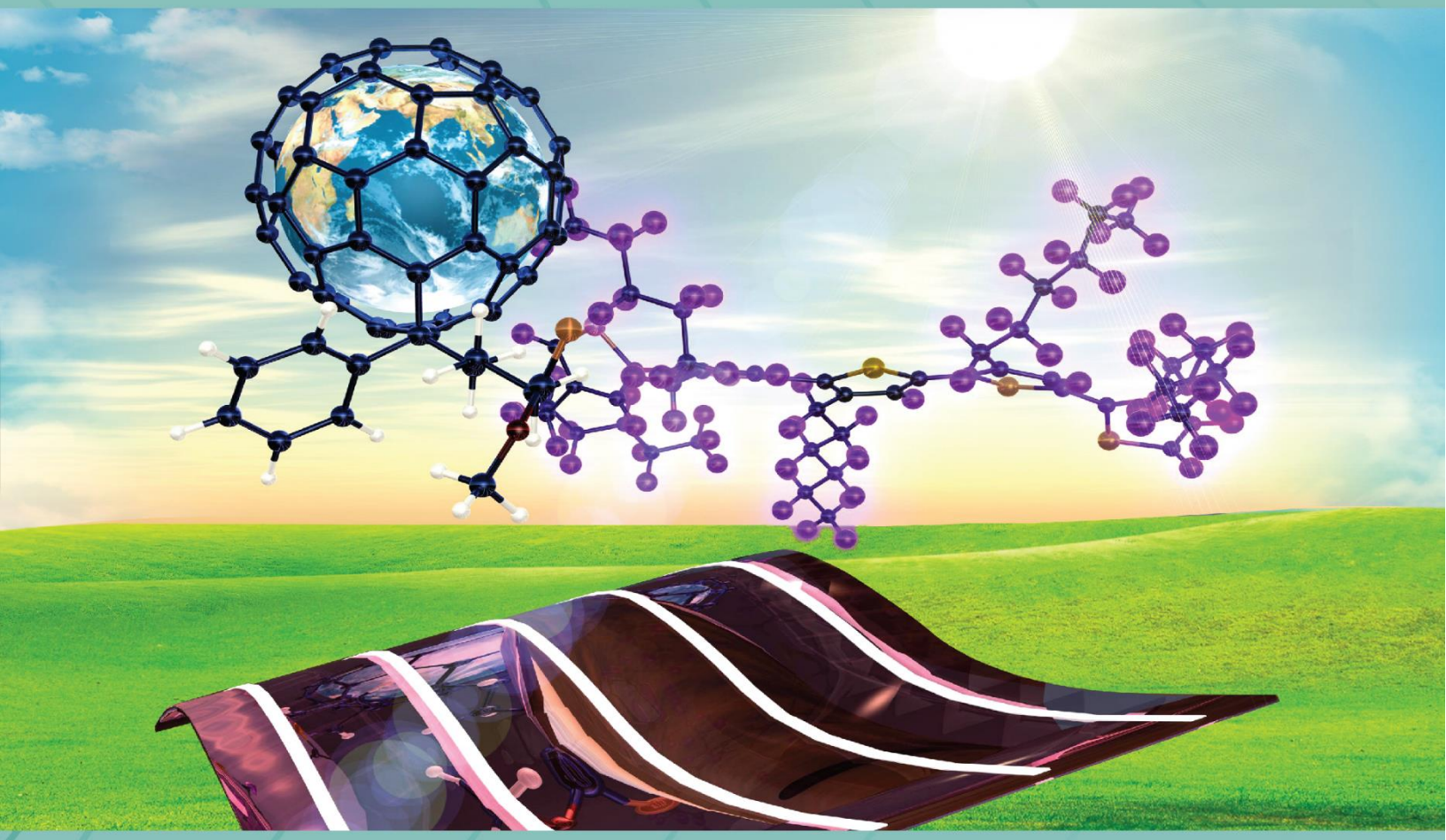

DOCTORAL THESIS
2023

DOCTORAL THESIS

Novel Strategies to Improve the Efficiency and Stability of Binary-Based Organic Photovoltaic Devices

Enas Moustafa Mohamed Abd Elghafar

Supervised by

Prof. Lluís Francesc Marsal Garví

Departament d'Enginyeria Electrònica, Elèctrica I Automàtica

Nanoelectronic and Photonic Systems (NePhoS)

UNIVERSITAT ROVIRA i VIRGILI

Tarragona

2022

Escola Tècnica Superior D'Enginyeria
Departament d'Enginyeria Electrònica, Elèctrica i Automàtica
Campus Sescelades
Avinguda dels Països Catalans, 26
43007 Tarragona
Espanya
Tel.: + 34 977 559 610 / 559 728
Fax: + 34 977 559 605

I State that the present study, entitled "**Novel Strategies to Improve the Efficiency and Stability of Binary-Based Organic Photovoltaic Devices"** presented by Enas Moustafa Mohamed Abd Elghafar for the award of the degree of Doctor, has been carried out under my supervision at the Department Electrical, Electronic, and Automatic Engineering of this university, and that it satisfies all requirements to obtain the doctoral degree with "International Distinction".

Tarragona, November 19th 2022

Doctoral Thesis Supervisor

MARSAL GARVI LUIS FRANCISCO - 39688257D

Firmado digitalmente por MARSAL GARVI LUIS FRANCISCO - 39688257D
Fecha: 2022.11.19 10:32:44 +01'00'

Dr. Lluis F. Marsal Garví

General Abstract

The power conversion efficiency (PCE) of organic photovoltaics (OPVs) has been promptly improved once emerging the recently developed non-fullerene small-molecules acceptors (NFAs) that replaced the fullerene counterpart, pushing the bulk-heterojunction (BHJ) based- OPVs to achieve efficiencies approaching 20 %. This remarkable increase in the PCEs was due to the significant enhancement in the light absorption along with diminishing the energy losses, particularly upon minimizing the trade-off behavior between voltage loss and charge generation in nonfullerene organic solar cells (NF–OPVs). Several strategies have been investigated to understand the limiting factors that significantly affect the performance of the OPV devices in order to boost their performance and stability. Some of these avenues concern the bulk-heterojunction photoactive blend microstructure through solvent additives, thermal treatment, deposition approaches, and introducing third component. Some other approaches determined the critical role of the interface materials stability and their compatibility with the contacted photo-active layer and electrodes, reflecting their importance for long-term stable OPVs. In this thesis, we combined the interfacial engineering, morphology control, and third component strategies to improve the OPV devices performance and stability. First, we conducted an intermittent spray pyrolysis approach to deposit the ZnO interfacial layers in fullerene based inverted OPVs. It significantly enhanced the interface morphology, resulting in remarkable stability behaviour of the sprayed devices. Then, we focused on optimizing the blend morphology based on the NF-OPV devices through solvent additives and thermal treatment. Furthermore, we presented an extremely efficient PDINO based cathode interlayer for iNF-OPVs, achieving excellent photostability behavior through avoiding the photo-induced shunts and the photocatalytic behavior, which are inevitably in the ZnO based inverted OPVs. Moreover, we demonstrated that a pre-thermal treatment approach as a facile passivation strategy that reduces the trap state density of the blend film, improves interface charge transfer, allows balanced electron/hole mobility, and thus significantly promotes the short-circuit current (J_{SC}) and PCE of treated devices. Finally, we investigated the use of the BHJ and layer by layer (LBL) deposition strategies in a binary system along with incorporating the perovskite $CsPbI_3$ QDs materials (PQDs) as a third counterpart to provide a novel NF-OPV ternary system. It significantly enhances the FF and V_{OC}, revealing the fine-tuned morphology. Our findings exhibited that QDs-third component through LBL processing method is an effective strategy to improve the morphology of the active layer and achieve high-performance OPVs.

Acknowledgement

First and foremost, I am deeply grateful to *Almighty Allah* for his endless guidance and support through all stages of my life, including my PhD journey. I sincerely hope that the research and analysis presented in this thesis will be benefit to others as a way of expressing my thanks and appreciation to Allah for all the countless blessings and opportunities *He* has given me.

I would like to present my sincere gratitude to my supervisors *Prof. Lluis Marsal* for his constant guidance, dedication, and commitment to my development as a researcher. It has been a pleasure to work with him and I am truly grateful not only for his encouragement and motivation but also for his gentleness. Thank you, *Prof. Lluis Marsal*, for your endless support during my PhD journey.

I would like to express my heartfelt gratitude to *Prof. Josep Pallarès* for his invaluable guidance and support throughout my research. His expertise and insights have been instrumental in the successful completion of this work. I am deeply grateful for his mentorship and for the opportunity to have worked with him. Thank you, *Prof. Josep Pallarès*, for your indispensable contribution to my research journey.

I owe my deepest thanks to *Prof. Jenny Nelson* for providing me with the opportunity to intern in her laboratory at the department of Physics, Imperial College London. The experience I gained during my internship was invaluable, and I am deeply grateful for the knowledge and skills I acquired under her supervision. Thank you, *Jenny*, for everything you have done for me during my four months stay. I am grateful for your support and for the opportunity to learn and grow as a researcher in your lab.

I would like to take this opportunity to extend my thanks to the group member, *Dr. Jun Yan, Dr. Flurin Eisner, Dr. Mohammed Azzouzi, Dr. He Zhicai, Dr. Gihan Ryu, Dr. Sachetan Tuladhar, Jolanda Müller, Brian Tam, Hang Yu*, Jack, and *Paloma*, not only for their constructive scientific discussion and the constant support during my stay but also for the kind and friendly environment they have created. They have provided a supportive and collaborative space for learning and exchanging ideas, and I am truly grateful for the opportunity to be a part of it.

I am greatly indebted to the excellent collaborators from ICIQ, Prof. Emilio Palomares and his research team, especially *Dr. Jose Sánchez* and *Dr. Maria Méndez* for their tremendous support, knowledge, valuable discussions, and experience that they gave throughout this work.

I am truly grateful to *Dr. Pilar Formentín* and *Dr. Josep Ferré* for their kindness and constant assistance during this work. I would also like to thank the URV Servei de Recursos Cientifics i Tècnics laboratory staff, especially *Dr. Eric Pedrol, Dr. Rita Marimon* and *Dr. Mariana Stankova*, for their invaluable

support, insights and expertise with the AFM and FE-SEM measurements and Eng. Ernist for his kind assistance in making the metallic mask of the spray pyrolysis setup.

I would also like to sincerely thank my marvelous colleagues and friends from NePhoS group: *Karen, Mohamed, Magaly, Pankaj, Anand, Alfonsina, Kandeel, Mahmoud, Nuria, Alejandro, Laura, Pili, Jakub, Akash, Tabish, Gohar,* and *Josep* for their unwavering support and encouragement throughout this journey. I would like also to express my deep thankful to *Reham* and *Fatima* for their welcoming demeanor, kindness, and generosity that made my stay so much enjoyable and comfortable. Special thanks go to my lovely friends: *Marwa, Ayaallah, Maghfera, Khaoula, Amal, Ikram,* and *Mariam* for their endless love and prayers.

My acknowledgement would be incomplete without thanking the biggest source of my strength, my beloved family. I am grateful for the love and support of my father *Moustafa*, and my dear brother *Ahmed*, as well as my sisters *Omnia* and *Ayat*, who always believed in me. Their care and encouragement have been a blessing to me. I would like to extend a special thanks to my mum *Safia* for her unwavering love and support throughout my entire life. Her constant encouragement and belief in me have been a driving force behind my success. I am deeply grateful to have such a strong and loving mother who has always been there for me, through every challenge and triumph. Thank you, Mum, for everything you have done for me. I love you.

سيكون عرفانى بالجميل غير مكتمل دون أن أشكر أكبر مصدر لقوتي ، عائلتي الحبيبة. أنا ممتنة لحب ودعم والدي مصطفى ، وشقيقي العزيز أحمد ، وكذلك شقيقاتي أمنية وآيات الذين هم دائمين الايمان بى. لقد كانت رعايتهم وتشجيعهم نعمة عظيمة بالنسبة لى.

أود أن أتقدم بشكر خاص لأمي صفية على حبها ودعمها الذي لا و لم يتزعزع طوال حياتي كلها. كان تشجيعها المستمر وإيمانها بي هما القوة الدافعة وراء نجاحي. أنا ممتنة للغاية لوجود أمى القوية والمحبة التي كانت دائمًا موجودة من أجلي ، من خلال كل تحد وانتصار. شكراً لك يا أمي الجميلة على كل ما فعلته من أجلي. أنا أحبك.

I wanted to take a moment to express my heartfelt thanks to my beloved husband *Ahmed*. His love and support mean the world to me and I am so grateful to have him by my side. His kindness, generosity, and understanding never go unnoticed, and I am thanking Allah for having him in my life. I love you more than words can say.

Lastly, I would like to acknowledge my funding agency for their financial support, which has made this research possible. The Agency for Management of University and Research Grants (AGAUR) for receiving the fund with grant number 2019 FI_B01102. The Spanish Ministerio de Ciencia, Innovación PDI2021-128342OB-I00. I would further acknowledge the Diptació de Tarragona 2021CM14 and the Catalan Institution for Research and Advanced Studies (ICREA) under the ICREA Academia Award.

This list of people could be extended much further; therefore, I am deeply grateful to all of those individuals not mentioned above and who have made contributions to my success.

Enas Moustafa Mohamed Abd Elghafar

List of Abbreviations

AFM	atomic force microscopy
Ag	silver
AM 1.5G	air mass 1.5 Global
BHJ	bulk heterojunction
BTP-4Cl (or Y7)	2,2'-((2Z,2'Z)-((12,13-bis(2-ethylhexyl)-3,9-diundecyl-12,13-dihydro[1,2,5]thiadiazolo[3,4e]thieno[2",3":4',5']thieno[2',3',:4,5]pyrrolo[3,2-g]thieno[2',3':4,5]thieno[3,2-b]indole-2,10-diyl) bis(methanyly-lidene))bis(5,6-dicholoro-3-oxo-2,3-dihydro-1H-indene-2,1-diylidene))dimalononitrile
BTP-4F (or Y6)	2,2'-((2Z,2'Z)-((12,13-bis(2-ethylhexyl)-3,9-diundecyl-12,13-dihydro-[1,2,5]thiadiazolo[3,4-e]thieno[2",3'':4',5']thieno [2',3':4,5]pyrrolo[3,2-g]thieno[2',3':4,5]thieno[3,2-b]indole-2,10-diyl)bis(methanylylidene))bis(5,6-difluoro-3-oxo-2,3-dihydro-1H-indene-2,1-diylidene))dimalononitrile
CB	chlorobenzene
CE	charge extraction
CN	1-chloronapthaline
$CsPbI_3$	Cesium Lead Iodide
CT-state	charge-transfer state
D/A	donor/acceptor
DC	direct current
DIO	1,8-diiodooctane
DOS	density of states
Eg	energy bandgap
EL	Electroluminescence
EQE	external quantum efficiency
ETL	electron transport layer
FF	fill factor
h	Planck's constant
HOMO	highest occupied molecular orbitals
HTL	hole transport layer
TPC	TPC
iOPVs	inverted organic Photovoltaics
IS	impedance spectroscopy
ITO	indium tin oxide
J	current density
J_{Ph}	photogenerated current
J_{SC}	short-circuit current density
J-V	current density versus voltage
J_0	reverse saturation current density of minority carriers
k_B	Boltzmann constant
LED	light emitting diode
LUMO	lowest unoccupied molecular orbitals
MPP	maximum power point
n	charge carrier density
NC	Nano-crystals
n_{id}	ideality factor
NREL	National Renewable Energy Laboratory
OSC	organic solar cell

OPV	organic photovoltaic
PBDB-T-2F (or PM6)	poly[2,6-(4,8-bis(5-(2-ethylhexyl-3-fluoro)thiophen-2-yl)benzo[1,2-b;4,5-b´]dithiophene))-alt-(5,5-(1',3'-di-2-thienyl-5',7'-bis(2-ethylhexyl)benzo [1',2'-c:4',5'-c']dithiophene-4,8-dione)]
PCE	power conversion efficiency
$PC_{70}BM$	[6,6]-phenyl-C71 butyric acid methyl ester
PDINO	2,9-bis[3-(dimethyloxidoamino)propyl]anthra[2,1,9-def:6,5,10-d'e'f']diisoquinoline-1,3,8,10(2H,9H)-tetrone
PEDOT:PSS	poly(3,4-ethylenedioxythiophene)-polystyrene sulfonate
PL	photoluminescence
PTB7-Th (or PCE10)	(poly[2,6-4,8-di(5-ethyl- hexylthienyl)benzo[1,2-b;3,3-b] dithiophene] [3-fluoro-2[(2-ethylhexyl)- carbonyl]thieno[3,4-b]thiophenediyl]
PV	photovoltaic
PQDs	Perovskite quantum dots
q	elementary charge
QDs	Quantum Dots
RMS	root-mean-square
R_S	series resistance
R_{Sh}	shunt resistance
SCLC	space-charge-limited-current
T	temperature
TPC	transient photocurrent
TPV	transient photovoltage
UV-vis	ultraviolet-visible
V	voltage
V_{MPP}	voltage at maximum power point
V_{OC}	open-circuit voltage
VTE	vacuum thermal evaporation
WF	work function
ZnO	zinc oxide
$Z^{\backslash}$	real impedance
$Z^{\backslash\backslash}$	imaginary impedance
μ	mobility
τ	charge carrier lifetime

List of Figures

List of Tables

List of Scientific Contributions

1. Patent

Spanish patent no. P202131074, "Pre-Thermal Treatment Approach for Enhancing Organic Photovoltaic devices", **Enas Moustafa**, Josep Pallarès, Lluis F. Marsal, Alfonsina Abat Amelenan Torimtubun, and José G. Sánchez, Registered.

2. Scientific Articles

1. **Enas Moustafa**, José G. Sánchez, L. F. Marsal, and J. Pallarès, "Stability Enhancement of High-Performance Inverted Polymer Solar Cells Using ZnO Electron Interfacial Layer Deposited by Intermittent Spray Pyrolysis Approach", ***ACS Appl. Energy Mater***. 4 (4), pp. 4099–4111, **2021**. https://doi.org/10.1021/acsaem.1c00455
2. **Enas Moustafa**, A.A.A. Torimtubun, J. Pallarès, and Lluis. F. Marsal, "Effect of Additives and Annealing on the Performance of Nonfullerene-Based Binary and Ternary Organic Photovoltaics.", ***Sol. RRL***, 2100480, **2021**. https://doi.org/10.1002/solr.202100480
3. **Enas Moustafa**, L. F. Marsal, and J. Pallarès, "Significant Stability Improvement of Fullerene Organic Photovoltaic via ZnO Film Modification through Intermittent Spray Pyrolysis Technique.", ***ACS Appl. Energy Mater***. 5, 4, pp. 4390–4403, **2022**. https://doi.org/10.1021/acsaem.1c03994
4. **Enas Moustafa**, M. Méndez, J. Pallarès, and L.F. Marsal, Low Temperature Based PDINO Cathode Interlayer for High Operational Photostable Inverted Non-Fullerene Organic Solar Cells.", ***Solar Energy Materials and Solar Cells***, 248, 111985, **2022**. https://doi.org/10.1016/j.solmat.2022.111985
5. **Enas Moustafa**, Maria Méndez, José G. Sánchez, J. Pallarès, Emilio Palomares, and Lluis. F. Marsal, "Thermal Activation of PEDOT:PSS/PM6:Y7 Based Films Leads to Unprecedent High Short-Circuit Current Density in Nonfullerene Organic Photovoltaics.", ***Advanced Energy Materials***, 13, 4, 2203241, **2023**. https://doi.org/10.1002/aenm.202203241
6. A. A. A. Torimtubun, M. Méndez, **Enas Moustafa**, J. Pallarès, E. Palomares and Lluis F. Marsal, "Achieving 17.7% Efficiency of Ternary Organic Solar Cells by Incorporating a High LUMO Level and Miscible Third Component", *submitted.*

7. **Enas Moustafa**, F. Eisner, J. Yan, M. Azzouzi, J. Pallarès, L. Marsal, and J. Nelson, "Charge transport mechanism of non-fullerene organic photovoltaic devices employing PQDs third component through LBL method", will be prepared.
8. **Enas Moustafa**, M. Samir, M. Ramírez-Como, L. F. Marsal, and J. Pallarès, "CPEPh-Na/PEDOT:PSS Bi-stack Hole Interfacial Layers for Enhancing the Performance of Nonfullerene Organic Photovoltaics", will be submitted.
9. **Enas Moustafa**, J. Pallarès, and L. F. Marsal, "Revealing the Influence of Layer Thickness Variation on the Non-Fullerene Base-OPV Devices Performance Through Impedance Spectroscopy Study", invitation to the ***Special Issue of the IEEE Journal of the Electron Devices Society on LAEDC 2022***, will be submitted.

3. Conferences Proceedings, Presentations, and Posters

The list of contributed presentations that were published in the conference proceedings:

1. **Enas Moustafa**, José G. Sanchez, Lluis. F. Marsal, J. Pallarès, "New Deposition Technique for Inverted Polymer Solar Cells Using ZnO-ETL", *IEEE Latin America Electron Devices Conference (LAEDC)*, pp. 1–4, **2020**. (Oral Presentation)
   DOI: 10.1109/LAEDC49063.2020.9073305.
2. **Enas Moustafa**, José G. Sánchez, Lluis. F. Marsal, and J. Pallarès, "High Efficiency Inverted Polymer Solar Cells Fabricated Based on ZnO-ETL Utilizing Spray Pyrolysis Technique," *European PV Solar Energy Conference (EU-PVSEC*20), pp. 738–741, **2020**, Online. (Poster Presentation)
   DOI: 10.4229/EUPVSEC20202020-3BV.2.55.
3. **Enas Moustafa**, José G. Sanchez, Lluis. F. Marsal, J. Pallarès, "Spray Pyrolysis Technique Utilized for the Fabrication of Inverted Polymer Solar Cells", *Imaginenano-Nano* Online conference, Bilbao, Spain, **2020**. (Oral presentation)
4. **Enas Moustafa**, José G. Sánchez, Lluis. F. Marsal, and J. Pallarès, "ZnO Thin Film Deposited by Spray Pyrolysis for Long-Term Stable Organic Solar Cells," *IEEE Latin America Electron Devices Conference (LAEDC21)*, pp. 1–4, **2021**. (Oral Presentation)
   DOI: 10.1109/LAEDC51812.2021.9437976.
5. **Enas Moustafa**, J. Pallarès and Lluis. F. Marsal, "Revealing the Influence of Annealing Treatment on the Performance of Non-Fullerene Organic Photovoltaics", *35th Symposium on Microelectronics Technology and Devices (SBMicro)*, pp. 1-4, **2021**. (Oral Presentation)
   DOI: 10.1109/SBMicro50945.2021.9585750.

6. **Enas Moustafa**, J. Pallarès and Lluis. F. Marsal, "Influence of Spray Pyrolysis Deposition Technique on the Performance and Stability of Polymer Solar Cells," *13th Spanish Conference on Electron Devices (CDE)*, pp. 37–40, **2021**. (Oral Presentation)
   DOI: 10.1109/CDE52135.2021.9455733.
7. **Enas Moustafa**, J. Pallarès and Lluis. F. Marsal," Effect of Additives and Annealing on the Performance of Nonfullerene-Based Binary and Ternary Organic Photovoltaics", *EU PVSEC*, **2021**. (Visual Presentation)
   DOI: org/10.1002/solr.202100480
8. **Enas Moustafa**, J. Pallarès and Lluis. F. Marsal, "Dependency of Current Generated Upon Thermal Treatment Duration in Non-fullerene Organic Solar Cells", *IEEE Latin America Electron Devices Conference (LAEDC)*, pp. 1-4, **2022.** (Oral Presentation)
   DOI: 10.1109/LAEDC54796.2022.9908224.
9. M. Ramírez-Como, **Enas Moustafa**, A.A.A. Torimtubun, J. Sanchez, J. Pallarès and Lluis. F. Marsal, "Preliminary Study of the Degradation of PM6:Y7-based Solar Cells", *IEEE Latin America Electron Devices Conference (LAEDC)*, pp. 1-5, **2022.**
   DOI: 10.1109/LAEDC54796.2022.9908202.
10. **Enas Moustafa**, L. F. Marsal, and J. Pallarès, "CPEPh-NA/MoO_3 Bi-stack Hole Interfacial Layers for Enhancing the Performance of Nonfullerene Organic Photovoltaics", *WCPEC-8*, Italy, pp. 331-334, **2022**. (Poster Presentation)
    DOI: 10.4229/WCPEC-82022-2AV.2.8.

The works in this thesis were presented in the following conferences:

11. **Poster Presentation, Enas Moustafa**, L. F. Marsal, and J. Pallarès, "Different Structures of Organic Solar Cells Based on Non-Fullerene Accepters", *NFA-Based Organic solar cells NanoGe*, **2021**.
    DOI: 10.13140/RG.2.2.34197.24808
12. **Poster Presentation**, **Enas Moustafa**, L. F. Marsal, and J. Pallarès, "Revealing the Effect of ZnO-Interface Roughness on the Performance and Stability of Organic Solar Cells upon the Intermittent Film Spraying", *HOPV21*, **2021**.
    DOI: 10.13140/RG.2.2.14064.58882
13. **Poster Presentation**, **Enas Moustafa**, L. F. Marsal, and J. Pallarès, "Effect of Additives and Annealing on the Performance of Nonfullerene – Based Binary Organic Photovoltaics", *nanoGe Spring Meeting*, **2022.**
    DOI: 10.29363/nanoge.nsm.2022.362

14. **Oral Presentation, Enas Moustafa**, L. F. Marsal, and J. Pallarès, "Dependency of the PM6:Y7 Binary Organic Photovoltaics Performance on the Role of the Solvent Additive and Thermal Treatment" *HOPV22*, **2022**.
DOI: 10.29363/nanoge.hopv.2022.110

4. Scientific activities

1. High school demo scientific activity, "Revolution of Solar Energy", *EU Researcher's Night,* November **2020**, Reus, Spain.
2. Attending scientific workshops, **2022**

- *Progress in Plastic Electronics*, Faculty of Natural Science, Imperial College London, London, UK
- NanoGe Online Meeting on Perovskite, Organic Photovoltaics and Optoelectronics (*IPEROP.22*)

"Be kind, for whenever kindness becomes part of something, it beautifies it"

Prophet Muhammad (peace be upon him)

Table of Contents

Chapter 1

Introduction

1.1 Background

Since the early 2000s, concerns about the climate changes specially global worming has received considerable attention as one of the most significant changes that is mainly driven by human activities[1,2]. Global warming is principally caused by fossil fuel ignition, exhibiting a clear increase in the heat-absorbing greenhouse gases level in the atmosphere of the earth[3]. As of 2018, the world's main energy sources come from 27 % of Coal, 34% of oil, and 24 % of natural gas[4] as illustrated in **Figure 1.1**. Hence, fossil fuels contribute 85 % to the world's primary energy consumption. Which means there is a net increase of billion tons of CO_2 per year, leading to global warming and ocean acidification[3,5]. Moreover, due to today's increased demands for energy supplies coupled with more concerns of environmental, the term of "Carbon neutrality" was proposed to refer net-zero CO_2 emission[6]. Correspondingly, alternative renewable, environmentally friendly as well as sustainable energy sources became desirable such as hydro, wind, geothermal, and solar power[7]. One such alternative is solar energy which is the cleanest and most abundant renewable energy source in the world[8].

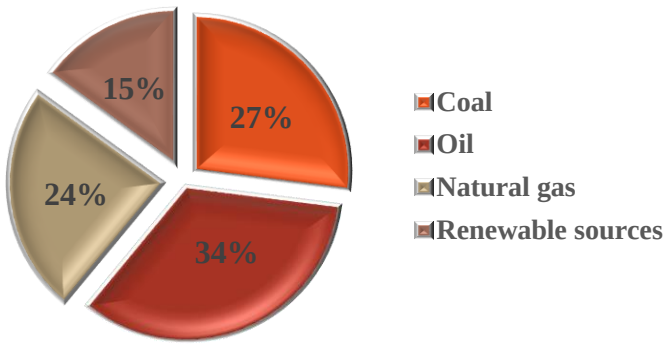

Figure 1.1 The primary energy consumption of the world.

Solar energy is predicted to play a pivotal role as an energy source for the future. This is because it is well known that the sun supplies the surface of the earth with about 120000 terawatts, which almost 6000 times the usual need of the world's energy consumption as well as it is equivalent to the output of 100 million modern fossil fuel or nuclear power stations [9,10]. Solar energy is a clean source for transportation, heating, cooling, and electricity[11]. Photovoltaic energy is one of the most promising future renewable energy resources which is successfully used for the entire latest mentioned needs[11]. One of the most powerful, sustainable, and greener applications that used solar energy sources is photovoltaics (PV) which emerged the 'carbon-free' technology that converts sunlight directly into electricity[9]. Devices that convert photovoltaic radiation

directly into electricity are termed as the "photovoltaic devices" or "solar cells", often abbreviated as PV. The term photovoltaic is derived from photo, the Greek word for light, while 'voltaic' refers to volt, which is the unit for electric voltage[11].

1.2 History of Photovoltaics

The history of photovoltaics goes back to the 19th century. Becquerel discovered of the photovoltaic effect in 1839 when he found a photovoltage between electrodes in electrolyte solutions[12]. The first working photovoltaic cells were constructed by Charles Fritts in 1883[13]. These prototype cells were made of selenium and achieved efficiencies of around 1% [13]. The modern era of photovoltaics started in 1954 when researchers at Bell Labs in the USA accidentally discovered that p-n junction diodes generated a voltage when the room lights were on, within a year, they had produced a 6% efficient Si p-n junction photovoltaic cell [13,14]. In 1973, the worldwide oil crisis, gallium arsenide (GaAs) heterostructure cells were also developed at IBM having 13% efficiency [15,16]. In 1980, at the University of Delaware, the first thin-film photovoltaic cell exceeds 10% efficiency using copper sulfide/cadmium sulfide (Cu_2S/CdS). In 1991, the first report of low-cost dye-sensitized photovoltaic cells (DSSC), the beginning efficiency of around 8% [16]. In 1992, University of South Florida develops a 15.9% efficient thin-film photovoltaic cell made of cadmium telluride (CdTe) [4,16]. In 1994, at National Renewable Energy Laboratory "NREL", GaInP/GaAs 2-terminal concentrator multijunction cell gives efficiency >30% [13], then in 1998, a Cu(InGa)Se_2 thin-film photovoltaic cell reaches 19% efficiency. Despite their high efficiency and stability, significant drawbacks were observed such as excess material consumption, manufacturing costs, and critical fabrication process. Hence, third-generation solar cells have exhibited high potential for commercial availability of efficient, low-production cost, flexible, and scalable solar cells in the recent decades. As in the 20 century the dye-sensitized cells "DSCC's" showed efficiency of around 8% that was improved to over 12% [16]. Moreover, recently developed organic semiconducting materials were very promising for photovoltaic applications due to its cost-effective up scaling by roll-to-roll printing techniques [18–20]. Accordingly, Organic photovoltaics (OPV) have grown dramatically in recent years achieving power conversion efficiencies approach over 18 %[21–25]. Recently, a perovskite photovoltaic cell with lead-based absorber has received a lot of attention from photovoltaic cell producers since it offers the promise of relatively cheap and efficient photovoltaic cells achieving over 20 %[26]. **Figure 1.2** demonstrates the chart of the photovoltaics efficiency records that summarized by NREL[27].

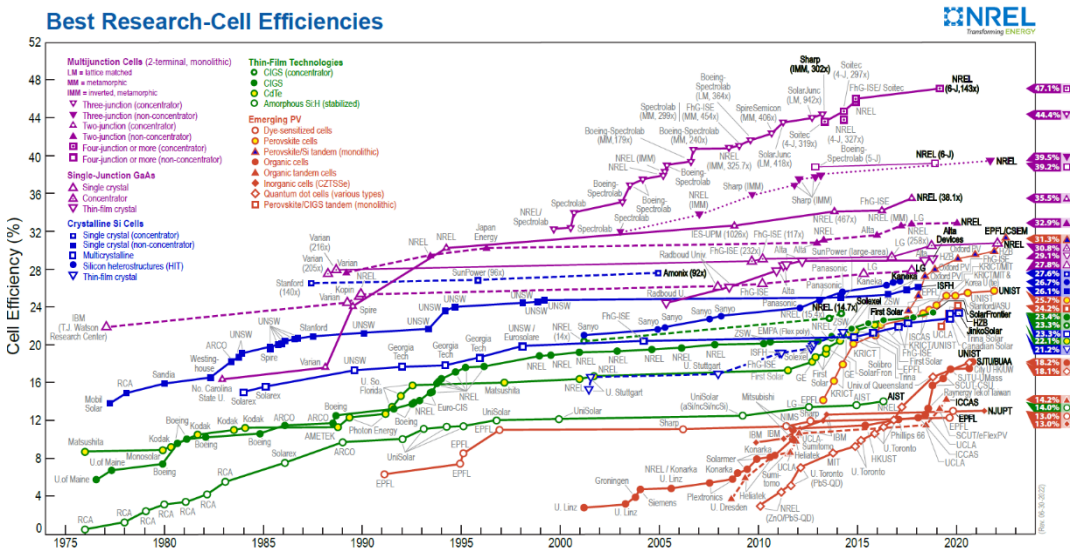

Figure 1.2 Chart of the recent photovoltaics efficiencies that summarized by NREL[27]

Organic photovoltaic cells" (OPV) are receiving enormous research attention nowadays and over the past decade. The advantage of this new generation of photovoltaic cells is their low cost production, i.e., likely less than 1U.S. $/peak watt[9]. Moreover, most OPVs can avoid the expensive, high vacuum and materials purification processes that are usually carried out for other thin-film solar cells. Since different thin film deposition techniques have been used for the fabrication of OPVs such as roll to roll[28], inkjet printing[29], spin coating (SC)[30,31] and spray pyrolysis (SP) techniques[32,33]. The spray pyrolysis technique is one of the most economic techniques that has many superior advantages that will be further discussed in Chapter 3. In addition, organic materials are abundantly available, hence the technology can be scaled up to the terawatt scale[9]. Furthermore, it is worth to mention that one of the important aspects of OPVs is the high absorption coefficient of the organic materials, providing thin devices (~100 nm) with high absorption[34]. However, the low charge-carrier mobility and small excitons diffusion length in the organic materials limit the efficiency of the devices[35]. Accordingly, enormous studies have performed new organic materials, investigated different designs, and examined the engineering of device architecture toward enhancing the OPVs performance and stability that will be comprehensively explained in Chapter 4, 5, 6, and 7.

1.3 Basic Principles of Organic Photovoltaics

In this section, basics principle of organic semiconductor materials along with the OPVs history, mechanism of the different device's architectures, and the working principle will be introduced.

1.3.1 Organic Semiconductors

The term organic semiconductor refers (1) that the compounds generally contain carbon-hydrogen bonds, possibly with a few heteroatoms such as oxygen, nitrogen and sulfur, and (2) that they exhibit features typically possessed by semiconductor materials [36]. Organic semiconductors are interesting because they have the potential to combine electrical properties of semiconducting materials with chemical and mechanical advantages of organic compounds. A semiconductor material has an electrical conductivity value falling in between that of a conductor and an insulator. Moreover, its conductive properties may be altered by introducing impurities, illumination or by external electric field[34]. Accordingly, the semiconducting properties of these materials depend on the interchanging between single and double carbon-carbon bonds (called conjugation) which limit the charge transport that plays a vital role in the property of materials. In such systems, the single bonds (called σ-bonds) are associated with localized electrons, and double bonds contain both σ and π-bonds. In the conjugated systems, (taking $(C_2H_2)_n$ polyacetylene as an example), carbon-carbon bonds is the backbone of polymers. The outer electron orbital of one carbon atom in the carbon-carbon bond contains three sp^2 hybrid orbitals and one p^z orbital as shown in **Figure 1.3a**, and each orbital has one electron. A sp^2 orbital of each carbon atoms overlaps with 1s orbital of one hydrogen atom and forms σ-bonds (sp^2-s). The other two sp^2 orbitals of one carbon atom form two σ-bonds (sp^2-sp^2) with two adjacent carbon atoms. Thus, the remaining one pure p^z orbital of one carbon atom overlaps sideways with the corresponding p^z orbital of other carbon atom, forming one π-bond. Hence, two bonds are shown between carbon and carbon (one π-bond and one σ-bond). The π-bond formed by the remaining p^z orbital increases the delocalization of electrons which is responsible for the semiconducting property. When these conjugated molecules are bound in π-bond, this overlap allows the π-electrons to delocalize and travel freely through the system resulting in enhancement the conductivity[37,38]. The charge carrier transport mechanism between inorganic and organic semiconductor materials is different. In inorganic semiconductor materials, atoms are connected through covalent or ionic bonds extended through the crystal, following band theory where the excited electrons are jumped from the occupied valence band (VB) to the unoccupied conduction band (CB) and the energy difference between CB and VB is termed as energy band gap (Eg)[39], as presented in **Figure 1.3b**. Hence, the photons absorbed in the band gap are converted directly into free charge carriers (electrons and holes) at room temperature[39]. In contrast to the photon absorption mechanism of the conjugated polymers which mainly rely on the antibonding π*-state near to the π-state. The organic molecules are connected through van der Waals force which is known to be a weak interaction. Moreover, the energy state of a single atom is depicted by discrete energy levels populated by electrons and upon the discontinuous energy the terms “Valence band” and “conduction band” are not appropriate to describe the energy levels of organic semiconductors. Thuse, the highest occupied molecular orbital (HOMO) and the lowest unoccupied molecular orbital (LUMO), respectively are used to analyze and explain the optical and electrical properties

of the organic semiconductors[40]. Where the interaction between the π-bonding orbitals generate the HOMO and the interaction between the π*-antibonding orbitals generate the LUMO as demonstrated in **Figure 1.3c**. The energy difference between HOMO and LUMO in photoactive materials is within the range of 1.1-3.5 eV and is termed as an energy bandgap (Eg) [41].

In organic semiconductors, the photon absorption mechanism is different than the inorganic ones as the organic semiconductor materials follow Frenkel excitons (electron-hole pairs) with low generated dielectric constant (typically 2-4)[41]. Accordingly, strong bounded excitons through Coulomb forces were obtained with binding energy about 0.3-0.5 eV by light absorption, resulting in lower exciton dissociation rate and in turn low free charge carriers' probability[42]. Hence, the charge transport mechanism in organic semiconductors mainly owing to intermolecular hopping between localized states. The hopping behaviour in organic π-conjugated materials is mainly ascribed by two theoretical models: Miller-Abraham's formalisms and the Marcus theory. Miller-Abrahams used the same formalisms for the hopping rates in both organic and inorganic semiconductors for simplicity[43]. While Marcus' expressions explain the hopping rate, considering the intermediate energetic barrier upon the energetic relaxation[44]. Moreover, it is worth noting that in organic materials, by changing the molecular structure such as the conjugation length and the electron withdrawing or donating ability of functional groups, the HOMO and the LUMO can be easily tuned. This vital advantage controls the property of these material to act as donor or acceptor. Accordingly, organic semiconductors that poses higher HOMO levels usually named as p-type semiconductors that used as electron-donor material with hole-transporting ability, while those with lower LUMO levels named as n-type semiconductors and work as electron-acceptor materials[41].

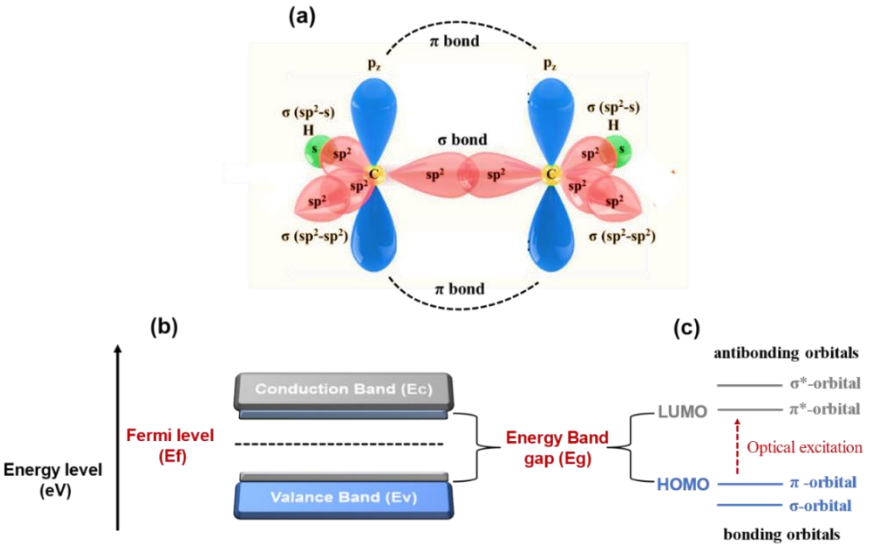

Figure 1.3 (a) Schematic diagram of sp^2 hybridized carbon atoms forming hybridized sp^2-orbitals called σ-bond and overlapped non-hybridized p^z-orbitals called π-bonds. Energy band diagram of (b) the inorganic semiconductor and (c) the organic semiconductor.

1.3.2 Progress of OPV

It is widely known that the first efficient OPV devices with two-layer OPV was demonstrated by Tang achieving 1% in 1986[45]. However, the first OPV was made by Gosch and Feng with 0.7% in 1978 using microcrystalline chlorophyll-a film was sandwiched between two metal electrodes[46]. The OPV technology has developed over the years reaching the most efficient active layer configuration: the bulk heterojunction (BHJ). The heterojunction era, which initiate the advent of devices with two organic materials in the active layer, evolved since 1986 from planar heterojunction (known as bilayer) to the BHJ devices in 1995 which introduced by Saricftci and Heeger and still widely used nowadays [47]. By using BHJ, donor/acceptor interface area is increased, resulting in enhancement of charge generation, separation, and transport. Upon this concept, enormous research has performed on optimizing the donor/acceptor interface or morphology through device processing and material design, to further improve device performance and stability achieving power conversion efficiencies exceeding 18 % [25].

1.3.3 OPVs Architectures

The classification of the OPVs structures depend on several groups: First, single junction regarding the photoactive materials that classified to single layer, bilayer, and bulk heterojunction layer. Second, single junction regarding the position of the interfacial materials that classified to conventional and inverted structure. Third, multi-junction that classified to tandem structure. All mentioned architectures are demonstrated in **Figure 1.4**. Single layer OPVs consist of organic layer (p-type) sandwiched between two electrodes, creating an electric field that assists the dissociation of the generated excitons in the depletion layer, then the free charges are collected at the corresponding electrodes, as shown in **Figure 1.4a**. In this structure, the electric field was not efficient enough to dissociate the excitons, thus the PCE was < 1%[46]. Then to enhance the electric field, two layers of donor (D-high ionization potential-p-type) and an acceptor (A-high electron affinity-n-type) materials stacked together with a planar interface between the conductive electrodes that named as bilayer structure, as depicted in **Figure 1.4b**. However, the PCE was still low because of the short exciton diffusion length (<10 nm), while donor layer requires a thickness of 80-100 nm to absorb the light, resulting in exciton recombination before reaching the interface to dissociate[45]. Finally, the bulk heterojunction (BHJ) structure was originated by interpenetrating donor and acceptor phases with average domain sizes on the order of tens of nanometers where the interfacial of D/A area was increased as illustrated in **Figure 1.4c**. Upon this blend network modification, the photogenerated excitons were traveling shorter distances, increasing the probability an exciton encounters a donor–acceptor interface and separates into free charge carriers before relaxing to the ground state, resulting in more collected free charges at the electrode and in turn higher PCE. The most widely studied BHJ systems are blends of conjugated electron donating polymers with electron accepting fullerene and non-fullerene derivatives[25,48–50]. Recently, BHJs

consisting of two small molecules, known as binary system, or three molecules, known as ternary system, deposited either by solution or vacuum sublimation have achieved impressive, the most popular and high-performing architecture till now with PCE exceeding 18%[51,52].

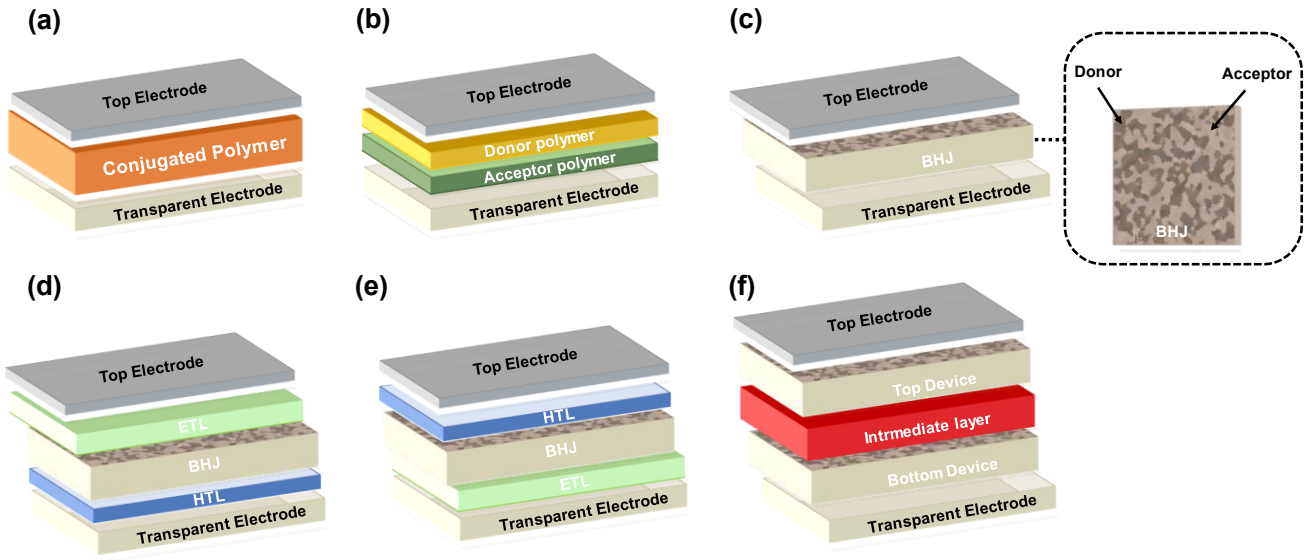

Figure 1.4 The architectures of (a) single layer, (b) bilayer, (c) bulk heterojunction, (d) conventional, (e) inverted, and (f) tandem organic photovoltaic devices.

To maximize the collected current, electrons should entirely flow in one direction. It is named a shunt that occurs when the wrong charge-carrier goes to an electrode, exhibiting recombination of the separated charge-carriers (non-geminate recombination). To control the shunting and push the uni-directional current flow, buffer layers (interfacial layers) are allocated between the active layer and the electrodes (shown in **Figure 1.4d and e**). These interlayers behave by either preventing one charge carrier from passing through (hole/electron blocking layer), and/or providing a better conduction to a specific charge-carrier (hole/electron transport layer, HTL/ETL, respectively) [53,54]. Furthermore, tandem OPVs consist of two cells with different bandgaps designed on top of each other, as presented in **Figure 1.4f**. The first cell that faces the illumination absorbs the higher-energy portion of the solar spectrum, which require to be transparent to allow the lower-energy photons to be absorbed by the second cell. The intermediate layer should align with the quasi-Fermi level of the acceptor of the first cell and the quasi-Fermi level of the donor of the second cell or vice-versa[55]. Due to the combination of two different bandgap materials, thermal losses are diminished and a large portion of the solar spectrum can be efficiently covered [56].

1.3.4 Working Principles of Bulk Heterojunction Photovoltaics

Although inorganic and organic PV devices both convert photons to electrical power, the fundamental physics and device architectures in organic photovoltaics differ significantly from inorganic photovoltaics. upon the low dielectric constant of organic semiconductor materials (approximately 2–4) absorbed photons create coulombically bound electron–hole pairs (excitons) that require an additional driving force to separate into free charges. Moreover, inorganic semiconductors charges move via band transport, while organic semiconductors charge transport mechanism is based on localized charge carriers that hop from state to state because of the disorder and weak intermolecular forces[57]. Then, in this section, the simplified working principle of the photocurrent generation in BHJ OPVs can be described in fundamental four consecutive stages namely: (a) light absorption, exciton generation, and diffusion, (b) charge transfer state and exciton dissociation, (c) charge carrier transport, and (d) charge carrier collection. **Figure 1.5** illustrates the four stages of BHJ OPVs photocurrent generation upon illumination from a to d along with the mechanism's band diagram in the BHJ organic photovoltaic devices (e).

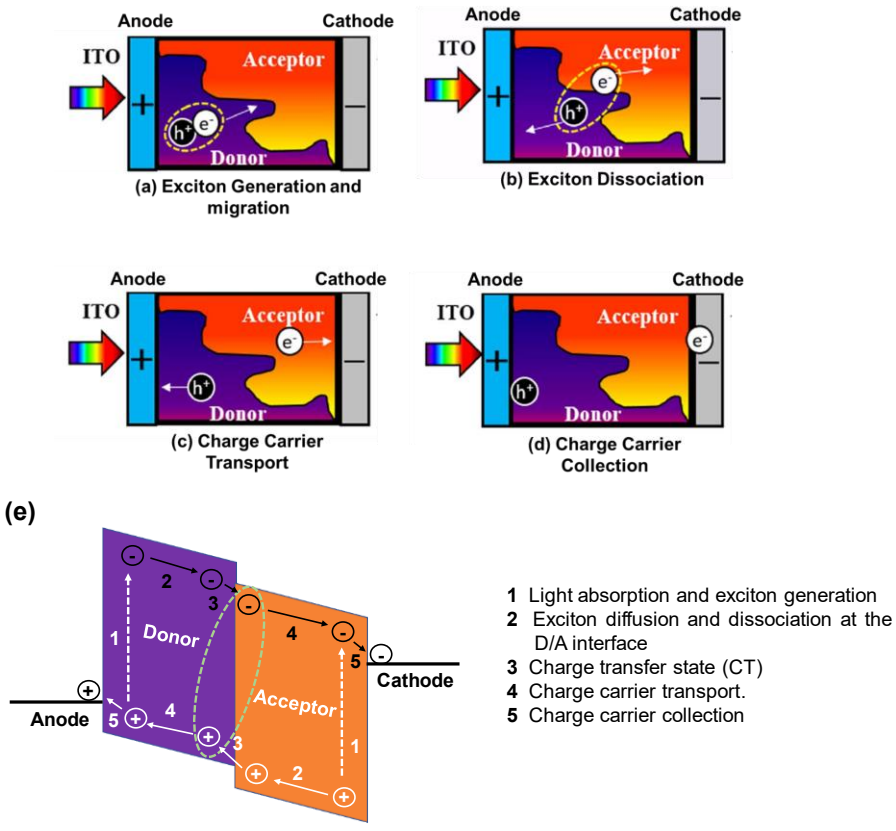

Figure 1.5 Illustration for the working principle of the photogenerated current in the BHJ OPVs devices via the steps of (a) exciton generation and migration, (b) exciton dissociation, (c) charge carrier transportation, and (d) charge carrier collection. (e) Band diagram of the photocurrent generation mechanism in a BHJ Photovoltaic devices.

(a) Light Absorption, Exciton Generation and Diffusion

When the light illuminated the device from the transparent conducting electrode (TCO) side, the photoactive layer absorber the incident light, mainly the donor portion of the BHJ, then an electron is excited from the HOMO to the LUMO through π- π* transition. It is not similar to inorganic semiconductors where the electron is excited from valence band to the conduction band, but as mentioned previously, a bind electron-hole pair (exciton) is generated due to their low dielectric constant[42]. The excitons are then migrated to the donor-acceptor interface, as shown in **Figure 1.5a**, because without external effect, these excitons might recombine via relaxing to the ground state within hundreds of picoseconds[58]. It is worth to mention that, as an essential step to enhance the efficiency of photovoltaics, the photoactive layer should absorb the maximum of the incident light which limited by the thickness of the photoactive layer along with the absorption coefficient of the conjugate polymer martial[59].

(b) Charge Transfer State and Exciton Dissociation

Ideally, the photogenerated holes and electrons at the D/A interface confront a strong Coulomb binding energy which bound the electron-hole pair (exciton). Then, the energy offset between the LUMO levels of the donor and acceptor materials overcomes this Columbic interaction in the exciton, resulting in exciton dissociation[60]. This takes place efficiently when the energy offset is higher than the exciton binding energy and the LUMO of the acceptor is lower than the LUMO of the donor. Then, at the D/A interface, the exciton from the donor dissociates via electron transfer to the acceptor unit, forming a charge transfer (CT) state exciton[61] as demonstrated in **Figure 1.5b**. Moreover, the short lifetime of the excitons is considered a major problem in conjugated polymers. This issue requires the excitons to be generated within their diffusion length, the distance where the excitons travel before decaying to the ground state, that is limited to few nanometers (< 20 nm in amorphous π-conjugated polymers and in the range of 20-47 nm in non-fullerene acceptors) which is shorter than the optical absorption pass length (≈ 100-200 nm)[57,59]. Thus, the donor or acceptor phase must be small enough for excitons to reach the D/A interfaces before decaying to insure the effective charge transfer in D/A blend. Upon this context the phase separation plays a crucial role for enhancing the device performance.

(c) Charge Carriers Transportation

The photogenerated free charge carrier should transport toward their corresponding electrodes. Where the free electrons move across the electron-acceptor portion of the photoactive bulk blend and the free holes travel through the electron-donor part of the photoactive bulk as demonstrated in **Figure 1.5c**. This transportation in organic semiconductors is mainly through the “hopping” from one localized state to another by the built-in electric field created by the asymmetry of the electrodes work functions (known as Drift-a

high work function, WF, anode and a low WF cathode create an internal electric field that determines the V_{OC} of the cell) or a charge-concentration gradient (diffusion)[59,60,62,63]. As mentioned previously, such carriers exhibit a low diffusion length along with low mobility, accordingly, the main energy losses in this process can be due to the recombination losses at the electrode interface during their journey to their respective ones. The main responsible for this recombination process in such amorphous organic materials is the localized density of states (DOS) which typically approximated with a Gaussian distribution[64]. Where DOS describes the energetic distribution of electronic states within the energy bands as defect states[65].

(d) Charge Carriers Collection

Finally, the photogenerated carriers from the photoactive layer that do not recombine are collected to their respective electrode and contribute to the photocurrent as demonstrated in **Figure 1.5d**. To get an efficient charge carrier collection, the potential barrier at the photoactive layer/electrodes interface must be reduced. Therefore, the LUMO of the acceptor should be higher than the WF of the cathode, while the HOMO of the donor should be lower than the WF of the anode[59,62]. If the WFs match well as described, then the contacts are said to be Ohmic contacts. If not, a Schottky contact is obtained that might origin electrical losses and inefficient charge injection. The charge collection efficiency is limited by different factors such as charge transfer, traps within the organic material, and charge recombination that discussed in details in the following section[59,61,64]. The steps of the charge collection at the respective electrodes from absorption of light to generation of photocurrent are concluded in **Figure 1.5e**.

1.3.5 Performance Parameters of Organic Photovoltaics

The performance of photovoltaic devices is commonly characterized by scanning the voltage and measuring the current under illumination and dark condition, providing the current density-voltage curves (J-V) as shown in **Figure 1.6a** for the illumination condition and **Figure 1.6b** in dark. The typical standard illumination test conditions for power output are radiation of Air Mass 1.5 Global (AM1.5G) and a cell temperature of 25°C. “Air Mass 1.5” refers to the 1.5 atmosphere thickness, corresponding to a solar zenith angle of 48.2° and G means “Global” that implies the incorporation of both direct and diffuse radiation. This AM1.5G spectrum standard has an integrated power of 1000 W/m^2 (100 mW/cm^2), also called 1-Sun condition[66,67]. Regarding the laboratory testing, solar simulators usually provide controllable illumination approximating standard AM1.5G.

To measure the performance parameters of the solar cells, it was modelled in an equivalent circuit as a current generator in parallel with a diode with a parasitic series (R_S) and shunt (R_{Sh}) resistances, as illustrated in **Figure 1.6c**. It interprets the solar cell J-V behavior into four constituent parts: a photocurrent source, diode, series resistor, and shunt resistor. The photocurrent source is simply the result of converting absorbed

photons to free charge by the PV device, the diode represents electron-hole recombination at the p-n junction, the series resistor refers the internal resistance of the cell to current flow, and the shunt resistor models the leakage current through the cells (e.g., via pinholes). Despite being in the dark there is no photocurrent, but it follows the diode behavior where the current flows in one direction. In an ideal photovoltaic behaviour, the J-V characteristics can be explained by following Shockley equation 1.1 where the R_S and R_{Sh} effects were negligible.

$$J = J_0[\exp(\frac{qV}{n_{id}k_BT}) - 1] \quad (1.1)$$

where J_0 is the reverse saturation current density, q the elementary charge, k_B Boltzmann constant, T the temperature, V is the output voltage, and n_{id} is the ideality factor, for this ideal n=1. It is worth noting that J_0 refers to the number of charges that overcome the energetic barrier in the reverse direction, which represents the minority charge density in the vicinity of the barrier[68]. While in illumination condition, the photovoltaic devices generate two opposing currents. These are added to deliver a net current density J at a given potential difference between the terminals, V following equation 1.2.

$$J = J_0\left(\exp\left(\frac{qV}{n_{id}k_BT}\right) - 1\right) - J_{Ph} \quad (1.2)$$

where J_{ph} represents the photogenerated current density delivered by the light. However, in a real photovoltaic behavior, R_S and R_{Sh} show a clear effect on the device performance, thus equation 1.2 was modified to become equation 1.3

$$J = J_0[\exp(\frac{e(V-JR_S)}{n_{id}k_BT}) - 1] + \frac{V-JR_S}{R_{Sh}} - J_{Ph} \quad (1.3)$$

It is worth noting that for Shockley-Read-Hall recombination (will discussed in details in the following section) due to defect states at the p-n junction, models were developed for $n_{id} > 1$[69,70]. For simplicity, equation 1.2 can be divided into 3 portions, the green part accounts for the recombination current that explains how a PV device acts as a diode in the dark. The red part for the shunt current represents the device leakages, due to defects such as pinholes, the edge of the device, or from localized defects upon the imperfections of the manufacturing process that enable parasitic current to move directly from one electrode to the other. The blue part refers to the photogenerated current as described previously. In **Figures 1.6a** and **1.6b**, regions I, II, and III illustrate how the different components of the PV devices equivalent circuit (**Figure 1.6c**) dominate the J-V response of the cell at different voltages. At low voltages (Region I), no current can flow because the drift of charge carriers to respective electrodes is high, thus the J-V characteristics are primarily determined by R_{Sh} (the slope in I region $=1/R_{Sh}$). At intermediate voltages (Region II), the J-V curve is an exponential line that controls by the diode parameters J_0 and n_{id} as the diffusion current overcomes the drift current. At

high voltages (Region III) by Rs (slope in region III=1/R_S), where the charges start to accumulate and modify the electric field in the medium. These regions provide useful rules when evaluating a J-V response curve: for instance, a steep slope in Region III generally means a low R_S

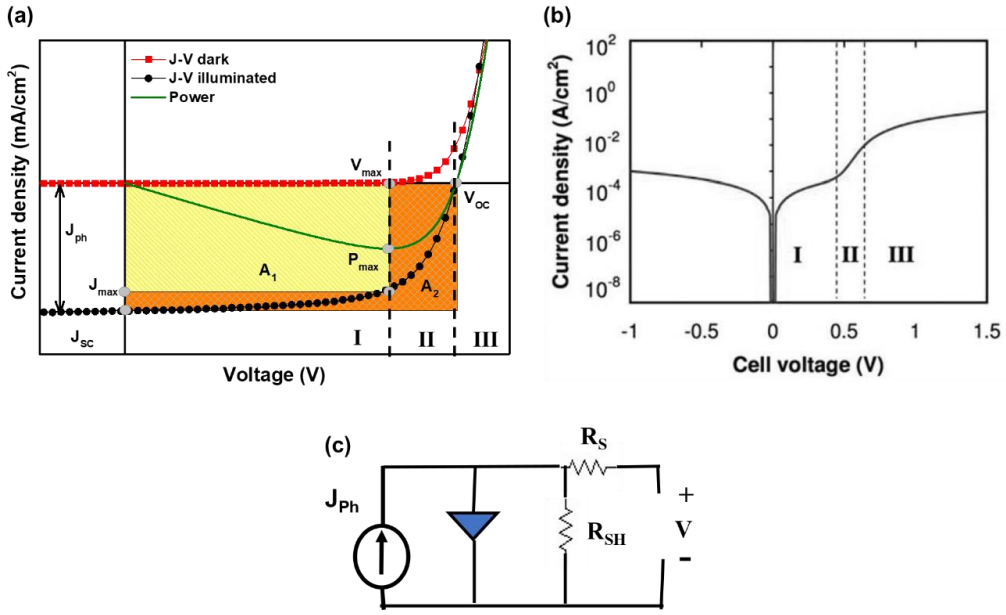

Figure 1.6 Typical J-V characteristic curve under (a) 1 Sun illumination and (b) in the dark in semi-log plot, (c) the equivalent circuit for practical PV. The three regions refer the different effects dominate: Region I accounts for leakage (shunt) current (R_{Sh}), Region II recombination currents (n_{id} and J_0), and Region III series resistance (R_S).

Then, to calculate the efficiency of the PV devices, three commonly used PV figures of merit are used: short circuit current density (Jsc), open circuit voltage (Voc), and fill factor. The power conversion efficiency is defined as the maximum of the extracted power density JV relative to the incident solar power (P_{in}). The output power reaches a maximum power (P_{max}) when the load is optimized, and the maximum power point (MPP) can be extracted from the JV curve when voltage sweep effectively simulates the presence of different loads, where the product of current density and applied bias voltage are maximin (J_m and V_m) as demonstrated in **Figure 1.6a**.

$$\eta = \frac{P_{max}}{P_{in}} = \frac{V_m J_m}{P_{in}} \tag{1.4}$$

and is equivalently written as:

$$\eta = \frac{Jsc\, Voc\, FF}{P_{in}} \tag{1.5}$$

where J_{SC} is the short circuit current density, V_{OC} is the open circuit voltage, and FF is the fill factor. In a short-circuit condition, where the output voltage bias is zero, the external load has zero or negligible resistance. The current density recorded at the short-circuit condition is called short-circuit current density (J_{SC}). Then V=0 and by applying this condition to equation 1.3 it provides equation 1.6.

$$I_{V=0} = J_{ph} = J_{SC} \tag{1.6}$$

The short-circuit current (I_{SC}) of photovoltaic devices relies mainly on the photon flux incident on the solar cell, which is determined by the incident light spectrum. Moreover, The I_{SC} depends on the area of the solar cell. Hence, to consider the device area onto Isc, often the J_{SC} term is used to describe the maximum current delivered by a solar cell in mA/cm^2 (J_{SC}=I_{SC}/cell area). The maximum current that the solar cell can deliver strongly depends on the optical properties of the solar cell, such as absorption in the photoactive absorber layer and reflection. Furthermore, it is affected by the active layer thickness and morphology that controls the diffusion lengths of minority carriers and in turn diffusion and dissociation rate of the generated excitons.

Similarly, the photovoltaics' open-circuit voltage, V_{OC}, is obtained when no external current flows, that is, J= 0 in (1.3). Assuming that $J_0 \ll J_{Ph}$ and $R_{Sh} \gg Voc/J_{Ph}$, V_{OC} is then given by equation 1.7. It is the maximum voltage that a solar cell can deliver.

$$V_{OC} = n_{id} \frac{k_B T}{q} \ln \left(\frac{J_{Ph}}{J_0} + 1\right) \tag{1.7}$$

Equation 1.6 shows that V_{OC} depends on the saturation current density of the photovoltaic devices and the photo-generated current. While J_{Ph} typically has a small variation, the key effect is the saturation current, since this may vary by orders of magnitude. Upon this context and as mentioned previously that the saturation current density, J_0, depends on the recombination in the solar cell, thus, V_{OC} is a measure of the amount of recombination in the device.

Regarding the fill factor (FF), it is the ratio between the maximum power ($P_{max} = J_m V_m$) generated by a photovoltaic device and the product of V_{OC} with J_{SC} as can be concluded from equation 1.4 and 1.5 that gives equation **1.8**. Thus, FF is the ratio of realistically achieved performance (V_{max} J_{max}) over ideally achievable performance ($V_{OC}J_{SC}$). In other words, the FF stands for how the realistically achieved performance filled the ideally achievable performance[71].

$$FF = \frac{J_M V_M}{J_{SC} V_{OC}} \tag{1.8}$$

As mentioned before, the subscript "MPP" denotes the maximum power point (MPP) of the solar cell. It is the point on the "square" of the J-V characteristic of the solar cell, at which the solar cell has the maximal power output (see **Figure 1.6a**). It is important to note that, to optimize the operation of PV devices, it is

necessary to operate it at the MPP tracking. Physically, FF can be regarded as how easily photo-generated carriers could be swept out under the field resulting from the build-in potential and external applied bias[71]. The ideal value for FF is unity, when the J–V curve is a rectangle, but in reality, it is always less than 1 upon how square the J-V curve is that indicated the quality of extracting the photogenerated carriers in the photovoltaic devices[72]. The non-ideality in the FF is mainly due to the parasitic resistances (R_S and R_{Sh}) that associate the photovoltaic devices as presented in the equivalent circuit model in **Figure 1.6c.** Then, R_S has a pronounced effect on the shape of J–V curve around V_{OC}, large R_S can divide the voltage from the diode, leading to a slower rise of J and in turn the J–V curve becomes less ‘‘square’’ and FF decreases. R_{Sh} governs the shape of the J–V curve around J_{SC}, small R_{Sh} divides the current from J_{Ph}, leading to J increasing with the reverse bias, i.e., the J–V curve becomes less ‘square’ and FF decreases as well as illustrated. Therefore, FF is more sensitive to the mobility-life time product of the bulk material, thickness of the active layer, and the morphology of the interfacial layers[72]. Generally, it is worth to link the parameters to the PV performance where J_0 relates to the ease of charge transport and injection over the junction and mainly influences the open-circuit voltage V_{OC}, while n_{id}, R_S, and R_{Sh} relate to the mechanism of charge recombination and affect bot V_{OC} the FF[61].

1.3.6 Recombination Processes that Limit the Efficiency of Organic Photovoltaic Devices

Ideally, every incident photon would be successfully converted into an electron and hole that are collected at the electrodes. However, in reality each step of the above-mentioned photovoltaic process from absorption to collection is wrought with potential loss mechanisms that limit the overall PCE of OPV devices. In this section, the factors limiting the performance of organic photovoltaic devices will be explained through the different recombination processes that take place from the initial step of absorbing the incident light to the charge carrier collection stage. The OPVs suffer from different types of recombination, commonly, such as the Exciton recombination, Geminate recombination and Nongeminate recombination[60,61]. **Figure 1.7** depicted the energy level diagram summarizing the main processes involved in charge photogeneration, recombination and collection in BHJ photovoltaics following Jablonski diagram[60,61].

Photoexcitation promotes an electron from the donor’s HOMO into the LUMO, generating the S_1 singlet exciton state. This donor S_1 state (the exciton) can be quenched by electron transfer from the donor to the acceptor. This initial electron transfer step generates an interfacial charge-transfer (CT) state. Recombination of the CT complexes is either radiative or nonradiative[73]. Once a photon is absorbed, the exciton only has a few nanoseconds to reach a donor–acceptor inter-face before it relaxes to the ground state (see a. in **Figure 1.7)**. In cases where the exciton is generated fare from the D/A interface and the domain sizes are larger than the exciton diffusion length, exciton recombination most likely takes place radiatively than separate. But, when the exciton is generated directly at the D/A interface, it might undergo a geminate recombination to

form either the ground state, S_0, or a triplet exciton, T_1, depending on their spin state[60] as presented in **Figure 1.7a**. The geminate or monomolecular recombination refers to the recombination of charge carriers that were generated from the same exciton, geminate bound pairs[61]. There are two prospects for this type of recombination. First, it could happen between the two Coulombically bound charges in the CT state. Second, if after overcoming their Coulombic attraction both charges persist confined by the physical sizes of their respective domains, where each electron can only recombine with its own hole, then recombination remains a monomolecular, geminate process[57,60] as demonstrated in red arrows in **Figure 1.7b**. Several factors are responsible for this type of recombination such as the delocalization of CT states, molecular reorganization energies, excess energy from above gap photons, phase purity and the internal electric field[57]. These factors may play a crucial role in the competition between geminate recombination and the generation of free charge carriers.

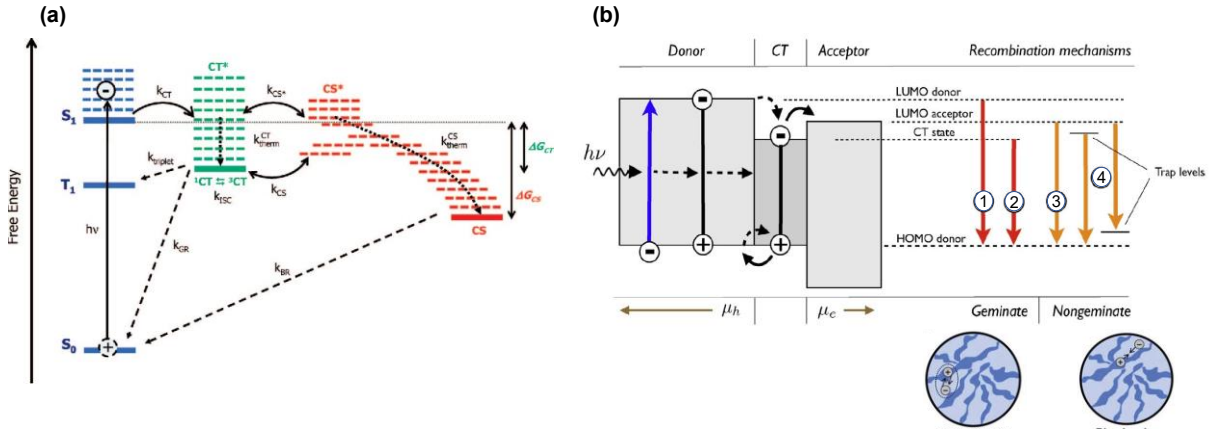

Figure 1.7 (a) The energy level diagram summarizing the main processes involved in charge photogeneration, recombination and collection in BHJ photovoltaics following Jablonski diagram[60,61]. hν: Photoexcitation to singlet exciton (S_1). k_{CT}: Exciton dissociation to form the hot charge-transfer (CT) state. k^{CT}_{therm}: Thermal relaxation of the CT state. k_{ISC}: Spin mixing of the ^{1}CT and ^{3}CT states. $k_{triplet}$: Geminate recombination of the ^{3}CT to the triplet exciton, T_1. k_{GR}: Geminate recombination of the ^{1}CT state back to the ground state, S_0. k_{CS*}: Dissociation of the hot CT state into a fully charge-separated (CS) state. k_{CS}: Dissociation of the thermally relaxed CT state into the CS state. k^{CS}_{therm}: Thermal relaxation of the CS state and migration away from the donor/acceptor interface, resulting in an increase in state degeneracy (entropy) and charge localization on lower energy sites (traps etc.). k_{BR}: Bimolecular recombination of the CS state. This diffusion-limited bimolecular process may result from either direct recombination or, more probably, reformation of interfacial charge-transfer states (shown as reversible arrows in processes k_{CS}* and k_{CS} and subsequent geminate recombination (k_{GR}))[74]. (b) Left: From left to right. Incoming light is absorbed in the donor material (blue arrow); a bound exciton is formed. The exciton diffuses toward the donor–acceptor interface. The exciton transfers onto the interface state i.e. CT state (dashed arrows), after which the exciton dissociates (solid arrows) and the free hole and electron drift through the donor and acceptor phase respectively, to the extracting contacts (brown arrows). Right: An overview of the four most encountered recombination mechanisms. The geminate mechanisms: (1) exciton decay after excitation, (2) recombination through the CT state, and the nongeminate mechanisms: (3) recombination of free holes and electrons, (4) recombination of free carrier with carrier trapped on sites within the band gap[57,75].

Alternatively, this CT state can undergo full charge separation to form dissociated charge carriers. These carriers can then diffuse away from one another and, if they fail in being collected at the electrodes, they face nongeminate recombination. This recombination process involves the recombination of fully dissociated charge carriers that did not previously belong to the same CT state or did not originate from the same photon[76] as illustrated by the orange arrow in **Figure 1.7b**. This nongeminate recombination process includes two main mechanisms: bimolecular (Langevin) and trap-assisted (Shockley-Read-Hall / SRH) recombination[57,69,70,76].

First, bimolecular recombination is a nongeminate recombination includes the recombination of a free electron and a free hole as presented by the orange arrow number 3 in **Figure 1.7b**. It is a primary loss mechanism that is commonly observed in OPV systems. In a disordered localized charge carriers semi-conductor system, bimolecular recombination is controlled by the charge carrier mobility[77]. Where, the faster charge carriers move, the faster they will find each other. Accordingly, the rate of bimolecular recombination is proportional to the charge carrier mobilities. This relation follows Langevin description using equation 1.9 that describe the recombination of two mobile opposing charge carriers attracted to each other in their mutual Coulomb field[78,79].

$$R_L = \frac{q}{\varepsilon}(\mu_n + \mu_p) \tag{1.9}$$

where q is the elementary charge, ε is the dielectric constant, μ_n is the mobility of the electrons through the LUMO of the acceptor, and μ_p is the mobility of the holes through the HOMO of the donor. From Langevin expression it might be expected that higher mobility materials provide higher recombination rates within OPV devices. However, the net bimolecular recombination rate in OPV devices diminishes with increasing the mobility [77,78]. This is because increased mobility also reduces the charge carrier density, resulting in improved charge extraction. Hence, in OPV devices, increased mobility is not expected to increase the nongeminate recombination. Contrarily, it is controlled by the slowest one, because if the charge carrier mobility is too low, sweeping out photogenerated charges will be inefficient, leading to more nongeminate recombination because the charge carrier density within the device will be higher[57,60,78,79].

Second, trap-assisted recombination (orange arrows number 4 in **Figure 1.7b**) which happen when a trapped electron (hole) recombines with a free hole (electron). It is a first order process where one electron and one hole recombine through a localized energetic trap. The recombination rate is described in inorganic semiconductors by the SRH recombination process where the recombination rate is determined by the amount of sites that act as traps and by how fast the free carrier can find the trapped sites[57,60,76]. It is worth noting that the measurement of V_{OC} as a function of light intensity consider a powerful tool to identify the presence of the trap assisted recombination in OPV devices [80,81] following equation 1.10.

$$V_{OC} = \frac{1}{q}[E_g - kT \ln\left(\frac{(1-P)\gamma N_C^2}{PG}\right)] \quad (1.10)$$

where P is the dissociation probability of a bound electron–hole pair into free charge carriers, G is the generation rate of bound electron-hole pairs, γ is the Langevin recombination constant, Eg is the energy difference between the HOMO of the donor and the LUMO of the acceptor, q is the elementary charge, k is the Boltzmann constant, T is the temperature in Kelvin, N_C is the density of states in the conduction band. This formula predicts the slope (S) of V_{OC} versus light intensity, since P and γ do not depend on intensity, while G is the only factor that is directly proportional to light intensity. Then, the S value should be equal to *kT/q* in bimolecular recombination process confirming its inescapable losses while in the presence of trap-assisted recombination, the S value increased to be more closer to $2kT/q$[79,80]. Consequently, there are several factors that can influence nongeminate recombination in OPV devices such as charge carrier mobilities, phase separation, energetic disorder, chemical impurities and active layer thickness[76].

1.4 Strategies to Improve the Performance and Stability of the Binary OPV Devices

Improving the performance of organic photovoltaic (OPV) devices is an active area of research, and several strategies were developed to achieve this goal as demonstrated in **Figure 1.8**. Tremendous attempts have been performed in the photoactive absorber material, interfacial device engineering, and various deposition approaches which affecting the device physics[82–84].

1.4.1 Photoactive Layer

Exploring new efficient organic materials for the photoactive layer with improved optical and electrical properties could generate highly efficient photovoltaic devices. Such as introducing the nonfullerene acceptors (NFAs) replacing the fullerene counterpart in organic photovoltaics (OPVs) that has pushed the bulk-heterojunction (BHJ)-based photovoltaics to achieve efficiencies approaching 20 %[22,83,85–87]. This dramatic increase in the power conversion efficiencies (PCEs) was particularly due to minimizing the trade-off behaviour between voltage loss and charge generation in nonfullerene organic solar cells (NF-OPVs)[88,89]. Where Small molecules with good crystallinity provide orderly arrangement and obtain ideal phase purity, thereby achieving improved charge transport efficiency and reduced energy loss. Therefore, the morphology of the photovoltaic active layer directly influences the charge transfer and transport mechanisms, making it one of the pronounced limiting factor for the performance of the OPV devices[83,90,91]. Thus, there are several further strategies have been investigated to tune the active blend morphology toward better film quality through controlling the miscibility between the donor and the acceptor, domain size and donor/acceptor (D/A) phase separation. This to secure sufficient exciton dissociation and improved charge transfer resulting in superior performance of the OPVs. [83,92–94]

Some of these avenues concern about the photoactive blend modification by solvent additives[83,95–97], thermal annealing[91,98] and further post treatments[85,97,99]. Actually, the thermal annealing and solvent additives have been widely adopted in fabricating the conventional BHJ OPVs to optimize their performances, because it can, on the one hand, increase the polymer's crystallinity, diminishing the bulk and interface defects, and on the other hand, improve the morphology in nanoscale and promote the contact between the polymer blends and electrodes thereby facilitating the charge transportation and collection[98,100,101]. Recently, some groups have been devoted to studying the intrinsic mechanisms on how thermal annealing affects the entire OPVs device performance[102,103]. However, due to the randomness of bicontinuous networks in BHJ OPVs, it is challenging to predict the impact of one variable change on the nanoscale morphology of the active layer[90]. The unoptimized bulk morphologies significantly affect the optical and electronic properties of BHJ blends and also influence their carrier dynamics[104,105].

Thus, deposition approaches played an essential role through fabricating the active layer by the sequential deposition method (SD) or so-called layer by layer (LBL) method. Hence, each layer can be individually regulated to form the superior vertical distributed structure that is feasible to create a p-i-n-like structure due to the interdiffusion of top layer into bottom one and higher gradient concentration of acceptors near the cathode and donors near the anode. This approach assists each component achieve the more accumulation on its respective electrode, which facilitates charge transmission and reduces charge recombination.

1.4.2 Interfacial Layers and Deposition Approaches

Interfacial layers are used in various locales within an OPV device where they play a number of roles, including matching or alignment of energy levels (for instance between the photoactive layer and an electrode surface), blocking electrons and/or holes to prevent recombination, adjusting of surface energetics and work function, and influencing the interfaces within the photoactive layer[106]. It is challenging to design an interfacial material between the organic photoactive layer and the metals because an interface with a barrier height of a few tens of mV may result in significant charge accumulation, and thus significant recombination loss and inferior photovoltaic (PV) performance[107]. Consequently, the interface between the BHJ and both the anode and cathode is of fundamental importance to the charge transport and extraction process, which determines the device performance and long term stability[106,108,109]. Tremendous efforts have been devoted to explaining and engineer the interface since the evolution of the OPVs. Particularly in solution-processed polymer photoactive layers, the surface properties of the bottom interface have a substantial influence on the film morphology, while the photoactive layers morphology grown above can be manipulated accordingly[75,106]. Furthermore, as shown by M. T. Lloyd et al. group work[110], B. MacLeod[111] and several other reported studies, the inverted architectures design has noticeably improved the OPV devices stability over the conventional structures from the scale of minutes up to years through avoiding the acidity effect of the PEDOT:PSS layer.[30,111,112] Therefore, several inverted OPVs based on selecting metal oxide such as ZnO

and TiO_x were used as the electron interfacial transporting material (ETL) for reinforcing the electron collection at the transparent conducting electrode and acquiring high performance and stable OPV.[111] This selection was mainly regarding its n-type conductivity and high optical transmission at vital wavelengths for solar energy conversion applications.[113–116] Furthermore, most of the metal oxides thin film was performed through various deposition techniques, including spin coating[111,117], atomic layer deposition[118], inkjet printing[29,119,120] and spray pyrolysis techniques.[32,121] That in turn influences the morphology, substrate coverage and the contact quality (roughness) of the interfacial layer with the organic absorber blend. These parameters are the most noteworthy factors in identifying the performance and stability of OPV devices.[112,122] Thus, Interface engineering has been a vital approach to facilitate carrier extraction to enhance the OPV performance and stability[123].

1.4.3 Device Design

One further strategy for improving the performance of organic photovoltaic (OPV) devices is to construct ternary and quaternary blends[124–126]. This is conducted to overcome the narrow absorption bands of organic semiconductor materials, which limit the ability of single-junction binary devices to fully utilize the energy from the solar spectrum[127]. Ternary and tandem OPVs have become popular in recent years, but the fabrication of tandem OPVs can be complex and may not be suitable for commercial applications[128,129]. Ternary blends, on the other hand, combine the advantages of binary and tandem OPVs through adding a third component to improve photon harvesting in a single-junction device, while maintaining the simplicity of single-step layer processing[130]. Selecting the third component and the host binary systems with complementary absorption spectrum can further broaden the absorption range along with enhance the insertion of light in the active layer through parallel-like or alloy-like model, resulting in improving the short-circuit current density (J_{SC}) of the OPVs devices[131]. Moreover, the matched energy levels cascade of the three materials in the photoactive layer can effectively enhance the open-circuit voltage (V_{OC}) of the devices and promote the charge transmission in the active layer[132]. Interestingly, the incorporation of the third counterpart can further regulate the accumulation and orientation of the molecule, as well as the phase separation of donor and acceptor [133,134]. Providing high crystallinity and ordered molecular stacking that can improve the charge transport, and inhibit the bimolecular recombination through well optimized phase separation, hence the ternary strategy is an effective method to enhance the exciton dissociation and advance charge transport and charge collection[135]. Accordingly, adding appropriate material to binary system is an emerging strategy to improve the morphology of active layer [136]. Therefore, the ternary strategy shows great potential in improving device performance, predicting to become the preferred scheme for the commercialization of OPVs in the future. However, most research on ternary strategies is based on BHJ system, which will further complicating the morphological regulation[130].

Consequently, the combination of ternary strategy and LBL deposition approach[135] to improve the performance of OPVs is worth considering as will be discussed in Chapter 7.

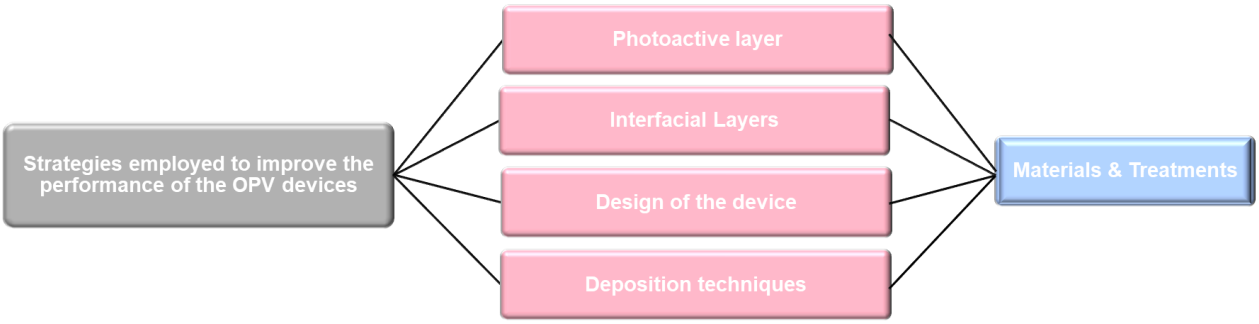

Figure 1.8 A schematic representation of the strategies used to improve the performance of organic photovoltaic devices.

1.5 Aims and Outlines of the Thesis

The aim of this thesis is to investigate and improve the performance and stability of organic photovoltaic (OPV) based devices through a combination of treatment approaches, deposition techniques, and material tuning. To achieve this goal, we conducted a series of experiments and analyses to identify and optimize the key parameters that contribute to enhance the performance and stability of such devices. In addition to examining the optical and electrical properties of the devices, we also aim to investigate the microstructure-morphology of the films as well as the underlying device physics in order to better understand the relationships between these factors and the overall performance of the devices.
My thesis structure is composed of seven themed chapters.

Chapter 1 introduces the background introduction to the development of organic semiconductors and organic photovoltaics. The basic photo-electric conversion, working principles, and photovoltaic performance parameters of organic solar cells are explained in detail afterward. Then, a summary of the strategies employed to enhance the performance of the OPV based devices is elaborated.

Chapter 2 is devoted to experimental methods and materials used in this thesis to elucidate the theoretical background given in Chapter 1. Chemical structures of photoactive materials will be provided, as well as detailed instructions on how to conduct the experiments. Working principles of spectroscopic techniques (absorption, PL, IS, TPV/TPC) and characterization setup will be introduced, along with its specifications.

Chapter 3 demonstrates the interfacial treatment conducted to the OPV devices through the zinc oxide interlayers that sprayed via the intermittent spray pyrolysis technique, exhibiting inverted BHJ-OPVs as efficient as the standard reported ones using the conventional laboratory-scale spin-coating technique. However, we record a pioneer stability behavior of the fabricated inverted fullerene organic photovoltaics (iF-OPVs) with various sprayed ZnO conditions. Thus, after optimizing the sprayed ZnO interfacial layer morphology by carefully inspecting the interdependence between the sprayed ZnO thin film morphology and the figures of merit of the optimized iF-OPVs, we conducted a distinct analysis on the optical and electric properties of the fresh and degraded devices.

Chapter 4 describes the morphological control of the binary (PM6:Y7) blend that was conducted through 1-chloronaphthalene (CN) solvent additive and thermal annealing (TA) treatment with respect to their influence on the photovoltaic performance. It explains the performance enhancement that was mainly upon suppressing the carrier recombination and assist the excitons in the photoactive layer blend to reach the donor/acceptor interface. Where the charge transport in the champion D-based devices exhibited the closest n_{id} value to 1, the highest Pdiss, the lowest leakage current, the highest J_{SC}, FF, and in turn the highest PCE. This indicates that tuning both the CN additives and TA treatments is crucial for prompting better film morphology, achieving the balance of exciton dissociation and charge collection, resulting in an increase in PCE.

Chapter 5 is an extend work for chapter 4 through conducting a systematic analysis on the fresh and photo-aged-inverted non-fullerene organic solar cells (iNF-OPVs) with different structures of the interfacial electron transporting layers (ZnO, ZnO/PDINO, and PDINO), through studying their optical and electric properties. Consequently, we presented PDINO as an efficient low temperature operation cathode interlayer for iNF-OPVs. Compared to the benchmark interface layers for i-OPVs such as ZnO, the PDINO interlayer used to replace the ZnO film, exhibiting a remarkable operational photostability. Where PDINO based iNF-OSCs demonstrated an extremely photostable behavior that is almost three times higher than the ZnO based devices under AM 1.5G (100 mW cm^{-2}) continuous illumination conditions. This behavior might be attributed to the PDINO interlayer properties, which undergoes with no photochemical reaction with the contacted PM6:Y7 photo-active layer, avoiding the inescapable photocatalytic effect that is commonly obtained by the ZnO interlayer.

Chapter 6 ascribes an effective approach to suppress traps formation as a potential route for enhancing the performance of nonfullerene organic photovoltaics (NF-OPVs) devices. Here, we achieved an extraordinary short-circuit current density (J_{SC}) value of 32.65 mA/cm^2, higher than the state-of-the art NF-OPVs reported, reaching high power conversion efficiency (PCE) of 17.92 %. This remarkable enhancement

was exhibited through the fine-tuning of PEDOT:PSS/PM6:Y7 films and interface morphologies via applying the Pre-Thermal Treatment approach (Pre-TT) to the devices, exhibiting J_{SC} and PCE enhancement of 21 % and 8 %, respectively, higher than the pristine devices. Accordingly, we investigated the dependence of the J_{SC} upon the Pre-TT approach through a range of morphological, optical, electrical, and advanced transient measurements. The Pre-TT based films were found to possess optimal smooth blend morphology with better dispersity owing to reduced domain size. Moreover, the measurements depicted that the optimized treated devices presented higher exciton dissociation probabilities and generation rate of the free charge carriers, showing an ideal balanced electron/hole mobility that reveal the J_{SC} and PCE enhancement. Hence, Pre-TT approach provides a facile passivation strategy that reduces the trap state density of the blend film, improves interface charge transfer, allows balanced electron/hole mobility, and thus promotes devices performance.

Chapter 7 describes the importance of material tuning and device design through a performance comparative study of the organic photovoltaic (OPV) devices based on a binary system using BHJ and LBL deposition approaches with D18 and Y6 as the host materials. We found that the devices prepared by the LBL processing method had a vertical distribution structure which facilitated charge transmission and collection, resulting in a higher J_{SC} and FF as compared to the BHJ OPV systems. Then, we developed a novel D18/PQDs/Y6 ternary system through the LBL approach, incorporating a perovskite $CsPbI_3$ quantum dots (PQDs) film as an interlayer between the D18/Y6 host system due to their complementary absorption and the proper electronic energy cascade levels of the three materials. The inclusion of the optimized PQDs film significantly improved the device performance, resulting in a PCE of 16.56% compared to the host binary system (PCE= 15.76%). Additionally, the incorporation of PQDs into an alloy structure with Y6 reduced bimolecular and trap-assisted recombination, improving exciton separation and charge transfer, leading to higher V_{OC}, J_{SC}, and FF in the PQDs-based device. Our findings reveal that the inclusion of PQDs as a third component through the LBL deposition approach is an effective strategy for improving the morphology of the active layers and achieving high-performance OPV devices.

Chapter 8 is the last chapter that summarizes the main results obtained from the appended papers of this thesis. The short outlook for future research through interface materials engineering, morphology control and third component counterpart in OPVs.

Chapter 2

Materials and Experimental Section

2.1 Materials

2.1.1 Photoactive Organic Semiconductor Materials

In the organic BHJ photovoltaic devices, the absorption takes place in the photoactive layer, which consists of the electron donor and the electron acceptor organic semiconductor materials. **Figure 2.1a** demonstrates the molecular structures of the conjugated donor polymers and small molecule fullerene, nonfullerene and QDs acceptors studied in this thesis. The donor polymers purchased are PBDTTT-EFT (known as PTB7-Th "[4,8-bis(5-(2-ethylhexyl) thiophen-2-yl) benzo[1,2-b:4,5-b] dithiophene-co−3-fluorothieno-[3,4 b]thiophene-2-carboxylate]", 1-Material) and PBDB-TF (known as PM6 "poly[2,6-(4,8-bis(5-(2-ethylhexyl-3-fluoro)thiophen-2-yl)benzo[1,2-b;4,5-b´]dithiophene)) -alt-(5,5-(1',3'-di-2-thienyl-5',7'-bis(2-ethylhexyl)benzo [1',2'-c:4',5' c'] dithiophene-4,8-dione)]", 1-Material), while DTBT (known as D18 " 1-[4 -[5- [4 -[amino- (propan-2-ylamino) methyl] phenyl] furan-2-yl] phenyl]- N-propan-2-yl-methanediamine", 1-Material) was performed during the placement period in the Blackett laboratory, physics department in Imperial College London, UK. The small molecule acceptor material of the fullerene derivative $PC_{70}BM$ "([6,6]-phenyl-C_{70}-butyric acid methyl ester)"was purchased from Solenne B.V., the nonfullerene materials BTP-4F (known as Y6 "2,2'- [[12,13-Bis (2-ethylhexyl) -12,13- dihydro- 3,9 diundecylbisthieno[2",3":4',5']thieno[2',3':4,5]pyrrolo[3,2-e:2',3'-g] [2,1,3] benzothiadiazole-2,10-diyl] bis[methylidyne (5,6-difluoro-3-oxo-1H-indene-2,1(3H)- diylidene)]] bis[propanedinitrile]"), BTP-4Cl (known as Y7 "2,2'- ((2Z,2'Z) -((12,13-bis (2-ethylhexyl) -3,9- diundecyl-12,13 -dihydro-[1,2,5] thiadiazolo [3,4-e]thieno[2",3":4',5'] thieno[2',3',:4,5]pyrrolo[3,2-g] thieno[2',3':4,5] thieno [3,2-b]indole-2,10-diyl)bis (methanylylidene)) bis (5,6-dicholoro-3-oxo-2,3-dihydro- 1H-indene-2,1-diylidene)) dimalononitrile)") were supplied by 1-Material as well, and the cesium lead iodide quantum dots "$CsPbI_3$ QDs" were purchased from Quantum Solution. The corresponding energy levels of the mentioned photoactive materials studied in this work are presented in **Figure 2.1b**. The solvents used to dissolve the photoactive materials during the synthesis were Chloroform (CF) and Chlorobenzene (CB) which both were supplied by Sigma-Aldrich. Furthermore, solvent additives were added to the photoactive BHJ blend to enhance the morphology of the layer and in turn improve the OPV devices performance. In which 1,8-diiodooctane (Alfa Aesar) and 1-chloronapthalene (Sigma-Aldrich) were used in this thesis.

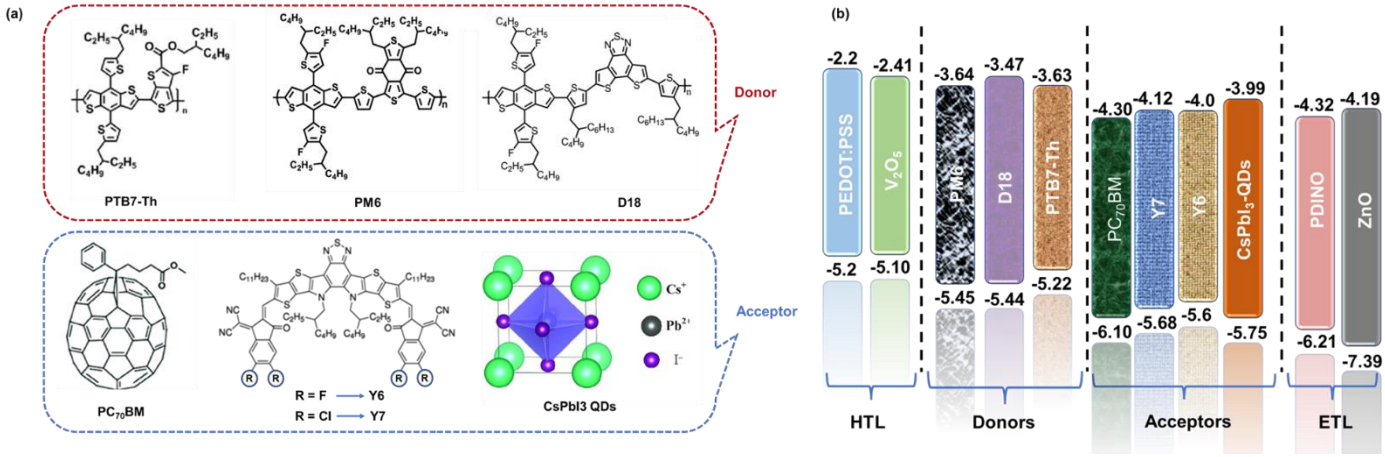

Figure 2.1 (a)The molecular structures of the conjugated donor polymers and small molecule fullerene, nonfullerene and QDs acceptors studied in this thesis, (b) The energy levels of the photoactive, ETLs and HTLs materials studied in this thesis.

2.1.2 Buffer Layers Materials

The buffer layers in both inverted and conventional structures are sandwiched between the photoactive layer and the electrodes as illustrated in Figure **1.4d** and **1.4e**. These interlayers play a crucial role in reducing interface barriers and selectively transporting the hole and electron carriers from the photoactive layer to the electrodes. Based on their function, they classified as hole transporting layer (HTL) and electron transport layer (ETL). In this thesis, the HTL materials used were PEDOT:PSS (Clevios TM) solution (without any purification, we directly used the commercially available) and vanadium oxide (V_2O_5, powder, Sigma-Aldrich). For ETL materials, organic small-molecule PDINO powder was purchased from 1-Materials and a prepared zinc oxide (ZnO) precursor solution. The ZnO- precursor solution was synthetized by sol-gel method, where zinc acetate dihydrate was dissolved in 2-methoxylethanol and ethanolamine that all were purchased from Sigma-Aldrich. The solvents used to dilute the ZnO and dissolve the PDINO powder during the synthesis were ethanol and methanol, respectively, which both were purchased from Sigma-Aldrich. **Figure 2.2** shows the mentioned buffer materials chemical structures used in the work of this thesis and their corresponding energy levels are demonstrated in **Figure 1.2b**.

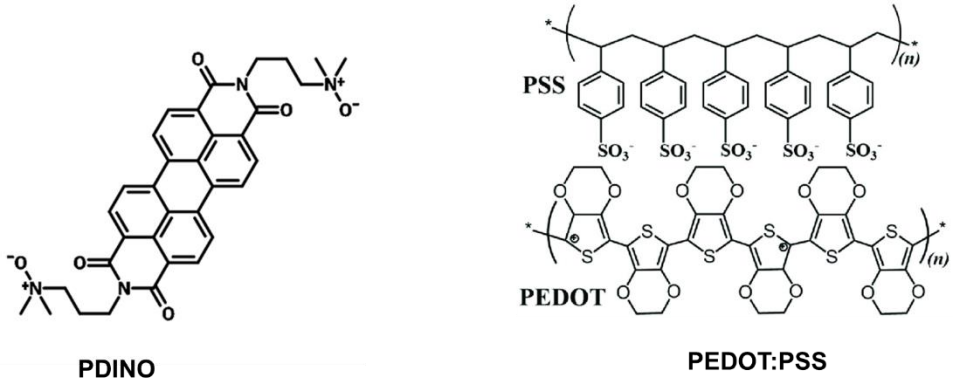

Figure 2.2 the chemical structures of the polymer and small molecule buffer interlayers used in this thesis.

2.1.3 Electrode Layers Materials

The transparent conducting electrode (TCO) used was Indium Tin Oxide (ITO) patterned glass substrates which were purchased from PsiOTec Ltd. The back contact electrodes were silver wire (Ag, high purity of 99.99%) and gold (Au) were supplied from Testbourne Ltd. and thermally evaporated under vacuum conditions.

2.2 Deposition Techniques

In this section, the thin film deposition techniques used for depositing the active layer, buffer layers and the contact electrodes will be explained in detail. The solution processed layers were deposited mainly using spin coating technique, while the ZnO precursor solution was additionally deposited by intermitted spray pyrolysis technique. Moreover, the powder buffer layers, and the metal top electrodes were deposited by vacuum thermal evaporation technique.

2.2.1 Spin Coating Technique

Spin coating technique (SC) is a common lab-scale based method that is used to apply highly uniform thin films to flat substrates from solution possessed materials with efficient thickness control. The spin coating working principle consists of four consecutive steps: deposition, spin-up, spin-off, and evaporation as illustrated in **Figure 2.3a**. The small amount from the dissolved material in a volatile solution was drooped over the center of the substrate, when the substrate accelerated to spin-up, the liquid flows radially driven by the centrifugal force then spin off and evaporation takes place for solvent removal and thinning the coated film. There are two main types of spin coting methods: static and dynamic. Both follow the mentioned four steps of deposition, but the main difference is that in the dynamic method, the solution is poured during the spinning of the substrate (after spin-up step) [137]. Moreover, dynamic method is mainly processed for the extremely high volatile solvents such as Chloroform. The speed unit used in the spin coating technique known

as rpm "revolution per minutes" that refers to the number of rounds in one minute and the thickness of the coated film is inversely related to the spin speed and depends mainly on the properties of the solution such as concentration, viscosity, and surface tension. On the other side, this technique is not compatible with the upscaling manufacturing prospective and showed low material efficiency, where about 95-98 % of the deposited solution is spreading away and discarded during the spinning and only 5-2% are coated over the substrate[137].

In this thesis, the static and dynamic spin coating methods were used to deposit the photoactive layers, while only static coating was used to deposit the solution processed buffer layers of PEDOT:PSS, PDINO, and ZnO. The lab spin-coater machine model was WS-400B-6NPP/LITE from Laurell Technologies Corporation as shown in **Figure 2.3b**.

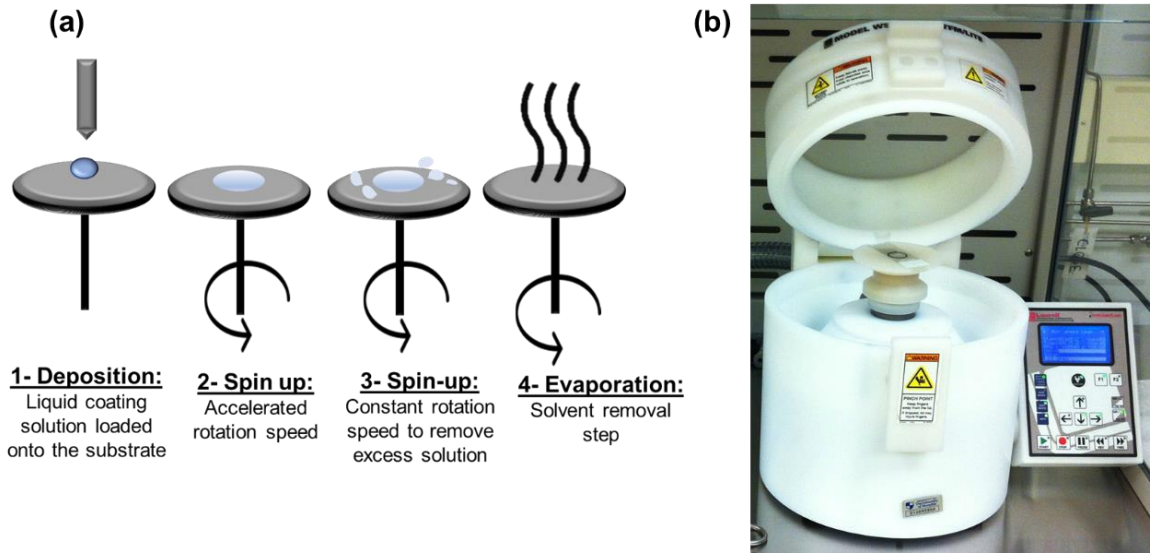

Figure 2.3 (a) The four stages of the spin coating procedures, (b) the lab spin coater machine used in this thesis.

2.2.2 Intermittent Spray Pyrolysis Technique

Spray pyrolysis (SP) is a sort of spray coating but needs a higher substrate temperature to assure the occurrence of the chemical decomposition of the liquid precursor needed to form a ceramic thin film. SP is a process in which a thin film is deposited by spraying a solution on a pre-heated substrate, where the constituents react to form the chemical compound acquired for the film. **Figure 2.4a** illustrates the working principle of the SP procedure where the spraying gun consists of a double nozzle sprayer that coaxially conjugated with quartz and a capillary tube inside. The prepared precursor solution inlets through the

capillary tube together with the quartz tube that passes the compressed air as a carrier gas in order to spray the precursor solution on the top of the preheated substrate. The most important parameters to be controlled in all these processes are the substrate temperature, carrier gas flow rate, nozzle-to-substrate distance (The distance between the nozzle gun and the substrate should be adjusted to cover the entire deposited surfaces), the spraying duration, and the solution concentration. It is worth mentioning that the conventional spraying pyrolysis procedure is usually a continuous deposition, but in this work, the approach of spraying procedure is different than the conventional continues spraying one. In this work, the spraying process was intermittently where each spraying running cycles (1R) step defined as 7 s of continuous spraying and 3 s hold, then repeating same attitude till spraying the corresponding number of R required as illustrated in the scheme in **Figure 2.4b**. Accordingly, it is called Intermittent SP technique as it used non continuous spraying procedure to avoid the accumulation that might produce defects in the film and as sequence affect film quality along with the performance of the device[138–140].

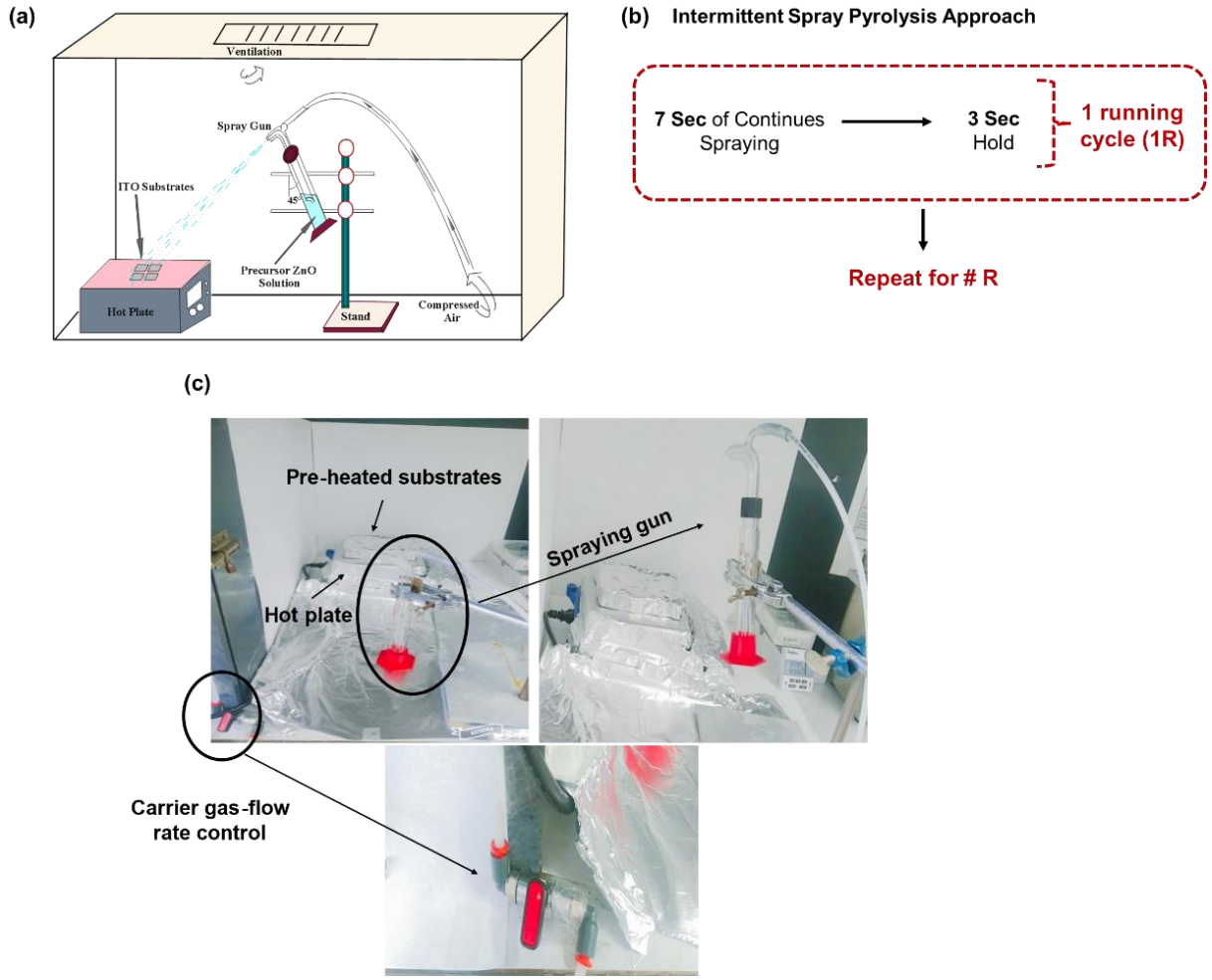

Figure 2.4 (a) The working principle sketch of the spray pyrolysis technique, (b) scheme illustrates the intermittent spray pyrolysis approach (c) the spray pyrolysis lab setup built and used to spray the ZnO precursor solution in this thesis.

Furthermore, it is important to note that the SP technique is one of the most economic techniques that has many superior advantages. It is a thick and thin film deposition technique that does not require any vacuum condition at any stage. That is a tremendously vital factor allows the process to scale-up for industrial production[32]. Furthermore, it is cost effective technique (especially regarding the equipment costs), easy to control the deposition parameters and reproducible the thin film. Moreover, the SP technique has the ability of fabricating the film by different compositions that enables preparing films with gradients through the film thickness which is highly effective for the optical applications[32,141,142]. In this thesis we build a spray pyrolysis lab-setup to spray the ZnO precursor solution on top of the Pre-heated ITO as demonstrated in **Figure 2.4c**.

2.2.3 Vacuum Thermal Evaporation Technique

One of the common methods of Physical Vapor Deposition (PVD) is the Vacuum Thermal Evaporation (VTE) technique. This is a thin film deposition technique for applying coatings of metals or powder materials in the thickness range of angstroms to microns in a highly precision control (±0.5 nm) and can be a single or multiple materials, in layered structure or in co-evaporated mixture[143]. **Figure 2.5a** depicts the working principle of VTE involves, where the solid material (metal or powder) inside a source of boat or filament was heated through passage of electrical current by resistive evaporation till it overcomes the melting point of the target material. This target source is placed at the bottom of a highly vacuumed chamber ($< 10^{-6}$ mbar) and the substrate (where the thin film will be coated over) placed at the top of the chamber toward the source evaporation direction. Then, the molecules of the source material move up to the cold surface of the substrate, forming the acquired thin films. It is worth mentioning that the rotation of the substrate holder inside the vacuum chamber during the deposition process assists the uniformity of the coated films. Moreover, the VTE system includes quartz crystal deposition control, whereby the deposition rate and the exhibited thickness can be monitored[143]. **Figure 2.5b** demonstrates the vacuum thermal evaporator used in our laboratory that is located in a glove-box model MB20/MB200 from MBRAUN to deposit the buffer layer of V_2O_5 film and the metal contact electrodes of Ag and Au films in this thesis.

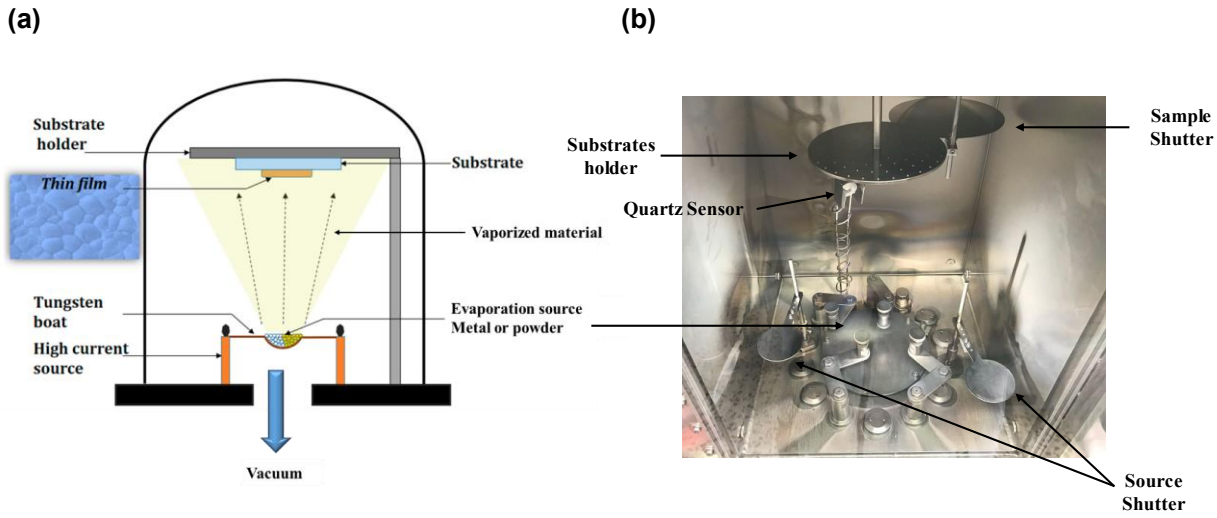

Figure 2.5 (a) The working principle diagram of the vacuum vapor deposition technique, (b) the vacuum thermal evaporator machine used in this thesis, top-inside view.

2.3 OPV Devices Fabrication

In this thesis, the OPVs devices were fabricated based on conventional and inverted device architectures, as sketched in **Figure 2.6**.

2.3.1 Cleaning the Transparent Conducting Oxide Substrates

In this thesis, both conventional and inverted OPVs structures used the patterned indium tin oxide (ITO) glass substrates with sheet resistance of 10 Ω sq^{-1}, processing the same cleaning procedures. ITO substrates were carefully cleaned by detergent and water, then subsequent 10 min ultrasonicated in acetone, methanol, and isopropanol. Then the substrates were blow-dried by nitrogen stream gun and placed in the oven at 100℃ for 10 min to remove any residual solvents. Then, the cleaned ITO substrates were transferred in ultraviolet-ozone chamber for 15 min to activate the ITO surfaces and to further remove any organic residues from their surfaces.

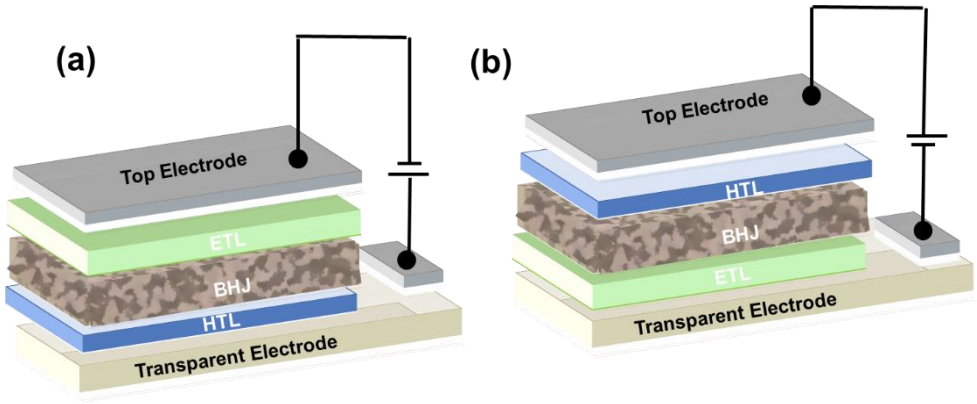

Figure 2.6 Devices architectures of OPVs with (a) conventional and (b) inverted structures fabricated in this thesis**.**

2.3.2 Conventional Structure OPV Fabrication

The conventional structure of OPV devices investigated in this thesis consists of ITO/HTL/photoactive layer/ETL/Ag as depicted in **Figure 2.6a**. PEDOT:PSS aqueous solution was used as the HTL that filtered through 0.45 µm PFTE filter (poly tetrafluoroethylene) then spun-coated on the pre-cleaned ITOs at 4000 rpm for 45 sec. The PEDOT:PSS film was annealed at 150 °C for 20 min in the air and left to cool down for 15 min to obtain thin films of 30 nm. The PEDOT:SS coated films were transferred to the glove box under nitrogen environment of 99.999 % N_2 electronic grade (H_2O < 0.1 ppm, O_2 < 0.1 ppm) directly after annealing to continue the deposition of the further films. The active layer was then spun coated over the PEDOT:PSS film. In this thesis, the studied active blends in conventional device structure were PM6:Y7, PM6:Y6, D18:Y6, PM6:QDs:Y7, PM6:QDs:Y6, and D18:QDs:Y6. It is worth mentioning that the D18:Y6 and D18:QDs:Y6 blends were spin coted in both architectures of BHJ blend and Layer By Layer (LBL) films using the dynamic spin coating deposition method as illustrated in Figure **2.7**. The preparation and deposition conditions of the mentioned active blends were summarized in **Table 2.1.** In this structure, PDINO was used as ETL and the PDINO solution was prepared by dissolving 1.5 mg/ml in methanol, then filtered and spun coated at 3000 rpm for 30 sec without any further thermal treatment. Finally, 100 nm thin film of Ag top back contact was thermally evaporated under high vacuum conditions (≤ 1 ×10-6 mbar) using shadow mask with device active area of 0.09 cm^2 as presented in Figure **2.7**.

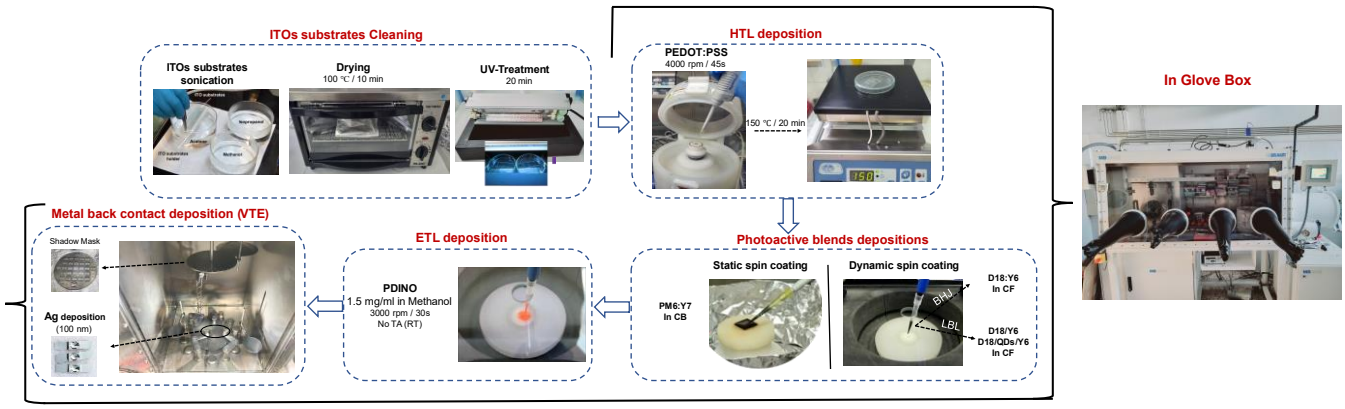

Figure 2.7 Schematic diagram illustration for the fabrication procedures of the conventional structure OPV devices in this thesis.

2.3.3 Inverted Structure OPV Fabrication

The inverted structure studied in this thesis was ITO/ETL/photoactive layer/HTL/Ag as sketched in **Figure 2.6b**. ZnO and PDINO materials were used as the ETL in this structure. The ZnO precursor solution was synthesized by sol-gel method of dissolving 150 mg of zinc acetate dihydrate in 1 mL of 2-methoxyethanol, then added 30 µL of Ethanolamine solution. Then, the mixture was left for 1 h under vigorous stirring at 70 °C. The prepared ZnO solution was diluted by methanol 1:1 v/v ratio to obtain the stock solution. It is noteworthy to mention that, in the OPVs inverted structure in this thesis, we deposited the ZnO precursor solution using two different techniques of lab-spin coating and the intermittent spray pyrolysis techniques as illustrated in **Figure 2.8.**

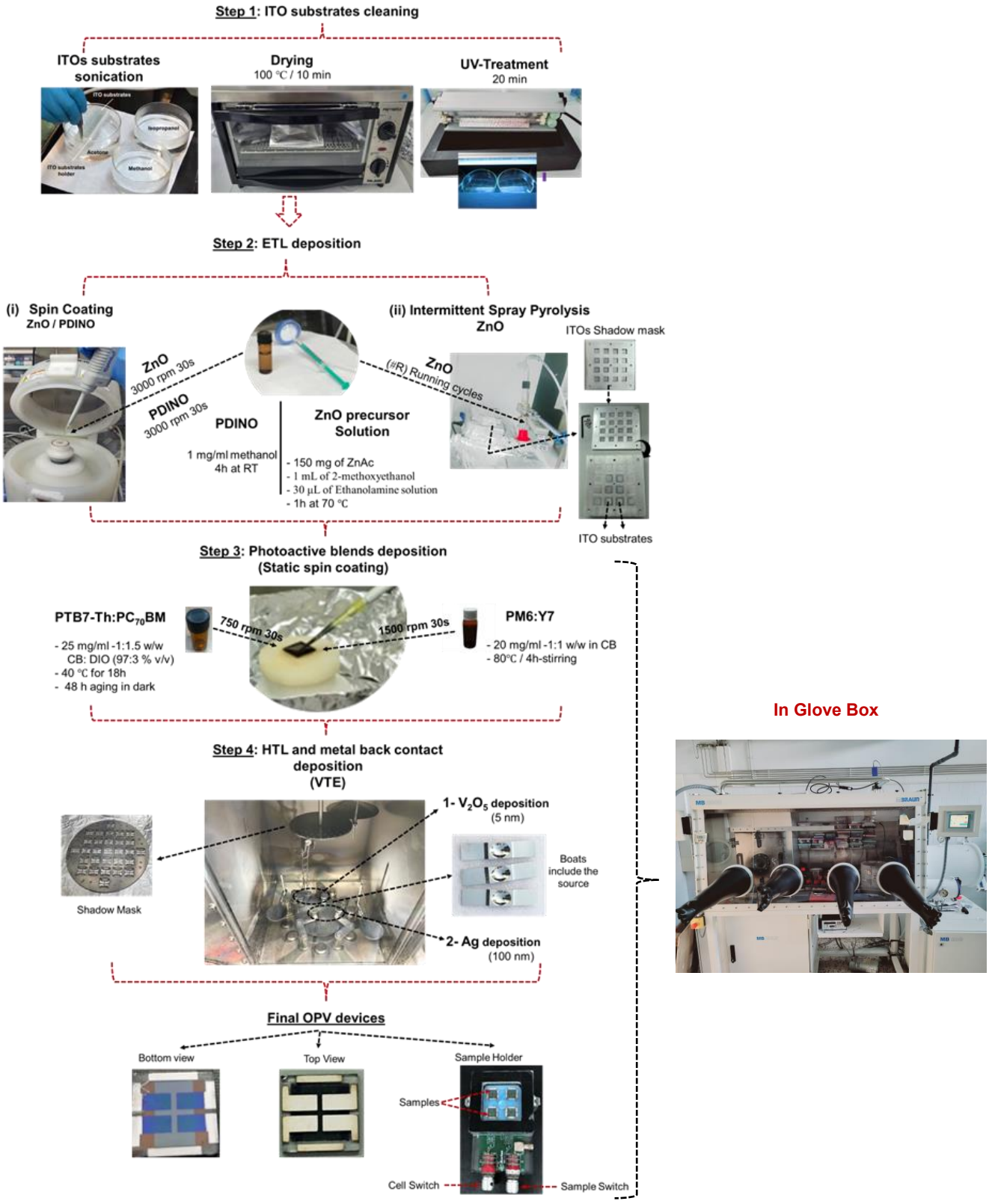

Figure 2.8 Schematic diagram illustration for the fabrication procedures of the inverted structure OPV devices in this thesis.

(i) ZnO Deposited by Spin Coating

In the spin coating method, the previously mentioned ZnO stock solution was spun coated on the top of the pre-cleaned ITO at 3000 rpm for 30 s, then left for 1 h annealing at 200 ℃ in air, coating a final ZnO-film thickness of 30 nm.

(ii) ZnO Deposited by Intermittent Spray Pyrolysis

In the intermittent SP technique, the ITOs substrates were left for 15 min to heated up to 350 ℃, then the synthesized stock solution was diluted with ethanol in different ratios and sprayed over the pre-heated ITOs, and the deposited films were left to annealed for 1 h. In this thesis, the variation of the ZnO concentration was investigated through two main categories of ZnO prepared solution, *low concentration ZnO* precursor solution with mass number spraying running cycles of *and high concentration ZnO* precursor solution with few numbers of spraying running cycles. The optimization deposition parameters of the ZnO film sprayed by the intermittent SP technique were listed in **Table 2.2.**

After cooling down the ZnO films deposited by both SC and SP techniques, the films transferred directly to the nitrogen filled glove box to deposit the further layers.

Regarding the PDINO used as ETL in this structure, 1 mg/ml PDINO powder was dissolved in methanol then stirred vigorously at room temperature for 4h inside the glove box. Then the PDINO solution was spun coated over the ITO and ZnO film to obtain different device structure as listed in **Table 2.2**. The photoactive blends employed in this structure were PTB7-Th:$PC_{70}BM$ and PM6:Y7 where their synthesis and deposition parameters were summarized in **Table 2.1**. The substrates were finally transferred into the thermally evaporation chamber inside the glove box where 5 nm of V_2O_5 and 100 nm Ag were sequentially deposited under high vacuum conditions ($\leq 1 \times 10^{-6}$ mbar). The V_2O_5 layer was deposited at a rate of 0.05 kÅ/s and the Ag film rate was 0.1 kÅ/s for the initial 10 nm thickness then increased to 0.4 Å/s till 100 nm film thickness that performed in 190 min with effective devices area of 0.09 cm^2. Lastly, we transferred the fabricated devices from the evaporator to the sample holder inside the glove box which was carefully sealed for the device's measurement steps as illustrated in **Figure 2.8**.

Table 2.1 The preparation and deposition conditions of the photoactive films employed in this thesis.

Photoactive Blend	Weight ratio (D:A)	Total concentration (mg/ml)	Solvents and additives	Stirring conditions	Spin Speed (rpm/sec)	Film treatment
PM6:Y7	1:1	20	99.5 vol% CB, 2 vol% CN	80℃/3h	2000/40	NA
			99.5 vol% CB, 2 vol% CN			100 ℃ / 1h
			CB			NA
			CB			100 ℃ / 1h
			99.5 vol% CB, 0.5 vol% CN		1500/30	90 ℃ /5 min
PTB7Th:$PC_{70}BM$	1:1.5	25	97 vol% CB, 3 vol% DIO	40 ℃ / 18h +48 h aging in dark	750	NA
BHJ	1:1.6 1:1.4	11	CF+ 0.5% CN	80℃/3h	4000/40	100℃/5 NA
LBL	**Step1.** D18: 3, 4, 5mg/ml		CF	3000/40		90℃/5
	Step2. Y6: 10 mg/ml		CF+ 0.5% CN	4000/40		
PQDs	**Step1**. D18: 4 mg/ml		CF	4000/40		90℃/5
	Step2. a) QDs: 10 mg/ml **b)** Washing		a) Octane b) EA solvent	1000/30		70℃/10
	Step3. Y6: 10 mg/ml		CF + 0.5% CN	3000/40		90℃/5

Table 2.2 The deposition parameters of the ZnO film sprayed by the intermittent SP technique and the PDINO in the inverted device architectures investigated in this thesis.

Device structure	ETL	ETL-deposition conditions	Photoactive blends	Stability conditions
ITO/**ZnO**/PTB7-Th:$PC_{70}BM$/V_2O_5/Ag	ZnO	SC 3000 rpm/30s	PTB7-Th:$PC_{70}BM$	Dark Inside the Glove box 99.999% N_2 H_2O < 0.1 ppm O_2 < 0.1 ppm
	ZnO (High concentrations)	SP-3R		
		SP-5R		
		SP-7R		
		SP-9R		
	ZnO (Low concentrations)			
		SP-15R		
		SP-20R		
		SP-25R		
		SP-30R		
ITO/**ZnO**/ PM6:Y7/V_2O_5/Ag	ZnO	SC 3000 rpm/30s	PM6:Y7	Photostability (AM1.5 G) Continuous illumination
ITO/**ZnO/PDINO**/ PM6:Y7/V_2O_5/Ag	ZnO/PDINO Bi-stack	ZnO (4000 rpm/40s) PDINO (4000 rpm/30s)		
ITO/**PDINO**/ PM6:Y7/V_2O_5/Ag	PDINO	3000 rpm/30s		

2.4 Characterization Techniques

In this thesis, all the electrical and photo-physics characterizations were performed under nitrogen environment (H_2O < 0.1 ppm and O_2 < 0.1 ppm). The devices were transferred from the evaporator chamber to the sample holder from Ikerlan Ltd. (see **Figure 2.8**) that was carefully sealed inside the glove box for the device's measurement steps. In order to avoid any degradation that might occur to the devices by the environment since all the characterization systems work under environmental conditions.

2.4.1 OPV Devices Characterizations

2.4.1.1 Current density-voltage characteristics

The current density – voltage (J-V) characteristics were carried out under illumination and dark conditions. J-V characteristics were extracted using a Keithley 2400 Source Measure Unit with a solar simulator (Abet Technologies model 11000 class type A, Xenon arc) as an artificial light source of AM 1.5G spectrum with the standard light intensity of 100 mW cm^{-2} as shown in **Figure 2.9**. The light intensity was calibrated by an NREL certified monocrystalline silicon photodiode. Furthermore, all the J-V characteristics were performed at room temperature in the forward direction from –1 to 1 V, with a scan step of 0.01 V and dwell time of 2 ms. For the J-V dark characteristics, equivalent circuit device models were operated in MATLAB software to fit the experimental data obtained from the OPV devices. The equivalent circuit models are useful for understanding the electrical behavior of semiconductor devices, considering the dominant effect of the diode, shunt and series resistance for a given voltage on the generated photocurrent of the device.

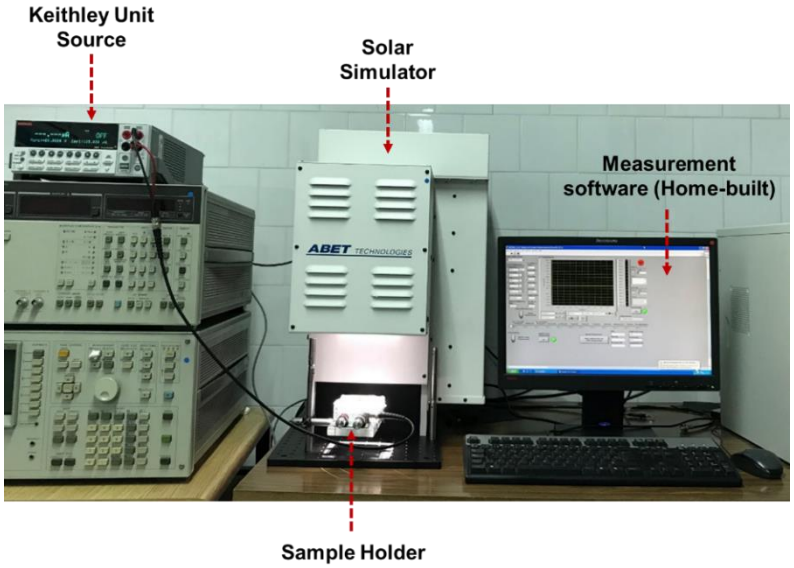

Figure 2.9 The experimental setup used for the measurement of J-V characteristics in this thesis.

The same experimental setup was used to measure the dependency of the J_{SC} and V_{OC} on the light intensity (P_{light}), using a set of optical density filters. These measurements were a powerful tool to gain more insights into the recombination kinetics inside the OPV devices[80,144]. The equation that represents the relation between the J_{SC} and the P_{Light} is J_{SC} α $(P_{Light}t)^{S1}$, where the power-law exponent S1 extracted from the log-log plotted curve of the J_{SC} vs P_{light}. The S1 value predicts the photocurrent losses under the short-circuit condition, where S1 value close to 1 refers the insignificant bimolecular recombination in an ideal photovoltaics behavior [89,144,145]. While from the V_{OC} vs P_{Light} semi-log curve, we can extract the ideality factor (n_{id}) following equation 1.10 that helps identifying the presence of the trap assisted recombination [81,146]. When the value of n_{id} is close to 1, it indicates that the bimolecular band-to-band recombination is the dominant recombination in the OPV devices[147], while n_{id} >1 (close to 2) denotes the presence of the trap assisted recombination mechanisms[144,148].

Moreover, the dependence of the photocurrent (J_{Ph}) on the effective voltage (V_{eff}) was calculated in this thesis to evaluate the exciton dissociation probabilities (P_{diss}), maximum amount of absorbed photons that provides the dissociation and generation of free carriers (G_{max}) and the generation rate (G_{rat}) of the free charge carriers in the fabricated devices[49,149]. Where J_{Ph} is the difference between light (J_L) and dark(J_D) current density, $V_{eff} = V_O - V$, where V_O is the voltage when $J_{Ph} = 0$ and V is the applied voltage[147,150,151]. We evaluated the values of the G_{max}, P_{diss}, and G_{rat} using the following equations 2.1, 2.2, and 2.3, respectively [49,149,151,152].

$$G_{max} = \frac{J_{sat}}{qL} \tag{2.1}$$

$$P_{diss} = \frac{J_{SC}}{J_{sat}} \tag{2.2}$$

$$G_{rat} = \frac{P_{diss}}{G_{max}} \tag{2.3}$$

where J_{sat} is the saturation current density, q is the elementary charge and L is the thickness of the blend film.

It is worth mentioning that the space charge limited current (SCLC) method was performed using the same setup but the configuration of the devices was different. This method is used to measure the electron and hole mobilities for the electron-only and hole-only devices with the structures of ITO/ZnO/photoactive film/PDINO/Ag and ITO/PEDOT:PSS/photoactive film/MoO_x/Au, respectively. Following Mott-Gurney equation 2.4, where the measured dark current was fitted to the SCLC model to determine the charge carrier mobility[153,154].

$$J_{SCLC} = \frac{9V^2}{8L^3}\varepsilon_0\varepsilon_r\mu_{SCLC} \tag{2.4}$$

where J_{SCLC} is the measured current density, ε_0 is the permittivity of vacuum (8.85 x 10^{-14} F cm^{-1}), ε_r is the relative dielectric constant of the materials (estimated to be 3 for organic semiconductors)[88], μ_{SCLC} is the charge carrier mobility, L is the thickness of the films (~100 nm). V is the difference between the applied voltage (V_{app}) and offset voltage (V_{bi}). The data are recorded with a Keithley 2400 through 1 to 9 V sweeping at a scan rate of 40 mV s^{-1}. The μ was calculated from the slope of 2 in the log-log dark J-V curve, as illustrated in **Figure 2.10**.

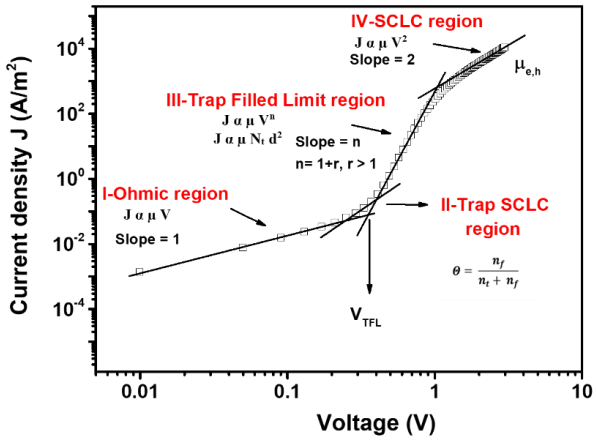

Figure 2.10 Typical SCLC behavior for organic semiconductors.

Furthermore, the SCLC is used to evaluate the density of trap states N_{trap} along with the the free (N_f) and trapped (N_t) carrier densities. In **Figure 2.10** there are four different regions in the SCLC curve. First, I-ohmic response region at low voltage (J α μ V). Second, II- trap-SCLC region where J α μ V^n, third III-trap-filled limit (TFL) region at intermediate voltages where the trap states are filled by the injected carriers and the voltage V_{TFL} is linearly proportional to the density of trap states N_{trap} (J α μ N_t d^2). Finally, the IV-Child's region or trap free region (J α μ V^2).

Accordingly, the voltage between the ohmic and TFL regions is called the trap-filled limit voltage (V_{TFL}), which can be used to calculate the N_{trap} by using equation 2.5[153–155]:

$$V_{TFL} = e\, N_{trap} L^2 / 2\varepsilon_0 \varepsilon_r \qquad (2.5)$$

Where e is the elementary charge, then we can calculate the free (N_f) and trapped (N_t) carrier densities using Θ as defined by trap factor parameter that can be determined from region II as shown in **Figure 2.10** follows equation 2.6 [154,156,157]

$$\Theta = \frac{N_f}{N_t + N_f} \qquad (2.6)$$

2.4.1.2 Quantum Efficiency (QE)

The external quantum efficiency (EQE) or known as incident-photon-to-current efficiency (IPCE) is the fraction of incident photons that create electron-hole pairs that collected by the PV devices. Or in another word it is the ratio of the number of charge carriers extracted by a PV device to the number of incident photons. These successfully collected photons are measured over different wavelengths of light. Because it is directly related to the short-circuit current of the PV devices, it is an excellent diagnostic tool to improve efficiency. This measurement is used to test structures and cellular materials, as well as to verify the reproducible production of PV devices. Moreover, EQE refers to the five main working principle procedures that take place in the PV devices as explained by equation 2.7.

$$\eta_{EQE} = \eta_A \times \eta_E \times \eta_{CS} \times \eta_{CT} \times \eta_{CC} \quad (2.7)$$

where η_A is the light absorption term, η_E is the exciton migration, η_{CS} is the charge separation, η_{CT} is the charge transport, and η_{CC} is the charge collection term. Moreover, equation 2.8 was applied to determine the value of the calculated EQE.

$$EQE = \frac{h\nu}{q} SR = \frac{h\nu\, J_{SC}}{q\, P_{in}} \quad (2.8)$$

where $h\nu$ is the photon energy, q is electron charge, SR is the spectral response = [current generated by the device (J_{SC}) / the incident light intensity (P_{in})][158]. Accordingly the integrated $J_{SC,EQE}$ of the PV device under illumination can be calculated using equation 2.9.

$$J_{SC} = \int qEQE\,(\lambda)\phi_{AM1.5G}(\lambda)d\lambda \quad (2.9)$$

where λ is the wavelength, $\phi_{AM1.5G}$ is the global AM1.5G value in W/m^2 (ASTM173-NREL)[159]. EQE spectrum can be converted into spectral response SR(λ) whose unit is Amp/Watt; while AM1.5G spectrum is in W/m^2. In this way, the integrated unit Amp/m^2 is the current density unit. The EQE quantum efficiency spectrum is measured under short-circuit conditions, therefore, it is called the integrated short-circuit current density $J_{SC,EQE}$ of the EQE spectrum under the AM1.5G spectrum. Then to verify the obtained value a comparison usually conducted between the the $J_{SC,JV}$ measured from the J-V characteristic under the solar simulator and the calculated $J_{SC,EQE}$ that is typically lower than the $J_{SC,JV}$ for OPVs with a deviation range of less than 10%.

In this thesis, the EQE experiments were conducted using the measurement system shown in **Figure 2.11** from Lasing, S.A. (IPCE-DC model, LS1109-232) equipped with a Newport 2936-R power-meter unit, a

Xenon lamp power supply, and a monochromator, where all the measurements were performed under forwarding wavelength sweep direction from 300 nm to 1100 nm.

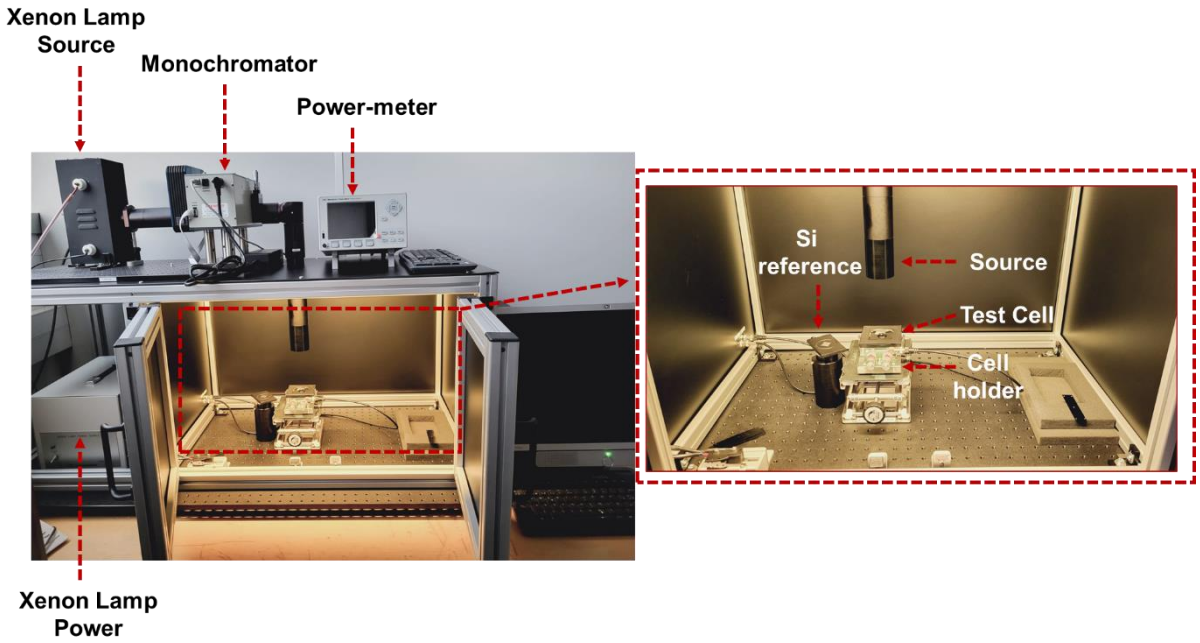

Figure 2.11 The EQE experimental set up used in this thesis.

It is well known that optical interference and parasitic absorbance in nonactive layers provide a pronounced effect on the shape of the measured EQE as a passive optical effect. Accordingly, it is a foremost to obtain the internal quantum efficiency (IQE) response since it neglects the multilayer optical phenomena and the parasitic absorptions in nonactive layers such as ITO, PEDOT/PSS, as ascribed by A. Armin et al[160]. IQE is employed to evaluate the charge generation, extraction, and collection processes of the devices within the photoactive layer, taking into account the recombination losses that might take place in the based devices. Following the correlation as described by Forrest et al.[161] and A. Armin et al. [160] that expressed as $\eta_{IQE}= \eta_{EQE}/\eta_A$, where η_{IQE} is the fractional internal quantum efficiency presented by the ratio of the number of the collected charges to the photons absorbed by the junction and η_A reveals the absorbed incident light amount by the photoactive layer. Hence, the IQE represents the photovoltaics response normalized by the number of photons actually absorbed by the photoactive layer and thus provides information about the behavior of the charge generation (exciton dissociation, charge transfer) and collection processes[161].

Furthermore, the logarithmic scale of the EQE vs the photon energy reflects the optical properties of the active blend film using the Urbach rule as following[162,163]:

$$\alpha(E) = \alpha_0 \, e^{(E-E_g)/E_U} \qquad (2.10)$$

where, α (E) is the optical absorption coefficient, α_0 is the optical absorption coefficient at the band edge, E is the photon energy and E_U is the Urbach Energy. the E_U value represents the density of state distribution that explains the energetic disorder in the molecular orbitals [162], which is considered as a valuable parameter revealing the influence of all possible defects.[164]

2.4.1.3 Impedance Spectroscopy (IS)

It is a powerful diagnostic technique for monitoring the recombination , carrier accumulation and transport behavior of each layer within the OPV devices[165–167]. It measures the phase shift and the amplitude of the current response obtained through applying an AC voltage to the devices at a given frequency range, which reveal different mechanisms taking place at various interfaces[165,168].these mechanisms were ivistigated through analyzing the observed Nyquist plot (or called Cole-Cole plots) behaviour.

Furthermore, capacitance-frequency (*Cf*) is one of the defect spectroscopy techniques that can be conducted using IS measurements setup that allows calculating the trap density of state (DOS) of the OPV devices, explaining the electric properties of the fabricated OPV devices, through investigating the interfacial charge transfer along with carrier recombination mechanisms [169].

It is well known that as the trap densities are high, then trapped charge carrier still can participate in the transportation by thermally hopping or tunneling (shallow traps), while deep traps creates recombination centers due to hardly excited back charges.[64] This characterization has been performed for OPVs in many research work to obtain the change in trap emission and disorder-induced tail states within the devices.[64,165,169–171]

The density of states (DOS) evaluation was performed for organic solar cells in many reported work to distinguish the change in trap emission and in turn the energetically disorder-induced tail states crated inside the devices [64,121,165,169–171]. Therefore, DOS at a given energy level, E_ω, can be calculated by varying the capacitance with respect to frequency of the device. This indicates the trapping and the charge release by shallow traps in the band gap close to the Fermi energy level as given by **Equation 2.11** [64,171]

$$\mathrm{DOS}(E_\omega)_{traps} = -\frac{V_{OC}\omega}{t\,q\,T\,k_B}\frac{\partial\,\mathrm{C}}{\partial\,\omega} \tag{2.11}$$

where, C is the measured capacitance, V_{OC} is the open circuit voltage obtained by the J-V characteristics under illumination conditions, ω is the angular frequency ($2\pi f$), t is the layer thickness, k_B is the Boltzmann constant, q is the electron charge, and T is room temperature (300K). Accordingly, we applied the following equation to obtain the trap-DOS as an energy dependent:

$$(E_\omega)_{traps} = k_B \, T \ln \frac{2\beta N}{\omega} = E_O - k_B \, T \ln\omega \quad (2.12)$$

where, β is the cross section and N is the effective density of state [172]. Since presuming that 2βN is independent on frequency value, in turn, the variation in its value is likely to be more related to the shift in the DOS values on energy scale (E_O).

From **Equation 2.12**, we get the energy dependence on the frequency for the cells comparison study such as A and B as $E_{0A} = k_B T \ln\frac{\alpha_A}{\omega}$ and $E_{0B} = k_B T \ln\frac{\alpha_B}{\omega}$, respectively, where the 2βN defined as α disorder parameter[173].

As a sequence, the energy's difference between the A and B devices can be determined as $E_B - E_A = E_{O(B)} - E_{O(A)} = k_B T \ln\alpha_B - k_B T \ln\alpha_A = k_B \, T \ln\frac{\alpha_B}{\alpha_A}$

Consistently, the shifting value due to photo-degradation can be calculated as

$$X = \exp\left(\frac{E_B - E_A}{k_B T}\right) = \frac{\alpha_B}{\alpha_A} = \frac{\beta_B . N_B}{\beta_A . N_A} \quad (2.13)$$

where β is the cross-section and N is the effective density of states. Furthermore, in **Equation 2.12,** the slope of the tail given by k_BT measures the extent of the distribution of localized states; in other words, it is an indirect measure of the disorder in the semiconductor[173]. Depending on their relative energetic position from the band edge, trap depth can be determined. Few k_BT from the band edge represents the shallow traps and several kT reveal the deep traps that lie further[174].

In this thesis, impedance spectroscopy (IS) measurements were carried out at different applied bias voltages (short circuit current at 0.0 V, near to the maximum power point voltage (V_{mpp}), V_{mpp}, and at open circuit voltage (V_{OC})) with an AC signal of 50 mV amplitude at frequency range 5 Hz -1 MHz utilizing the same AM 1.5G illumination conditions that recorded by a HP-4192A impedance analyzer presented in **Figure 2.12**. The extracted data was fitted through several equivalent circuit models such as the 3RC and Debye models. Furthermore, to calculate the DOS by *C*f measurement, the capacitance-voltage (C-V) measurement should be performed in dark conditions at a frequency 1 MHz, 5mV amplitude and voltage scan from -1 to 1 V to get the value of built-in voltage (V_{bi}).

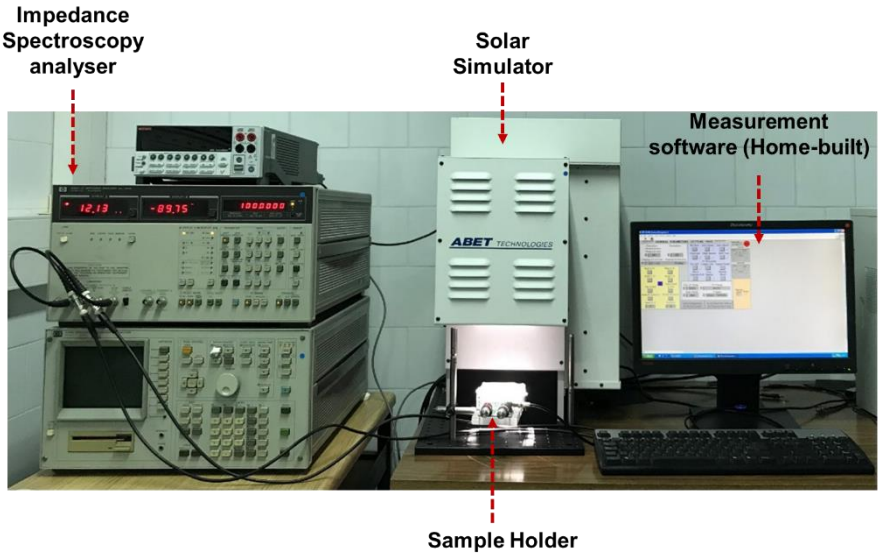

Figure 2.12 The experimental setup of the impedance spectroscopy used in this thesis.

2.4.1.4 Photovoltage/Photocurrent Transient Techniques (Time-resolved techniques)

Characterization of OPV devices by means of photovoltage and photocurrent transients provide important information related to the properties of the devices, such as the charge carrier lifetime. In these techniques the device is perturbed by a modulated light and the photovoltage/photocurrent is conducted in the time or frequency domain, from which information on charge transport, accumulation and recombination can be recorded.

(i) Transient Photovoltage Technique (TPV)

Transient Photo-Voltage (TPV) is a time-resolved technique employed to study carrier recombination processes in OPV devices. This technique is based on the excitation of the device by a fast and small perturbation of incoming light perturbing the device open-circuit voltage (V_{OC}).In order to perform a TPV, the cell is continuously irradiated using a light source, that promotes a constant and stable V_{OC}. The OPV device is kept at open-circuit conditions, so no current can flow through the contacts and the cell is connected to an oscilloscope that can register the changes in voltage over time (**Figure 2.13a**). After reaching a stable V_{OC}, the solar cell is excited with an additional short-lived laser pulse that generates a small perturbation of the V_{OC} (**Figure 2.13b**). This process was conducted using a nanosecond nitrogen laser (PTI GL-3300) to control the 590 nm excitation wavelength (the emission of Rhodamine 6G dye) to hold the solar cells in approximately V_{OC} condition. Then, to trigger the laser pulse, an analogue function generator (Aim-TTi

TG330) has been used to generate a square wave pulse with a duration of 1.5 ns. A semitransparent optical filer was utilized to adjust the laser pulse intensity. Accordingly, the variation of the V_{OC} (ΔV) is proportional

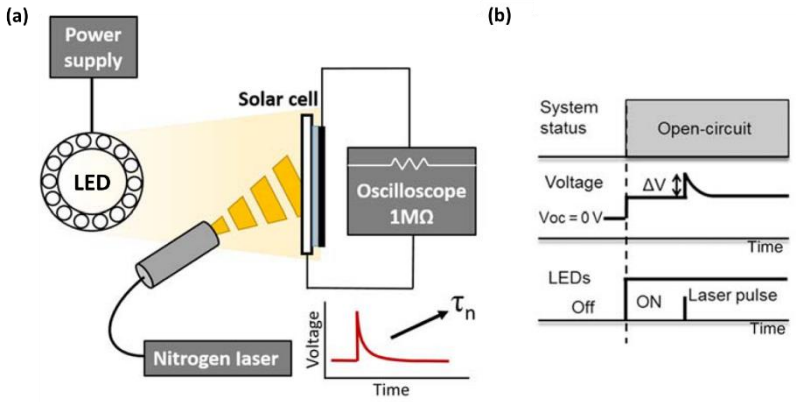

to the photo-generated carriers by the laser pulse. As the cell is in open-circuit, the "extra" photo-generated carriers are forced to recombine, which leads to the registration of the transient to the initial V_{OC}, depicting the carrier recombination process in OPV device[175].

Figure 2.13 (a) Schematic illustration of the transient photovoltage setup and (b) the demonstrated corresponding signals that can be monitored at the oscilloscope[175].

(ii) Transient Photovoltage Technique (TPV)

It is a powerful time-resolved method used to measure the charge carrier lifetime along with the charge density in OPV device through the Differential Capacitance analysis (DC). It measures the extra carriers in the cell that are generated by laser pulse-induced perturbation in short-circuit conditions. The TPC measurement setup (see **Figure 2.14a**) is quite similar to the TPV measurement setup, with the exception that the device is connected to a small resistance (50 Ω) whilst kept in short-circuit condition. To perform TPC, a small perturbation in the cell current generated by the laser pulse is measured on the oscilloscope as a voltage drop across the resistor that can easily be converted into a transient current by using Ohm's law, the current response monitored by the oscilloscope illustrated in Figure 2.14b. The transient current generated

by the nitrogen laser pulse is measured and integrated over time so that the amount of the photo-generated charges (ΔQ) can be calculated[175].

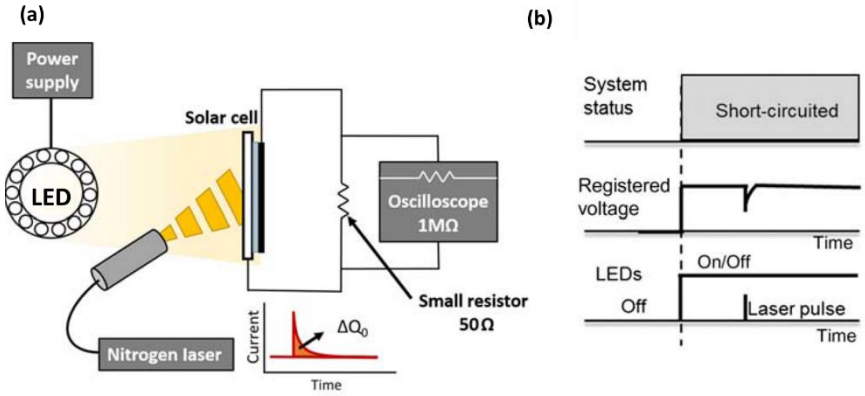

Figure 2.14 (a) Scheme of the setup employed for transient photo-current measurements and (b) the representation of the corresponding running process at the oscilloscope[175].

(iii) Charge Extraction (CE)

Charge extraction (CE) is a large modulation technique that measures the amount of stored charge present in the PV devices. Where, in the setup shown in **Figure 2.15a**, the solar cell is placed in front of a white LED array (LED from LUXEON Lumileds and powered by an Aim-TTi PLH120-P power supply), where the light intensities of white LED can be modulated to match the V_{OC} of the cell that used to measure the TPV decays. Then, the cell is short-circuited (V = 0V) through a circuit containing a small resistance (50 Ω) whilst the light source is simultaneously switched off. When short circuited, most of the free charges in the device move through the resistor to create a current transient due to the device discharged through the contacts, **Figure 2.15b** demonstrates the corresponding process at the oscilloscope. It is important to note that CE extracts all the kinds of charges like carries and the geometrical charges presented at the cell at a given voltage. Thus, charge extraction must be faster than the carrier recombination to prevent the charge losses before the cell is short-circuited[175].

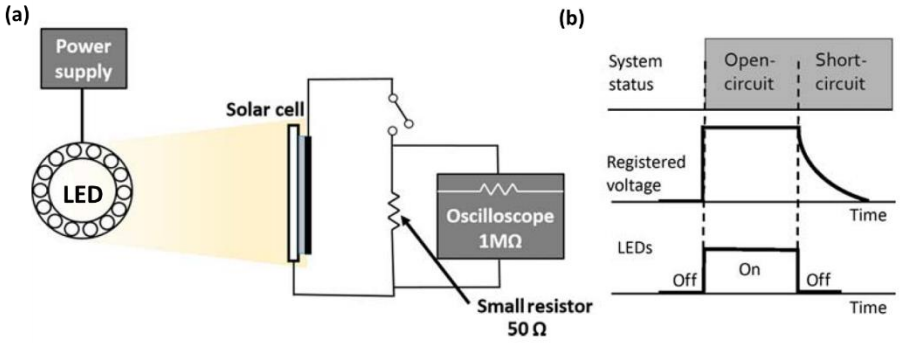

Figure 2.15 (a) Schematic illustration of the charge extraction setup. (b) Representation of the running process at the oscilloscope.

In this thesis, the experimental setup for charge extraction and transient photovoltage/photocurrent measurements are shown in **Figure 2.16** that was conducted in the Institute of Chemical Research of Catalonia (ICIQ-BIST). Hence, it is worth acknowledging Dr. Maria Méndez under the supervision of Prof. Emilio Palomares for her precious assistance in measuring and analyzing the experimental results obtained by the CE and TPV/TPC measurements.

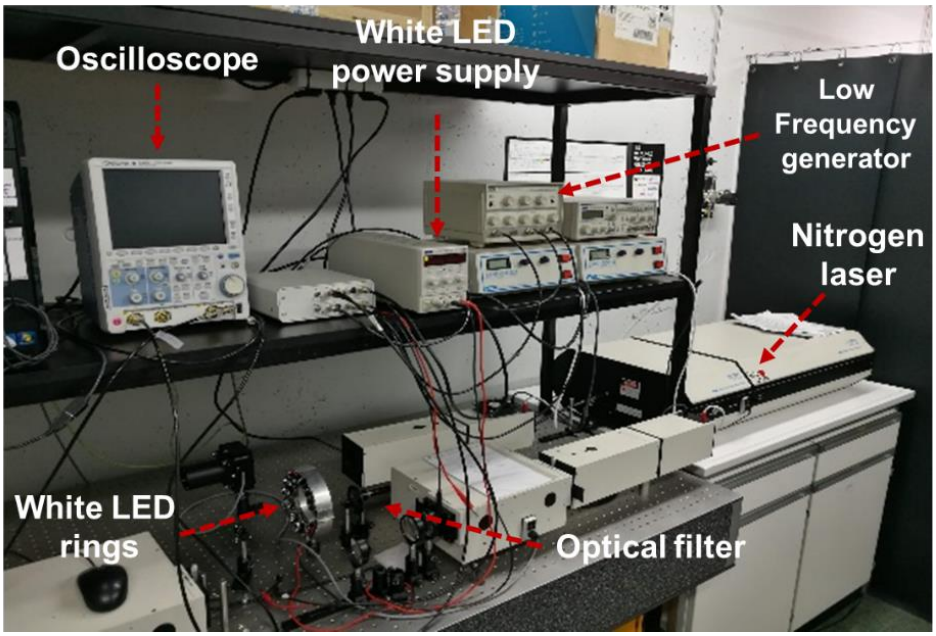

Figure 2.16 The experimental setup used in this thesis for charge extraction and transient photovoltage/photocurrent measurements in ICIQ.

2.4.2 Film Characterizations

2.4.2.1 Steady State UV-Vis Spectroscopy

The ultraviolet-visible (UV-vis) spectroscopy is employed to gain information about the absorbance / reflectance / transmittance spectra of a compound in a solution or a thin-film phase. It is an analytical technique that measures the amount of discrete wavelengths of UV or visible light that are absorbed by or transmitted through a sample in comparison to a reference or blank sample. The %R and %T spectra were recorded on a Perkin Elmer UV-Visible-NIR Lambda 950 spectrophotometer using an integrator sphere (see **Figure 2.17**) at room temperature in the wavelength range from 300 to 900 nm and the absorbance was calculated by Kirchoff's radiation law in equation 2.14

$$1 = \rho + \tau + \alpha \qquad 2.14$$

where ρ is the reflectance, τ the transmittance and α the absorbance spectra. The different absorption spectra observed in different wavelength is due to the different chromophore responses to different electrons excitation behaviour of theλ material by the absorbance of light energy or electromagnetic radiation. Moreover, this technique is used to calculate the energy of the optical bandgap (E_g^{opt}) following equation 2.15.

$$E_g^{opt} = h \times \frac{c}{\lambda} \approx \frac{1240}{\lambda} \qquad 2.15$$

where λ (nm) is the wavelength offset at the absorption peak edge.

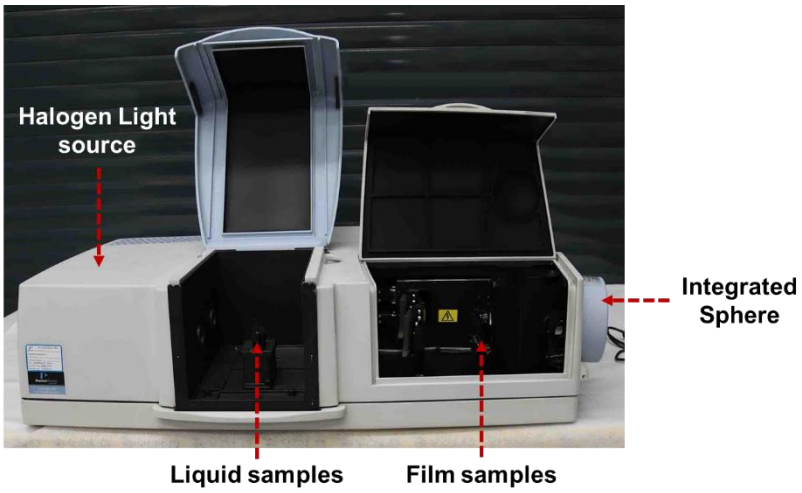

Figure 2.17 The experimental setup of UV-vis spectrophotometer used in this thesis.

2.4.2.2 Steady State Photoluminescence Spectroscopy (PL)

Photoluminescence (PL) measurements were carried out on different compositions of photoactive layers, which were recorded on fluorolog Horiba Jobin Yvon steady state spectrofluorometer equipped with a photomultiplier (UV-vis) detector in the wavelength range from 250 to 850 nm, double monochromator and Xenon light source (See **Figure 2.18**) at room temperature. The fluorescence spectrum was corrected for the optical density of the sample at the excitation wavelength and for the detection sensitivity of the detector. The PL is a process of photon excitation followed by photon emission and is important for determining band gap, purity, crystalline quality, and impurity defect levels of semiconducting material. It deals with transitions from the excited state to the ground state. Thus, PL is usually related to the number of excitons in OPV devices. The high PL intensity indicates that a large number of excitons exist in the active layer. The low PL intensity indicates that the excitons are efficiently dissociated into charge carriers[176]. In this thesis, the thin-film sample was prepared by spin-coating the photoactive blend solution under the same condition of the devices. Then, a protective coating of a transparent optical adhesive layer was deposited over the photoactive layer to avoid any environmental degradation that might take place to the organic film. In this thesis, the PL measurements were conducted in ICIQ with the kind help of Dr. Maria Méndez.

Figure 2.18 The experimental setup of PL spectrophotometer used in this thesis.

2.4.2.3 Atomic Force Microscope (AFM)

Atomic force microscopy (AFM) is a common technique to investigate the surface morphology and the roughness of thin films. AFM has three differing operation modes: contact mode, tapping mode and non-contact mode. In this thesis, AFM measurements were carried out in tapping mode, where the tip lightly taps on the surface of the specimen during scanning. The cantilever in tapping mode oscillates at its resonant

frequency and the changes in the oscillation amplitude can be used to measure the distance between the tip and the specimen surface. The specimens for AFM characterization were prepared under the same condition compared with the interfacial and photoactive layer deposition of the OPVs devices. The cantilever used was silicon probes with a typical spring constant of 1 – 5 N m-1 and a resonant frequency of 75 kHz operated under ambient conditions. The images were processed using a Molecular Imaging Pico SPM II instrument (pico +) software. **Figure 2.19** depicts the AFM setup used in this thesis.

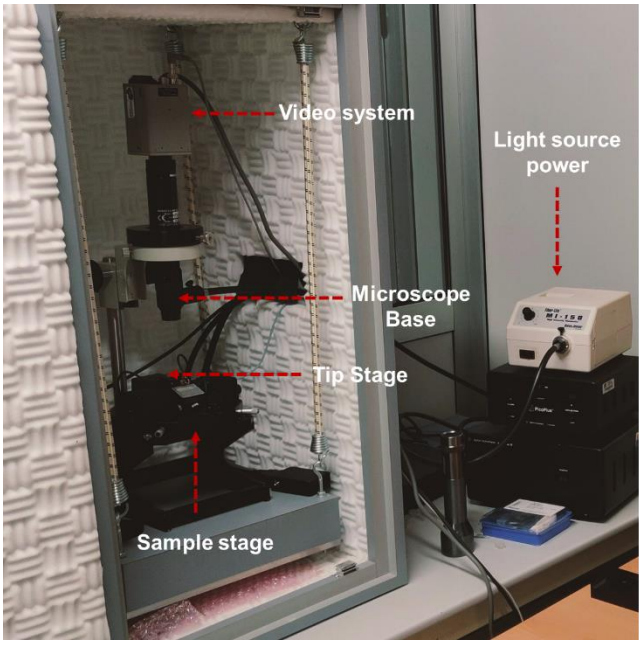

Figure 2.19 The experimental atomic force microscope setup used in this thesis.

2.4.2.4 Field Emission Scanning Electron Microscope (FE-SEM)

In this thesis, the surface microstructure images were derived from field emission scanning electron microscope, Thermo Fisher Scientific-Scico2-High Resolution FE-SEM as presented in **Figure 2.20**.

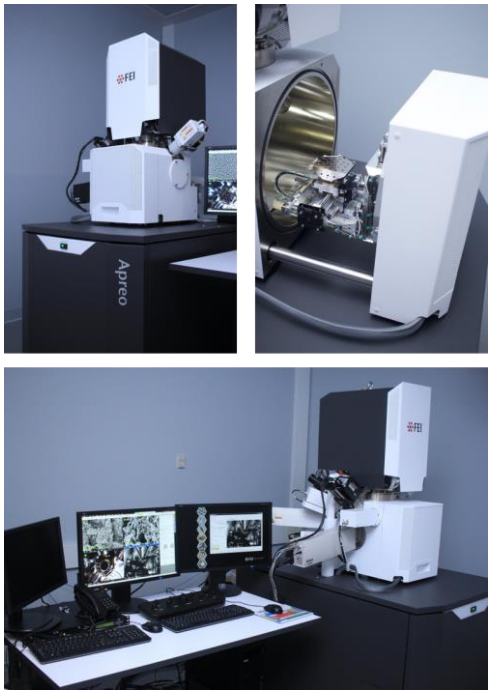

Figure 2.20 Field Emission Scanning Electron Microscope (FE-SEM) used in this thesis.

2.4.2.5 Surface Profilometer

The thicknesses of the prepared interfacial and photoactive films within the devices were measured by the surface profilometer (AMBIOSTECHNOLOGY-XP 1) as presented in **Figure 2.20** that placed on a vibration isolation table.

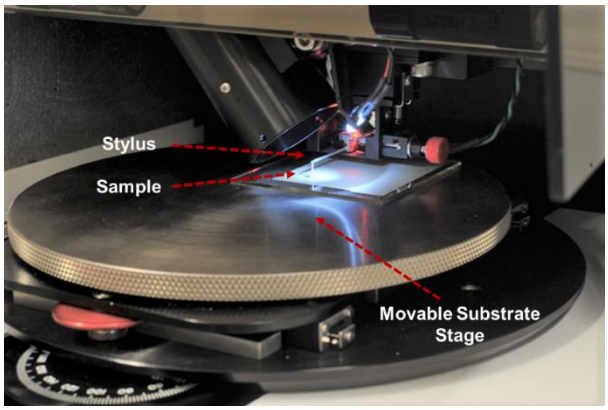

Figure 2.21 The surface profilometer setup used in this thesis.

Thesis Work Flow-Chart

The structure of the results and discussions in this thesis are summarized in the following flow chart in **Figure 3.**

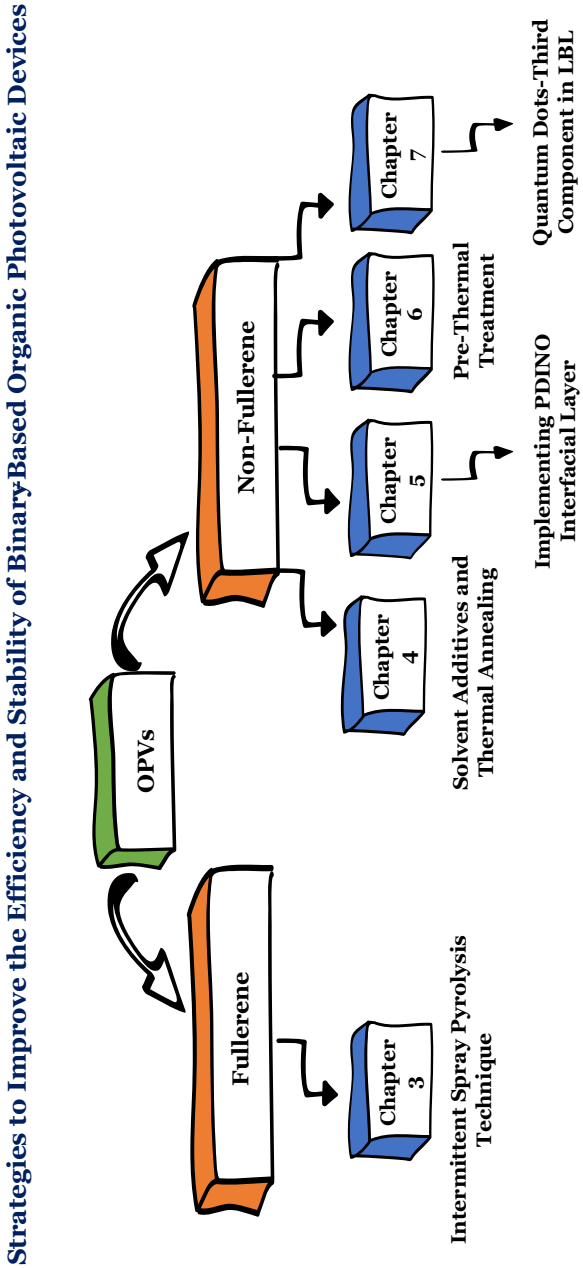

Figure 3.1 The flow chart of the conducted work in this thesis

Chapter 3

Stability Boosting of Fullerene-Based Inverted Organic Photovoltaic via ZnO film Modification Deposited by Intermittent Spray Pyrolysis Technique

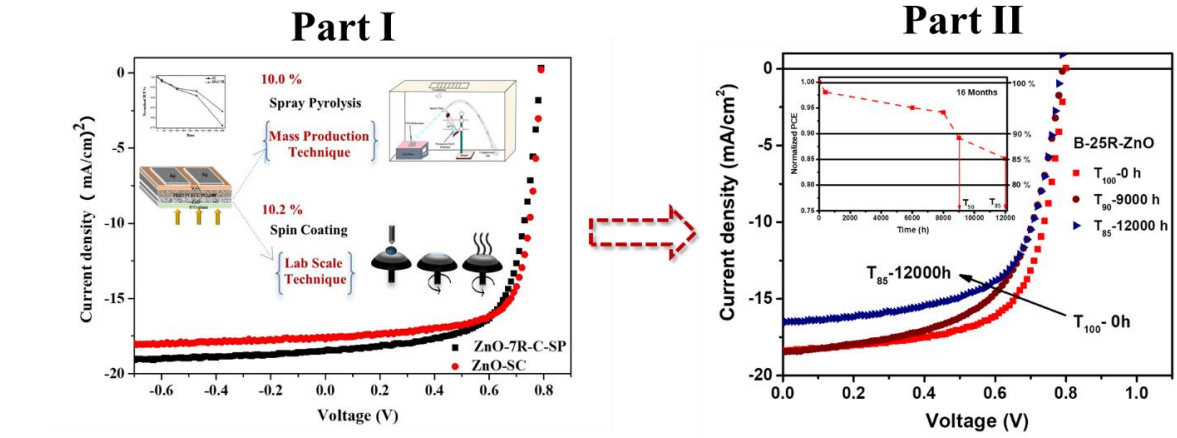

This chapter consists of two parts, Part I describes a comparison study between the devices performance based on the spin coating technique and a novel spray pyrolysis technique termed as "Intermittent Spray Pyrolysis" to deposit highly concentrated ZnO precursor solutions. In this study, several modification parameters were conducted to optimize the intermittent spray pyrolysis method. In Part II, further optimization was performed for ZnO precursor solution concentrations combined with the optimized deposition parameters achieved in Part I. In both parts, a stability study was conducted for the champion optimized OPV devices with the structure of ITO/ZnO/ PTB7-Th: $PC_{70}BM/V_2O_5$/Ag.

This chapter is based on the published works:

Part I: Enas Moustafa, J. Sánchez, L. F. Marsal, and J. Pallarès, "Stability Enhancement of High-Performance Inverted Polymer Solar Cells Using ZnO Electron Interfacial Layer Deposited by Intermittent Spray Pyrolysis Approach", ***ACS Applied Energy Materials***, **2021**, 4 (4), 4099-4111.

Part II: Enas Moustafa, L. F. Marsal, and J. Pallarès, Significant Stability Improvement of Fullerene Organic Photovoltaics via ZnO Film Modification through the Intermittent Spray Pyrolysis Technique, ***ACS Applied Energy Materials***, **2022**, 5 (4), 4390-4403.

3.1 Introduction and Aim of the Work

Since 2005, it has been proposed that polymer-based solution-processed organic photovoltaics (OPVs) with 10% power conversion efficiency (PCE) would be adequate for initiating the commercialization, which would in turn assist the cost savings of broad materials development.[177] However production of OPV on large scale and at a competitive price is a breakthrough waiting to be achieved. Importantly, while OPVs will essentially continue incremental progress in PCE, the devices will also require advanced stability for long-term operation to be able to compete in the commercial applications field. Hence, the stability of the OPVs is still a crucial issue to investigate the origin of the degradation processes and the mechanisms of the intrinsic or extrinsic degradation leads to device instability[171,178,179]. Most of the literatures pointed to overcome the extrinsic instability by the encapsulation to prevent the degradation due to the humidity and oxygen[166]. While, the intrinsic degradation was studied through investigating different interfacial layers and thin film materials[171]. Therefore, there are tremendous attempts that have been performed to understand the degradation mechanisms and improve the OPV device stability, counting the enhancement of active blend materials that stated more photochemical stability[180], the insertion of the polymeric side-chains that improve thermal stability[181–183], as well as the encapsulation techniques.[184,185]

Moreover, some other avenues concern about interlayers tuning morphology toward better film quality through controlling the selection of interfacial materials, interfacial device engineering, and the approach of the inverted structure along with the layer deposition techniques.[32,82,83,121,186,187] Regarding the latest mention approaches, as shown by M. T. Lloyd et al. group work[110], B. MacLeod[111] and several other reported studies, that the conventional structure suffers from rapid degradation due to the use of Poly (3,4 ethylenedioxythiophene): poly (styrene sulfonate) (PEDOT: PSS) as an anode buffer layer which is hygroscopic and acidic[188]. Accordingly, the implementation of inverted architectures has noticeably improved the OPV devices stability over the conventional structures from the scale of minutes up to years.[30,110–112] Therefore, up on this context, in this chapter, an inverted fullerene-based OPVs (iF-OPVs) based on selecting zinc oxide (ZnO) as the electron transporting interfacial material (ETL) were fabricated for reinforcing the electron collection at the transparent conducting electrode and acquiring high performance and stable OPV.[111] This selection was mainly regarding its n-type conductivity and high optical transmission at vital wavelengths for solar energy conversion applications.[113–116,189,190] Furthermore, ZnO thin film can be performed through a number of deposition techniques, including spin coating[111,117], atomic layer deposition[118], inkjet printing[29,119,120] and spray pyrolysis techniques [32,108,121,185].That in turn influences the morphology, substrate coverage and the contact quality (roughness) of the ZnO layer at the interface with the organic absorber blend. These parameters are the most significant factors in identifying the performance and stability of OPV devices[112,122,186].

The spray pyrolysis technique is one of the most economic techniques that has many superior advantages. It is a very simple thin film deposition technique that does not require any vacuum condition at any stage. That is a tremendously vital factor allows the process to scale-up for industrial approach [141,191,192]. Furthermore, it is a cost effective technique (especially regarding to the equipment costs), easy to control the deposition parameters and reproducible thin film deposition technique[191,192]. Moreover, the SP technique has the ability of fabricating the film by different compositions that enables preparing films with gradients through the film thickness which is highly effective for the optical applications[141,142]. Several studies were reported on the fabrication of thin film ZnO ETL with SP technique in OPV devices[139,193]. However, none of the reports that applied the SP technique achieved high power conversion efficiency with the structure of ITO/ZnO/ PTB7-Th: $PC_{70}BM/V_2O_5$/Ag because it is challenging to scale up from laboratory to production approach.

In this part of chapter 3, iF-OPVs were fabricated based on the semiconducting donor polymer PBDTTT-EFT (known as PTB7-Th) that blended with the $PC_{70}BM$ fullerene acceptor to compose the optically active layer. Thin film of ZnO was employed as ETL, vanadium oxide (V_2O_5) was used as HTL followed by silver (Ag) as a metal contact. It is important to mention that the ZnO-ETL presented in this work were deposited using spray pyrolysis thin film deposition technique with the intermittent approach mentioned previously in Chapter 2 in **Figure 2.4**. That gave the niche of producing high ZnO-film quality along with retaining the high performance of the fabricated devices. Furthermore, different ZnO precursor solution concentrations and various spraying parameters were investigated and optimized to perform efficient and highly stable iF-OPVs. In parallel with the iF-OPVs fabricated by the SP, a lab-scale spin coating technique was used to deposit ZnO-ETL as a controlled reference device. Moreover, to focus on the study of the intrinsic degradation behavior of the fabricated devices, we stored and analyzed the samples in an inert atmosphere of <0.1 ppm O_2 <0.1 ppm H_2O using a well-sealed sample holder inside the glove box to avoid the possible degradations that might arise from the oxygen and the ambient moisture.

Hence, deep insight studies for the fresh and degraded iF-OPVs were carried out using electrical, optical, and morphological characteristics to investigate the effect of the SP and SC deposition techniques on the properties of the obtained ZnO film.

3.2 Experimental Procedures

This section reports the details of the ZnO and the blend solution synthesis, the deposition conditions employed for ZnO solution, and device fabrication procedures of the iF-OPVs conducted in the two parts of this chapter that based on ITO/ZnO/PTB7:Th:$C_{70}BM/V_2O_5$/Ag structure as demonstrated in **Figure 3.2**.

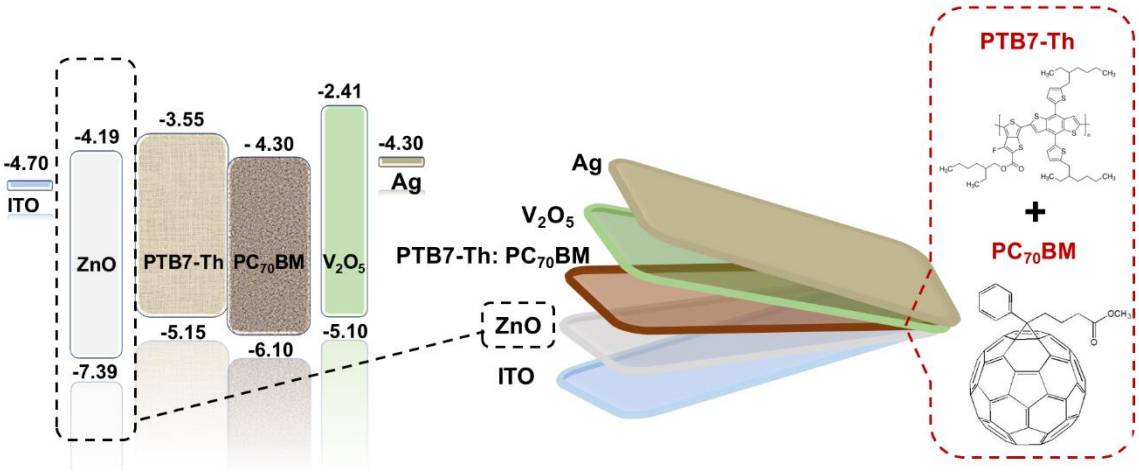

Figure 3.2 Scheme of the fabricated inverted fullerene organic photovoltaic device with the chemical structure of the PTB7-Th: $PC_{70}BM$ active blend and the energy level alignment of each layer within the device.

The schematic diagram for the fabrication procedures of the inverted structure OPV devices in this thesis is prior illustrated in Figure 2.8 in chapter 2. In the case of fabricating the reference devices using SC technique (A sample), ZnO stock solution was spun coated on the top of the pre-cleaned ITO at 3000 rpm for 30 s, then left for 1 h annealing at 200 °C. While, for the intermittent SP technique, the synthesized stock solution was diluted with ethanol then sprayed over the pre-heated ITOs at 350 °C (as demonstrated in Figure 2.4), and the deposited films were left to annealed for 1 h.

For the study in Part I, three different concentration ratios of ZnO solution were prepared, B samples with 1:6 v/v ratio, C samples with 1:4 v/v ratio, and D samples with 1:2 v/v ratio. Moreover, each concentration of the mentioned samples (B, C, and D) was used to spray the ZnO solution by applying different numbers of running cycles (3R, 5R, 7R, and 9R), see Figure 2.4b, for the optimization purpose. Furthermore, the other parameters related to optimizing the SP setup were conducted and fixed during the entire work duration, such as the distance between the spraying nozzle and the substrates, the angle of spraying (45°), spraying rate (applied pressure) and the substrates temperature (350 ℃).

For the study in Part II, the ZnO stock solution was further diluted by ethanol with 0.5:9.5 (v/v) and various numbers of spraying running cycles (R) of 15R, 20R, 25R, and 30R were conducted to deposit different thickness of ZnO film obtaining I, II, II, and IV devices, respectively.

The photoactive blend solution was prepared by dissolving 25 mg of PTB7-Th:$PC_{70}BM$ with 1:1.5 (w/w) ratio in 1 mL of chlorobenzene: DIO (97:3, %v/v). The solution was kept under stirring at 40 ℃ for 48 h

before deposition. Approximately a 100 nm thick PTB7-Th:$PC_{70}BM$ based active layer was spin-coated (750 rpm, 30 s) on glass/ITO/ZnO inside a N_2 filled glove box. Finally, the samples were introduced to a vacuum chamber to thermally evaporate V_2O_5 followed by Ag as aforestated.

3.3 Results and Discussion

3.3.1 Part I: Comparison study between the devices performance based on the spin coating and Intermittent Spray Pyrolysis to deposit highly concentrated ZnO precursor solutions.

In this part, the dependency of different high concentrated ZnO precursor solutions and the spraying conditions by intermittent SP technique on the performance and the stability of iF-OPVs were investigated. Then, the optimized iF-OPV device using SP were compared to the state-of-the-art reference cells fabricated by the lab-scale SC technique (sample A: ZnO-SC).

3.3.1.1 Optimization of The ZnO-Film Deposited by Intermittent Spray Pyrolysis Approach

In order to optimize the ZnO film deposition by intermittent SP technique, three different concentrations of ZnO solution, B (1:6), C (1:4), and D (1:2) were sprayed with four different numbers of running cycles (3R, 5R, 7R, and 9R) as described in the experimental section. The fabricated iF-OPVs were identified as B-ZnO-SP, C-ZnO-SP, and D-ZnO-SP, respectively. The performance parameters of the mentioned devices were extracted from the J-V characteristic curves shown in **Figure 3.3a**. **Table 3.1** lists the performance parameters of B-ZnO-SP, C-ZnO-SP, and D-ZnO-SP devices. It was noticeable that the performance of the iF-OPVs improved as the concentration of ZnO-precursor solution increased from B to C but decreased in D concentration. Furthermore, as the number of running cycles increased from 3R to 7R the performance of the devices enhanced except for 9R, which decreased again as illustrated in **Figure 3.3b and 3.3c**. It is worth noting that at B, C, and D concentrations, the iF-OPVs conducted by the 7R-SP have followed the same trend of showing higher performance among those prepared by 3R, 5R, and 9R. For B-ZnO-SP devices fabricated by 7R-SP technique, the measured values of open circuit voltage (V_{OC}), current density (J_{SC}), fill factor (FF), series resistance (R_S), shunt resistance (R_{Sh}), and power conversion efficiency (PCE) were 0.79 V, 18.78 mA/cm^2, 67.20 %, 2.47 Ω.cm^2, 616 Ω.cm^2, and 9.97 % respectively. While for the C-ZnO-SP cells performed with 7R, the V_{OC}, J_{SC}, FF, R_S, R_{Sh} and PCE were 0.79 V, 18.46 mA/cm^2, 68.61 %, 2.83 Ω.cm^2, 720 Ω.cm^2, and 10.00% respectively. The D-ZnO-SP devices with 7R obtained V_{OC}=0.76 V, J_{SC}=19.02 mA/cm^2, FF=64.20 %, R_S=2.00 Ω.cm^2, R_{Sh}=499 Ω.cm^2 and PCE of 9.30 %. Hence, the lower performance of sample D-ZnO-SP might be due to the highest concentration of the ZnO precursor solution D, as well as high numbers of running cycles (9R) deposited which increase the thickness along with decreasing R_{Sh} that affected negatively on the performance of the devices. In contrast to the devices with C concentration that showed the highest performance as illustrated in **Figure 3.3c**.

Upon the exhibited results, the iF-OPVs with 7R for B, C, and D concentrations were nominated for a comparison with the reference-controlled devices fabricated by the lab-scale SC technique (Sample A: ZnO-SC) since revealing the champion performance among the other iF-OPVs devices.

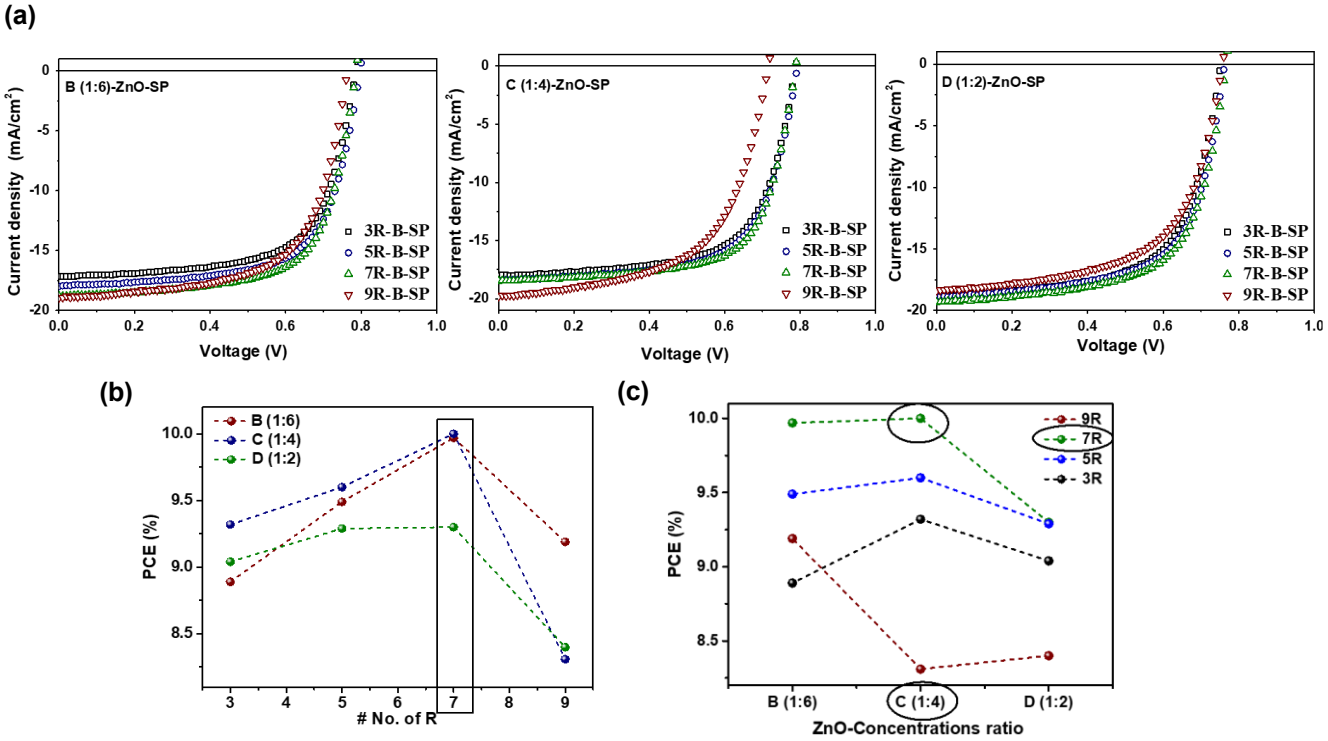

Figure 3.3 (a) J-V characteristic curves of the iF-OPVs devices fabricated by intermittent SP technique at running cycles of 3R, 5R, 7R, and 9R for each ZnO precursor solution concentration under illumination, (b) PCE vs R (c) PCE of the iF-OPVs vs B, C and D ZnO precursor solution concentrations.

Table 3.1 The performance parameters of B-ZnO-SP, C-ZnO-SP, and D-ZnO-SP iF-OPVs fabricated by the intermittent SP technique with running cycles of 3R, 5R, 7R, 9R along with the ZnO-SC-reference.

	V_{OC} (V)	J_{SC} (mA/cm^2)	FF (%)	PCE (%)	R_S (Ω.cm^2)	R_{SH} (Ω.cm^2)
B (1:6)						
9R	0.75±0.01	18.51±0.43	63.61±0.39	9.00±0.19	1.96±0.15	610±22
Best	0.76	18.94	64.00	9.19	2.11	582
7R	0.78±0.01	18.14±0.64	67.00±0.20	9.73±0.24	3.04±0.12	610±6
Best	0.79	18.78	67.20	9.97	2.47	616
5R	0.79±0.01	17.46±0.54	65.41±0.59	9.23±0.26	2.43±0.45	664±7
Best	0.80	18.00	66.00	9.49	2.88	671
3R	0.78±0.01	16.69±0.55	65.86±0.24	8.61±1.28	3.00±0.38	642±13
Best	0.79	17.24	66.10	8.89	3.08	655
C (1:4)						
9R	0.71±0.01	19.37±0.27	58.38±0.62	8.11±20	3.21±0.25	298±12
Best	0.72	19.64	59.00	8.31	2.79	300
7R	0.79±0.01	18.04±0.42	68.04±0.57	9.82±0.18	2.80±0.20	734±20
Best	0.79	18.46	68.61	10.00	2.83	720
5R	0.78±0.01	17.79±0.60	66.57±0.46	9.48±0.12	2.96±0.23	604±7
Best	0.79	18.39	67.03	9.60	2.89	611
3R	0.78±0.01	17.54±0.45	65.86±0.46	8.78±0.54	3.40±0.31	758±16
Best	0.79	17.99	66.32	9.32	2.98	764
D (1:2)						
9R	0.75±0.01	17.94±0.45	59.65±0.35	8.21±0.19	2.46±0.19	400±17
Best	0.76	18.39	60.00	8.40	2.67	417
7R	0.75±0.01	18.70±0.32	63.80±0.40	9.15±0.15	2.23±0.60	490±28
Best	0.76	19.02	64.20	9.30	2.00	499
5R	0.74±0.02	18.86±0.20	63.29±0.71	9.08±0.21	1.87±0.24	564±26
Best	0.76	19.06	64.00	9.29	2.07	590
3R	0.75±0.02	18.74±0.23	62.91±0.209	8.95±0.09	2.63±0.19	511±17
Best	0.75	18.97	63.20	9.04	2.11	524
ZnO-SC	0.79±0.01	17.45±0.28	72.60±0.40	10.00±0.20	1.90±0.13	1129±13
Best	0.79	17.69	73.00	10.19	1.03	1140

The average parameters were calculated from a minimum of 8 fabricated cells of each condition.

3.3.1.2 Comparative Study Between the Controlled Reference iF-OPVs Conducted by SC Method and the Optimal Devices of 7R-SP Based Devices.

The following section explains in detail the dependency of ZnO precursor solution concentrations (B, C, and D) sprayed by 7R-SP intermittently on the film formation, the interfacial roughness along with the performance of the corresponding B, C, and D based devices that were further compared to the standard reference ZnO-SC ones. As presented in **Figure 3.4**, AFM images show the surface roughness topographical profile for the ZnO films deposited by both SC and intermittent SP techniques. The estimated root mean square (RMS) surface roughness values of the ZnO films were 1.97 nm, 2.95 nm, 3.06 nm, and 3.99 nm for SC, B-7R-SP, C-7R-SP, and D-7R-SP, respectively. The average thicknesses of ZnO-film were 30 nm, 20

nm, 25 nm, and 50 nm for ZnO-SC, B-7R-SP, C-7R-SP, and D-7R-SP, respectively. Thus, it can be observed that the ZnO films prepared by the SP technique possess higher surface roughness values than those deposited by the SC technique. This indicates that the coating method itself has an impact on the film morphology and roughness where the SC technique usually performs smooth and uniform film. While SP technique is known as randomly spraying method which produces more rough film than the SC technique[32,194]. Moreover, regarding the ZnO films sprayed by the SP, as the concentration of the prepared ZnO solution increases, the thickness along with the roughness increased.

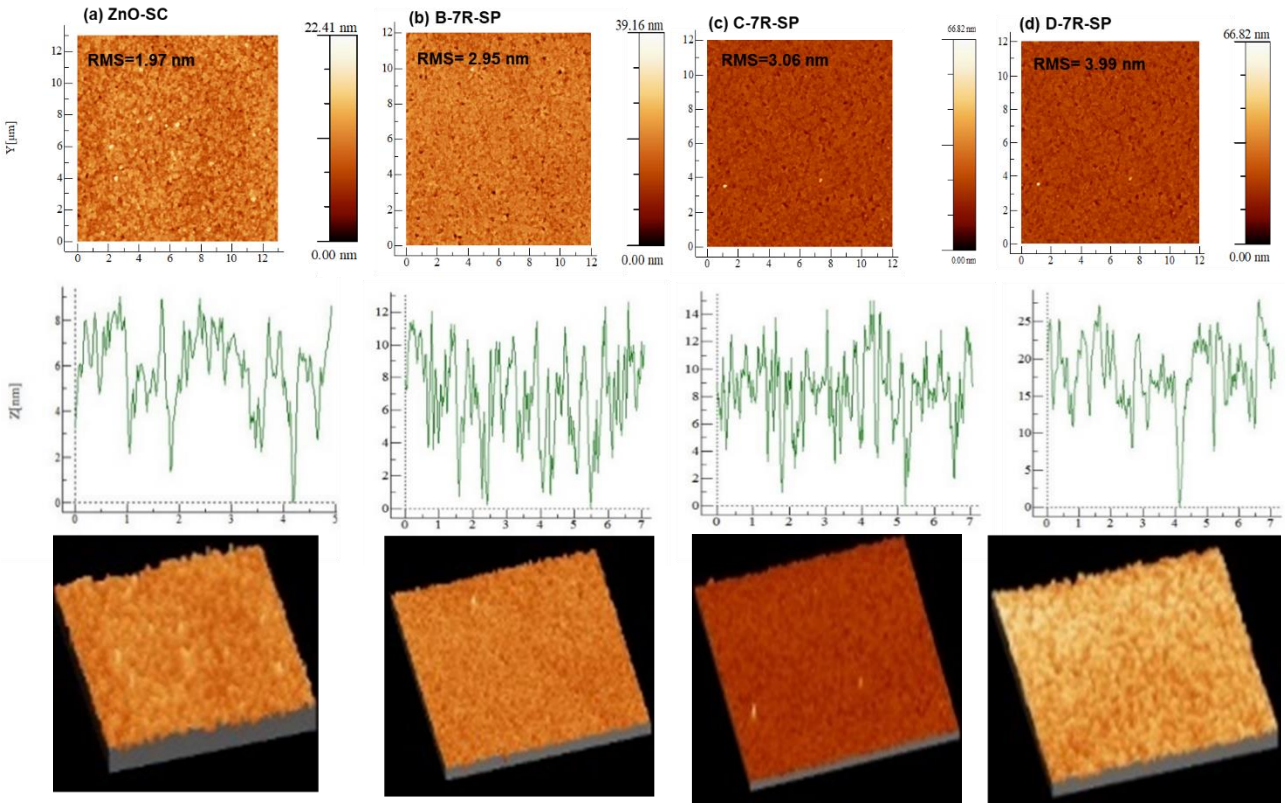

Figure 3.4 AFM topographical images of the ZnO films deposited by SC (a) and 7R-SP devices of B (b), C (c) and D (d) concentrations.

Figure 3.5a illustrates the illuminated J-V measurements of the iF-OPVs performed by 7R-SP with B, C, and D-ZnO concentrations along with the ZnO-SC controlled reference cells. The detailed comparison of the performance parameters is summarized in **Table 3.1** and **Figure 3.5b**. Despite that the best PCE value was obtained for the reference ZnO-SC iPSCs, these devices have the lowest short-circuit current value. This can be due to the difference in the thickness and surface roughness of the ZnO film sprayed by SP which proves that there is a dependence on the device's performance on the thickness and roughness of the sprayed ZnO films. Moreover, the lowest performance of D-7R-SP iPSCs can be attributed to the interface mismatch as a consequence of higher concentration and ZnO-surface roughness.

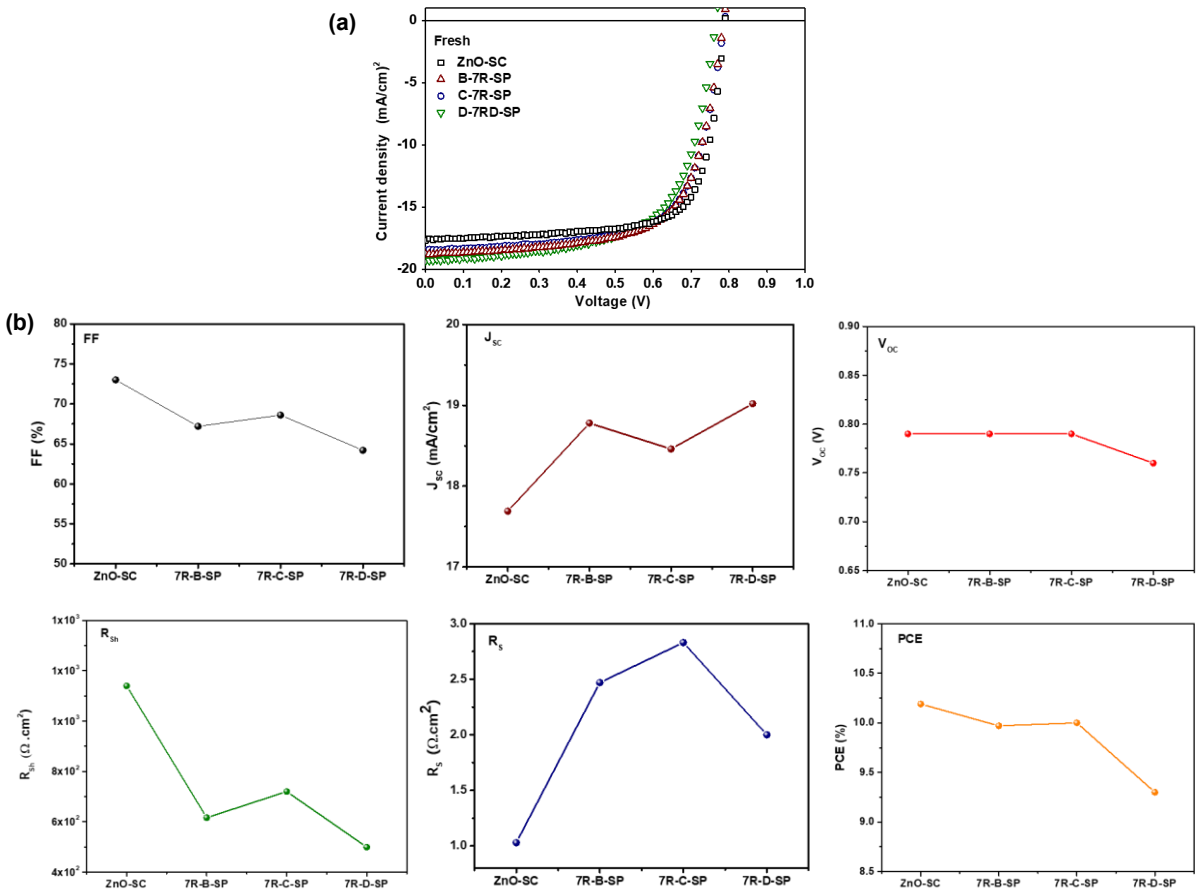

Figure 3.5 Comparative analysis between B-7R-SP, C-7R-SP, and D-7R-SP device fabricated by SP along with the reference cell ZnO-SC fabricated by lab-scale SC under illumination conditions (AM 1.5) through (a) J-V characteristic curves (b) the extracted performance parameters of the FF, J_{SC}, R_{Sh}, R_S, V_{OC}, and PCE.

Figure 3.6a presents the J-V characteristic curves at dark conditions for the B, C, and D 7R-SP based devices in a comparison with the ZnO-SC ones. This figure shows the experimental data (symbols) and the fitting model values (line) using two diodes equivalent model as illustrated in **Figure 3.6b**. It is woth to

mention that not only the usual series and shunt resistances are included but also a space charge limiting current (SCLC) element was provided to properly fit the experimental fresh ZnO-SP data at the reverse and low forward voltages due to their observed high leakage current density (J_{rev}) following equation 3.1.

$$V = V_S + V_B$$

$$V_S = J \times R_S$$

$$J = J_{D1} + J_{D2} + J_{Sh} + J_{SCLC} = \sum_{i=1}^{2} J_{Oi} \times \left[exp\left(\frac{V_B}{n_i V_T}\right) - 1 \right] + \frac{V_B}{R_{SH}} + K \times V_B^m \qquad \textbf{3.1}$$

where $J_{01,2}$ and $n_{1,2}$ are the reverse saturation current and the ideality factor of the two diodes, respectively, V_T is the thermal voltage, R_S and R_{Sh} are the series and shunt resistances, respectively, k and m are the SCLC parameters. For an applied voltage given, V, the two diodes equivalent model clearly separate the voltage drop in the junction, V_B, and bulk, V_S, regions. The total current density, J, can flow thorough two exponential mechanisms, a shunt and a series resistances in addition to a space-charge limited current (SCLC) term expressed by the equations 3.1[195,196]. Thus, the SP-based devices showed a non-ideal PV behavior as exhibited from the fitting values listed in **Table 3.2**.

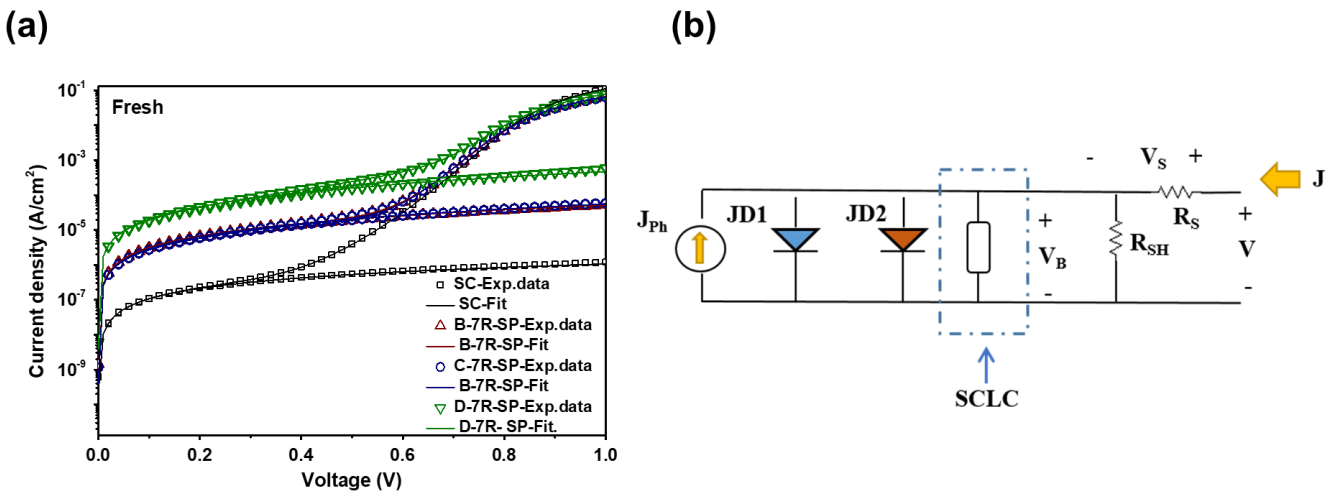

Figure 3.6 (a) J-V characteristic curves of B-7R-SP, C-7R-SP, D-7R-SP, and ZnO-SC based devices at dark condition (symbols for experimental data and the lines for the fitted data). (b)Equivalent electrical circuit employed to fit the experimental J-V dark measurements (at J_{Ph} = 0) for the ZnO-SP and ZnO-SC based devices.

Table 3.2 The fitting values of the fresh devices obtained by employing the electrical equivalent circuit shown in Figure 3.6b using equation 3.1.

	n_1	J_{O1} ($\times 10^{-12}$ A cm^{-2})	n_2	J_{O2} ($\times 10^{-12}$ A cm^{-2})	R_S (Ω cm^2)	R_{SH} ($\times 10^3$ Ω cm^2)	K ($\times 10^{-6}$ A V^{-m}cm^{-2})	m
ZnO-SC	1.20	0.06	2.0	195	1.05	940	N/A	N/A
B-7R -SP	1.24	0.20	2.0	205	2.09	33.6	22	2.0
C-7R -SP	1.29	0.58	2.0	55.3	2.13	38.3	30	2.0
D-7R-SP	1.20	0.12	4.0	759000	1.90	5.85	300	2.0

The samples showed a similar exponential mechanism with n_1 around 1.25 at medium forward voltages and saturation current density values of $0.6 < J_{01}$ (10^{-13} A/cm^2) < 5.8. Furthermore, the J_{rev} for D-7R-ZnO-SP samples is higher than that of B-7R-ZnO-SP and C-7R-ZnO-SP devices. This confirms the effect of surface roughness of the film because D-7R-ZnO-SP devices have the highest surface roughness of the ZnO film which consequently, affected the D-7R-SP cells' performance by having the lowest R_{Sh}, resulting in more leakage current that declines the PCE of the D-based devices. This attitude might be ascribed to the trapping sites that created due to the aggregated ZnO particles on the film surface upon the high concentration of D-based ZnO sprayed solution[195–198]. In fact, ZnO-SC devices showed a higher performance but a lower J_{SC} and J_{rev} while D-7R-SP iPSCs showed a lower performance but a higher J_{SC} and J_{rev}. On one hand, the diminished V_{OC} and FF as R_{Sh} decreases can be found elsewhere[72,146]. On the other hand, the enhancement of J_{SC} as R_{Sh} reduces cannot be explained using electrical parameters but optically in the following section.

Figure 3.7a displays the external quantum efficiency (EQE) spectra for the fabricated devices which have a similar range of absorption. However, a slight difference in the intensities and the spectral absorption position between devices were exhibited that probably due to the difference in the light reflection properties of the ZnO-ETL layers in each device regarding the roughness and thickness variations. The calculated J_{SC} from the integration of the EQE spectra for the SC-ZnO, B-7R-SP, C-7R-SP, and D-7R-SP iPSCs were 17.57 mA/cm^2, 18.43 mA/cm^2, 18.01 mA/cm^2, and 18.82 mA/cm^2, respectively which consistent with the measured J_{SC} values from the J-V characteristics under illumination listed in **Table 3.1**. The exhibited results showed an increment in the J_{SC} for the ZnO-SP based devices more than the ZnO-SC ones. This observation indicates the enhanced photons absorption as confirmed by UV-Vis analysis for the calculated absorbance spectra

in **Figure 3.7b** for the ITO/ZnO/photoactive layer structure. Where the spray-coated ZnO-based films showed higher absorbance than the ZnO-SC ones. Furthermore, **Figure 3.7c** demonstrates that the transmission for the ITO/ZnO-SP/photoactive layer structures was lower than the ITO/ZnO-SC/photoactive layer structures, revealing that the photoactive layer in the ZnO-SP- based devices absorbed more incident light than the ZnO-SC devices. Moreover, it is worth mentioning that D-7R-SP iPSCs exhibit the highest J_{SC} and the highest ZnO-film roughness. That is in good agreement with the observed phenomena reporting that "As the film roughness increases, it assists the light trapping inside the PV devices that plays a crucial role in enhancing the light absorbance by the active absorber layer[8,39]. Consequently, higher photogeneration of charges can be exhibited providing higher J_{SC} value of the corresponding devices. [199–201]. Moreover, the reflectance depends on the surface roughness for each layer as well affects the interfaces related to the light trapping takes place inside the cell[199,200]. Accordingly, the reflectance declines as the roughness increases, resulting in improving the absorbance upon the effect of light trapping that occurred inside the cell[11,200–202]as confirmed in **Figure 3.7d** for the ZnO-SP based devices. Consequently, the observed lower transmittance and reflectance of the ZnO-7R-SP samples than the ZnO-SC ones were due to the higher interface roughness between the ZnO layer and the active layer. This interface roughness assisted the light trapping inside the cells, enhancing the light absorbance and in turn the current generation J_{SC}. This context explains the lowest reflectance and thus the best light trapping upon the higher interface roughness noticed for the D-7R-SP based device.

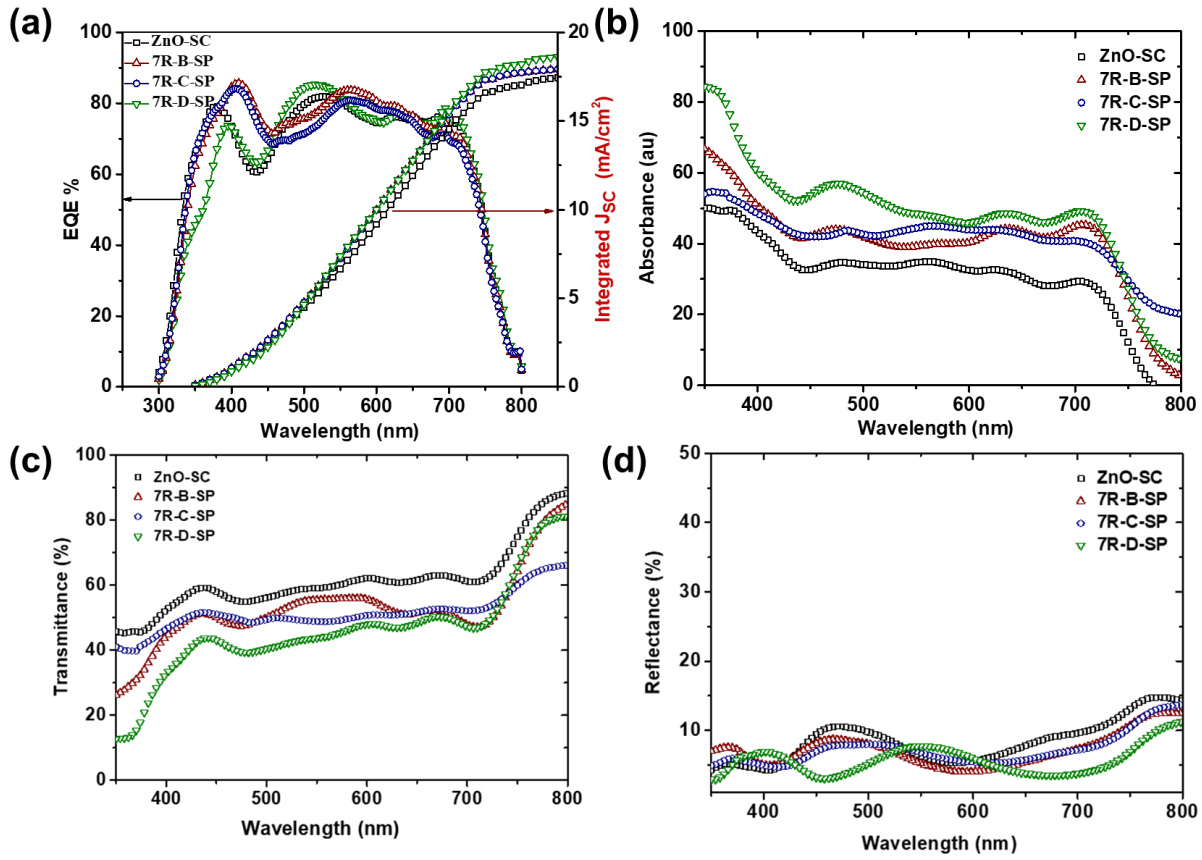

Figure 3.7 (a) EQE spectra (left) and the integrated short circuit current (right), (b) calculated absorbance, (c) transmittance, (d) reflectance UV-visible measurements of the ITO/ZnO/photoactive layer structure of the devices.

3.3.1.3 Stability Study of ZnO-SC and the Optimal ZnO-7R-SP iF-OPVs.

In this part, a degradation study of the fabricated devices was conducted by storing them inside a dry glove box at dark in electronic grade of 99.999% N_2 (H_2O humidity < 0.1 ppm; Oxygen < 0.1 ppm) during the entire examination time. The samples expose to light during the electrical measurements and then store back to the glove box. The main goal of this study is to manifest the modification effect of the ZnO-film by the intermittent spray pyrolysis approach as compared to the ZnO-SC one on the stability behavior of the devices. In addition, it is crucial to indicate the intrinsic degradation mechanisms upon the influence of the interfacial layers.

Figure 3.8a shows the illuminated J-V characteristics of the studied devices with respect to aging time until they achieved 80% of their initial efficiencies, known as T_{80}. The T_{100} (the time of the initial PCE), T_{95} (the time reaching 95 % of the efficiency initial value), T_{90} (the time reaching 90 % of the efficiency initial

value) and T_{85} (the time reaching 85 % of the efficiency initial value) are described in the protocol.[203] More detailed photovoltaic performance statistics of the devices over time were summarized in Table 3.3. Furthermore, Figure 3.8b displays the decay of the normalized PCE of the 7R-SP based devices and the ZnO-SC based ones after 5000 h (T_{80}). It depicted that the T_{80} degradation for the ZnO-7R-SP iF-OPVs were slower than the ZnO-SC devices where the normalized PCE % for the fabricated ZnO-SC, B-7R-SP, C-7R-SP, and D-7R-SP iPSCs were 76.42 %, 79.68 %, 84.20 %, and 82.72 %, respectively. **Furthermore,** by analyzing the transient normalized performance parameters plotted in Figure 3.9, it can be noticed that the V_{OC} values of the entire devices were maintained during the degradation test for 5000 h (see Figure 3.9a) which might represent the stability of the photoactive layer as it retained inside the glove box[22,23]. In addition, we can notice that J_{SC} values were changed in a different trend as it first enhanced then decreased slowly as shown in **Figure 3.9b**. Also, the values of R_{Sh} declined for the ZnO- SC based devices, while there was a fluctuation between increasing and decreasing for the SP-7R iPSCs (**Figure 3.9c)**. But the R_S was obviously increased for the whole devices (**Figure 3.9d)**. Furthermore, there was a clear diminishing in the FF which might be due to the increment of the R_S of the devices over time as clarified from the normalized FF curve of the degraded iF-OPVs in **Figure 3.8c**. Thus, the latest mentioned Figures confirmed that the decrease in the FF is the main factor that significantly reduces the PCE over time indicating the presence of electrodes or interfacial layers degradation[22,25]. Consequently, it is worth to emphasize that the decay of the performance parameters related to the ZnO-SC based devices were faster than the 7R-SP ones, indicating the higher intrinsic stability of the ZnO-SP based devices. Furthermore, the PCE decay rate over the time for the C-7R-SP based devices was the slowest which might be attributed to the enhanced interface morphology between the photoactive layer and the sprayed ZnO film. Furthermore, these obtained results greatly matched with the dark J-V characteristics as shown in **Figure 3.10**. The figure showed a clear increase in the leakage current upon degradation for the entire devices as confirmed by the fitting parameters for the T_{80} and T_{90} (devices reached 90% from the initial value) listed in Table 3.4 using the mentioned equivalent electric circuit aforementioned in Figure 3.6b. Interestingly, these results present a similar behavior as reported in the previous **works of the long lifetime devices conducted only under nitrogen environment[62,63].**

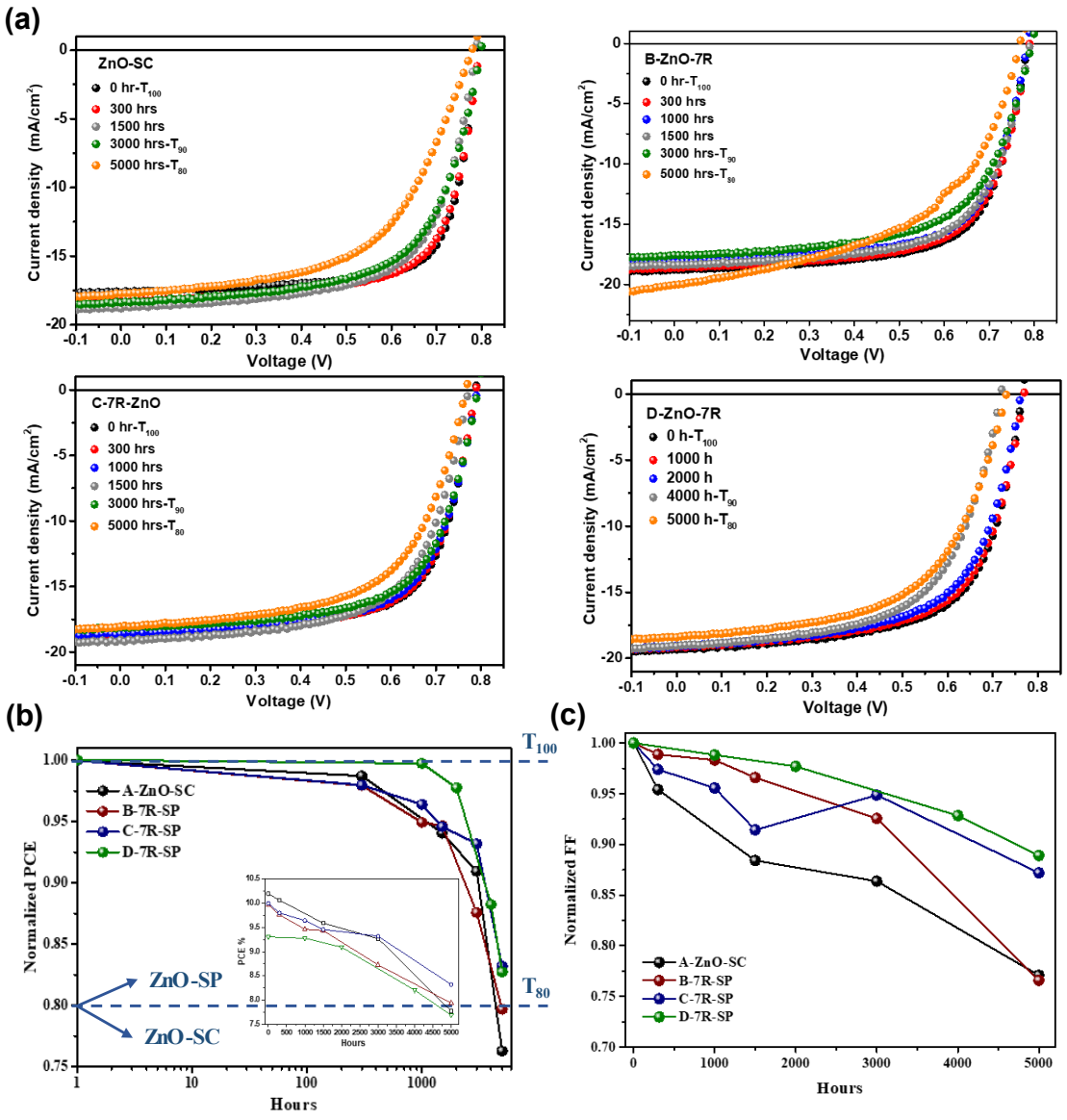

Figure 3.8 (a) J-V characteristic curves, (b) Normalized PCE (c) Normalized FF of the devices over the aging time reaching the T_{80}.

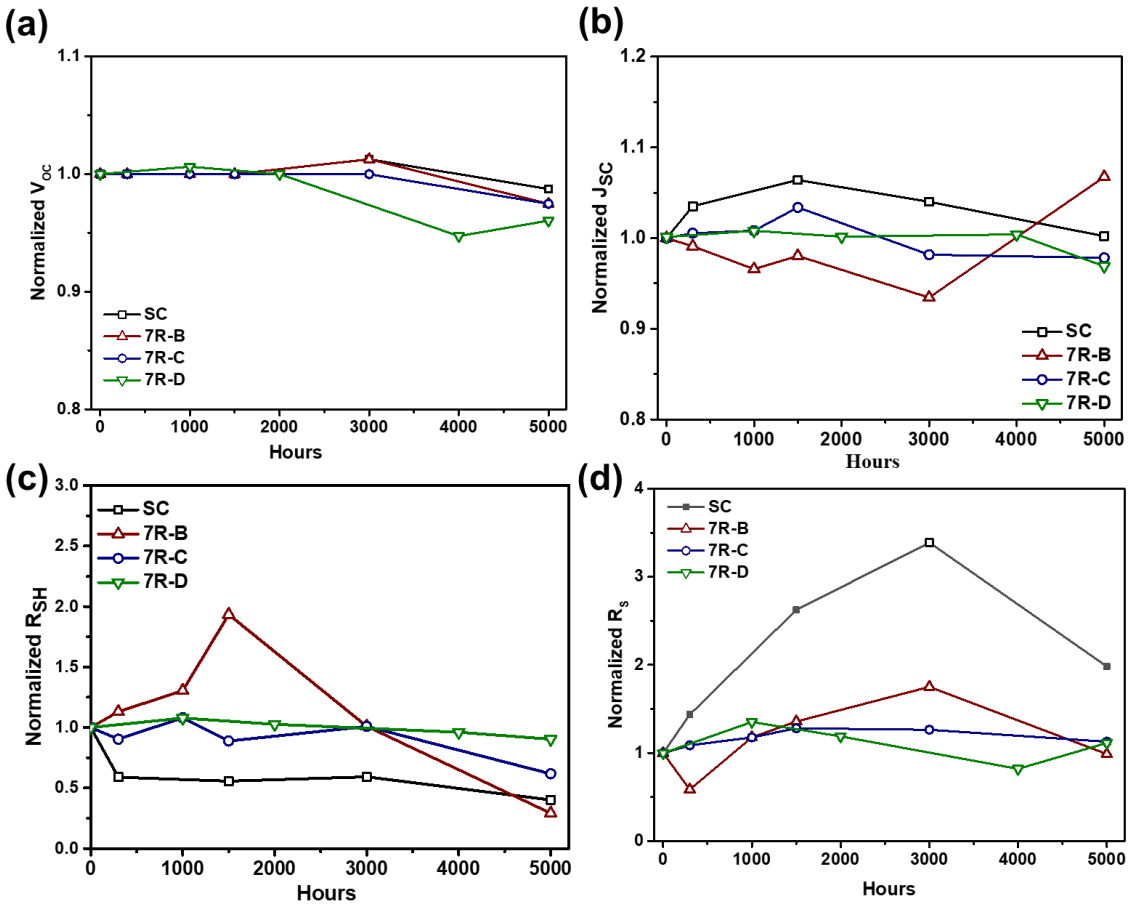

Figure 3.9 (a) Normalized V_{OC}, (b) Normalized J_{SC}, (c) Normalized R_{Sh}, (d) Normalized R_S of the degraded iF-OPVs with respect to the aging time (5000 h)- devices stability study.

Table 3.3 The performance parameters of B-7R-SP, C-7R-SP, D-7R-SP, and ZnO-SC based devices during the degradation analysis over time. The data average of 6 devices for each configuration.

Ddevices	Aging Time (h)	Normalized PCE (%)	V_{OC} (V)	J_{SC} (mA/cm^2)	FF (%)	PCE (%)	R_S (Ω.cm^2)	R_{Sh} (Ω.cm^2)
ZnO-SC	0 (T_{100})	100	0.79	17.69	73.00	10.19	1.03	1140
	300	98.74	0.79	18.30	69.58	10.06	1.48	674
	1500	94.06	0.79	18.82	64.48	9.59	2.71	636
	3000 (~T_{90})	90.95	0.80	18.39	62.99	9.27	3.49	677
	5000 (~T_{80})	76.24	0.78	17.73	56.23	7.77	2.04	458
B-7R-SP	0 (T_{100})	100	0.79	18.78	67.20	9.97	2.47	616
	300	97.96	0.79	18.61	66.39	9.76	1.45	696
	1000	94.95	0.79	18.14	66.02	9.46	2.91	804
	1500	94.67	0.79	18.41	64.86	9.44	3.36	1190
	3000 (~T_{90})	87.58	0.80	17.55	62.15	8.73	4.33	622
	5000 (~T_{80})	79.68	0.77	20.05	51.43	7.94	2.45	179
C-7R-SP	0 (T_{100})	100	0.79	18.46	68.61	10.00	2.83	720
	300	97.99	0.79	18.56	66.85	9.80	3.08	650
	1000	96.42	0.79	18.61	65.59	9.64	3.34	778
	1500	94.59	0.79	19.08	62.75	9.46	3.63	639
	3000 (~T_{90})	93.20	0.79	18.12	65.12	9.32	3.58	727
	5000 (~T_{80})	84.20	0.77	18.05	59.85	8.32	3.20	444
D-7R-SP	0 (T_{100})	100	0.76	19.02	64.21	9.30	2.00	499
	1000	99.76	0.76	19.15	63.61	9.28	2.70	538
	2000	97.78	0.76	19.03	62.88	9.09	2.38	513
	4000 (~T_{90})	88.24	0.71	19.07	59.76	8.21	1.64	480
	5000 (~T_{80})	82.72	0.72	18.41	57.25	7.69	2.23	451

Table 3.4. Fitting values of the degraded (~T_{90} and T_{80}) ZnO-SC and ZnO-SP based devices using SCLC mechanism at reverse Voltage.

T_{90}	n_1	J_{O1} (10^{-12}A/cm^2)	n_2	J_{O2} (A/cm^2)	R_S (Ω.cm^2)	R_{Sh} (Ω.cm^2)	K (A/V^{m}cm^2)	m
ZnO-SC	1.24	0.13	2.0	3.11E-10	2.54	1.85E5	2.00E-6	2.0
7R-B-SP	1.30	0.36	2.0	2.16E-10	3.10	4.04E4	1.85E-5	2.0
7R-C-SP	1.36	1.57	2.0	9.36E-11	2.70	1.92E4	5.50E-5	2.0
7R-D-SP	1.30	1.20	4.5	2.40E-6	1.80	6.02E3	1.80E-4	2.0
T_{80}								
ZnO-SC	1.49	11.00	2.5	4.33E-9	5.59	1.80E5	1.00E-5	2.0
7R-B-SP	1.47	23.10	6.0	2.61E-5	4.80	1.76E2	8.50E-3	2.0
7R-C-SP	1.44	5.50	2.5	5.58E-9	4.20	5.0E3	2.80E-4	2.0
7R-D-SP	1.50	266.00	5.0	9.00E-6	8.39	2.74E3	6.00E-4	2.0

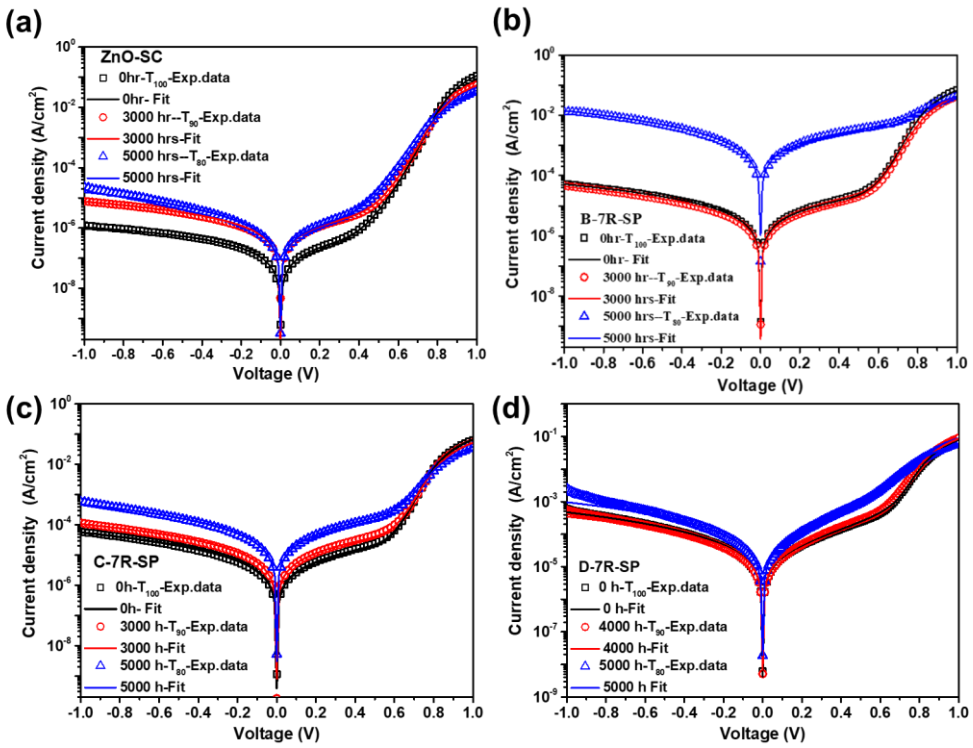

Figure 3.10 J-V characteristic at dark of the ZnO-SC (a), B-7R-SP (b), C-7R-SP (c) and D-7R-SP (d) devices over time (h) under nitrogen environment.

3.3.1.4 Impedance Spectroscopy Insight Analysis for Studying the Effect of ZnO-Interfacial Deposited Layer through SC and 7R-SP Techniques of the Fresh and Aged iF-OPV Devices.

Impedance spectroscopy (IS) characteristics were conducted to gain a comprehensive understanding regarding the electric properties of the fresh and degraded devices upon the interfacial charge transfer and carrier recombination[165] due to the modification of the ZnO-film within the iF-OPVs upon various deposition techniques. IS was used to measure the response of the device when an external alternating current was applied[20464,65]. **Figure 3.11 and 3.12** shows the Cole-Cole plots for the T_{100} fresh and T_{80} degraded devices under illumination at the V_{OC} bias voltage with their corresponding Bode plots which reveals the efficient transfer at the active layer/electrode interfaces.[165] It is worth mentioning that the comparison were performed between the real Z′(Ω) and imaginary Z′′ (Ω) parts of the impedance measurements for the champion devices, C-7R-SP and the controlled reference cell ZnO-SC ones and the other comparisons of the B and D-7R-SP based devices were added in the supporting information Appendence part. On one hand, **Figure 3.11a** shows a typical semicircle behavior of the Cole-Cole plot for the freshly T_{100} ZnO-SC and C-7R-SP based devices. It demonstrates a lower impedance and smaller arc radius size for the ZnO-SC based devices than the C-7R-SP ones. This arc radius variation correlated to the different charge injection or extraction takes

place within the device[165,167,205]. Thus, these obtained results are consistent with the lower R_S values obtained for the ZnO-SC based devices through the J-V characteristics under same illumination conditions (**Table 3.1**). One the other hand, **Figure 3.11b** illustrates the Cole-Cole plot of the aged devices at T_{80} with arc deviation behaviour from the typical shape. Where, only ZnO-SC based devices exhibited a second arc at high frequency. Moreover, it showed a higher arc radius than the C-7R-SP devices.

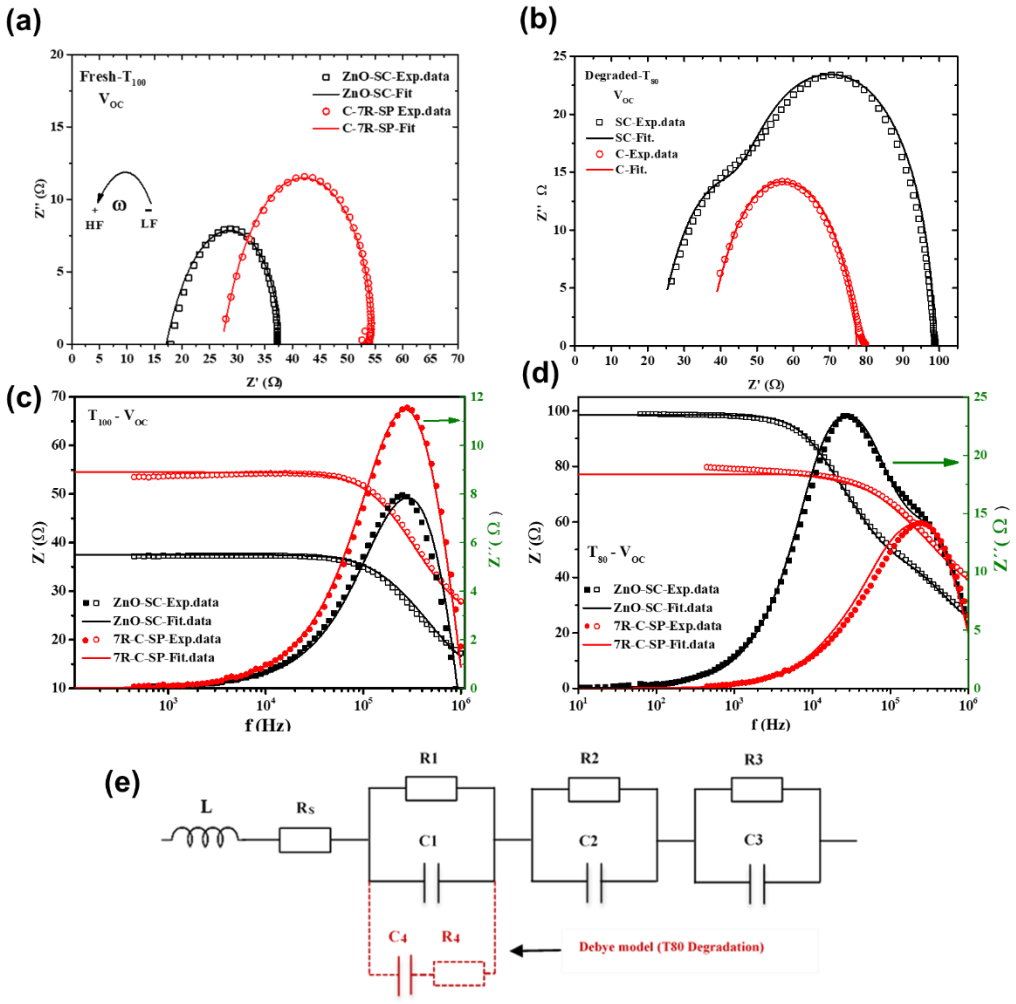

Figure 3.11 Impedance spectra measured under illumination (IS- AM1.5) for ZnO-SC and C-7R-SP iF-OPVs at V_{OC} (a) for the T_{100} freshly prepared devices, (b) for the degraded devices after 5000 h (T_{80}) and the corresponding Bode plots of (c) the T_{100} Fresh devices, and (d) T_{80} aged devices. Using symbols for the experimental data and the fitting results in solid lines by applying the equivalent circuit model (e) 3RC solid black lines for the freshly prepared iF-OPVs and the added dashed red lines for the T_{80} degraded ones following Debye model.

Furthermore, as Arredondo et al. suggested that the low frequency impedance arc indicates the charge accumulation, reflecting inadequate charge extracted by the contacts of the device.[206] Thus, in **Figure 3.11b** we can notice that the low frequency arc was the smallest for the C-7R-SP based devices as well as the arc

size. This behavior reflects the effective charge extraction in the device, confirming the faster degradation behavior of the ZnO-SC based devices as they possess a higher low frequency arc which might be related to the more pronounced charge accumulation effect[91]. The same behaviors were observed in the Cole-Cole plot at V_{MPP} bias voltage of 0.5 V illustrated in **Figure A.1** for the T_{100} and T_{80} conditions in the Appendices part.

As a sequence, to get a deep insight regarding the physical parameters of the fresh and degraded cells and to understand this behavior, we conducted an electrical equivalent circuit to fit the experimental Z´-Z´´ data. The basic electrical circuit components used to fit the plots (Solid lines) presented in Figure 3.11e for the T_{100}-fresh and T_{80} aged cells. It is worth to mention that the components used to fit the plots with one arc, fresh devices, are shown in black solid lines whereas the additional components used to fit the second arc that appeared at high frequency, T_{80} degraded SC-ZnO based ones, are presented in red dashed lines. The proper fitted parameters were listed in Table 3.5. This equivalent circuit possesses a distributed resistor (R) which refers to the electron transportation resistance of each layer within the device. Hence, R_1, R_2 and R_3 components are for ZnO, PTB7-Th:$PC_{70}BM$ active blend layer and the V_2O_5 layer, respectively. In addition, C represents the geometrical capacitance values of each layer, exhibiting a parallel association of resistor and capacitor for 3 RC resistive/capacitive components in series. Moreover, the R_S component represents the metallic wires series resistance as well as the resistance from the ohmic components such as ITO films and Ag electrodes[121,165] and L is the inductor used for proper fitting of the data at high frequency.[165] It is interesting to notice that the model consist of an extra included R_4C_4 in series that connected in parallel to the R_1C_1 of the ZnO film following Debye model,[121,207] considering the presence of a single type of trap created in the corresponding film.[207] Hence, Debye model was the most proper one used to fit the obtained experimental data smiultaneously, clarifying the effect of the modified ZnO-film upon the deposition techniques on the performance and stability behavior of the iF-OPVs devices.

From the fitting values listed in Table 3.5, we manifested that the fitting values of the capacitance of each layer matched greatly with the theoretical ones summarized in Table 3.6. This might reflect that at V_{OC}, the impedance data was governed by the geometrical capacitances given by the metal insulator-metal (MIM) model indicating fully depleted layers behavior.[208,209] Regarding the resistance values obtained from the fitting, several few differences were found for the ZnO-SC vs C-7R-SP iPSCs. But the key variation depicted from the R_S element as the ZnO film deposited by SP technique has higher values than that produced from the ZnO film deposited by SC technique. This explained the higher arc radius along with higher low frequency shift observed for the fresh T_{100} C-7R-SP plot than the ZnO-SC shown in Figure 3.11a. Where, the R_S values for the fresh ZnO-SC were around 7 Ω which might be referred to the ITO film resistance. While for the C-7R-SP, the R_S values were around 12 Ω which could be attributed to the ITO film resistance in addition to the interface resistance between the ZnO- SP based film and the ITO. This observed result is correlated with the Bode plot at V_{OC} and 0.5 V in Figure 3.11x and Figure A1, respectively. This might be

related to the higher interface roughness between the ITO and the ZnO layer coated by SP. Moreover, it is worth noting that the V_{OC} of the entire devices almost did not show a sever change regarding the deposition technique or even for the degradation procedures. Thus, it can be assumed that the main effect was related to the ZnO/ITO interface. Because ITO was the main layer exposed to high temperature of 350 °C during the SP deposition which might affect its interface resistance with the ZnO layer. This revealing the increment of the resistance was not related to the layer itself even it has been deposited by different techniques, but it was related to the interfaces effect.

Table 3.5. The evaluated RC circuits fitting parameters of 7R-C-SP and ZnO-SC iF-OPVs by the 3RC equivalent circuit model for the fresh samples (T_{100}) and Debye model for the degraded devices after 5000 h (~T_{80}) at various applied voltages. For the V_2O_5 layer of the degraded devices, the parameter $\tau = R_4 \times C_4$ where R_4 parameter were demonstrated in Figure 3.11e.

Parameters of Fresh ZnO-SC-iPSCs	**0.8 V (V_{OC})**			**0.5 V**		
V_2O_5	R_S = 7.0 Ω L = 1.7E-6 H	R_1= 8.0 Ω	C_1= 99.0 nF	R_S = 7.0 Ω L =1.7E-6 H	R_1= 9.5 Ω	C_1= 99.0 nF
ZnO		R_2= 17.5 Ω	C_2= 16.0 nF		R_2= 22.8 Ω	C_2= 16.0 nF
The Blend		R_3= 5.0 Ω	C_3= 2.8 nF		R_3= 5.0 Ω	C_3= 2.80 nF
Parameters of degraded ZnO-SC-iPSCs-Debye model	**0.78 V (V_{OC})**			**0.5 V**		
V_2O_5	R_S =4.5 Ω L = 1.7E-6 H	R_1= 53.0 Ω τ = 7.0 µs	C_1= 99.0 nF C_4= 41.0 nF	R_S = 6.0 Ω L= 1.7E-6 H	R_1= 49.0 Ω τ = 8.0 µs	C_1= 99.0 nF C_4= 56.0 nF
ZnO		R_2= 22.0 Ω	C_2= 16.0 nF		R_2= 28.0 Ω	C_2= 16.0 nF
The Blend		R_3= 19.0 Ω	C_3= 2.8 nF		R_3= 19.0 Ω	C_3= 2.8 nF
Parameters of Fresh ZnO-C-7R-SP iPSCs	**0.8 V (V_{OC})**			**0.5 V**		
V_2O_5	R_S = 12.0 Ω L = 1.7E-6 H	R_1= 9.0 Ω	C_1= 99.0 nF	R_S =14.5 Ω L=1.7 E-6 H	R_1= 12.0 Ω	C_1= 99.0 nF
ZnO		R_2= 20.5 Ω	C_2= 19.0 nF		R_2= 24 Ω	C_2= 19.0 nF
The Blend		R_3= 13.0 Ω	C_3= 2.8 nF		R_3= 9.0 Ω	C_3= 2.8 nF
Parameters of degraded ZnO-C-7R-SP iPSCs--Debye model	**0.77 V (V_{OC})**			**0.5 V**		
V_2O_5	R_S = 17.8 Ω L =1.7 E-6 H	R_1= 17.8 Ω τ = 6.0 µs	C_1= 99.0 nF C_4= 41.0 nF	R_S =16.0 Ω L =1.7E-6 H	R_1= 19.0 Ω τ = 6.0 µs	C_1= 99.0 nF C_4= 61.0 nF
ZnO		R_2= 21.0 Ω	C_2= 19.0 nF		R_2= 26.0 Ω	C_2= 19.0 nF
The Blend		R_3= 20.6 Ω	C_3= 2.8 nF		R_3= 24.0 Ω	C_3= 2.8 nF

Table 3.6 Dielectric constants and calculated capacitances for each layer

Layer	ε_{Layer}	**Capacitance (nF)**	**Thickness (nm) d_{Layer}**
V_2O_5	5[166]	99	4
ZnO-SC	6[210]	16	30
ZnO-B-7R-SP	6	24	20
ZnO-C-7R-SP	6	19	25
ZnO-D-7R-SP	6	10	50
Blend	3.5[211,58,212]	2.8	100

The capacitance (C) for each layer has been calculated using the following formula:

$$C = \varepsilon_0 \varepsilon_{Layer} \frac{A}{d_{Layer}}$$

where A is the Active area, d_{Layer} the thickness for each layer, ε_0 vacuum dialectic permittivity and ε_{Layer} the relative dielectric permittivity (the referred values extracted from the references [166], [210], [211],[58], and [212].

Table 3.7 The calculated τ (extracting charge time) of each layer and the total for the fresh and ~T_{80} degraded 7R-C-SP and SC-ZnO iF-OPVs at V_{MPP} (0.5 V) and V_{OC}.

τ (s)/ For ZnO-SC-Fresh iPSCs (T_{100})	**0.5V**	**V_{OC}**	**τ (s)/ For SC-degraded iPSCs (~T_{80})**	**0.5 V**	**V_{OC}**	**τ (s)/ For C-7R-SP-Fresh iPSCs (T_{100})**	**0.5 V**	**V_{OC}**	**τ (s)/ For C-7R-SP-degraded iPSCs (~T_{80})**	**0.5 V**	**V_{OC}**
V_2O_5	9.4E-07	7.9E-07	**V_2O_5**	8.0E-06	7.0E-06	**V_2O_5**	1.2E-06	8.9E-07	**V_2O_5**	6.0E-06	6.0E-06
ZnO	3.7E-07	2.8E-07	**ZnO**	4.5E-07	3.5E-07	**ZnO**	4.6E-07	3.9E-07	**ZnO**	4.9E-07	4.0E-07
Blend	1.4E-08	1.4E-08	**Blend**	5.3E-08	5.3E-08	**Blend**	2.5E-08	3.6E-08	**Blend**	6.7E-08	5.8E-08
τ (s)-Total	1.3E-06	1.1E-06	**τ (s)-Total**	8.5E-06	7.4E-06	**τ (s)-Total**	1.7E-06	1.3E-06	**τ (s)-Total**	6.6E-06	6.5E-06

Furthermore, **Table 3.7** summarizes the extracted charge time (TAU-τ) values for the T_{100} fresh devices at V_{OC} and 0.5 V. Where, at V_{OC} for the fresh prepared iPSCs, the τ of the ZnO-SC ($1.1x10^{-6}$ s) was quite smaller than the ones for the C-7R-SP ($1.3x10^{-6}$ s) which also correlated with the previous obtained results providing quit higher performance of the fresh ZnO-SC devices. The same trend of the results has been observed for the devices at 0.5 V (see **Table 3.7**).

Regarding to the additional arc observed in **Figure 3.11b** at high frequency for the T_{80} ZnO-SC based degraded devices, it was successfully fitted by the extra R_4C_4 circuit through Debye model[73]. On one side, it is essential to note that the extra C_4 value of the V_2O_5 layer of both ZnO-SC and C-7R-SP were almost the same giving the highest layer capacitance in the devices which limits the performance for both devices, revealing the implementation of a single type of traps in the V_2O_5 layer during the degradation process. On the other side, this second arc could be explained by the noticeable increment in the resistance of the V_2O_5 layer in the T_{80} degraded ZnO-SC iPSCs (53.0 Ω) in comparison with the C-7R-SP cells (17.8 Ω) as showed in **Table 3.5**. Moreover, **Figure 3.11d Figures A.1d** illustrates the Bode plots of the ZnO-SC and C-7R-SP based devices at V_{OC} and 0.5 V for T_{80} degraded iF-OPVs. These plots confirm the higher resistance observed by the ZnO-SC devices after T_{80} degradation which result in declining the devices performance along with

the stability. In addition, the τ for the degraded ZnO-SC iPSCs (7.4 x 10^{-6} s) was higher than the ones of C-7R-SP (6.5 x 10^{-6} s) at V_{OC} as shown in **Table 3.7**. As it was limited by V_2O_5 layer upon the highest R and C values. Same considered behavior observed at 0.5 V for the T_{80} degraded IF-OPVs. That might be the same reason of increasing the arc size for the T_{80}-degraded ZnO-SC devices more than the C-7R-SP devices at **Figure 3.11b.** Upon this context, this could be attributed to the interfacial effect takes place upon the ZnO deposition mechanism using the SP where tiny spray droplets quickly dried on a hot substrate (350 °C) which immediately evaporates on top of the ITO, avoiding the accumulation or retaining of any solvents or moisture inside the ZnO layer during the deposition, resulting in enhancing the ZnO film quality. In turn, it minimizes the defects in the ZnO film, avoiding the ZnO and contacted layers degradation and consequently stabilizes the entire device. Furthermore, the same behavior of the Cole-Cole plots and the Bode corresponding plots were detected for the B-7R-SP and D-7R-SP samples as shown in **Figure A.2** and the summarized fitting parameters in **Table A.1** in the Appendices part. Finally, it can be noticed that the C and τ were quite equal for both fresh ZnO-SC and C-7R-SP based devices. However, the T_{80} stability test depicts that C-7R-SP based devices showed lower τ and lower performance decay than the ZnO-SC ones, indicating enhanced stability behavior that as well confirmed by the aforementioned J-V analysis**.**

A further procedure to study the behavior of the recombination mechanisms through impedance spectroscopy technique is the capacitance-frequency (Cf) measurements to evaluate the trap density of state (DOS). As known that the main source of traps in the organic photovoltaic reveal to the disorder.[64] Therefore, this characterization was carried out for OPVs in many reported research work to investigate the change in trap emission along with the imperfection and energetically disorder-exhibited tail states inside the cells[64,121,165,171169]. It is well known that as the trap densities are high, then trapped charge carrier still can participate in the transportation by thermally hopping or tunneling (shallow traps), while deep traps creates recombination centers due to hardly excited back charges.[64] This characterization has been performed for OPVs in many research work to obtain the change in trap emission and disorder-induced tail states within the devices.[64,165,169–171] Accordingly, at a given energy level, E_ω, we can calculate the traps DOS by varying the capacitance with respect to the frequency of the device. This corresponds the charge release by shallow traps in the band gap close to the Fermi energy level as given by the Equation 3.2[64,171]

$$\mathrm{DOS}(E_\omega)_{traps} = -\frac{V_{OC}\omega}{t\,q\,T\,k_B}\frac{\partial\,\mathrm{C}}{\partial\,\omega} \qquad \textbf{3.2}$$

where, V_{OC} is the open circuit voltage from the J-V characteristics (see **Table 3.1**) under illumination conditions, C is the measured capacitance, ω is the angular frequency, k_B is the Boltzmann constant, t is the thickness of the layer, q is the electron charge and T is room temperature (around 300K).

To evaluate the relation of the dependency of energy on the trap-DOS, we applied the following equation 3.3:

$$(E_\omega)_{traps} = k_B \, T \ln \frac{2\beta N}{\omega} = E_O - k_B \, T \ln\omega \qquad \textbf{3.3}$$

where, N is the effective density of state and β is the cross section.[172] By assuming that 2βN does not depend on of the value of the frequency, hence, the value variation is corelated to the shift in the DOS values on energy scale (E_O).[171] **Figure 3.12** displays the calculated trap-DOS plotted as a function of energy for T_{100} and T_{80} devices. We noticed that, all samples exhibited the same carrier response and trap activation energy, showing a single exponential trap distribution with almost same slope values.[58] However, for the T_{100} fresh samples in **Figure 3.12a**, D-7R-SP based devices depicted the lowest DOS values for a given frequency.

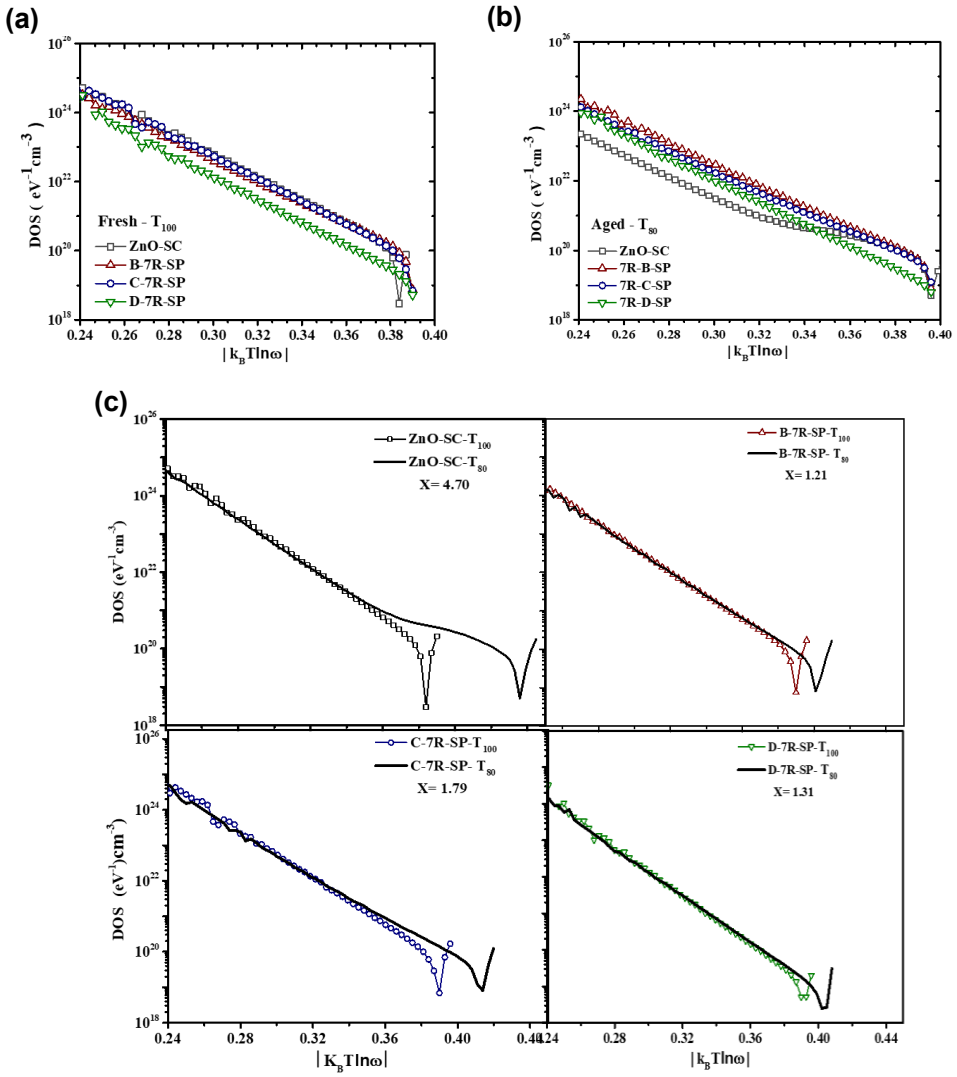

Figure 3.12 Density of state (DOS) as a function of energy at V_{OC} for (a) the freshly prepared T_{100} devices (b) T_{80} degraded devices (c) the freshly prepared T_{100} and ~T_{80} degraded iF-OPVs illustrated by the shifting value (X).

This behaviour might be explained through Equation 3.3, as a shift in the E_O value due to the increase of the β.N value. Accordingly, it expected to have the lower energy due to higher traps located (deep traps attitude) in the device which confirm the low performance of the D-7R-SP based samples. In **Figure 3.12b**, it can be found that the T_{80} degraded ZnO-SC devices create more trapping sites than the ZnO-SP based devices. Furthermore, it can be noticed that a deep traps states behavior was observed only for the ZnO-SC based devices due to the degradation process. On the other hand, the devices fabricated by ZnO-SP technique showed only shallow traps of tail states. This exhibited observation is greatly matches with the IS measurements in **Figure 3.11b**, showing a second arc implemented for the ZnO-SC based devices.

Furthermore, by calculating the energy shift values (X) of the T_{100} fresh and the T_{80} aged devices through the following equations:

As $(E_\omega)_{traps} = k_B\,T \ln\frac{2\beta N}{\omega} = E_o - k_B T \ln\omega$ and $\alpha = 2\beta N$

So, $E_{Fresh} = k_B T \ln\frac{\alpha_F}{\omega}$ and $E_{Degraded} = k_B T \ln\frac{\alpha_D}{\omega}$

Hence, to get the value of the shifting upon the degradation shown in **Figure 3.12b** we apply the following calculations assuming a frequency given

$E_D - E_F = E_{OD} - E_{OF} = k_B T \ln\alpha_D - k_B T \ln\alpha_F = k_B\,T \ln\frac{\alpha_D}{\alpha_F}$

$$\frac{\alpha_D}{\alpha_F} = \exp\left(\frac{E_D - E_F}{k_B T}\right) = \frac{\beta_D . N_D}{\beta_F . N_F} = X \qquad \textbf{3.4}$$

Consequently, through comparing the energy shift values of the T_{100} fresh and the T_{80} degraded samples shown in **Figure 3.12c,** we obtained that the T_{80} degraded ZnO-SC based devices possessed almost five times trapping sites more than the T_{100} fresh ones. While the T_{80} degraded ZnO-SP based devices showed less than double trapping of tail state only. Accordingly, after 5000 h of degradation it can be said that the ZnO- SP iF-OPVs revealed higher stability behaviour than ZnO-SC devices, confirming the previously mentioned J-V and IS degradation analysis.

3.3.2 Part II: Further Modification through Low Concentrated ZnO Precursor Solution.

In this part of the work, we report the use of intermittent spray pyrolysis technique, applying the optimized deposition parameters achieved in Part I, to modify the ZnO film using low concentrations of ZnO precursor solution aforestated in the **3.2 experimental section**. The investigation was mainly towards modifying the substrate coverage and surface morphology of the ZnO films and pointing out the morphological compact spot where ZnO films can achieve similar benchmark efficiency along with improved stability behavior. Then, relating the exhibited microstructure-morphology- of the ZnO film with the photovoltaic performance

of the fabricated fresh and aged devices. Accordingly, the insight gained into the importance of the surface morphology of sprayed ZnO films highly assisted the development of the film quality[111,116,122,190].The demonstrated PCE values of the fabricated devices are either better than or comparable to Part I reports accounted by different ZnO precursor solution concentration as well as conventional spin coating technique [30,112,121] .However, in this part, a novel and pioneer record behavior of the iF-OPVs is presented via significant enhancement of its stability achieving 12000 hours (16.7 months). This improvement was provided through the modification of the ZnO interfacial layer concentration along with the spraying deposition parameters.

For easy distinguish the optimization performed on the ZnO film, we labelled the fabricated iF-OPVs as I, II, III and IV for the devices with 15R, 20R, 25R and 30R spraying number of running cycles to optimize the ZnO layer, respectively. **Figure 3.13** displays the current density-voltage (J-V) characteristics of the freshly fabricated iF-OPVs-T_{100}- with different processing of ZnO-spraying running cycles measured under illumination and dark conditions. The obtained photovoltaic parameters statistics of the corresponding devices are listed in **Table 3.8**. As demonstrated in **Figure 3.13a**, it can be noticed that all the devices have almost the same open circuit voltage value (V_{OC}). Moreover, III based devices (25R-ZnO) demonstrated the champion performance, as it exhibited maximum PCE of 9.86 %, with an average V_{OC} of 0.8 V, a current density (J_{SC}) of 18.42 mA cm^{-2}, fill factor (FF) of 0.67, series resistance (R_S) of 2.31 Ω cm^2 and shunt resistance (R_{Sh}) of 774 Ω cm^2. On the other hand, devices I (15R-ZnO) possessed the lowest performance parameters with maximum PCE, average V_{OC}, J_{SC}, FF, R_S and R_{Sh} of 7.76 %, 0.78 V, 17.17 mA cm^{-2}, 0.54, 4.63 Ω cm^2, and 429 Ω cm^2, respectively. Furthermore, devices II (20R-ZnO) showed performance parameters with maximum PCE, average V_{OC}, J_{SC}, FF, R_S, and R_{Sh} of 9.80%, 0.79 V, 18.26 mA cm^{-2}, 0.66, 2.83 Ω cm^2, and 765 Ω cm^2, respectively, and devices IV (30R-ZnO) with 9.60 %, 0.78 V, 18.88 mA cm^{-2}, 0.63, 3.07 Ω cm^2, and 381 Ω cm^2, respectively.

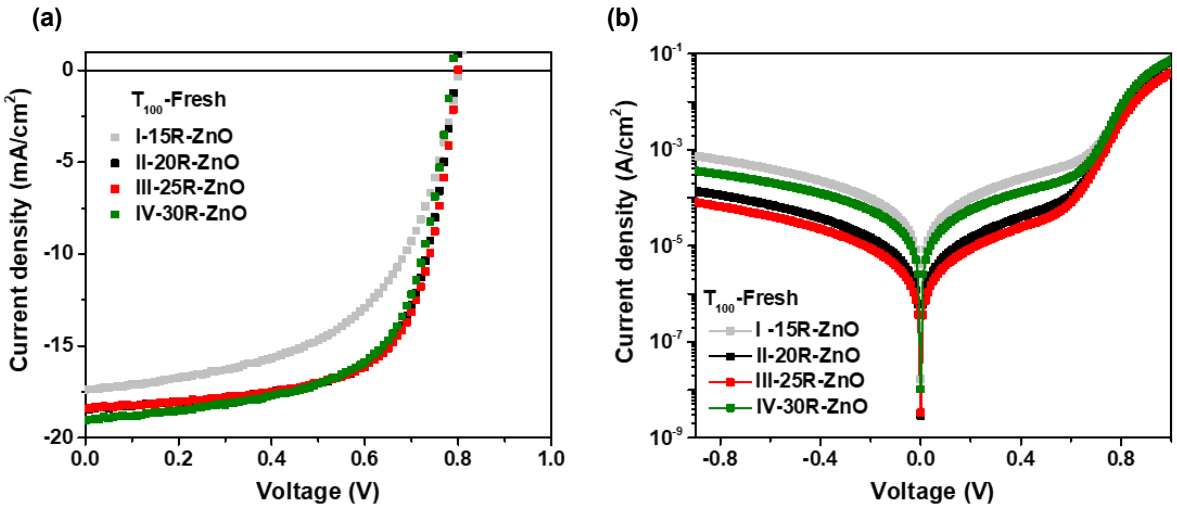

Figure 3.13 Current density- voltage (J-V) characteristic curves (a) under AM 1.5 G illumination (b) at dark condition of fresh iF-OPVs.

It is worth mentioning that the number of spraying running cycles (R) controls the thickness of the formed ZnO film. Hence, we observed that as the ZnO thickness increases (R-increases), the J_{SC} of the fabricated devices improves. However, in devices IV (30R-ZnO), the slight enhancement of the J_{SC} was at the expense of marginal reduction of the V_{OC}, FF and as a sequence diminishing the PCE as shown in **Table 3.8**. **Figure 3.12b** shows the dark J-V curves for the freshly fabricated iF-OPVs. Under reverse bias, we obtained one order of magnitude lower leakage current for II and III devices than I and IV ones**.** This obtained less leakage current in the II and III devices might be attributed to the higher shunt resistance R_{Sh}[91] values of 1.64 x 10^4 in device II and 2.69 x 10^4 Ω cm^2 in devices III than 2.32 x 10^3 of devices I and 3.88 x 10^3 Ω cm^2 of devices IV at dark. This enhancement in the R_{Sh} in the II and III based devices discloses the lower charge carrier recombination in the active blend film[95] .This behavior agrees with the enhanced FF observed for devices II and III (**Table 3.8**). In addition, the diminished FF and J_{SC} value for devices I under illumination (**Figure 3.13a**) matches the highest leakage current obtained under dark that shown in **Figure 3.13b.**

Table 3.8. Photovoltaic performance parameters statistics of the devices, extracted from an average of at least 9 devices.

DEVICE T_{100}	V_{OC} (V)	J_{SC} (mA/cm^2)	FF	PCE (%)	PCE_{MAX} (%)	R_S (Ω cm^2)	R_{SH} (Ω cm^2)
I-15R-ZnO	0.78 ± 0.02	17.17 ± 0.20	0.54 ± 0.02	7.53 ± 0.23	7.76	4.63 ± 0.41	429 ± 26
II-20R-ZnO	0.79 ± 0.01	18.26 ± 0.12	0.66 ± 0.01	9.71 ± 0.09	9.80	2.83 ± 0.32	765 ± 17
III-25R-ZnO	0.80 ± 0.02	18.42 ± 0.19	0.67 ± 0.04	9.80 ± 0.11	9.86	2.31 ± 0.11	774 ± 24
IV-30R-ZnO	0.78 ± 0.01	18.88 ± 0.31	0.63 ± 0.03	9.46 ± 0.14	9.60	3.07 ± 0.43	381 ± 19

Figure 3.14 illustrates the AFM surface topographic and phase images of ZnO thin film deposited by the spray pyrolysis onto glass substrate to investigate the morphological variations of the sprayed ZnO-Films. The average thickness of the ZnO films were optimized as a function of the number of spraying running cycles, where the varied number of running cycles of 15R-ZnO, 20R-ZnO, 25R-ZnO and 30R-ZnO corresponded to 10, 18, 25, and 35 nm, respectively. As can be noticed in the 15R-ZnO film in Figure 3.14a, it contains many defects that lead to erratic surface with RMS of 2.86 nm. While, after increasing the number of spraying running cycles to 20R and 25R, the thicknesses increased, however, the ZnO film obtained was featureless and homogenous that leads to roughness reduction to RMS of 2.13 and 1.77 nm, respectively as presented in Figure 3.14b,c. In addition, by further increasing the spraying running cycles to 30R, the roughness increased to RMS of 2.61 nm (**Figure 3.14d**). Interestingly, same behavior was obtained for L. Jagadamma et.al and Z. Ma works.[112,122] The relation between the ZnO film thicknesses and the RMS values demonstrated in Figure 3.14e. We imply that the effect might be due to the ZnO surface coverage during the ZnO precursor solution spraying processes as simplified in **Figure 3.14f**. Where in the 15R based film, the surface was not fully covered which cause some surface imperfection. That basically matches with the Low FF, R_{Sh} and high R_S values observed from the I based cells. Then, by increasing the spraying running cycles to 20R and 25R, we noticed that the film roughness diminished, reflecting uniform sprayed ZnO-film along with better dense and quality. This surprising behavior confirms the higher R_{Sh}, FF and the lower R_S values obtained for B and C based devices. Moreover, regarding the 30R-ZnO film, the higher roughness might be attributed to the excess of the ZnO-precursor solution sprayed that leads to some surface aggregations and non-homogenous ZnO film that may cause the rise of the film roughness. Consequently, we observed that 15R and 30R based ZnO films possessed the highest surface roughness that declare the higher leakage current[213] obtained from I and IV based devices as previously discussed in **Figure 3.13b**. It is worthy to notice that, as compared to Part I reported work as well as L. Jagadamma et.al work [112,121], we found out that the mentioned surface modification performed for the ZnO-film in the current work via the intermittent spray pyrolysis approach using low concentration of ZnO solution (section 3.2 Experimental Methods) suppressed the surface roughness of the deposited ZnO film, exhibiting better film quality along with providing higher based devices performance.

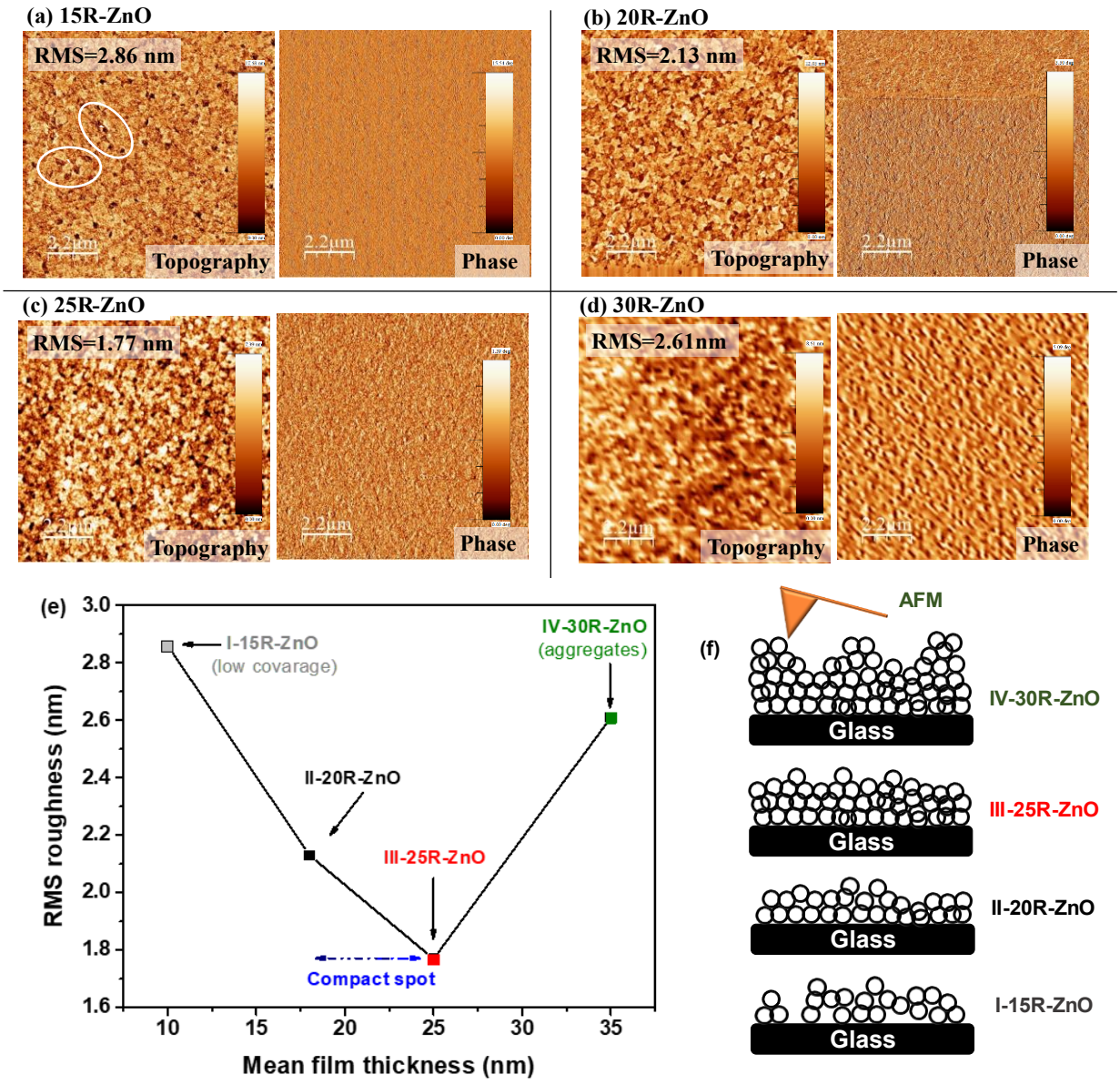

Figure 3.14 AFM topographic and phase images of the ZnO film with (a) 15R (Thickness=10 nm), (b) 20R (Thickness=18 nm), (c) 25R (Thickness=25 nm), and (d) 30R (Thickness=35 nm). (e) RMS surface roughness of ZnO films as a function of film thickness. (f) Schematics simplifying the evaluated ZnO surface morphology measured by the AFM tip.

Figure 3.15a implies the external quantum efficiency (EQE) response of the fabricated devices. As shown, the trend of EQE is almost similar to J_{SC} of the fabricated iF-OPVs with different thicknesses of ZnO-film. Regarding the absorption spectra of donor and acceptor materials, all devices display photo-response spectra with broad range of 300 to 800 nm which mainly attributed to the absorption spectra of PTB7-Th:PC_{70}BM blend.[31] Devices based I-15R-ZnO showed the lowest maximum plateau-photoresponses of 80 %, while II and IV based devices possessed 90% and III devices exhibited the highest plateau value of 95%. This

observed reduction in the spectra of devices I might be related to the insufficient charge extraction and transport mechanism that highly matches their low obtained performance parameters, as listed in Table 3.8. Furthermore, we note that the calculated integrated J_{SC} values from the EQE spectra are 15.79, 17.98, 18.01 and 17.12 mA cm^{-2} for I, II, III and IV devices respectively. These calculated J_{SC} basically confirm the obtained values by the J-V measurements under illumination with approximate error percentage less than 10 (Table 3.8). For farther understanding the influence of different R to perform the ZnO-film on the underlying PTB7-Th: $PC_{70}BM$ blend films and investigate the relation regard enhancing the J_{SC} in the fabricated cells, the UV-visible transmittance spectrum was conducted for the sprayed ZnO films with different, R, thicknesses as presented in Figure 3.15b. On one hand, we compare the effect of the deposition techniques on the transmittance (T %) of the performed ZnO-Film. As, in Figure 3.15b, we demonstrated the transmittance of ZnO films fabricated by the spin coating technique (ZnO-SC) in the Part I work and the current studied ones deposited by the intermittent-SP technique. It was interesting to manifest that the ZnO film sprayed by the SP technique (ZnO-SP) exhibited higher T% compared to the ZnO film deposited by the spin coating films (ZnO-SC). That can be noticed by the naked eye as demonstrated in the inset photos of the ZnO-films in Figure 3.15b. This means that the ZnO-SP films allow more light passed to be absorbed by the active layer and therefore enhances the photogeneration of charges. Interestingly, this behavior was confirmed by the UV-Visible absorbance spectra of the ZnO/active blend for each based device configuration as illustrated in Figure 3.15c. This reveals the enhancement of the J_{SC} values that were noticeable for the ZnO-SP based devices. On the other hand, in the current work, we compare the transmittance of the ZnO sprayed films with different thicknesses. The obtained results followed the logical trend where transmittance decreases as thickness increases. Furthermore, it is important to mention that, however, I-15R-ZnO based film has the lowest thickness, the highest transmittance (Figure 3.15b) and high absorbance respond (Figure 3.15c), but it exhibited lowest J_{SC} value (Table 3.8). This might be attributed to the major defects obtained in the 15R-ZnO-film as discussed previously (Figure 3.14a) that lead to higher film roughness. This behavior devoted the high R_S and low R_{Sh} values that explain the diminishing in the FF and as a sequence the reduction of the PCE of I based devices (15R-ZnO) (Table 3.8). Moreover, we can see that IV-30R-ZnO-film possessed the lower transmittance (Figure 3.15b), but the IV based devices own the highest J_{SC} value, which might be attributed to the highest absorbance responses observed in Figure 3.15c. Similar behavior was noticed in our Part I work which suggested to be related to the film roughness. As the film roughness increases, it assists the light trapping inside the solar cells that plays an important role in increasing the light absorbance by the active absorber layer.[199,200] Consequently, higher photogeneration of charges can be exhibited resulting in higher J_{SC} value of the fabricated devices.

Furthermore, it was interesting to observe the reason behind diminishing the J_{SC}, V_{OC} and the PCE of the I based devices through investigating the blend film optical properties using the Urbach Equation as following[162,163]:

$$\alpha(E) = \alpha_0 \, e^{(E-E_g)/E_U} \qquad \textbf{3.5}$$

where, α (E) is the optical absorption coefficient, α_0 is the band edge optical absorption coefficient, E is the photon energy and E_U is the Urbach Energy. The E_U value describes the energetic disorder in the molecular orbitals as it features the density of state distribution[162] which is considered as a valuable parameter revealing the influence of all possible defects.[164] Upon this context, the smaller E_U value reveals the abrupt band edge[100,163]. **Figure 3.15d** showed the double logarithmic scale of the EQE vs the photon energy to manifest the effect of the ZnO-film thickness sprayed by SP on the optical properties of the blend active layer. We noticed that all the devices obtained a similar slope of tail state distribution at low energy regime. This behavior describes the quiet negligible effect of the energetic disorder of the active blend.[8] Moreover, the calculated E_U values (in the inset of **Figure 3.15d**) were a bit close for all cells; however, the lowest E_U value was obtained for devices III. This might reflect the less induced disorder distribution in the III based devices that matches with their highest V_{OC} value and provides the champion performance among the other cells (**Table 3.8**). In contrast to the I based devices which have the highest E_U value, indicating a bit higher disorder that leads to suppress the V_{OC}, J_{SC} and FF of I based devices and consequently the device PCE as confirmed by the J-V characteristics (**Figure 3.13, Table 3.8**). As known that the charge carrier extraction possibility can be used to unravel the mechanisms behind the current loss during charge extraction, which is basically counted by the carrier transport layers and the interfaces between these layers and the active layers.[186,214] Accordingly, for more consistent comparison between the fabricated iF-OPVs, we calculated the dependence of the photocurrent (J_{Ph}) on the effective voltage (V_{eff}) to determine the exciton dissociation probabilities (P_{diss}), the generation rate (G_{rat}) of the free charge carriers and the maximum amount of absorbed photons that impart the dissociation and generation of free carriers (G_{max}) in the fabricated iF-OPVs as mentioned previously in Chapter 2[49,149] **.**J_{Ph} is described as J_L - J_D, where J_L is the current density under light illumination and J_D is the current density at dark. V_{eff} is defined as V_O -V, where V_O is the voltage when J_{Ph} = 0 and V is the applied voltage.[147,150,151] The $G_{max,}$ values were obtained by calculating G_{max}= J_{sat} / qL,[49,149,151,152] where J_{sat} is the saturation current density, L is the thickness of the blend film and q is the elementary charge. Then we evaluated P_{diss}, and G_{rat} values from the equations[49,149,151,152]of , P_{diss} = J_{SC} / J_{sat} and G_{rat}= P_{diss} G_{max},. **Table 3.9** lists the calculated optoelectronic parameters from the J_{ph}-V_{eff} characteristics. In **Figure 3.15e**, we depicted the curves of J_{ph} -V_{eff} in double logarithmic scale for the cells. The exhibited results denoted that the J_{Ph} of the devices increased linearly at low V_{eff} (V_{eff} < 0.5 V for I based devices and V_{eff} < 0.2 V for the II, III and IV based devices), then, it tends to saturate indicating the proper charge carrier

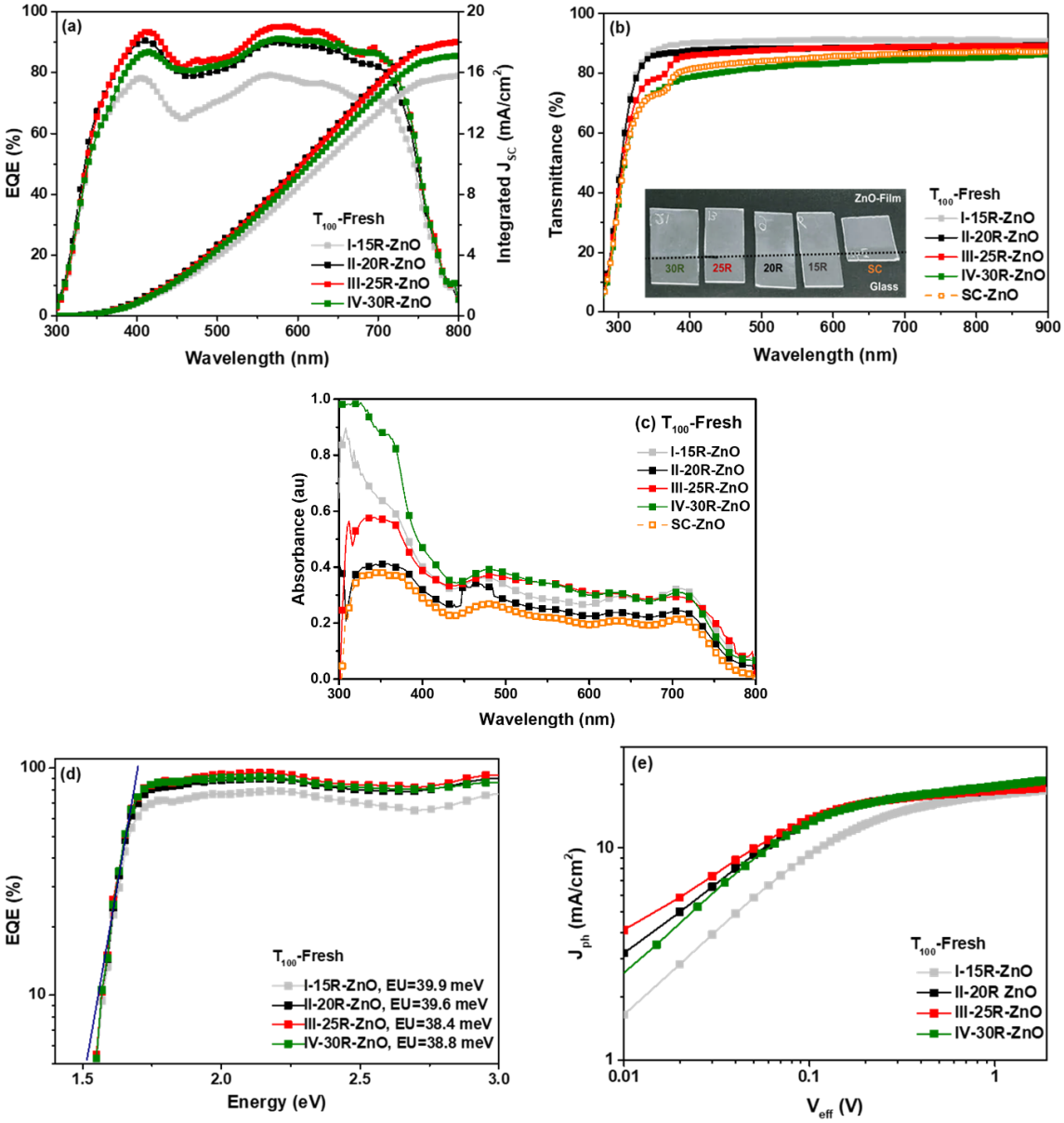

Figure 3.15 (a) EQE spectra (left) and the integrated short circuit current (right) of the fresh fabricated iF-OPVs, (b) UV-vis optical transmittance characteristics, (c) UV-Vis optical absorbance characteristics of the various ZnO-Films deposited by intermittent spray pyrolysis (15R, 20R, 25R and 30R) along with the ZnO film coated by spin coating technique reported in our previous work[121], (d) EQE vs photon energy of the fresh iF-OPVs with the inset values of Urbach energy (E_U), (e) J_{Ph} versus V_{eff} curves of the fresh iF-OPVs with various thicknesses of ZnO-interfacial layer.

separation.[149] Moreover, the J_{sat} values evaluated from **Figure 3.15e**, showed that B, C and D based cells have more efficient charge carriers separation within the interfaces of the active absorber layer [147,149] than the

A based devices (**Table 2**).In addition, the values of the G_{max} for the I, II, III and IV devices were 1.11×10^{28}, 1.16×10^{28}, 1.17 and 1.22×10^{28} m^{-3} s^{-1}, respectively. It is interesting to notice that the highest value of the G_{max} was for IV based devices consisting with its highest J_{SC} value obtained from the J-V characteristics under illumination (**Figure 3.13a**). In turn, this behavior matched with the G_{rat} values (**Table 3.9**) of the devices, indicating the effective dissociation of the photogenerated excitons for II, III and IV based devices than I cells which consistent with the corresponding performance of the devices (**Table 3.8**). However, the P_{diss} value was higher for II and III devices more than I and IV ones which correlate with their highest FFs and PCEs values (**Table 3.8**). In addition, the maximum value of P_{diss} was achieved for the III based devices (98.51 %) with 25R-ZnO film of 25 nm thickness that may imply that the 25R modification condition provided the highest level of surface passivation to the device.[214] This observation is highly matched with the lowest film roughness obtained for the 25R-ZnO film showing better surface coverage **Figure 3.14**.

Table 3.9 Optoelectronic parameters calculated from the J_{ph} -V_{eff} curves of the fresh fabricated iF-OPVs.

DEVICE T_{100}	J-sat (mA/cm^2)	G_{max} (× 10^{28} m^{-3} s^{-1})	P_{diss} (%)	G_{rat} (× 10^{30} m^{-3} s^{-1})
I-15R-ZnO	17.80	1.11	97.60	1.08
II-20R-ZnO	18.66	1.16	98.51	1.15
III-25R-ZnO	18.75	1.17	98.24	1.15
IV-30R-ZnO	19.60	1.22	97.15	1.19

In the following part, we performed a degradation study, following the same conditions as Part I. The goal of this study is to manifest the modification effect of the ZnO-film by the intermittent spray pyrolysis approach on the stability behavior of the fabricated devices. In addition, it is crucial to indicate the intrinsic degradation mechanisms upon the influence of the interfacial layers. Figure 3.16a shows the illuminated J-V characteristics of the studied devices with respect to aging time until they achieved about T_{80}. More detailed photovoltaic performance statistics of the devices over time were listed in Table 3.10. In addition, the decrease in the performance of the degraded devices over time was described in Figure A.3. It is worth mentioning that I-15R-ZnO based devices were excluded from the degradation comparison as it showed the lowest performance behavior. Hence, we focused on comparing the champion devices of III-25R-ZnO with the high performance iF-OPVs of II-20R-ZnO and IV-30R-ZnO ones. On one hand, it can be generally observed that the J-V curves of the entire degraded cells (after 12000 h) showed a pronounced shift to lower J_{SC} respect to the fresh devices (T_{100}). On the other hand, the change in the V_{OC} was not noticeable for the degraded cells compared to the fresh ones. These behaviors were clearly observed in Figure 3.16b for the V_{OC} and J_{SC} normalized parameters of the degraded devices over aging time.

Moreover, it was interesting to notice that devices II and IV reached their 80 % of their initial PCE after 12000 h (16.7 months), while devices III still retaining 85 % of their initial PCE as illustrated in the normalized PCE with respect to the time in Figure 3.16b. Remarkably, by considering the results in Part I, we can clearly notice that the ZnO-SC and the C-ZnO-SP (sprayed via -7R- high concentration of ZnO precursor solution) based iF-OPV devices achieved almost T_{80} after 5000 h only, demonstrating lower stability performance as compared to the work in Part II as illustrated in Figure 3.16b.

Furthermore, the FF showed a higher stable behavior for III based devices than II and IV cells, where after 12000 h the FF values were 0.66, 0.57 and 0.57 for III, II and IV devices, respectively (Table 3.10). That might be devoted to the slight increase as well as the marginal decrease of the R_S and R_{Sh}, respectively, of III based devices during the degradation time as presented in Figure 3.16b. Accordingly, it might be the main reason for retaining devices III with the highest performance after 12000 h rendering the most stable behavior among the other devices.

It was interesting to observe an increase in the J_{SC} values of the II-20R-ZnO device after 8000 h then declined again till T_{80}. A similar behavior was exhibited for the III-25R-ZnO and IV-30R-ZnO devices after 9000 h, then decrease till the 12000 h. This increment in the J_{SC} values may deliver from the UV-irradiation dependence, reported as light-soaking effect occurred during the measurements of the degraded devices, , when the UV components from the solar simulator spectrum irradiate the cells[215]. This phenomenon was widely observed for the degraded inverted OPVs using ZnO or other metal oxide materials as ETL[215]. There are two main suggested mechanisms behind the origin of this phenomenon. First, it may obtain from the photo-induced rearrangement of the Fermi levels at the ITO/metal oxides interfaces upon the filling of trap states during the light exposure, that diminishes the potential barrier and thus enhance the electron extraction through the ITO/metal oxide interface[215]. Second, the interfacial dipole clue role between the metal-oxide and the organic blend film interface as reported elsewhere [216]. This behavior was confirmed by a bit reduction in the R_S values during degradation (Figure 3.16b) followed by a rapid increase, which reflects the slightly enhanced FF as well then diminishing again till 12000 h for the degraded devices (Figure 3.16b). Hence, these obtained results along with the compared L. Jagadamma et al. reported work[112]carried out with same condition of degradation providing maximum of 13 month of degradation, we indicated higher performance as well as stability behavior for the III based device regarding the modified ZnO-film sprayed with 25R. In addition, up on the context in Table 3.11, it is worth to clarify that, our ZnO-film modified based iF-OPVs devices presented a pioneer record of stability behavior among the previous reported studies using same photoactive absorber blend in N_2 atmosphere without encapsulation. Figure 3.16c presents the evaluation of the J-V characteristics at dark of the representative degraded devices. The devices showed an increase in the leakage current by one order of magnitude difference between the fresh and degraded cells. That greatly matched with the noticed reduction in the J_{SC} values of the degraded devices in Figure 3.16a. Moreover, it

was surprising to find that IV-30R-ZnO devices showed a bit lower leakage current after 8000 h, then increased by twofold till the T_{80}. This behavior might be attributed to the mentioned light soaking phenomena of the inverted OPVs through diminishing the photoinduced shunts which enhance the R_{Sh} [215,216] then further increased as illustrated in Figure 5b, confirming the increment of the J_{SC}[72]during degradation then decline till 12000 has discussed previously.

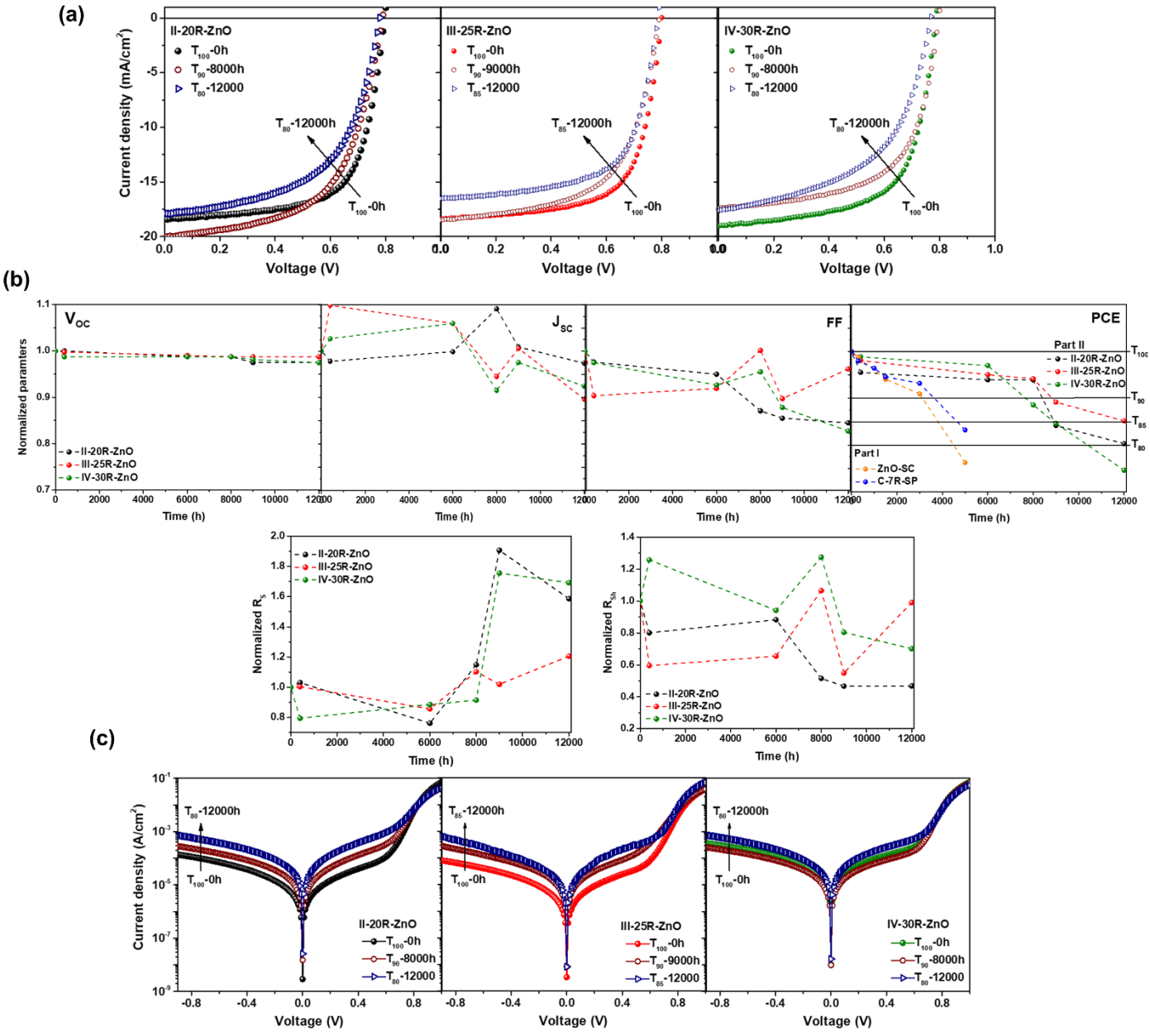

Figure 3.16 (a) Current density- voltage (J-V) characteristic curves under AM 1.5 G illumination, (b) the normalized performance parameters, (c) J-V characteristic curves at dark of the degraded iF-OPVs with respect to the aging time (12000 h)- devices stability study.

Table 3.10. Photovoltaic performance parameters statistics of the aged iF-OPVs that presented from average of at least 9 devices.

AGING TIME (h)		V_{OC} (V)	J_{SC} (mA/cm²)	FF	PCE (%)	PCE_{MAX} (%)	NORMALIZED PCE (%)	R_S (Ω cm²)	R_{SH} (Ω cm²)
B-20R									
T100	**0**	0.79 ± 0.01	18.26±0.12	0.66 ± 0.01	9.71 ± 0.09	9.80	100	2.83 ± 0.32	765 ± 17
≈T95	**400**	0.79 ± 0.01	17.98 ± 0.21	0.65 ±0.01	9.26 ± 0.10	9.36	95	2.92 ± 0.44	613 ± 21
	6000	0.79 ± 0.01	17.96 ± 0.09	0.63 ± 0.01	9.01 ± 0.20	9.21	93	2.81 ± 0.17	676±25
≈T90	**8000**	0.79 ± 0.01	18.03 ± 0.49	0.58 ± 0.02	9.00 ± 0.10	9.10	90	3.26 ± 0.31	394 ± 19
≈T85	**9000**	0.78 ± 0.01	17.98 ± 0.26	0.57 ± 0.02	8.11 ± 0.14	8.25	84	4.40 ±0.92	357 ± 52
≈T80	**12000**	0.78 ± 0.01	17.00 ± 0.91	0.56 ± 0.02	7.72 ± 0.15	7.87	80	4.50 ± 0.66	352 ± 12
C-25R									
T100	**0**	0.80 ± 0.01	18.42 ± 0.19	0.67± 0.04	9.80 ± 0.06	9.86	100	2.31 ± 0.11	774 ± 24
	400	0.80 ± 0.01	19.46 ± 0.73	0.61 ± 0.06	9.62 ± 0.05	9.67	98	2.39 ± 0.10	520 ± 17
≈T95	**6000**	0.79 ± 0.01	19.23 ± 0.61	0.62 ± 0.08	9.32 ± 0.05	9.37	95	2.46 ± 0.03	416 ± 52
	8000	0.79 ± 0.01	17.44 ± 0.33	0.66 ±0.02	9.18 ± 0.10	9.28	94	2.53 ± 0.22	757 ± 11
≈T90	**9000**	0.79 ± 0.01	18.39 ± 0.29	0.60 ± 0.07	8.66 ± 0.13	8.79	89	2.73 ± 0.16	387 ± 72
≈T85	**12000**	0.79 ± 0.01	16.51 ± 0.25	0.64 ± 0.04	8.37 ±0.03	8.40	85	2.91 ± 0.09	698 ± 13
D-30R									
T100	**0**	0.78 ± 0.02	18.88 ± 0.31	0.63 ± 0.03	9.46 ± 0.14	9.60	100	3.07 ± 0.43	381 ± 19
	400	0.78 ± 0.02	19.03 ± 0.61	0.62 ± 0.02	9.23 ± 0.26	9.49	99	3.09 ± 0.16	480 ± 09
≈T95	**6000**	0.78 ± 0.02	19.17 ± 0.22	0.60 ± 0.01	9.11 ± 0.20	9.31	97	3.36 ± 0.48	359 ± 12
≈T90	**8000**	0.78 ± 0.02	17.44 ± 0.19	0.61 ± 0.03	8.46 ± 0.04	8.51	87	3.40 ± 0.17	486 ± 07
≈T85	**9000**	0.78 ± 0.02	18.60 ± 0.21	0.58 ± 0.02	8.03 ± 0.10	8.13	85	4.61 ± 0.11	307 ± 16
≈T80	**12000**	0.77 ± 0.01	17.63 ± 0.15	0.57 ± 0.01	7.02 ± 0.14	7.16	76	4.80 ± 0.29	268 ± 13

Table 3.11 The photovoltaic performance parameters of the previously reported iF-OPVs devices before and after aging, PCE_A: the power conversion efficiency of the aged devices, PCE_F: the power conversion efficiency of the fresh devices.

Device structure	Evaluated Aging Time (h)	V_{oc} (V)	J_{sc} (mA/cm^2)	FF	Fresh PCE (%)	Aged PCE (%)	PCE_A/PCE_F (%)	Ref.
C-25R-ZnO ITO/ZnO/ Blend /V_2O_5/Ag	12000	0.80	18.42	0.67	9.86%	8.40	85	This work Part II
ZnO-SC ITO/ZnO/ Blend /MoO_x/Ag	8600	0.74	14.20	0.63	6.50	5.85	90	112
ZnO-SC ITO/ZnO/ Blend /V_2O_5/Ag	5000	0.79	17.69	0.73	10.19	7.77	76	121 Part I work
C-7R-ZnO-SP ITO/ZnO/ Blend /V_2O_5/Ag		0.79	18.46	0.68	10.00	8.32	83	
ITO/PEDOT:PSS/Blend/PFN/Ag	2400 [a]	0.74	19.30	0.57	8.20	4.10	50 [a]	206,217
Inv-ML-ST ITO/ZnO/Blend/MoO_x/Ag	1900	0.75	10.0	0.72	5.37	5.14	80	218
Inv-ST ITO/ZnO/Blend/MoO_x/Ag	750	0.73	8.09	0.74	4.39	3.51		
Inv-Opaque ITO/ZnO/Blend/MoO_x/Ag	250	0.75	13.26	0.73	7.27	5.82		
ITO/ZnO/Blend/MoO_x/Ag	1000	0.82	14.19	0.53	6.25	3.83	61	219
ITO/PFN/Blend/MoO_x/Ag	1460	0.81	16.2	0.68	8.9	4.81	54	220
ITO/FGr/Blend/MoO_x/Ag		0.81	17.2	0.68	9.5	9.03	95	
ITO/PEDOT:PSS/Blend/ PDINO/Ag	630	0.79	16.22	0.68	8.78	4.66	53	221
ITO/ BiOCl-NPs /Blend/ PDINO/Ag		0.79	18.42	0.68	9.92	7.92	80	
ITO/TiO_X/ Blend/MoO_x/Ag	500	0.71	14.80	0.62	6.5	2.28	35	
ITO/TiO_X/TPPZn/Blend/MoO_x/Ag		0.72	14.90	0.66	7.1	3.55	50	
ITO/TiO_X/ TPPCOOHZn /Blend/MoO_x/Ag		0.73	15.70	0.67	7.7	4.62	60	
ITO/ZnO/Blend/MoO_x/Ag	4300	0.74	14.30	0.67	7.10	5.54	78	220
ITO/ZnO/Al/Blend/MoO_x/Ag		0.75	15.20	0.70	8.00	6.80	85	
ITO/PEDOT:PSS/Blend/ PDINO/Ag	1200	0.81	16.50	0.66	8.60	6.71	78	222
ITO/PEDOT:PSS/Blend/ PDINO/PCB/Ag		0.82	17.60	0.70	9.9	9.70	98	
ITO/PEDOT:PSS/Blend/ C60/Al	24	0.76	16.30	0.70	8.70	6.53	75	223
ITO/PEDOT:PSS/Blend/ C60/Au		0.76	15.80	0.71	8.60	8.51	99	
ITO/Cu-Gr/PEDOT:PSS/Blend/ C60/Au	720	0.80	16.3	0.65	8.5	8.33	98	224

[a] The estimated value from degradation curve in the references.

Despite the information provided from the J-V characteristics that explained the effect of the ZnO modification on the performance parameters as well as the degradation behavior of the devices. But they could not introduce an in-deep insight to understand the performance deterioration of the fresh and degraded cells. Hence, impedance spectroscopy (IS) characteristics were conducted to gain a comprehensive understanding regarding the electric properties of the fresh and degraded devices upon the interfacial charge transfer and carrier recombination[165] due to the modification of the ZnO-film within the iF-OPVs.

Figure 3.17a shows the Cole-Cole plots for the T_{100} fresh and 12000 h degraded devices under illumination at the open circuit bias voltage with their corresponding Bode plots in Figure 3.17b which reveals the efficient transfer at the active layer/electrode interfaces.[165] Figure 3.17a for the T_{100} fresh and 12000 h degraded samples illustrates a typical semicircle curves with Z´(Ω) real part of impedance as x-axis and Z´´(Ω) imaginary part as y-axis. It can be noticed that the semicircle radiuses showed a variation sizes from device to another, that is basically correlated to the different charge injection or extraction takes place within the device.[165,167,205] Then, we observed that the III based devices presented smaller arc radius as well as lower impedance than the II and IV based ones. The same behavior was obtained for the T_{90} degraded samples demonstrated in Figure A.4. It is worth mentioning that the diameter of the arc radius increases as the aging time increases. However, the increase in the arc radius was noticeable for the II and IV based T_{80}-12000 h degraded cells more than the III (T_{85}-12000 h) based ones, verifying the higher stability behavior of III devices. In addition, in Figure 3.17a it can be noticed that the low frequency arc was the smallest for the III based devices as well as the arc size. This behavior reflects the effective charge extraction in the device leading to lower leakage current (Figure 3.13b, Figure 3.16c), higher V_{OC} and as a result, enhanced device performance and stability (Table 3.8, Figure 3.16b, Table 3.10). On the other hand, this detected behavior confirms the lower performance of devices II and IV (20R and 30R-ZnO- Table 3.8) as they possess a higher low frequency arc which might be related to the more pronounced charge accumulation effect that could be derived from the disorder of blend morphology over the corresponded sprayed ZnO-films.[91] This consideration is correlated with the higher ZnO-surface roughness obtained for II and IV based films (Figure 3.14b,d), higher leakage current and lower V_{oc} of the II and IV based devices. Moreover, this behavior is in a good agreement with a prior work. [100] Interestingly, we exhibited a typical Cole-Cole plots attitude through applying similar measurements of Z´(Ω) vs Z´´(Ω) at maximum power point applied voltage (V_{MPP}) and the short circuit current for the T_{100}-fresh, T_{90} and 12000 h degraded samples shown in A.5.

As a sequence, to get a deep insight regarding the physical parameters of the fresh and degraded cells and to understand this behavior, we conducted an electrical equivalent circuit to fit the experimental Z´-Z´´ data. The basic electrical circuit components used to fit the plots (Solid lines) presented in Figure 3.17c for the T_{100}-fresh and 12000 h degraded cells. The proper fitted parameters were listed in Table 3.12. It is interesting to notice that the model consist of an extra included R_4C_4 in series that connected in parallel to the R_2C_2 of

the PTB7-Th:$PC_{70}BM$ blend film following Debye model,[121,207] considering the presence of a single type of trap created in the corresponding film.[207] Hence, Debye model was the most proper one used to fit the obtained experimental data, clarifying the effect of the modified ZnO-film on the performance and stability behavior of the iF-OPVs devices.

From the fitting values listed in Table 3.12, we manifested that the fitting values of the capacitance of each layer matched greatly with the theoretical ones summarized in Table 3.6. Regarding the values of the resistance from the fitted data, we found out that for both T_{100}-fresh and 12000 h degraded devices, insignificant changes observed for the R_S values from one device to another as well as upon the aging time. This might reflect the negligible influence of the ZnO–film modification on the resistance of the ITO film.

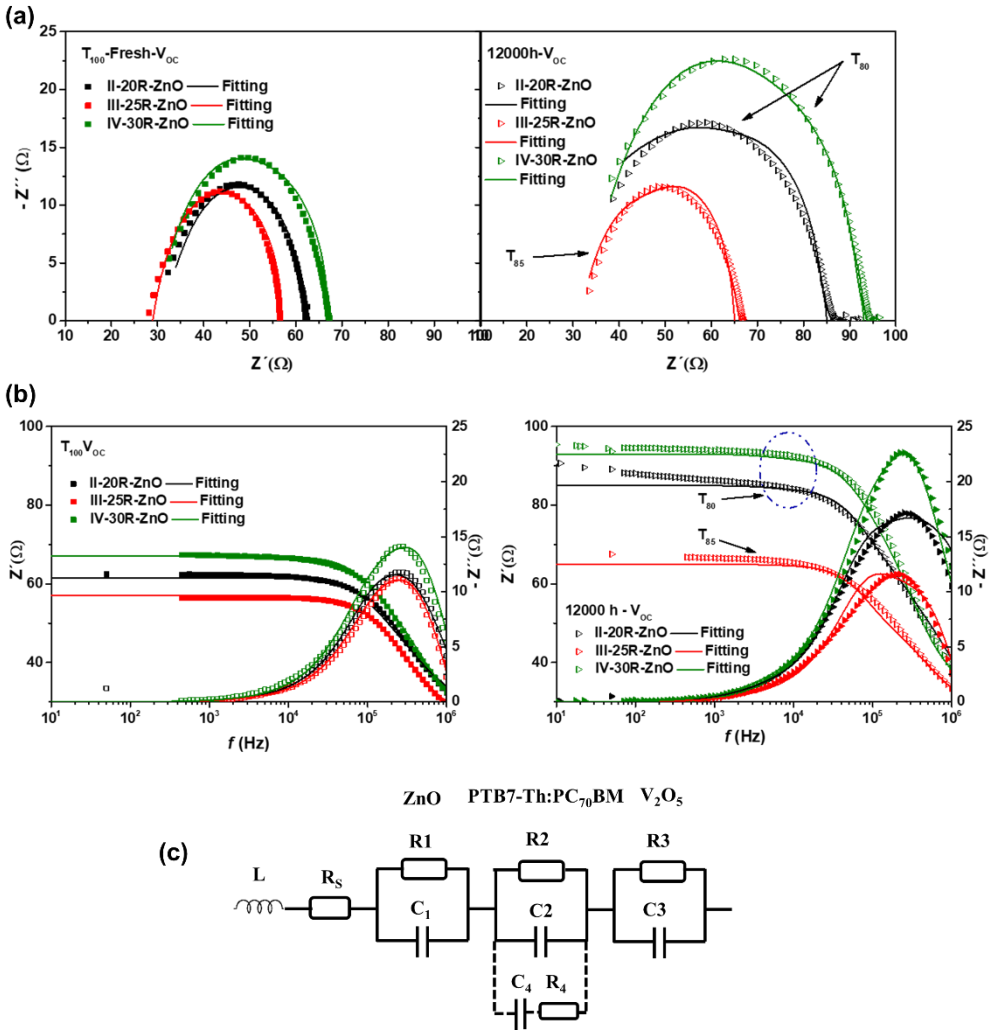

Figure 3.17 (a) Cole-Cole curves under AM 1.5G illumination at V_{OC} of the T_{100}-fresh (left) and 12000 h aged devices (right), symbols were presented for the experimental data and the fitting results in solid lines applying (b) the equivalent circuit using Debye model. (c) The Bode plot: experimental (symbols) and fitted (lines) values for the real part (left axis) and the imaginary part (right axis) of T_{100} for the fresh devices (left) and after 12000 h for the degraded cells (right) at V_{OC}. The fitted lines are obtained using data demonstrated in Table 3.11.

First, by detecting the effect of ZnO-Film modification on the T_{100} fresh devices, we found that the R_1 values for the ZnO-film of III based devices (17.0 Ω) less than that obtained in II and IV devices (18.0 and 24.0 Ω, respectively). Furthermore, the Value of R_2 for the blend layer deposited over the sprayed ZnO films was 18.5, 10.0 and 13.0 Ω for the II, III and IV based devices. Then, it can be clearly observes that the 25R of ZnO film suppresses the R_2 value for the blend performing better film quality that assists the charge transportation paths within the active blend layer providing less impeded traps within the film.[165] This behavior confirms the enhancement in the interface between the blend film and the ZnO interfacial film which might attributed to the homogeneity of the film morphology observed for the 25R-ZnO films as discussed previously in the AFM analysis (Figure 3.14c). Regarding the V_2O_5 interfacial layer, we revealed no obvious effect upon the ZnO-film modification within the fabricated devices. Accordingly, the total resistance values (R_{Total}) evaluated for the cells (summarized in Table 3.12) were mainly controlled by the R_1 of the ZnO-film. As it showed the same trend behavior of R_1 via representing the higher values for II and IV based devices confirming their low performance, the smallest R_{Total} and Z´ values along with the smallest arc radius obtained for devices III confirming the enhanced iF-OPVs performance.

Table 3.12. The fitted parameters of the equivalent circuit using Debye model at V_{OC} for the fabricated T_{100}-fresh and 12000 h degraded devices. The parameter $\tau = R_4 \times C_4$, where R_4, C_4 parameters were demonstrated in the equivalent circuit in Figure 3.17c.

Physical Parameters of the T_{100}-Fresh iF-OPVs	**Device II (20R-ZnO)**			**Device III (25R-ZnO)**		
ZnO	R_S = 14.0 Ω L = 1.20 µH	R_1= 18.0 Ω	C_1= 26.2 nF	R_S = 17.0 Ω L = 1.20 µH	R_1= 17.0 Ω	C_1= 19.1 nF
PTB7-Th-$PC_{70}BM$		R_2= 18.5 Ω τ = 30.0 µs	C_2= 2.8 nF C_4= 30.0 nF		R_2= 10.0 Ω τ = 30.0 µs	C_2= 2.8 nF C_4= 50.0 nF
V_2O_5		R_3= 11.0 Ω	C_3= 99.0 nF		R_3= 12.0 Ω	C_3= 99.0 nF
		R_{Total} = 61.5 Ω			R_{Total} = 56.0 Ω	
	Device IV (30R-ZnO)					
ZnO	R_S = 16.0 Ω L = 1.20 µH	R_1= 24.0 Ω	C_1= 13.7 nF			
PTB7-Th-$PC_{70}BM$		R_2= 13.0 Ω τ = 30.0 µs	C_2= 2.8 nF C_4= 100.0 nF			
V_2O_5		R_3= 14.0 Ω	C_3= 99.0 nF			
		R_{Total} = 67.0 Ω				
Physical Parameters of the T_{80}- Degraded iF-OPVs	**Device II (20R-ZnO)**			**Device III (25R-ZnO)**		
ZnO	R_S = 14.0 Ω L = 1.20 µH	R_1= 17.0 Ω	C_1= 26.6 nF	R_S = 17.0 Ω L = 1.20 µH	R_1= 16.0 Ω	C_1= 19.1 nF
PTB7-Th-$PC_{70}BM$		R_2= 34.0 Ω τ = 30.0 µs	C_2= 2.8 nF C_4= 30.0 nF		R_2= 14.0 Ω τ = 30.0 µs	C_2= 2.8 nF C_4= 50.0 nF
V_2O_5		R_3= 20.0 Ω	C_3= 99.0 nF		R_3= 18.0 Ω	C_3= 99.0nF
		R_{Total} = 85.0 Ω			R_{Total} = 65.0 Ω	
	Device IV (30R-ZnO)					
ZnO	R_S = 17.0 Ω L = 1.20 µH	R_1= 35.0 Ω	C_1= 13.7 nF			
PTB7-Th-$PC_{70}BM$		R_2= 21.0 Ω τ = 30.0 µs	C_2= 2.8 nF C_4= 100.0 nF			
V_2O_5		R_3= 20.0 Ω	C_3= 99.0 nF			
		R_{Total} = 93.0 Ω				

Furthermore, it can be noticed that the mentioned resistance behavior obtained for the devices was verified by the Bode plot in Figure 3.17b-T_{100}. Interestingly, these observed results greatly matched with the lowest value of R_S, highest value of FF and in turn the champion PCE of the III based devices from the J-V characteristics under similar illumination condition (Figure 3.13, Table 3.8).

Second, regarding the fitted resistance values of 12000 h degraded devices listed in Table 3.12, we noticed that R_1 values related to the ZnO-film maintained lower for III based devices (16.0 Ω) than II and IV ones (17.0 and 35.0 Ω). However, II and III based devices succeeded to keep their similar initial resistance value (T_{100}) after 12000 h, but the degraded IV based devices showed a pronounced enlarging of their R_1 value by 45% than the fresh ones (Figure 3.18, Table 3.12). Furthermore, the observed fitted R_2 values (of the blend) for the 12000 h devices were increased by 70, 30 and 43% of their initial values (T_{100}) for the II, III and IV based cells, respectively. Otherwise, the R_3 values of the V_2O_5 film were increased by almost similar percentage of ≈ 40 % for the entire degraded cells (Figure 3.18). Since the R_S values (regarding the ITO) were almost similar for the fresh and degraded devices. Hence, we can assume that the traps created during the time of the degradation mainly affect the blend interface with ZnO-ETL and the V_2O_5- HTL. Accordingly, we can disclose that the degraded devices were controlled by the R_2 of the blend as the R_{Total} obeyed similar trend by showing lowest value for the III based devices (65.0 Ω) and the highest for the IV based devices (93.0 Ω) as listed in Table 3.12. That might confirm the lowest Z´ values measured and their lowest arc size (Figure 3.17a-12000 h) of the C devices reflecting the highest stability obtained for the corresponding devices (Figure 3.18). This variation of the resistance behavior obtained was clarified by the Bode plots in Figure 3.17c 12000 h. That can be described by the fact that less pronounced defects were created within the blend layer of the III devices as ascribed by value of resistance evaluated from the Debye model.[207] Therefore, Figure 3.18 demonstrates that III based devices own the highest consistency of the resistance values in each layer till 12000 h.

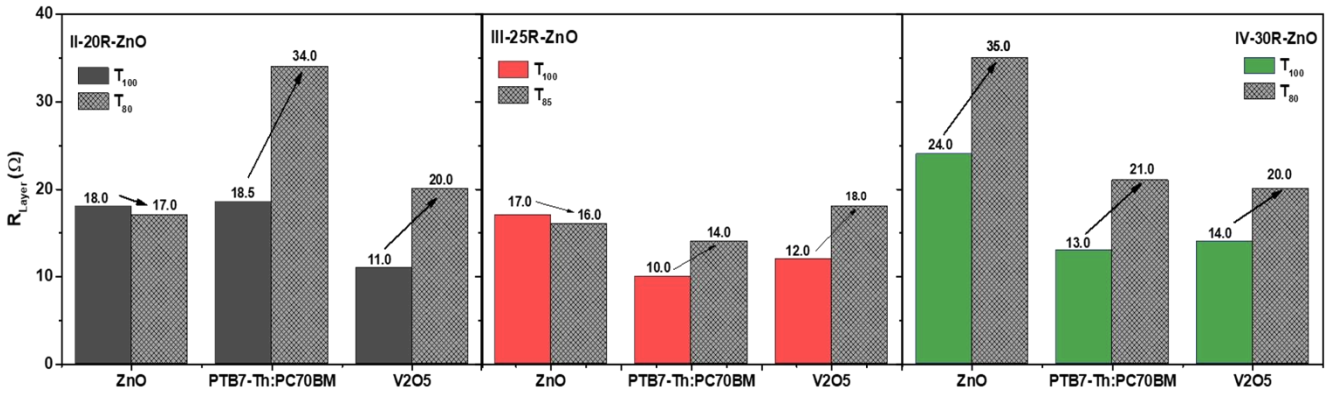

Figure 3.18 The resistance values of each layer for the T_{100}-fresh and T_{80}-degraded II (20R-ZnO), III (25R-ZnO) and IV (30R-ZnO) based iF-OPVs. The values were extracted from the Debye model for the T_{100} fresh and 12000 h degraded devices.

In addition, this observation confirmed the J-V characteristic for the stability study which clarifies that after 12000 h, III devices retained their 85 % of performance while the other iF-OPVs reached their 80 %. Based on these results, it is apparent that the properties of the electron transporting interfacial layer (ZnO-film modification) can have a significant impact on the stability of the organic photovoltaic devices.

It was surprising to note that all the degraded devices prepared by the intermittent spray pyrolysis technique showed a single arc of impedance which in agreement with Part I work.[121] However, in Part I, the Cole-Cole plots showed an extra arc for the degraded samples prepared by the spin coating technique, which verify the efficient degradation inhibition provided by the modification of the ZnO interfacial layer upon the variation of the deposition techniques. Furthermore, the comparison between the previous and current samples prepared by intermittent spray pyrolysis technique provides that the concentration of the ZnO precursor solution as well as the deposition parameters play a crucial role in enhancing the device performance and stability.

A further study for the behavior of the recombination mechanisms through impedance spectroscopy, capacitance-frequency (Cf) measurements were conducted to evaluate the trap density of state (DOS). Figure 7 displays the calculated trap-DOS plotted as a function of energy for T_{100} and 12000 h devices. We noticed that, all samples exhibited the same carrier response and trap activation energy, showing a single exponential trap distribution with almost same slope values.[58] For the T_{100} fresh samples, we did not observe a significant change in the DOS value for all devices. However, III based devices presented a bit higher DOS values compared to the others. This behavior is greatly consistent with the E_U results discussed previously in Figure 3.15d and clarifying the impedance behavior as well in Figure 3.17a along with explaining the higher FF and V_{OC} obtained for III based devices in Figure 3.13a and Table 3.8. Thus, it might be correlated to the enhanced 25R-ZnO-film quality as discussed previously in Figure 3.14c.

Then, at the 12000 h degraded devices we can observe a diminishing in the DOS values for a given frequency, depicting a shift in the E_O value. Hence, the degraded devices showed lower energy representing higher interfacial induced defects in the devices compared to the fresh ones as an intrinsic source of tarps.[64,121,172,225] Moreover, it was interesting to find out that the DOS value was higher for the 12000 h degraded III based devices than II and IV based devices (**Figure 3.19a-12000 h**). As by performing a comparative analysis for the values of the energy shift (X), explained in Part I, of the 12000 h degraded devices in **Figure 3.19b** we obtained that the II and IV based devices exhibited higher shifting value than the III based one. That indicates less trapped sites located in devices III verifying their superior stable behavior toward the degradation. This detected behavior was interestingly agreed with the obtained 12000 h J-V characteristics in **Figure 3.16** as well as the impedance behavior given in **Figure 3.17a**. In contrast to the behavior of IV based devices that confirms the increment of the interface density of states values for this

sample, correlating its lower V_{OC}, PCE as well as the drop diminished stability behavior. Interestingly, same attitude was distinguished for the T_{90} degraded devices presented in **Figure A.6**.

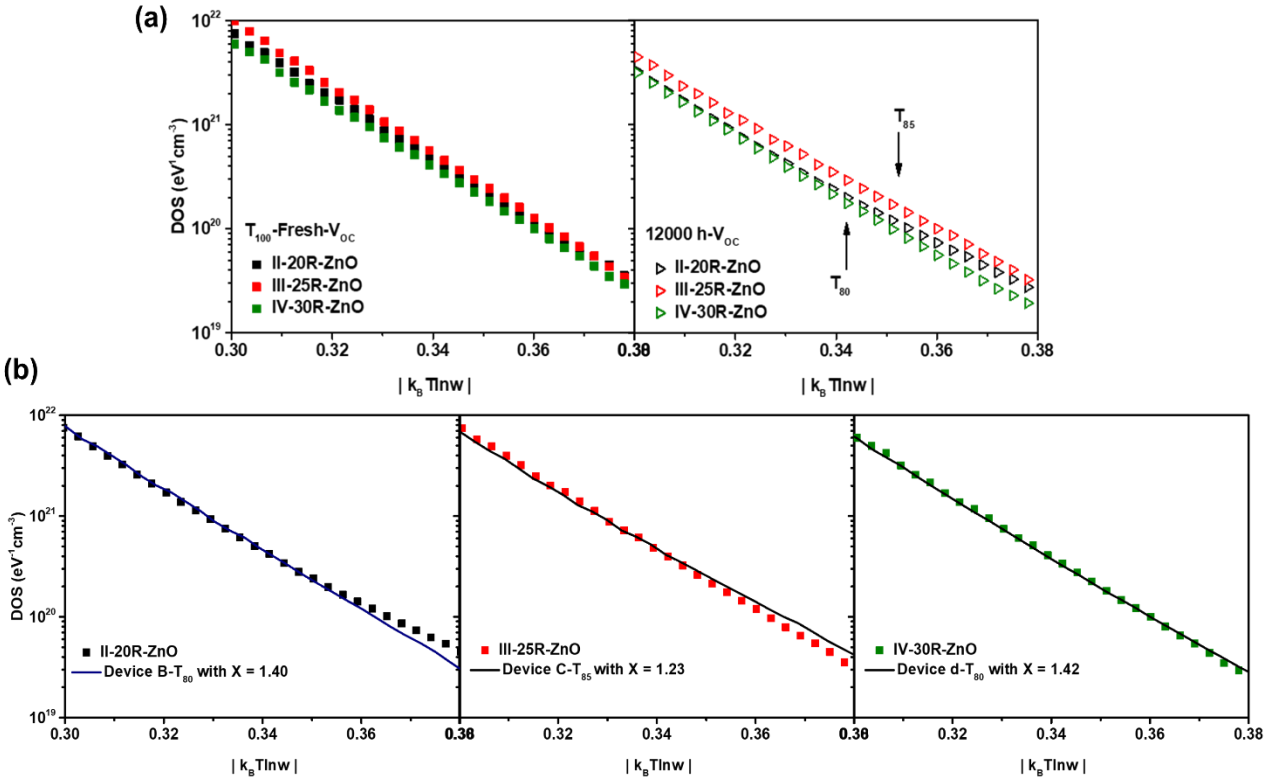

Figure 3.19 DOS vs $|k_BT\ln\omega|$ under AM 1.5G illumination at V_{OC} of (a) the T_{100} fresh devices (left) and the 12000 h degraded (right) iF-OPVs. (b) the T_{100} fresh (symbols) and the 12000 h degraded devices (line with shifting value of X value).

Accordingly, the observed data exhibited that modifying the ZnO-Film via spraying 25R using the intermittent spray pyrolysis approach enhanced the ZnO-film quality as well as the attached active blend film. Therefore, it was interesting to mention that this modification assists the stability of the based performed devices (III based devices) more than the other cells. In addition as to compare with the Part I work [121], we can clearly notice the significant stability enhancement obtained by the Modified 25R-ZnO film sprayed by low concentration of ZnO precursor solution (reached T_{85} after 12000 h) than the ZnO spin coated as along with the ZnO sprayed using high concentration of ZnO precursor solution (reached T_{85} after 5000 h). That might be attributed to the better ZnO film quality obtained by the 25R of low ZnO precursor solution which

provides less defect sites for the over coated blend layer which in turn plays an important role in enhancing the device performance and stability[58].

3.4 Conclusion

In summary, the importance of the surface roughness of the ZnO film (ETL) in identifying the performance of the iF-OPVs was detected by using PTB7-Th: $PC_{70}BM$ as the photoactive layer. We demonstrated that the carefully tuning of the microstructure features -morphology- and the properties of sprayed ZnO film via high and low concentrations of ZnO precursor solution depend sensitively on the chosen number of spraying running cycles using the intermittent spray pyrolysis approach. Then we conducted a comparison between the ZnO-SP based devices and the ZnO-SC ones to reveal the devices performance and stability behavior. For the ZnO-SP based devices with high ZnO concentration precursor solutions, the results demonstrated that the C-7R-SP based devices showed higher J_{SC} than the lab-scale ZnO-SC based ones and fairly similar performance, achieving devices with same V_{OC} (0.79 V) as well efficiency of 10 %. It was noticeable that the main difference between the ZnO-SC and C-7R-SP based devices is the interface roughness effect between the ITO and the ZnO deposited film. The bright side of being textured surface that enhances the light trapping inside the solar cell which increases the absorbance of the incident light and generates higher J_{SC}. Furthermore, this proper interface contact with the active layer enhances the overall stability for the ZnO-SP based devices, where the rate of degradation of the ZnO-SP based devices was slower than the ZnO-SC one. However, the deficient side was regarding the effect of the interface between the ZnO sprayed layer and the ITO that increases the R_S.

Thus, these investigated results in part I point out that the deposition techniques have a vital role that affects the film formation as well as the performance and stability of the devices. Taking these facts into account leads to the next step of improving the interface between the ZnO layer and the ITO to perform lower R_S which might enhance the device stability and performance. Accordingly, we further optimized the morphology of the sprayed ZnO in part II with lowest roughness and full surface coverage that is achieved through 25R with 0.5:9.5 ration of ZnO precursor solution concentration, yielding the benchmark performance of 10 % PCE along with enhanced average V_{OC} (0.80 V) and FF (0.70) of III based devices. Furthermore, we tested their stability behavior that demonstrated a pioneer record with respect to device ZnO-7R-SP and ZnO-SC based devices, maintaining 85% of their starting efficiency even after 16.7 months of storage inside a nitrogen glove box without encapsulation. The difference in the devices performance and stability appears to originate from the different obtained ZnO surface morphologies that control the presence of defects at the surface and their subsequent adjacent organic active layer blend. As a sequence, the surface

roughness determines the effective interfacial region between the active layer and the ZnO layer and ITO, thus the density of trap sites at the interface that was investigated by the IS measurements for the fresh and degraded iF-OPVs. Therefore, the proposed electrical equivalent circuit module accounted to fit the experimental data of the IS, allowed us to recognize the impact of each interlayer on the device performance and the correlated stability behavior. Accordingly, we obtained that the remarkable stability enhancement behavior of the III based devices correlates with the marginally interface density of states values for this sample among the others. These models presented a simple way to diagnose the loss mechanisms and investigate degradation mechanisms and stability issues in the fabricated devices. Finally, it is worthy mentioning that the obtained high efficiency and excellent stability of the fabricated inverted OPVs using intermittent spray pyrolysis approach could facilitate their scaling up to the industrial production perspective.

Chapter 4

Dependency of Non-fullerene Binary Organic Photovoltaics Performance on Solvent Additives and Thermal Annealing

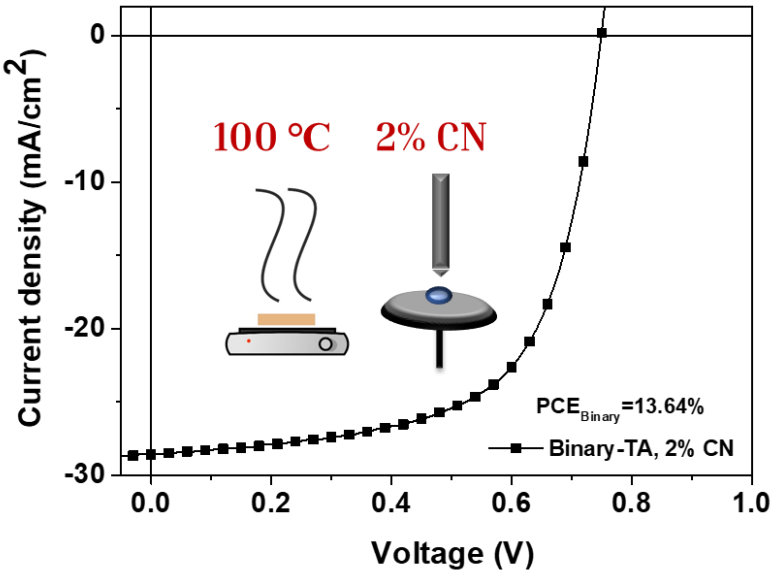

This chapter is based on the published works: Enas Moustafa, A.A.A.Torimtubun, J. Pallarès, and L.F. Marsal, "Effect of Additives and Annealing on the Performance of Nonfullerene-Based Binary and Ternary Organic Photovoltaics", ***Sol. RRL***, **2022**, 6: 2100480.

4.1 Introduction

The inception of merging nonfullerene acceptors (NFAs) replacing the fullerene counterpart in organic photovoltaics (OPVs) has pushed the bulk-heterojunction (BHJ) based- photovoltaics to achieve efficiencies approaching 20%[22,83,85–87]. This reflects the tremendous attempts that have been performed in the photoactive absorber material, interfacial device engineering and device physics[82,83,226]. Moreover, this dramatic increase in the power conversion efficiencies (PCEs) was particularly due to minimizing the trade-off behaviour between voltage loss and charge generation in nonfullerene organic photovoltaics (NF-OPVs)[88,89]. This is attributed to the design of the central fused ring unit of these low band gap NFAs molecules such as Y6 (BTP-4F) and Y7 (BTP-4Cl) with the virtue of their anisotropic structure [86,125,227,228]. Moreover, they have the ability of tuning their energy levels and their strong absorption in the near-infrared region with the donor polymers[126,227–229]. These properties lead to barrierless free charge generation, low charge trapping, and high charge mobilities of the corresponding devices[230]. These great advantages provide efficient ways to improve the performance of the NF-OPVs [89,227]. Furthermore, the bulk morphology of the photovoltaic active layer directly influences the charge transfer and transport mechanisms, making it one of the pronounced limiting factor for the performance of BHJ OPVs[83,90,91]. For instance, the insufficient hole transfer from Y6 to PM6 (PBDB-T-2F) limits the exciton decay that affects the cell performance as described by J. Wu et al. due to morphology defects[231]. This declaration reflects the possibility of enhancing the NF-OPVs performance through the optimization of the morphology of the photoactive blend.

There are several strategies were investigated to tune the active blend morphology toward better film quality through controlling the miscibility between the donor and the acceptor, domain size and donor/acceptor (D/A) phase separation. This to secure sufficient exciton dissociation and improved charge transfer resulting in superior performance of the OPVs. [83,92–94] Some of these avenues concern about the photoactive blend modification by solvent additives[83,95–97], thermal annealing[91,98] and further post treatments[85,97,99]. Among the strategies, moderating the morphology by the construction of ternary and quaternary blends performing ternary and quaternary OPVs[124–126,232,233]. Regarding the first approach, 1-chloronaphthalene (CN) has been the most reported solvent additive to fine-tune the morphology of PM6:Y6 OPVs, achieving 15.7% efficiency as compared to its non-additive ones (15%) as presented by J. Lv et al.[83]. Furthermore, the influence of thermal annealing and post treatments were significant in enhancing both of the blend morphology along with the interface matching with the interfacial layers[91,163,234]. As reported by S. Lui et al., they minimized the degree of energetic disorder and reduced the energy losses due to less non-radiative recombination of 0.17 eV resulting in high PCEs up to 16.5 %[163].

The scenario in this chapter, we demonstrate an interesting correlation between the CN solvent additives and the thermal annealing treatment on the optical and physical properties of the binary inverted nonfullerene

organic photovoltaics (iNF-OPVs) based on PM6:Y7 photoactive blend. Subsequently, we related the observed results with the photovoltaic performance of the devices. Hence, we perform a systematic investigation to reveal the effect of the mentioned treatments on the morphology of the binary blend layer. Moreover, a particular study was performed on the electric properties and the correlated charge transfer, separation and recombination mechanisms using impedance spectroscopy and Mott Schottky analysis of the treated and non-treated binary devices.

4.2 Experimental Procedures

This section reports the details of the ZnO and the blend solution synthesis along with the device fabrication procedures of the inverted NF-OPVs conducted in this chapter based on the structure of ITO/ZnO/PM6:Y7/V_2O_5/Ag as Illustrated in **Figure 4.1**. ZnO and V_2O_5 were used as n-type and p-type charge transport interfacial layers, respectively, moreover, a binary BHJ of PM6:Y7 was employed as the photoactive layer. The chemical structures of the PM6 polymer donor and Y7 nonfullerene acceptor acceptor with the energy level alignment for binary devices are demonstrated in **Figure 4.1b** and **4.1c**, respectively. The energy positions of the band edges for the semiconductors and the metals work functions were taken from[235], [117], and [30] references. The schematic diagram for the fabrication procedures of the inverted structure OPV devices in this thesis is prior illustrated in **Figure 2.8** in Chapter 2. For fabricating the NF-OPVs binary devices, ZnO stock solution was spun coated on the top of the pre-cleaned ITO at 3000 rpm for 30 s, then left for 1 h annealing at 200 °C. The ZnO-coated ITO substrates were brought to a nitrogen-filled glove box for the active layer deposition. The binary PM6:Y7 blends with the weight ratio of 1:1 were dissolved in chlorobenzene to prepare the total concentration of 20 mg mL^{-1} solution. All blend solutions were stirred and heated on a hotplate at 80°C for 3 h. Different concentration (0 vol% to 2 vol%) of 1-chloronapthalene was added as the solvent additives before device fabrication to study the effect of addition of the additives for all blends. The blend solutions were spin-coated onto the ZnO/ITO substrates to obtain an active layer thickness around 100 nm. Then, the prepared films were treated with and without thermal annealing at 100°C for 10 min, 30 min, and 1 h to study the effect of thermal annealing treatment on the performance of the corresponding devices. The substrates were finally transferred into the vacuum thermal evaporation chamber inside the glove box where 5 nm of V_2O_5 and 100 nm Ag were sequentially evaporated as aforestated in Chapter 2 in **Figure 2.8**.

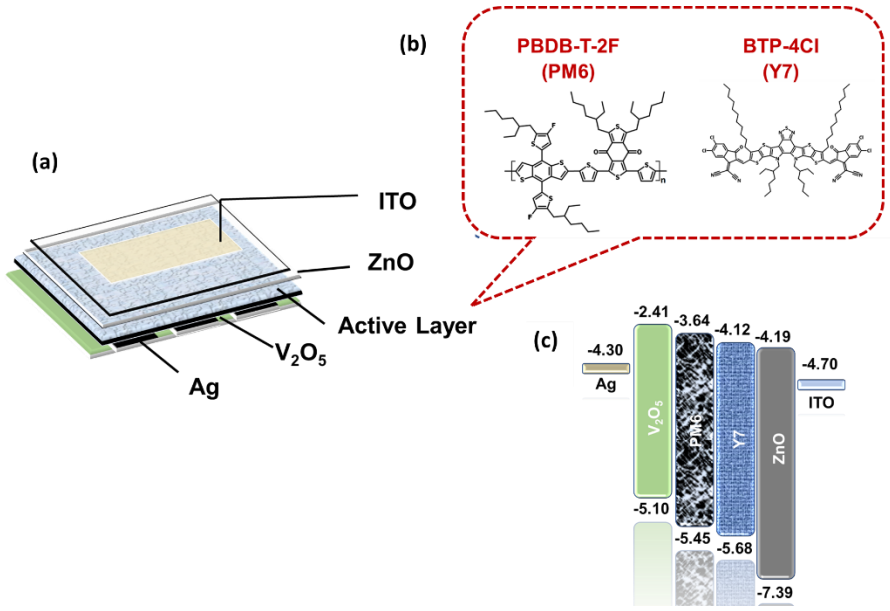

Figure 4.1 (a) The schematic diagram of the fabricated iNF-OPVs structure, (b) the chemical structures of PM6-donor, Y7-nonfullerene acceptor, (c) the energy band diagrams of the inverted binary NF-OPVs.

4.3 Results and Discussion

4.3.1 Photovoltaic Performance Properties

The effect of additives and thermal annealing treatment on the performance of the champion iNF-OPVs were investigated in this chapter. To better distinguish the parameters given, we labelled the binary iNF-OPV as a Roman capital letters A-D. As shown in **Figure 4.2**, Type A and B in binary iNF-OPVs are the non-annealed (NA) devices treated without (0%) and with 2% v/v chloronaphthalene (CN) solvent additive, respectively. Moreover, type C and D are thermally annealed (TA) devices treated with 0% and 2% v/v CN,

respectively.

Figure 4.2 Schematic illustration of the nanomorphology models of the binary BHJ films under different treatment conditions**.**

Figure 4.3 displays the current density-voltage (J-V) characteristics of the fabricated devices with different processing treatment measured under illuminated AM 1.5G (100 mW/cm^2) and dark conditions. The photovoltaic parameters of the corresponding cells are listed in **Table 4.1**. As shown in **Figure 4.3a**, on one hand, regarding the effect of CN additives, without thermal annealing treatment, devices A (NA, 0% CN-pristine) exhibit a maximum power conversion efficiency (PCE_{max}) of 8.26% with an average open-circuit voltage (V_{OC}) of 0.69 V, short-circuit current density (J_{SC}) of 21.23 mA/cm^2, and fill factor (FF) of 0.56. After 2 % CN additives, the devices B (NA, 2% CN) performance was improved to provide a PCE_{max} of 11.64 % (with average V_{OC} = 0.71 V, J_{SC} = 26.12 mA/cm^2, and FF = 0.63). It can be clearly seen that the entire performance parameters of devices B were enhanced upon the addition of 2 % CN. Moreover, it was interesting to observe the same behavior for the thermally annealed C (TA, 0% CN) and D (TA, 2% CN) samples, where 2 % of CN additives increases the PCE_{max}, average V_{OC}, J_{SC} and FF from 10.09 %, 0.74 V, 22.06 mA/cm^2 and 0.61, respectively, in C based devices to 13.62 %, 0.75 V, 28.61 mA/cm^2, and 0.64, respectively, in D based devices. Furthermore, it is worth noticing that the J_{SC} values were highly pronounced by the CN additives as shown in **Figure 4.3a** for devices B and D based devices which may explain the improvement in their PCEs. The enhancement of J_{SC} is consistent with the obtained EQE values and photocurrent charge carrier density vs effective voltage analysis, as will be discussed later. Another factor that assists the enhancement of the PCE comes from the increase of the FF due to the distinguished decrease in the series resistance average values (R_S) from 3.03, 1.48 in devices A and devices C (with 0% CN), respectively to 1.68 in devices B and 1.20 in devices D (with 2% CN). We obtained the same effect of improving the performance parameters upon 1 % CN of the non-annealed and annealed devices as shown in **Figure A7,** noting a better performance for the 2% CN based devices. Thus, it is obvious that the overall photovoltaic parameters for the devices with and without TA treatment was enhanced upon the addition of 2% CN, suggesting that solvent additive is an effective strategy to improve device performance in different blend systems.

On the other hand, the obtained data remarked the effect of TA on the fabricated devices. By comparing A devices with C ones and B devices D ones, we noticed that all the photovoltaics parameters were enhanced but at the expense of slightly reduced R_{Sh} values for the corresponding thermally annealed devices (C and D based devices). However, the noticeable decline in the R_S average values of the thermally annealed samples (R_S of devices C= 1.48 Ω cm^2 and R_S of devices D= 1.20 Ω cm^2) might be the reason of enhancing the FF and in turn the PCEs of these cells. Furthermore, we can say that the major effect of TA was obtained by improving the FF and the V_{OC} of the TA cells (C and D devices). Despite there was not a clear effect observed due to the TA on the J_{SC} values of devices C, but it was more noticeable in devices D. Accordingly, it is worth noting that D based devices illustrated the dual benefit of the 2% CN additives as well as the TA in fabricating efficient high-performance devices. Moreover, it was interesting to detect the same impact trend

due to CN additives and TA using additional percentage of CN (1 % v/v) along with various time of annealing (10 min and 30 min at 100 ℃) as shown in **Figure A.8** and the obtained performance parameters statistics were listed in **Table A.2**.

Figure 4.3b depicts the J-V curves at dark condition for the devices. It was noticeable that a lower leakage current under reverse bias was obtained for the 2% CN based devices (B and D devices) than the 0% CN ones (A and C devices). This lower leakage current in the 2% CN based devices leads to increasing the shunt resistance R_{Sh}[91] from 4.33 x 10^4 in A devices to 3.80 x 10^6 Ω.cm² in B based devices and from 2.34 x 10^4 in C devices to 2.09 x 10^6 Ω.cm^2 in D devices at dark.

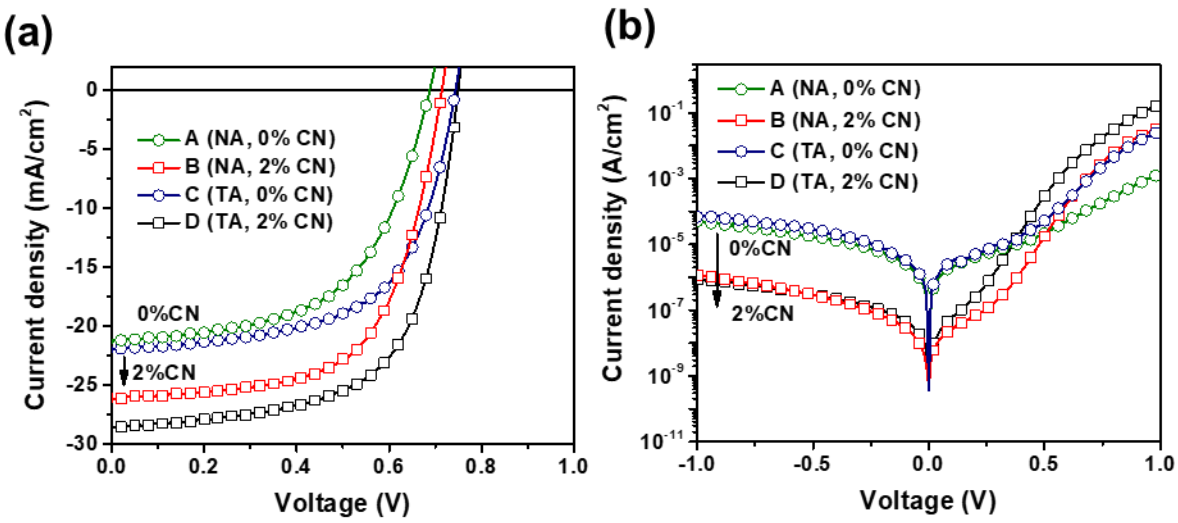

Figure 4.3 Current density-voltage (J-V) characteristic curves (a,b) under AM 1.5 G illumination of binary and ternary iNF-OPVs, (c,d) at dark condition of binary and Ternary iNF-OPVs.

Table 4.1 Photovoltaic performance parameters statistics of the fabricated binary inverted NF-OPVs. The open circuit voltage (V_{OC}), short circuit current density (J_{SC}), fill factor (FF), power conversion efficiency (PCE), series (R_S) and shunt (R_{Sh}) resistances were presented from an average of at least 8 devices.

Device type	V_{OC} (V)	J_{SC} (mA/cm^2)	FF	PCE (%)	PCE_{max} (%)	R_S (Ω cm^2)	R_{Sh} (Ω cm^2)
A (NA, 0% CN)	0.69 ± 0.02	21.23 ± 1.18	0.56 ± 0.02	8.04 ± 0.22	8.26	3.03 ± 0.85	389 ± 22
B (NA, 2 % CN)	0.71± 0.01	26.12 ± 1.62	0.63 ± 0.06	11.12 ± 0.52	11.64	1.68 ± 0.24	462 ± 32
C (TA, 0% CN)	0.74 ± 0.01	22.06 ± 0.74	0.61 ±0.04	10.00 ± 0.09	10.09	1.48 ± 0.44	271 ± 12
D (TA, 2% CN)	0.75 ± 0.01	28.61 ± 0.43	0.64 ± 0.08	13.04 ± 0.58	13.62	1.20 ± 0.09	382 ± 57

This enhancement in the R_{Sh} reveals a lower charge carrier recombination in the active layer blend[95]. This behavior confirms the higher J_{SC} and FF observed for B and D devices with 2% CN under illumination condition in **Figure 3a**. Furthermore, at forward bias (V > 0.3 V), we noticed a steep slope of the J-V curves for binary TA-devices (C and D) more than the NA cells (A and B) that indicates low R_S[75] devices (R_S-A devices = 1188.1, R_S-B devices= 47.53, R_S-C devices= 59.19, and R_S-D device= 9.43 **Ω** cm^2) which in good agreement with the obtained R_S values in under illumination condition **Table 4.1**.

The dramatic increase in the J_{SC} for the iNF-OPVs with 2% CN-devices (type B and D) compared to that in 0% CN-devices (type C and D) under different processing treatment were confirmed by the external quantum efficiency (EQE) response with AM 1.5G reference spectrum as shown in **Figure 4.4a**. It can be noticed that the entire devices have similar wavelength broad photoresponses ranging from 300 to 950 nm. However, the absorption intensity at short wavelengths range of 300-400 is still low due to the limited absorption of the polymer donor in this region[117,163]. It can be revealed, the pristine devices (A) showed different response than the other cells by a sharp reduction in the absorption range of 450 - 800 nm. This obtained reduction in the spectra suggested to be related to the insufficient charge extraction and transport mechanism which greatly matches with the low performance parameters of A based devices aforementioned in **Table 4.1**. Otherwise, the EQE spectra from 450 to 800 nm exhibited strong photoresponses for the 2 % CN devices with a maximum plateau achieving around 80 % for the devices B, around 90 % for devices D and medium response around 65 % for devices C with 0 % CN. It was interesting to see that the calculated integrated J_{SC} values from the EQE spectra were 19.44, 24.74, 21.49 and 26.24 mA/cm^2 for device A, B, C, and D, respectively, showing great matching with the values obtained from the J-V measurements under AM 1.5G illumination with the maximum error values less than 10% (**Table 1.4**).

To further determine the effect of CN additives and TA treatment on the underlying PM6:Y7 films and investigate the relation toward improving the J_{SC} in the fabricated devices, we performed the UV-visible absorption spectrum of the PM6:Y7 pristine and treated blend films as presented in **Figure 4b**. Compared to the pristine films of binary (A), PM6 has an almost unchanged absorption peaks position (500-750 nm) with 2 % CN additive films. But surprisingly, the main change appeared in the absorption intensity of PM6, where the 2 % CN additives showed a bit lower absorption intensity than the 0 % CN blends. In contrast, Y7 peak intensity showed higher absorption for the 2% CN modified blends. That provides more absorption from the Y7 acceptor that efficiently converted into photocurrent[237]. Consequently, Y7 implies the major pronounced effect within the blend than the PM6 by providing higher J_{SC} as well as better device performance for the 2 % CN modified cells. It is worth mentioning that this behavior explains the enhancement of the EQE response

of the 2% CN devices above 800 nm more than the 0 % CN ones, where similar results were obtained by the X. Wang et al. [236].

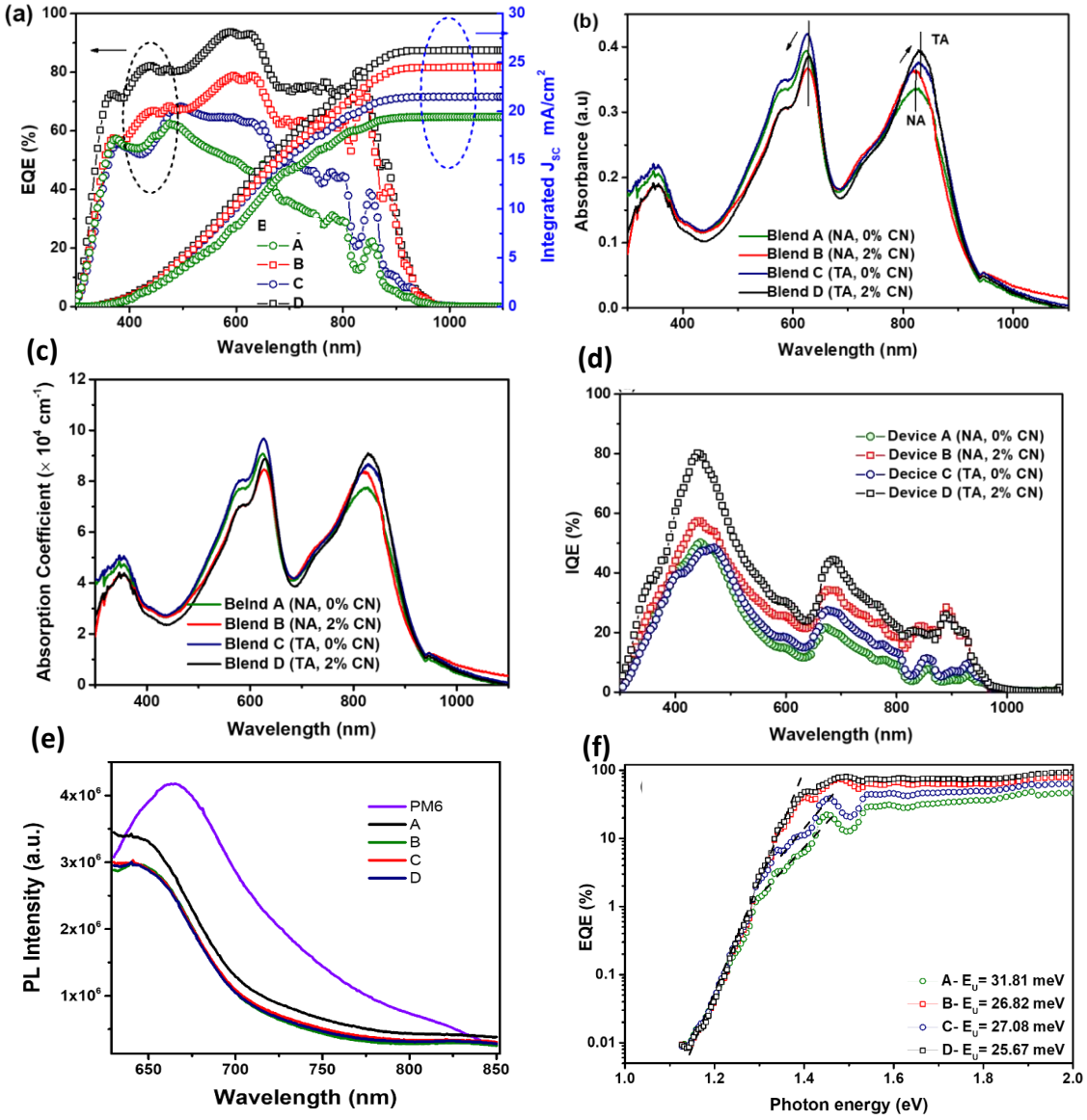

Figure 4.4 Different treatment conditions measurement of (a) EQE spectra (left) and the integrated short circuit current (right) of iNF-OPVs, (b) UV-vis optical characteristics of the PM6:Y7 binary blend films (c) Absorption coefficients of the PM6:Y7 blend film, (d) IQE of the iNF-OPVs devices, (e) PL spectra of the PM6:Y7 based blend films, (f) EQE vs photon energy of the iNF-OPVs with the inset values of Urbach energy (E_U).

Moreover, a different behavior was exhibited for the TA blend films, it was clearly seen that all absorption spectra intensity enhanced for the TA devices more than the NA ones. In which C based devices showed a bit higher absorption intensity than A device (the same for devices D and B) for both PM6 and Y7 related

peaks. Moreover, the Y7 peak position (700-900 nm) demonstrated a redshift of 8 nm from 826 to 834 nm (maximum peak), indicating further ordering of Y7 molecules that became more tight aggregation, which is typically ascribed to π-π interactions[236],. Interestingly, the same behavior was exhibited from the calculated absorption coefficients of the binary blends as illustrated in **Figure 4c**. From the obtained absorption coefficients, one may assume that the contributions of light harvesting from the treated devices were higher than the absorbed by the pristine ones. Accordingly, the overall evaluation of the UV-Vis spectra and the absorption coefficient reflects that 2 % CN additives and TA treatment manifest a significant influence on Y7 molecular order and PM6, respectively. Hence, the EQE spectra verifies the paired improvement effect obtained from the CN additives and the TA step by showing the higher intensity for the champion device D with 2% CN and TA treatment devices. Furthermore, we calculated the internal quantum efficiency-IQE (IQE=EQE/Absorption of the active layer) of the corresponding devices to estimate the efficient charge collection from the devices within the active layer taking into account the recombination losses that might take place in the devices[160]. **Figure 4.3d** showed the highest IQE intensities obtained for 2% CN devices of B and D, indicating the declined recombination losses which greatly matches with their superior J_{SC} values (**Table 4.1**). Furthermore, the highest IQE response exhibited for the champion device D that possessed the highest J_{SC} value. Moreover, to investigate the optical properties behavior and the interfacial charge transfer efficiency, photoluminescence (PL) spectra were conducted for all blends. From **Figure 4.3e**, it is shown that the photoluminescence peak of all blends shifts to a lower energy or higher wavelength (about 650 nm) than those of the absorption peak (about 620 nm) in the wavelength window from 600 nm to 850 nm which is corresponding to the PM6 characteristic. It indicates that the photoluminescence and absorption measurement in this study is reliable since this phenomenon occurred due to the relaxation state of electrons within the atoms of PM6 to the lower energy level and it can emit the photon. As it is well known that PL measurement provides information about the energy transfer from the donor to the acceptor. Therefore, device B, C and D have similar energy transfer, while the as-cast binary A has a different energy transfer, indicating that the TA and additive treatments implied a positive impact for the energy transfer in the treated devices.

Accordingly, it was interesting to investigate the low J_{SC}, V_{OC} as well as PCEs obtained by the 0 % CN binary devices (A and C) through studying the optical properties of the blend film using the Urbach rule as explained previously in chapter 2 using equation 2.10[162,163]. The obtained results in **Figure 4.3f** manifests that the curves of the 0 % CN exhibited two different slopes at low energy region of tail state distribution explaining the high disorder in these 0 % CN cells[163]. Moreover, this behavior proof that the 0% CN devices have more trap states than the 2 % CN, resulting in reducing their device performance (**Table 4.1**). Interestingly, this behaviour confirms the dip intensity of the EQE response appeared for the 0% CN devices (A and C) above 800 nm (**Figure 4.3a**). In addition, the calculated values of the E_U (in the inset of **Figure**

4.3f) were quite close for all devices, however, they still have lower values for B devices than A devices and for devices D than devices C, reflecting the less disorder distribution presented in the B and D based devices due to 2 % CN additives modification.

For further understanding the reason behind the improvement in the performance of the iNF-OPVs prepared by 2 % CN additives and the TA treatment, the recombination characteristics of the fabricated devices were calculated through measuring the dependance of J_{SC} and V_{OC} on the incident light intensity (P_{Light}). The equation that represent the relation between the J_{SC} and the P_{Light} is J_{SC} α $(P_{Light})^{S1}$, where the power-law exponent S_1 close to 1 represents the insignificant bimolecular recombination [89,144,145]. **Figure 4.5a** demonstrates the J_{SC} dependance on the P_{Light} of the fabricated devices, we noticed the difference in the dependency behavior at low and high light intensities. At low P_{Light} (< 1 mw/cm^2), the S_1 values for the entire devices were almost the same (around 0.6 - 0.7 which is less than 1) that indicates a major effect of bimolecular recombination. But different attitude was observed for the S_1 values at high P_{Light} (>10 mW/cm^2) for A, B, C and D devices which are 0.810, 0.860, 0927 and 0.998, respectively. It can be noticed that the pristine devices (A – NA, 0% CN) suffer from the major effect of the bimolecular recombination (S_1 < 1) than the other devices. In addition, device B (NA, 2%CN) possessed higher S_1 value representing a bit less bimolecular recombination effect than device A. Concerning the thermally annealed devices, the S_1 value tends to 1 that indicative of the lowest bimolecular recombination excite in devices C and D. However, it is worth mentioning that device D possessed the closest S_1 value to 1 due to the virtue of 2 % CN additives along with the TA effect which highly matched with its prior performance. Furthermore, the measurement of V_{OC} as a function of P_{Light} helps identifying the presence of the trap assisted recombination[81,146]. Hence, **Figure 4.5b** illustrates the logarithmic dependence of the V_{OC} on the P_{light} of the binary and ternary systems which are represented by Shockley diode equation 4.1

$$V_{OC}\ \alpha\ S_2\left(\frac{KT}{q}\right) Ln\left(P_{light}\right) \alpha\ n_{id}\left(\frac{KT}{q}\right) Ln\left(J_{SC}\right) \quad (4.1)$$

where, n_{id} is the ideality factor of the diode ($n_{id}=S_2/S_1$), k is the Boltzmann constant, T is the temperature, and q is the elementary charge. When the value of n_{id} is close to 1, it indicates that the bimolecular recombination is the main form of recombination in the OSC devices[147], while n_{id} >1 explains the presence of the trap assisted recombination mechanisms[144,148]. The S_2 values in binary iNF-OPV were calculated by fitting equation 4.1 and obtaining values of 1.746, 1.296, 1.350, 1.212 that gives n_{id} values of 2.156, 1.507, 1.456, and 1.214 (at P_{Light} >10 mW/cm^2) for A, B, C, and D based devices, respectively. It can be noticed that the n_{id} values higher than 1 for the 0 % CN devices (A and C) than the 2 % CN (B and C) ones, revealing the energetic disorder due to the non-geminate recombination[239] of the 0% CN based devices. In contrast, the n_{id} values were closer to 1 for the TA (C and D) devices than the NA cells (A and B), attributing to a less

concentration of traps in the bulk, resulting in higher FF values of the treated ones. Accordingly, we suggested that the trap-assisted recombination was mitigated for the devices treated with the 2 % CN as well TA devices. All these factors approve the enhanced FF as well as the PCEs observed in the B and D treated binary devices.

Moreover, the dependence of the photocurrent (J_{Ph}) on the effective voltage (V_{eff}) was calculated to evaluate the exciton dissociation probabilities (P_{diss}), maximum amount of absorbed photons that provides the dissociation and generation of free carriers (G_{max}) and the generation rate (G_{rat}) of the free charge carriers in the fabricated devices[49,149]. Where J_{Ph} is the difference between light (J_L) and dark(J_D) current density, V_{eff} =V_O -V, where V_O is the voltage when J_{Ph} = 0 and V is the applied voltage[147,150,151]. We evaluated the values of the $G_{max,}$ P_{diss}, and G_{rat} as previously explained using equations 2.1, 2.2, and 2.3[49,149,151,152]. In **Figure 4.5c,** a double logarithmic scale curves of J_{ph} vs V_{eff} were plotted for pristine and the treated devices. The obtained results exhibited that the J_{Ph} of the devices increased linearly at low V_{eff} (< 0.1 V). Then, it tends to saturate by increasing the V_{eff} > 0.2 V representing an efficient charge carrier separation[149]. From the J_{sat} values extracted from **Figure 4.5c**, it can observed that the effect of 2% CN additives in B and D based showed more sufficient charge carriers separation within the interfaces of the active layer blend[147,149] than the 0% CN devices A and C devices. However, the TA devices showed a bit higher saturation behavior than the NA cells, but the effect of the 2 % CN additives was more dominant than the TA effect. **Table 4.2** summarizes the optoelectronic parameters calculated from the J_{ph}-V_{eff} curves. Thus, the values of the G_{max} for the NA devices - A and B were 1.37×10^{28} and 1.66×10^{28} m^{-3} s^{-1}, respectively, which indicate more sufficient free carriers generation and dissociation takes place in device B due to the 2 % CN additive. It is worthy to mention the highest value of G_{max} was exhibited for the D based device, consisting with its highest J_{SC} values provided by the J-V and EQE characteristics. In turn, these observed results matched with the G_{rat} values (listed in **Table 4.2**) for the devices which confirm that the photogenerated excitons were efficiently dissociated into free carriers upon the 2% CN additives (device B) as well as TA ones (device D) which correlated with the corresponding performance of the devices (**Table 4.1**). Furthermore, the P_{diss} of these devices followed the same trend of D (98.44 %) > B (98.05 %) and C (97.79 %) > A (96.56 %). Accordingly, the highest P_{diss} values correlate with the lower recombination that observed for the devices D based NF-OPVs (**Figure 4.5a,b**), reflecting their high FFs, J_{SC}, and PCEs (**Table 4.1**). It is worth mentioning that all P_{diss} values are above 90%, indicating the efficient exciton dissociation and charge collection in our fabricated devices.

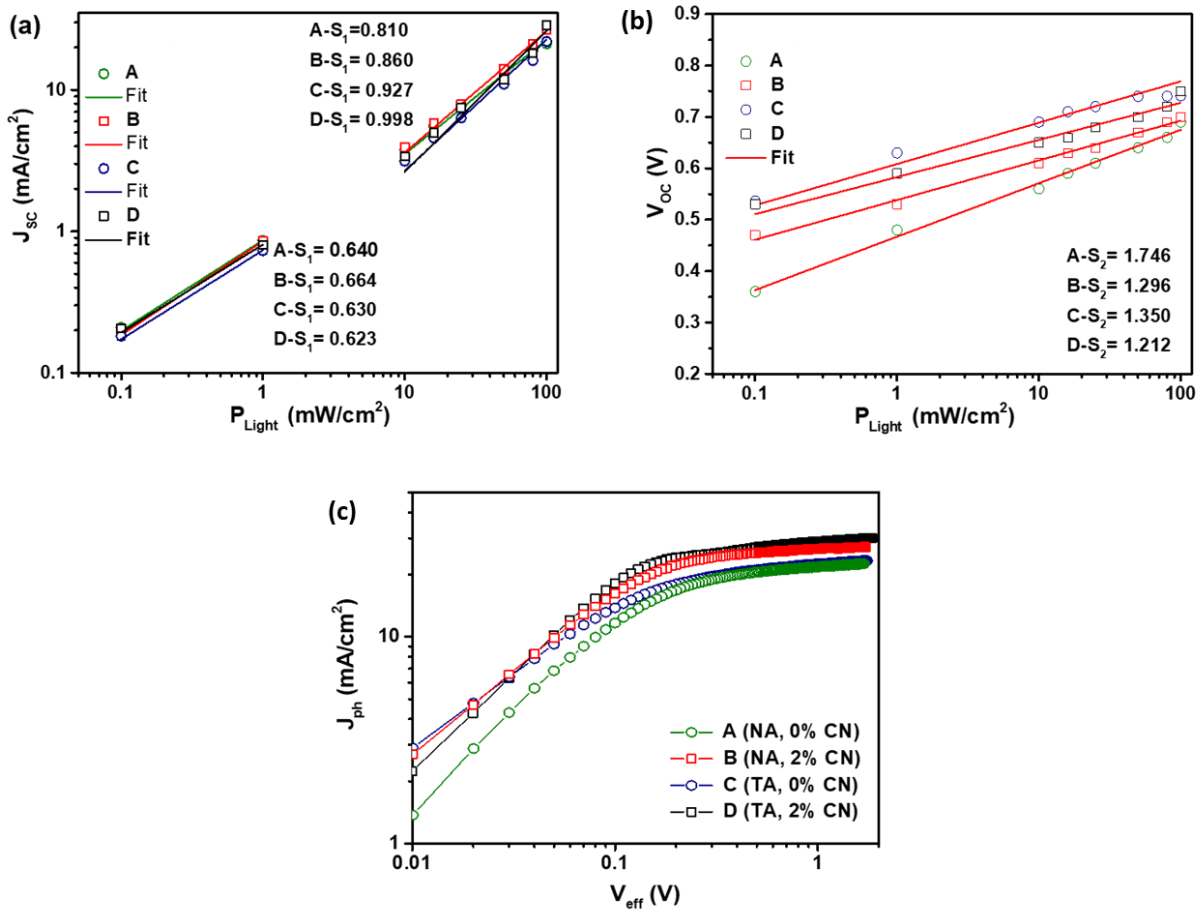

Figure 4.5 Device performance parameters versus the light intensity (a) the J_{SC} and (b) the V_{OC}, symbols for the experimental data and the red line for the fitted data (c) J_{Ph} versus V_{eff} characteristics of the devices under different treatment conditions.

Table 4.2 Optoelectronic parameters calculated from the J_{ph} -V_{eff} curves of iNF-OPVs in **Figure 5c**.

Devices	J-sat (mA/cm^2)	G_{max} ($\times 10^{28}$ m^{-3} s^{-1})	J_{SC} (mA/cm^2)	P_{diss} (%)	G_{rat} ($\times 10^{30}$ m^{-3} s^{-1})
Binary					
A	21.99	1.37	21.23	96.56	1.33
B	26.64	1.66	26.12	98.05	1.63
C	22.45	1.40	22.06	97.79	1.37
D	29.06	1.81	28.61	98.44	1.79

4.3.2 Thin-Film Surface Properties

The morphology of the binary PM6:Y7 blend film (pristine-NA, 0% CN), (NA, 2% CN), (TA, 0% CN), and (TA, 2% CN) films were investigated using AFM with morphology and phase modes shown in **Figure 4.6**. Interestingly, we observed two different trends regarding the effect of 2 % CN additives and the TA. Firstly, for the NA films, where the addition of 2% CN increased the film roughness root mean square (RMS) from 2.88 nm (Pristine films - **Figure 4.6a**) to 3.67 nm (**Figure 4.6b**), secondly and differently, for the TA films, 2 % CN provides more smother film surface from RMS of 1.73 nm (**Figure 4.6c**) to 1.43 nm (**Figure 4.6d**). Thus, the surface morphology in **Figure 6a and c** for 0% CN films reveals a strong aggregation in the film blend that commonly produces large phase separation domains that traps the exciton and hinder the charge transport[240]. As a sequence, it affects the charge dissociation that leads to diminishing the J_{SC} and FF of the fabricated devices as verified in devices A and C (**Table 4.1, Figure 4.3a**) which possessed the highest leakage current (**Figure 4.3b**) and in turn lower PCEs. In case of device B, however the 2% CN-based blend films (**Figure 4.6b**) showed higher surface roughness due to 2 %CN additives than the pristine film-A, but it demonstrates higher performance parameters than device A. Hence, we suggested that the 2 % CN additives has the dominant effect on the physical properties of the film by enhancing the order of the blend microstructure morphology as it has high boiling point that allows the blend to uniformly mix[241], decreasing the effect of Coulomb interaction with delocalization as well as decreasing the domain size that leads to efficient separation of the exciton providing higher J_{SC} and better FF (**Table 4.1**) that make morphological roughness effects less pronounced[83,242,243]. Regarding the TA effect, the TA films showed smoother homogenous surfaces for the 0% CN (**Figure 4.6c**) and 2% CN (**Figure 4.4d**) more than the NA blend films. A network of fiber with less defined phase separation reflecting the well homogenous mix of that PM6 and Y7. This characteristics indicating the adequate inhibition of the molecular aggregation due to the high thermal stability of the norfullerene acceptors[91]. Moreover, this behavior suppressed the carrier recombination and assist the excitons in the active layer blend to reach the donor/acceptor interface, and in turn dissociate into free carriers[237] which typically contribute to enhance the J_{SC} and FF of the based devices. This obtained results in line with the performance of D based devices, possessing the lower RMS as well as more enhanced film crystallization (**phase-Figure 4.6d**). That likely facilitated the charge transport which correlated with the closest n_{id} value to 1, highest P_{diss} (**Figure 4.5c**), lowest leakage current (**Figure 4.3b**), highest J_{SC}, FF, and PCE_{max} (**Table 4.1**). Accordingly, the tunning of both CN additives and TA step are crucial for achieving the balance of exciton dissociation and charge collection, prompting better film morphology and increase in the PCE as confirmed by the case of device D.

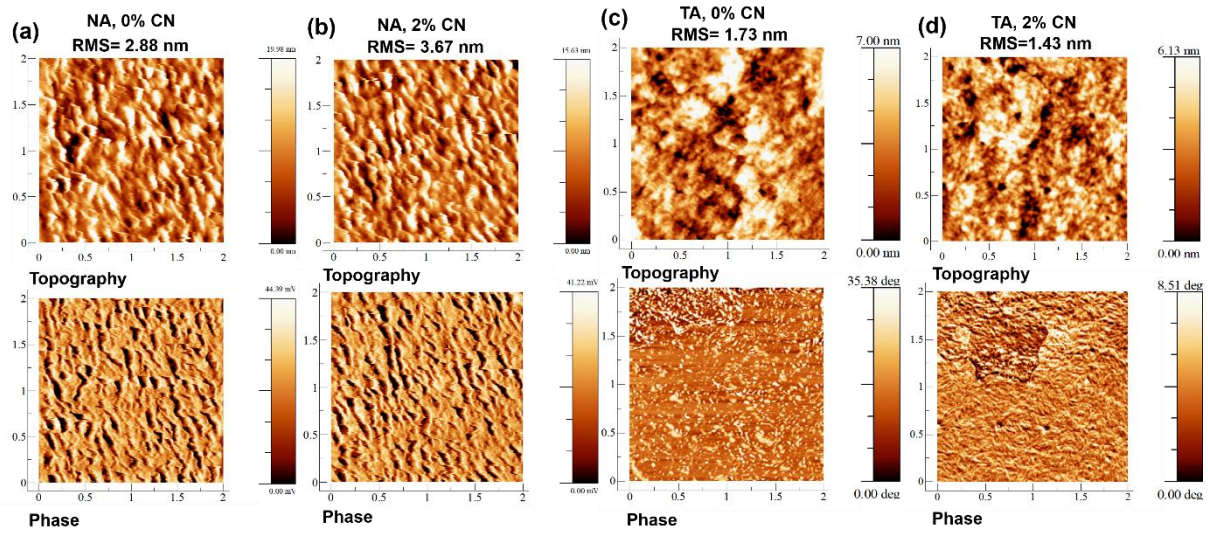

Figure 4.6. AFM topography and phase images of the PM6:Y7 blend films of (a) pristine -NA, 0 % CN, (b) NA, 2 %CN, (c) TA, 0% CN, and (d) TA, 2% CN.

4.3.3 Impedance Spectroscopy-Based Studies

To further investigate the impact of 2% CN additives along with the TA treatment step on the blend film surface and based devices performance, C-V measurements were carried out on the fabricated devices in dark, as shown in **Figure 4.7a**. It illustrates the Mott-Schottky ($A^{-2}C^{-2}$-V) plots of A, B, C, and D based devices, the built-in potential (V_{bi}) can be evaluated by the intercept of the curve with x-axis as demonstrated in the figure. The obtained values of V_{bi} were 0.29, 0.39, 0.36, 0.43 V for, B, C, and D devices, respectively. We noticed that the V_{bi} values was increased by 2% CN additives (devices B higher than A) as well as for the TA devices (D higher than C), thus, the lowest value was for the pristine A device (NA, 0 % CN) and the highest value was for device D (2 % CN and TA). Consequently, at lower V_{bi} the photovoltaic cells do not work efficiently since at forward voltages, the net field in the device reverses, thereby impeding charge carrier extraction instead of helping it[91]. therefore, the low V_{bi} leads to low FF accompanied by diminishing the Voc[91] which is in line with the obtained values in device A and C (**Table 4.1**), confirming the reduction in the PCEs of the corresponding cells. It is worth mentioning that device D demonstrate a prior high chemical capacitance among the other iNF-OPVs as shown in **Figure 4.7a** due to the tunning of both 2% CN additives and TA treatment which resulting in less localized states in the band gap[91] that leads to better V_{OC} and FF [244]. Then, impedance spectroscopy measurements through Nyquist plots were conducted to gain more information about the electric properties of the fabricated devices regarding the interfacial charge transfer

and carrier recombination[165]. **Figure 4.7b** shows the Nyquist plots for the fabricated devices at open circuit bias voltage under illumination which correlated the efficient transfer at the active layer/electrode interface[165]. The figure demonstrates a typical semicircle behavior with real part of impedance (Z´(Ω)) as x-axis and imaginary part (Z´´(Ω)) as y-axis at open-circuit condition. As shown in **Figure 4.7b**, we observed that the 2% CN additives devices (B and D) showed smaller arc radius than the 0% CN (A and C) ones. In addition, regarding the TA devices, devices C and D showed lower impedance and smaller arc radius than devices A and B, respectively. Furthermore, as Arredondo et al. proposed that the impedance arc at low frequency is an indication for the charge accumulation that cannot be extracted by the contacts of the device[206]. Hence, it can be seen that for the low frequency arc decreases by the addition of 2 % CN as well as the TA treatment which in the same line as the arc size. This behavior confirms the lower performance of device A (NA. 0% CN- **Table 4.1**) as it possesses the highest low frequency arc which describes the more pronounced charge accumulation impact that could be originated from pristine morphology disorder of the blend[91]. This consideration is correlated with the high leakage current and low V_{bi} of the pristine devices A. On the other hand, for device D, which has the less low frequency arc reflecting the efficient charge extraction through the device, resulting in lower leakage current, higher V_{bi} and as a sequence, better device performance. Same behavior was obtained for the devices at short circuit current condition (Voltage = 0 V) in **Figure 4.7c**, indicating the rapid charge extraction, which is contributed to the J_{SC} values of the devices, consisting with the results from **Table 4.1**, the optical analysis, and the J_{SC} of the corresponding devices that contributes more to the PCE enhancement. Moreover, same attitude was exhibited at maximum power point voltage (V_{mpp}) in **Figure A.9.**

Therefore, to get more information about the physical parameters of the fabricated cells, we performed an electrical equivalent circuit to fit the experimental Z´-Z´´ data. The electrical component used to fit the plot (Solid lines) illustrated in the inset of **Figure 4.7b**. The fitted parameters were summarized in **Table 4.3**. The mentioned equivalent circuit consists of resistive/capacitive (RC) elements where a distributed resistor (R) represents the resistance of electrons transportation in each layer where R_1, R_2 and R_3 refers to ZnO, blend active layer and the V_2O_5 layer, respectively. In addition, C refers to the geometrical capacitance values of each layer, proving a parallel association of resistor and capacitor for 3 RC elements in series. R_S represents the series resistance from the metallic wires and the ohmic components such as ITO layer Ag electrodes[121,165] and L is the added inductor to fit the data at high frequency[165]. It is important to mention that the model composed of an extra implemented R_4C_4 in series which attached in parallel to R_2C_2 corresponding the photoactive blend layer obeying Debye model[207]. This model was the most suitable to fit the experimental data to explain the effect of the 2% CN additives and thermal annealing treatment carried out in the binary blend. From the fitting data listed in **Table 4.3**, we exhibited that the fitting capacitance values for each layer were in good agreement with the theoretical values shown in **Table 4.4**. This might indicate that at V_{OC}, the

IS data was controlled by the geometrical capacitances provided by the metal insulator-metal (MIM) model reflecting the presence of fully depleted layers[208]. From the fitted resistance values for each layer of the fabricated devices (**Table 4.3**), it can be seen that the R_S value is low in all devices within the range of 2.0-3.0 Ω. First, by investigating the effect of 2% CN additives, we found that the R_2 value of B device (17.0 Ω) was less than that obtained in A device (22.0 Ω) . In addition, device D showed R_2 value of 20.0 Ω which is lower than the one of device C (25.0 Ω). Thus, the 2 % CN additives suppresses the R_2, performing better path for charge transportation within the blend film[165]. This result is in good agreement with the R_S values obtained from dark J-V characteristic in which 2% CN-treated devices showed lower R_S values than 0% CN devices (**Figure 4.3b**).

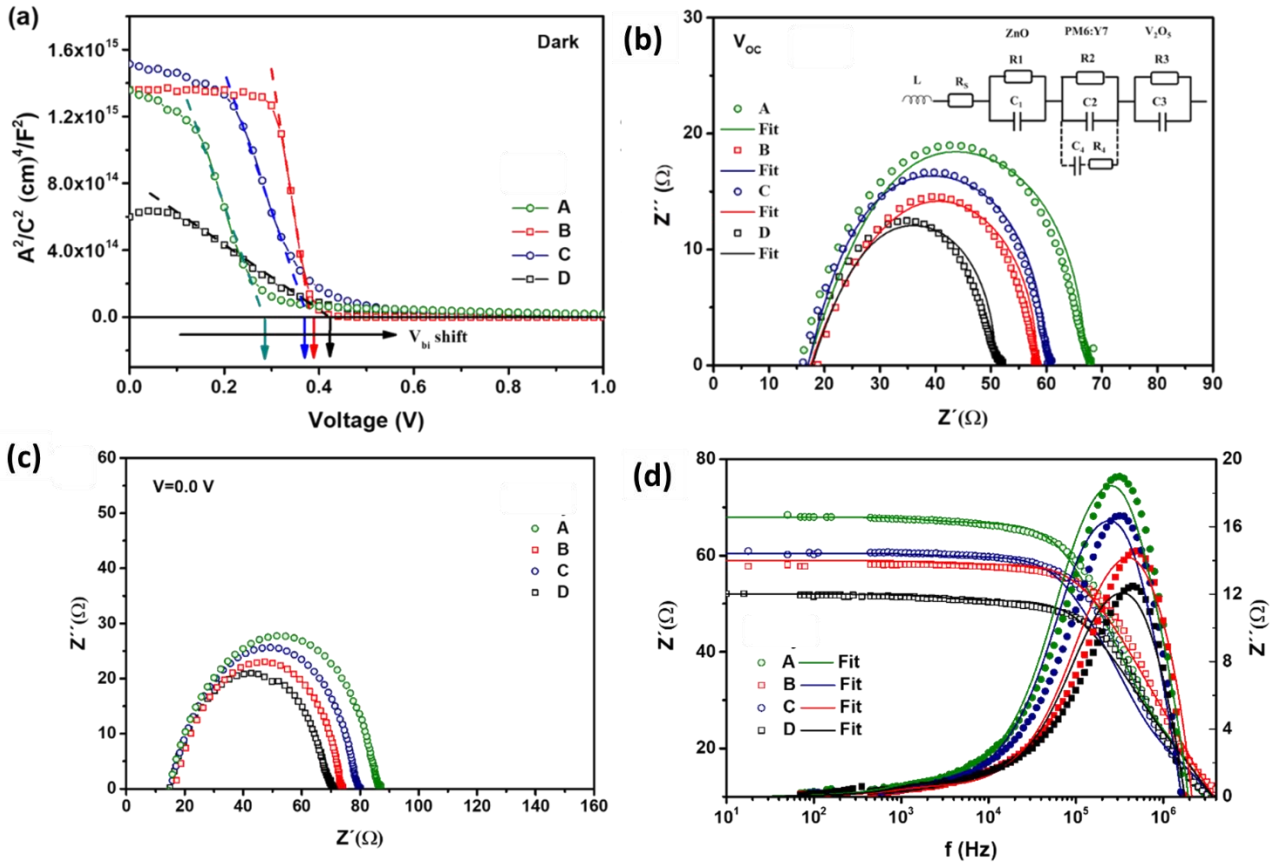

Figure 4.7 (a) Mott Schottky plot under dark at 1 kHz of the binary iNF-OPVs. Nyquist plots (b) at V_{OC}, using symbols for the experimental data and the fitting results in solid lines by applying the equivalent circuit in the inset of the figure, (c) at V_{MPP}, under AM 1.5G illumination of the iNF-OPVs devices. (d) The Bode plot: experimental (symbols) and fitted (lines) values for the real part (left axis) and the imaginary part (right axis) of the fabricated devices at V_{OC}. The fitted lines are obtained using data demonstrated in Table 4.3.

Table 4.3 The fitted parameters of the equivalent circuit using Debye model at V_{OC} for the fabricated iNF-OPVs devices, the parameter $\tau = R_4 \times C_4$ where R_4 parameter were demonstrated in the equivalent circuit in the inset of Figure 4.7b.

Physical parameters of the Binary iNF-OPVs	**Device A (NA, 0% CN)**			**Device B (NA, 2% CN)**		
ZnO	R_S = 2.0 Ω L = 1.3 µH	R_1= 26.0 Ω	C_1= 16.0 nF	R_S = 2.0 Ω L = 1.3 µH	R_1= 24.5 Ω	C_1= 16.0 nF
PM6:Y7		R_2= 22.0 Ω τ = 80.0 µs	C_2= 2.8 nF C_4= 200.0 nF		R_2= 17 Ω τ = 80.0 µs	C_2= 2.8 nF C_4= 200.0 nF
V_2O_5		R_3= 18 Ω	C_3= 79.7 nF		R_3= 17.5 Ω	C_3= 79.7 nF
		R_{Total} = 68.0 Ω			R_{Total} = 61.0 Ω	
	Device C (TA, 0% CN)			**Device D (TA, 2% CN)**		
ZnO	R_S =3.0 Ω L = 1.3 µH	R_1= 19 Ω	C_1= 16.0 nF	R_S = 2.0 Ω L= 1.3 µH	R_1= 18.0 Ω	C_1= 16.0 nF
PM6:Y7		R_2= 25 Ω τ = 80.0 µs	C_2= 2.8 nF C_4= 100.0 nF		R_2= 20.0 Ω τ = 60.0 µs	C_2= 2.8 nF C_4= 200.0 nF
V_2O_5		R_3= 12 Ω	C_3= 79.7 nF		R_3= 12 Ω	C_3= 79.7 nF
		R_{Total} = 59 Ω			R_{Total} = 52 Ω	
		R_{Total} = 43.0 Ω			R_{Total} = 41.0 Ω	

Table 4.4 Dielectric constants and calculated capacitances for each layer of the fabricated iNF-OPVs.

Layer	ε_{Layer}	**Capacitance (nF)**	**Thickness (nm) d_{Layer}**
ZnO	6[121,210]	16	30
Blend	3.5[58,211,212]	2.79	100
V_2O_5	5[166]	79.7	5

The capacitance (C) for each layer were calculated using formula of $\boldsymbol{C = \varepsilon_0 \varepsilon_{Layer} \frac{A}{d_{Layer}}}$, where A is the Active area, d_{Layer} the thickness for each layer, ε_0 vacuum dialectic permittivity and ε_{Layer} the relative dielectric permittivity (the referred values extracted from the references [58,121,166,210–212].

Regarding the ZnO and V_2O_5 interfacial layer within theiNF-OPVs devices, we revealed no clear effect upon the 2% CN additives. Thus, the total resistance (R_{Total}) evaluated for the devices (listed in **Table 4.3**) was mainly controlled by the R_2 of the blend. Accordingly, R_{Tota} followed the same trend of R_2 showing higher value for A and C based devices, verifying their low iNF-OPVs performance, and the smaller R_{Total} value for devices B and D devices confirming the enhanced iNF-OPVs performance. This trend of the resistance obtained for the devices was confirmed by the Bode plot curve in **Figure 4.7d**. Furthermore, this obtained behavior agreed with the R_S values obtained by the J-V characteristics under illumination (**Table 4.1**).

Second, as for the TA effect, by comparing device A with C and device B with D, we manifested that the R_2 values of the TA blends were a bit higher than NA films for both 0 % and 2 % CN devices as presented in **Table 4.3**. But, it was surprising that the R_1 and R_3 for the interfacial layers (ZnO and V_2O_5) were clearly diminished resulting in reducing the R_{Total} of the TA devices. This observation confirms the enhancement in the interface between the blend and the interfacial layers which might be due to the homogenous film morphology obtained for the TA-blend films as discussed previously. Hence, it was interesting to find that both of 2 %CN and TA treatments contributed to decline the impedance of the fabricated devices, indicating less imbedded traps in the related blend film that highly matched with the provided high film quality (**Figure 4.6d**) and the calculated n_{id} value observed for devices D. In addition, this behavior followed the same trend obtained in the previously discussed characteristics confirming the enhancement effect upon combining multiple treatments.

An alternative way for understanding the recombination mechanisms using IS technique is the measurement of the capacitance-frequency (Cf) to calculate the trap density of state (DOS). This characterization has been performed for OPVs in many research work to obtain the change in trap emission and disorder-induced tail states within the devices[64,165,169–171,]. Therefore, the traps DOS at a given energy level, E_ω, can be evaluated by the variation of the capacitance of the device with the frequency. This correlated the trapping and the charge release by shallow traps in the band gap near to the Fermi energy level as explained by equation 4.2[64,171]

$$\mathrm{DOS}(E_\omega)_{traps} = -\frac{V_{OC}\omega}{t\ q\ T\ k_B}\frac{\partial\ \mathrm{C}}{\partial\ \omega} \tag{4.2}$$

where, C is the measured capacitance, V_{OC} is the open circuit voltage obtained by the J-V characteristics under illumination conditions, ω is the angular frequency, t is the layer thickness, k_B is the Boltzmann constant, q is the electron charge and T is room temperature (300K).

To observe the relation of the trap-DOS as an energy dependent, the following equation has been applied:

$$(E_\omega)_{traps} = k_B\ \mathrm{T}\ \ln\frac{2\beta \mathrm{N}}{\omega} = \mathrm{E_O}\text{- }k_B\ \mathrm{T}\ \ln\omega \tag{4.3}$$

where, β is the cross section and N is the effective density of state[172]. Since assuming that 2βN is independent of the frequency value, the change in its value is related to the shift in the DOS values on energy scale (E_O)[75].

. **Figure 4.8a** displays the calculated trap-DOS plotted as a function of energy for the fabricated binary devices. It shows a single exponential trap distribution for all samples where almost same slope values were detected which defines the same trap activation energy and carrier response[58]. Regarding the TA treatment,

we did not see much change in the DOS value from device A to C or from B to D. However, a shift in E_O value was observed showing bit higher DOS of B and D devices with 2 % CN more than device A and C devices with 0 % CN. This behavior can be explained by Equation 3.3, assuming that this small shift of E_O or higher DOS values might be result from decreasing in the βN value, which means higher obtained energy because of less localized shallow trap sites created due to the addition of 2% CN to the blend film[64,121,172,225,245]. Furthermore, the shifting value of the 0 % CN devices shown in **Figure 4.8b** and **4.8c**, X, has been calculated as follows[121]:

Using equation 4.3 in the manuscript, we get the energy dependence on the frequency for the 2 % CN treated and 0% CN cells as $E_{2\%\ CN} = k_B T \ln\frac{\alpha_{2\%\ CN}}{\omega}$ and $E_{0\%\ CN} = k_B T \ln\frac{\alpha_{0\%\ CN}}{\omega}$, respectively, where the parameter $\alpha = 2\beta N$ has been defined.

So, the energy's difference between the 0% CN and 2 % CN devices can be ascribed as

$$E_{0\%\ CN} - E_{2\%\ CN} = E_{O\ (0\%\ CN)} - E_{O\ (2\%\ CN)} = k_B T \ln\alpha_{0\%\ CN} - k_B T \ln\alpha_{2\%\ CN} = k_B T \ln\frac{\alpha_{0\%\ CN}}{\alpha_{2\%\ CN}}$$

Finally, the shifting value due to degradation can be obtained as

$$X = \exp\left(\frac{E_{0\%\ CN} - E_{2\%\ CN}}{k_B T}\right) = \frac{\alpha_{0\%\ CN}}{\alpha_{2\%\ CN}} = \frac{\beta_{0\%\ CN}.N_{0\%\ CN}}{\beta_{2\%\ CN}.N_{2\%\ CN}} \quad (4.4)$$

where β is the cross-section and N is the effective density of states.

By comparing the energy shift values (equation 4.4) of the 0 % CN devices (A and C) and the 2 % CN ones (B and D) as shown in **Figure 4.8b** and **4.8c**, we obtained that the 0 % CN devices exhibited almost double trapping sites more than the 2% CN treated ones. This observation confirms the superior performance of the B and D devices due to the addition of 2% CN that diminished the presence of defects inside the devices. This behavior was interestingly highly matched with the E_U study discussed previously in **Figure 4.4e** and with the impedance behavior in **Figure 4.7b** along with the performance obtained in **Figure 4.3a** which explains the higher FF, V_{OC} and J_{SC} obtained for these based devices

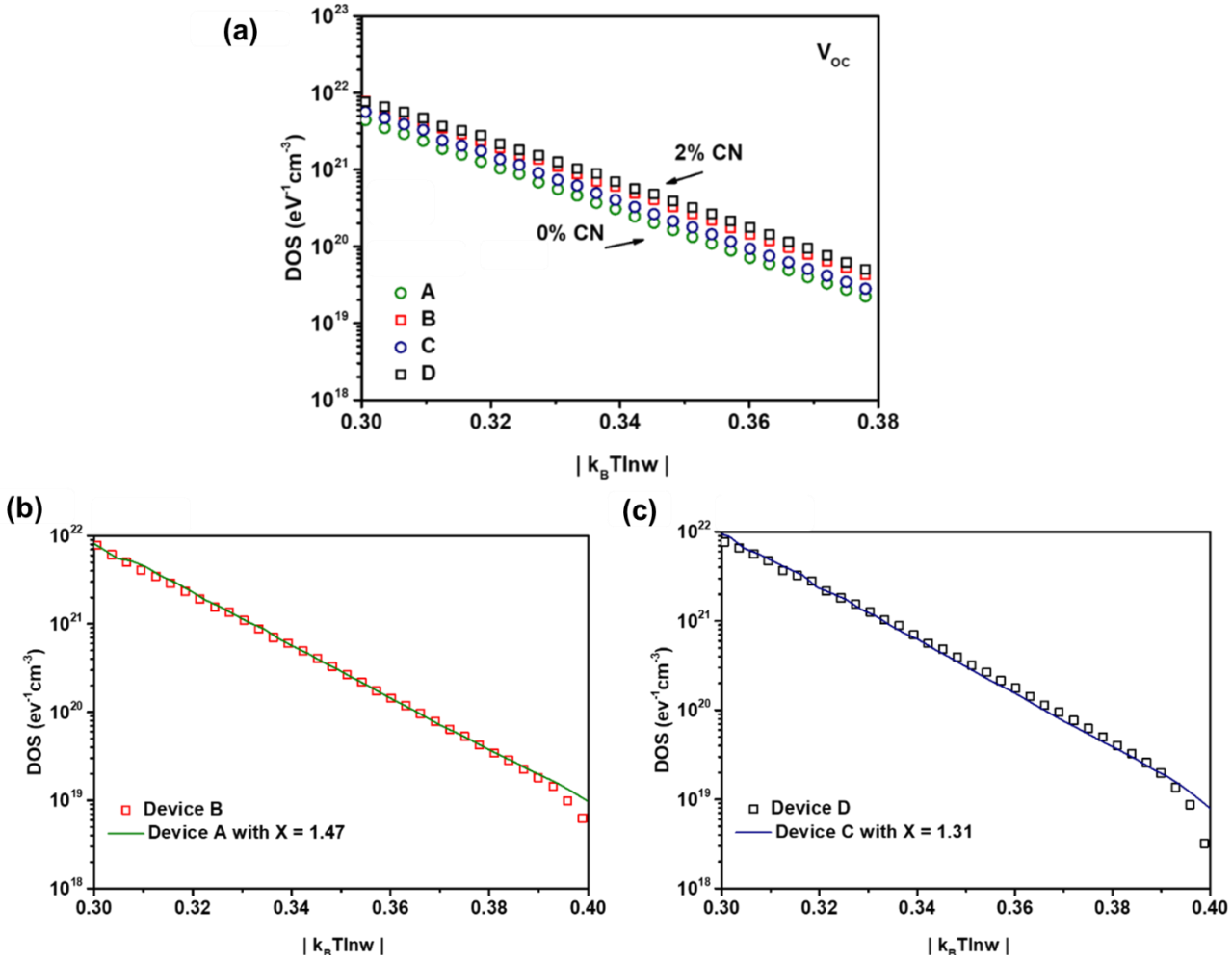

Figure 4.8 (a) DOS as function of $|k_BTln\omega|$ at V_{OC} under AM 1.5G illumination of the iNF-OPVs devices. the shifting value (X) to superpose the 2% CN treated devices (b) A and B based devices, (c) C and D based devices.

4.4 Conclusions

In summary, fine-tuning of blend morphology is a key factor that limits the performance of the bulk-heterojunction organic photovoltaics (BHJ-OPVs). Here, morphological control of the binary PM6:Y7 blends was conducted through 1-chloronaphthalene (CN, 2%) solvent additives and thermal annealing treatment (TA, 100 °C) with respect to their influence on the photovoltaic performance. Moreover, a distinct study was accomplished on the optical and electric properties of the treated and non-treated based devices by external quantum efficiency measurements and impedance spectroscopy. The results indicated that the 2 % CN solvent addition showed pronounced increment of the J_{SC} by ≈ 27 % and FF by ≈ 12.5 %. Furthermore, the TA treatment provides a higher PCE for the iNF-OPV mainly due to the increment of the V_{OC}. These performance enhancement was mainly upon suppressing the carrier recombination and assist the excitons in the photoactive layer blend to reach the donor/acceptor interface, and in turn easily dissociated into free carriers[237] which typically contributed to enhance the J_{SC} and FF of the based devices. Moreover, the low RMS as well as more enhanced film crystallization were exhibited for the champion D based devices that conducted the dual modifications of 2 % CN solvent additives along with the TA treatments. That likely facilitated the charge transport providing the closest n_{id} value to 1, highest P_{diss}, lowest leakage current, highest J_{SC}, FF, and in turn the best PCE_{max} Accordingly, the tunning of both CN additives and TA treatments are crucial for achieving the balance of exciton dissociation and charge collection, prompting better film morphology and increase in the PCE as confirmed by the case of D based devices.

Chapter 5

Enhancing the Photostability of Inverted Nonfullerene Organic Solar Cell Devices Implementing PDINO Interfacial Layer

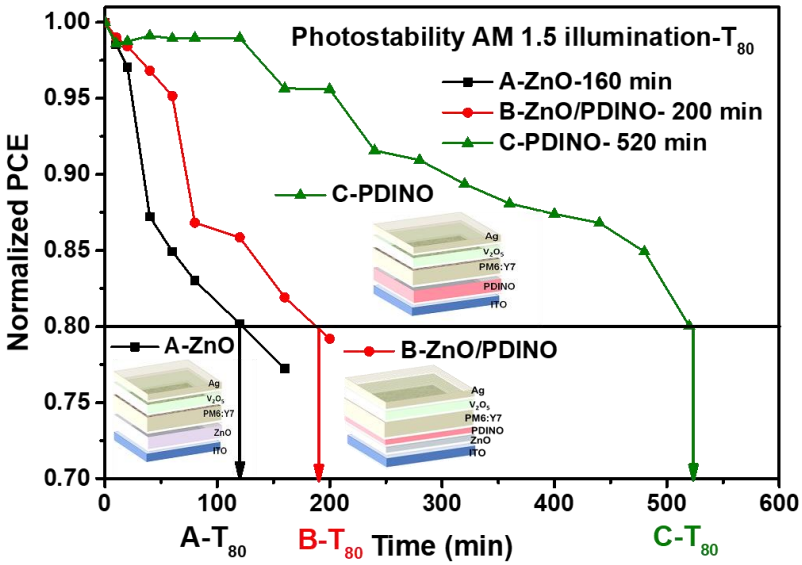

This chapter is based on the published works: Enas Moustafa, M. Méndez, J. Pallarès, and L.F. Marsal, Low Temperature Based PDINO Cathode Interlayer for High Operational Photostable Inverted Non-Fullerene Organic Solar Cells. ***Solar Energy Materials and Solar Cells***, **2022**, 248, 111985.

5.1 Introduction

The power conversion efficiency (PCE) of organic solar cells (OSCs) has been promptly improved once emerging the recently developed non-fullerene small-molecules acceptors (NFAs), approaching PCE of 20% [22,83,85–87,246]. This remarkable increase in the power conversion efficiencies was due to the significant enhancement in the light absorption along with diminishing the energy losses [22,24,125,229,234,247], particularly upon minimizing the trade-off behaviour between voltage loss and charge generation in nonfullerene organic solar cells (NF-OSCs) [88,89,248]. Despite the efficiency, long-term operational stability, particularly illumination stability, considers as a major challenging issue that must be confronted for the commercialization of OSCs [176,249–251]. Several strategies have been investigated to understand the intrinsic photo-degradation mechanism in order to overcome this recent demanding subject. Some of these avenues concern about the stability of the bulk-heterojunction photoactive blend microstructure through additives modifications to tune the properties of the photoactive layer [213,252–254]. Some other approaches determined the critical role of the interface materials stability and their compatibility with the contacted photoactive layer and electrodes, reflecting their importance for long-term stable OSCs [249,251,255–257]. This interface-induced instability approach is less frequently studied and still debatable even for high-performance systems. Moreover, the architecture of the OSCs has a pronounced impact on the stability of the devices as shown by M. T. Lloyd et al. group work[110], B. MacLeod[111]and several other reported studies, where the inverted structure assists the OSCs stability over the conventional structures from the scale of minutes up to years [30,110–112,257–259].

Furthermore, zinc oxide (ZnO) is the typically used cathode interlayer in inverted OSCs (i-OSCs), which exhibit better oxygen and humidity resistance as compared to the interface materials used in the conventional structure [30,110–112,257,260]. However, it possesses inescapable photo-instability behavior upon ultraviolet (UV) illumination, known as photocatalytic effect [261], resulting in photoinduced shunts and cause charge carrier recombination at the ZnO/photoactive layer interface, which in turn dramatically diminishing the performance of the corresponding devices [262]. Therefore, developing a compatible and photostable cathode inter layer materials that could provide efficient and photostable OSCs classified as an urgent need for the scalability of OSCs. Thus, herein, we demonstrate the use of PDINO as a promising low temperature operation cathode interlayer that provides a highly photostable inverted non-fullerene organic solar cells (iNF-OSCs).

5.2 Experimental Methods.

This part reports the details of the PDINO and ZnO interfacial layers employing the previously optimized PM6:Y7 blend solution synthesis in Chapter 4. Furthermore, explaining the device fabrication procedures of the inverted NF-OSCs conducted in this chapter based on the structure of ITO/*ETL*/PM6:Y7/V_2O_5/Ag as

Illustrated in **Figure 5.1a** with the energy level alignment for the fabricated devices, demonstrated in **Figure 5.1b**. The energy positions of the band edges for the semiconductors and the metals work functions were taken from [235], [117], 30 ,and [263] references. ZnO, ZnO/PDINO bi-stack, and PDINO were used as n-type charge transport interfacial layers while V_2O_5 applied as p-type. Moreover, a binary BHJ of PM6:Y7 was employed as the photoactive layer. The schematic diagram for the fabrication procedures of the inverted structure OPV devices in this thesis is prior illustrated in **Figure 2.8** in Chapter 2. For fabricating the NF-OPVs binary devices, The ZnO precursor solution was spun-coated on the top of the precleaned ITO substrates to deposit 30 and 30, 20 nm ZnO-film thicknesses for the A-ZnO-ETL and the optimization of B-ZnO/PDINO based devices, respectively, then annealed in air for 1 h at 200 °C. The ZnO-coated ITO substrates were transferred to a nitrogen-filled glove box for the PDINO and photoactive layer deposition. Regarding the PDINO based devices, we prepared 1 mg/ml PDINO/methanol solution that stirred for 4 h. Then, the PDINO solution was deposited over the ZnO film to obtain thicknesses of 10 and 15 nm for the optimization of B-ZnO/PDINO based devices, then 10, 20, and 35 nm for the optimization process of the C-PDINO based ones. It is important to note that all the device fabrication steps for C based devices were conducted inside the glove box. The PM6:Y7 blend solution was synthesized upon the optimized parameters achieved from Chapter 4, with the weight ratio of 1:1 dissolved in chlorobenzene to prepare the total concentration of 20 mg mL^{-1} solution. Then, the blend solution was stirred and heated at 80 °C for 3 h. 2 vol% of 1-chloronapthalene was added as solvent additives to the blend. The blend solution was spun-coated onto the A-ZnO, B-ZnO/PDINO and C-PDINO substrates to obtain an active layer thickness around 100 nm. Then, the prepared films were treated with 100 °C for 1 h. The substrates were finally transferred into the vacuum thermal evaporation chamber inside the glove box where 5 nm of V_2O_5 and 100 nm Ag were sequentially evaporated as aforestated in Chapter 2 in **Figure 2.8**. Finally, we transferred the fabricated devices from the evaporator to the sample holder inside the glove box which was carefully sealed for the device's measurement steps.

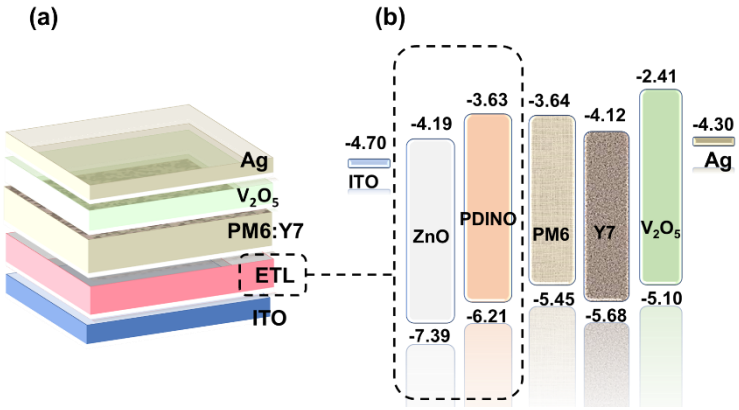

Figure 5.1 (a) Schematic diagram of the fabricated iNF-OSCs structure, (b) the energy band diagrams of the inverted OSCs.

5.3 Results and Discussions

5.3.1 Device Optimization Procedures and Performance Properties

In this work, we fabricated the iNF-OSCs using three different structures of electron interfacial layers. Where, bilayer stack of PDINO/ZnO (named Type B-based devices) and PDINO (named Type C- based devices) were operated as cathode interlayers to fabricate iNF-OSCs with the configuration of ITO/*ETL*/PM6:Y7/V_2O_5/Ag as illustrated in **Figure 5.1a**. Moreover, control devices with ZnO as cathode electron transporting layer (ETLs) that optimized in our previous work[100] were used for comparison (named Type A- based devices). The performance of the fabricated iNF-OSCs to optimize the interlayers in Type B and C based devices incorporating different thickness of ZnO and PDINO films was displayed in **Figure 5.2a** and 5.2b using the representative current density-voltage (J-V) characteristics under simulated AM 1.5G illumination at 100 mW cm^{-2}. In addition, the photovoltaic performance parameters statistics were summarized in Table 5.1.

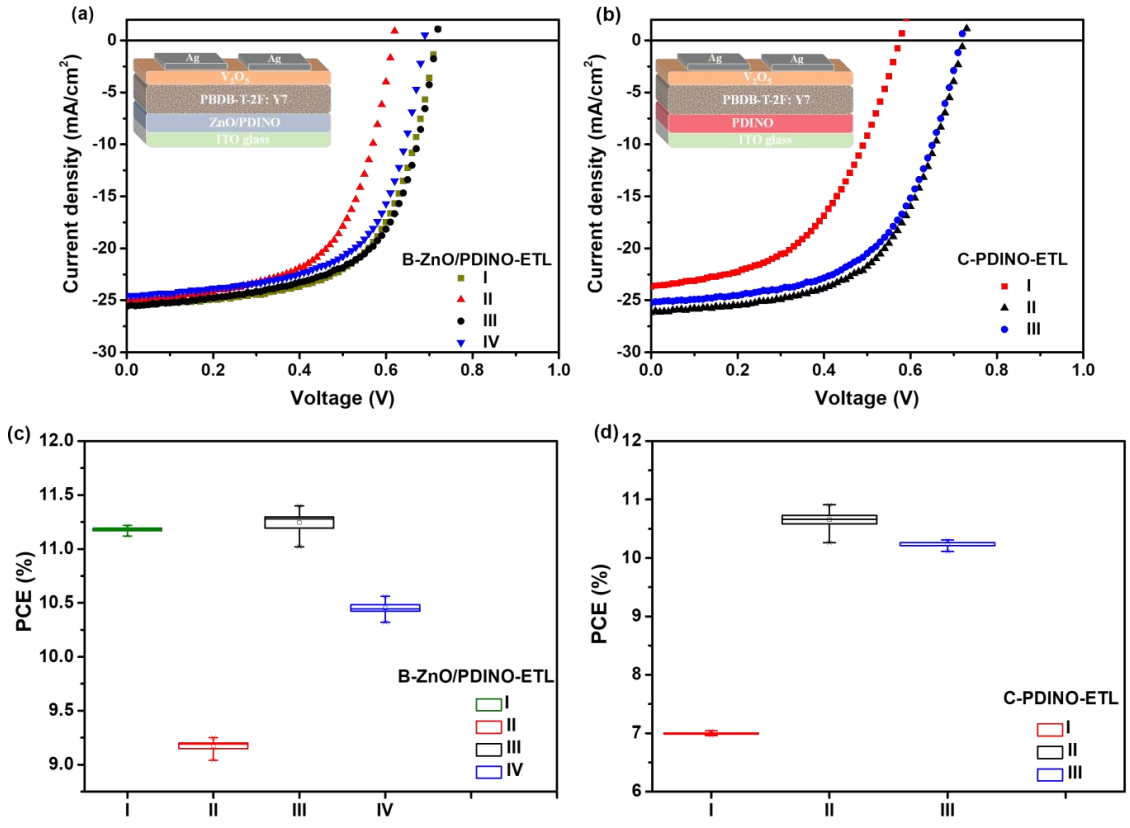

Figure 5.2 Current density-voltage (J-V) characteristic curves under AM 1.5 G illumination of (a) B-ZnO/PDINO based iNF-OSCs with different thickness of ZnO and PDINO layers, (b) C-PDINO based iNF-OSCs with different thickness of PDINO layer. PCE % box plot of (c) B-based devices, and (d) C-based devices.

Table 5.1. Inverted organic solar cells performance parameters statistics under AM 1.5 G illumination condition during the optimization step of devices B and C in **Figure 5.1**.

Thicknesses (nm)			V_{OC} (V)	J_{SC} (mA/cm^2)	FF	PCE (%)	PCE_{MAX} (%)	R_S (Ω cm^2)	R_{Sh} (Ω cm^2)
Type A		ZnO	A-ZnO-ETL [100]						
A-ZnO		30	0.75 ± 0.02	28.61 ± 0.33	0.64 ± 0.09	13.04 ± 0.58	13.62	1.20 ± 0.13	382 ± 61
Type B	ZnO	PDINO	B-ZnO/PDINO-ETL						
I	30	10	0.72 ± 0.01	25.51 ± 0.18	0.61 ± 0.02	11.12 ± 0.10	11.22	1.84 ± 0.45	395 ± 11
II	30	15	0.62 ± 0.02	24.97 ± 0.20	0.60 ± 0.02	9.04 ± 0.21	9.25	1.65 ± 0.21	329 ± 32
III	20	10	0.72 ± 0.01	25.77 ± 0.21	0.61 ± 0.02	11.00 ± 0.40	11.40	1.65 ± 0.14	344 ± 22
IV	20	15	0.69 ± 0.02	24.54 ± 0.11	0.62 ± 0.01	10.32 ± 0.24	10.56	1.57 ± 0.44	361 ± 16
Type C		PDINO	C-PDINO-ETL						
I		35	0.57 ± 0.02	24.62 ± 0.11	0.50 ± 0.04	6.96 ± 0.07	7.04	3.11 ± 0.36	198 ± 91
II		20	0.72 ± 0.01	26.15 ± 0.23	0.58 ± 0.04	10.26 ± 0.65	10.91	4.71 ± 0.23	397 ± 51
III		10	0.70 ± 0.01	25.25 ± 0.42	0.57 ± 0.02	10.11 ± 0.19	10.30	4.64 ± 0.81	428 ± 47

The data were presented from an average of at least 9 devices

Accordingly, we selected devices-III of type B (III-B) with ZnO/PDINO bilayers thicknesses of 20/10 nm, respectively and devices II of type C (II-C) with PDINO film thickness of 20 nm as the optimized devices that illustrated in the PCE % box plots in **Figure 5.2c,d** and **Table 5.1**. The control ZnO-based devices (A-ZnO-ETL) in our previous report[100] exhibited a maximum power conversion efficiency (PCE_{Max}) of 13.62 % with an average open-circuit voltage (V_{OC}) of 0.75 V, a short circuit current density (J_{SC}) of 28.61 mA cm^{-2}, fill factor (FF) of 0.64, series (R_S) and shunt (R_{Sh}) resistances of 1.20 and 382 Ω cm^2, respectively. Using the optimized ZnO/PDINO stacking bilayer cathode (B-ZnO/PDINO-ETL) based devices, we obtained a reduction of the PCE_{Max} to 11.40 % and the J_{SC} to 25.77 mA cm^{-2} as well as a slight diminishing in the average V_{OC} (0.72 V), FF (0.61) and R_{Sh} (344 Ω cm^2) along with a bit increase in the R_S average values to 1.65 Ω cm^2. Same behaviour was observed for the PDINO-based devices (C-PDINO-ETL) that revealed a PCE_{Max}, average V_{OC}, J_{SC}, FF, and R_S of 10.91 %, 0.72 V, 26.15 mA cm^{-2}, 0.58 and 4.71 Ω cm^2, respectively. In contrast, the R_{Sh} values where slightly improved to 397 Ω cm^2 as listed in Table 5.1.

5.3.2 Photostability Study Under AM 1.5G Continues Illumination Condition

The previously mentioned devices of types A (A-ZnO), B (B-ZnO/PDINO) and C (C-PDINO) were determined to perform the photostability aging test under continues exposure of simulated AM 1.5G

illumination condition (100 mW cm^{-2}) as demonstrated in **Figure 2.9** in Chapter 2, following the international Summit on OSC Stability ISOS Standard [203] till achieving 80 % of their initial PCE-T_{100} values (T_{80}). The T_{100} is the time of the initial PCE values of the fresh-prepared devices, T_{90} is the time reaching 90% of their initial PCE as explained by the protocol [203]. During the Photo-aging test measurements, the devices were kept under continues light exposure and measured every 10 minutes for the first 20 minutes, then every 20 minutes till the 80 minutes, then every 40 minutes till the T_{80} degradation time as presented in the inset labels of **Figure 5.3**. In this study, we pointed out the significant effect obtained by the photo-aging test. Therefore, it was conducted in an inert atmosphere of <0.1 ppm O_2 <0.1 ppm H_2O using the sealed samples holder mentioned previously, to avoid the possible degradations that might arise from the oxygen and the ambient moisture.

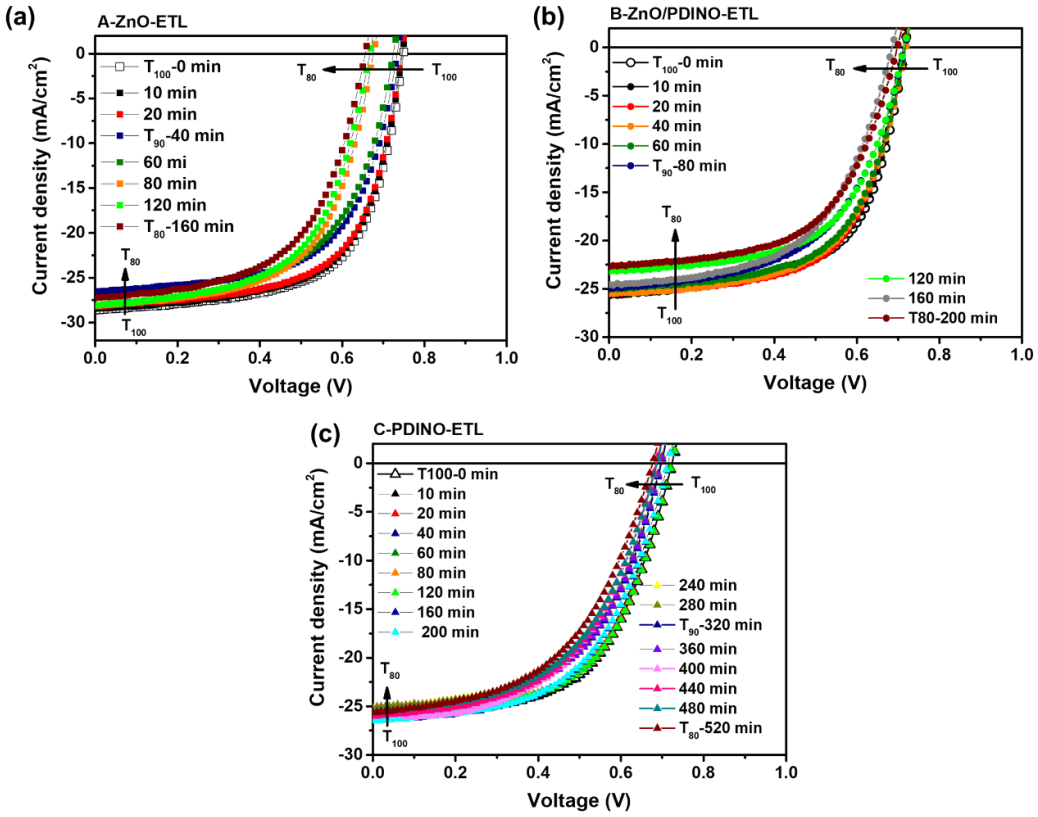

Figure 5.3 Current density-voltage (J-V) characteristic curves under AM 1.5 G illumination of the (c) A-ZnO (d) B-ZnO/PDINO and (e) C-PDINO based devices over the photo-aging time till achieving T_{80}.

Figure 5.4a,b,c depict the T_{100}, T_{90}, and T_{80} J-V characteristics of the A-ZnO, B-ZnO/PDINO, and C-PDINO based devices under continues illumination. Moreover, the T_{90} and T_{80} lifetimes of the corresponding devices are listed in Table 5.2. Moreover, the normalized PCE values are summarized in **Figure 5.5a**. It was

surprising to obtain that the lowest T_{100} performance devices possessed by the PDINO interlayer (C-PDINO) exhibited excellent photostability, maintaining 80% of their efficiency after 520 min illumination, while the B-ZnO/PDINO based devices showed a lower photostability by reaching their T_{80} after 200 min. However, the highest T_{100} performance ZnO-based control iNF-OSCs demonstrated a rapid decay in the PCE presenting an accelerated degradation, achieving T_{80} after 160 min only under same condition, which agreed with the recent work reported by M. Cui et al.[249]. Hence, it is worthy to notice that after achieving T_{80}, the C-PDINO based devices showed almost 3 times longer lifetime than the ZnO-based devices (control-A-ZnO and B-ZnO/PDINO) under same photo-aging conditions as simplified in **Table 5.3**. Furthermore, it is important to note that in the early minutes, the ZnO based devices (Type A and B) demonstrated a faster decay than the C-PDINO based devices that clarified in **Figure 5.5a**. This phenomenon is known as a "burn in loss" degradation behavior which is commonly observed performance loss under light [253,264]. This intrinsic light-driven degradation is believed to be due to the material properties[252,265,266] and the photochemical reaction between the interfacial layers and the photoactive layer [251,264,267,268]. Hence, we can observe that the C-PDINO based devices exhibited insignificant burn in loss effect that reflecting their outstanding photostable behavior.

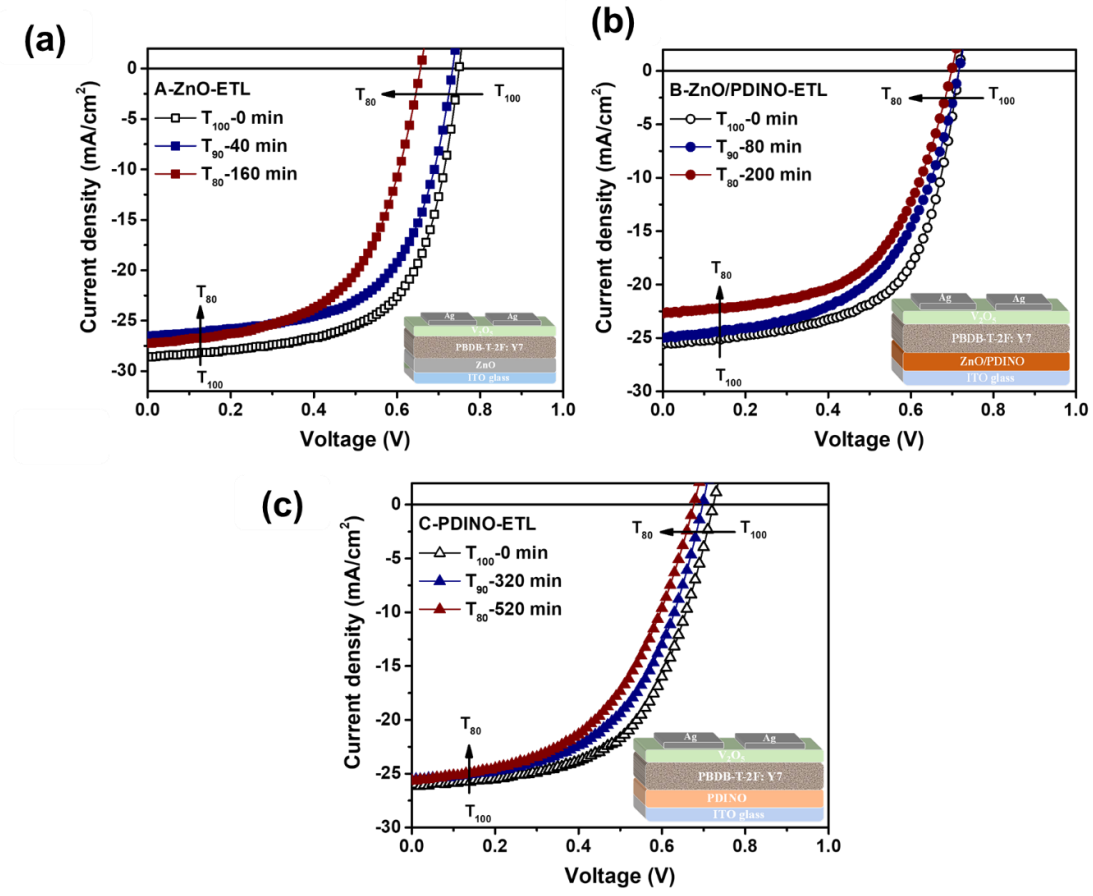

Figure 5.4 Current density-voltage (J-V) characteristic curves under AM 1.5 G illumination of the photo-aged (c) A-ZnO (d) B-ZnO/PDINO and (e) C-PDINO based devices.

Table 5.2 Inverted organic solar cells performance parameters statistics of the T_{100} fresh, T_{90} and T_{80} photo-degraded devices over photo-aging times under AM 1.5 G illumination.

Device Type	V_{OC} (V)	J_{SC} (mA/cm^2)	FF	PCE (%)	PCE_{MAX} * (%)	R_S (Ω cm^2)	R_{Sh} (Ω cm^2)
A-ZnO-ETL							
T_{100}- 0 min[100]	0.75 ± 0.02	28.61 ± 0.33	0.64 ± 0.09	13.04 ± 0.58	13.62	1.20 ± 0.13	382 ± 61
T_{90}- 40 min	0.73± 0.01	26.12 ± 0.82	0.61 ± 0.03	11.46 ± 0.42	11.88	1.31 ± 0.24	362 ± 26
T_{80}- 160 min	0.66 ± 0.01	27.01 ± 0.62	0.52 ±0.04	10.11 ± 0.41	10.52	2.41± 0.14	314 ± 12
B-ZnO/PDINO-ETL							
T_{100}- 0 min	0.72 ± 0.01	25.77 ± 0.21	0.61 ± 0.02	11.00 ± 0.40	11.40	1.65 ± 0.14	344 ±22
T_{90}- 80 min	0.72 ± 0.01	25.01 ± 61	0.55 ± 0.06	9.81 ± 0.08	9.89	2.15 ± 0.21	289 ± 24
T_{80}- 200 min	0.70 ±0.01	22.69 ± 0.47	0.57 ± 0.04	9.00 ± 0.03	9.03	2.05 ± 0.11	342 ± 46
C-PDINO-ETL							
T_{100}-0 min	0.72 ± 0.01	26.15 ± 0.23	0.58 ± 0.04	10.26 ± 0.65	10.91	4.71 ± 0.23	397 ± 51
T_{90}- 320 min	0.70 ± 0.02	25.80 ± 0.42	0.54 ± 0.03	9.55 ± 0.20	9.75	3.64 ± 0.61	364 ± 46
T_{80}- 520 min	0.68 ± 0.02	25.62 ± 0.63	0.51 ± 0.02	8.63 ± 0.21	8.84	4.88 ± 0.19	238 ± 61

The statistics average values of the performance parameters based on 9 devices.

Table 5.3 Photostability lifetime of the photo-aged iNF-OSCs under AM 1.5G illumination.

Standard lifetime	A-ZnO-ETL	B-ZnO/PDINO-ETL	C-PDINO-ETL
T_{90} (min)	40	80	320
T_{80}(min)	160	200	520

Moreover, we can clearly see a sharp burn in loss of the V_{OC} and FF values regarding the control A-ZnO based devices as shown in **Figure 5.5b,c**, V_{OC} reached 88% while the FF achieved 82 % after only 160 min of illumination. This detected attitude might reveal the fast photo-degradation behavior observed for Type A devices. Unlike the stabilized V_{OC} and FF for the C-PDINO based devices, V_{OC} showed a consistence slow decrease and maintained 95 % (**Figure 5.5b**) and the FF remained 88 % (**Figure 5.5c**) after prolonged 520 min illumination, providing a remarkable photostability behavior. It is worth mentioning that the V_{OC} losses commonly obtained due to the light-induced trap states/defects which reveal the traps in the devices as reported by N. Gasparini et al. work [269]. Upon this context, we can depict that the C-PDINO based devices possessed lower photo–induced defects within the devices than the ZnO based ones (Type A and B). This might attributed to replacing the ZnO layer with the PDINO film that avoids the inescapable photocatalytic behavior of the ZnO that would facilitate the decomposition of the organic active blend result in photo-instability issues upon the UV illumination as exhibited elsewhere [249,261,266,270].

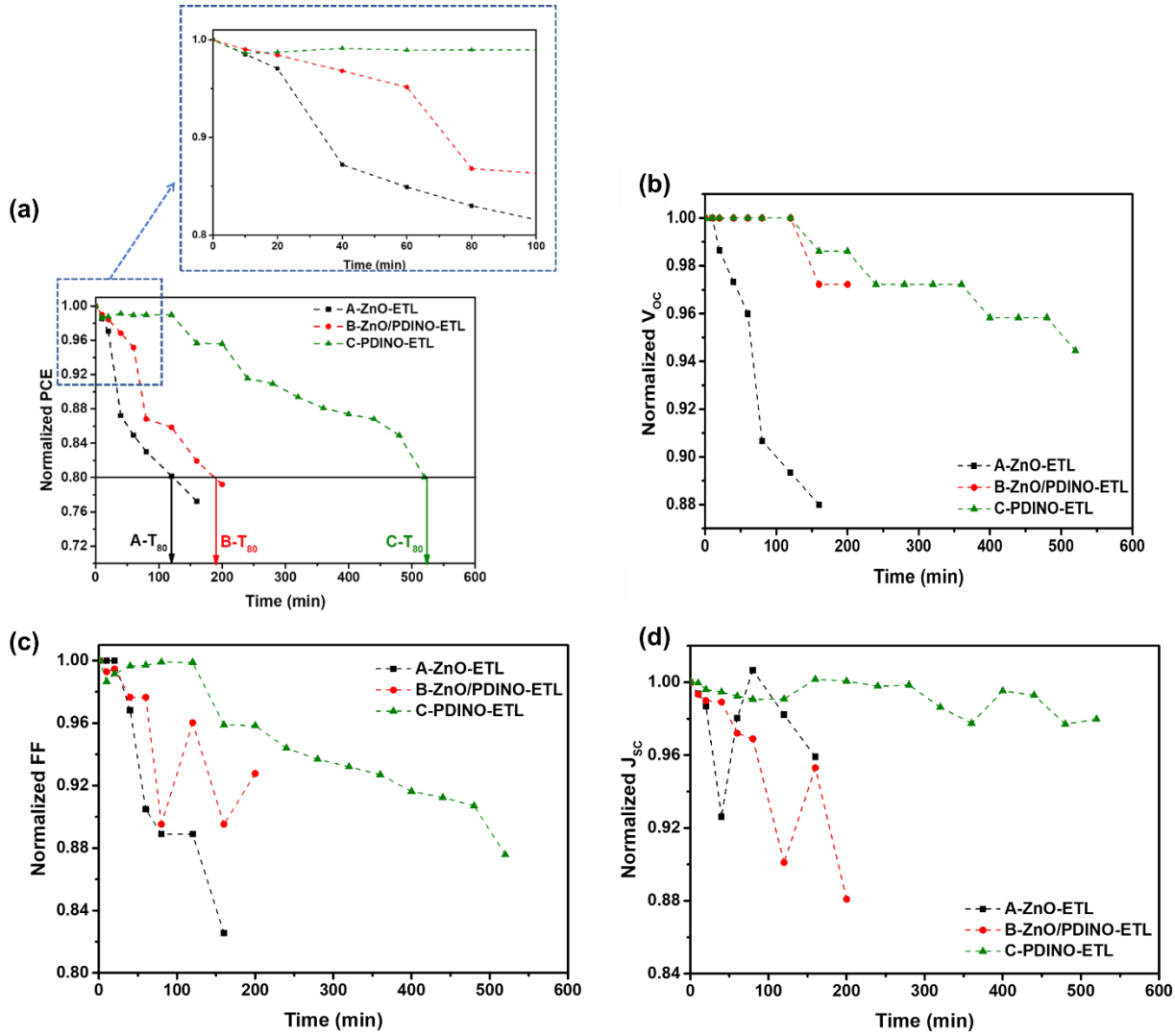

Figure 5.5 Normalized performance parameters of the iNF-OSCs (a) PCE, (b) V_{OC}, (c) FF, and (d) J_{SC} of the iNF-OSCs over photo-aging time.

Interestingly, the overall J_{SC} values were diminished for both A-ZnO-ETL and B-ZnO/PDINO based devices (**Figure 5.4a,b**, **Figure 5.5d**) over photo-aged time, in contrast to the C-PDINO based devices that almost maintained its J_{SC} values till 520 min (T_{80}-almost 9 h) (**Figure 5.4c**, **Figure 5.4d**). However, it was interesting to observe a 2 % increase in respect of the J_{SC} initial values after 90 min of illumination for the A-ZnO based cells, then a sharp decrease till the T_{80} after 160 min. This increment in the J_{SC} values may deliver from the UV-irradiation dependence, reported as light-soaking effect [215,271]. This light-soaking phenomenon was widely observed for the inverted OSCs using ZnO or other metal oxide materials as ETL as well as it is highly considered to evaluate the photostability behavior of the photo-aged OSCs [272–274]. There

are two main suggested mechanisms behind the origin of this phenomenon. First, it may obtain from the photo-induced rearrangement of the Fermi levels at the ITO/metal oxides interfaces upon the filling of trap states during the illumination, that diminishes the potential barrier and thus enhance the electron extraction through the ITO/metal oxide interface.[215,273,275,276] Second, the interfacial dipole clue role between the metal-oxide/organic blend film interface as reported elsewhere [216,275,277]. Interestingly, this observed effect for the A-ZnO based devices was highly matched with the previously discussed PCE, V_{OC} and FF burn in loss behavior that verifies the rapid photo-degradation of these devices. Accordingly, we think that the different T_{80} lifetimes between the fabricated devices systems are due to the intrinsic photostability variation of the ZnO and PDINO ETLs. Moreover, it was pronounced that the insertion of the PDINO layer between the active blend and the ZnO film in the B-ZnO/PDINO based devices acts as a shield that partially suppresses the accelerated photo-degradation arise from the ZnO photocatalytic effect appeared in the A-ZnO based devices. Therefore, by avoiding the ZnO in the C-PDINO based devices, they did not manifest any light soaking behavior reflecting the good quality of the devices [275] along with obtaining very week effect of burn in loss providing stunning photostability behavior.

For further investigation regarding the obtained performance parameters of the photo-aged fabricated i-OSCs, the J-V characteristic for the T_{100} fresh, the T_{90} and T_{80} i-OSCs at dark were conducted as shown in **Figure 5.6a,b,c**. As displayed in **Figure 5.6a**, the A-ZnO based devices suffered from an almost two orders in magnitude increased leakage current under the reverse bias condition as compared to the fresh devices after 2.5 h continuous illumination. Such behavior indicates a high shunt possibility recognized as "photo-induced shunts" that responsible for diminishing the charge carrier at the semiconductor/ZnO selective interface [278], which is responsible for lowering the J_{SC} in the device, in addition, low R_{Sh} is in charge of the low FF in the OSCs [178]. This obtained result agreed with the fast performance decay upon the illumination as demonstrated in **Figure 5.5a** and **Table 5.2**. In clear contrast, B-ZnO/PDINO and C-PDINO based devices (**Figure 5.6b,c**) revealed more stable behavior even after longer time of photo-degradation. This underlines the remarkable photostability of the PDINO based devices, especially the C-PDINO ones that showed inconsiderable change even after almost 9 h of constant illumination.

Furthermore, **Figure 5.6d** demonstrates the UV-visible absorption spectra for the PM6:Y7 blend over the ITO/ZnO (A-ZnO-ETL), ITO/ZnO/PDINO (B-ZnO/PDINO-ETL) and ITO/PDINO (C-PDINO-ETL) samples before (T_{100}) and after (T_{80}-as Listed in **Table 5.3**) the AM 1.5G illumination to evaluate the absorption spectra under same photo-aging conditions. After the illumination, we can see that the ZnO-based films (Type A and B) illustrate a significant diminishing in the peaks intensity (inset photo), reflecting the interface and blend decomposition via the photocatalytic activity of the ZnO, which in agreement with the work by M. Cui and co-workers [249]. In contrary, the C-PDINO based films showed more sustained absorption spectra even after prolonged 520 min of illumination.

As further evidence that the remarkable reduced photocatalytic activity of the PDINO is responsible for the lifetime enhancement, we investigated the previously mentioned T_{100} and T_{80} aged films through photoluminescence (PL) spectroscopy as presented in **Figure 5.6e.** The photo-degraded ZnO based films showed a dramatically increased PL intensity of 88% for A-ZnO based films. This implies a crucial inhibition of the exciton dissociation for the respective photo-aged devices, which is considered one of the key reasons for the rapid initial photo-degradation [176,250,279]. Same behavior was observed by L.Duan et al. using different fullerene and non-fullerene active blend, indicating that the presence of ZnO assists the decomposition of the contacted blend layer upon illumination due to the previously discussed photocatalytic effect of the ZnO [176]. Unlike the C-PDINO based films, where the PL spectrum increased only 7% compared to the fresh films upon 520 min under light. This indicated that the excitons maintain their efficient dissociation ability into charge carriers [176,250,279] even after longer time of exposure announcing the champion photostability behavior of C-PDINO based films.

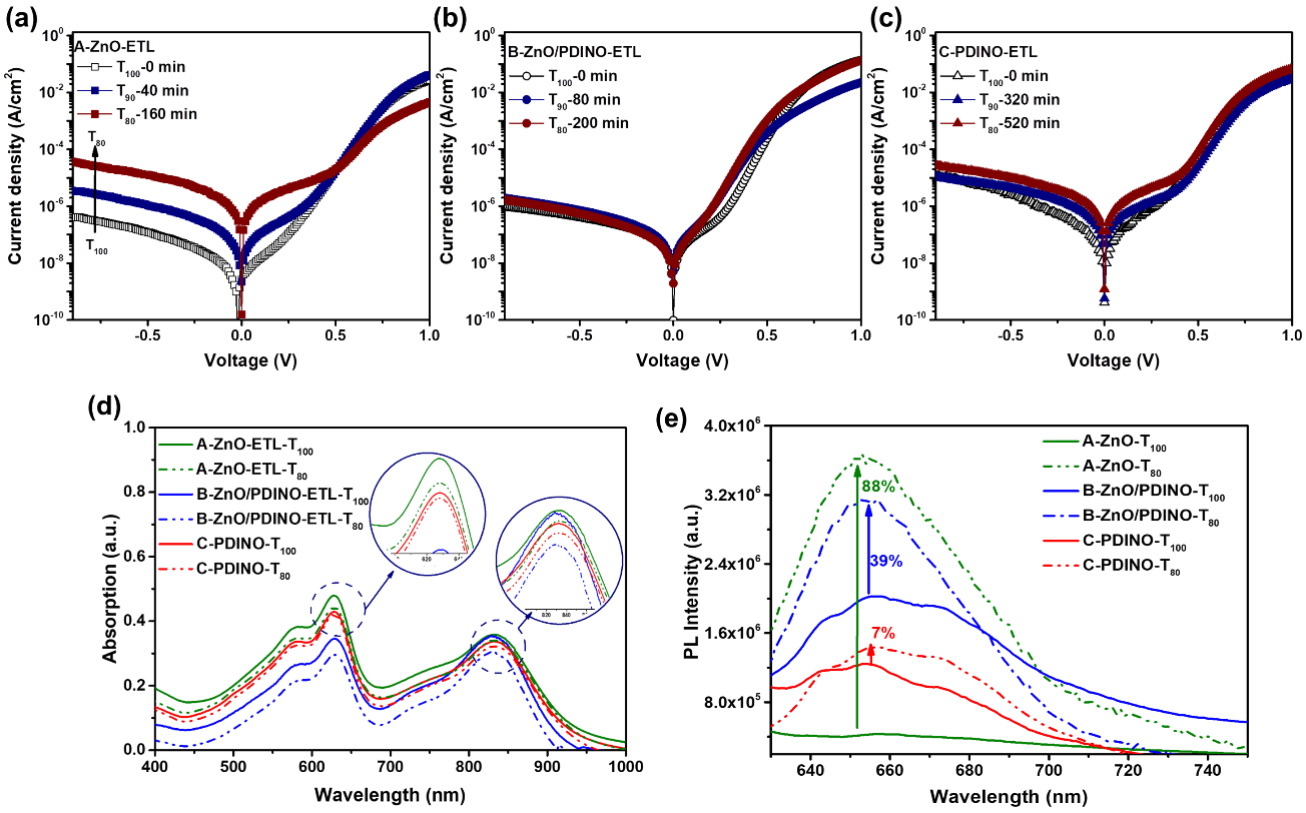

Figure 5.6 J-V characteristic curves of the T_{100} fresh and T_{90}, T_{80} photo-degraded iNF-OSCs at dark of (a) A-ZnO, (b) B-ZnO/PDINO, and (c) C-PDINO based devices, (d) UV-vis optical characteristics of the T_{100} and T_{80} photo-aged PM6:Y7 blend films over different ETLs, (e) Photoluminescence spectra of the T_{100} and T_{80} photo-aged PM6:Y7 blend films over different ETLs

Finally, it was interesting to find that the B-ZnO/PDINO based film showed an increment of the PL intensity by 39 % after 200 min which is right between the A-ZnO and the C-PDINO based films, providing a clear proof that the presence of PDINO reduced the photocatalytic activity along with improving the lifetime of the fabricated devices. Herein, this observation is highly consistent with the obtained performance results for the corresponding devices from the J-V characteristics.

The charge recombination mechanisms within the devices regarding the photo-aging test were further explored through investigating the light intensity (P_{Light}, from 0.1 to 100 mW cm^{-2}) dependence of the T_{100}-fresh and T_{80}-photodegraded i-OSCs J-V characteristics. The J_{SC} and V_{OC} as a function of P_{Light} were plotted in logarithmic scale along with the linear fitting as presented in **Figure 5.7a,b,c** and **5.7d,e,f**, respectively. The relation between the J_{SC} and P_{Light} was modeled as J_{SC} α $\boldsymbol{P_{Light}^{S1}}$, where S_1 represents the power law exponent. Under short circuit condition, S_1 value should approach 1 if the bimolecular recombination is insignificant, and values less than 1 implies that the bimolecular recombination of the free charge carriers will limit the photocurrent of devices [280,281]. In **Figure 5.7a,b,c**, we observed a difference in the dependency behavior at low and high light intensities. At low P_{Light} (< 1 mw/cm^2), the linearly fitted S_1 values for all devices were quite similar as well as at T_{100} and T_{80} conditions (around 0.62 - 0.64 which is less than 1) that pronounces a major effect of bimolecular recombination. But different attitude was observed for the S_1 values at high P_{Light} (>10 mW/cm^2), where the S_1 values for the T_{100} fresh A-ZnO, B-ZnO/PDINO and C-PDINO devices were 0.99, 0.96, and 0.91, respectively. Despite these observed values depicted that the A-ZnO based iNF-OSCs exhibited the lowest bimolecular recombination which greatly matched with its highest initial performance (**Table 5.2**). But S_1 values for the entire T_{100} devices are close to unity. Hence, it is worth to note that, regarding the T_{100} fresh prepared devices, the diminishing in the J_{SC} of structure B and C based devices as compared to A ones, might be due to the transmittance behavior of the ETLs as presented in **Figure 5.7g** not because of the recombination behavior. Where B-ZnO/PDINO and C-PDINO based films showed the lower film transmittance, indicating lower amount of light could reach the photo-active blend and in turn lower value of generated current (**Table 5.2**). However, after the T_{80} photo-aged of the device (listed in Table 5.3), we exhibited that the S_1 values were 0.89, 0.91, and 0.97, respectively, reflecting more implemented bimolecular recombination within the A-ZnO based devices upon the illumination (for 2.5 h only) than the others. This behavior explains the rapid photo-degradation behavior that is observed for Type A devices as previously discussed (**Figure 5.5a**). Interestingly, C-PDINO based devices showed a pioneer behavior in photo-degradation resistance with smaller extent of bimolecular recombination presenting almost same S_1 value after prolonged illumination time of 520 min. This attitude verifies the stable J_{SC} values over the illumination aging time test and in turn the highest photostability of this kind of devices. Hence, it can be noticed that the order of the T_{80}-S_1 values of the corresponding iNF-OSCs is consistent with their obtained photostability behavior (**Figure 5.5a**).

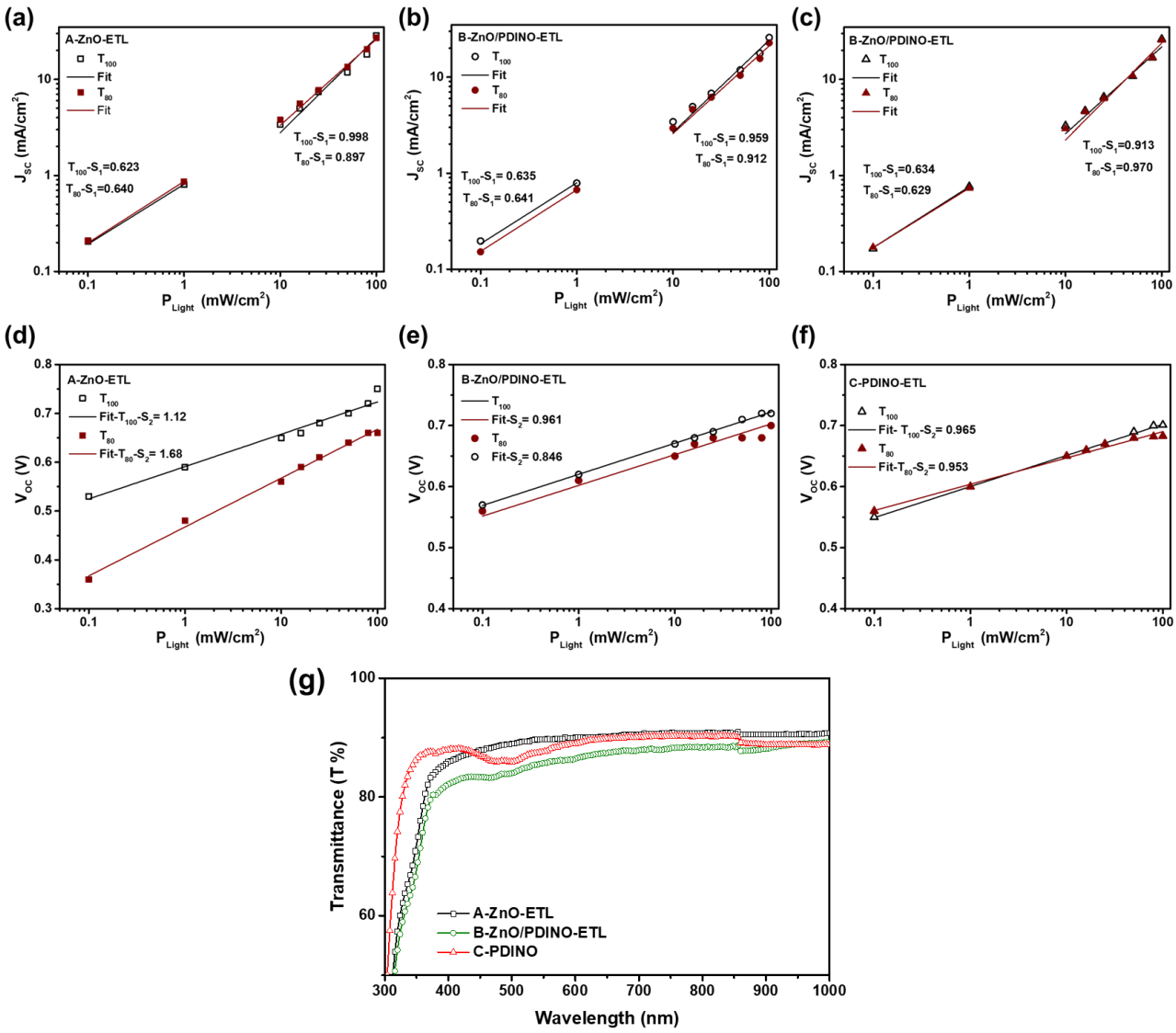

Figure 5.7 T_{100} and T_{80} iNF-OSCs (a,b,c) J_{SC} and (d,e,f) V_{OC} versus the light intensity (P_{light}), symbols for the experimental data and the line for the fitted data.(g) UV-vis optical transmittance characteristics of the various ETL-Films.

To gain more insights into the recombination kinetics inside the fresh and photo-degraded devices, we display their semi-logarithmic V_{OC} dependence vs P_{Light} (**Figure 5.7d,e,f**) that followed the Shockley diode equation [80,81,146] 5.1

$$\boldsymbol{V_{OC}\,\alpha\, S_2\left(\frac{KT}{q}\right) Ln\left(P_{light}\right)\alpha\, n_{id}\left(\frac{KT}{q}\right) Ln\left(J_{SC}\right)} \qquad (5.1)$$

where, n_{id} is the ideality factor of the diode ($n_{id}=S_2/S_1$), k is the Boltzmann constant, T is the temperature, and q is the elementary charge. S_2 values (**Figure 5.7d,e,f** insets) were calculated by fitting equation 5.1,

then obtaining the n_{id} values of 1.12, 1.01 and 1.06 for the T_{100} fresh A-ZnO, B-ZnO/PDINO and C-PDINO i-OSCs, respectively. It is apparent that all fresh devices has almost similar n_{id} values, indicating that the bimolecular recombination is governing the charge recombination in the fresh iNF-OSC devices along with insignificant trap-assisted recombination process [147,214,282]. After the illumination of T_{80} times of the examined devices, the n_{id} value for the A-ZnO was clearly escalated to 1.87 (**Figure 5.7d**), underlining the dominated trap-assisted recombination mechanism upon 2.5 h of the samples photo-aging due to the increase of trap density [144,148]. In contrary, we surprisingly found that the n_{id} values of the both T_{80} photo-aged B-ZnO/PDINO and C-PDINO based devices were 1.00 and 1.01(**Figure 5.7e,f**), implying a negligible trap-assisted recombination behavior within the devices, resulting in most stable V_{OC} values over aging time. We suggest that, in case of the PDINO based devices, the interfacial trap-assisted recombination was effectively diminished upon the photo-induced light which enhances the photostability of the devices. These observations are coherent with the observed photostability behavior of the photo-aged devices (**Figure 5.4, 5.5**). It explains the rapid decay of the V_{OC}, FF and in turn the PCE over the AM 1.5G aging time upon the light-induced trap formation in the A-ZnO based devices. In addition, it clarifies the remarkable photo-stability behavior of the entire performance parameters in the photo-aged C-PDINO based i-OSCs (**Figure 5.4, 5.5 and Table 5.2**).

To further understand the charge dynamics behind the dramatic decrease of the performance of the ZnO based device as well as the perceptible photostability of the C-PDINO based cells upon the photo-aging test, we measured the photocurrent density (J_{Ph}) vs the effective voltage (V_{eff}) of the fresh and photo-aged devices in double logarithmic scale as plotted in **Figure 5.8a,b,c**. J_{Ph} equals J_L-J_D, where $J_L$and J_D are the photocurrent densities under illumination and dark current densities, respectively. V_{eff} is defined as V_O –V, where V_O is the voltage when J_L=J_D and V is the applied bias voltage [147,150,151]. This dependence of the J_{Ph} on the V_{eff} assists the calculation of the exciton dissociation probabilities (P_{diss}), maximum amount of absorbed photons that provides the dissociation and generation of free carriers (G_{max}) and the generation rate (G_{rat}) of the free charge carriers in the fabricated devices[49,149] as listed in Table 5.4 of the T_{100}-fresh and the photo-aged (T_{90} and T_{80}) samples (calculation details explained previously in Chapter 2, equations 2.1, 2.2, and 2.3). For the entire tested samples, we found that the J_{Ph} increased linearly at low V_{eff} (< 0.3 V), then it starts to saturate by increasing the V_{eff} > 0.3 V, representing an efficient photogenerated charge carrier that can extracted by the electrodes.[149,283] Regarding the P_{diss} of the fresh devices, A-ZnO, B-ZnO/PDINO and C-PDINO based devices were calculated as 98.44, 98.10, and 98.58 %, respectively, then after exposure to light till T_{80} they obtained values of 96.57 % (within 160 min), 96.94 (within 200 min) and 96.32% (within 520 min), respectively. For fair comparison, it worthy to notice, despite all the devices presented almost same value of P_{diss} over the photo-aging time, but C-PDINO based devices showed the longest time to achieve this value, which is closely related to the high photostability of the devices, in contrast to the other ZnO based cells.

These results were in good matching with the stabilized performance parameters over photo-aging time for the C-PDINO based devices (**Figure 5.4, 5.5**), as well as correlated with the lowest T_{80} recombination behaviors discussed in **Figure 5.7c,f**. Furthermore, the G_{max} and the G_{rat} for the fresh devices were following the same trend of their performances (Table 5.2), where A-ZnO > B-ZnO/PDINO > C-PDINO as listed in Table 5.4. However, by approaching the T_{90} and T_{80} of the samples photo-aging test, we disclosed that the G_{max} and the G_{rat} were decreased for types A and B samples, but it showed a fascinating sustained behavior even with longer photo-aged time than the others (**Table 5.4**).

By combining the obtained results from the light intensity dependence on J_{SC} and V_{OC}, along with the voltage dependence of J_{Ph}, a side from the PCE values, C-PDINO based devices revealed week recombination losses in addition to highest resistance time toward the photo-aging test, which accounting their superior improvement of its operational photostability.

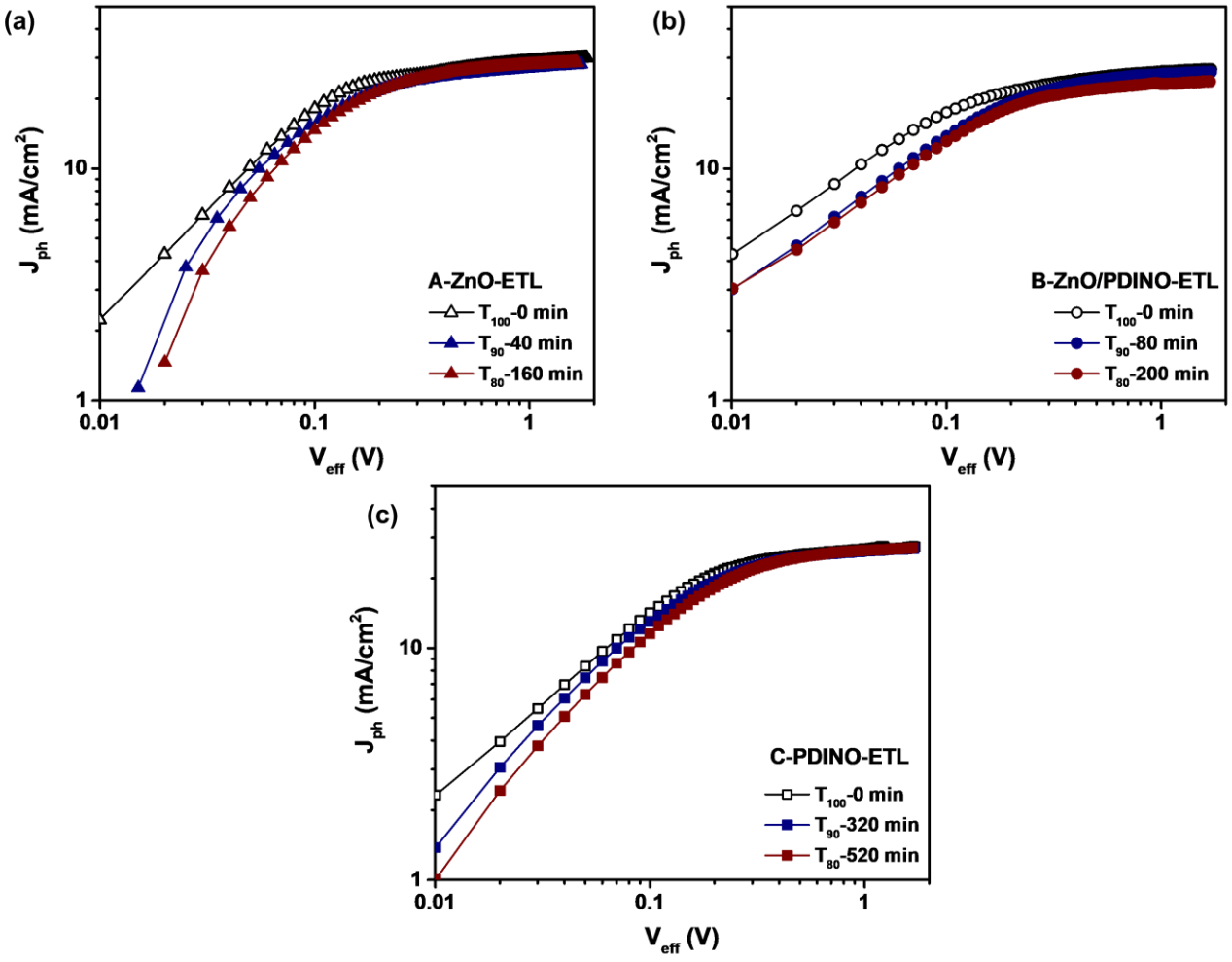

Figure 5.8 J_{Ph} versus V_{eff} characteristics of the T_{100}, T_{90} and T_{80} (a) A-ZnO, (b) B-ZnO/PDINO, and (c) C-PDINO based devices over photo-aging time.

Table 5.4 Optoelectronic parameters calculated from the J_{ph} -V_{eff} curves of the T_{100}, T_{90} and T_{80} photo-aged iNF-OSCs **in Figure 5.6 g,h,i**.

Devices	J-sat (mA/cm^2)	G_{max} ($\times 10^{28}$ m^{-3} s^{-1})	P_{diss} (%)	G_{rat} ($\times 10^{30}$ m^{-3} s^{-1})
A-ZnO-ETL				
T_{100}-0 min	29.06	1.81	98.44	1.79
T_{90}-40 min	27.61	1.72	95.99	1.65
T_{80}-160 min	28.20	1.76	96.57	1.70
B-ZnO/PDINO-ETL				
T_{100}-0 min	25.93	1.68	98.10	1.64
T_{90}-80 min	25.76	1.61	96.94	1.56
T_{80}-200 min	23.41	1.46	96.94	1.42
C-PDINO-ETL				
T_{100}-0 min	26.53	1.66	98.58	1.63
T_{90}-320 min	26.53	1.66	96.51	1.60
T_{80}-520 min	26.60	1.66	96.32	1.60

As a part of investigating the mechanism behind the photo-degradation within the fabricated iN-OSCs, external quantum efficiency (EQE) measurements were conducted for the fresh and the photo-aged devices. It is worth mentioning that all measurements were performed under the same condition of 1 sun, AM 1.5G illumination to evaluate a proper comparison with the other characteristics.

Figure 5.9a,b,c depict the plots of EQE versus the photon energy for A-ZnO, B-ZnO/PDINO and C-PDINO based devices, respectively. it can be seen that the photocurrent spectrum response of the entire devices is up to 1.4 eV [163] regarding same photo-active blend of PM6:Y7. Hence, the higher photocurrent response of the devices is more probably correlated to the excitation of the active polymer blend, and the lower photocurrent response than 1.4 eV is more likely attributed to the charge transfer states [284,285]. Accordingly, the Urbach energy (E_U) of the devices was defined with the absorption tail (known as Urbach tail) below 1.4 eV by following equation 2.10[162,163]. The E_U value reveals the trap-mediated charge recombination[286] which represents the energetic disorder in the molecular orbitals [162,284]. The extracted E_U values of the fresh and photo-aged i-OSCs were presented in the corresponding insets in **Figure 5.9a,b,c.** We manifested that both photo-aged types of A and B ZnO-based devices showed a noticeable increase in the T_{90} and T_{80} E_U values as compared to the T_{100}-fresh corresponding devices. A higher E_U usually indicates a higher energetic disorder that originates the reduction of the device performance via implemented density of state distributions that assist the recombination[286], which determined as a common reason for fast initial photo-degradation of the photo-aged devices. This observation gives a proper declaration regarding the V_{OC} and FF burn in losses [287] along with the produced trap-assisted recombination that leads to the rapid photo-degradation behavior exhibited by the ZnO-based devices, particularly A-ZnO ones, as presented in the previously discussed characteristics. However, by avoiding the presence of the ZnO in the C-PDINO based

devices, we obtained the most stable E_U values over the photo-aging test time (inset of **Figure 5.9c**). This withstand attitude pointed out the insignificant existence of trap-mediated charge recombination and in turn less displayed energetic disorder upon 520 min of continues illumination.

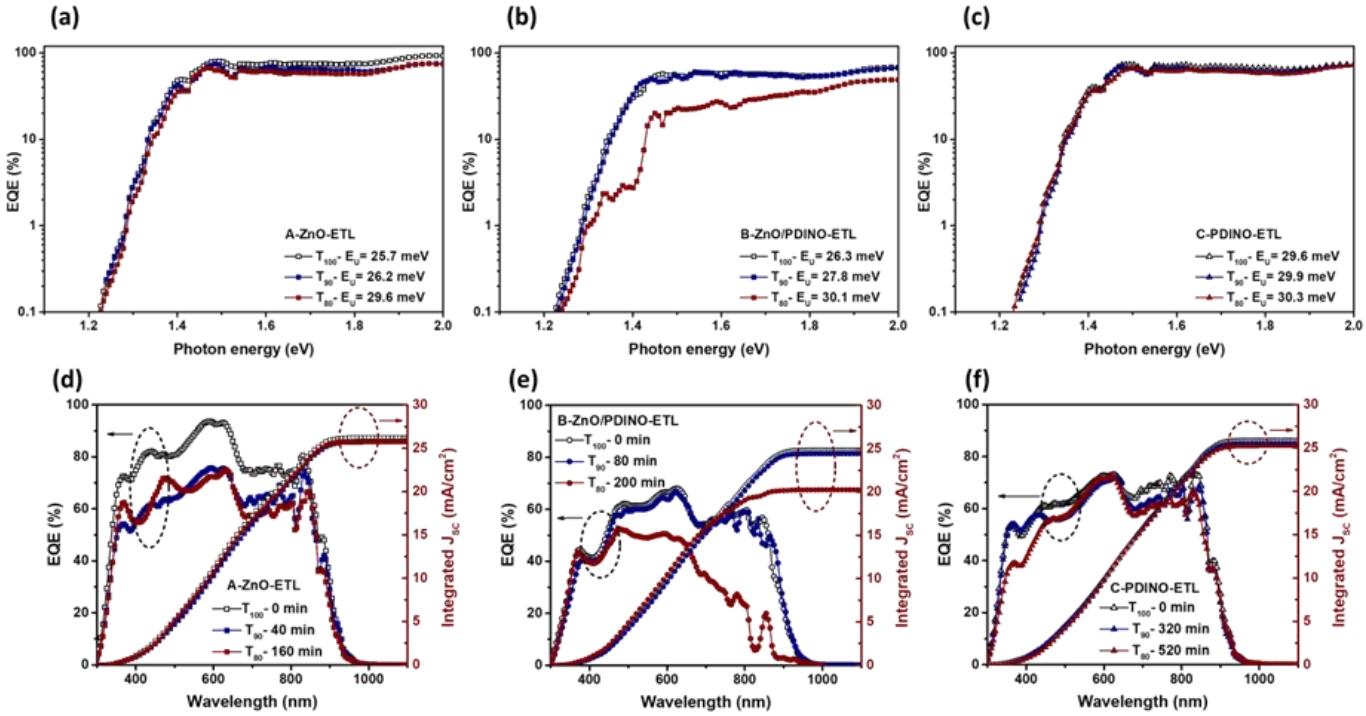

Figure 5.9 EQE vs photon energy of the (a) A-ZnO (b) B-ZnO/PDINO, (c) C-PDINO iNF-OSCs with the inset values of Urbach energy (E_U), EQE spectra (left) and the integrated short circuit current (right) of T_{100}, T_{90} and T_{80} photo-aged (d) A-ZnO (e) B-ZnO/PDINO, and (f) C-PDINO iNF-OSCs.

Table 5.5. The integrated J_{SC} values are evaluated from the EQE measurements in **Figure 5.9.**

Integrated J_{SC} from the EQE	**A-ZnO-ETL**	**B-ZnO/PDINO-ETL**	**C-PDINO-ETL**
T_{100}	26.24	24.85	25.50
T_{90}	25.79	24.41	25.50
T_{80}	25.88	20.24	25.19

Figures 5.9d,e,f illustrate the EQE response of the fresh and photo-degraded samples over wavelength rang of 300-1100 nm. Regarding A-ZnO based devices, the photo-aged devices showed a noticed diminishing

in the absorption over the full range (**Figure 5.9c**), which suggested to be related to the insufficient charge extraction and transport mechanism, which greatly matched with the performance drop obtained for the photo-aged A-ZnO cells with in 160 min, discussed in the J-V characteristics (**Figure 5.4, 5.5**). Moreover, in case of the photo-aged B-ZnO/PDINO based cells, we can observe that at T_{80}, the absorption reduction did not carry out over the full wavelength range (such A-ZnO cell), but it started from 500 nm then sharply decreased (**Figure 5.9e**). This obtained behavior might reflects that despite the presence of the PDINO layer between the ZnO and photoactive blend may partially assist the device resistance toward photo-degradation and extended the cells lifetime to 200 min, but the ZnO still has the pronounced photocatalytic contribution of degrading the contacted layers and as a sequence assists the decay of the device performance. Furthermore, the exhibited EQE reduction for both types of A and B photo-aged devices is consistent with the observed J_{SC} loss from the J-V characteristics (**Figure 5.5d**). While the photo-aged C-PDINO based devices signify inconsiderable decrease of the EQE absorption response, indicating the most photo-stable behavior over aging test time (for 520 min) as compared to the fresh ones (**Figure 5.9f**). This obtained behavior is perfectly coherent with the stabilized J_{SC} values obtained over photo-aging time by the J-V characteristics in **Figure 5.5d**. Furthermore, the calculated integrated J_{SC} values from the EQE spectra for the fresh T_{90}, and T_{80} photo-aged devices were listed in Table 5.5, which consistent with the values obtained from the J-V measurements under AM 1.5G illumination with the maximum error values less than 10% (Table 5.2).

Impedance spectroscopy was carried out under AM 1.5G illumination condition as an alternative insight study to investigate the electric properties of the fabricated devices with respect to the interfacial charge transfer and carrier recombination[165] along with providing the mechanisms behind the performance deterioration of the photo-aged tested devices. Hence, we conducted the capacitance-frequency (Cf) measurements to calculate the trap density of state (DOS) that explained in Chapter 2 in equation **2.11, 2.12**. **Figure 5.10** displays the evaluated trap-DOS curve as a function of energy for the fresh and the T_{80} photo-degraded devices. It demonstrates a single exponential trap distribution which defines the same trap activation energy and carrier response within the devices [58,171]. Furthermore, after the T_{80} photo-aging time (Table 5.3), a decline in the DOS values for a given frequency can be revealed for all devices. This behavior can be explained as DOS energy shift of E_O (explained by equation **2.13**). Thus, the T_{80} photo-aged devices demonstrated lower energy, reflecting higher interfacial induced defects in the devices compared to the T_{100} fresh ones as an intrinsic origin of tarps [64,121,172,225,245]. In consequence, we measured the values of the energy shifting (X) for the T_{80} photo-degraded cells, explained in **Chapter 2**, equation **2.13**, presented by the blue line in **Figure 5.10**. We detected that the order of energy sifting value (X) is following the trend of A-ZnO > B-ZnO/PDINO > C-PDINO. Hence, C-PDINO based cells provided lower shifting value of X than the ZnO-

based ones, indicating less trapped sites implemented in these cells, confirming their superior photostable behavior toward the illumination.

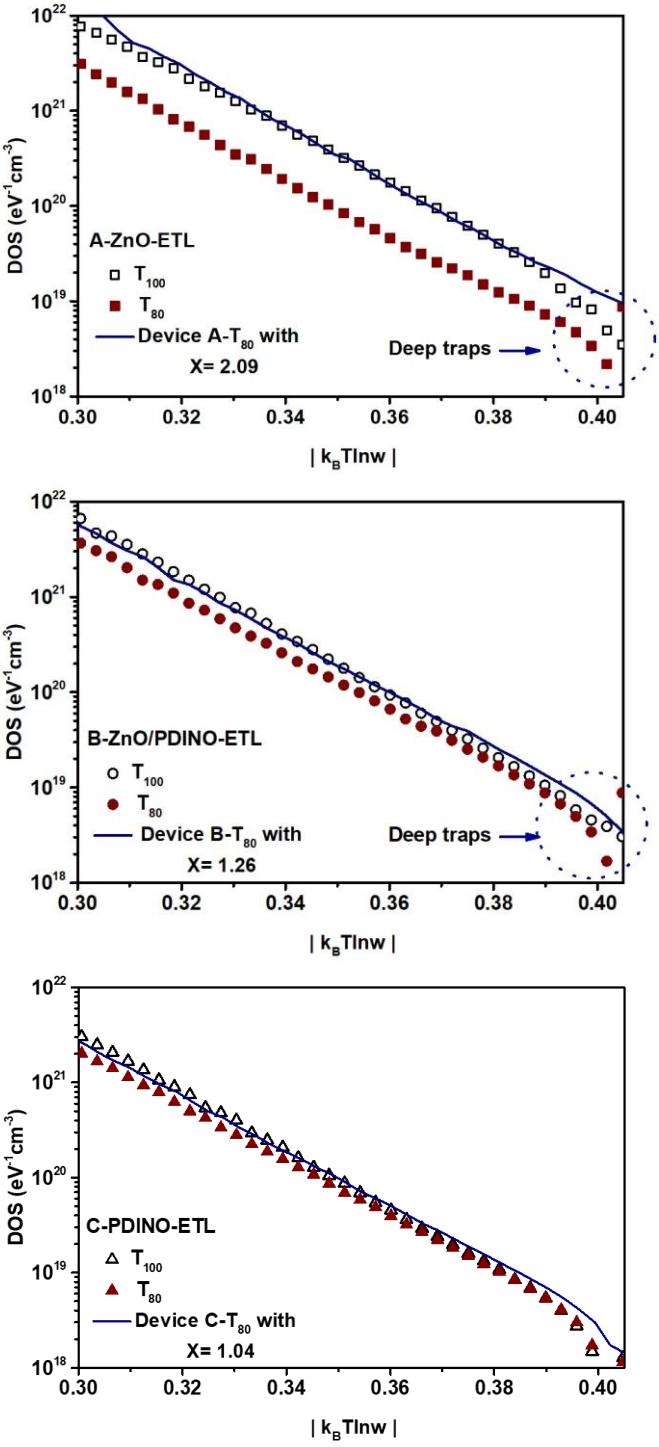

Figure 5.10 DOS as function of $|k_BTln\omega|$ at V_{OC} under AM 1.5G illumination of the T_{100} and T_{80} photo-aged iNF-OPVs over times (blue line with shifting value of X), (a) A-ZnO, (b) B-ZnO/PDINO, and (c) C-PDINO based devices.

Interestingly, A-ZnO based devices showed the highest X value of double, demonstrating highest contribution of photo-induced traps within the device. Moreover, we can clearly notice that the T_{80} ZnO-based devices (A and B types) possessed an additional impeded deep-trap sites[171,288] (**Figure 5.10a,b**), that did not observe for the T_{80} C-PDINO based i-OSCs (**Figure 5.10c**), consisting with their rapid photo-degradation performance, particularly the drop in the FF and V_{OC}[287,289], presented by the J-V and EQE characteristics. It is worth to mention that this sequence of attitude is highly matched with the obtained sequence behavior of the previously discussed E_U values over photo-aging times in **Figure 5.9a,b,c**, depicting same observation of energy disorder upon trap creation.

Furthermore, impedance Nyquist test was performed to gain a better understating of the photo-degradation effect within the tested devices. The obtained data from the IS was originated from the response testing of the devices under AM 1.5G illumination and an applied AC signal with 5 mV amplitude in the frequency range between 5 Hz to 2 MHz. **Figure 5.11** shows typical Nyquist plots that were obtained for the T_{100} fresh and T_{80} photo-aged iNF-OSC and their corresponding Bode plots [266] at V_{OC}. All Nyquist plots exhibited a semicircle shape, reflecting the efficient transfer at the active layer/electrode interface [165]. As an initial observation, we can notice that all the devices obtained a single process represented by one arc behavior. In addition, the diameter of the arc increased for the photo-aged devices over aging times (Table 5.3), considering the increment in the bulk resistance of the devices upon the continuous light exposure [166]. Nevertheless, it was interesting to notice that this increment is much higher in the A-ZnO based devices, unlike C-PDINO based ones. Same behavior was observed for photo-aged devices at maximum power point voltage (V_{mpp}) and short circuit current (Voltage = 0 V) in **Figure A.10**. Accordingly, it is worth to mention that the size of the arc is commonly correlated to the device resistance [165]. Hence, to gain more information about the physical parameters of each layer within the fresh and photo-aged cells, we analyzed the plots with an electrical equivalent circuit using Debye model[100,207]shown in 5.12, which provided a proper fitting for the experimental data (presented as solid lines in **Figure 5.11**). The equivalent circuit contains, R_S represents the series resistance which indicates the resistance of the contact and the ohmic components [121,165]. A parallel association of resistor (R) and capacitor (C) for 3 RC elements in series, where R represents the resistance of electrons transportation in each layer as R_1, R_2 and R_3 refers to ETL, PM6:Y7 and the V_2O_5 layer, respectively. In addition, C refers to the geometrical dielectric component capacitance values of each layer. Moreover, the R_4C_4 were in series which attached in parallel to R_2C_2 corresponding the photoactive layer (PM6:Y7) obeying Debye model[207], explaining the effect of the photo-degradation behavior that carried out in the photoactive blend within the A, B, and C based devices regarding the variation of the contacted ETLs. This model considers the existence of a single type of trap implemented in one layer [207] upon the continuous illumination process. Finally, L is the included inductor applied to fit the data properly at high frequency [165]. Then, the extracted parameters from the fitting were listed in Table 5.6. The exhibited fitting capacitance

values for each layer were highly matched with the theoretical values shown in Table A.3. This might imply that at V_{OC}, the IS data was controlled by the geometrical capacitances provided by the metal insulator-metal model indicating the presence of fully depleted layers [208].

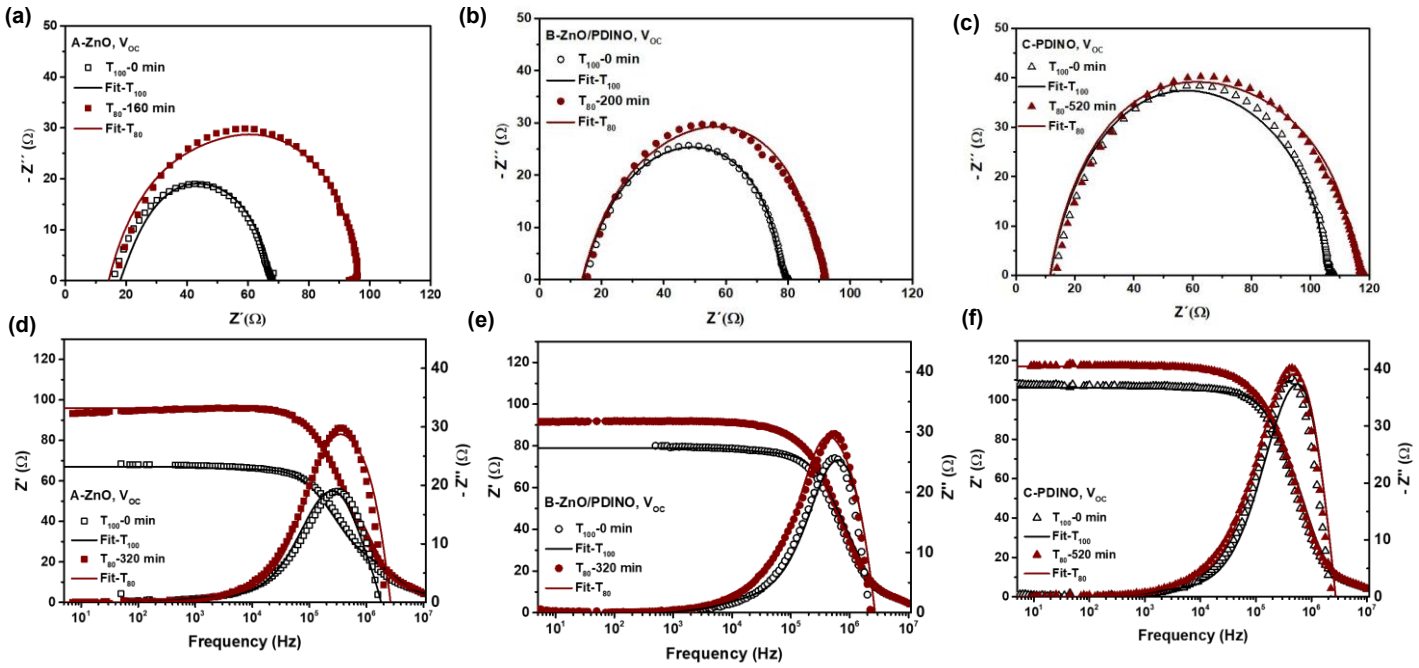

Figure 5.11 Nyquist plots and Bode Plots at V_{OC} under AM 1.5G illumination of the T_{100} and T_{80} photo-aged (a,d) A-ZnO, (b,e) B-ZnO/PDINO, and (c,f) C-PDINO based devices, using symbols for the experimental data and the fitting results in solid lines by applying the equivalent circuit in the **Figure 9.11**

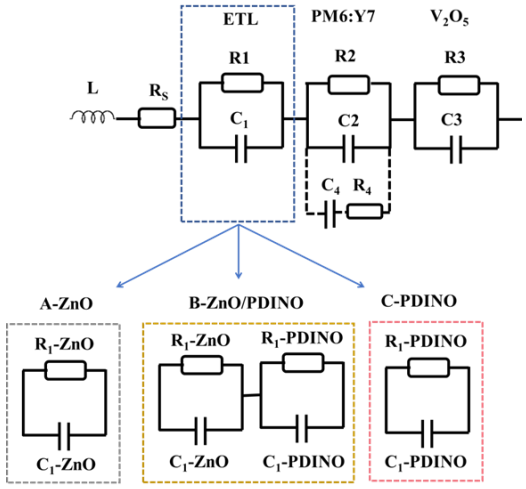

Figure 5.12 The equivalent circuit used to fit the experimental data in **Figure 5.11** applying Debye model.

Table 5.6. The fitted parameters of the experimental data in **Figure 5.11** using Debye model at V_{OC} for the fabricated T_{100}-fresh and T_{80} Photo-aged devices. The parameter $\tau = R_4 \times C_4$, where R_4, C_4 parameters were demonstrated in the equivalent circuit in **Figure 5.12**.

Physical Parameters of the i-OSCs (Debye Model)	**T_{100}-Fresh-0 min A-ZnO-Contol devices**			**T_{80}-Photo-aging-160 min A-ZnO-Contol devices**		
ZnO	R_S = 3.0 Ω L = 1.3 µH	R_1= 28.0 Ω	C_1= 16.0 nF	R_S =5.0 Ω L =1.3 µH	R_1= 33.0 Ω	C_1= 16.0 nF
PM6:Y7		R_2= 20.0 Ω τ = 100.0 µs	C_2= 2.8 nF C_4= 300.0 nF		R_2= 43.0 Ω τ = 70.0 µs	C_2= 2.8 nF C_4= 30.0 nF
V_2O_5		R_3= 16.0 Ω	C_3= 79.7 nF		R_3= 16.0 Ω	C_3= 79.7 nF
		R_{Total} = 67.0 Ω			R_{Total} = 97.0 Ω	
	T_{100}-Fresh-0 min B-ZnO/PDINO-ETL			**T_{80}-Photo-aging-200 min B-ZnO/PDINO-ETL**		
ZnO/PDINO	R_S = 4.0 Ω L =1.30 µH	R_1-ZnO=22.0 Ω R_1-PDINO=8.0 Ω	C_1-ZnO = 24.0 nF C_1-PDINO= 39.8 nF	R_S =4.0 Ω L =1.3 µH	R_1-ZnO=28.0 Ω R_1-PDINO=11.0 Ω	C_1-ZnO = 24.0 nF C_1-PDINO= 39.8 nF
PM6:Y7		R_2= 40.0 Ω τ = 10.0 µs	C_2= 2.8 nF C_4= 10.0 nF		R_2= 43.0 Ω τ = 10.0 µs	C_2= 2.8 nF C_4= 20.0 nF
V_2O_5		R_3= 5.0 Ω	C_3= 79.7 nF		R_3= 8.0 Ω	C_3= 79.7 nF
		R_{Total} = 79.0 Ω			R_{Total} = 92.0 Ω	
	T_{100}-Fresh-0 min C-PDINO-ETL			**T_{80}-Photo-aging-520 min C-PDINO-ETL**		
PDINO	R_S = 5.0 Ω L = 1.3 µH	R_1= 25.0 Ω	C_1= 19.9 nF	R_S =5.0 Ω L =1.3 µH	R_1= 30.0 Ω	C_1= 19.9 nF
PM6:Y7		R_2= 64.0 Ω τ = 50.0 µs	C_2= 2.8 nF C_4= 20.0 nF		R_2= 66.0 Ω τ = 30.0 µs	C_2= 2.8 nF C_4= 20.0 nF
V_2O_5		R_3= 12.0 Ω	C_3= 79.7 nF		R_3= 16.0 Ω	C_3= 79.7 nF
		R_{Total} = 106.0 Ω			R_{Total} = 117.0 Ω	

Regarding the fitted resistance values for each layer of the T_{100} fresh and T_{80} photo-aged devices (Table 5.6), it can be seen that the R_S values were at the range of 3.0-5.0 Ω in the entire devices. This might indicate that the different ETLs did not show a significant effect in the ITO/ETL interface upon the photo-aging test. Similar behavior was observed for the V_2O_5 layers, which show consistent resistance values (R_3) before and after the photo-aging test for the entire devices as presented in **Table 5.6** and **Figure 5.13**.

On one hand, as for the T_{100} and T_{80} A-ZnO based devices, we found that the R_1 values of the ZnO layer slightly increased from 28 to 33 Ω, respectively. While the R_2 values were almost doubled from 20 to 43 Ω (**Figure 5.13a**). In turn, the total resistance (R_{total}) of the device were increased from 67 to 79 Ω (**Table 5.6**), which controlled by the photoactive blend resistance (R_2). This obtained behavior is greatly matched with the escalated R_S values obtained by the J-V measurements under illumination over aging times (**Table 5.2**). Moreover, it confirms the burn in losses effect observed for the A-ZnO performance parameters, especially the V_{OC} and FF parameters, which leads to their rapid photo degradation behavior (**Figure 1,2**).

On the other hand, regarding the B-ZnO/PDINO based devices, the R_1-ZnO values were 22 and 28 **Ω** for the T_{100} and T_{80} photo-aging time, respectively, while R_1-PDINO values were 8 and 11 **Ω**, respectively. In addition, the R_2 values were 64 **Ω** for the T_{100} devices and 66 **Ω** for the photo-aged devices (**Figure 5.13b**). From the obtained fitted values, we can notice that both R_1 and R_2 values showed a slight increment in their resistance values after the photo-aging test (200 min), where the R_{Total} values rather increased from 79 to 92 **Ω** (**Table 5.6**). This attitude confirms their higher photo-stability as compared to the A-ZnO ones (**Figure 5.5a**). Furthermore, T_{80} C-PDINO based cells showed the highest stable R_1 and R_2 values (**Figure 5.13c**) with respect to the longest exposure time to the light (520 min) as compared to the T_{100} fresh ones. Where, the R_1, R_2 and R_{Total} presented a bit increase from 25 to 30 **Ω**, from 64 to 66 **Ω** and from 106 to 117 **Ω**, respectively. This explains the steady R_S values obtained by the J-V measurements (**Table 5.2**) over aging time which in turn provided a superior J_{SC} photo-stability behavior (**Figure 5.5d**). Accordingly, to perform a fair comparison regarding the fitted resistance values between the T_{100} and T_{80} of each device, we considered the thickness difference of each device and then calculated the variation of R_{Total}/thickness percentage as illustrated in **Figure 5.13d**. We found that A-ZnO based devices exhibited the highest ratio of resistance increment by 22.2 %, while the B-ZnO/PDINO cells increased by 9.6 % and the C-PDINO based ones increased by only 8.8 %. These obtained results explain the much higher variation in the arc diameters that obtained for the A-ZnO-devices (**Figure 5.11a**) and the less variation exhibited for the C-PDINO based devices (**Figure 5.11c**). With respect to the T_{80} times (Table 5.3), it was considered the lowest for A-ZnO devices, revealing their fast photo-degradation behavior, and the highest for the C-PDINO cells, marking their impressive photostable behavior.

Finally, it is worth to mention that the key reason of the highest resistance variation obtained by the A-ZnO based devices might be attributed to photocatalytic effect of the ZnO film, which highly accelerated the photo-degradation the photoactive blend (**Figure 5.13a**) and in turn the entire devices [261]. Interestingly, the resistance variation was diminished by adding the PDINO layer between the ZnO and the photo-active blend as observed in the B-ZnO/PDINO devices. Thus, this difference in the resistance values was highly suppressed by replacing the ZnO with PDINO, which avoids the photo-degradation of the photoactive blend and showing better resistance toward the illumination.

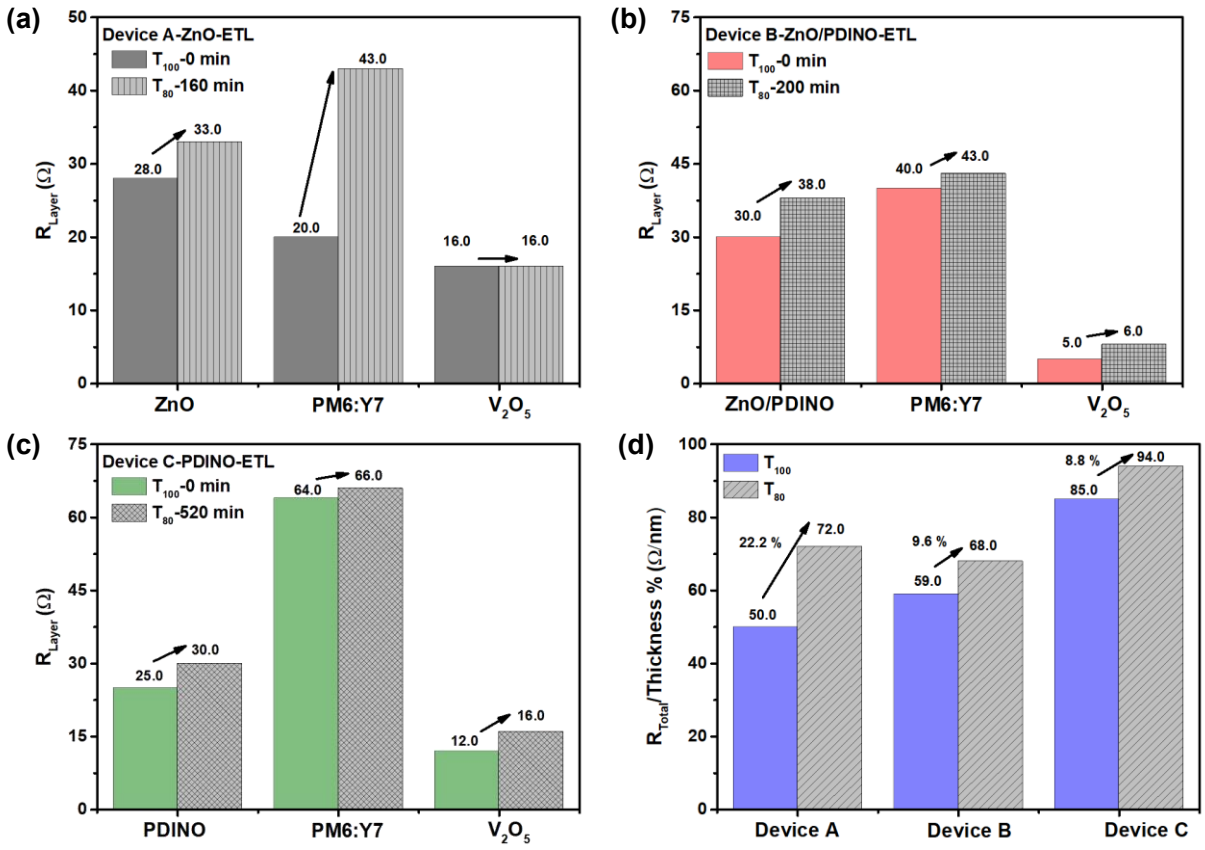

Figure 5.13 The resistance values of each layer for the T_{100}-fresh and T_{80} photo-aged (a) A-ZnO, (b) B-ZnO/PDINO and (c) c-PDINO based iNF-OSCs. The values were extracted from the Debye model listed in Table 5.6. (d) the total resistance variation of the T_{100} and T_{80} iNF-OSCs with respect to the total thickness within each device.

Atomic force microscope (AFM) characteristics were performed to investigate the active blend morphology changes during the photo-aging test. AFM images and the corresponding phases were demonstrated in **Figure 5.14** for both T_{100} fresh and T_{80} photo-aged tested based films of ITO/ETLs/active blend, considering the T_{80} photo-aging times of the corresponding devices as listed in Table 5.3. Regarding the T_{100} fresh films, we can clearly see that the A-ZnO based films (ITO/ZnO/PM6:Y7 film) showed the lowest root mean square (RMS) value of 1.43 nm (**Figure 5.14a**), representing lowest surface roughness. Moreover, B-ZnO/PDIBO (ITO/ZnO/PDINO/PM6:Y7) and C-PDINO (ITO/ PDINO/PM6:Y7) based films exhibited higher RMS values of 3.51 and 4.21 nm, respectively (**Figure 5.14b,c**). This behavior agreed with the lowest R_S along with the highest FF values obtained for the T_{100} A-ZnO based devices and the contrary behavior of the B and C based devices as obtained from the J-V characteristics (**Table 5.2**) due to their higher surface roughness. Furthermore, this observation might reveal the higher performance of the T_{100} fresh A-

ZnO based devices than the others. However, after the T_{80} photo-aging test, we found that a huge increase in the surface roughness with RMS value of 8.19 nm (7 times higher than T_{100}) was observed for the A-ZnO based exposed films (**Figure 5.14d**), explaining the FF as well the PCE burn in photo-degradation behavior (**Figure 5.5**) along with the highest leakage current (**Figure 5.6a**) exhibited for the A-ZnO based devices within short time of 2.5 h.

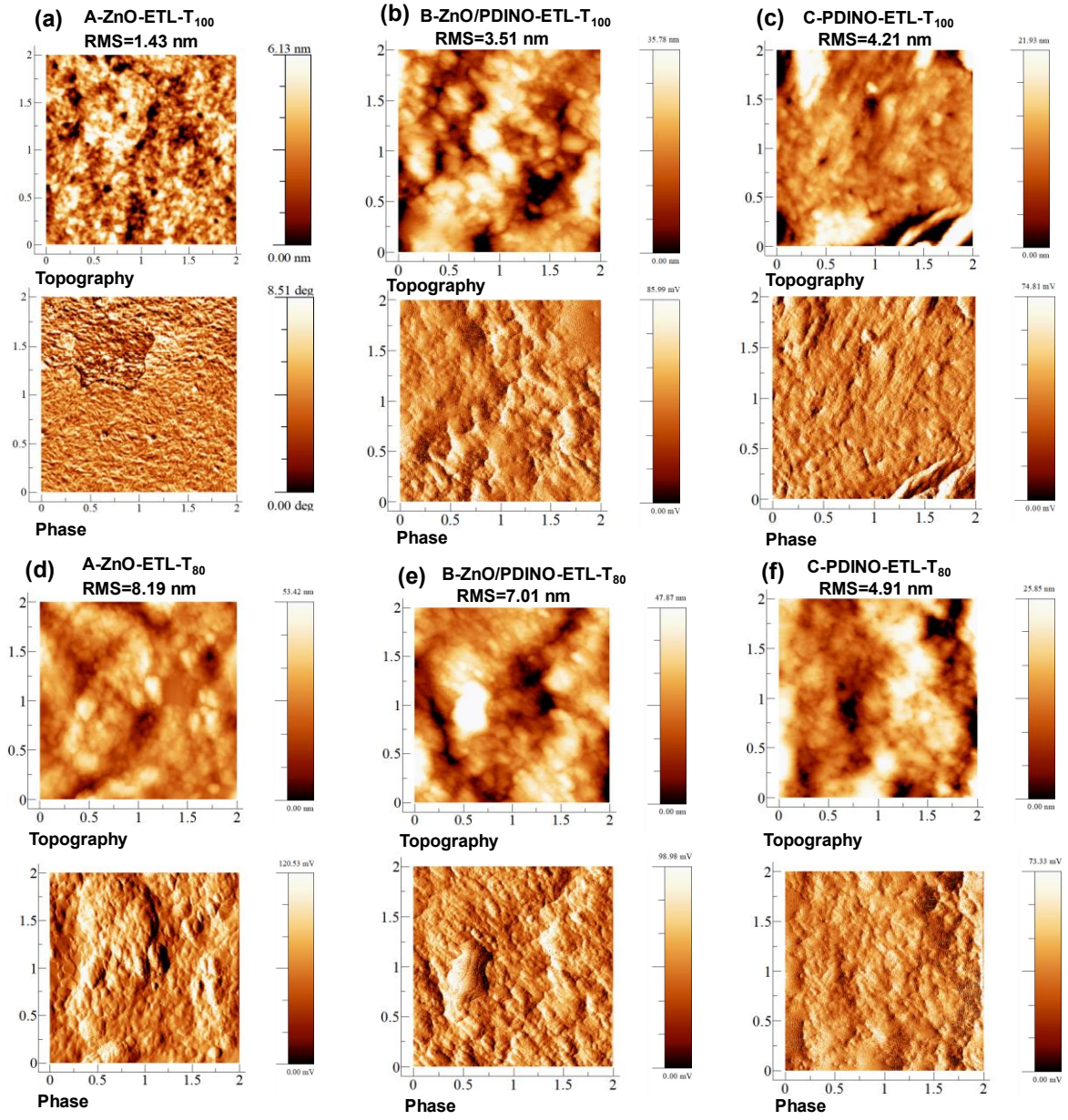

Figure 5.14 AFM topography and phase images of the PM6:Y7 blend films over different ETLs of T_{100} (a) A-ZnO, (b) B-ZnO/PDINO, (c) C-PDINO based films and the T_{80} photo-degraded (d) A-ZnO, (e) B-ZnO/PDINO, (f) C-PDINO based films.

Interestingly, same behavior was observed from the reported work of L.Duan et al. [266]. In addition, a more stable attitude was obtained by B-ZnO/PDINO based films, where the RMS values were doubled to 7.01 nm (**Figure 5.14e**). Surprisingly, T_{80} C-PDINO based exposed film presented a quite similar RMS value of 4.91 as compared to the T_{100} fresh films even after prolonged photo-aging time of 520 min. In addition, it showed lower RMS value among the further T_{80} devices, conserving the suitable phase separation and better pathways in the active layer [283]. Hence, we observed a noticeable effect regarding the photo-aging response upon changing the ETL. First, with reference to the A-ZnO based films, during the photo-degradation, it is suspected that photocatalytic effect plays a significant role in transferring the degradation to the contacted active blend, appeared to induce a greater extent of the film surface roughness. Where, the high RMS value with rough surface morphology indicated significant aggregation existence inside the active blend, which correspond the large phase separated domains with more excitons traps that in turn affect the charge dissociation process.[176,290,291] This observation is highly matched with the obtained R_2 fitted value (Table 5.6) from the previously discussed IS measurements, which showed a great increase in its value after the T_{80} photo-aging test along with a noticeable enlargement in the arc diameter of the A-ZnO-based devices (**Figure 5.11a**).

Second, with respect to the C-PDINO based films, we suggested that the PDINO layer resist the photo-degradation and in turn preserve the blend film from degradation that present in maintaining the roughness of the films over the photo-aging time. This agreed with the consistency of the resistance fitted values, R_1 and R_2 of the C-PDINO based devices that characterized by the IS discussed in **Figure 5.11c**, along with the J_{SC} and R_S values obtained by the J-V characteristic over photo-aging times (**Figure 5.5, Table 5.2**) as well as the constant leakage current behavior (**Figure 5.3c**). Finally, it was interesting to find that the B-ZnO/PDINO films as well as the B-based devices performance showed a moderate behavior between both A and C ones, reflecting the effect of adding the PDINO film in increasing the photostability of the blend and in turn the full devices. Upon this context, we noticed that the photostability of the fabricated iNF-OSCs enhanced through avoiding the interface contact between the active layer and the ZnO film along with providing a good compatibility with the PDINO host system.

5.4 Conclusion

In conclusion, we presented an extremely efficient PDINO based cathode interlayer for iNF-OSCs, achieving excellent photostability behavior. The iNF-OSCs incorporating the PDINO interlayer (C-PDINO based devices) maintained 80 % of the initial efficiency after continuous illumination (AM 1.5G, 100 mW cm^{-2}) for 520 min, while the ZnO-based control iNF-OSCs (A-ZnO based devices) remained only for 160 min under same conditions. The remarkable photostability of the C-PDINO based devices were mainly attributed to the avoidance of the photo-induced shunts and the photocatalytic behavior, which are inevitably in the ZnO based i-OSCs. Moreover, C-PDINO based devices refrained from the burn-in photo-degradation phenomena, which cause a significant reduction in the performance of the exposed devices by providing negative effects on energy transfer, exciton dissociation and charge recombination processes which may be more related to the bulk of the active layer as appeared for the ZnO based iNF-OSCs. Hence, this piece of work clearly demonstrates that PDINO is a promising cathode interlayer for tremendously photostable iNF-OSCs, particularly for large-scale production. As it fits the requirements of low-temperature fabrication, can be used in very fine-tuned thicknesses, showing great resistance behavior toward light, and does not react with the contacted active layers and electrodes.

Chapter 6

Extraordinary Current Generated in PM6:Y7 Based Organic Photovoltaic Devices Assisted by Pre-Thermal Treatment Approach

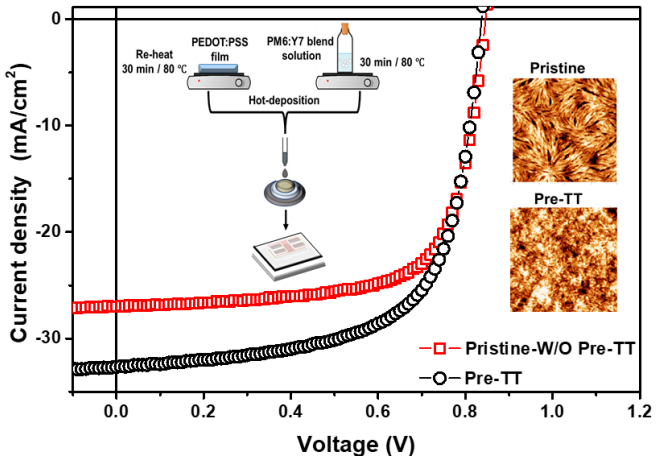

This chapter is based on two articles

1. **Enas Moustafa**, M. Méndez, J. G. Sánchez, J. Pallarès, E. Palomares, and L. F. Marsal, Thermal Activation of PM6:Y7 Based blend leads to Unprecedent High Short-Circuit Current Density in Nonfullerene Organic Photovoltaics, ***Advanced Energy Materials***, **2023**, 13, 4, 2203241.
2. Enas Moustafa, J. Pallarès, and L. F. Marsal, Revealing the Influence of Layer Thickness Variation on the Non-Fullerene Based Organic Photovoltaic Devices Performance Through Impedance Spectroscopy Study, to be published.

Patent

The Universitat Rovira i Virgili has registered this work for a Spanish patent no. P202131074, in the name of the five authors Enas Moustafa, Josep Pallarès, Lluis F. Marsal, Alfonsina Abat Amelenan Torimtubun, and José G. Sánchez.

6.1 Introduction

Over the past two decades, tremendous efforts were dedicated to organic photovoltaics (OPVs) which have led to the breaking barrier of 20% power conversion efficiencies (PCEs) for single-junction devices.[24,117,227,292–295] Recently, the non-fullerene low bandgap acceptor materials (NFA) receive considerable attention regarding their thermal stability [23,296], broad absorption spectrum which lead to efficient solar photons harvesting and thus high output current density[87], diminishing the non-radiative energy losses, providing high voltages[163,297], and easy tunable energy level.[227,298299] From the device point of view, enhancing both photocurrent and photovoltage of NF-OPVs are the most straightforward strategy to improve the photovoltaic performance.[292] In addition, it is well known that the molecular orientation between the donor and acceptor materials plays a vital role in the charge transfer kinetics.[300] Hence, the anisotropic structure of NFA (such as Y6 and Y7) secures an efficient π-π interaction that matches the coupling with the donors which tuned the phase separation.[50] As a result, the NF-OPVs demonstrate an efficient capability by separating excitons with negligible driving energies, obtaining high PCEs with respect to the energy levels of the used donor materials.[301,302] Thus, these remarkable advantages, avoiding the trade-off behaviour between the voltage loss and charge generation[89], provide barrierless free charge generation, suppressed charge carrier recombination, and enhanced charge mobilities of the resulting devices.[86,89,227]

Furthermore, the device structure as well as the bulk morphology and thickness play a crucial role that critically influence the performance of the NF-OPVs.[83,89,303] These factors mainly control the exciton binding energy and diffusion length[304] to avoid the undesirable static disorder that exhibit intrinsic sources of traps in the devices and in turn affecting the overall performance.[64,305] Upon these contexts, several optimization strategies were performed to control the phase morphology and thicknesses of the photoactive layer of the NF-OPVs. [304,306–309] Furthermore, thermal treatment is one of the effective avenues conducted to tune the bulk and interface morphologies to perform an efficient charge separation at the donor/acceptor interface[36,310] as well as to modify the interfaces between the active blend and the interfacial layers to enhance the charge carrier collection and transportation.[98,100,298,311,312] For instance, the morphology defects described by Wu et al. were the main obstacles that hinder the hole transfer from Y6 to PM6, limiting the exciton decay and consequently declining the overall cell performance.[231] These observations reflect the improvement ability of the NF-OPVs through fine tuning of the active blend and interfacial morphologies.

Accordingly, in this chapter, the proposed device architecture is ITO/PEDOT:PSS/PM6:Y7/PDINO/Ag as shown in **Figure 6.1.** Herein, we report pioneer enhancement in the generated current density (J_{SC}) of 32.62 mA/cm^2 with a maximum PCE of 17.92 % for the optimized single junction NF-OPVs by introducing Pre-Thermal Treatment approach (Pre-TT). Therefore, first, we conducted an optimization process to the devices through varying the thicknesses of the PEDOT:PSS, PM6:Y7, and PDINO layers. Then, to

investigate the reason behind the enhanced J_{SC}, we conducted a comparison between the pristine and the Pre-TT treated devices. Exhibiting an interesting dependency of the blend and interface morphologies, the J_{SC}, and in turn the overall device photovoltaic performance upon the applied Pre-TT to the PEDOT:PSS/PM6:Y7 layers. The Pre-TT approach procedure was described in detail in the **6.2 Experimental Procedures** section and simplified in **Figure 6.2**.

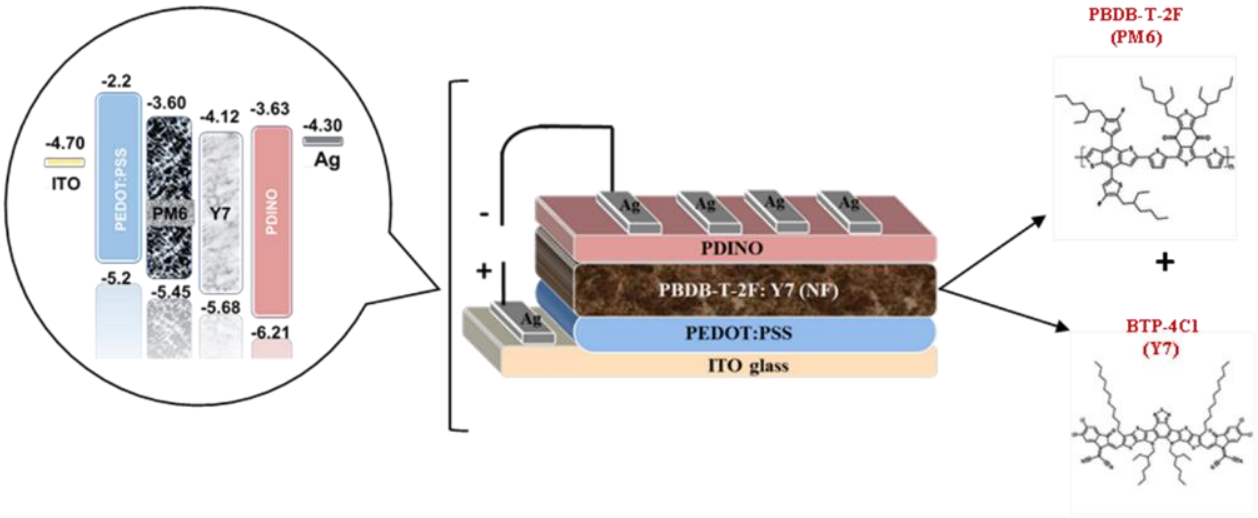

Figure 6.1 The schematic diagram of the fabricated conventional NF-OPVs structure with the energy band cascade and PM6:Y7 chemical structures. The energy positions of the band edges for the semiconductors and the metals work functions were taken from [117], [235], and [313] references.

6.2 Experimental Procedures

In this section the synthesis and optimization details of the PEDOT:PSS, PDINO interfacial layers, and the PM6:Y7 photoactive layers along with the Pre-TT Approach were reported. Furthermore, explicating the device fabrication procedures of the conventional NF-OPVs conducted in this chapter. The schematic diagram for the fabrication procedures is prior illustrated in **Figure 2.7** in Chapter 2.

6.2.1 Device Fabrication Procedures

For fabricating the NF-OPVs devices, the PEDOT:PSS aqueous solution was filtered through 0.45 µm PFTE filter (poly tetrafluoroethylene) then spun-coated on the pre-cleaned ITOs. The PEDOT:PSS film was annealed at 150 °C for 20 min in the air and left to cool down for 15 min to obtain thin films of 45 nm (Device 6-D6), 30 nm (Device 2 - D2), and 20 nm (Device 7- D7). 20 mg/ml blend solution of PM6 donor and Y7 acceptor was prepared by dissolving the 1:1 ratio in CB with 0.5 wt % CN additive and stirred for at least 3 h at 80 °C. Afterward, the prepared solution was filtered by 0.2 µm PVDF filter then spun-coated over the

PEDOT:PSS layer at 1200, 1500, 1600, 1800 and 2000 rpm obtaining films with thicknesses of 150 nm (Device 1– D1), 100 nm (Device 2-D2), 95 nm (Device 3–D3), 80 nm (Device 4 - D4), and 70 nm (Device 5 – D5). Then the PM6:Y7 deposited film was left to anneal at 90 ℃ for 5 min and then cool down for 15 min. The PDINO solutions were prepared by dissolving 1.0 mg/ml, 1.5 mg/ml and 2.0 mg/ml in methanol, then filtered and spun coated to form 10 nm (Device 2-D2), 20 nm (Device 8 - D8), and 30 nm (Device 9 – D9) thin films, respectively. The substrates were finally transferred into the vacuum thermal evaporation chamber inside the glove box 100 nm Ag was evaporated as aforestated in Chapter 2 in **Figure 2.7**. Finally, we transferred the fabricated devices from the evaporator to the sample holder inside the glove box which was carefully sealed for the device's measurement steps.

6.2.2 Pre-Thermal Treatment Approach (Pre-TT) to Fabricate the Pre-TT Based Devices

Regarding the Per-Thermal Treatment approach (Pre-TT), we conducted an additional hot deposition step to the PEDOT:PSS film along with the PM6:Y7 blend solution as clarified in **Figure 6.2**.

1- Before the PM6:Y7 deposition step, the cooled down PEDOT:PSS film and the filtrated PM6:Y7 solution (as described above) were both re-heated at 80 ℃ for 30 min.
2- After 30 min, the hot filtered solution of PM6:Y7 blend was hot-deposited over the hot PEDOT:PSS film.
3- Then, the PEDOT:PSS/PM6:Y7 films were left to annealed for 5 min at 90 ℃, and finally we followed the fabrication procedure of PDINO and Ag depositions as previously described .

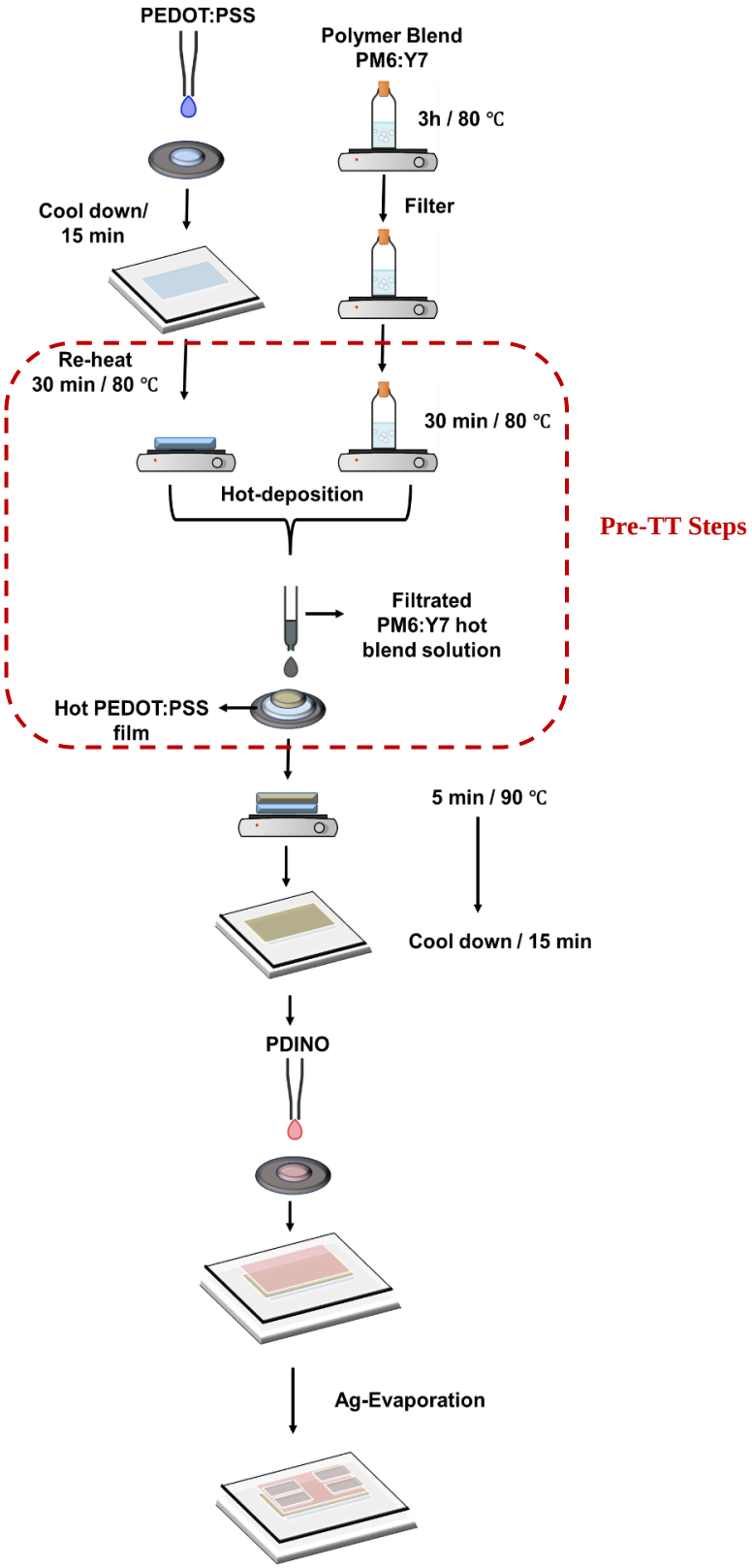

Figure 6.2 Scheme of the proposed Pre-Thermal Treatment (Pre-TT) Approach procedures for the Pre-TT NF-OPVs based devices.

6.3 Results and Discussions

6.3.1 Optimization Study of the NF-OPVs Devices through Varying Layers Thickness.

Careful optimization steps were conducted to improve the performance of the resulting NF-OPVs through revitalizing the thickness of each layer within the device. First, we started with the PM6:Y7 absorber active layer using five different thicknesses of 150 nm (Device 1-D1), 100 nm (Device 2-D2), 95 nm (Device 3-D3), 80 nm (Device 4-D4), and 70 nm (Device 5-D5). As displayed in **Figure 6.3a**, the best performance was observed by D2 (100 nm) as listed in **Table 6.1**. Hence, we selected D2 to continue the further optimization steps through optimizing the thickness of the interfacial layers. The second optimization step was through the PEDOT:PSS, hole transporting layer (HTL), investigating three thicknesses of 45 nm (Device 6-D6), 30 nm (Device 2-D2), and 20 nm (Device 7-D7). We found that D2 retained the highest performance among the others (**Figure 6.3b, Table 6.1**). Last step was conducted via the PDINO electron transporting layer (ETL) using three concentrations of 1.0 mg/ml, 1.5 mg/ml, and 2.0 mg/ml to obtain 10 nm (Device 2-D2), 20 nm (Device 8-D8), and 30 nm (Device 9-D9) film thickness, respectively. Finally, D8 showed the pioneer recorded performance in comparison to the other devices (**Figure 6.3c, Table 6.1**). Hence, the best performance was recorded for D8 through the proper optimization of the PM6:Y7 absorber active layer thickness along with the cathode interfacial layer thickness of PDINO.

6.3.1.1 Optimization of the NF-OPV Devices through Different Photoactive Layer Thicknesses

In this section, the correlation between the active layer thickness and the performance of the fabricated devices was described. It is important to clarify that the other thicknesses related to the interfacial layers (PEDOT:PSS and PDINO) were kept constant in this stage of study to conduct a systematic comparison.

Figure 6.3a displays the current density-voltage (J-V) characteristics under illumination conditions for the five representative devices (Device 1-Device 5) with different thicknesses of PM6:Y7 photo-absorber layer aforestated. Moreover, to confirm the high performance presented by our devices, we remeasured some devices such as D2 and D3 in the ICIQ facilities which exhibited quite similar performance as listed in **Table 6.1,** labelled as D2-ICIQ and D3-ICIQ. The results exhibited that the 100 nm photoactive layer thickness - Device 2- based devices possessed the highest performance parameters of FF, R_{Sh}, and PCE with 67.40 %, 508 $\Omega.cm^2$, and 17.33 %, respectively, which quite well consistent with the reported literatures[117,227]. In contrast to the Device 1 (150 nm) based devices that showed the lowest values of V_{OC} = 0.81 V, FF = 0.59, R_{SH} = 315 $\Omega.cm^2$ and PCE = 15.04 %. It was noticeable that, by increasing the absorber film thickness from 70 nm to 100 nm, obvious increase in FF was improved from 63.83 % for Device 5, to 64.09 % for device 4, to 66.85 % for device 3 and 67.40 for Device 2, which in turn improves the overall efficiencies of the corresponding

Table 6.1 Photovoltaic performance parameters statistics of the fabricated devices with variable thicknesses of the PM6:Y7, PEDOT:PSS and PDINO layers.

Device	PM6:Y7	PEDOT:PSS	PDINO	V_{OC} (V)	J_{SC} (mA/cm^2)	FF (%)	PCE (%)	R_S (Ω.cm^2)	R_{SH} (Ω.cm^2)
D1	150 nm	30 nm	10 nm	**0.81** 0.80±0.1	**31.56** 29.69±1.87	**58.85** 60.36±1.51	**15.04** 14.20±0.84	**0.94** 0.81±0.13	**315** 305±10
D2	100 nm			**0.84** 0.84±0.01	**30.60** 30.63±0.08	**67.40** 65.55±1.85	**17.33** 16.78±0.55	**0.69** 0.71±0.08	**508** 465±43
D2-ICIQ	95 nm			**0.85**	**31.28**	**0.66**	**17.61**	**1.26**	**489**
D3				**0.85** 0.85±0.01	**30.04** 30.12±0.66	**66.85** 66.75±0.10	**17.07** 16.30±0.77	**0.76** 1.14±0.42	**403** 398±30
D3-ICIQ	80 nm			**0.85**	**32.08**	**0.61**	**17.31**	**1.12**	**512**
D4				**0.83** 0.83±0.01	**30.88** 30.78±0.37	**64.09** 62.95±1.27	**16.425** 16.08±0.43	**0.72** 0.71±0.08	**389** 380±20
D5	70 nm			**0.83** 0.83±0.01	**30.34** 30.96±0.53	**63.83** 64.34±0.52	**16.08** 15.82±0.26	**0.78** 0.68±0.21	**350** 348±32
D6	100 nm	45 nm		**0.83** 0.83±0.01	**31.36** 31.43±0.11	**62.08** 61.45±0.74	**16.16** 15.91±0.25	**1.36** 1.12±0.80	**321** 342±42
D7		20 nm		**0.83** 0.83±0.01	**31.33** 31.11±0.22	**63.35** 63.24±0.43	**16.48** 16.33±0.17	**0.73** 0.78±0.12	**340** 413±80
D8		30 nm	20 nm	**0.85** 0.84±0.10	**32.65** 31.44±1.36	**65.53** 65.82±0.63	**17.92** 17.61±0.31	**1.13** 0.80±0.52	**372** 374±29
D9			30 nm	**0.84** 0.84±0.10	**30.61** 30.18±0.43	**66.91** 66.68±0.23	**17.21** 16.70±0.51	**0.91** 1.14±0.28	**447** 464±75

All the devices were measured under standard conditions (100 mW/cm^2 simulator irradiation at AM 1.5G) and the average parameters were calculated from a minimum of 9 fabricated devices for each configuration.

devices to 16.08 %, 16.43 %, 17.07 %, and 17.33 %, respectively as demonstrated in **Figure 6.3c**. This exhibited results are consistence with the reported work of J. Yuan et al. and L. Zhan et al.[89,237]. Hence, this behavior could be attributed to the diminishing of the series resistance (R_S) along with the increment of R_{Sh}, providing better FF corresponding devices. While the drop of FF in Device 1 might be assigned to increased bulk recombination sites upon higher PM6:Y7 thickness, resulting in a noticeable decline in the R_{Sh} values [88]. Interestingly, the J_{SC} and V_{OC} values showed insignificant influence upon the photoactive layer thickness increment till 100 nm that is barely changed as demonstrated in **Figure 6.3d**, which matched with the workpresented by Y. Cui et al. and N. Tokmoldin et al.[117,88]. In contrast to Device 1-150 nm-based devices, where the J_{SC} along with the R_S increased and the V_{OC} reduced as listed in **Table 6.1**.

Figure 3.6b depicts the J-V curves of the mentioned five fabricated devices under dark condition. It was noticeable that the thicker photoactive layer-based devices (D1-150 nm) exhibited the highest leakage current, resulting in shunting behavior. Furthermore, D2 (100 nm) and D3 (95 nm) based devices showed lower values of leakage current behavior than D4 (80nm) and D5 (70 nm). This attitude is greatly matched with the obtained R_{Sh} value of the corresponding devices (**Table 6.1**). Thus, the R_{Sh} showed a noticeable increment with minimum leakage current for the D2 based devices and vice versa for D1 ones. This variation

in leakage current in the fabricated devices is common in organic solar cells due to many reasons and importantly the film thickness[146, 314].

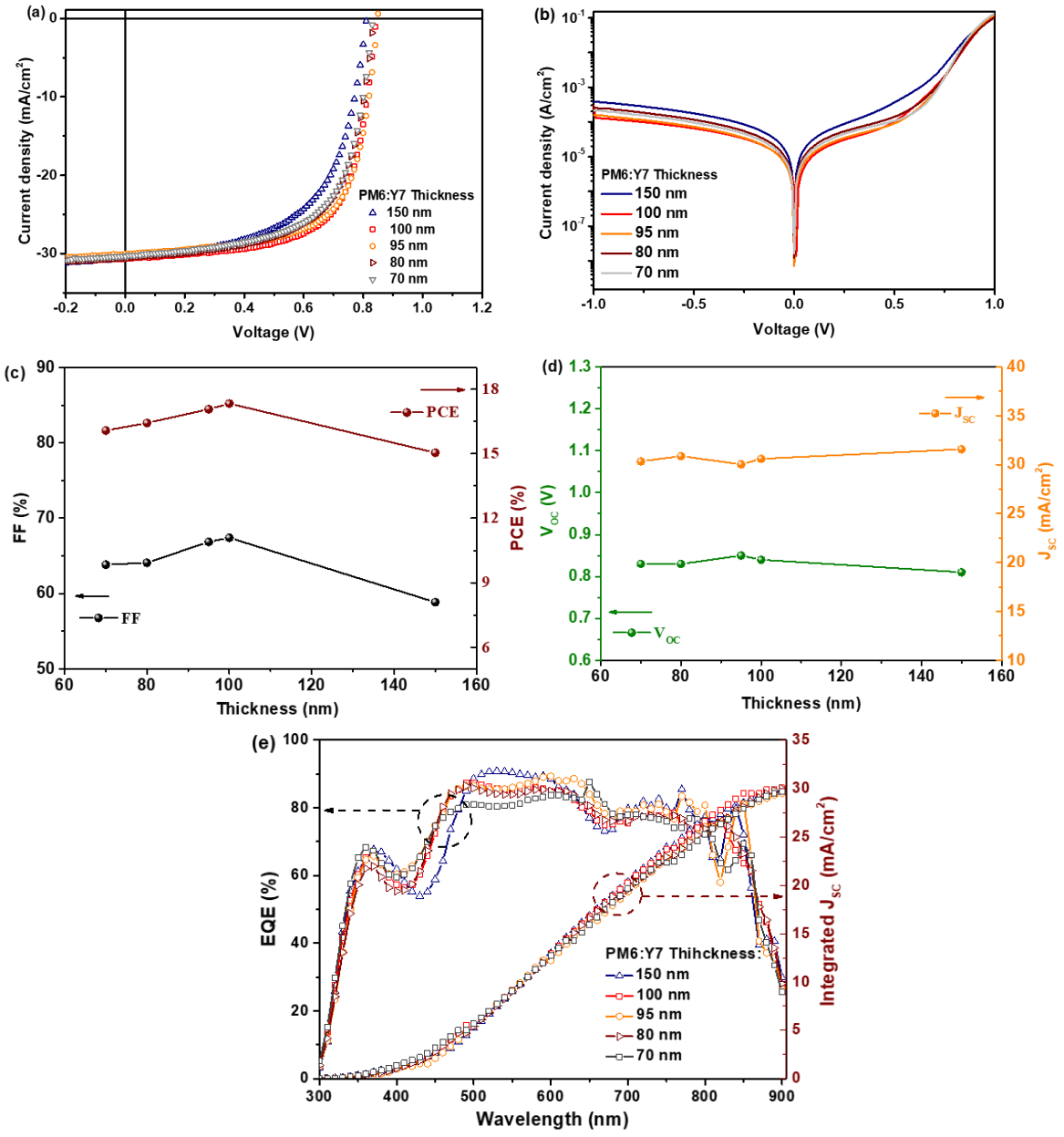

Figure 6.3 J-V characteristic curves of the NF-OPVs fabricated with different absorber-active layer thicknesses (a) under Illumination (AM 1.5G), (b) at dark. (c) EQE spectra (left) and the integrated short circuit current density (right) of the different PM6:Y7 thicknesses-based devices. Devices performance parameters optimization of (a) FF (left) and PCE (right), (b) V_{OC} (left) and J_{SC} (right). The lines are only for eyes guide.

Figure 6.3c displays the external quantum efficiency (EQE) spectra with AM 1.5 G reference spectrum for 1, 2, 3, 4, and 5 based devices with different photoactive layer thicknesses. It showed that all the devices exhibit barley enhanced EQE response by increasing the absorber active layer thickness. Furthermore, the entire devices possess similar wavelength range of absorption from 300 nm to 900 nm however, the absorption intensity at short wavelengths 300-450 still low due to the limited absorption of the polymer donor in this region. Otherwise, the EQE spectra from 450 to 800 nm exhibited strong photoresponses with an average plateau achieving around 80 % with the highest value of 86 % at 540 nm for the D1 (150 nm) based devices. In addition, the integrated J_{SC} values from the EQE spectra (listed in **Table 6.2**) showed a good proof for the impressive high current generated along with being consistent with the J_{SC} trend values of the corresponding devices as measured by the J-V under illumination (**Table 6.1**).

Table 6.2 The values of J_{SC} integrated of the conventional NF-OPVs based devices calculated from the EQE measurements in **Figure 6.3e.**

Device	PM6:Y7	PDEOT:PSS	PDINO	J_{SC} (mA/cm^2)
D1	150 nm	30 nm	10 nm	28.99
D2	100 nm			30.04
D3	95 nm			29.50
D4	80 nm			30.00
D5	70 nm			29.67
D6	100 nm	45 nm		30.54
D7		20 nm		29.33
D8		30 nm	20 nm	32.10
D9			30 nm	30.05

Then, impedance spectroscopy was carried out under AM 1.5G illumination condition as an alternative insight study to investigate the electric properties of the fabricated devices with respect to the interfacial charge transfer and carrier recombination[165] along with providing the mechanisms behind the performance swap upon thickness variation. **Figure 6.4a** shows a typical semicircle behavior of Cole-Cole plot for the NF-OPVs based on different PM6:Y7 layer thickness at V_{OC} bias voltage which correlated the efficient transfer happened at the active layer/electrode interface[165,166]. Moreover, It is worth to mention that the size of the arc is commonly correlated to the device resistance [165]. We noticed that D2 showed the smallest arc radius among the other devices. Furthermore, D2 based devices exhibited the smallest frequency arc, describing the less pronounced charge accumulation impact as compared to the other devices. [91]Therefore,

this behaviour reveals that D2 based devices possessed the lowest device resistance that efficiently assist the charge transfer and collection, resulting in better device performance. Interestingly, this behavior confirms the lowest R_S value observed by the D2 based devices in the previously discussed J-V characteristics under illumination (**table 6.1**). Moreover, the same behavior was recorded for the entire devices at 0.0 V, 0.2 V and 0.5 V applied bias voltages as shown in **A.11**. **Figure 6.4b** displays the calculated trap-DOS plotted as a function of energy for the fabricated devices. It shows a single exponential trap distribution for all samples where almost same slope values were detected which defines the same trap activation energy and carrier response[58]. However, a shift in E_O value was observed from the lower DOS of D1 based on 150 nm absorber film thickness than the others. We can explain this by equation **2.11. 2.12** suggesting that this shift might be due to the lower obtained energy regarding more localized trap sites created in thicker active layer based devices[172,245,64,225]. This behavior explains the highest device impedance, lowest shunt resistance, lowest FF, and in turn the PCE drop obtained by D1 based devices.

Upon the obtained results, D2 exhibited the less pronounced trap sites, lowest R_S, highest R_{Sh} and as a sequence, better PCE. Accordingly, D2 based devices were selected to be the optimized PM6:Y7 film with 100 nm thickness for future interfacial layers optimization processes.

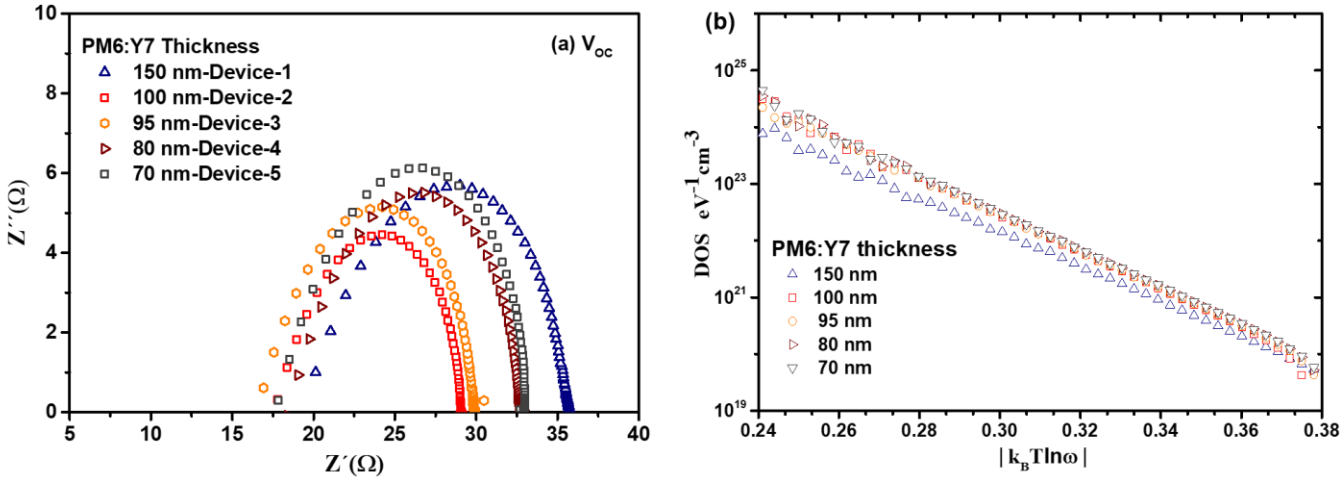

Figure 6.4 (a) Cole-Cole plots, (b) DOS as function of $|k_BTln\omega|$ at V_{OC} under AM1.5 G illumination, of different thicknesses of the PM6:Y7 photoactive layer-based NF-OPVs.

6.3.1.2 Optimization of the NF-OPV Devices Through Different PEDOT:PSS Film Thicknesses

Following same sequence of procedures, we studied three different thicknesses of PEDO:PSS based on the previously mentioned optimized D2 devices, maintaining constant thickness of PM6:Y7 (100 nm) and PDINO (10 nm- 1 mg/ml) layers. **Figure 6.5a** shows the J-V curve for the fabricated D6, D2 and D7 based

devices with different PEDOT:PSS thicknesses of 45, 30, and 20 nm, respectively, under illumination conditions. It can be noticed that the V_{OC} was barely changed for the entire devices. Moreover, insignificant differences were recorded between the performance parameters D6 and D7 devices as listed in Table **6.1**. It is worth mentioning that the pronounced variation was revealed by the FF, where D2 based devices showed a higher value of 0.67 than D6 and D7 based devices, exhibited 0.62 and 0.63, respectively. This might be attributed to the lowest R_S value of 0.69 Ωcm^2 and highest R_{Sh} value of 508 Ωcm^2 obtained by the D2 based devices, resulting in better FF and in turn higher PCE. Furthermore, it was noticed that the higher leakage current was observed from the thicker PEDOT-PSS layer in D6 based devices as displayed in **Figure 6.5b.** This might explain the diminishing of the R_{Sh} value in such a device, explaining the decline of the FF and the PCE. Moreover, **Figure 6.5c** shows the EQE spectral response and the calculated integrated J_{SC} values that greatly matched with the J_{SC} values obtained by the J-V characteristics under illumination (**Table 6.1**).

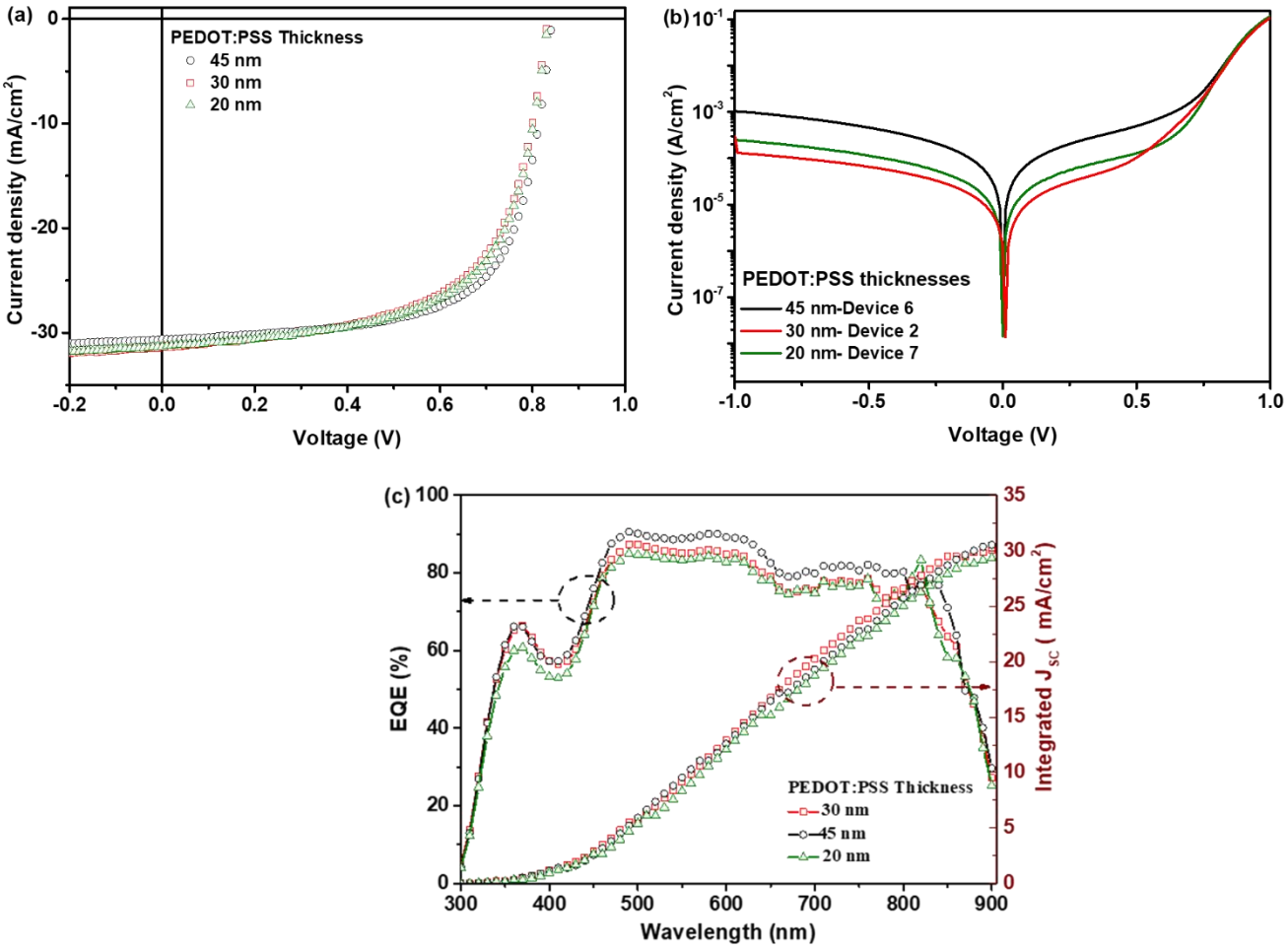

Figure 6.5 Characteristic curves of the NF-OPVs fabricated with different PEDOT:PSS thicknesses (a) J-V under Illumination (AM 1.5G), (b) J-V at dark, and (c) EQE spectra (left) and the integrated short circuit current density (right).

Figure 6.6 presents the Cole-Cole plots for the NF-OPVs based on different PEDOT:PSS thicknesses at V_{OC} bias voltage. All devices showed the typical Nyquist arc; however, a clear variation was observed regarding the arc radius response. Where, the Cole-Cole plot of D2 showed much lower impedance as well as smaller arc radius size than the other devices. In contrast to D6, that showed the higher arc radius along with the highest arc frequency, revealing the pronounced charge accumulation takes place that hinder their collection, resulting in charge recombination upon increment of the PEDOT:PSS layer thickness. This attitude was similarly detected for all samples at 0.0 V, 0.2 V, and 0.5 V illustrated in **Figure A.12**. Moreover, the shifting of E_0 value obtained in **Figure 6.5b** confirms the presence of an extra recombination centers that might be impeded in the D6 based devices upon the thicker layer of PEDO:PSS which increased its resistance as well declined its performance[64]. Therefore, it is important to notice that the film thickness of the PEDOT:PSS in the NF-OPVs showed a vital role in limiting the performance of the devices. Thus, D2 based devices with 100 nm of PM6:Y7 and 30 nm of PEDOT:PSS were further chosen as a reference for the next investigation steps with the PDINO thickness layer variation.

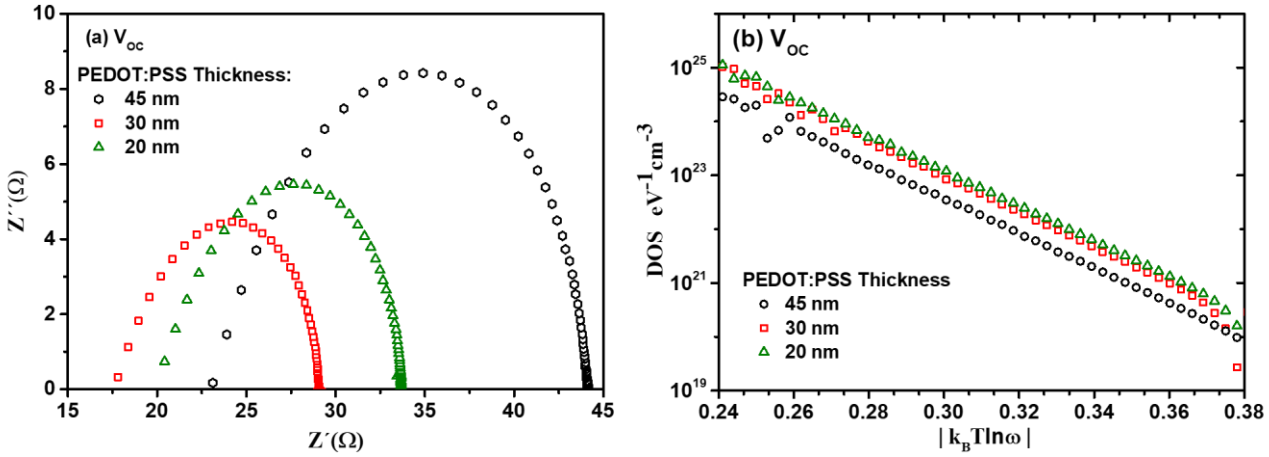

Figure 6.6 (a) Cole-Cole plots, (b) DOS as function of $|k_BTln\omega|$ at V_{OC} under AM1.5 G illumination of different PEDOT:PSS thicknesses-based NF-OPVs.

6.3.1.3 Optimization of the NF-OPV Devices Through Different PDINO Film Thicknesses

To cover the study of NF-OPVs performance dependence on the film thicknesses within the device, we went further for optimizing the ETL by using different solution concentrations correlated with the film thickness of the PDINO as described in the **6.2 Experimental** section. **Figure 6.7a** illustrates the measured J-V curves of three representative cells with different thicknesses of the PDINO-ETL: Device 2 -10 nm (1 mg/ml – the selected device upon the previous optimization steps), Device 8 – 20 nm (1.5 mg/ml), and Device

9 – 30 nm (2 mg/ml). Regarding D2 and D9 based devices, both showed almost similar perform parameters. Furthermore, the J-V characteristics at dark (**Figure 6.7b**) manifested insignificant difference between the behavior of the devices. Surprisingly, we noticed that Device 8 presents the highest of both J_{SC} and V_{OC} of 32.65 mA/cm^2 and 0.85 V with the increment of the PDINO thickness to 20 nm film thickness. However, the FF of D8 based devices was slightly reduced to 0.65 which might be due to increasing the R_S of the film to 1.173 Ωcm^2 along with decreasing the R_{Sh} to 372 Ωcm^{2}as shown in **Table 6.1**. Thus, strategies to optimize one parameter might oppositely affect another one, making it challenging to optimize the entire parameters at the same time. Therefore, even we got higher J_{SC}, V_{OC}, and PCE, that sacrifices with a quite diminishes in the FF. Moreover, the extraordinarily high J_{SC} value observed in D8 base devices was further confirmed by the EQE- spectra shown in **Figure 6.7b** and the calculated integrated J_{SC} listed in **Table 6.3**. As it showed that the entire devices absorbed in the same wavelength range (300-900 nm) and the maximum absorption intensities for D2 and D9 based devices were about 85 -90 % while for D8 based ones was > 95 %.

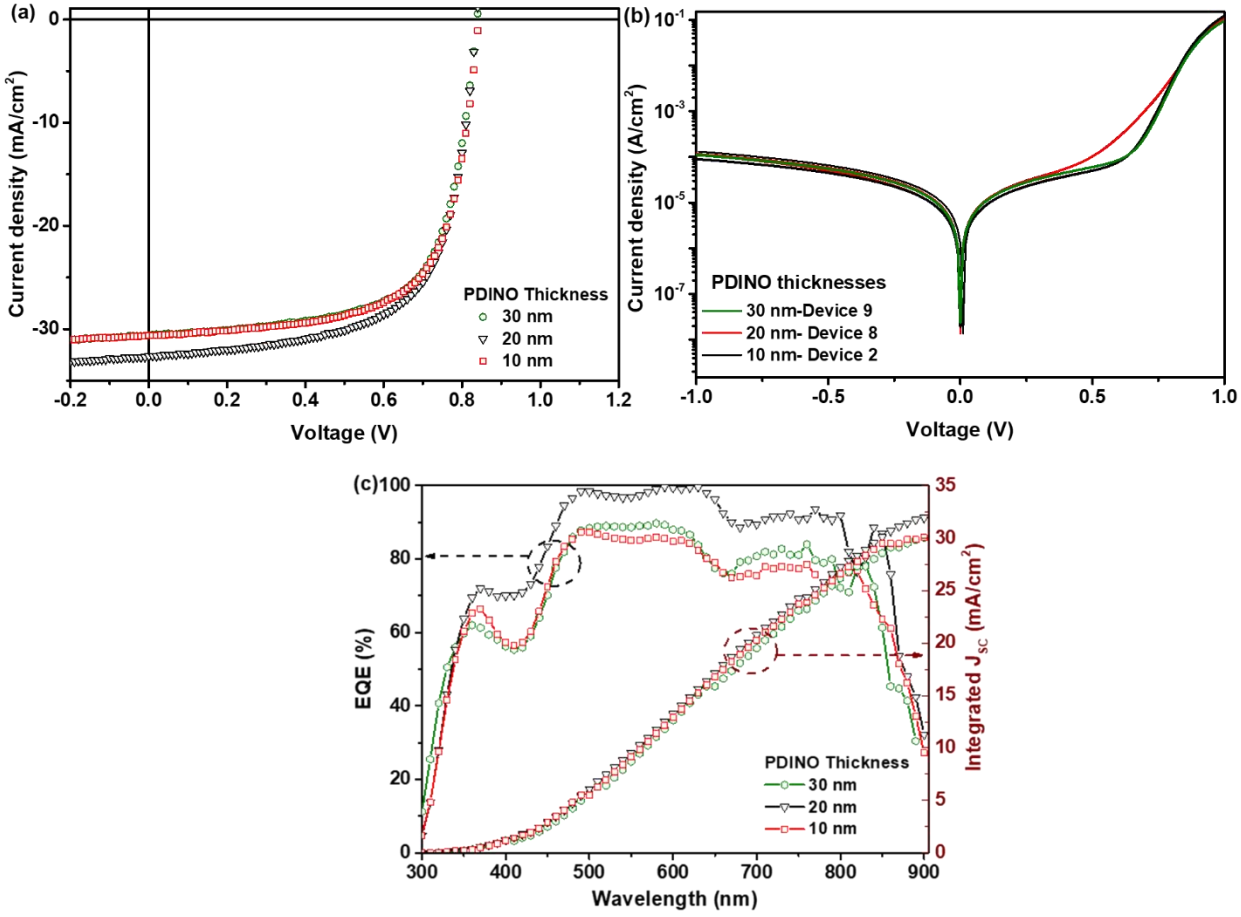

Figure 6.7 Characteristic curves of the NF-OPVs fabricated with different PDINO thicknesses (a) J-V under Illumination (AM 1.5G), (b) J-V at dark, and (c) EQE spectra (left) and the integrated short circuit current density (right).

Figure 6.8a displays the Cole-Cole plots for the NF-OPVs devices based on different PDINO ETL thickness at V_{OC} bias voltage. All devices showed the typical Cole-Cole curve with quite similar behavior. It showed that the arc size and frequency increased significantly for the D9 based devices that possessed the 30 nm PDINO layer thickness. Thus, high PDINO film thickness causes noticeable increment in the device resistance and assists the charge accumulation process. In contrast to the D8 and D2 based devices, both showed lower arc radius and smaller arc frequency, specifying D8 based ones. This behavior was similarly recorded for the devices at 0.0 V. 0.2 V and 0.5 applied voltages as presented in **Figure A.13**. Furthermore, **Figure 6.8b** showed a bit shifting in E_O value obtained for D9 which might explain the quite low performance of these cells, that agree with the Cole-Cole behaviour, confirming the noticeable defects upon the trap sites exhibited in cuch devices more than the others. Finally, however, the entire fabricated devices possessed high generated current, but we interestingly observed that when the cathode interfacial PDINO ETL is optimized, the J_{SC} reaches its maximum value along with the efficiency as presented by D8 based devices.

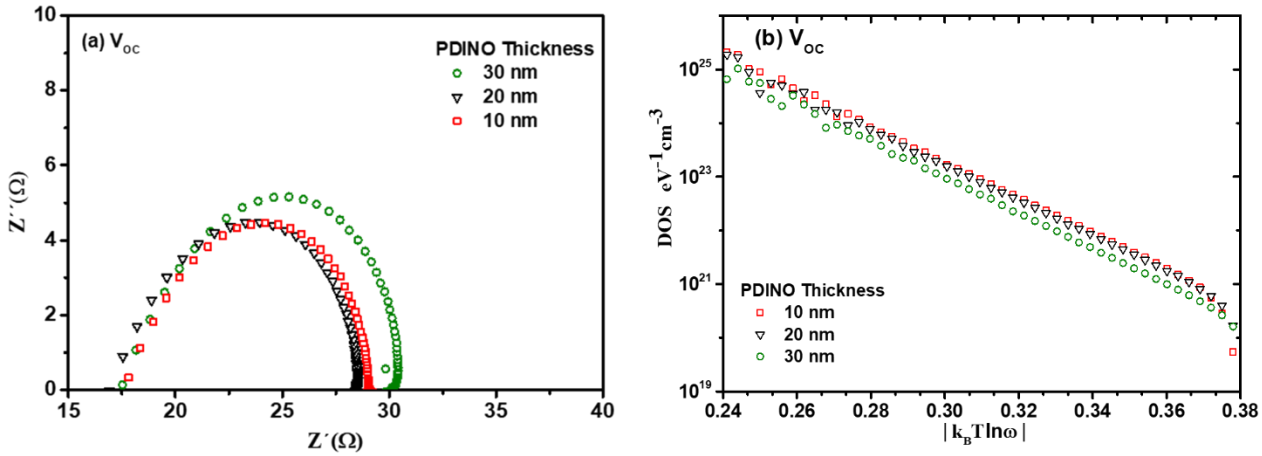

Figure 6.8 (a) Cole-Cole plots, (b) DOS as function of $|k_BTln\omega|$ at V_{OC} under AM1.5 G illumination of different PDINO thicknesses-based NF-OPVs.

Accordingly, the champion performance was exhibited through optimizing the PM6:Y7 to 100 nm, PEDOT:PSS to 30 nm, and the PDINO film to 20 nm (1.5 mg/ml), providing D8 based devices.

6.3.2 Revealing the Influence of the Pre-TT Approach on the NF-OPVs Based Device Properties.

Up on the aforementioned optimization processes, we depicted that the champion performance was recorded for D8 based devices through the proper optimization of the PM6:Y7 absorber active layer thickness along with the cathode interfacial layer thickness of PDINO. Hence, to further understand the reason behind the enhanced J_{SC}, we selected D1 as the non-optimized cells and D8 as the champion optimized ones, then we applied the investigation study of the Pre-TT approach through comparative insights on the morphological, optical, optoelectronic, electrical properties and related charge recombination dynamics of both, the pristine (non-treated-W/O Pre-TT) and the treated (Pre-TT) devices of D1 and D8 NF-OPVs. We examined the devices via current density voltage (J-V) under different illumination intensities, at 0.1, 1, 10, 16, 25, 50, 80, and 100 mW/cm^2, external quantum efficiency (EQE), mobility measurements, charge extraction (CE) and transient photovoltage/photocurrent (TPV/TPC) techniques. Furthermore, impedance spectroscopy (IS) measurements were performed through capacitance-voltage (CV) and capacitance-frequency (C*f*) to understand the device behaviour dependency on the Pre-TT approach.

6.3.2.1 Devices Performance

To evaluate the photovoltaic performance of the pristine and treated D1 and D8 based devices, current density-voltage (J-V) characteristics under AM 1.5G illumination conditions were performed as shown in **Figure 6.9a,** the detailed statistic performance parameters were collected in **Table 6.3** and the photovoltaic PCE % statistics diagrams in **Figure A.14**. The non-optimized pristine NF-OPVs of Device 1 (D1-W/O Pre-TT) exhibited a maximum PCE of 13.94 %, with a V_{OC} of 0.83 V, short circuit current density (J_{SC}) of 26.06 mA cm^{-2}, fill factor (FF) of 0.65, series and shunt resistances (R_S and R_{Sh}) of 0.98, and 473 Ω cm^2, respectively. For the non-optimized Per-TT based devices (D1-Pre-TT), the J_{SC} and PCE were remarkably enhanced to 31.56 mA cm^{-2} and 15.04 %, respectively, while the FF, R_{Sh} and V_{OC} were slightly diminished to 0.60, 315 Ω cm^2, and 0.81 V, respectively as listed in **Table 6.3**. Surprisingly, D8 Pre-TT demonstrated a similar behaviour toward the Pre-TT effect on D1 based devices ,where the pristine devices of D8-W/O Pre-TT showed PCE of 16.07 % with V_{OC} of 0.85 V, J_{SC} of 26.98 mA cm^{-2}, FF of 0.70, R_S, and R_{Sh} of 1.45 and 724 Ω cm^2, respectively which consistent with the reported results.[83,89,227] Interestingly, the Pre-TT D8 devices (D8-Pre-TT) obtained extraordinary increase in the J_{SC} of 32.65 mA cm^{-2} and in turn the PCE were highly improved to 17.92 % (see **Table 6.3**). However, the V_{OC} was the same (0.85 V), but the FF and R_S were slightly decreased to 1.13 Ω cm^2 and 0.66, respectively, as well as the R_{Sh} to 372 Ω cm^2. Thus, The Pre-TT devices of both D1 and D8 demonstrate slight decrease in their FF values and inconspicuous in their V_{OC} values as presented in **Figure 6.9b.** This trivial change in the FF might correlates the decline in the shunt resistances (R_{Sh}) of the Pre-TT based devices, as displayed in **Table 6.3**. However, both Pre-TT device types

(D1-non-optimized and D8-optimized) exhibited a remarkable enhancement in their PCEs upon the great improvement in their J_{SC} values as presented in **Figure 6.9b**. Hence, it is worth mentioning that the strategies to optimize one parameter might oppositely affect another one, making it challenging to optimize the entire parameters at the same time. Therefore, even we got higher J_{SC} and PCE, that sacrifices with bit diminishing the FF as previously reported in Y. Cui et al. [117] and J. Yuan [89] works. Overall, an outstanding J_{SC} value of 32.65 mA cm^{-2} is recorded for the D8 Pre-TT optimized based devices, which represent the top result for the non-fullerene OPVs devices as it is higher than the recently reported results in the literature [22,227,236,237]using the same active blend.

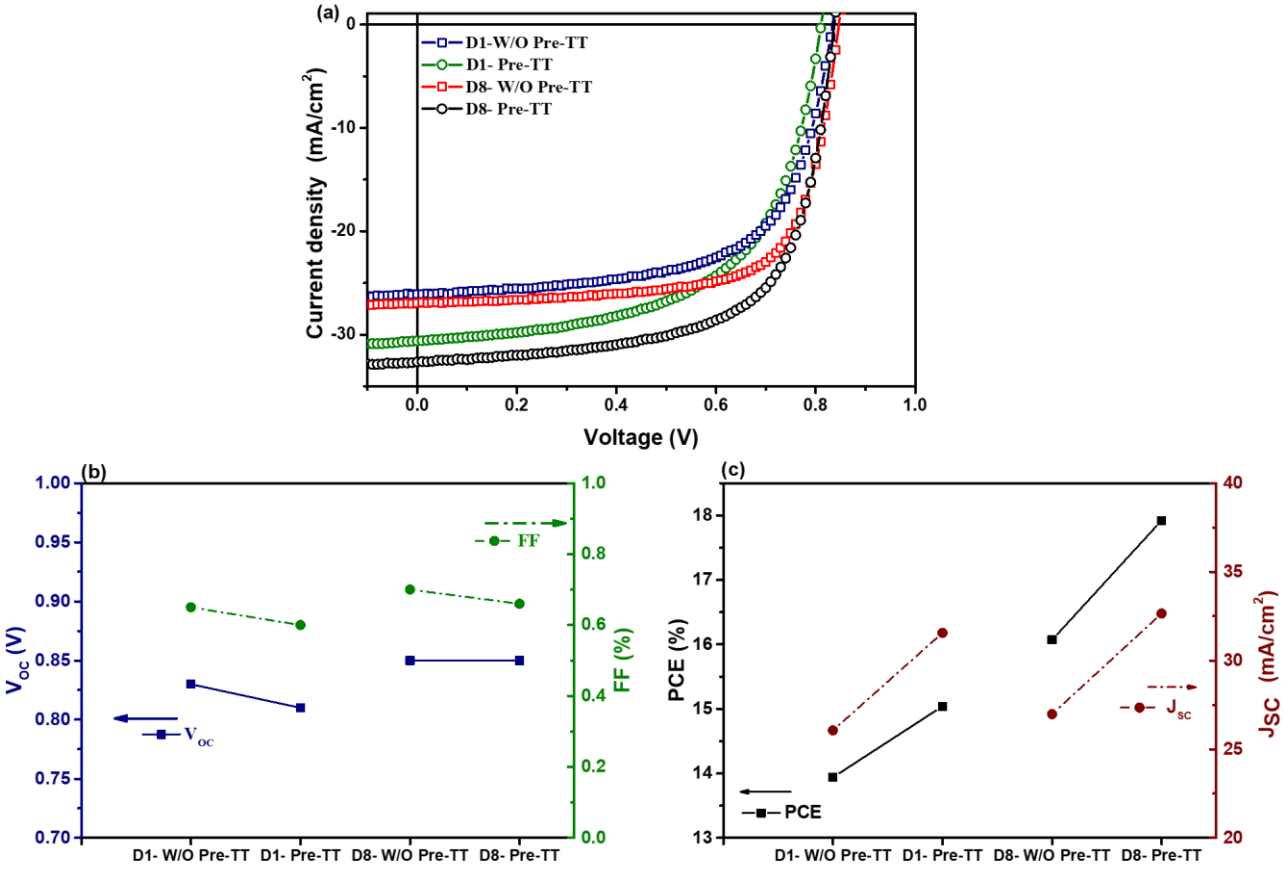

Figure 6.9 J-V characteristic curves of the pristine and the Pre-TT NF-OPVs of D1 and D8 under Illumination (AM 1.5 G). Cells' performance parameters for D1 and D8 Pristine and Pre-TT devices (b) V_{OC} (left) and FF (right), (c) PCE (left) and J_{SC} (right), the lines are only for eyes guide.

Table 6.3 Main performance parameters of the pristine and the Pre-TT fabricated D1 and D8 NF-OPVs.

Device	V_{OC} (V)	J_{SC} (mA/cm^2)	FF	PCE (%)	R_S (Ω cm^2)	R_{Sh} (Ω cm^2)
D1-W/O Pre-TT	**0.83** 0.82±0.10	**26.06** 27.25±2.12	**0.65** 0.62±0.02	**13.94** 13.53±0.60	**0.98** 1.26±0.62	**473** 397±76
D1- Pre-TT	**0.81** 0.80 ± 0.10	**31.56** 29.69±1.87	**0.60** 0.61±0.02	**15.04** 14.20±0.84	**0..94** 0.81±0.13	**315** 305±10
D8-W/O Pre-TT	**0.85** 0.84±0.10	**26.98** 27.15 ± 1.82	**0.70** 0.69 ± 0.02	**16.07** 15.82±0.61	**1.45** 1.18±0.27	**424** 625±99
D8- Pre-TT	**0.85** 0.84±0.10	**32.65** 31.44±1.36	**0.66** 0.65±0.06	**17.92** 17.61±0.31	**1.13** 0.80±0.52	**372** 374±29

All the devices measured under standard conditions (100 mW/cm^2 simulator irradiation at AM 1.5G) and the average parameters were calculated from minimum of 9 fabricated devices for each configuration.

For further investigation of the Pre-TT NF-OPVs, we performed the J-V characteristic for the pristine and the treated devices in dark condition as shown in **Figure 6.10a**. On one hand, the highest leakage current was obtained from the thicker absorber active layer in Device 1 (D1-150 nm) showing a high shunt, possibly recognized as "induced shunts" that responsible for diminishing the charge carrier at the interface.[278] This attitude might explain the lowest FF along with the PCE for these devices (D1), in contrast to the optimized D8 devices (100 nm), listed in **Table 6.3**. On the other hand, we found that the Pre-TT devices (of both D1 and D8) present almost one order of magnitude lower leakage current under the reverse bias conditions as compared to the pristine ones, indicating a higher shunt resistance.[72] Such behavior reveals the enhancement in the J_{SC} [72,178] of the Pre-TT devices than the pristine cells. Furthermore, to gain more insights we fitted the experimental data of the J-V at dark conditions through operating 2 diodes equivalent circuit model to calculate the series resistance (R_S) and shunt resistance (R_{Sh}) as demonstrated in **Figure 6.10b**. Where the symbols in **Figure 6.10b** referred to the experimental data and the lines to the fitting values that are listed in **Table 6.4**. For an applied voltage given, V, the two diodes equivalent model showed in **Figure 66.10n** clearly separate the voltage drop in the junction, V_B, and bulk, V_S, regions. The total current density, J, can flow thorough two exponential mechanisms, a shunt and a series resistances expressed by the equations 6.1, 6.2, and 6.3[195,315]

$$\mathbf{V=V_S+V_B} \quad 6.1$$

$$\mathbf{V_S = JR_S} \quad 6.2$$

$$J = J_{D1} + J_{D2} + J_{Rsh} = \sum_{i=1}^{2} J_{S-i}\left[\exp\left(\frac{V_B}{n_i V_T}\right) - 1\right] + \frac{V_B}{R_{SH}} \quad 6.3$$

where $J_{S1,2}$ and $n_{1,2}$ are the reverse saturation current and the ideality factor of the two exponential currents, respectively, V_T is the thermal voltage, R_S and R_{Sh} are the series and shunt resistances, respectively. It is well known that the meaning of J_S in OPVs is associated with the number of charges capable of jumping the energetic barrier in the reverse direction. It represents the minority charge density in the nearness of the barrier[30]. The devices achieving high efficiencies always show the lowest values of J_S as presented in our fabricated devices. The same trend has been observed for the ideality factor (n1 and n2) obtained by **equation 6.3** for all the devices. Where, the fitting data showed an exponential region ($0.65 < V\ (V) < 0.85$) with higher ideality factor (n1) values of 2.01 and 1.27 for the pristine devices of D1 W/O Pre-TT and D8 W/O Pre-TT, respectively, in comparison to the n1 of 1.35 and 1.15 for the D1 Pre-TT and D8 Pre-T, respectively. Moreover, the fitted values in **Table 6.4** depicted a noticeable increase in the R_{sh} values for the Pre-TT D1 ($3.2\times10^3\ \Omega\ cm^2$) and D8 devices ($1.1\times10^4\ \Omega\ cm^2$) in comparison to those for the pristine cells (R_{Sh} of D1 W/O Pre-TT= $2.9\times10^3\ \Omega\ cm^2$ and R_{Sh} of D8 W/O Pre-TT= $3.9\times10^3\ \Omega\ cm^2$). These obtained results explain the diminishing of the leakage current behavior observed for the Pre-TT devices [278], especially for the optimized D8 Pre-TT that possessed the champion performance. This variation in leakage current in the fabricated devices is common in OPVs due to many reasons and directly related to the thickness, quality and morphology of the films.[146,314]

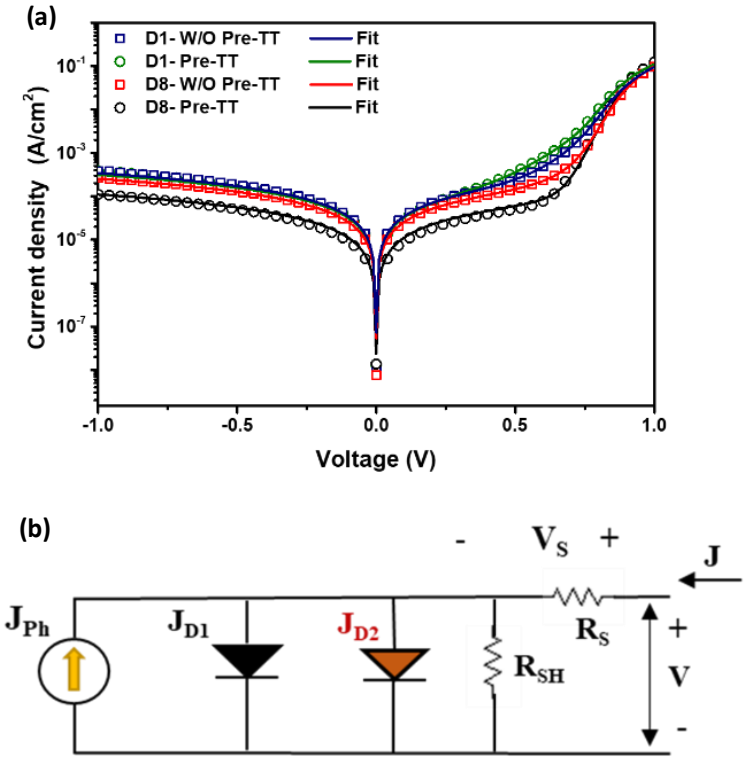

Figure 6.10 (a) J-V characteristic curves of the pristine and the Pre-TT NF-OPVs of D1 and D8 at dark condition (symbols for experimental data and the lines for the fitting). (b) Equivalent electrical circuit used to fit the experimental dark current-voltage measurements ($J_{Ph} = 0$) of the NF-OPVs corresponding devices.

Table 6.4. Fitting values from the of J-V characteristics under dark conditions of the pristine D1- W/O Pre-TTand D8-W/O Pre-TT as well as the D1 and D8 Pre-TT devices.

Devices	J_{S1} (A/cm^2)	n1	J_{S2} (A/cm^2)	n2	R_S (Ω cm^2)	R_{SH} (Ω cm^2)
D1-150 nm - W/O Pre-TT	1.59×10^{-9}	2.01	4.35×10^{-7}	4.31	0.65	2900
D1-150 nm - Pre-TT	9.27×10^{-13}	1.35	9.90×10^{-7}	3.60	0.90	3200
D8-100 nm - W/O Pre-TT	9.80×10^{-14}	1.27	3.03×10^{-8}	2.99	0.90	3940
D8-100 nm - Pre-TT	1.13×10^{-14}	1.15	2.18×10^{-10}	2.03	0.82	1.10×10^{4}

Figure 6.11a displays the external quantum efficiency (EQE) response with AM 1.5 G reference spectrum of the pristine and Pre-TT devices. It can be noticed that the entire devices have a similar wavelength range of a broad photoresponses from 300 to 900 nm, indicating the contribution of both donor and NF acceptor to the overall generated photocurrent. We can see that, the EQE intensity at short wavelengths range of 300-450 is lower due to the limited absorption of the polymer donor in this region.[117,163] However, the EQE spectra from 450 to 800 nm exhibited stronger photoresponses with a maximum plateau achieving around 80 % for the pristine devices (D1-W/O Pre-TT and D8-W/O Pre-TT), around 90 % for D1-Pre-TT and > 95 % for D8-Pre-TT. In addition, we calculated the integrated J_{SC} from the EQE spectra (listed in **Table 6.5**) which are consistent with the values obtained from the J-V listed in **Table 6.3**. Interestingly, the observed EQE response provides good proof for the extraordinary high current generated from the devices fabricated with Pre-TT approach. It is worth noting that in the absorption range of 450-850 nm, the pristine based devices showed different EQE spectral shape response than Pre-TT based ones. However, it is well known that optical interference and parasitic absorbance in nonactive layers provide a pronounced effect on the shape of the measured EQE as a passive optical effect. But, the BHJ layer thickness (and therefore the resulting film roughness) has a first order effect on the spectral dependence of the EQE[316]. Hence, we suggested that it might be attributed to the higher roughness observed for the pristine based films as will be explained in the **6.3.2.5 Morphology** section. Thus, in our case different microstructures reveal a more pronounced influence on the EQE spectral shape which is provided upon thickness variation and Pre-TT factors. Therefore , it is a foremost to obtain the internal quantum efficiency response (we will return to this measurement in the following parts) since it neglects the multilayer optical phenomena and the parasitic absorptions in nonactive layers such as ITO, PEDOT/PSS, as ascribed by A. Armin et al[160].

For further investigation related to the phenomena beyond the improvement of the generated current density for the Pre-TT devices, we measured the UV-visible absorption spectra of the ITO/PEDOT:PSS/PM6:Y7 structure for the pristine and the Pre-TT based films as shown in **Figure 6.11b**. We can explicitly see the enhancement in the light absorption of the D1 and D8 Pre-TT based films without any bathochromic shift. Furthermore, the inset images in **Figure 6.11b** show the real photo of the pristine

and Pre-TT devices. The colour of the active blend turns to darker upon the Pre-TT steps in both D1 and D8 devices, showing the potential to improve the photon harvesting of the host blend in the Pre-TT based devices (D1-Pre-TT and D8-Pre-TT) which in turn enhances the generated J_{SC} as confirmed by the previously discussed J-V curves. This behaviour was previously reported by T. Hua[317], ascribing that the improved absorption was attributed to the refining of the active layer morphology upon the Pre-TT (will be discussed in details in the **6.3.2.5 Morphology** section). In addition, it is worth to mention that the V_{OC} values of the corresponding pristine and Pre-TT devices (listed in **Table 6.3**) did not show a remarkable change that is greatly matches the consistency of the PM6:Y7 peak position in **Figure 6.11b**. Accordingly, the enhancement in the EQE spectra due to the Pre-TT approach might be attributed to the modulation of the absorption energy in the active blend.[163] This behaviour perfectly matches with S. Liu, et.al research work.[163]. Furthermore, to evaluate the charge generation, extraction, and collection processes of the devices within the photoactive layer, taking into account the recombination losses that might take place in the based devices. We calculated the internal quantum efficiency-IQE, following the correlation as described by Forrest et al.[161] and A. Armin et al. [160] that expressed as $\eta_{IQE}= \eta_{EQE}/\eta_A$, where η_{IQE} is the fractional internal quantum efficiency presented by the ratio of the number of the collected charges to the photons absorbed by the junction and η_A reveals the absorbed incident light amount by the photoactive layer. Hence, the IQE represents the photovoltaics response normalized by the number of photons actually absorbed by the photoactive layer and thus provides information about the behavior of the charge generation (exciton dissociation, charge transfer) and collection processes[161]. **Figure A.14** display the IQE of the pristine and Pre-TT based devices. The overall IQE intensities of the Pre-TT based devices are higher than the corresponding pristine ones. However, the contributed efficiency was varied from both donor and acceptor regions. Where, high IQE values in the range of 400 to 550 nm were 99.68%, 92.12%, 90.06%, and 88.86 % for the D8-Pre-TT, D8-WO Pre-TT, D1-Pre-TT, and D1- WO Pe-TT, respectively, and 52.42 %, 35.52%, 42.82%, and 25.03%, respectively, in the range of 650 to 800 nm. The IQE >900 nm has been omitted regarding the absorption falling edge at these wavelengths. Accordingly, it can be exhibited that the pristine based devices possessed lower IQE intensities than the Pre-TT ones, revealing the less efficient exciton dissociation and free charge extraction. In contrast to the Pre-TT-based device, specifying D8-Pre-TT optimized devices, suggesting that a significantly larger portion of the absorbed photons are converted to free charge carriers which are then collected by the corresponding electrodes which greatly matches with their superior EQE response (**Figure 6.11a**) and their J_{SC} values (**Table 6.3**). This might be facilitated by the fine-tuning of the Pre-TT based blend morphology (in the **6.3.2.5 Morphology** section), revealing that excitons generated can therefore reach the D/A interface and efficiently dissociate, resulting in high IQE values.

Interestingly, **Figure 6.11c** showed the logarithmic scale of the EQE vs the photon energy to confirm the effect of the Pre-TT step on the optical properties of the photoactive blend film using the Urbach rule as following[162,163]:

$$\alpha(E) = \alpha_0 \, e^{(E-E_g)/E_U} \quad (6.4)$$

where, α (E) is the optical absorption coefficient, α_0 is the optical absorption coefficient at the band edge, E is the photon energy and E_U is the Urbach Energy. It can be noticed that the photocurrent spectrum response of the entire devices is up to 1.4 eV that relates to the same photo-active blend of PM6:Y7.[163] Therefore, the higher photocurrent response of the devices is more likely correlated to the excitation of the active blend, and the lower photocurrent response than 1.4 eV is more attributed to the charge transfer states.[284,285] Accordingly, the Urbach energy of the devices was defined with the absorption tail (known as Urbach tail) below 1.4 eV as described in equation 2.10. Hence, the E_U value represents the density of state distribution that explains the energetic disorder in the molecular orbitals [162], which is considered as a valuable parameter revealing the influence of all possible defects.[164] Upon this context, the smaller E_U value corresponds the abrupt band edge.[163] The extracted E_U values of the devices are quite similarity (around 25 meV) which comparable to the thermal energy k_BT (25.8 meV) at room temperature.[162] However, they follow the same trend of devices performance (as listed in the inset of **Figure 6.11c**), where lower E_U values were exhibited for the Pre-TT devices that possessed better performance than the pristine ones. This obtained behavior from the Pre-TT samples might be due to diminishing the energetic disorder in the active blend as revealed by the morphological characteristics discussed in the following sections and in turn improving its optical properties.[163] Furthermore, these observations were verified by the optimized D8-Pre-TT devices which present the lowest E_U value, indicating the lowest energetic disorder that originates the superior device performance via declining the density of state distributions that in turn retard decreasing the recombination[286].

Moreover, to examine the exciton dissociation behaviour and the charge transfer processes, we performed photoluminescence (PL) measurements of the pristine and the Pre-TT pure blend films over the PEDOT:PSS layer to get a fair comparison regarding the Pre-TT approach as demonstrated in **Figure 6.11d**. The observed results indicate that the PL spectra of pristine films present higher intensity than the Pre-TT ones, where the PL response is quenched by 13 % and 35 % for D1 Pre- TT and D8 Pre-TT, respectively. This remarkable PL quench of the Pre-TT films, especially for the optimized D8 Pre-TT film, implies an efficient charge transfer at the interfaces of the PEDOT:PSS/PM6:Y7, resulting in higher generated current along with better device performance. [155,318] The PL results follow the same trend of the J_{SC} values of the corresponding based devices obtained (**Table 6.3**) as well as their EQE response in **Figure 6.11a**. Same response was further noticed for the PEDOT:PSS/PM6 films performed as a reference of D1 and D8 pristine and Pre-TT films as

shown in **Figure SA.15a** and **SA.15b**, respectively. Interestingly, same behaviour was reported by the F. Jin et al. upon the thermal annealing effect.[98]

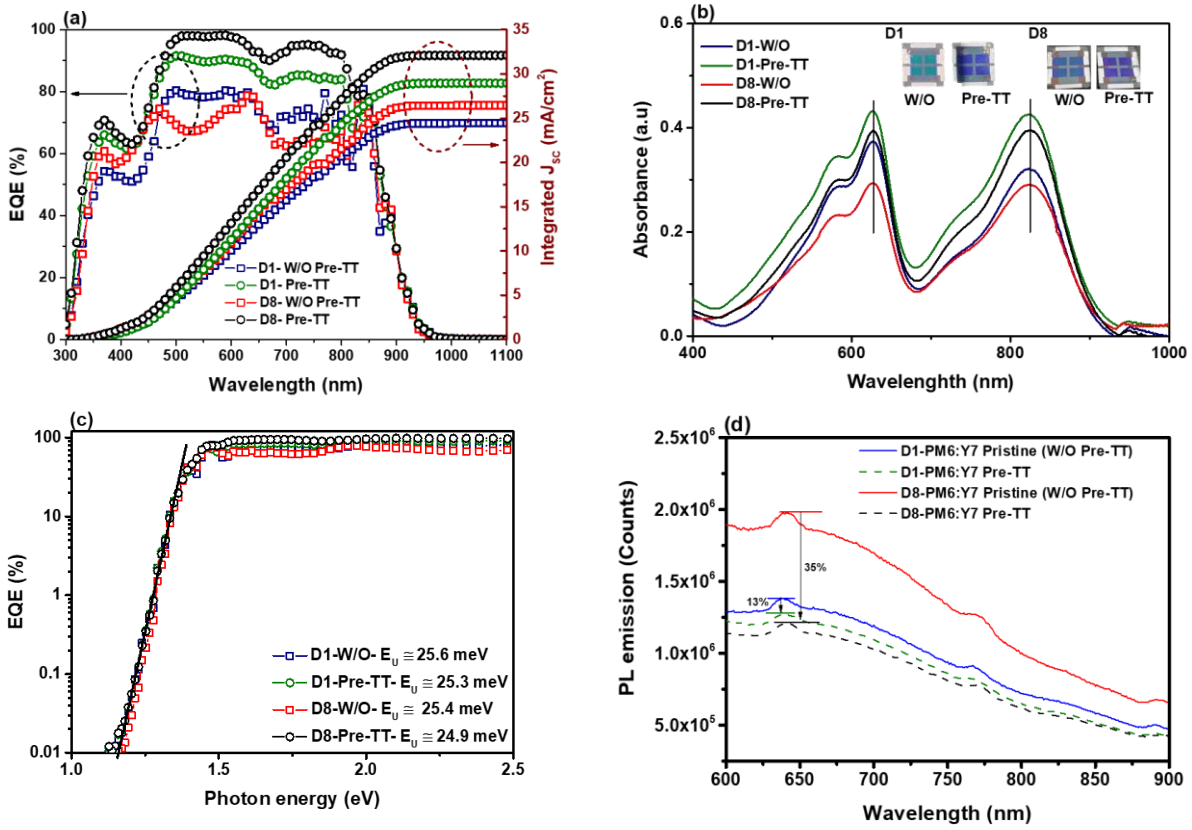

Figure 6.11 (a) EQE spectra (left axis) and the integrated short circuit current (right axis) of the NF-OPVs pristine and Pre-TT of D1 and D8 devices, (b) UV-vis absorption spectra of the ITO/PEDOT:PSS/PM6:Y7 structure based on D1 and D8 with an inset photos of the fabricated devices. (c) EQE vs photon energy of the pristine and PreTT NF-OPVs devices, and (d) PL spectra of the pristine and the Pre-TT pure blend films over the PEDOT:PSS.

Table 6.5 The values of the integrated J_{SC} extracted from the EQE-spectra analysis of the fabricated pristine and Pre-TT NF-OPVs.

Device	PM6:Y7 Thickness	Integrated J_{SC} (mA/cm^2)
D1- W/O Pre-TT	150 nm	24.44
D1-Pre-TT	150 nm	28.99
D8- W/O Pre-TT	100 nm	26.43
D8- Pre-TT	100 nm	32.10

6.3.2.2 Carrer Dynamics

In order to better understand the improvement of the treated devices upon the effect of the Pre-TT approach, we further measured the carriers dynamics of the devices via the advanced photoinduced spectroscopic techniques through charge extraction (CE), transient photovoltage (TPV) and transient photocurrent (TPC), evaluating the variation of charge transport, accumulation, and recombination that take place in the devices (see **Figure A.16** for more information).[167,175] **Figure 6.12a** presents the photogenerated charge density of the pristine and Pre-TT devices under different light bias from 1 Sun to dark, providing different V_{OC} values. The symbols indicate the geometrical and the chemical capacitance or in other words, the charges accumulated at the interfaces and in the bulk, respectively. Consequently, to disclose clear interpretation of the obtained data, we subtracted the geometrical capacitance obtaining the solid lines at the bottom of **Figure 6.12a**, revealing the charges presented at the bulk.[319] We noticed that the Pre-TT devices (D1-Pre-TT and D8 Pre-TT) exhibited higher number of charges (solid lines) compared to the pristine ones, describing the higher J_{SC} values obtained by J-V characteristics (**Figure 6.9a**) of the Pre-TT devices (**Table 6.3**). Moreover, we found that all devices present similar slope at 0.4-0.6 V range, indicating insignificant differences in the energy level position of the pristine devices and their corresponding Pre-TT cells [320,321], clarifying the consistency of their V_{OC} values.

Moreover, **Figure 6.12b** shows the charge carrier lifetimes scale with voltage, extracted from the TPV decays. The recombination was faster for the pristine devices, confirming their lower J_{SC} as well as PCE. However, for a proper comparison, **Figure 6.12c** displays carrier recombination lifetime (tau) versus charge density to evaluate the carrier recombination dependence on the charges of the corresponding devices. We observed that, for the same number of charges, recombination is slightly faster for the pristine devices. Hence, it is worth noting that the Pre-TT NF-OPVs demonstrated more charge generation which neither lead to recombination behaviour nor affecting Voc, exhibiting better performance than their pristine counterparts. This behaviour might be attributed to the presence of defect states[167,321,322] in the pristine devices that efficiently reduced by the Pre-TT approach. These results agree well with the PL characteristics (**Figure 6.11d**) and consequently better J_{SC} along with overall enhanced performance of the Pre-TT devices.

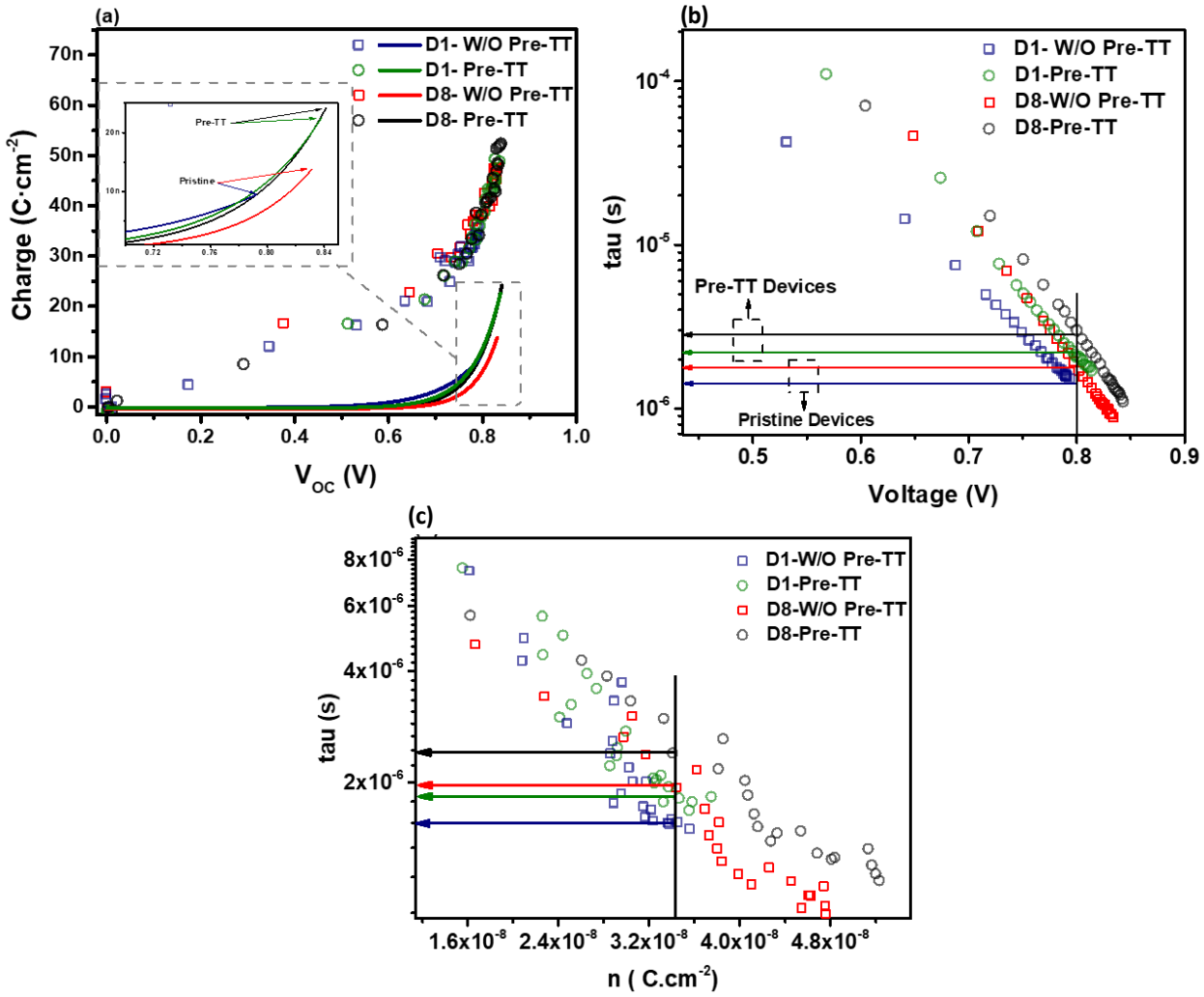

Figure 6.12 (a) Charge measured at different light biases for the pristine and Pre-TT devices. The symbols correspond to both geometrical capacitance and chemical capacitance. The solid lines at the bottom represent only the exponential part: $y=Be^{Cx}$ (chemical capacitance) after subtraction of the geometrical capacitance, (b) TPV versus voltage of the pristine and Pre-TT NF-OPVs devices, (c) charge measured by CE versus the carrier lifetime obtained via TPV for the pristine and Pre-TT devices.

Furthermore, we noticed that the CE and TPV characteristics did not demonstrate a significant difference regarding the recombination behaviour within our devices. Therefore, we further investigated the nature of the recombination occurred for the fabricated pristine and the Pre-TT devices through studying the dependence of J_{SC} and V_{OC} on the incident light intensity (P_{light})[145] under AM 1.5 G illumination condition as shown in **Figure 6.13,** gaining more insights to understand the improvement of the J_{SC} for the Pre-TT devices.

Figure 6.13a displays the J_{SC} power law dependence on the light intensity (P_{light}) that following the proportional relation of J_{SC} α P_{light}^{S1} in principle, where S_1 is the exponential factor that represents the bimolecular recombination in devices along with the ability of extracting the free carries through the corresponding electrodes[145,227,263]. Basically, under short circuit condition, the S_1 value is unity when there is negligible bimolecular recombination appears in the donor/acceptor blend films and less than 1 in case of the presence of the bimolecular recombination.[147,144] The fitted values of S_1 were 0.799, 0.800, 0.825 and 0.865 for D1-W/O Pre-TT, D1-Pre-TT, D8-W/O Pre-TT, and D8-Pre-TT, respectively. As a sequence, the obtained results showed a linear behaviour which indicate a presence of bimolecular recombination for the entire devices[323,263] as a significant loss mechanism in the OPVs.[81] We noticed that both Pre-TT devices possessed S_1 values closer to 1 in comparison to the corresponding pristine devices. Interestingly, the closest S_1 value to 1 was obtained for the optimized D8 Pre-TT which might reflect the less contribution of non-geminate charge recombination.[68,144] This behaviour is highly matched with the lower leakage current (**Figure 6.10b**) and the highest J_{SC} regarding the D8-Pre-TT devices in the J-V characteristics (**Table 6.3**).

Moreover, it is well known that the ΔV_{OC} dependence of the $\Delta \ln (P_{light})$ has been effectively used to identify the presence of the trap assisted recombination.[146,81] Hence, **Figure 6.13b** illustrates the logarithmic dependence of the V_{OC} on the P_{light} of the fabricated devices, representing the diode equation 6.5 of

$$V_{OC}\, \alpha\, S_2 \left(\frac{k_B T}{q}\right) Ln\left(P_{light}\right) \alpha\, n_{id} \left(\frac{k_B T}{q}\right) Ln\left(J_{SC}\right) \quad (6.5)$$

where, n_{id} is the ideality factor of the diode ($n_{id}=S_2/S_1$), k_B is the Boltzmann constant, T is the temperature, and q is the elementary charge. The n_{id} value specifies that the bimolecular recombination is the exclusive form of recombination in the OPV devices when it close to 1[147], while higher n_{id} value than 1 designates the presence of the trap assisted recombination mechanisms.[148,144] The values of S_2 were extracted by fitting equation **6.4**, obtaining values of 1.627, 1.139, 1.174, and 1.024 that leads to n_{id} values of 2.089, 1.418, 1.401, and 1.184 for the based devices of D1-W/O Pre-TT, D1-Pre-TT, D8-W/O Pre-TT, and D8-Pre-TT, respectively. First, it can be noticed that the n_{id} values for D1 are higher than those for D8 which might be related to the non-optimized PM6:Y7 thickness in the D1 based devices, explaining the recombination observed in these devices. Second, it was surprising to find that the Pre-TT based devices showed n_{id} values close to 1 in comparison to both pristine non treated devices. These observed results suggest that the Pre-TT approach suppress the trap assisted recombination mechanisms which may reflect the efficient charge transport and extraction of the devices.[148,144] It is worth to mention that this behaviour might explain the previously observed lower E_U values for the Pre-TT devices along with confirming the higher J_{SC} values, EQE and PL responses in comparison to the pristine devices.

Moreover, it was interesting to detect that at low light intensities (<10 mW/cm^2), the pristine devices behaved differently than the pre-TT ones as shown in **Figure 6.13b**. Where the pristine D1-W/O Pre-TT and D8-W/O Pre-TT devices exhibited higher S_2 values of 3.28 and 3.16, respectively, and in turn a n_{id} values of

4.21 and 3.98, respectively. It is well known that at low voltage and low light intensities (< 10 mW/cm^2), the region is governed by R_{Sh}, exhibiting shunt behavior that can be clearly identified as a rapid voltage drop[71,324]. Then after 10 mW/cm^2 the diode is entering its real diffusion current dominated regime, where ideality factor can be determines as ascribed by K. Tvingstedt et al[324]. Accordingly, the high n_{id} values and the different linear behaviour at low P_{light} of the pristine based devices might be attributed to the pronounced shunt recombination loss mechanisms, preventing a sufficient carrier density to be maintained. [324] and being dominated by the trap-assisted recombination mechanisms SRH.[81] In contrast to the Pre-TT devices (D1 and D8) that have no remarkable shunt paths across their PN junction as well as less nonideal recombination behavior is taking place[68], possessing mainly bimolecular recombination form under open circuit and short circuit conditions. Specifically, the D8-Pre-TT based devices which showed the champion n_{id} value (closest to 1), provided a lower slope which implies trap-free recombination behavior.[145,325] Then, it might be the main reason of their superior performance of J_{SC} and PCE over the other devices. Furthermore, it was surprising to find that the obtained n_{id} values from the V_{OC} and P_{light} dependency were in excellent agreement with the obtained n_1 values from the dark J-V characteristics discussed previously (**Table 6.6**).

Moreover, the dependence of the photocurrent density (J_{Ph}) on the effective voltage (V_{eff}) was calculated to depict the exciton dissociation probabilities (P_{diss}), maximum amount of absorbed photons that leads to the dissociation and generation of free carriers (G_{max}) and the generation rate (G_{rat}) of the free charge carriers for the pristine and the Pre-TT fabricated NF-OPVs.[49,72,149] The J_{Ph} is defined as J_L- J_D, where the J_L and J_D are the current densities at dark and under illumination, respectively. V_{eff} is described as V_O -V, where V_O is the voltage when J_{Ph} = 0 and V is the applied voltage[150,147,151]. We calculated the values of the $G_{max,}$ P_{diss}, and G_{rat} using the following reference equations of [49,149,151,152] $G_{max}= J_{sat} / qL$, $P_{diss} = J_{SC} / J_{sat}$, and $G_{rat}= P_{diss} G_{max}$, where J_{sat} is the saturation current density at 0.2 V, q is the elementary charge and L is the thickness of the blend film.

From the double logarithmic scale plot of J_{ph} vs V_{eff} in **Figure 6.13c**, we disclosed that almost all photo-generated charge carriers were collected at high field of $V_{eff} > 0.2$ V, where at low field of $V_{eff} < 0.2$ V the J_{ph} of the devices was increasing linearly. Then, it saturates by increasing the $V_{eff} > 0.2$ V revealing an efficient charge carrier separation.[149] Hence, from the calculated J_{sat} in **Figure 6.13c**, we can observe that the Pre-TT based devices (D1-Pre-TT and D8-Pre-TT) manifest better charge carriers separation through the interfaces of the active layer blend[149,147] more than the pristine devices (D1-W/O Pre-TT and D8- W/O Pre-TT). Then, **Table 6.6** summarizes the optoelectronic parameters calculated from the J_{ph} vs V_{eff} curves. The values of the G_{max} were 1.17×10^{28} and 1.76×10^{28} m^{-3} s^{-1} for the pristine D1-W/O Pre-TT and D8-W/O Pre-TT devices, respectively, while the G_{max} values for the Pre-TT D1 and D8 devices were 1.37×10^{28} and 2.09×10^{28} m^{-3} s^{-1}, respectively. It is worthy to mention that the Pre-TT devices showed a noticeable increase in the G_{max} rather than the pristine devices, consisting with their extraordinary enhanced J_{SC} values (**Table 6.3**).

The high values of the G_{max} represent the excellent energy harvesting due to the efficient exciton generation in the fabricated devices.[49,151] Moreover, these observed results matched with the higher G_{rat} values of Pre-TT devices in comparison to the pristine ones (listed in **Table 6.6**), confirming that the photogenerated excitons were more efficiently dissociated into free carriers owing to the Pre-TT post treatment approach. Furthermore, the P_{diss} values of the fabricated devices followed the same trend of the other parameters, being as D8-Pre-TT (97.46 %) > D8-W/O-Pre-TT (95.56 %) and D1-Pre-TT (93.02 %) > D1-W/O-Pre-TT (92.36 %), which is greatly complies the obtained n_{id} values of the corresponding devices discussed previously.

To validate the P_{diss} values obtained from **Figure 6.13c**, we plotted the J_{ph} to their saturation value ($qG_{max}L$ in **equation 6.4**) as shown in **Figure A.17** for the fabricated NF-OPVs. The photocurrent indicates the dissociation efficiency in the saturation region at V_{eff} > 0.2 V.[147,306] It shows that applying the Pre-TT approach to the films leads to an enhancement in the dissociation efficiency in the V_{eff} region < 0.2 V which in accordance with the obtained P_{diss} values. In addition, the most significant difference appeared for D1 and D8 at V_{eff} < 0.2 in **Figure 6.13** and **A.17** is mainly due to the FF as a result of the thickness variation in the PM6:Y7 film in the representative devices which in turn affect the recombination and the P_{diss} within the devices. Accordingly, greater P_{diss} values correlate with the lower recombination as presented by the D8 based NF-OPVs, reflecting their higher performance.

Table 6.6 Optoelectronic parameters calculated from the J_{ph} -V_{eff} curves.

Device	J_{sat} (mA cm^{-2})	J_{SC} (mA cm^{-2})	G_{max} (× 10^{28} m^{-3} s^{-1})	P_{diss} (%)	G_{rat} (× 10^{30} m^{-3} s^{-1})
D1-W/O-Pre-TT	28.07	26.06	1.17	92.36	1.08
D1- Pre-TT	32.90	31.56	1.37	93.02	1.27
D8-W/O-Pre-TT	28.23	26.98	1.76	95.56	1.68
D1- Pre-TT	33.50	32.65	2.09	97.46	2.04

J_{sat}: Average values of J_{ph} under condition where V_{eff} in the saturation region

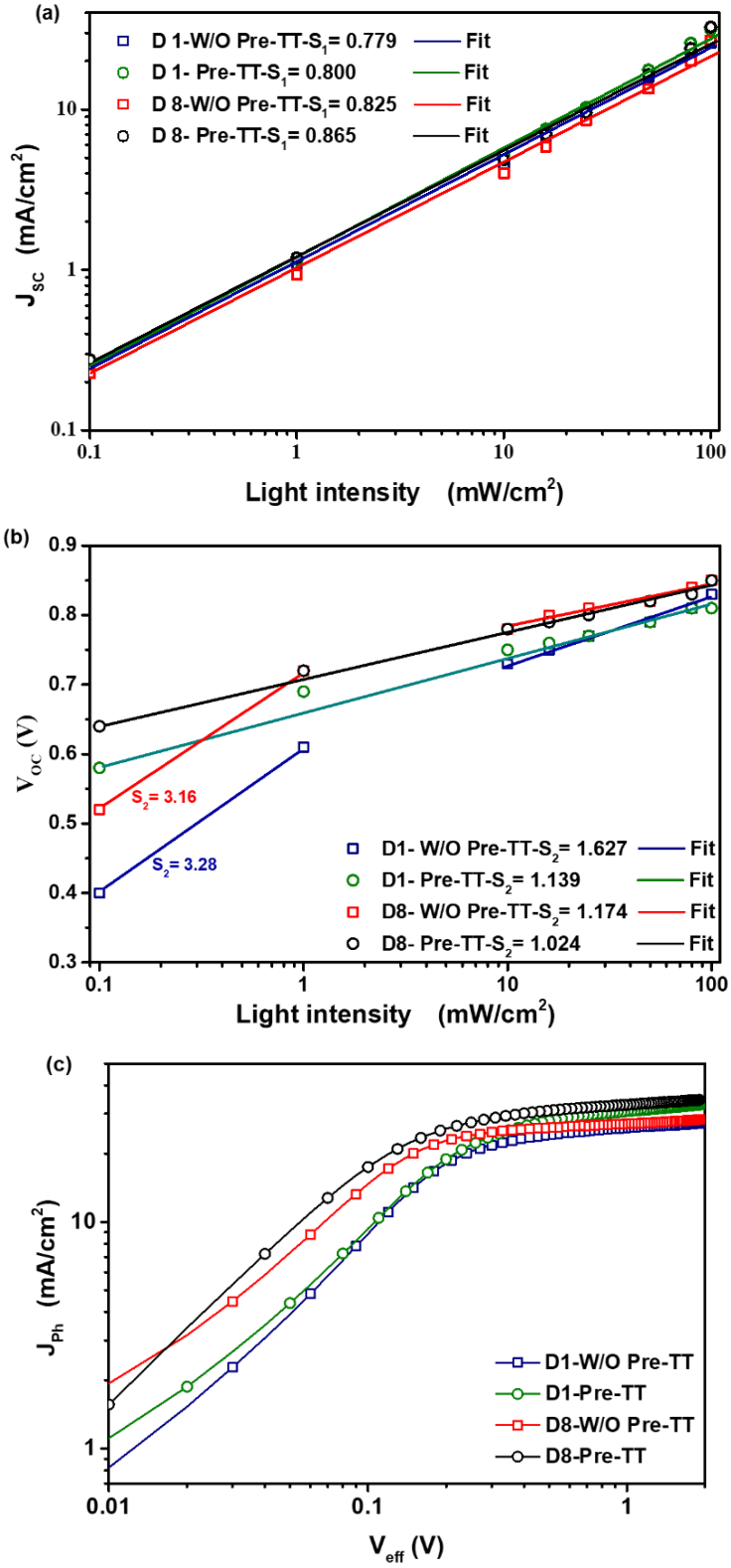

Figure 6.13 (a) J_{SC} and (b) V_{OC} versus the light intensity, symbols refer the experimental data and lines for the fitted data, (c) J_{Ph} versus V_{eff} characteristics of the pristine and Pre-TT of D_1 and D_8 NF-OPVs devices.

6.3.2.3. Charge Mobility

Furthermore, the space-charge-limited current (SCLC) measurements were probed to calculate the e/h mobilities, the trapped filled limit voltage (V_{TFL}) and the trap density (N_{trap}) of the pristine and the treated blend-based films of D1- W/O Pre-TT, D1-Pre-TT, D8-W/O Pre-TT, and D8-Pre-TT) as explained in **Figure 2.10** with the calculation details in Chapter 2, section 2.4.1.1. The tested hole-only devices are presented by using a sandwich capacitor like architecture of ITO/PEDOT:PSS/Active blend/Au and the electron-only devices with structure of ITO/ZnO/Active blend/PDINO/Ag in the dark as illustrated in **Figure 6.14 a, b**, respectively. **Figure 6.14c** displays the SCLC curves of the electron-only devices of the pristine and Pre-TT devices. The electron mobility values (μ_e) of the fabricated devices were calculated following the Mott-Gurney model[153,154] of $J_{SCLC} = 9/8\varepsilon_0\varepsilon_r\mu_{SCLC}\, V^2/L^3$. We depicted that the μ_e values of the pristine D1-W/O Pre-TT and D8-W/O Pre-TT were 9.31×10^{-4} and 7.97×10^{-4} $cm^2V^{-1}S^{-1}$, respectively, while the μ_e values of the Pre-TT devices were D1-Pre-TT= 3.51×10^{-3} $cm^2V^{-1}S^{-1}$ and μ_e of D8-Pre-TT= 3.72×10^{-3} $cm^2V^{-1}S^{-1}$. Accordingly, we noticed that despite the blend thickness variation from 150 nm in D1 and 100 nm in D8 which did not express a noticeable effect on the μ_e same as found elsewhere[326]as we use the same blend ratio, but the Pre-TT devices provided a higher μ_e than the pristine ones.

Moreover, it is important to note that the μ_e values of the Pre-TT devices are about an order of magnitude higher than most of the other blends reported [327–329] as well as close to N. Tokmoldin work, explaining the same reason behind the high J_{SC} values obtained for their corresponding devices.[88] Moreover, by considering the thickness of the blend film for D1(150 nm) and D8 (100 nm), we found that the estimated values of the N_{trap} for the Pre-TT devices (D1- Pre-TT=3.96×10^{15} cm^{-3} and D8- Pre-TT =5.81×10^{15} cm^{-3}) were lower than the pristine ones (D1-W/O Pre-TT=5.94×10^{15} cm^{-3} and D8-W/O Pre-TT =10.11×10^{15} cm^{-3}) as listed in **Table 6.7**, which showed an excellent match with the lower E_U values observed for the Pre-TT devices as discussed previously. Moreover, it is worth to mention that the values of the V_{TFL} were diminished for the Pre-TT devices, as listed in the inset of **Figure 6.14c**. This behaviour indicates that the Pre-TT approach passivated the trap states of the treated devices, providing an enhanced path for an efficient charge carrier transfer and collection by suppressing the defect density and the recombination mechanisms. [153,154,330] That also explains their superior P_{diss}, G_{max}, J_{SC} along with their boosting PCE in comparison to the pristine devices. Moreover, in order to confirm the charge trap density behavior in the pristine and the Pre-TT devices, the hole-only devices were also examined by the SCLC measurements, evaluating same previous observations of terminating V_{TFL} and the N_{trap} values for the Pre-TT devices as showed in **Figure A.18** and **Table A.4**. Furthermore, it is well known that the mobility balance (μ_e/μ_h) is a key factor governing the overall performance of the OPVs devices[331]. The unbalanced mobility leads to space charge formation along with significant recombination, because in case of unbalanced charge transport, the cells performance is mainly limited by the slower carrier, resulting in determination in the J_{SC} along with the PCE of the devices.[85,331]

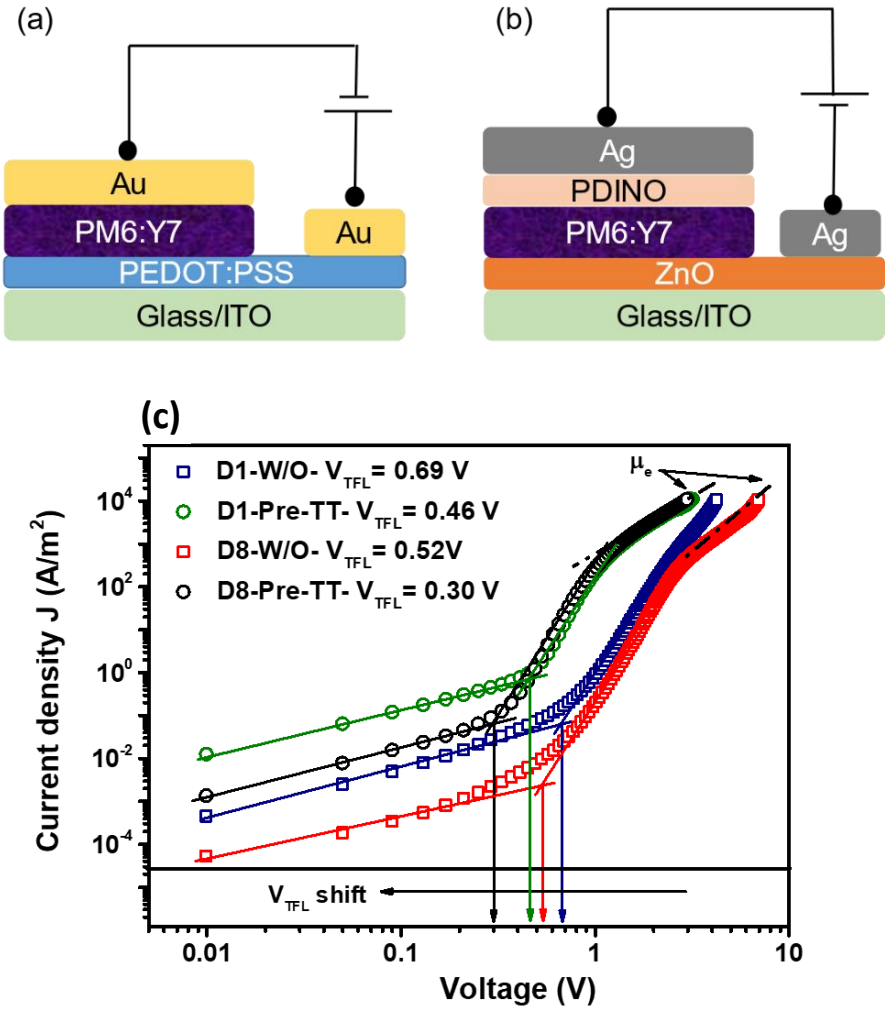

Figure 6.14 The structure diagram of the (a) hole-only and (b) electron-only devices tested by SCLC, (c) The SCLC curves of the electron-only pristine and Pre-TT based devices.

Table 6.7 The evaluated values of V_{TFL}, N_t and N_f for the pristine and Pre-TT electron only devices.

Electron only devices	V_{TFL} (V)	N_t (× 10^{15} cm^{-3})	N_f (× 10^{12} cm^{-3})
D1-W/O Pre-TT	0.69	5.94	1.81
D1-Pre-TT	0.46	3.96	15.43
D8-W/O Pre-TT	0.52	10.11	0.23
D8-Pre-TT	0.30	5.81	5.06

In contrast, the performance of the PV devices maximized when the μ_e/μ_h ratio is close to unity, meaning balanced carrier mobilities which are beneficial to enhance the charge transport and in turn the device

performance.[319,331–333] Accordingly, we plot the logarithmic curve of the mobility balance (μ_e/μ_h) against the voltage as displayed in **Figure 6.15a** to estimate the μ_e/μ_h of the different devices. Our results presented that, at V_{OC}, the pristine devices showed μ_e/μ_h values of 4.0 and 2.3 for the D1-W/O Pre-TT and D8-W/O Pre-TT devices, respectively. This imbalanced carrier mobility might be detrimental to the overall charge collection [319], revealing the drop of their J_{SC} and PCE values obtained (**Table 6.3** on the contrary, well-balanced μ_e/μ_h of 1.4 and 1.3 were obtained for D1-Pre-TT and D8-Pre-TT NF-OPVs, respectively. Moreover, it was interesting to notice that at high voltage around the maximum power point voltage (V_{mpp}) and the V_{OC}, only the Pre-TT devices demonstrated the mobility balance close to one, in contrast to the pristine NF-OPVs, as can be seen in **Figure 6.15b**. Consequently, the extraordinary enhancement in the J_{SC} and PCE values of the Pre-TT devices might be attributed to deteriorating the recombination mechanisms as well as ameliorative charge transport [334], which as well revealed by the previously discussed characteristics. These results confirm that the Pre-TT approach has effective influence to assist balancing the electron and hole transport. In addition, it was interesting to note that the devices performance increase as the balanced carrier mobility close to unity as clearly observed for the champion optimized D8-Pre-TT based devices. Accordingly, it was interesting to correlate that the more balanced e/h transport (Pre-TT devices) decreases the E_U values in combination with low non-geminate recombination represented by the high G_{rat} might be the key parameters that led to a remarkable enhancement in the performance of the Pre-TT devices as further observed by Y. Firdaus et. al.[85] and S. Athanasopoulos et. al.[335]

As an alternative way to interpret the obtained results, the diffusion length, (L_d) of the pristine and Pre-TT NF-OPVs can be calculated using the formula: $L_d = \sqrt{\mu t \frac{T k_B}{q}}$, where μ is mobility, and t is the carrier recombination lifetime (tau).

The tau values are extracted from the TPV measurements (**Figure 6.12c**) and the electron and hole mobility values obtained from SCLC measurements (**Figure 6.14a** and **Figure A.18**). We found that the estimate electron L_d values of the devices were 121 nm in D1-W/O Pre-TT, 128 nm in D1 Pre-TT, 139 nm in D8-W/O Pre-TT, and 156 nm in D8 Pre-TT devices. Moreover, the hole L_d values of the devices were 41 nm in D1-W/O Pre-TT, 44 nm in D1 Pre-TT, 48 nm in D8-W/O Pre-TT, and 54 nm in D8 Pre-TT devices. Hence, these rather higher estimated carrier diffusion length values in the Pre-TT devices in comparison to the pristine cells that may justify their observed better device performance, specifically, the high J_{SC} values[336] and especially for the D8- Pre-TT optimized devices.

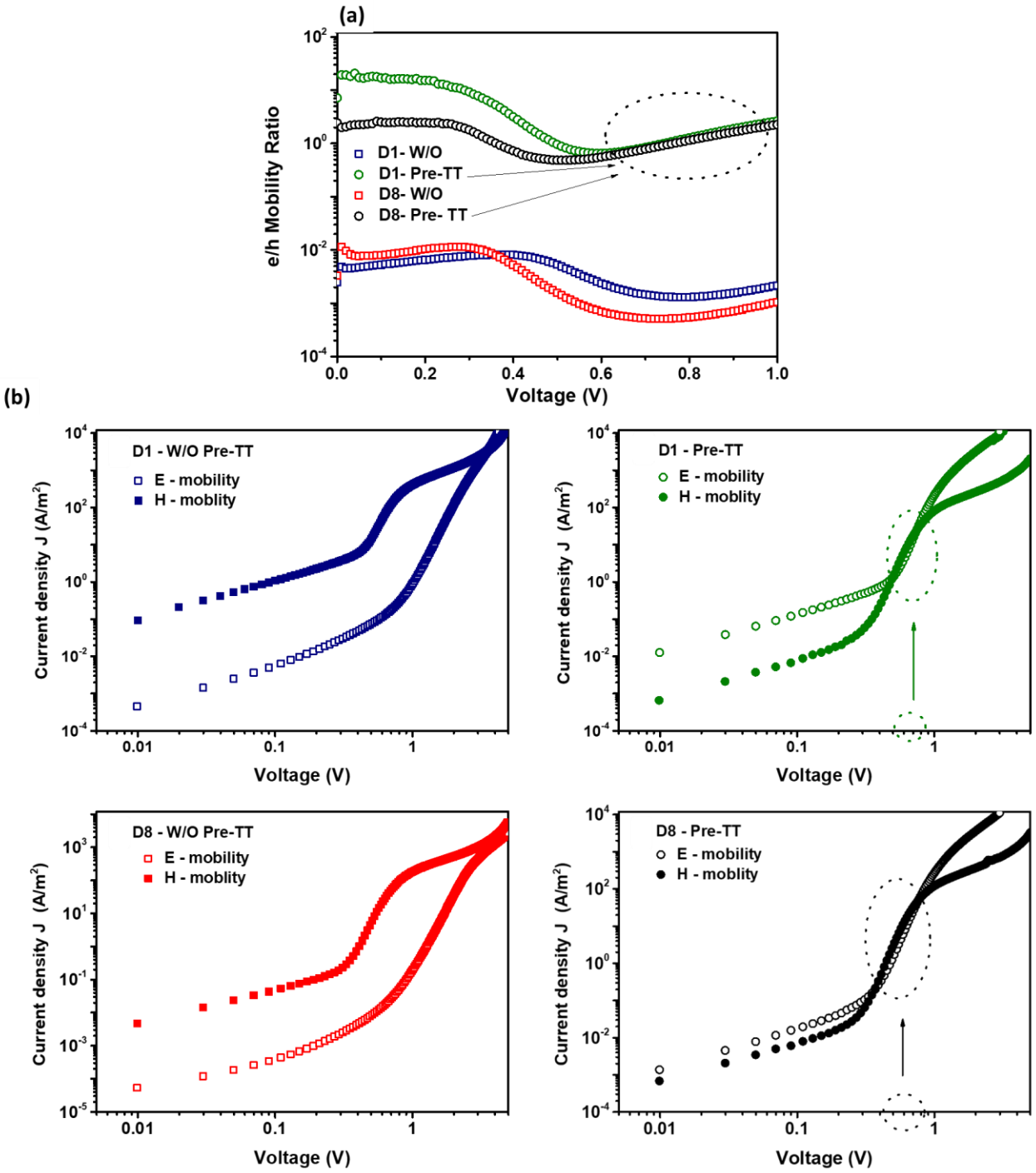

Figure 6.15 The SCLC curves of (a) e/h mobility balance of pristine and Pre-TT devices, (b) electron and hole-only devices of D1-W/O Pre-TT, D1-Pre-TT, D8-W/O Pre-TT, and D8-Pre-TT based devices.

6.3.2.4. Impedance Spectroscopy

Impedance spectroscopy (IS) characterization technique has been carried out as an insight analysis to study the effect of Pre-TT approach on the performance of the fabricated NF-OPVs. It is a powerful diagnostic technique for monitoring the recombination , carrier accumulation and transport behavior of each layer within the OPVs.[165–167] It measures the phase shift and the amplitude of the current response obtained through applying an AC voltage to the devices at a given frequency range, which reveal different mechanisms taking place at various interfaces.[165,168]

Figure 6.16a shows a typical semicircle Cole-Cole plot for the fabricated pristine and Pre-TT based NF-OPVs at V_{OC} and their corresponding Bode plots presented in **Figure 6.16b**, demonstrating the efficient transfer at the active layer/electrode interface.[165,166] We can see that all the analyzed NF-OPVs derived a single process illustrated by one arc attitude. First, regarding the types of devices, we observed that D8 based devices exhibited smaller arc radius along with lower impedance than D1 based devices. This might be attributed to the optimization process performed to the D8 NF-OPVs discussed before, revealing their better performance. Second, regarding the Pre-TT approach, we noticed that both types of D1 and D8 based devices showed smaller arc radii for the Pre-TT based devices than their corresponding pristine ones. This might consider the diminishing in the Pre-TT devices resistance[100,165,166], matching their lower R_S obtained by the J-V characteristics (**Table 6.3**) . Moreover, it was interesting to record the same behavior at short circuit voltage (0.0 V), near to the maximum power point voltage (V_{MPP} = 0.2 V) and at V_{MPP} of 0.5 V applied bias voltages as shown in **Figure A.19**, respectively.

Furthermore, the lower frequency arc decreases for the Pre-TT devices (D1-Pre-TT and D8- Pre-TT) which in the same behavior of arc size. We can interpret that the generated charge can be efficiently extracted through the contacts of the Pre-TT devices more than the pristine ones, as proposed by Arredondo et al.[206] This behavior confirms the effective contribution of the Pre-TT approach that improve the devices performance (**Table 6.2**), especially D8-Pre-TT as it possessed the lowest low-frequency arc which describes the less pronounced charge accumulation effect, correlating with the lowest leakage current (**Figure 3a**), lowest R_S, highest J_{SC} and as a sequence, reflecting their champion PCE. In contrast to the pristine devices, which have a higher low-frequency arc as well as higher leakage current (**Figure 3a**) and lower J_{SC} values, indicating their drop performance behavior (**Table 6.3**). Same behavior was observed in our previous reported work[100,337]as well as Upama et al.[304] Another important consideration in short circuit conditions (**Figure A.19**), as the Pre-TT based devices showed lower Z´ (real part-X axis) -Z´´ (imaginary part-Y axis) values than the pristine based ones. It indicates that the Pre-TT devices show rapid charge extraction, whereas the pristine devices demonstrate lower charge extraction, that contributes to the J_{SC} values of the devices which are highly consistent with the results of the J-V characteristics (listed in **Table 6.3**) and the previously discussed photo-physics measurements (**Figure 6.12**) as well as the performed optical analysis (**Figure 6.11**),

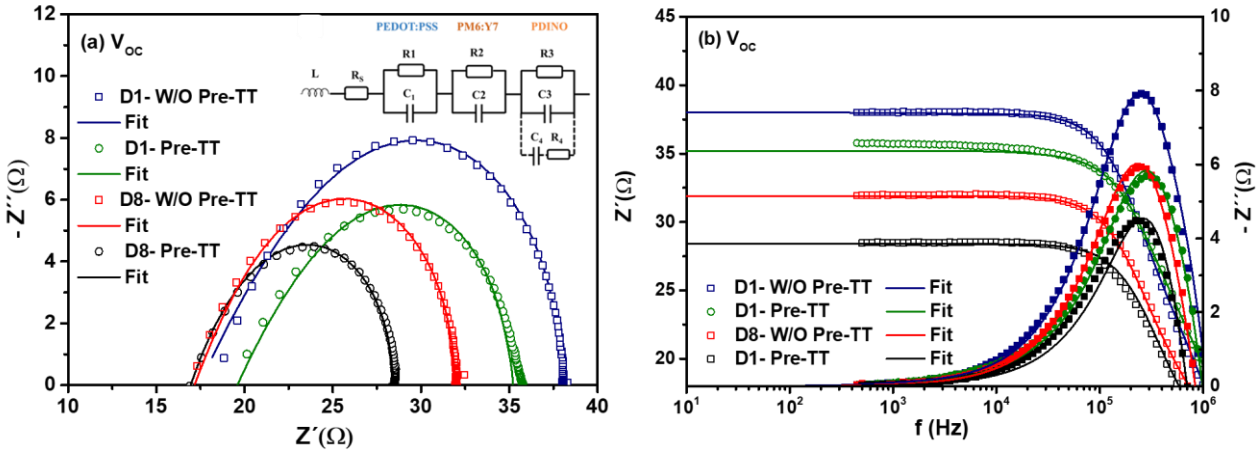

Figure 6.16 (a) Cole-Cole plots at V_{OC} under AM 1.5G illumination, using symbols for the experimental data and the fitting results in solid lines by applying the inset equivalent circuit of Debye model, (b) Bode plots of the D1 and D8 Pristine and Pre-TT devices at V_{OC}.

revealing that the improvement of the J_{SC} of the Pre-TT devices has the main contribution to the PCE enhancement. To get more perception regarding the physical parameters of the fabricated NF-OPVs, we carried out an electrical equivalent circuit to fit the experimental Z´-Z´´. The electrical component used to properly fit the plots (Solid lines) illustrated in the inset of **Figure 6.16a**, the fitted parameters were summarized in **Table 6.8**. We used Debye model[207] equivalent circuit that consists of a parallel association of resistors (R) and capacitor (C) providing 3RC elements in series, where a distributed resistors (R) represent the resistance of electrons transportation in each layer where R_1, R_2 and R_3 referring to PEDOT:PSS, PM6:Y7 and the PDINO layer, respectively. In addition, C refers to the geometrical capacitance values of each corresponding layer. R_S represents the series resistance from the ITO layer as well the ohmic contact resistance due to the interface between the ITO and the HTL in the conventional structure of the OPVs[121,165,166] and L is the added inductor to fit the data at high frequency.[165] Moreover, it is important to mention that the R_4C_4 elements where in series and attached in parallel to R_3C_3, representing the PDINO interfacial layer as proposed by Debye model.[207]

Table 6.8 The fitted parameters of the equivalent circuit at V_{OC} for the fabricated pristine and Pre-TT NF-OPVs using Debye model. The parameter $\tau = R_4 \times C_4$ where R_4 parameter were demonstrated in the equivalent circuit in the manuscript in the inset of Figure 7a.

NF-OPVs – V_{OC}	**D1-W/O Pre-TT Based on 150 nm – PM6:Y7**			**D1- Pre-TT**		
R1/C1- PEDOT:PSS	R_S = 1.00 Ω	R1 = 17.00 Ω	C1 = 5.84 nF	R_S = 2.60 Ω	R1 =15.60 Ω	C1 = 5.84 nF
R2/C2- PM6:Y7	L = 1.70 µHz	R2 = 4.00 Ω	C2 = 1.86 nF	L = 1.70 µHz	R2 = 4.00 Ω	C2 = 1.86 nF
R3/C3-PDINO		R3 = 16.00 Ω	C3 = 39.80 nF C4 = 65.00 nF τ = 0.63 µs		R3 =13.0 Ω	C3 = 39.80 nF C4 = 50.00 nF τ = 0.51 µs
		R_{Total} = 37.90 Ω ***HF/τ $_{Total}$** = 95.10 µs			R_{Total} = 35.20 Ω ***HF/τ $_{Total}$** = 7.10 µs	
	D8-W/O Pre-TT Based on 100 nm – PM6:Y7			**D8- Pre-TT**		
R1/C1- PEDOT:PSS	R_S =1.50 Ω	R1 = 11.40 Ω	C1 = 5.84 nF	R_S =3.80 Ω	R1 = 7.30 Ω	C1 = 5.84 nF
R2/C2- PM6:Y7	L =1.70 µHz	R2 = 2.00 Ω	C2 = 2.79 nF	L =1.70 µHz	R2 = 2.00 Ω	C2 = 2.79 nF
R3/C3-PDINO		R3 = 17.00 Ω	C3 = 19.92 nF C4 = 30.00 nF τ = 0.37 µs		R3 =15.30 Ω	C3 = 19.92 nF C4 = 26.56 nF τ = 0.29 µs
		R_{Total} = 31.90 Ω ***HF/τ $_{Total}$** = 0.7 µs			R_{Total} = 28.40 Ω ***HF/τ $_{Total}$** = 0.14 µs	
***HF**: High Frequency						

Table 6.9 Dielectric constants for each layer

Layer	ε_{Layer}
PEDOT:PSS	2.2[88]
PM6:Y7	3.5[88,211]
PDINO	5[88]

The capacitance (C) for each layer was calculated through the formula of $\boldsymbol{C = \varepsilon_0 \varepsilon_{Layer} \frac{A}{d_{Layer}}}$ (6.5)

where A is the Active area, d_{Layer} the thickness for each layer, ε_0 vacuum dialectic permittivity and ε_{Layer} the relative dielectric permittivity (the referred values were taken from the source [88] and [211]).

Table 6.10 The theoretical values of the geometrical capacitance (C_g) for each cell configuration.

PM6:Y7 Thickness -$d_{Layer\ (nm)}$	**C_g – (nF) Theoretical**	**PDINO Thickness- d_{Layer}**	**C_g – (nF) Theoretical**	**PEDOT:PSS Thickness- d_{Layer}**	**C_g – (nF) Theoretical**
Device 1- 150 nm	1.86	**Device 1- 10 nm**	39.84	**30 nm**	5.84
Device 8- 100 nm	2.79	**Device 8- 20 nm**	19.92		

Regarding the fitted data used to interpret the obtained results, it is worth to notice that the fitted capacitance values for each layer in the device were in an excellent agreement with the theoretical values (Listed in **Table 6.8** and calculated using **equation 6.5** and **Table 6.9** and **6.10**), indicating that the obtained Z´-Z´´ data at V_{OC} were governed by the metal-insulator-metal model (MIM)[208], depicting the presence of

fully depleted layers approach.[88,208] In addition, we observed that the C_4 values, representing the extra impeded traps in the PDINO layer, were reduced upon the Pre-TT step as listed in **Table 6.8**. It reveals that more trap defects were created in the PDINO layer in the pristine devices, hindering the charge carrier collection and transportation that in turn lowering their performance in contrary to the Pre-TT devices.[121,207]

Regarding the fitted resistance values listed in **Table 6.8**, it can be seen that the R_S value showed an insignificant increase for the Pre-TT devices more than the pristine ones. Moreover, as illustrated in **Figure 6.17a**, on one hand, in both devices of D1 and D8, we detected that the values of R_1 and R_3 representing the interfacial layers of PEDOT:PSS and PDINO layers, respectively, were declined upon applying the Pre-TT approach to the Pre-TT devices. Where R_1 values of D1 and D8 reduced from 17.0 to 15.6 **Ω** and 11.4 to 7.3 **Ω**, respectively, for the pristine and the Pre-TT cells, respectively. In the same way, R_3 values of D1 and D8 were declined from 16.0 to 13.0 and 17.0 to 15.3, respectively, for the pristine and the Pre-TT devices, respectively. On the other hand, it was interesting to find that the values of R_2 representing the PM6:Y7 active layer did not show any difference upon the Pre-TT step for both D1 and D8 devices as shown in **Figure 6.17a**. Accordingly, the R_{total} values were more controlled by the resistance of the interfacial layers, that rather diminished from 37.9 to 35.2 **Ω** of the D1-W/O Pre-TT and D1- Pre-TT, respectively, and from 31.9 to 28.4 **Ω** for the D8-W/O Pre-TT and D8- Pre-TT, respectively, as displayed in **Figure 6.17b**. Hence, this obtained behavior for the Pre-TT based cells showed a remarkable enhancement in suppressing the PEDOT:PSS and PDINO films resistance (R1 and R3), leading to an enhanced path of charge transportation and charge carriers collection, diminishing the recombination in the treated devices [165,330] as verified in the previous sections. In addition, we suggested that this enhancement in the interfaces between the blend and the interfacial layers might be attributed to the homogenous film morphology obtained for the Pre-TT films as observed by the AFM analysis in the following discussion, which further explain their enhanced NF-OPVs performance obtained by the J-V characteristics under same illumination conditions (**Table 6.3**) regarding the incorporation of the Pre-TT approach.

Furthermore, by analyzing the fitted data and estimating the total value of the extracted charge time (τ_{Total}) for the fabricated devices listed in **Table 6.8**, we can see significant diminish in the τ_{Total} values for the Pre-TT cells than the pristine ones as illustrated in **Figure 6.17c**, which confirm the CE and TPV behavior (**Figure 6.12**) as well as endorse their superior J_{SC} extracted and in turn their enhanced PCE (**Table 6.3**). Upon these obtained results, we found that the Pre-TT approach contributed to reducing the impedance of the fabricated Pre-TT NF-OPVs, reflecting less implanted trap sites in the corresponding blend and interfaces within the layers of the treated devices, assisting charge transportation and collection, that highly matched with the calculated n_{id} (**Figure 6.13b**) and the E_U values (**Figure 6.11c**) observed for the Pre- TT devices. In addition, this behavior similarly followed the observed trend in the previous characteristics, endorsing the improvement effect upon applying the Pre-TT approach.

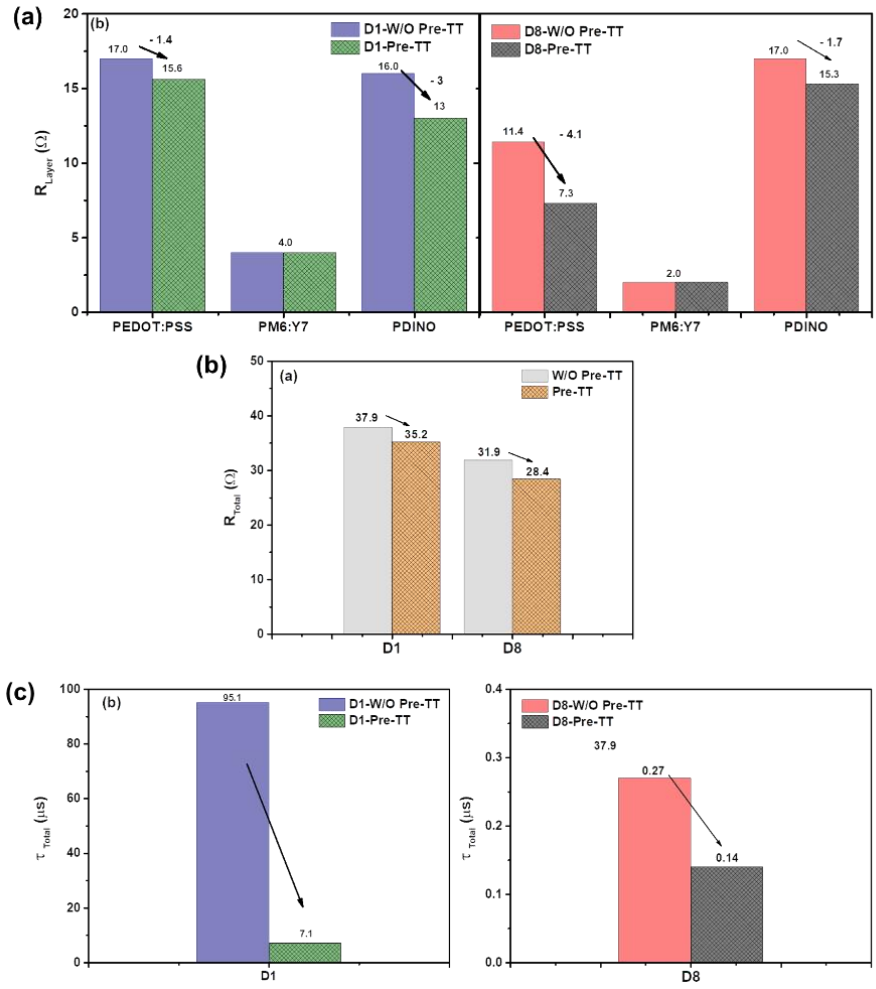

Figure 6.17 (a) The resistance of each layer, (b) the total resistance values of the pristine and Pre-TT NF-OPVs of D1 and D8 based devices, (c) the total extraction lifetime of the pristine and Pre-TT of D1 and D8. The values were extracted from the Debye model listed in **Table 6.8.**

IS technique was performed in an alternative methodology, explaining the mechanisms behind the performance enhancement of the Pre-TT devices using the capacitance-frequency (Cf) measurements to calculate the trap density of state (DOS) of the devices. It allows us to understand the electric properties of the fabricated devices, through investigating the interfacial charge transfer along with carrier recombination mechanisms.[169] It is well known that as the trap densities are high, then trapped charge carrier still can participate in the transportation by thermally hopping or tunneling (shallow traps), while deep traps creates recombination centers due to hardly excited back charges.[64] This characterization has been performed for OPVs in many research work to obtain the change in trap emission and disorder-induced tail states within the devices.[64,165,169–171] Consequently, the traps DOS at a given energy level, E_ω, can be determined by varying

the capacitance of the device with frequency. This reveals the trapping and the charge release by shallow traps in the band gap near to the Fermi energy level as proposed in **equation 6.6, 6.7** as follows

$$\mathrm{DOS}(E_\omega)_{traps} = -\frac{V_{OC}\,\omega}{t\,q\,T\,k_B}\frac{\partial\,\mathrm{C}}{\partial\,\omega} \tag{6.6}$$

where, C is the measured capacitance, V_{OC} is the open circuit voltage obtained by the J-V characteristics (**Table1**), ω is the angular frequency, t is the layer thickness, k_B is the Boltzmann constant, q is the electron charge and T is room temperature (300 K). Then, the following **equation 6.7** considers the relation of the trap-DOS as function of energy dependent

$$(E_\omega)_{traps} = k_B\,\mathrm{T}\,\ln\frac{2\beta\mathrm{N}}{\omega} = \mathrm{E_O} - k_B\mathrm{T}\,\ln\omega \tag{6.7}$$

where, β is the cross-section and N is the effective density of state.[172] Assuming 2βN as an independent of the frequency value, hence, the change in its value is correlated to the shift in the DOS values as a function of energy (E_O)[121]. The shifting of the pristine devices shown in **Figure 6.18b,c**, defined by X, was calculated as follows[121]:

From **equation 6.6**, we get the energy dependence on the frequency for the Pre-TT and Pristine cells as $E_{0\ \text{Pre-TT}} = k_B\mathrm{T}\ln\frac{\alpha_{Pre-TT}}{\omega}$ and $E_{0\ \text{Pristine}} = k_B\mathrm{T}\ln\frac{\alpha_{Pristine}}{\omega}$, respectively, where the 2βN defined as α parameter, β is the cross-section and N is the effective density of states.

As a sequence, the energy's difference between the pristine and Pre-TT based devices can be determined as $E_{pristine} - E_{Pre\text{-}TT} = E_{O\ (pristine)} - E_{O\ (Pre\text{-}TT)} = k_B\mathrm{T}\ln\alpha_{Pristine} - k_B\mathrm{T}\ln\alpha_{Pre\text{-}TT} = k_B\,\mathrm{T}\ln\frac{\alpha_{Pristine}}{\alpha_{Pre-TT}}$

Consistently, the shifting values between the pristine and the Pre-TT devices can be calculated as

$$\mathrm{X} = \exp\left(\frac{E_{pristine}-E_{Pre-TT}}{k_B T}\right) = \frac{\alpha_{pristine}}{\alpha_{Pre-TT}} = \frac{\beta_{pristine}\cdot N_{pristine}}{\beta_{pre-TT}\cdot N_{Pre-TT}} \tag{6.8}$$

Figure 6.18a displays the plot of the calculated trap-DOS as a function of energy for the fabricated devices. It describes a single exponential trap distribution for all devices, revealing the same trap activation energy and carrier response.[58] However, a bit higher DOS values were observed for D1 and D8 Pre-TT devices represented in the shift of E_O value, we explained this by equation **6.7**, calculating the values of the energy shifting (X) for the pristine cells, presented by the solid lines in **Figure 6.18b**. Where, the Pre-TT devices demonstrated higher energy by one order of magnitude than the pristine ones, reflecting less localized interfacial induced defects compared to the pristine devices.[64,121,172,225,245] This behavior was interestingly matched with the suppressing of recombination behavior in **Figure 6.13** which explains the higher J_{SC}

obtained for the treated devices through the Pre-TT approach. Furthermore, in **equation 6.7,** the slope of the tail given by k_BT measures the extent of the distribution of localized states; in other words, it is an indirect measure of the disorder in the semiconductor[173]. Depending on their relative energetic position from the band edge, trap depth can be determined. Few k_BT from the band edge represents the shallow traps and several kT reveal the deep traps that lie further[174]. In **Figure 6.18a**, we depicted that the tail of localized state was a bit reduced for the Pre-TT as compared to the pristine ones. This behaviour indicates that the pristine based devices possess deeper traps in the tail state HOMO. Such deep states act as recombination centers for charge carriers, resulting in reducing their overall lifetime and in turn devices performance [64]. Interestingly, this behaviour is consistent with the E_U values aforementioned in **Figure 6.11c**.

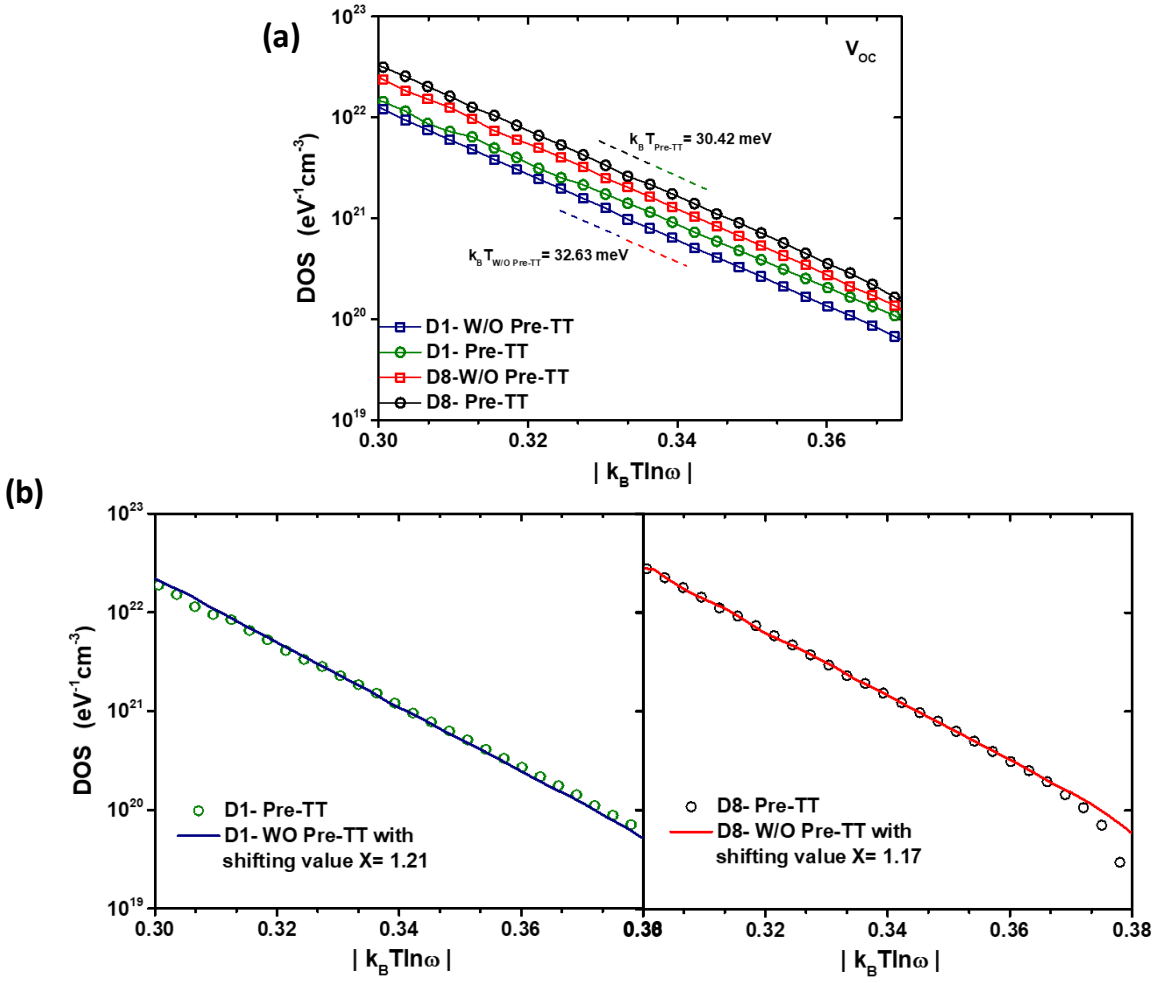

Figure 6.18 (a) DOS as function of $|k_BTln\omega|$ at V_{OC} under AM 1.5G illumination of the pristine and Pre-TT NF-OPVs, (b) lines present the shifting value of X for the pristine device compared to the Pre-TT ones.

To get further insight into the influence of the Pre-TT approach on the fabricated devices, we used the IS to investigate the dark and light intensity-dependent capacitance– voltage (C-V) characteristics. First, **Figure 6.19a** explains the Mott–Schottky of C-V data measured in the dark at the applied frequency of 1 MHz for NF-OPVs with pristine and Pre-TT devices. Two regions have been recorded from the entire samples, the linear region 1 from 0.0 V to 1.0 V, corresponding to the contribution from the PM6 donor phase and region 2 from 0.0 V to 1.0 V that attributed to the Y7 acceptor phase [171,338] as demonstrated in the inset of **Figure 6.19a**. We observed that the slope of the curves in region 2 is almost the same, while region 1 has shown different slopes, indicating various traps contribution in each device.[171] Accordingly, from region 1, we evaluated the built-in voltage (V_{bi}), by finding the plot intercept with the x-axis as demonstrated in the inset of **Figure 6.19a**. The values of V_{bi} were 0.89 V, 0.93 V, 0.87 V, and 0.98 V for D1- W/O Pre-TT, D1- Pre-TT, D8- W/O Pre-TT, and D8- Pre-TT, respectively. It was interesting to find that the Pre-TT devices possessed higher V_{bi} values than their corresponding pristine NF-OPVs. The enhanced V_{bi} assists the collection of holes and repel electrons at the interfaces, reducing the interfacial recombination, thereby enhancing the device performance[330] as presented by our Pre-TT devices. Therefore, the low V_{bi} values signify that the photovoltaic devices work inefficiently through impeding the charge carriers extraction instead of assisting it[100,304], confirming the lower performance obtained by the pristine devices. As a sequence, these results demonstrated that the Pre-TT approach not only reduced the trapes states in the blend films, but also improves the interfaces charge transport, leading to overall improvement in the device performance. Moreover, it is worth to mention that the Pre-TT devices showed a higher chemical capacitance than the pristine ones (**Figure 6.19a**), resulting in less localized stated in the bandgap that leads to diminishing the carrier recombination [165,304].

Second, for further investigation regarding these observed traps sites for the fabricated NF-OPVs, we followed the standard Mott-Schottky analysis to calculate the charge carrier density (N_{PM6}) in region 1 using equation **6.6** [88,171,338]

$$\left(\frac{A}{C}\right)^2 = \frac{2(V-V_{Bi})}{q\varepsilon_O\varepsilon_{PM6}N_{PM6}} \tag{6.9}$$

where A is the active area of the device, C is the capacitance, V is the applied voltage, V_{Bi} is the built-in voltage, q is the elementary charge, ε_O is the vacuum permittivity, ε_{PM6} is the relative dielectric constant of PM6 donor polymer.

Moreover, To calculate the charge carrier concentration in the Y7 acceptor phase (N_{Y7}) (region 2- in **Figure 6.19a**) for the fabricated devices of D1 and D8, we suggested that the donor PM6 phase is fully depleted of charges and equation 6.10 was applied[171,338].

$$V_2 = V_{Bi} + \left(\frac{q}{2\varepsilon_O\varepsilon_{Y7}}\right)N_{Y7}d^2 \tag{6.10}$$

where V_2 is the intercept of region 2 with the voltage axis, ε_{NY7} is the relative dielectric constant of Y7 and d is the thickness of the PM6 phase. The calculated charge carrier concentration of the Y7 phase vs. the PM6:Y7 film thicknesses at dark and applied frequency is shown in **Figure 6.19b**.

Thus, Under the assumption of $N_{Y7} >> N_{PM6}$ as presented in **Figure 6.19b**, then applying equation 6.9 to the C-V measurements at 1 MHz under different illumination intensities (P_{light}) for pristine and Pre-TT devices, we obtained the N_{PM6} vs the P_{light} illustrated in **Figure 6.19c**. It can be seen that the charge carrier concentration increased upon light intensities for the entire devices as predicted phenomena of charge photogeneration in the bulk.[64] However, on one hand, it was interesting to detect that the slopes of D1-W/O Pre-TT and D8-W/O Pre-TT were increased more sharply than the slopes of D1-Pre-TT and D8-Pre-TT cells. This attitude for the pristine devices might be ascribed to significant located trap states into the bulk [171,339,64] which correlate with the measurements of the DOS in **Figure 6.18**. On the other hand, the slope of the D1-PreTT and D8-Pre-TT devices were steadier upon the effect of the light intensities which reflects the less contribution regarding traps.[64] Accordingly, the Pre-TT approach provides less recombination behavior which leads to higher charge carrier concentration (**Figure 6.19c**) that reflects the extraordinary J_{SC} obtained from D1- Pre-TT and D8-Pre-TT devices that is greatly matching the CE and TPV characteristics (**Figure 6.12**)

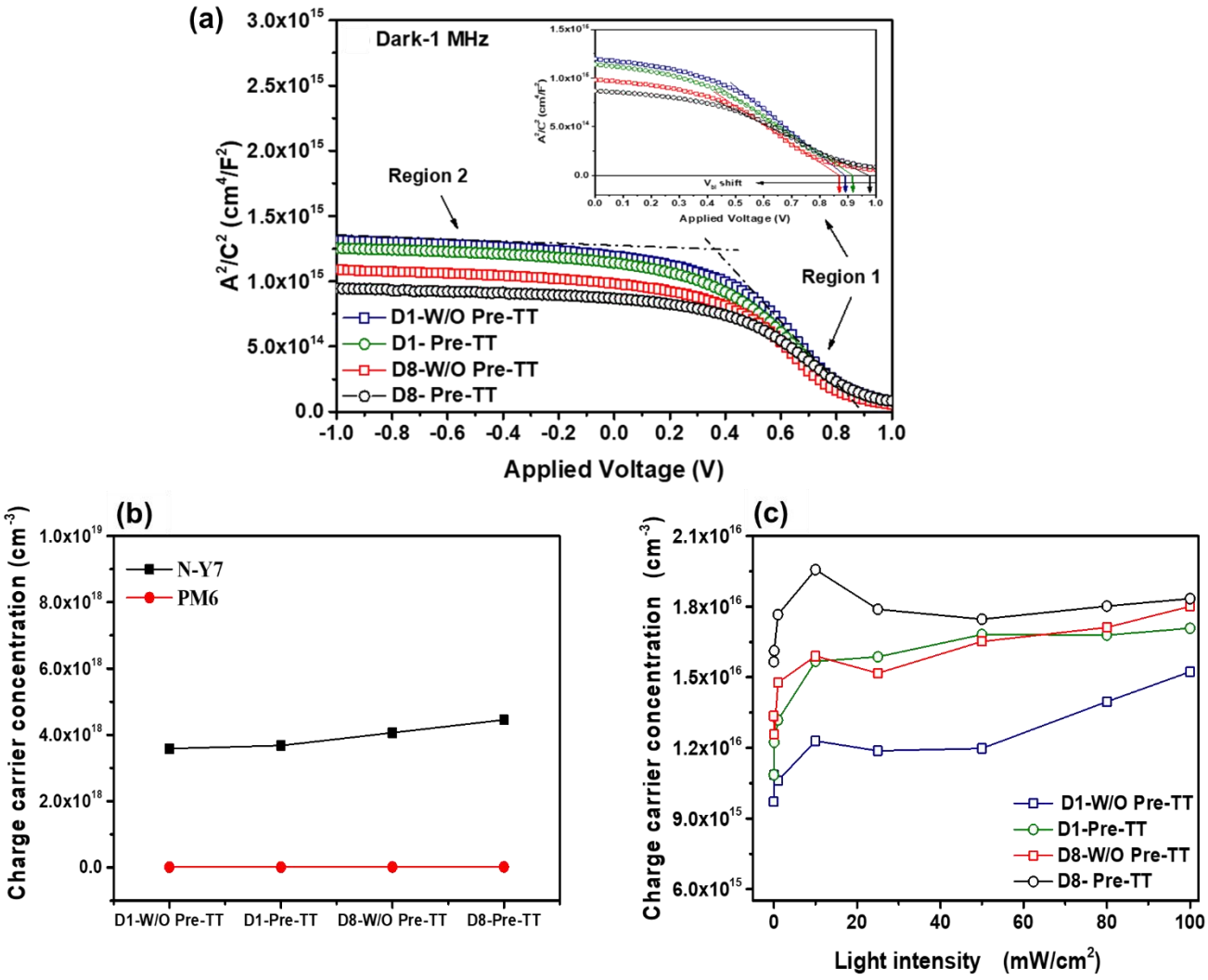

Figure 6.19 (a) Mott Schottky plot at dark at 1 MHz of the pristine and Pre-TT D1 and D8 NF-OPVs. (b) Charge carrier concentration in region 1 (PM6-donor polymer) and region 2 (Y7-acceptor polymer) plot for the fabricated pristine and Pre-TT D1 and D8 devices, this data extracted from the CV measurements taken at 1 MHz under dark (in Figure 6.19a) applying equation 6.6 then equation 6.7. (c) Charge carrier concentration in region 1 (PM6-donor polymer) plot vs the illumination intensities for the devices. The values extracted from the CV measurements were taken at 1 MHz for each P_{light} condition, then applied equation 6.6.

6.3.2.5 Morphological study

A microscopic view characteristic was performed through atomic force microscope (AFM) to investigate the active blend morphology variation upon the effect of Pre-TT approach. We carried out the morphological characterization of the PM6:Y7 blend films over the PEDOT:PSS layer, considering same conditions of the pristine (W/O Pre-TT) as well as the Pre-TT based devices of D1 and D8, as the Pre-TT approach combines the treatment of both PEDOT:PSS along with the active blend PM6:Y7 film as explained in **Figure 6.2** at the **6.2 Experimental section**. **Figure 6.20** displays the AFM topography images and the corresponding phases of the blend films of the mentioned based devices. We can notice that the root mean square surface roughness (RMS) values of the Pre-TT blend films were lower than the pristine ones. Where the RMS of the pristine blend film of D1-W/O Pre-TT is 4.28 nm (**Figure 6.20a**) which is doubled the RMS of the D1-Pre-TT film (2.20 nm – **Figure 6.20b**). Moreover, the same behavior was obtained for the pristine blend film of D8-W/O Pre-TT with RMS of 2.01 nm (**Figure 6.20c**), which is as well higher than the D8-Pre-TT film of RMS =1.44 nm- as shown in **Figure 6.20 d**. First, regarding the blend thickness, the surface roughness and the size of the domain increase as the thickness of the PM6:Y7 film increases[36] as shown in D1 (150 nm), in contrast to the optimized D8 (100 nm) that presented less PM6:Y7 film roughness in both cases of pristine and Pre-TT based films. Second, regarding the Pre-TT approach, it is noticeable that the surface roughness and the phase features of Pre-TT films were different than the pristine films for both of D1 and D8, where the diminishing in the RMS values of the Pre-TT films, providing smoother surface, might be ascribed to the decline in the size of the domains.[36] As already reported by H. Zhang and C. Guo [340,341], temperature causes a pre-aggregation of the PM6 already in the solution, resulting in smaller PM6 fibrillar domain size, which affects the miscibility and crystallinity of non-fullerene acceptors resulting in a better nanoscale phase separation[342,343]. Furthermore, the field emission-scanning electron microscope images displayed in **Figure 6.20** was conducted for the pristine and Pre-TT D8 based films (PEDOT:PSS/PM6:Y7). It demonstrates that the pristine based films showed the strongest aggregation, in contrast to the P*re-TT based films that exhibited more fine, uniform, and compact film morphology.* Consequently, despite the simplicity of the incorporation of this additional Pre-TT step, but it presents obvious effect on the morphology of the treated films that led to a remarkably smooth surface (lower values of RMS) and enhanced phase order separation features with better dispersity.[89] Since the small domain sizes assist the excitons in the active layer blend to reach the donor/acceptor interface, and in turn dissociate into free carriers.[36]

Hence, it is worth mentioning that this enhanced morphology of the Pre-TT based films might reflects the enhancement of their based film absorption (**Figure 6.11b**), J_{SC} their based devices (**Figure 6.9a** and **Table 6.3)** as well as manifesting the lowest R_S and leakage current [91,100](**Figure 6.10**), resulting in improving

their PCE. Furthermore, this observation supports the IS characteristics in **Figure 6.17a**, where the pristine devices possessed the highest low-frequency arc that describes more pronounced charge accumulation effect that could be originated from the pristine morphology disorder of the blend, providing lower overall performance. In contrast to the Pre-TT devices, as it exhibited less traps contribution as confirmed by the closest n_{id} to 1, lowest E_U values, highest P_{diss} along with the optical and the previously discussed electrical IS characteristics, that might be emanated from the fine-tuning of their based film morphology upon the Pre-TT approach. Thus, the Pre-TT approach provides a morphological control which is beneficial for tuning the film surface morphology that greatly enhances the overall performance of the device.

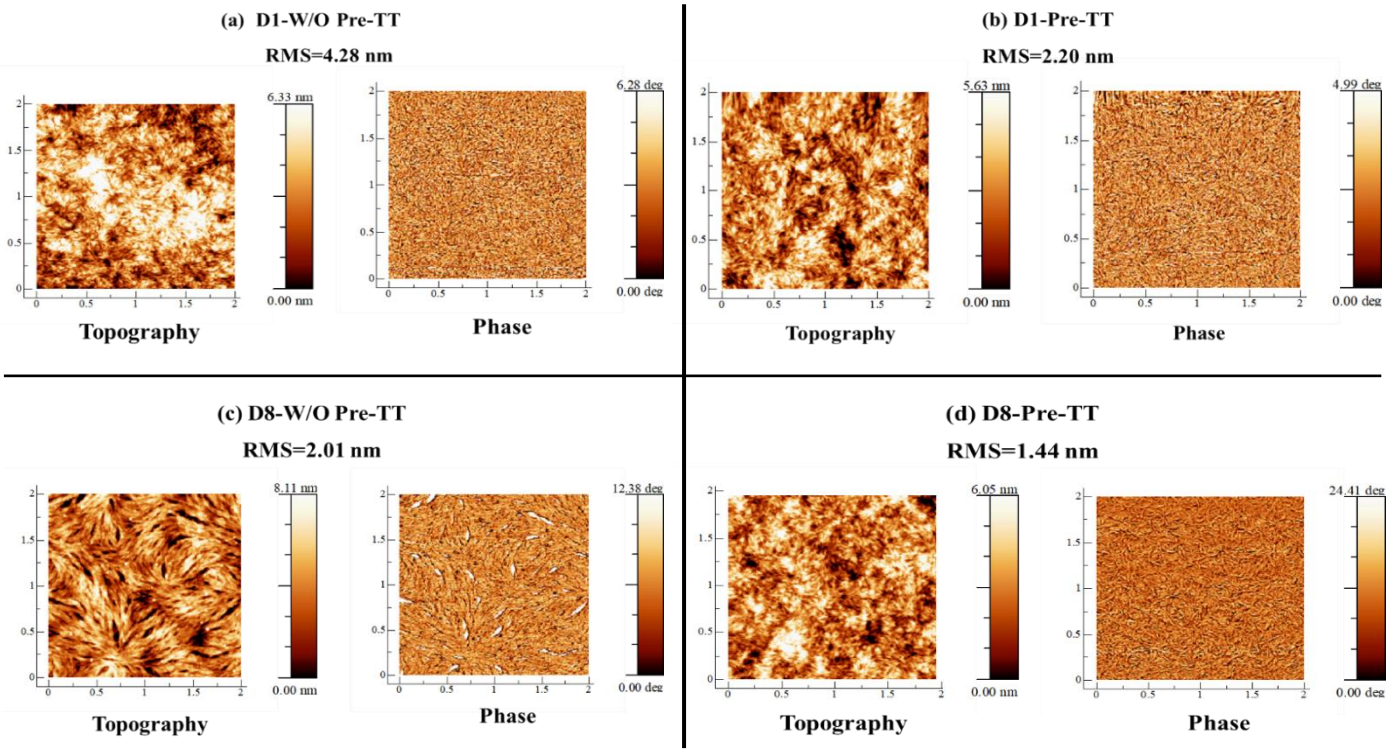

Figure 6.20 AFM topography and phase images of the PM6:Y7 blend films based on the fabricated devices (a) D1- W/O Pre-TT, (b) D1- Pre-TT, (c) D8- W/O Pre-TT, and (d) D8-Pre-TT.

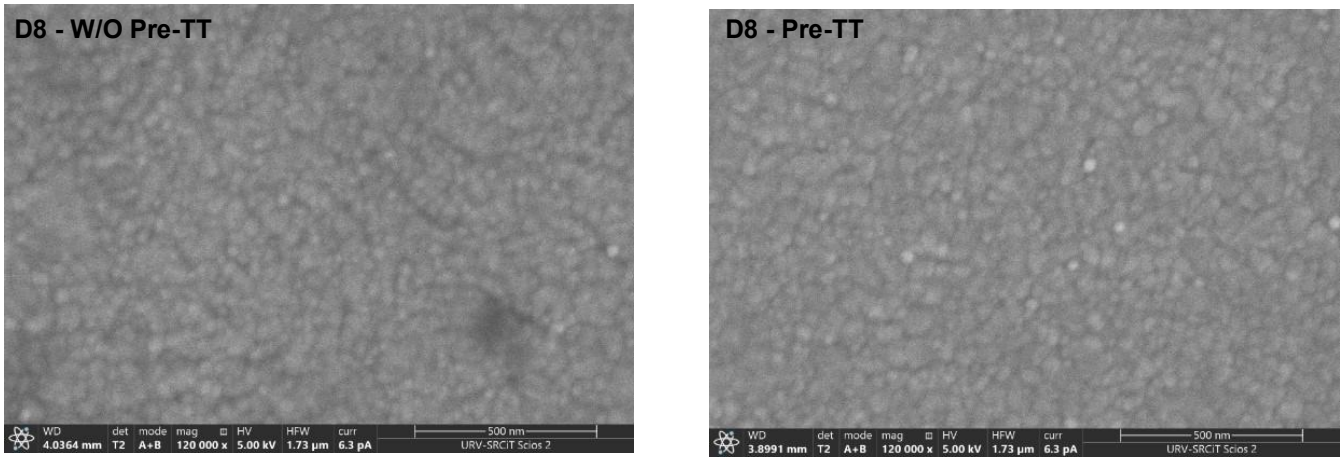

Figure 6.21 Field emission scanning electron microscope images of the D8 pristine and Pre-TT PEDOT:PSS/PM6:Y7 based films.

6.4 Conclusion

In summary, aiming to enhance the photovoltaic performance, we explicitly conducted a systematic investigation regarding the influence of the Pre-TT approach on the performance of the NF-OPVs. But first, optimization process was conducted to the devices through sequential thicknesses variation of PM6:Y7, PEDOT:PSS, and PDINO layers to investigate the impact of each layer on the overall device behavior. The obtained results revealed that the key limiting effect was related to the PM6:Y7 layer where the PCE % enhanced by 15% upon reducing its thickness from 150 nm to 100 nm. Surprisingly, another important factor was corelated to the PDINO film which increases the J_{SC} by 7% owing to increment the concentration of the PDINO precursor solution from 1 mg/ml to 1.5 mg/ml in methanol. Then, conducting the Pre-TT step critically affects the PEDOT:PSS/PM6:Y7 blend morphologies and thus the overall performance of the devices. Interestingly, this chapter puts the spotlight on the extraordinary J_{SC} values obtained by the Pre-TT devices, where the optimized treated devices of D8-Pre-TT exhibited a pioneer enhanced J_{SC} value of 32.65 mA/cm^2 along with improved PCE of 17.92. We observed that the treated based films exhibited smoother surface roughness, revealing their lower R_S, and lower leakage current, which leads to high carrier transport and suppressed charge carrier recombination in the resulting NF-OPVs based devices. Indispensably, a critical challenge for the current NFA-based OPVs is to avoid the strong phase separation upon blending and deposition, which applied through the Pre-TT approach, leading to balanced hole and electron mobility along with low non-geminate recombination that might be the key parameter leading to the remarkable enhancement observed in the performance of the Pre-TT NF-OPVs. Moreover, the enhanced J_{SC} values noticed for the Pre-TT devices were mainly due to their high EQE values and high P_{diss} than the corresponding pristine NF-OPVs, correlating their remarkable PL quench of the Pre-TT films, reflecting the efficient charge transfer at the PEDOT:PSS/PM6:Y7 interfaces Furthermore, the recombination study using P_{light} vs the J_{SC} showed the presence of recombination, but it did not distinguish between each device as it showed all devices have equal contribution of the bimolecular recombination. While the IS characteristics were conducted through investigating the Nyquist plot, Cf -DOS calculations and the C-V characteristics, providing an efficient insight study that accurately detected the recombination contribution that was more obvious for the pristine devices which disclose their lower performance. Accordingly, the Pre-TT approach diminishes the traps and enhances the interface charge transfer through enhancing the carrier dynamics of the treated devices, triggering a promising approach for boosting the J_{SC} along with the photovoltaic performance of the treated devices.

Chapter 7

PQDs Third Component Provides Efficient NF-OPVs Devices Employing BHJ and LBL Deposited Donor-Acceptor Layers

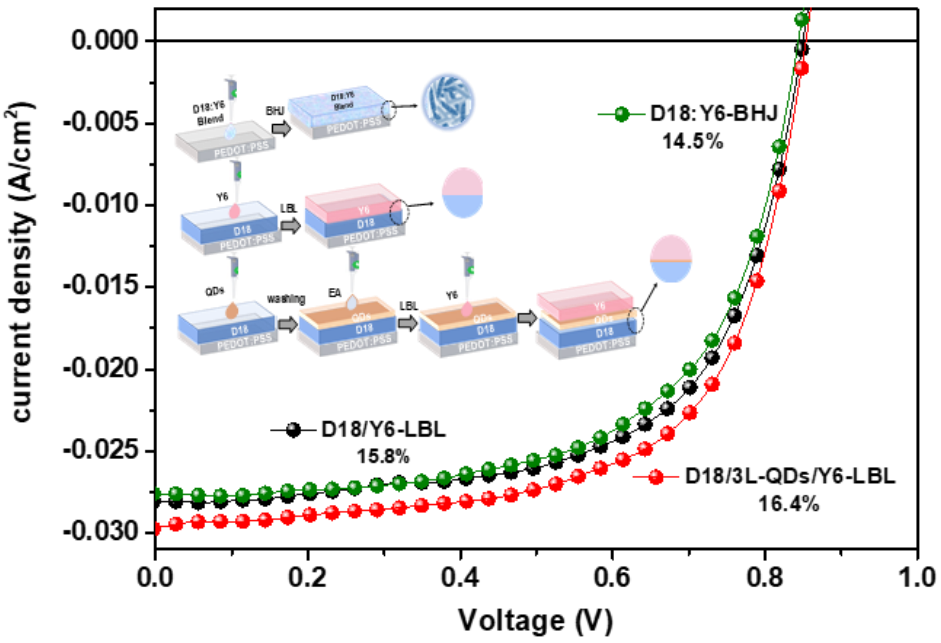

This chapter is based on a collaboration work with Prof. Jenny Nelson group at the Faculty of Natural Science, Physics department at Imperial College London, UK.

The work conducted in this chapter is under preparation: Enas Moustafa, F. Eisner, J. Yan, M. Azzouzi, J. Pallarès, L. Marsal, and J. Nelson, "Charge transport mechanism of non-fullerene organic photovoltaic devices employing QDs third component through LBL method", to be published.

7.1 Introduction

Organic Photovoltaics (OPVs) have received widespread attention and research, owing to their unique advantages like inexpensive, light weight, flexible, processable and less environmental pollution[22,83,85–87]. In the past decades, due to the efforts made in device engineering and material replacement[307,344], bulk heterojunction (BHJ) OPVs has developed rapidly with power conversion efficiency (PCE) reaching 19% [345,346]. However, due to the randomness of bicontinuous networks in BHJ OPVs, it is challenging to predict the impact of one variable change on the nanoscale morphology of the active layer[90]. The unoptimized bulk morphologies significantly affect the optical and electronic properties of BHJ blends and also influence their carrier dynamics[104,105]. In fact, before the BHJ concept, Tang et al. initially reported a vacuum evaporated bilayer OPV to form a planar heterojunction (PHJ) configuration in 1986[45]. However, the insufficient contact surface between donor and acceptor in PHJ OPVs exhibited low exciton dissociation efficiency that limited its development in the past three decades[347]. To overcome the drawbacks of bilayer devices, as early as 1998, Friend et al. fabricated a D/D:A/A structure (D:A is a mixed blend of donor and acceptor materials) by coating donor and acceptor materials on the corresponding contacts[348]. The resulting p–i–n-like structure (D/D:A/A, named layer-by-layer (LBL)) revealed greatly improved exciton dissociation and charge transport[135,349,350]. Recently, the investigated LBL solar cells exhibited PCEs as high as 18.0%, which is higher than that of their BHJ counterparts (17.1%)[135]. Unlike the BHJ approach, LBL processing strategies avoids the difficulty of controlling the bulk morphology through forming a proper vertical phase separation that can be controlled, which is efficient for the charge transportation and collection at the corresponding electrodes[351]. Furthermore, p–i–n-like bilayer structure enable easier exciton dissociation at the D/A interface and can reduce charge carrier recombination loss[352]. Accordingly, the sequential deposition method allows the carefully controlled arrangement and orientation of the organic molecules, leading to improved photovoltaic performance.

To further improve the performance of nonfullerene organic solar cells, ternary strategy was evolved by adding a proper third component to the binary system[128]. To obtain an efficient charge transfer, the HOMO and LUMO energy levels of the third component should be located between those of the host donor and host acceptor, forming a cascade energy alignment[128]. This cascade energy level can avoid energy traps and can facilitate the charge separation and charge transfer at the D/A interface due to the functionality of the third component as a charge relay for electron and hole transport. Moreover, the matched energy levels cascade of the three materials in the photoactive layer can effectively enhance the open-circuit voltage (V_{OC}) of the devices and promote the charge transmission in the active layer[132]. Furthermore, selecting the third component and the host binary systems with complementary absorption spectrum can further broaden the absorption range along with enhance the insertion of light in the active layer, resulting in improving the short-circuit current density (J_{SC}) of the OPVs devices[131]. Interestingly, the incorporation of the third counterpart

can further regulate the accumulation and orientation of the molecule, as well as the phase separation of donor and acceptor [133,134]. Providing high crystallinity and ordered molecular stacking that can improve the charge transport, and inhibit the bimolecular recombination through well optimized phase separation, hence the ternary strategy is an effective method to enhance the exciton dissociation and advance charge transport and charge collection[135]. Furthermore, adding appropriate material to binary system is an emerging strategy to improve the morphology of active layer [136]. Therefore, the ternary strategy shows great potential in improving device performance, predicting to become the preferred scheme for the commercialization of OPVs in the future. However, most research on ternary strategies is based on BHJ system, which will further complicating the morphological regulation. Consequently, the combination of ternary strategy and LBL deposition approach to improve the performance of OPVs is worth considering.

Hence, in this chapter, we compared the binary host system of the wide band gap polymer donor D18 and the nonfullerene acceptor (NFA) Y6 using both the bulk heterojunction (BHJ) and layer-by-layer (LBL) approaches as illustrated in **Figure 7.1a**. We found that the LBL-based devices showed improved performance compared to the BHJ devices. Subsequently, we explored the potential of a novel D18/PQDs/Y6 ternary system employing the optimized LBL approach, introducing the perovskite $CsPbI_3$ QDs (PQDs) film as an interlayer between the D18/Y6 host system in view of their complementary absorption along with the proper energy band cascade of these three materials as demonstrated in **Figure 7.1b**.

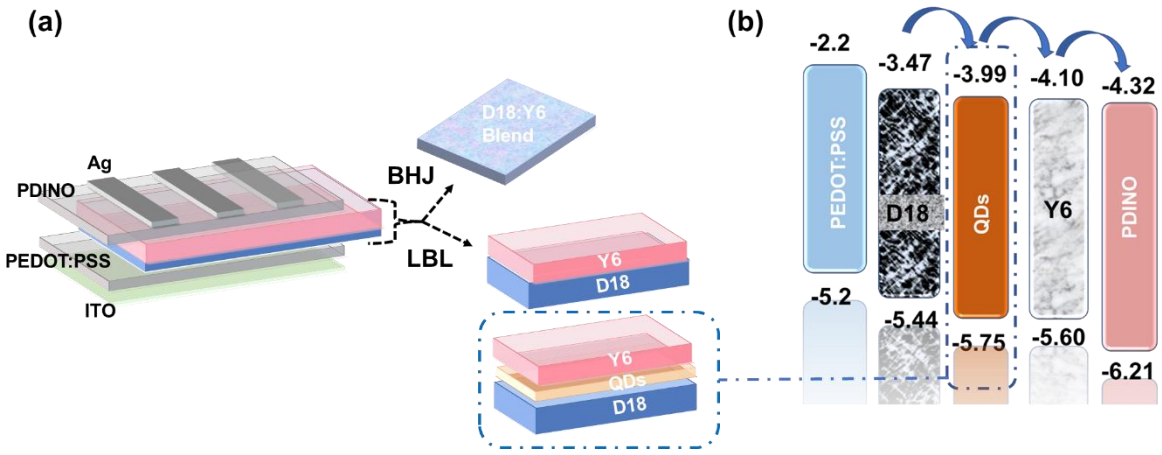

Figure 7.1 (a) Schematic diagram of the fabricated NF-OPVs based on the BHJ and LBL deposition approaches, (b) the energy band diagrams of the based devices.

7.2 Experimental Procedures

This section reports the details of the photoactive materials synthesis of D18:Y6 blend solution for BHJ deposition method, D18/Y6, D18/QDs/Y6 separate solutions for sequential LBL deposition method, and the $CsPbI_3$ quantum dots nanocrystals ($CsPbI_3$-QDs-NCs) Ligand exchange procedures. Moreover, it explains the BHJ and LBL deposition conditions that were conducted for the binary and ternary based devices as illustrated in **Figure 7.3**, based on the structure of ITO/PEDOT:PSS/photoactive layers/PDINO/Ag as presented in **Figure 7.1**.

7.2.1 Ligand Exchange Procedures of $CsPbI_3$ QDs

The purchased $CsPbI_3$ QDs solution was further modified through liquid ligand exchange procedure (LE) to replace the oleic acid and oleylamine capping agents (OA and OAm-long chain organic ligand) with 2,2-Iminodibenzoic acid (IDA-short ligand). This procedure was conducted through direct adding powder of IDA to the pristine QDs solution. After completely mixing the NCs-$CsPbI_3$ solution with IDA for 6 hours, at room temperature under vigorous stirring, purification step was conducted through high-speed centrifugation (8000 rpm for 5 min) was applied to remove the excess IDA powder as illustrated in **Figure 7.2**. It is worth noting that, after film deposition step of the LE- QDs, washing step was performed for the solid film using ethyl acetate (EA) solvent to remove any further residuals of the OA and OAm from the film surface as presented in **Figure 7.3c**.

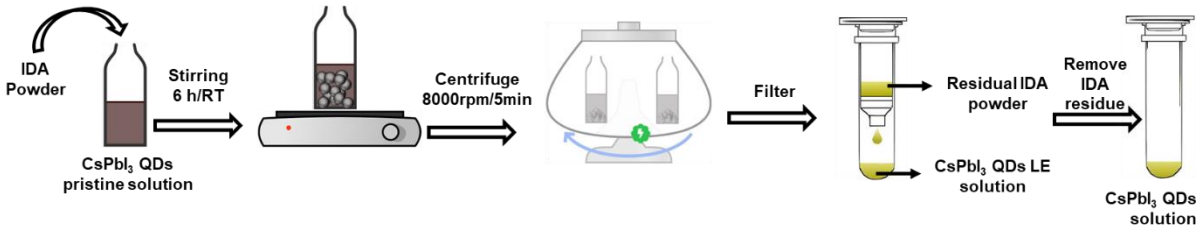

Figure 7.2 Ligand exchange procedures of the $CsPbI_3$ QDs solution using IDA ligand.

7.2.2 Device Fabrication Procedures

For fabricating the NF-OPVs devices, the HTL of PEDOT:PSS aqueous solution was filtered through 0.45 µm PFTE filter (poly tetrafluoroethylene) then spun-coated on the pre-cleaned ITOs. The PEDOT:PSS film was annealed at 150 °C for 20 min in the air and left to cool down for 15 min to obtain thin films of 45 nm. The photoactive layers of D18:Y6 BHJ, D18/Y6 LBL, and D18/QDs/LBL were dynamically spin coated as demonstrated in **Figure 7.3** with the conditions listed in Table **7.1**. The ETL of PDINO was then spin-coated from methanol solution (1 mg/ml) on the active layers at 3000 rpm/30 s. Finally, the substrates were transferred into the vacuum thermal evaporation chamber inside the glove box where 100 nm Ag was

evaporated. Then the devices were moved from the evaporator to the sample holder inside the glove box which was carefully sealed for the device's measurement steps as aforestated in Chapter 2 in **Figure 2.7**.

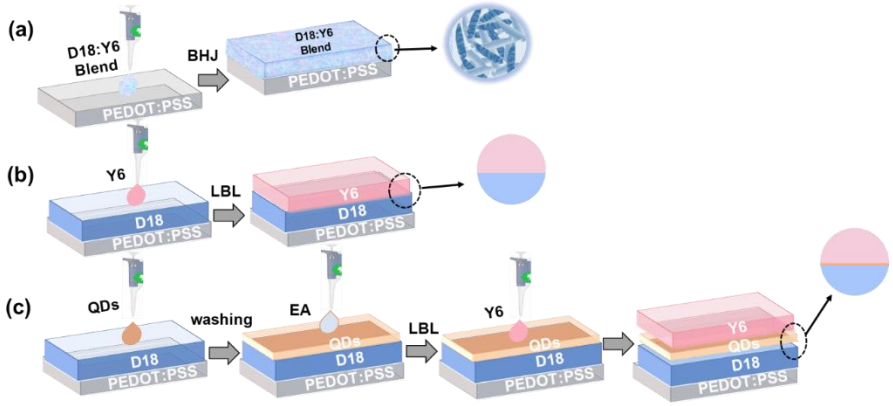

Figure 7.3 Schematic illustration of the photoactive layer formation employing (a) D18:Y6 blend BHJ structure of binary based devices, (b) D18/Y6 LBL structure of binary based devices, (c) D18/QDs/Y6 LBL structure of ternary based devices.

Table 7.1 The synthesis and fabriction conditions of the photoactive layers employed on the binary and ternary BHJ and LBL based devices.

Devices	Fabrication conditions			
	Concentration	rpm/sec	Thermal treatment	Thickness (nm)
ITO/PEDOT:PSS/D18:Y6/PDINO/Ag **BHJ-one step (Figure 7.3a)**				
A-BHJ	1:1.6 (11mg/ml) in CF+ 0.5% CN	4000/30	No	≈ 110 nm
B-BHJ	1:1.6 (11mg/ml) in CF+ 0.5% CN	4000/30	100°C/5	≈ 110 nm
C-BHJ	1:1.4 (11mg/ml) in CF+ 0.5% CN	4000/30	100°C/5	≈ 95 nm
ITO/PEDOT:PSS/D18/Y6/PDINO/Ag **Binary-LBL-sequential deposition (Figure 7.3b)**				
A-LBL	**Step1.** D18: 5mg/ml in CF	3000/40	90°C/5	≈70 nm
	Step2. Y6: 10 mg/ml in CF+ 0.5% CN			≈65 nm
B-LBL	**Step1.** D18: 4 mg/ml in CF	3000/40		≈ 55 nm
	Step2. Y6: 10 mg/ml in CF+ 0.5% CN			≈ 65 nm
C-LBL	**Step1.** D18: 4 mg/ml in CF	4000/40		≈ 45 nm
	Step2. Y6: 10 mg/ml in CF + 0.5% CN	3000/40		≈ 65 nm
D-LBL	**Step1.** D18: 3 mg/ml in CF	4000/40		≈ 35 nm
	Step2.Y6: 10 mg/ml in CF + 0.5% CN			≈ 50 nm
ITO/PEDOT:PSS/D18/QDs/Y6/PDINO/Ag **Ternary-LBL-sequential deposition (Figure 7.3c)**				
QDs-1L	**Step1.** D18: 4 mg/ml in CF	4000/40	90°C/5	≈ 45 nm
	Step2. a) QDs:10 mg/ml in Octane-1L **b)** Washing by EA solvent	1000/30-1L	70°C/10	≈ 8 nm
	Step3. Y6:10 mg/ml in CF + 0.5% CN	3000/40	90°C/5	≈ 65 nm
QDs-3L	**Step1.** D18: 4 mg/ml in CF	4000/40	90°C/5	≈ 45 nm
	Step2. a) QDs: 10 mg/ml in Octane **b)** Washing by EA solvent	1000/30-3L	70°C/10	≈ 20 nm
	Step3. Y6: 10 mg/ml in CF + 0.5% CN	3000/40	90°C/5	≈ 65 nm

7.3 Results and Discussions

In this section, first, we conducted a comparative study between the BHJ and LBL binary based devices. The champion optimized binary devices were exhibited by the LBL method which selected as a control reference. Second, $CsPbI_3$ QDs were modified through ligand exchange process then employed as a third component for a further strategy to improve the binary based devices combined with LBL deposition method.

7.3.1 Optimization of the Binary Based Devices through BHJ and LBL Deposition Methods

Optimization and comparative studies were conducted for the bulk-heterojunction (BHJ) and layer by layer (LBL) based devices with variable fabrication condition that aforementioned in **Table 7.1**. **Figure 7.4a** displays the J-V characteristic curves under AM 1.5G illumination condition of the LBL and BHJ binary based devices with related performance metrics listed in **Table 7.2**. On one hand, regarding the LBL binary based devices, we manifested that C-LBL cells possessed the optimal performance parameters values of 0.85 V, 27.68 mA cm^{-2}, 0.65, and 15.76 %, for V_{OC}, J_{SC}, FF, and PCE respectively, as compared to the A, B, and D based LBL ones. While A-LBL based devices showed lower V_{OC}, J_{SC}, FF, and PCE of 0.83 V, 27.71 mA cm^{-2}, 0.63, and 13.39 %. It was interesting to find that however the D18 thickness of A-LBL cells is higher than the other LBL based devices, but the J_{SC} is significantly diminished. This might explain as when the thickness of the photoactive layer is increased, the total number of charges created in the active layer is also increased upon higher absorption. However, as the thickness of the photoactive layer is increased, the photogenerated electrons and holes must travel a greater distance through the active layer in order to reach their respective electrodes. Assuming a constant recombination lifetime, the charges have a higher probability of recombination before reaching their respective electrodes. Upon this simple picture we can expect that as photoactive layer thickness increases, the photocurrent will be increased due to greater charge generation unless it will be limited by higher recombination[353,354]. Thus, it was the case of A-LBL based devices with higher D18 concentration of 5 mg/ml (thickness ≈70 nm) than the other ones, reflecting the recombination losses take place in such devices resulting in diminishing the J_{SC}, V_{OC}, R_{Sh} and in turn the PCE as listed in **Table 7.2**. Furthermore, it is well known that the difference between J_{SC} and FF can usually be adjusted by thickness control of active layers, mostly reducing the thickness will optimize the performance of the FF[72] as demonstrated by the higher FF of C-LBL than the other-LBL based devices. Then, regarding the D-LBL ones with the lower D18 concentration (3 mg/ml) and thickness of 35 nm, it reveals the reduced J_{SC} to 26.11 mA cm^{-2} upon the thinner absorber photo active film.

While for the BHJ-based cells, the B devices showed the best performance values of .84 V, 27.54 mA/cm^2, 0.62, and 14.50 %, for V_{OC}, J_{SC}, FF, and PCE respectively, among the A and C BHJ based ones as listed in **Table 7.2**. It can be noticed that the performance of the A-BHJ based devices were significantly reduced, reflecting the importance of the thermal treatment as discussed previously in chapter 4 and 6. Moreover, C-BHJ based showed the worth performance due to the non-optimized ratio between the D18 and Y6 components. This sensitive ratio optimization step has a great influence on the film microstructure morphology, thickness and absorption that greatly affect the charge transfer and recombination behaviour and thus the overall device performance[151,311,355].

On the other hand, it can be noticed that the LBL based devices exhibited higher values for all performance parameters than the BHJ ones, specifying the FF of the C-LBL based cells. This might be attributed to the lowest R_S value of 5.08 **Ω** cm^2 and highest R_{SH} values of 301.22 **Ω** cm^2 [178]. This might be generated from the better morphological control of the photoactive films[71] revealed by the p-i-n LBL deposition method as reported previously by C. Jinglong et.al [356], W. Kangkang et.al[307], and S. Rui et.al[357]. They declared that the benefit of the combined fibril network morphology and non-fullerene acceptor properties along with the controllable p-i-n morphology strategy exhibit a good charge transport and extraction properties, reflecting the champion performance observed by the C-LBL base devices in **Figure 7.4a** and **Table 7.2**. Moreover, the enhancement in the V_{OC} of the optimized LBL based devices than the BHJ ones was suggested to be upon the reduced D-A interface in LBL OPVs that would reduce the nonradiative carrier recombination as reported by Azzouzi. M et.al[358].

Furthermore, **Figure 7.4b** shows the J-V curves of the LBL and BHJ binary based devices in dark condition. It is worth noting that the C-LBL based devices showed almost one order of magnitude lower leakage current under the reverse bias conditions as compared to the other LBL and BHJ based ones. Such behavior indicates insignificant shunt possibility, resulting in enhancing the transport of the charge carrier at the selective interfaces [278], which is responsible for improving the V_{OC} and J_{SC} in the device[72] as listed in **Table 7.2**. Upon the obtained results, C-LBL based devices were selected as a control reference for applying a further optimization procedure using $CsPbI_3$ QDs as a third component along with using the LBL deposition approach as ascribed in the following sections.

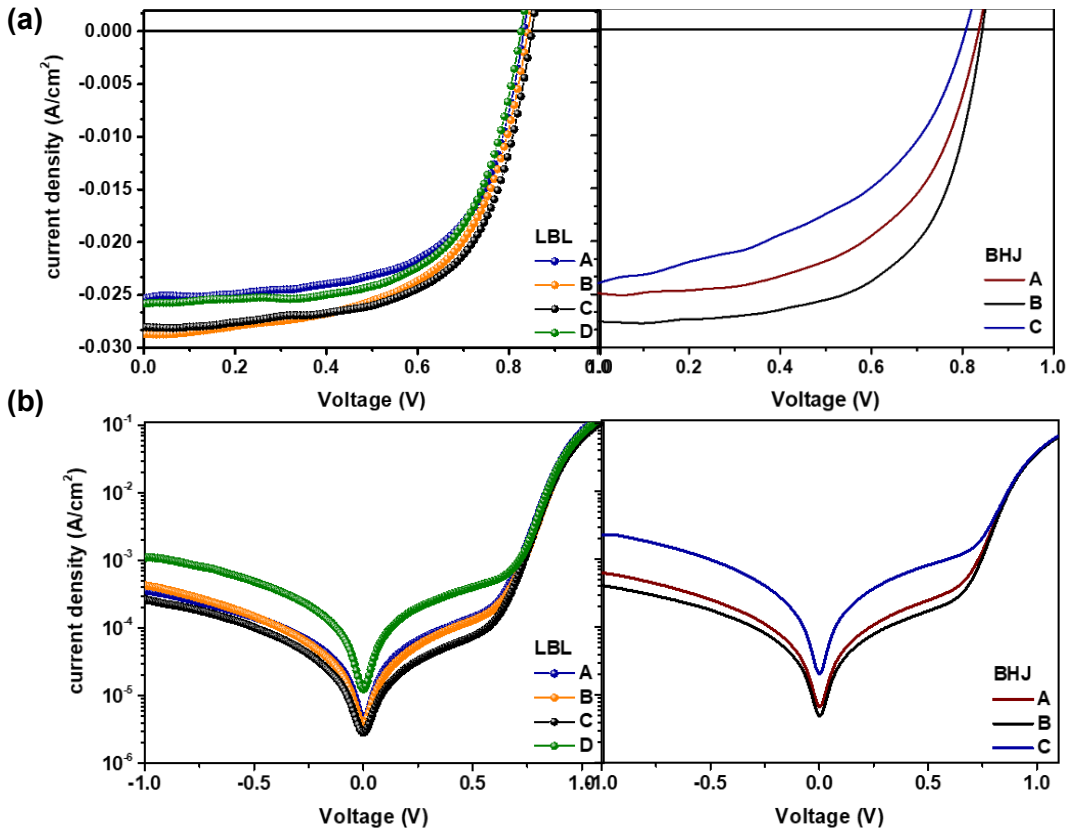

Figure 7.4 J-V characteristic curves of the LBL and BHJ binary based devices under (a) AM 1.5G illumination condition, (b) dark condition.

Table 7.2 Photovoltaic performance parameters statistics of the BHJ and LBL binary NF-OPV based devices.

Devices	J_{SC} [mA/cm^2]	V_{OC} [V]	FF	PCE [%]	R_S (Ω.cm^2)	R_{Sh} (Ω.cm^2)
ITO/PEDOT:PSS/D18/Y6/PDINO/Ag LBL						
A-LBL	25.71	0.83	0.63	13.39	6.79	297.62
B-LBL	27.93	0.84	0.61	14.53	6.89	193.05
C-LBL	27.68	0.85	0.65	15.76	5.08	301.22
D-LBL	26.11	0.83	0.61	13.22	6.01	133.51
ITO/PEDOT:PSS/D18:Y6/PDINO/Ag BHJ						
A-BHJ	24.92	0.83	0.57	11.89	6.49	240.14
B-BHJ	27.54	0.84	0.62	14.50	5.83	300.07
C-BHJ	24.08	0.81	0.51	10.01	8.56	101.94

7.3.2 Studying the $CsPbI_3$ QDs Ligand Exchange Behaviour

Aforementioned in the **7.2 experimental procedures** section in **Figure 7.2**, ligand exchange (LE) and purification procedures were conducted to the pristine $CsPbI_3$ QDs solution to replace the long chain organic OA and OAm to shorter chain ligand of IDA. However, OA and OAm act as capping agents to prevent the QDs from aggregation. But this LE step is mandatory to remove the OA and OAm as it acts as potential barriers on the $CsPbI_3$ QDs surface, thereby preventing electrical coupling and detrimental to the carrier transport/hopping between adjacent QDs[359]. Moreover, they cause a significant surface trapping for the based devices, resulting in losing the generated current and diminishing the FF and in turn reducing the overall based devices performance[360]. Hence, we replace it with shorter ligand to enhance the electrical property of the deposited film[360].

Figure 7.5a displays the PL spectra for the pristine and ligand exchanged $CsPbI_3$ QD-NCs to investigate the influence of the LE step on the pristine $CsPbI_3$ QDs solution. Regarding the pristine $CsPbI_3$ QDs, we can manifest that the EA washing step showed a blue shift effect along with higher PL intensity for the washed $CsPbI_3$ QDs as compared to the pristine one. Moreover, it can be noticed that the LE $CsPbI_3$ QDs showed more significant PL intensity with blue peak shift that might be attributed to the smaller QDs shell size exhibited, in another word, after changing the long OA and OAm ligands by the short IDA ligand, we assume that the $CsPbI_3$ dots shell became smaller in size and not compact to each upon the bulk structure of the IDA, providing confinement[359,361,362]. Furthermore, it is worth to mention that after ligand exchange-LE (Red dots), there is no significant effect regarding the washing step, depicting that most of the OAs already removed by LE step and a few remining amount was further removed by EA through the final washing step for the LE-$CsPbI_3$ QDs solid film[360]. Accordingly, the IDA ligand exchange procedures might be successful to passivate the $CsPbI_3$ QDs film through binding the IDA to the PbI_2-rich surfaces through dual carboxyl groups, which can reduce the surface traps.

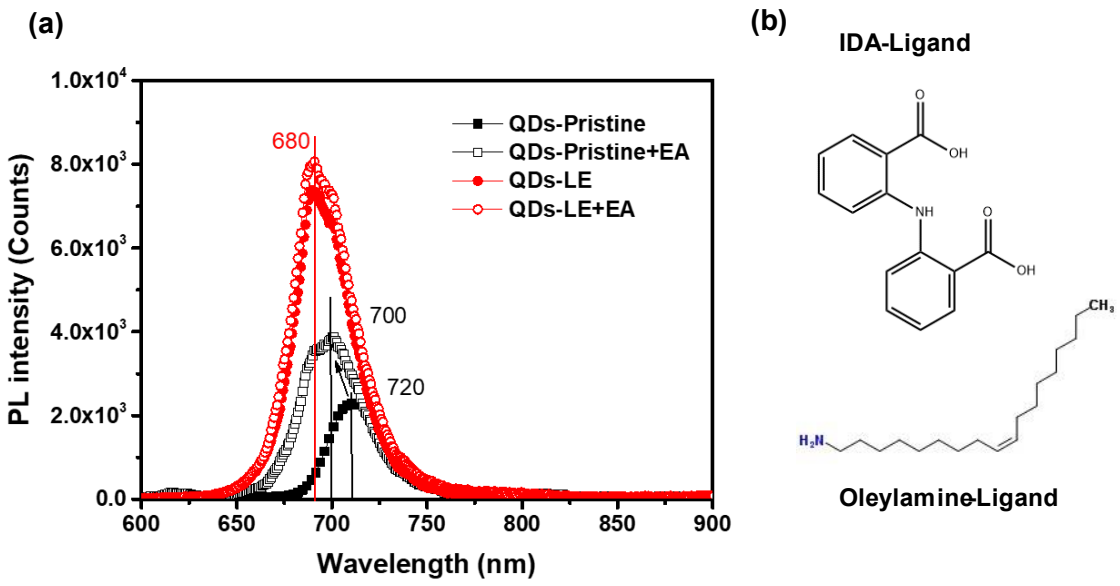

Figure 7.5 (a) photoluminescence spectra of the pristine and the ligand exchanged modified $CsPbI_3$ QDs based films, (b) the molecular structure of the oleylamine capping agent (long ligand) and f 2,2'-Iminodibenzoic acid (short ligand-IDA).

7.3.3 Photovoltaic Performance Based on Employing $CsPbI_3$ QDs as a Third Component to the Binary Based NF-OPV through LBL Approach.

In this section, optimization processes were conducted for employing the ligand exchanged $CsPbI_3$ QDs as a third component for further enhancing the performance of the binary based conventional NF-OPVs structure through LBL approach. The architecture of the fabricated devices was ITO/PEDOT:PSS/D18/QDs/Y6/PDINO/Ag as demonstrated in **Figure 1a**. In this study, the performance of C-LBL controlled based devices was compared to that of QD-1L and QDs-3L based ones. The QD-1L devices consisted of a sandwich structure with a layer of LE-$CsPbI_3$ QDs (≈ 8 nm) between D18 and Y6 films, while the QDs-3L devices had three layers of $CsPbI_3$ QDs (≈ 20 nm) consecutive spin coated between D18 and Y6 films, as shown in **Figure 7.3c**.

Figure 7.6a displays the J-V curves under illumination condition (AM 1.5G) of the NF-OPVs processed with $CsPbI_3$-QDs as compared to the C-LBL cells. The performance parameters of the devices were summarized in **Table 7.3**. Interestingly, the QDs-1L based devices showed a significant enhancement in the FF and J_{SC} achieving 0.67 and 30.07 mA/cm^2, respectively, resulting in an improved PCE of 16.65%. Moreover, the QDs-3L based devices exhibited a noticeable enhancement in the V_{OC}, J_{SC}, and FF of 0.86 V, 29.51 mA/cm^2, and 0.66, respectively, and in turn the PCE was enhanced to 16.43% as compared to the C-LBL binary based NF-OPVs. Furthermore, **Figure 7.6b** implies the J-V curves at dark condition of the

corresponding devices. It is worth to note that, under the reverse bias conditions, QDs based devices showed a bit reduced leakage current than the C-LBL ones, consisting with their enhanced FF[72].

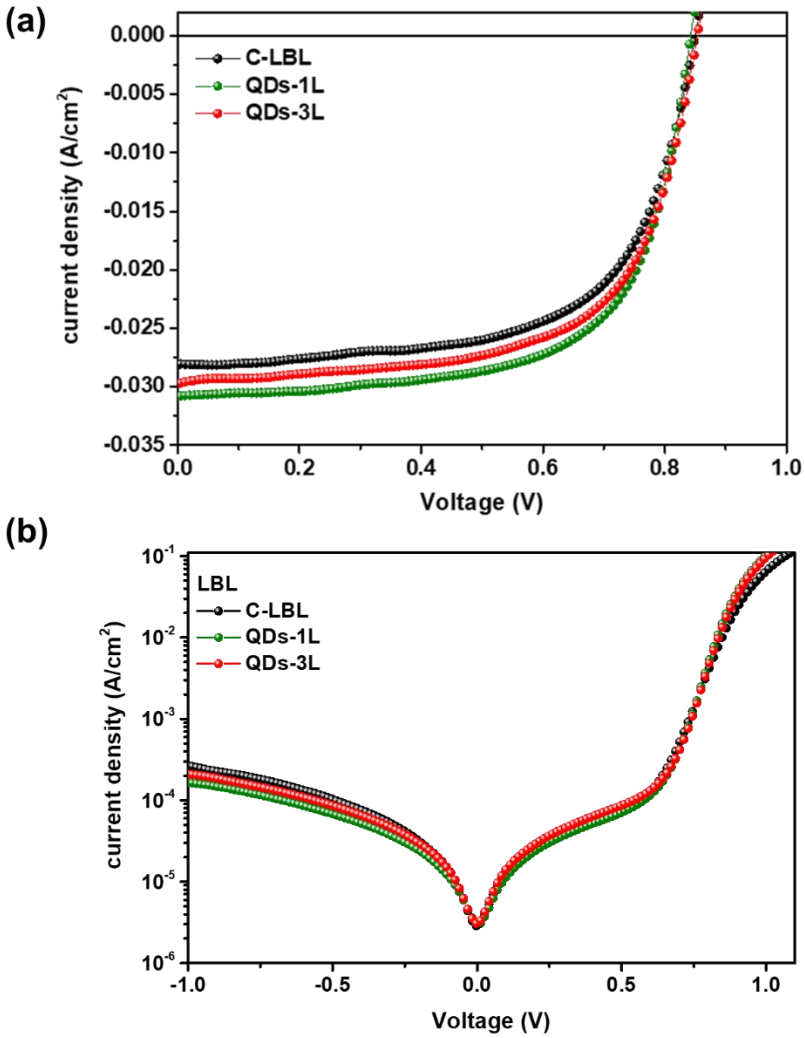

Figure 7.6 J-V characteristic curves of the LBL binary and QDs-based ternary NF-OPV based devices under (a) illumination AM 1.5G, and (b) dark conditions.

Table 7.3 Photovoltaic performance parameters statistics of the LBL binary and ternary NF-OPVs based devices.

Devices	J_{SC} [mA/cm^2]	V_{OC} [V]	FF	PCE [%]	R_S (Ω.cm^2)	R_{Sh} (Ω.cm^2)
C-LBL	27.68	0.85	0.65	15.76	5.08	301.22
QDs-1L	30.07	0.85	0.67	16.65	3.66	297.62
QDs-3L	29.51	0.86	0.66	16.43	4.20	287.01

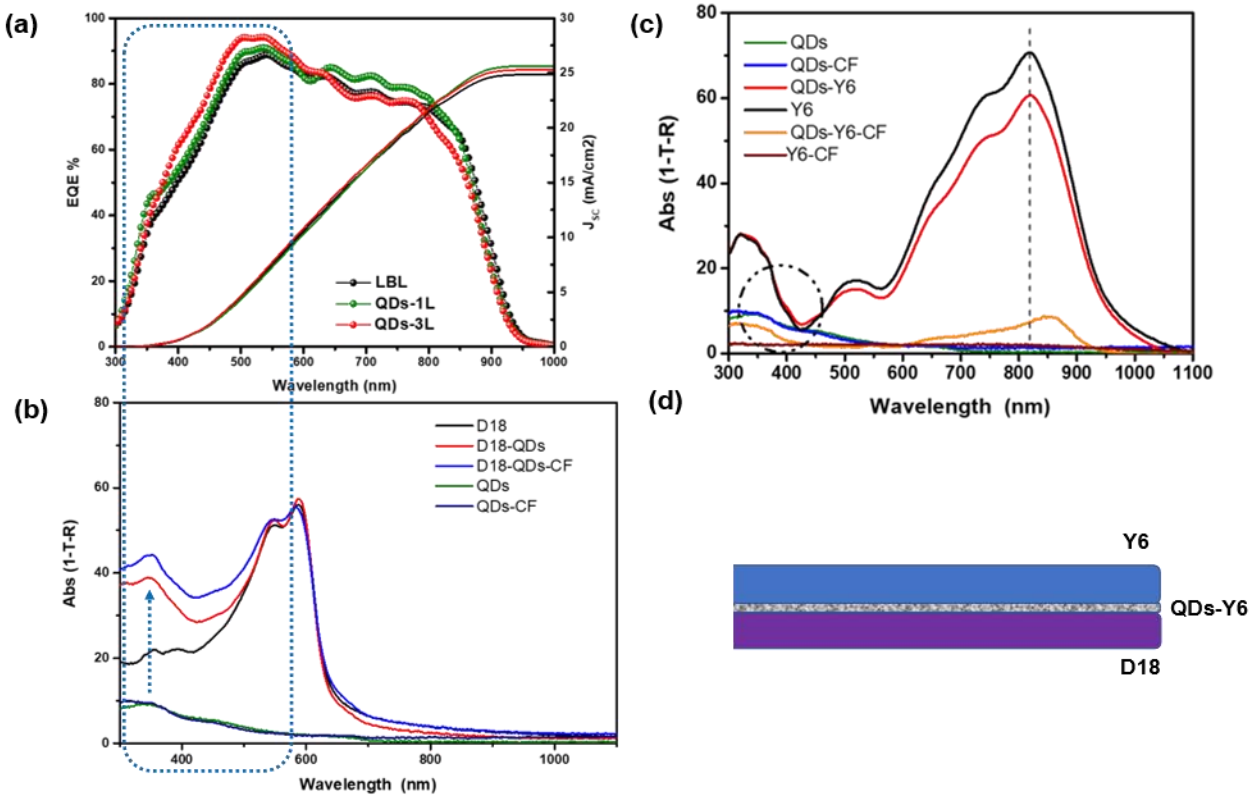

Figure 7.7 (a) EQE spectra of the LBL binary and QDs-ternary based NF-OPV devices. (b) and (c) UV-visible absorption spectra of different films structures. (d) schematic architecture for the QDs-ternary based photoactive layer.

For further insights into the reason behind the enhanced performance of the QDs based devices, external quantum efficiency (EQE) characteristics were conducted for the corresponding devices as shown in **Figure 7.7a**. It presented that all devices exhibited an absorption range from 300 to 900 nm with an average plateau of 85 % for the C-LBL binary based devices and 90 % for the QDs based ones. Furthermore, it was interesting to see that the calculated integrated J_{SC} values from the EQE spectra were 24.81, 25.84, and 25.31 mA/cm^2 for device C-LBL, QDs-1L, and QDs-3L, respectively, showing great matching with the values obtained from the J-V measurements under same AM 1.5G illumination condition (**Table 1.4**), confirming the higher J_{SC} obtained by the QDs based devices than the control binary ones. It is worth noting that the EQE spectral intensity in the WL range of 350-600 was noticeably enhanced for the PQDs based devices. This might be explained by the contribution of the $CsPbI_3$ QDs counterpart absorption as presented in **Figure 7.7b**, where the absorption spectra intensity of the D18/QDs film was enhanced at the same range of 350-600 than the D18 pristine film.

Then, we further performed the UV-Visible absorption characteristics for different films structures as presented in **Figure 7.7b** and **7.7c** to study the nature of the interface upon adding the $CsPbI_3$ QDs between the D18 and Y6 that leads to the boosting in the performance of the QDs based devices. To study the absorption impact of the QDs on the D18 film, it might be complicated to observe the absorption difference of the $CsPbI_3$ QDs and Y6 as both absorb in the same range as presented in **Figure 7.7c**. Thus, we separated the D18 based films in **Figure 7.7b** and the Y6 based film in **Figure 7.6c**. First, both D18/QDs and D18/QDs/CF (D18/QDs washed by CF) films showed almost the same absorption spectra, depicting that washing the QDs by CF solvent did not show any significant effect on the absorption properties of the D18/QDs film. We conducted this experiment to make sure that the deposition of the Y6 solution (dissolved in CF) over the QDs film would not dissolve it during the device fabrication. Furthermore, this step was confirmed by the measured PQDs and QDs/CF (PQDs washed by CF), exhibiting the same behaviour. Interestingly, washing the QDs with CF over the D18 layer did not affect the D18 film as well, as presented in **Figure 7.7b**. Then, we further measured the FE-SEM cross-section of the binary C-LBL and the QD-3L based devices as displayed in **Figure A.20** to analyze the corresponding structure**s.** As for the C-LBL based cross-section view image in **Figure A.20a**, we can clearly see that insignificant features were observed between the layers, indicating that all of the films are organic. In contrast to the QDs-3L based ones, showing different features, confirming the presence of the inorganic PQDs film as shown in **Figure A.20b**. Second, another comparison was carried out between the QDs/Y6 and the QDs/Y6/CF films as demonstrated in **Figure 7.6c**. We disclose that after washing the QDs/Y6 film with CF solvent, some residue from the Y6 still existed (orange line), which might explain that some of the Y6 was passivating the QDs as reported previously by Yuan. J et.al[363]. Thus, we assumed that Y6 might intermixed with the surface of QDs forming a passivated sub-layer as illustrated in **Figure 7.7 d**, that is why it did not totally remove by CF washing step.

This step was further confirmed by washing the pristine Y6 film by CF (dynamic spin coating), revealing that all Y6 was removed (dark red line).

Furthermore, in order to further analyze the microstructure morphology of the corresponding films, we conducted the AFM topography images as shown in **Figure 7.8.** First, **Figure 7.8a** reveals the fibril microstructure of the D18 film, while **Figur**e **7.8b** implies the D18/PQDs image which shows that the QDs film form a net that covered most of the D18 film as compared to the topographical features of the pristine D18 and QDs films shown in **Figure 7.8a** and **7.8c,** respectively. Furthermore, it can be noticeable that there is no distinguish difference between the surface morphology of QDs/Y6 and pristine Y6 films as presented in **Figure 7.8d** and **7.8e,** respectively**.** This behaviour might reflect the good coverage of the Y6 over the QDs film, forming a compact film with almost same RMS of both films. Then, **Figure 7.8f** implies the QDs/Y6 film washed by the CF solvent, depicting that when we washed the QDs/Y6 film with CF, features from the Y6 was remaining on the PQDs film, confirming the UV-Vis in **Figure 7.7c** and the presence of intermixing sub layer of Y6 with PQDs. Upon this observation, we assumed that the QDs formed a net that is not fully covering the D18 film, and it was further passivated by the Y6, allowing the Y6 to still in a contact with the D18 but with more controlled and aligned structure through the QDs film and the sequential LBL deposition method.

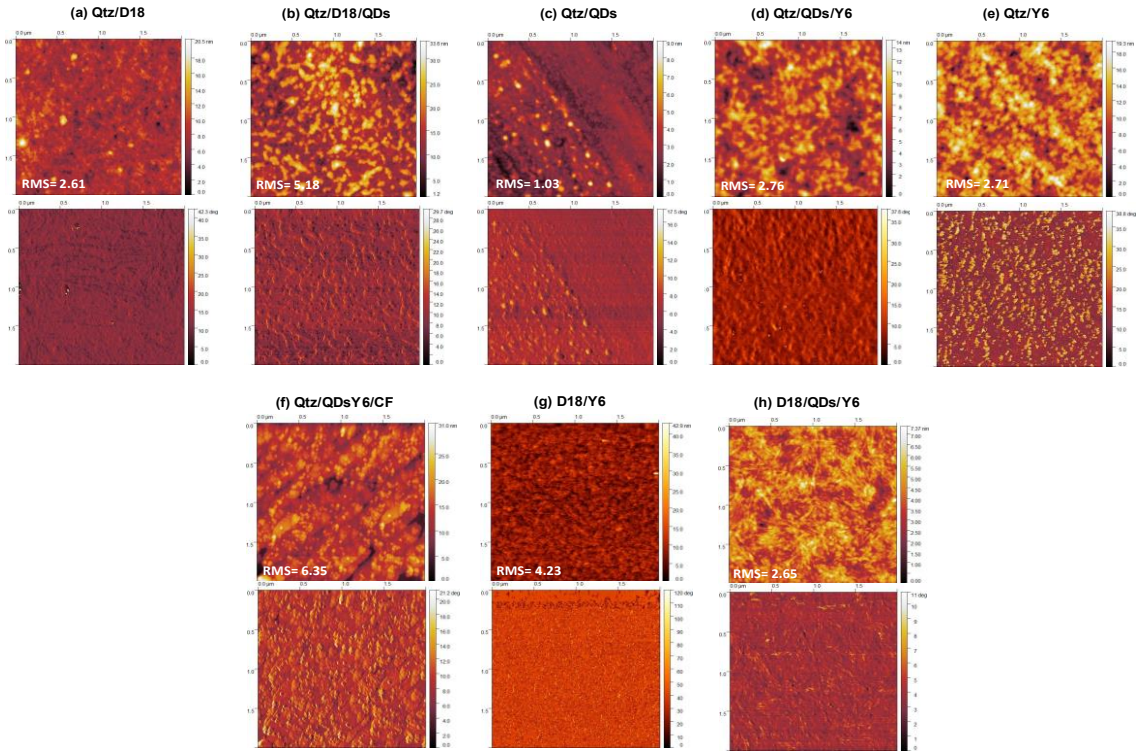

Figure 7.8 AFM topography and phase images of (a) pristine D18 film, (b) D18/QDs LBL film, (c) pristine QDs film, (d) QDs/Y6 LBL film, (e) pristine Y6 film, and (f) QDs/Y6 LBL film washed by CF.

In order to better understand the improved performance of the PQDs based devices upon including the PQDs counterpart, we further studied the recombination behaviour of the C-LBL as compared to the PQDs based devices. **Figure 7.9a** displays the photoluminescence (PL) spectra of the corresponding devices. Interestingly, we found that the QDs based devices exhibited strong PL quenching compared to the C-LBL based ones, reflecting the efficient exciton dissociation and better charge transfer.

This behavior is consistent with the AFM measurements, where the D18/QDs/Y6 film (**Figure 7.8h**) exhibited smoother surface than the D18/QDs (**Figure 7.8a**) and the D18/QDs/Y6 (**Figure 7.8g**), exhibiting rather uniform fibril texture that closer backed with a significantly reduced RMS value of 2.65 nm. This homogeneous film behaviour could be helpful for the contact between the active layers and electrodes, which benefits the exciton separation, and charge transport, indicating that the PQDs film was well aligned and passivated via the short-chain IDA capping ligands along with Y6 NFA, reveling the efficient electrons injection into the QDs and Y6 resulting in suppressed interfacial recombination of photocarriers, cranking up the electron coupling, accelerating charge transfer and facilitating carrier transportation[359,362,364] which greatly agreed with the significant enhanced the FF and J_{SC} of the QDs based cells (**Figure 7.6a**, **Table 7.3**). In addition, this behaviour in a consistence with the reported work by Pan .J et.al[360] and Yuan. J et.al[363].

Moreover, this result consents the enhanced electroluminescence (EL) peak intensity for QDs based devices as compared to the C-LBL ones as shown **Figure 7.9b**, indicating the diminished non radiative paths through the enhanced radiated recombination emission which explains the improved V_{OC} observed for the QDs-3L based devices. Furthermore, it is worth to mention that the EL emission of the QDs based devices slight red shifted as compared to the C-LBL ones which might be attributed to the interdot interaction at the QDs interface providing a compact film upon the efficient surface passivation through the IDA and Y6, revealing the improved FF and J_{SC} obtained by the QDs based devices (**Table 7.3**).

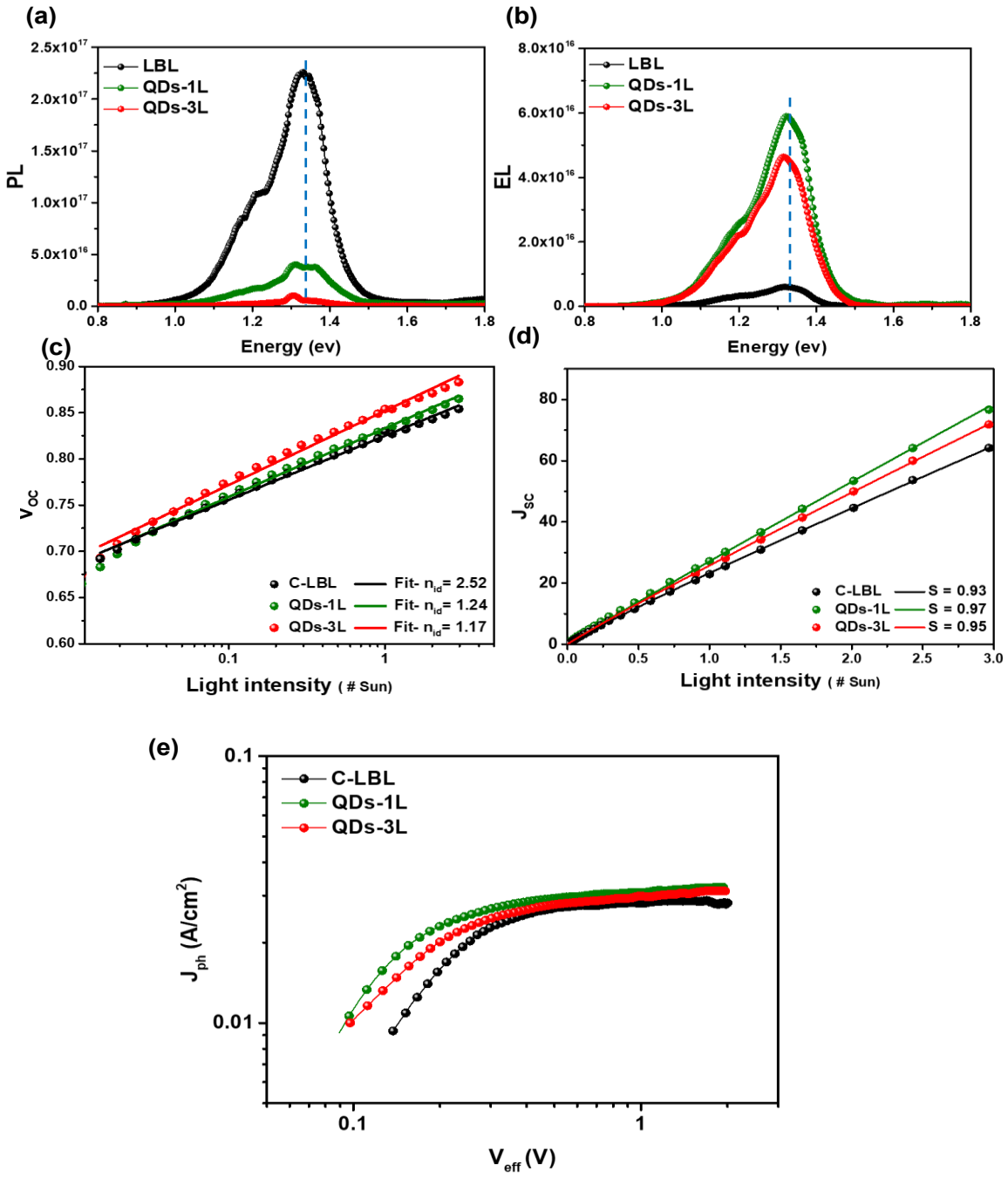

Figure 7.9 (a) PL, (b) EL, (c) V_{OC} vs the light intensities, and (d) J_{SC} vs the light intensities of the C-LBL binary and PQDs based full devices.

Then, The recombination mechanisms were further studied through examining the dependence of V_{OC} and J_{SC} on the incident light intensity (P_{light})[145] under AM 1.5 G illumination condition as shown in **Figure 7.9c and 7.9d,** respectively, gaining more insights to understand the improvement of the J_{SC} for the PQDs based devices.

At the open-circuit potential, the recombination can be reflected via V_{OC} α $n_{id}(k_BT/q)\ln(P_{light})$, where n_{id}, k_B, T, and q are the ideality factor, Boltzmann constant, temperature in kelvin, and elementary charge, respectively. When the value of n_{id} is close to 1, it indicates that the bimolecular band-to-band recombination is the dominant recombination in the OPV devices[147], while n_{id} >1 (close to 2) denotes the serious presence of the trap assisted recombination mechanisms[144,148]. As demonstrated in **Figure 7.9c**, n_{id} values of 1.17 and 1.24 were found for the QD-3L and QDs-1L based devices, respectively, which is lower than that of the host binary reference C-LBL devices (n_{id}=2.52). This suggests that trap-assisted recombination can be efficiently inhibited by the incorporation of the PQDs as an interlayer between the host D18/Y6, thus contributing to the improved J_{SC} and FF values in the ternary QDs based device. It is worth to mention that QDs-3L based devices showed lower n_{id} values than the QDs-1L ones, assuming that the sequential deposition of three layers of the PQDs provides better film coverage and well passivated surface which reduces the surface traps recombination, exhibiting lower n_{id} and higher V_{OC} values as compared to the one layer of PQDs cells.

Figure 7.9d displays the J_{SC} power law dependence on the light intensity (P_{light}) that following the proportional relation of J_{SC} α $P_{light}^{S_1}$ in principle, where S_1 is the exponential factor that describing the bimolecular recombination in devices and the capability of the corresponding electrodes to extract the free carries [145,227,263]. Thus, under short circuit condition, the S_1 value is unity when bimolecular recombination is insignificant in the donor/acceptor films and less than 1 in case of the presence of the bimolecular recombination.[147,144] The fitted values of S_1 were 0.93, 0.97, and 0.95 for C-LBL, QDs-1L, and QDs-3L, respectively. Consequently, the obtained results showed a linear behaviour, indicating the presence of bimolecular recombination for the entire devices[323,263] as a significant loss mechanism in the OPVs.[81] We noticed that QDs-based cells possessed S_1 values closer to 1 in comparison to the corresponding control C-LBL devices, reflecting that the non-geminate charge recombination is reduced[68,144] in the PQDs layered third-component structure active layers and it thus helps to elucidate the higher FF and J_{SC} in the ternary devices. This is also coincident with the lower leakage current (**Figure 7.6b**) and the highest J_{SC} obtained by the QDs based devices in the aforementioned J-V characteristics (**Figure 5.6a** and **Table 6.3**) as compared to the C-LBL devices.

As given in **Table 7.3**, the J_{SC} and FF values of the third PQDs based devices are higher than those of the binary C-LBL devices. To seek more for the cause behind the improvements of J_{SC} and FF in the QDs based devices we studied the charge generation and separation process of the C-LBL and the PQDs devices by plotting the double-logarithmic scale curves (J_{ph}–V_{eff}) as presented in **Figure 7.9e** for the devices to calculate

the saturation current density (J_{Sat}), the exciton dissociation probabilities (P_{diss}), maximum amount of absorbed photons that provides the dissociation and generation of free carriers (G_{max}) and the generation rate (G_{rat}) of the free charge carriers in the fabricated devices[49,149], the values are listed in **Table 7.4** and the calculation details explained previously in Chapter 2, equations 2.1, 2.2, and 2.3. Where J_{Ph} equals J_L-J_D, where $J_L$and J_D are the photocurrent densities under illumination and dark current densities, respectively, and V_{eff} is defined as V_O –V, where V_O is the voltage when J_L=J_D and V is the applied bias voltage [147,150,151]. We found that for the J_{Ph} increased linearly at low V_{eff}, then it starts to saturate by increasing the V_{eff} > 0.3 V for the PQDs based cells and > 0.4 V for the C-LBL based ones, representing that the PQDs suppressed the charge recombination, implying more efficient photogenerated charge carrier that can extracted by the electrodes[149,283] than the C-LBL devices. The J_{sat} of the QDs-1L and QDs-3L are 30.13 and 29.68 mA cm^{-2}, respectively, which is higher than that of the hosting C-LBL devices (28.23 mA cm^{-2}), according well with the variation tendency of the J_{SC} values provided in the J–V plots (see **Table 7.3**). The improved J_{sat} value of the QDs device indicates that the addition of the PQDs as the third component might assist the photo-harvesting of the host D18/Y6 system and benefits exciton generation and separation in the D18/PQDs/Y6 system. Furthermore, regarding the P_{diss} of the QD-1L and QDs-3L based devices were calculated as 98.06 % and 99.87 %, respectively, which was higher than that of the C-LBL devices (99.40 %). This result implies that the incorporated PQDs third counterpart can effectively promote the charge separation in the ternary devices, thus contributing to a higher J_{SC} and FF of the QDs based devices as compared with the binary C-LBL ones. Morover, the values of the G_{max} for the C-LBL, QDs-1L, and QDs-3L devices were 1.76×10^{28}, 1.88×10^{28}, 1.85 and 1.22×10^{28} m^{-3} s^{-1}, respectively. It is interesting to notice that the highest values of the G_{max} were for the PQDs based devices consisting with its highest J_{SC} value obtained from the J-V characteristics (**Figure 7.6a**). In turn, this behavior matched with the G_{rat} values (**Table 7.4**) of the devices, indicating the effective dissociation of the photogenerated excitons for PQDs based devices than C-LBL cells which consistent with the corresponding performance of the devices (**Table 7.3**).

Table 7.4 Optoelectronic parameters calculated from the J_{ph} -V_{eff} curves.

Device	J_{sat} (mA cm^{-2})	G_{max} (× 10^{28} m^{-3} s^{-1})	P_{diss} (%)	G_{rat} (× 10^{30} m^{-3} s^{-1})
C-LBL	28.23	1.76	98.06	1.73
1L-QDs	30.13	1.88	99.87	1.88
3L-QDs	29.68	1.85	99.40	1.84

J_{sat}: Average values of J_{ph} under condition where V_{eff} in the saturation region

7.4 Conclusion

In conclusion, first, we comparatively studied the binary system based on BHJ and LBL deposition approaches with D18 and Y6 as the host binary system. The devices prepared by LBL processing method form a vertical distribution structure facilitating the charge transmission and charge collection which brings a higher J_{SC} and FF than BHJ OPVs systems. Second, we have developed a novel D18/PQDs/Y6 ternary system employing LBL approach, introducing a $CsPbI_3$ QDs (PQDs) film as an interlayer between the D18/Y6 host system in view of their complementary absorption and the proper electronic energy cascade levels of these three materials. It is worth mentioning that the incorporation of the optimized PQDs film has a great influence on the device performance, exhibiting an enhanced PCE of 16.56 % as compared to the host binary system (PCE= 15.76 %). Moreover, the addition of PQDs to create alloy structure with the Y6 was beneficial for reducing bimolecular and trap-assisted recombination, improving exciton separation, and charge transfer, resulting in the higher, V_{OC}, J_{SC}, and FF of the PQDs based device. Finally, our findings evidence that the incorporation of the $CsPbI_3$ QDs as a third component through LBL deposition approach is an effective strategy to improve the morphology of the active layers and achieve high-performance OPV devices.

Chapter 8

Conclusion and Future Directions

8.1 Conclusion

In **Chapter 3**, the surface roughness of the zinc oxide (ZnO) film as electron transport layer (ETL) was found to be important for the performance of inverted organic photovoltaics (iF-OPVs) using PTB7-Th:$PC_{70}BM$ as the photoactive layer. By using an intermittent spray pyrolysis approach, the microstructure features and properties of the sprayed ZnO film were carefully controlled by varying the concentration of the ZnO precursor solution and the number of spraying cycles. Then we conducted a comparison between the ZnO-SP based devices and the ZnO-SC ones to reveal the devices performance and stability behavior. The results showed that the ZnO-SP based devices with high ZnO concentration (C-7R-SP based devices) manifested higher J_{SC} than the lab-scale ZnO-SC based ones and fairly similar performance, achieving devices with same V_{OC} (0.79 V) as well efficiency of 10 %. It was noticeable that the main difference between the ZnO-SC and C-7R-SP based devices is the interface roughness effect between the ITO and the ZnO deposited film. The bright side of being textured surface that enhances the light trapping inside the solar cell which increases the absorbance of the incident light and generates higher J_{SC}. Furthermore, this proper interface contact with the active layer enhances the overall stability for the ZnO-SP based devices, where the rate of degradation of the ZnO-SP based devices was slower than the ZnO-SC one. However, the deficient side was regarding the effect of the interface between the ZnO sprayed layer and the ITO that increases the R_S. Thus, these investigated results in part I point out that the deposition techniques have a vital role that affects the film formation as well as the performance and stability of the devices. Taking these facts into account leads to the next step of improving the interface between the ZnO layer and the ITO to perform lower R_S which might enhance the device stability and performance. Accordingly, we further optimized the morphology of the sprayed ZnO in part II with lowest roughness and full surface coverage that is achieved through 25R with 0.5:9.5 ration of ZnO precursor solution concentration, yielding the benchmark performance of 10 % PCE along with enhanced average V_{OC} (0.80 V) and FF (0.70) of III based devices. Furthermore, we tested their stability behavior that demonstrated a pioneer record with respect to device ZnO-7R-SP and ZnO-SC based devices, maintaining 85% of their starting efficiency even after 16.7 months of storage inside a nitrogen glove box without encapsulation. The difference in the devices performance and stability appears to originate from the different obtained ZnO surface morphologies that control the presence of defects at the surface and their subsequent adjacent organic active layer blend. As a sequence, the surface roughness determines the effective interfacial

region between the active layer and the ZnO layer and ITO, thus the density of trap sites at the interface that was investigated by the IS measurements for the fresh and degraded iF-OPVs. The proposed electrical equivalent circuit module accounted to fit the experimental data of the IS, allowed us to recognize the impact of each interlayer on the device performance and the correlated stability behavior. Accordingly, we obtained that the remarkable stability enhancement behavior of the III based devices correlates with the marginally interface density of states values for this sample among the others. These models presented a simple way to diagnose the loss mechanisms and investigate degradation mechanisms and stability issues in the fabricated devices. Finally, it is worth mentioning that the obtained high efficiency and excellent stability of the fabricated inverted OPVs using intermittent spray pyrolysis approach could facilitate their scaling up to the industrial production perspective.

In **Chapter 4**, fine-tuning of blend morphology is a key factor that limits the performance of the bulk-heterojunction organic photovoltaics (BHJ-OPVs). Here, morphological control of the binary PM6:Y7 blends was conducted through 1-chloronaphthalene (CN, 2%) solvent additives and thermal annealing treatment (TA, 100 °C) with respect to their influence on the photovoltaic performance. Moreover, a distinct study was accomplished on the optical and electric properties of the treated and non-treated based devices by external quantum efficiency measurements and impedance spectroscopy. The results indicated that the 2 % CN solvent addition showed pronounced increment of the J_{SC} by ≈ 27 % and FF by ≈ 12.5 %. Furthermore, the TA treatment provides a higher PCE for the iNF-OPV mainly due to the enhancement of the V_{OC}. These performance improvement was mainly upon suppressing the carrier recombination and assist the excitons in the photoactive layer blend to reach the donor/acceptor interface, and in turn easily dissociated into free carriers[237] which typically contributed to enhance the J_{SC} and FF of the based devices. Moreover, the low RMS as well as more enhanced film crystallization were exhibited for the champion D based devices that conducted the dual modifications of 2 % CN solvent additives along with the TA treatments. That likely facilitated the charge transport providing the closest n_{id} value to 1, highest P_{diss}, lowest leakage current, highest J_{SC}, FF, and in turn the best PCE_{max} Accordingly, the tunning of both CN additives and TA treatments are crucial for achieving the balance of exciton dissociation and charge collection, prompting better film morphology and increase in the PCE as confirmed by the case of D based devices.

In **Chapter 5**, we presented a highly efficient PDINO based cathode interlayer for iNF-OPVs, achieving excellent photostability behavior. The iNF-OPVs incorporating the PDINO interlayer (C-PDINO based devices) maintained 80 % of the initial efficiency after continuous illumination (AM 1.5G, 100 mW cm^{-2}) for 520 min, while the ZnO-based control iNF-OPV (A-ZnO based devices) remained only for 160 min under same conditions. The remarkable photostability of the C-PDINO based devices were mainly attributed to the avoidance of the photo-induced shunts and the photocatalytic behavior, which are inevitably in the ZnO based i-OPVs. Moreover, C-PDINO based devices refrained from the burn-in photo-degradation phenomena, which cause a significant reduction in the performance of the exposed devices by providing negative effects on energy transfer, exciton dissociation and charge recombination processes which may be more related to the bulk of the active layer as appeared for the ZnO based iNF-OSCs. Hence, this piece of work clearly demonstrates that PDINO is a promising cathode interlayer for tremendously photostable i-OPVs, particularly for large-scale production. As it fits the requirements of low-temperature fabrication, can be used in very fine-tuned thicknesses, showing great resistance behavior toward light, and does not react with the contacted active layers and electrodes.

In **Chapter 6**, aiming to enhance the photovoltaic performance, we explicitly conducted a systematic investigation regarding the influence of the Pre-TT approach on the performance of the NF-OPVs. But first, optimization process was conducted to the devices through sequential thicknesses variation of PM6:Y7, PEDOT:PSS, and PDINO layers to investigate the impact of each layer on the overall device behavior. The obtained results revealed that the key limiting effect was related to the PM6:Y7 layer where the PCE % enhanced by 15% upon reducing its thickness from 150 nm to 100 nm. Surprisingly, another important factor was correlated to the PDINO film which increases the J_{SC} by 7% owing to increment the concentration of the PDINO precursor solution from 1 mg/ml to 1.5 mg/ml in methanol. Then, conducting the Pre-TT step critically affects the PEDOT:PSS/PM6:Y7 blend morphologies and thus the overall performance of the devices. Interestingly, this chapter puts the spotlight on the extraordinary J_{SC} values obtained by the Pre-TT devices, where the optimized treated devices of D8-Pre-TT exhibited a pioneer enhanced J_{SC} value of 32.65 mA/cm^2 along with improved PCE of 17.92. We observed that the treated based films exhibited smoother surface roughness, revealing their lower R_S, and lower leakage current, which leads to high carrier transport and suppressed charge carrier recombination in the resulting NF-OPVs based devices. Indispensably, a critical challenge for the current NFA-based OPVs is to avoid the strong phase separation upon blending and deposition, which applied through the Pre-TT approach, leading to balanced hole and electron mobility along with low non-geminate recombination that might be the key parameter leading to the remarkable enhancement observed in the performance of the Pre-TT NF-OPVs. Moreover, the enhanced J_{SC} values noticed for the Pre-TT devices were mainly due to their high EQE values and high P_{diss} than the corresponding

pristine NF-OPVs, correlating their remarkable PL quench of the Pre-TT films, reflecting the efficient charge transfer at the PEDOT:PSS/PM6:Y7 interfaces Furthermore, the recombination study using P_{light} vs the J_{SC} showed the presence of recombination, but it did not distinguish between each device as it showed all devices have equal contribution of the bimolecular recombination. While the IS characteristics were conducted through investigating the Nyquist plot, Cf -DOS calculations and the C-V characteristics, providing an efficient insight study that accurately detected the recombination contribution that was more obvious for the pristine devices which disclose their lower performance. Accordingly, the Pre-TT approach diminishes the traps and enhances the interface charge transfer through enhancing the carrier dynamics of the treated devices, triggering a promising approach for boosting the J_{SC} along with the photovoltaic performance of the treated devices.

In **Chapter 7**, first, we have conducted a comparative study of binary systems based on bulk-heterojunction (BHJ) and layer-by-layer (LBL) deposition approaches using D18 and Y6 as the host binary system. The devices prepared by the LBL processing method are known by their vertical distribution structure that facilitated charge transmission and collection, resulting in higher J_{SC} and FF values as compared to the BHJ OPV systems. Second, we have developed a novel D18/PQDs/Y6 ternary system employing the LBL approach, with a perovskite $CsPbI_3$ quantum dot (PQD) film serving as an interlayer between the D18/Y6 host system due to their complementary absorption and suitable electronic energy cascade levels. The incorporation of the optimized PQD film had a significant impact on device performance, resulting in an enhanced PCE of 16.56% compared to the host binary system (PCE= 15.76%). The addition of PQDs to create an alloy structure with Y6 was also beneficial for reducing bimolecular and trap-assisted recombination, improving exciton separation, and charge transfer, resulting in V_{OC}, J_{SC}, and FF values for the PQD-based device. Finally, our findings suggest that the incorporation of $CsPbI_3$ QDs as a third component through the LBL deposition approach is an effective strategy for improving the morphology of the active layers and achieving high-performance OPV devices.

8.2 Future Directions

In the future, there will be a focus on:

1- Low temperature SP to facilitate R2R techniques for conventional OPVs.
2- Combining the QDs-third component in different OPV systems.
3- Working on different types of organic and inorganic ligand exchange for replacing the capping agent of QDs, providing less surface recombination behaviour and as a result boosting the OPV device performance.
4- In-deep insights required to understand the QDs phase transition behaviour within the BHJ OPVs systems.
5- Assumption of D/A1/A2, D18 has intermixed with QDs or separate layers or parallel like model or alloy like model with the D18 and investigating the mechanism of the energy transfer through FRET depending on the spectral gap between absorption and emission.

References

References

(1) Frölicher, T. L.; Fischer, E. M.; Gruber, N. Marine Heatwaves under Global Warming. *Nature* **2018**, *560* (7718), 360–364.

(2) Tapley, B. D.; Watkins, M. M.; Flechtner, F.; Reigber, C.; Bettadpur, S.; Rodell, M.; Sasgen, I.; Famiglietti, J. S.; Landerer, F. W.; Chambers, D. P.; Reager, J. T.; Gardner, A. S.; Save, H.; Ivins, E. R.; Swenson, S. C.; Boening, C.; Dahle, C.; Wiese, D. N.; Dobslaw, H.; Tamisiea, M. E.; Velicogna, I. Contributions of GRACE to Understanding Climate Change. *Nature Climate Change* **2019**, *9* (5), 358–369.

(3) IPCC. *Climate Change 2022: Mitigation of Climate Change. Contribution of Working Group III to the Sixth Assessment Report of the Intergovernmental Panel on Climate Change*; 2022.

(4) p.l.c. Statistical Review of World Energy https://www.bp.com/en/global/corporate/energy-economics/statistical-review-of-world-energy.html.

(5) Doss-Gollin, J.; Farnham, D. J.; Lall, U.; Modi, V. How Unprecedented Was the February 2021 Texas Cold Snap? *Environmental Research Letters* **2021**, *16* (6), 064056.

(6) Liu, Z.; Deng, Z.; He, G.; Wang, H.; Zhang, X.; Lin, J.; Qi, Y.; Liang, X. Challenges and Opportunities for Carbon Neutrality in China. *Nature Reviews Earth and Environment* **2022**, *3* (2), 141–155.

(7) Owusu, P. A.; Asumadu-Sarkodie, S. A Review of Renewable Energy Sources, Sustainability Issues and Climate Change Mitigation. *Cogent Engineering* **2016**, *3* (1), 1167990.

(8) Brown, E. W. *An Introduction to Solar Energy*; 1988.

(9) Grätzel, M. Recent Advances in Sensitized Mesoscopic Solar Cells. *Accounts of Chemical Research* **2009**, *42* (11), 1788–1798.

(10) Lynn, P. A. *Electricity from Sunlight: An Introduction to Photovoltaics*; 2010.

(11) Haberlin, H. *PHOTOVOLTAICs SYSTEM DESIGN AND PRACTICE*; 2012; Vol. 1.

(12) E. Becquerel. On Electron Effects under the Influence of Solar Radiation. *Comptes rendus l'Académie des Sci. IX* **1839**, *9*, 561.

(13) Hegedus, S. S.; Luque, A. *Status, Trends, Challenges and the Bright Future of Solar Electricity from Photovoltaics*.

(14) Fritts, C. E. On a New Form of Selenium Cell, and Some Electrical Discoveries Made by Its Use. *Am. J. Sci* **1883**, *23–26*, 465–472.

(15) Century, B. C. Solar Technology Isn ' t New . Its History Spans from the 7th Century B . C . to Today . We Started out Concentrating the Sun ' s Heat with Glass and Mirrors to Light Fires . Today , We Have Everything from Solar-Powered Buildings to Solar- Powered Vehicl. **2000**.

(16) Park, N.-G. Organometal Perovskite Light Absorbers Toward a 20% Efficiency Low-Cost Solid-State Mesoscopic Solar Cell. *Journal of Physical Chemistry Letters* **2013**, *4* (15), 2423–2429.

(17) Thermopedia. Solar Energy. **2014**, 1–10.

(18) Shaheen, S. E.; Brabec, C. J.; Sariciftci, N. S.; Padinger, F.; Fromherz, T.; Hummelen, J. C. 2 . 5 % Efficient Organic Plastic Solar Cells. *APPLIED PHYSICS LETTERS* **2001**, *78* (6), 841–843.

(19) Bagher, A. M.; Mahmoud, M.; Vahid, A.; Mohsen, M. Types of Solar Cells and Application. *American Journal of Optics and Photonics* **2015**, *3* (5), 94–113.

(20) Brabec, B. C. J.; Sariciftci, N. S.; Hummelen, J. C. Plastic Solar Cells. *Advanced Functional Materials* **2001**, *11* (1), 15–26.

(21) Ma, L.; Zhang, S.; Wang, J.; Xu, Y.; Hou, J. Recent Advances in Non-Fullerene Organic Solar Cells: From Lab to Fab. *Chemical Communications* **2020**, *56* (92), 14337–14352.

(22) Upama, M. B.; Mahmud, M. A.; Conibeer, G.; Uddin, A. Trendsetters in High-Efficiency Organic Solar Cells: Toward 20% Power Conversion Efficiency. *Solar RRL* **2020**, *4* (1), 1–16.

(23) Armin, A.; Li, W.; Sandberg, O. J.; Xiao, Z.; Ding, L.; Nelson, J.; Neher, D.; Vandewal, K.; Shoaee, S.; Wang, T.; Ade, H.; Heumüller, T.; Brabec, C.; Meredith, P. A History and Perspective of Non-Fullerene Electron Acceptors for Organic Solar Cells. *Advanced Energy Materials* **2021**, *11* (15), 1–42.

(24) Liu, Q.; Jiang, Y.; Jin, K.; Qin, J.; Xu, J.; Li, W.; Xiong, J.; Liu, J.; Xiao, Z.; Sun, K.; Yang, S.; Zhang, X.; Ding, L. 18% Efficiency Organic Solar Cells. *Science Bulletin* **2020**, *65* (4), 272–275.

(25) Luo, D.; Jang, W.; Babu, D. D.; Kim, M. S.; Wang, D. H.; Kyaw, A. K. K. Recent Progress in Organic Solar Cells Based on Non-Fullerene Acceptors: Materials to Devices. *Journal of Materials Chemistry A* **2022**, *10* (7), 3255–3295.

(26) Yan, J.; Savenije, T. J.; Mazzarella, L.; Isabella, O. Progress and Challenges on Scaling up of Perovskite Solar Cell Technology. *Sustainable Energy and Fuels* **2022**, *6* (2), 243–266.

(27) NREL. National Renewable Energy Laboratory, Best Research-Cell Efficiencies Chart, https://www.nrel.gov/pv/assets/pdfs/best-research-cell-efficiencies.html.

(28) Søndergaard, R.; Hösel, M.; Angmo, D.; Larsen-Olsen, T. T.; Krebs, F. C. Roll-to-Roll Fabrication of Polymer Solar Cells. *Materials Today*. Elsevier Ltd 2012, pp 36–49. https://doi.org/10.1016/S1369-7021(12)70019-6.

(29) Sánchez, J. G.; Balderrama, V. S.; Garduño, S. I.; Osorio, E.; Viterisi, A.; Estrada, M.; Ferré-Borrull, J.; Pallarès, J.; Marsal, L. F. Impact of Inkjet Printed ZnO Electron Transport Layer on the Characteristics of Polymer Solar Cells. *RSC Advances* **2018**, *8* (24), 13094–13102.

(30) Balderrama, V. S.; Sánchez, J. G.; Lastra, G.; Cambarau, W.; Arias, S.; Pallarès, J.; Palomares, E.; Estrada, M.; Marsal, L. F. High-Efficiency Organic Solar Cells Based on a Halide Salt and Polyfluorene Polymer with a High Alignment-Level of the Cathode Selective Contact. *Journal of Materials Chemistry A* **2018**, *6* (45), 22534–22544.

(31) Torimtubun, A. A. A.; Sánchez, J. G.; Pallarès, J.; Marsal, L. F. A Cathode Interface Engineering Approach for the Comprehensive Study of Indoor Performance Enhancement in Organic Photovoltaics. *Sustainable Energy and Fuels* **2020**, *4* (7), 3378–3387.

(32) Eslamian, M. Spray-on Thin Film PV Solar Cells: Advances, Potentials and Challenges. *Coatings* **2014**, *4* (1), 60–84.

(33) Aziz, F.; Ismail, A. F. Spray Coating Methods for Polymer Solar Cells Fabrication: A Review. *Materials Science in Semiconductor Processing* **2015**, *39*, 416–425.

(34) Li, G.; Zhu, R.; Yang, Y. Polymer Solar Cells. *Nature Photonics* **2012**, *6* (3), 153–161.

(35) Brabec, C. J. Organic Photovoltaics: Technology and Market. *Solar Energy Materials and Solar Cells* **2004**, *83* (2–3), 273–292.

(36) Gu, S.; Neugebauer, H.; Sariciftci, N. S. Conjugated Polymer-Based Organic Solar Cells. *Chem. Rev.* **2007**, *107* (4), 1324–1338.

(37) Silinsh, E. A.; Cápek, V. *Organic Molecular Crystals : Interaction, Localization, and Transport Phenomena*; 1994.

(38) Zhuravleva, T. S.; Vannikov, a. V. Polymer Solar Cells. *Materials Science Forum* **1987**, *21* (June), 203–0. https://doi.org/10.4028/www.scientific.net/MSF.21.203.

(39) Käfer, D.; El Helou, M.; Gemel, C.; Witte, G. Packing of Planar Organic Molecules: Interplay of van Der Waals and Electrostatic Interaction. *Crystal Growth and Design* **2008**, *8* (8), 3053–3057.

(40) Köhler, A.; Bassler, H. *Related Titles Physics of Organic Self-Organized Organic OLED Displays Fundamentals The Photophysics behind Photovoltaics and Photonics*; 2015.

References

(41) Wu, J.; Cha, H.; Du, T.; Dong, Y.; Xu, W.; Lin, C. T.; Durrant, J. R. A Comparison of Charge Carrier Dynamics in Organic and Perovskite Solar Cells. *Advanced Materials* **2022**, *34* (2), 2101833.

(42) Poelking, C.; Andrienko, D. Design Rules for Organic Donor-Acceptor Heterojunctions: Pathway for Charge Splitting and Detrapping. *Journal of the American Chemical Society* **2015**, *137* (19), 6320–6326.

(43) Miller, A.; Abrahams, E. Impurity Conduction at Low Concentrations. *Phys. Rev.* **1960**, *120* (3), 745–755. https://doi.org/10.1103/PhysRev.120.745.

(44) Marcus, R. A. Electron Transfer Reactions in Chemistry: Theory and Experiment (Nobel Lecture). *Angewandte Chemie International Edition in English* **1993**, *32* (8), 1111–1121.

(45) Tang, C. W. Two-Layer Organic Photovoltaic Cell. *Applied Physics Letters* **1986**, *48* (2), 183–185.

(46) Ghosh, A. K.; Feng, T. Merocyanine Organic Solar Cells Merocyanine Organic Solar Cells. *Appl. Phys. Lett.* **1978**, *49* (August), 5982.

(47) Yu, G.; Gao, J.; Hummelen, J. C.; Wudl, F.; Heeger, A. J. Polymer Photovoltaic Cells: Enhanced Efficiencies via a Network of Internal Donor-Acceptor Heterojunctions. *Science* **1995**, *270* (5243), 1789.

(48) Hou, J.; Inganas, O.; Friend, R. H.; Gao, F. Organic Solar Cells Based on Non-Fullerene Acceptors. *Nature Materials* **2018**, *17* (2), 119–128.

(49) Mihailetchi, V. D.; Koster, L. J. A.; Hummelen, J. C.; Blom, P. W. M. Photocurrent Generation in Polymer-Fullerene Bulk Heterojunctions. *Physical Review Letters* **2004**, *93* (21), 19–22.

(50) Kang, H.; Lee, W.; Oh, J.; Kim, T.; Lee, C.; Kim, B. J. From Fullerene-Polymer to All-Polymer Solar Cells: The Importance of Molecular Packing, Orientation, and Morphology Control. *Accounts of Chemical Research* **2016**, *49* (11), 2424–2434.

(51) Lu, B.; Wang, J.; Zhang, Z.; Wang, J.; Yuan, X.; Ding, Y.; Wang, Y.; Yao, Y. Recent Progress of Y-series Electron Acceptors for Organic Solar Cells. *Nano Select* **2021**, *2* (11), 2029–2039.

(52) Ma, L.; Zhang, S.; Wang, J.; Xu, Y.; Hou, J. Recent Advances in Non-Fullerene Organic Solar Cells: From Lab to Fab. *Chemical Communications* **2020**, *56* (92), 14337–14352.

(53) Sun, Y.; Seo, J. H.; Takacs, C. J.; Seifter, J.; Heeger, A. J. Inverted Polymer Solar Cells Integrated with a Low-Temperature-Annealed Sol-Gel-Derived ZnO Film as an Electron Transport Layer. *Advanced Materials* **2011**, *23* (14), 1679–1683.

(54) White, M. S.; Olson, D. C.; Shaheen, S. E.; Kopidakis, N.; Ginley, D. S. Inverted Bulk-Heterojunction Organic Photovoltaic Device Using a Solution-Derived ZnO Underlayer. *Applied Physics Letters* **2006**, *89* (14), 87–90.

(55) Kumar, K.; Das, A.; Kumawat, U. K.; Dhawan, A. Tandem Organic Solar Cells Containing Plasmonic Nanospheres and Nanostars for Enhancement in Short Circuit Current Density. *Optics Express* **2019**, *27* (22), 31599.

(56) Jia, Z.; Qin, S.; Meng, L.; Ma, Q.; Angunawela, I.; Zhang, J.; Li, X.; He, Y.; Lai, W.; Li, N.; Ade, H.; Brabec, C. J.; Li, Y. High Performance Tandem Organic Solar Cells via a Strongly Infrared-Absorbing Narrow Bandgap Acceptor. *Nature Communications* **2021**, *12* (1), 1–10.

(57) Proctor, C. M.; Kuik, M.; Nguyen, T. Q. Charge Carrier Recombination in Organic Solar Cells. *Progress in Polymer Science*. Elsevier Ltd 2013, pp 1941–1960.

(58) Garcia-Belmonte, G.; Munar, A.; Barea, E. M.; Bisquert, J.; Ugarte, I.; Pacios, R. Charge Carrier Mobility and Lifetime of Organic Bulk Heterojunctions Analyzed by Impedance Spectroscopy. *Organic Electronics* **2008**, *9* (5), 847–851.

(59) Rafique, S.; Abdullah, S. M.; Sulaiman, K.; Iwamoto, M. Fundamentals of Bulk Heterojunction Organic Solar Cells: An Overview of Stability/Degradation Issues and Strategies for Improvement. *Renewable and Sustainable Energy Reviews* **2018**, *84* (December 2017), 43–53.

(60) Clarke, T. M.; Durrant, J. R. Charge Photogeneration in Organic Solar Cells. *Chemical Reviews* **2010**, *110* (11), 6736–6767.

(61) Janssen, R. A. J.; Nelson, J. Factors Limiting Device Efficiency in Organic Photovoltaics. *Advanced Materials* **2013**, *25* (13), 1847–1858.

(62) Giannini, S.; Blumberger, J. Charge Transport in Organic Semiconductors: The Perspective from Nonadiabatic Molecular Dynamics. *Accounts of Chemical Research* **2022**, *55* (6), 819–830.

(63) Hu, R.; Liu, Y.; Peng, J.; Jiang, J.; Qing, M.; He, X.; Huo, M. M.; Zhang, W. Charge Photogeneration and Recombination in Fluorine-Substituted Polymer Solar Cells. *Frontiers in Chemistry* **2022**, *10*, 1–12.

(64) Haneef, H. F.; Zeidell, A. M.; Jurchescu, O. D. Charge Carrier Traps in Organic Semiconductors: A Review on the Underlying Physics and Impact on Electronic Devices. *Journal of Materials Chemistry C* **2020**, *8* (3), 759–787.

(65) Boix, P. P.; Garcia-Belmonte, G.; Muñecas, U.; Neophytou, M.; Waldauf, C.; Pacios, R. Determination of Gap Defect States in Organic Bulk Heterojunction Solar Cells from Capacitance Measurements. *Applied Physics Letters* **2009**, *95* (23), 233302.

(66) Heston, N. AM1 . 5 Solar Simulator User Guide.

(67) Laboratory, N. R. E. L. Reference Air Mass 1.5 Spectra | Grid Modernization.

(68) Meyer, E. L. Extraction of Saturation Current and Ideality Factor from Measuring Voc and Isc of Photovoltaic Modules. *International Journal of Photoenergy* **2017**, *2017*, 1–9.

(69) W. SHOCKLEY. The Theory of P-n Junctions in Semiconductors and p-n Junction Transistors. *The Bell System Technical Journal* **1948**, *28* (3), 435–489.

(70) Shockley, W.; Read, W. T. Statistics of the Recombinations of Holes and Electrons. *physical review Journal* **1952**, *87* (46), 835.

(71) Jao, M. H.; Liao, H. C.; Su, W. F. Achieving a High Fill Factor for Organic Solar Cells. *Journal of Materials Chemistry A* **2016**, *4* (16), 5784–5801.

(72) Qi, B.; Wang, J. Fill Factor in Organic Solar Cells. *Physical Chemistry Chemical Physics* **2013**, *15* (23), 8972–8982.

(73) Deibe, C.; Strobe, T.; Dyakonov, V. Role of the Charge Transfer State in Organic Donor-Acceptor Solar Cells. *Advanced Materials* **2010**, *22* (37), 4097–4111.

(74) Yi, Y.; Coropceanu, V.; Brédas, J. L. Exciton-Dissociation and Charge-Recombination Processes in Pentacene/C 60 Solar Cells: Theoretical Insight into the Impact of Interface Geometry. *Journal of the American Chemical Society* **2009**, *131* (43), 15777–15783.

(75) Servaites, J. D.; Ratner, M. A.; Marks, T. J. Organic Solar Cells: A New Look at Traditional Models. *Energy and Environmental Science*. 2011, pp 4410–4422.

(76) Fukuhara, T.; Tamai, Y.; Ohkita, H. Nongeminate Charge Recombination in Organic Photovoltaics. *Sustainable Energy and Fuels* **2020**, *4* (9), 4321–4351.

(77) Blom, P. W. M.; Mihailetchi, V. D.; Koster, L. J. A.; Markov, D. E. Device Physics of Polymer:Fullerene Bulk Heterojunction Solar Cells. *Advanced Materials* **2007**, *19* (12), 1551–1566.

(78) Langevin, M. Recombinaison et Diffusion Des Ions. *Ann Chim Phys* **1905**, *4* (1), 322–333.

(79) Mihailetchi, V. D. Bimolecular Recombination in Polymer / Fullerene Bulk Heterojunction Solar Cells Bimolecular Recombination in Polymer / Fullerene Bulk Heterojunction Solar Cells. *Appl. Phys. Lett.* **2006**, *88*, 052104.

(80) Brus, V. V. Light Dependent Open-Circuit Voltage of Organic Bulk Heterojunction Solar Cells in the Presence

of Surface Recombination. *Organic Electronics* **2016**, *29* (February 2016), 1–6.

(81) Juka, G.; Arlauskas, K. Charge Carrier Recombination in Bulk Heterojunction Organic Solar Cells. *Solar Energy* **2010**, *38*, 1941–1960.

(82) Liang, Z.; Tong, J.; Li, H.; Wang, Y.; Wang, N.; Li, J.; Yang, C.; Xia, Y. The Comprehensive Utilization of the Synergistic Effect of Fullerene and Non-Fullerene Acceptors to Achieve Highly Efficient Polymer Solar Cells. *Journal of Materials Chemistry A* **2019**, *7* (26), 15841–15850.

(83) Lv, J.; Tang, H.; Huang, J.; Yan, C.; Liu, K.; Yang, Q.; Hu, D.; Singh, R.; Lee, J.; Lu, S.; Li, G.; Kan, Z. Additive-Induced Miscibility Regulation and Hierarchical Morphology Enable 17.5% Binary Organic Solar Cells. *Energy & Environmental Science* **2021**, *14* (5), 3044–3052.

(84) Hu, M.; Zhang, Y.; Liu, X.; Zhao, X.; Hu, Y.; Yang, Z.; Yang, C.; Yuan, Z.; Chen, Y. Layer-by-Layer Solution-Processed Organic Solar Cells with Perylene Diimides as Acceptors. *ACS Applied Materials and Interfaces* **2021**, *13* (25), 29876–29884.

(85) Firdaus, Y.; Le Corre, V. M.; Khan, J. I.; Kan, Z.; Laquai, F.; Beaujuge, P. M.; Anthopoulos, T. D. Key Parameters Requirements for Non-Fullerene-Based Organic Solar Cells with Power Conversion Efficiency >20%. *Advanced Science* **2019**, *6* (9), 1802028.

(86) Cui, Y.; Yao, H.; Zhang, J.; Xian, K.; Zhang, T.; Hong, L.; Wang, Y.; Xu, Y.; Ma, K.; An, C.; He, C.; Wei, Z.; Gao, F.; Hou, J. Single-Junction Organic Photovoltaic Cells with Approaching 18% Efficiency. *Advanced Materials* **2020**, *32* (19), 1–7.

(87) Kan, B.; Zhang, J.; Liu, F.; Wan, X.; Li, C.; Ke, X.; Wang, Y.; Feng, H.; Zhang, Y.; Long, G.; Friend, R. H.; Bakulin, A. A.; Chen, Y. Fine-Tuning the Energy Levels of a Nonfullerene Small-Molecule Acceptor to Achieve a High Short-Circuit Current and a Power Conversion Efficiency over 12% in Organic Solar Cells. *Advanced Materials* **2018**, *30* (3), 1–8.

(88) Tokmoldin, N.; Hosseini, S. M.; Raoufi, M.; Phuong, L. Q.; Sandberg, O. J.; Guan, H.; Zou, Y.; Neher, D.; Shoaee, S. Extraordinarily Long Diffusion Length in PM6:Y6 Organic Solar Cells. *Journal of Materials Chemistry A* **2020**, *8* (16), 7854–7860.

(89) Yuan, J.; Zhang, Y.; Zhou, L.; Zhang, G.; Yip, H. L.; Lau, T. K.; Lu, X.; Zhu, C.; Peng, H.; Johnson, P. A.; Leclerc, M.; Cao, Y.; Ulanski, J.; Li, Y.; Zou, Y. Single-Junction Organic Solar Cell with over 15% Efficiency Using Fused-Ring Acceptor with Electron-Deficient Core. *Joule* **2019**, *3* (4), 1140–1151.

(90) Brabec, C. J.; Heeney, M.; Mc Culloch, I.; Nelson, J. Influence of Blend Microstructure on Bulk Heterojunction Organic Photovoltaic Performance. *Chemical Society Reviews* **2011**, *40* (3), 1185–1199.

(91) Upama, M. B.; Elumalai, N. K.; Mahmud, M. A.; Wright, M.; Wang, D.; Xu, C.; Uddin, A. Effect of Annealing Dependent Blend Morphology and Dielectric Properties on the Performance and Stability of Non-Fullerene Organic Solar Cells. *Solar Energy Materials and Solar Cells* **2018**, *176*, 109–118.

(92) Ma, W.; Tumbleston, J. R.; Wang, M.; Gann, E.; Huang, F.; Ade, H. Domain Purity, Miscibility, and Molecular Orientation at Donor/Acceptor Interfaces in High Performance Organic Solar Cells: Paths to Further Improvement. *Advanced Energy Materials* **2013**, *3* (7), 864–872.

(93) Li, J.; Wang, Y.; Liang, Z.; Wang, N.; Tong, J.; Yang, C.; Bao, X.; Xia, Y. Enhanced Organic Photovoltaic Performance through Modulating Vertical Composition Distribution and Promoting Crystallinity of the Photoactive Layer by Diphenyl Sulfide Additives. *ACS Applied Materials and Interfaces* **2019**, *11* (7), 7022–7029.

(94) Ji, Y.; Xu, L.; Hao, X.; Gao, K. Energy Loss in Organic Solar Cells: Mechanisms, Strategies, and Prospects. *Solar RRL* **2020**, *4* (7), 1–17.

(95) Huang, D.; Li, Y.; Xu, Z.; Zhao, S.; Zhao, L.; Zhao, J. Enhanced Performance and Morphological Evolution of PTB7:PC71BM Polymer Solar Cells by Using Solvent Mixtures with Different Additives. *Physical Chemistry Chemical Physics* **2015**, *17* (12), 8053–8060.

(96) Wienhold, K. S.; Körstgens, V.; Grott, S.; Jiang, X.; Schwartzkopf, M.; Roth, S. V.; Müller-Buschbaum, P. Effect of Solvent Additives on the Morphology and Device Performance of Printed Nonfullerene Acceptor Based Organic Solar Cells. *ACS Applied Materials and Interfaces* **2019**, *11*, 42313–42321.

(97) Qin, M.; Cheng, P.; Mai, J.; Lau, T. K.; Zhang, Q.; Wang, J.; Yan, C.; Liu, K.; Su, C. J.; You, W.; Lu, X.; Zhan, X. Enhancing Efficiency and Stability of Organic Solar Cells by UV Absorbent. *Solar RRL* **2017**, *1* (12), 1–7.

(98) Jin, F.; Ding, G.; Wang, Y.; Yuan, J.; Guo, W.; Yuan, H.; Sheng, C.; Ma, W.; Zhao, H. Thermal Annealing Effect on Ultrafast Charge Transfer in All-Polymer Solar Cells with a Non-Fullerene Acceptor N2200. *Journal of Physical Chemistry C* **2017**, *121* (16), 8804–8811.

(99) Adhikari, N.; Khatiwada, D.; Dubey, A.; Qiao, Q. Device and Morphological Engineering of Organic Solar Cells for Enhanced Charge Transport and Photovoltaic Performance. *Journal of Photonics for Energy* **2015**, *5* (1), 057207.

(100) Moustafa, E.; Torimtubun, A. A. A.; Pallarès, J.; Marsal, L. F. Effect of Additives and Annealing on the Performance of Nonfullerene-Based Binary and Ternary Organic Photovoltaics. *Solar RRL* **2021**, *2100480*, 1–16.

(101) Grott, S.; Kotobi, A.; Reb, L. K.; Weindl, C. L.; Guo, R.; Yin, S.; Wienhold, K. S.; Chen, W.; Ameri, T.; Schwartzkopf, M.; Roth, S. V.; Müller-Buschbaum, P. Solvent Tuning of the Active Layer Morphology of Non-Fullerene Based Organic Solar Cells. *Solar RRL* **2022**, *6* (6), 1–7.

(102) Moustafa, E.; Méndez, M.; Sánchez, J. G.; Pallarès, J.; Palomares, E.; Marsal, L. F. Thermal Activation of PEDOT : PSS / PM6 : Y7 Based Films Leads to Unprecedent High Short-Circuit Current Density in Nonfullerene Organic Photovoltaics. *Advanced Energy Materials* **2022**, 2203241.

(103) Murari, N. M.; Crane, M. J.; Earmme, T.; Hwang, Y. J.; Jenekhe, S. A. Annealing Temperature Dependence of the Efficiency and Vertical Phase Segregation of Polymer/Polymer Bulk Heterojunction Photovoltaic Cells. *Applied Physics Letters* **2014**, *104* (22), 223906.

(104) Shoaee, S.; Stolterfoht, M.; Neher, D. The Role of Mobility on Charge Generation, Recombination, and Extraction in Polymer-Based Solar Cells. *Advanced Energy Materials* **2018**, *8* (28), 1–20.

(105) Han, G.; Yi, Y.; Shuai, Z. From Molecular Packing Structures to Electronic Processes: Theoretical Simulations for Organic Solar Cells. *Advanced Energy Materials* **2018**, *8* (28), 1–16.

(106) Cao, B.; He, X.; Fetterly, C. R.; Olsen, B. C.; Luber, E. J.; Buriak, J. M. Role of Interfacial Layers in Organic Solar Cells: Energy Level Pinning versus Phase Segregation. *ACS Applied Materials and Interfaces* **2016**, *8* (28), 18238–18248.

(107) Chen, L. M.; Xu, Z.; Hong, Z.; Yang, Y. Interface Investigation and Engineering - Achieving High Performance Polymer Photovoltaic Devices. *Journal of Materials Chemistry* **2010**, *20* (13), 2575–2598.

(108) Moustafa, E.; Marsal, L. F.; Pallarès, J. Significant Stability Improvement of Fullerene Organic Photovoltaics via ZnO Film Modification through the Intermittent Spray Pyrolysis Technique. *ACS Applied Energy Materials* **2022**.

(109) Moustafa, E.; Méndez, M.; Pallarès, J.; Marsal, L. F. Low Temperature Based PDINO Cathode Interlayer for High Operational Photostable Inverted Non-Fullerene Organic Solar Cells. *Solar Energy Materials and Solar Cells* **2022**, *248*, 111985.

(110) Lloyd, M. T.; Olson, D. C.; Lu, P.; Fang, E.; Moore, D. L.; White, M. S.; Reese, M. O.; Ginley, D. S.; Hsu, J. W. P. Impact of Contact Evolution on the Shelf Life of Organic Solar Cells. *Journal of Materials Chemistry* **2009**, *19* (41), 7638–7642.

(111) Macleod, B. A.; Tremolet De Villers, B. J.; Schulz, P.; Ndione, P. F.; Kim, H.; Giordano, A. J.; Zhu, K.; Marder, S. R.; Graham, S.; Berry, J. J.; Kahn, A.; Olson, D. C. Stability of Inverted Organic Solar Cells with ZnO Contact Layers Deposited from Precursor Solutions. *Energy and Environmental Science* **2015**, *8* (2), 592–601.

(112) Jagadamma, L. K.; Abdelsamie, M.; El Labban, A.; Aresu, E.; Ngongang Ndjawa, G. O.; Anjum, D. H.; Cha,

References

D.; Beaujuge, P. M.; Amassian, A. Efficient Inverted Bulk-Heterojunction Solar Cells from Low-Temperature Processing of Amorphous ZnO Buffer Layers. *Journal of Materials Chemistry A* **2014**, *2* (33), 13321–13331.

(113) Duan, L.; Hoex, B.; Uddin, A. Progress in Semitransparent Organic Solar Cells. *Solar RRL* **2021**, *5* (5), 1–23.

(114) Lee, Y. J.; Wang, J.; Cheng, S. R.; Hsu, J. W. P. Solution Processed ZnO Hybrid Nanocomposite with Tailored Work Function for Improved Electron Transport Layer in Organic Photovoltaic Devices. *ACS Applied Materials and Interfaces* **2013**, *5* (18), 9128–9133.

(115) Upama, M. B.; Mahmud, M. A.; Conibeer, G.; Uddin, A. Trendsetters in High-Efficiency Organic Solar Cells: Toward 20% Power Conversion Efficiency. *Solar RRL* **2020**, *4* (1), 1900342.

(116) Özgür, Ü.; Alivov, Y. I.; Liu, C.; Teke, A.; Reshchikov, M. A.; Doğan, S.; Avrutin, V.; Cho, S. J.; Morkoç, H. A Comprehensive Review of ZnO Materials and Devices. *Journal of Applied Physics* **2005**, *98* (4), 1–103.

(117) Cui, Y.; Yao, H.; Zhang, J.; Zhang, T.; Wang, Y.; Hong, L.; Xian, K.; Xu, B.; Zhang, S.; Peng, J.; Wei, Z.; Gao, F.; Hou, J. Over 16% Efficiency Organic Photovoltaic Cells Enabled by a Chlorinated Acceptor with Increased Open-Circuit Voltages. *Nature Communications* **2019**, *10* (1), 1–8.

(118) Crisp, R. W.; Hashemi, F. S. M.; Alkemade, J.; Kirkwood, N.; Grimaldi, G.; Kinge, S.; Siebbeles, L. D. A.; van Ommen, J. R.; Houtepen, A. J. Atomic Layer Deposition of ZnO on InP Quantum Dot Films for Charge Separation, Stabilization, and Solar Cell Formation. *Advanced Materials Interfaces* **2020**, *7* (4), 1–8.

(119) Jayakumar, O. D.; Tyagi, A. K. Piezoelectric Inkjet Printed Films and Patterns of ZnO and Mn Doped ZnO: Formation of Bifunctional Zn0.98Mn0.02O Films. *Journal of Materials Chemistry* **2011**, *21* (33), 12246–12250.

(120) Kwon, J.; Hong, S.; Lee, H.; Yeo, J.; Lee, S. S.; Ko, S. H. Direct Selective Growth of ZnO Nanowire Arrays from Inkjet-Printed Zinc Acetate Precursor on a Heated Substrate. *Nanoscale Research Letters* **2013**, *8* (1), 1–6.

(121) Moustafa, E.; Sánchez, J. G.; Marsal, L. F.; Pallarès, J. Stability Enhancement of High-Performance Inverted Polymer Solar Cells Using ZnO Electron Interfacial Layer Deposited by Intermittent Spray Pyrolysis Approach. *ACS Applied Energy Materials* **2021**, *4* (4), 4099–4111.

(122) Ma, Z.; Tang, Z.; Wang, E.; Andersson, M. R.; Inganäs, O.; Zhang, F. Influences of Surface Roughness of ZnO Electron Transport Layer on the Photovoltaic Performance of Organic Inverted Solar Cells. *Journal of Physical Chemistry C* **2012**, *116* (46), 24462–24468.

(123) Steim, R.; Kogler, F. R.; Brabec, C. J. Interface Materials for Organic Solar Cells. *Journal of Materials Chemistry* **2010**, *20* (13), 2499–2512.

(124) Corzo, D.; Almasabi, K.; Bihar, E.; Macphee, S.; Rosas-Villalva, D.; Gasparini, N.; Inal, S.; Baran, D. Digital Inkjet Printing of High-Efficiency Large-Area Nonfullerene Organic Solar Cells. *Advanced Materials Technologies* **2019**, *4* (7), 1–9.

(125) Fu, H.; Wang, Z.; Sun, Y. Advances in Non-Fullerene Acceptor Based Ternary Organic Solar Cells. *Solar RRL* **2018**, *2* (1), 1–18.

(126) Wang, D.; Liu, H.; Li, Y.; Zhou, G.; Zhan, L.; Zhu, H.; Lu, X.; Chen, H.; Li, C. Z. High-Performance and Eco-Friendly Semitransparent Organic Solar Cells for Greenhouse Applications. *Joule* **2021**, *5* (4), 945–957.

(127) Liu, X.; Yan, Y.; Yao, Y.; Liang, Z. Ternary Blend Strategy for Achieving High-Efficiency Organic Solar Cells with Nonfullerene Acceptors Involved. *Advanced Functional Materials* **2018**, *28* (29), 1802004.

(128) Doumon, N. Y.; Yang, L.; Rosei, F. Ternary Organic Solar Cells: A Review of the Role of the Third Element. *Nano Energy* **2022**, *94* (January), 106915. https://doi.org/10.1016/j.nanoen.2021.106915.

(129) Ho, C. H. Y.; Kim, T.; Xiong, Y.; Firdaus, Y.; Yi, X.; Dong, Q.; Rech, J. J.; Gadisa, A.; Booth, R.; O'Connor, B. T.; Amassian, A.; Ade, H.; You, W.; Anthopoulos, T. D.; So, F. High-Performance Tandem Organic Solar Cells Using HSolar as the Interconnecting Layer. *Advanced Energy Materials* **2020**, *10* (25), 2000823.

(130) Wang, X.; Sun, Q.; Gao, J.; Wang, J.; Xu, C.; Ma, X.; Zhang, F. Recent Progress of Organic Photovoltaics with Efficiency over 17%. *Energies* **2021**, *14* (14), 4200.

(131) An, Q.; Ma, X.; Gao, J.; Zhang, F. Solvent Additive-Free Ternary Polymer Solar Cells with 16.27% Efficiency. *Science Bulletin* **2019**, *64* (8), 504–506.

(132) Ma, X.; Wang, J.; Gao, J.; Hu, Z.; Xu, C.; Zhang, X.; Zhang, F. Achieving 17.4% Efficiency of Ternary Organic Photovoltaics with Two Well-Compatible Nonfullerene Acceptors for Minimizing Energy Loss. *Advanced Energy Materials* **2020**, *10* (31), 1–9.

(133) Li, M.; Lin, H.; Ma, B.; Yu, X.; Du, X.; Yang, G.; Zheng, C.; Tao, S. Non-Fullerene Acceptor Alloy Strategy Enabling Stable Ternary Polymer Solar Cells with Efficiency of 17.74%. *Journal of Materials Chemistry C* **2022**, *10* (8), 3207–3216.

(134) Xu, X.; Li, Y.; Peng, Q. Ternary Blend Organic Solar Cells: Understanding the Morphology from Recent Progress. *Advanced Materials* **2022**, *2107476*, 1–30.

(135) Zhu, R.; Li, X.; Cao, L.; Du, X.; Lin, H.; Yang, G.; Zheng, C.; Chen, Z.; Tao, S. Sequential Deposition Method Processed Ternary Organic Solar Cells with Efficiency of 17.92%. *Organic Electronics* **2022**, *111*, 106651.

(136) Jung, S.; Cho, Y.; Kang, S. H.; Yoon, S. J.; Yang, C. Effect of Third Component on Efficiency and Stability in Ternary Organic Solar Cells: More than a Simple Superposition. *Solar RRL* **2022**, *6* (2), 1–29.

(137) Tyona, M. D. A Theoritical Study on Spin Coating Technique. *Advances in material research* **2013**, *2* (4), 195–208.

(138) Lehraki, N.; Aida, M. S.; Abed, S.; Attaf, N.; Attaf, A.; Poulain, M. ZnO Thin Films Deposition by Spray Pyrolysis: Influence of Precursor Solution Properties. *Current Applied Physics* **2012**, *12* (5), 1283–1287.

(139) Noh, Y. J.; Na, S. I.; Kim, S. S. Inverted Polymer Solar Cells Including ZnO Electron Transport Layer Fabricated by Facile Spray Pyrolysis. *Solar Energy Materials and Solar Cells* **2013**, *117*, 139–144.

(140) Ji, R.; Zheng, D.; Zhou, C.; Cheng, J.; Yu, J.; Li, L. Low-Temperature Preparation of Tungsten Oxide Anode Buffer Layer via Ultrasonic Spray Pyrolysis Method for Large-Area Organic Solar Cells. *Materials* **2017**, *10* (7), 820.

(141) Adamopoulos, G.; Bashir, A.; Wöbkenberg, P. H.; Bradley, D. D. C.; Anthopoulos, T. D. Electronic Properties of ZnO Field-Effect Transistors Fabricated by Spray Pyrolysis in Ambient Air. *Applied Physics Letters* **2009**, *95* (13), 133507.

(142) SINGH, D. V. K. Thin Film Deposition by Spray Pyroysis Techniques. *Emerging Technologies and Innovative Research (JETIR)* **2017**, *4* (11), 1–9.

(143) Forrest, S. R. The Path to Ubiquitous and Low-Cost Organic Electronic Appliances on Plastic. *Nature* **2004**, *428*, 911–918.

(144) Hartnagel, P.; Kirchartz, T. Understanding the Light-Intensity Dependence of the Short-Circuit Current of Organic Solar Cells. *Advanced Theory and Simulations* **2020**, *3* (10), 2000116.

(145) Cowan, S. R.; Roy, A.; Heeger, A. J. Recombination in Polymer-Fullerene Bulk Heterojunction Solar Cells. *Physical Review B - Condensed Matter and Materials Physics* **2010**, *82* (24), 1–10.

(146) Proctor, C. M.; Nguyen, T. Q. Effect of Leakage Current and Shunt Resistance on the Light Intensity Dependence of Organic Solar Cells. *Applied Physics Letters* **2015**, *106* (8), 083301.

(147) Liu, Z.; Wang, N. Small Energy Loss in Ternary Organic Solar Cells with a Blend of Cascade Energy Levels: Two Fullerene-Free Acceptors as the Electron Acceptor. *Journal of Materials Chemistry C* **2019**, *7* (32), 10039–10048.

(148) Gupta, V.; Kyaw, A. K. K.; Wang, D. H.; Chand, S.; Bazan, G. C.; Heeger, A. J. Barium: An Efficient Cathode Layer for Bulk-Heterojunction Solar Cells. *Scientific Reports* **2013**, *3*, 6–11.

(149) Mihailetchi, V. D.; Koster, L. J. A.; Blom, P. W. M.; Melzer, C.; De Boer, B.; Van Duren, J. K. J.; Janssen, R. A. J. Compositional Dependence of the Performance of Poly(p-Phenylene Vinylene):Methanofullerene Bulk-Heterojunction Solar Cells. *Advanced Functional Materials* **2005**, *15* (5), 795–801.

(150) Wu, J.-L.; Chen, F.-C.; Hsiao, Y.-S.; Chien, F.-C.; Chen, P.; Kuo, C.-H.; Huang, M. H.; Hsu, C.-S. Nanoparticles on the Performance of Polymer Bulk Heterojunction Solar Cells. *ACS nano* **2011**, *5* (2), 959–967.

(151) Jiang, B. H.; Wang, Y. P.; Liao, C. Y.; Chang, Y. M.; Su, Y. W.; Jeng, R. J.; Chen, C. P. Improved Blend Film Morphology and Free Carrier Generation Provide a High-Performance Ternary Polymer Solar Cell. *ACS Applied Materials and Interfaces* **2021**, *13* (1), 1076–1085.

(152) Zhao, J.; Li, Y.; Lin, H.; Liu, Y.; Jiang, K.; Mu, C.; Ma, T.; Lin Lai, J. Y.; Hu, H.; Yu, D.; Yan, H. High-Efficiency Non-Fullerene Organic Solar Cells Enabled by a Difluorobenzothiadiazole-Based Donor Polymer Combined with a Properly Matched Small Molecule Acceptor. *Energy and Environmental Science* **2015**, *8* (2), 520–525.

(153) Röhr, J. A.; Moia, D.; Haque, S. A.; Kirchartz, T.; Nelson, J. Exploring the Validity and Limitations of the Mott-Gurney Law for Charge-Carrier Mobility Determination of Semiconducting Thin-Films. *Journal of Physics Condensed Matter* **2018**, *30* (10), 105901.

(154) Moiz, S. A.; Khan, I. A.; Younis, W. A.; Karimov, K. S. Space Charge–Limited Current Model for Polymers. In *Conducting Polymers*; 2016; pp 91–117.

(155) Xing, G.; Mathews, N.; Sun, S.; Lim, S. S.; Lam, Y. M.; Graïzel, M.; Mhaisalkar, S.; Sum, T. C. Long-Range Balanced Electron-and Hole-Transport Lengths in Organic-Inorganic CH3NH3PbI3. *Science* **2013**, *342* (6156), 344–347.

(156) Moiz, S. A.; Ahmed, M. M.; Karimov, K. S. Estimation of Electrical Parameters of OD Organic Semiconductor Diode from Measured I-V Characteristics. *ETRI Journal* **2005**, *27* (3), 319–324.

(157) Pospisil, J.; Zmeskal, O.; Nespurek, S.; Krajcovic, J.; Weiter, M.; Kovalenko, A. Density of Bulk Trap States of Hybrid Lead Halide Perovskite Single Crystals: Temperature Modulated Space-Charge-Limited-Currents. *Scientific Reports* **2019**, *9* (1), 1–8.

(158) Ananda, W. External Quantum Efficiency Measurement of Solar Cell. *QiR 2017 - 2017 15th International Conference on Quality in Research (QiR): International Symposium on Electrical and Computer Engineering* **2017**, 450–456.

(159) NREL. Reference Air Mass 1.5 Spectra.

(160) Armin, A.; Velusamy, M.; Wolfer, P.; Zhang, Y.; Burn, P. L.; Meredith, P.; Pivrikas, A. Quantum Efficiency of Organic Solar Cells: Electro-Optical Cavity Considerations. *ACS Photonics* **2014**, *1* (3), 173–181.

(161) Forrest, S. R. The Limits to Organic Photovoltaic Cell Efficiency. *MRS Bulletin* **2005**, *30* (1), 28–32.

(162) Urbach, F. The Long-Wavelength Edge of Photographic Sensitivity and of the Electronic Absorption of Solids. *Physical Review* **1953**, *92* (5), 1324.

(163) Liu, S.; Yuan, J.; Deng, W.; Luo, M.; Xie, Y.; Liang, Q.; Zou, Y.; He, Z.; Wu, H.; Cao, Y. High-Efficiency Organic Solar Cells with Low Non-Radiative Recombination Loss and Low Energetic Disorder. *Nature Photonics* **2020**, *14* (5), 300–305.

(164) Wang, F.; Yang, M.; Zhang, Y.; Yang, L.; Fan, L.; Lv, S.; Liu, X.; Han, D.; Yang, J. Activating Old Materials with New Architecture: Boosting Performance of Perovskite Solar Cells with H 2 O-Assisted Hierarchical Electron Transporting Layers. *Advanced Science* **2019**, *6* (4), 1801170.

(165) Von Hauff, E. Impedance Spectroscopy for Emerging Photovoltaics. *Journal of Physical Chemistry C* **2019**, *123* (18), 11329–11346.

(166) Osorio, E.; Sánchez, J. G.; Acquaroli, L. N.; Pacio, M.; Ferré-Borrull, J.; Pallarès, J.; Marsal, L. F. Degradation

Analysis of Encapsulated and Nonencapsulated TiO2/PTB7:PC70BM/V2O5 Solar Cells under Ambient Conditions via Impedance Spectroscopy. *ACS Omega* **2017**, *2* (7), 3091–3097.

(167) Pockett, A.; Lee, H. K. H.; Coles, B. L.; Tsoi, W. C.; Carnie, M. J. A Combined Transient Photovoltage and Impedance Spectroscopy Approach for a Comprehensive Study of Interlayer Degradation in Non-Fullerene Acceptor Organic Solar Cells. *Nanoscale* **2019**, *11* (22), 10872–10883.

(168) Contreras-Bernal, L.; Ramos-Terrón, S.; Riquelme, A.; Boix, P. P.; Idígoras, J.; Mora-Seró, I.; Anta, J. A. Impedance Analysis of Perovskite Solar Cells: A Case Study. *Journal of Materials Chemistry A* **2019**, *7* (19), 12191–12200.

(169) Hegedus, S. S.; Fagen, E. A. Midgap States in A-Si:H and a-SiGe:H p-i-n Solar Cells and Schottky Junctions by Capacitance Techniques. *Journal of Applied Physics* **1992**, *71* (12), 5941–5951.

(170) Wang, S.; Kaienburg, P.; Klingebiel, B.; Schillings, D.; Kirchartz, T. Understanding Thermal Admittance Spectroscopy in Low-Mobility Semiconductors. *Journal of Physical Chemistry C* **2018**, *122* (18), 9795–9803.

(171) Ecker, B.; Nolasco, J. C.; Pallarés, J.; Marsal, L. F.; Posdorfer, J.; Parisi, J.; Von Hauff, E. Degradation Effects Related to the Hole Transport Layer in Organic Solar Cells. *Advanced Functional Materials* **2011**, *21* (14), 2705–2711.

(172) Walter, T.; Herberholz, R.; Müller, C.; Schock, H. W. Determination of Defect Distributions from Admittance Measurements and Application to Cu(In,Ga)Se2 Based Heterojunctions. *Journal of Applied Physics* **1996**, *80* (8), 4411–4420.

(173) Chen, Z.; Wang, T.; Wen, Z.; Lu, P.; Qin, W.; Yin, H.; Hao, X. Trap State Induced Recombination Effects on Indoor Organic Photovoltaic Cells. *ACS Energy Letters* **2021**, *6*, 3203–3211.

(174) Kaiser, C.; Sandberg, O. J.; Zarrabi, N.; Li, W.; Meredith, P.; Armin, A. A Universal Urbach Rule for Disordered Organic Semiconductors. *Nature Communications* **2021**, *12* (1), 3988.

(175) Emilio Palomares1, Nuria F. Montcada, M. M.; Jesus Jime´nezLopez, W. Y. and G. B. Characterization Techniques for Perovskite Solar Cell Materials. In *Micro and Nano Technologies, Chapter 3 - Optical absorption and photoluminescence spectroscopy, Elsevier*; 2020; pp 49–79.

(176) Duan, L.; Yi, H.; Zhang, Y.; Haque, F.; Xu, C.; Uddin, A. Comparative Study of Light- and Thermal-Induced Degradation for Both Fullerene and Non-Fullerene-Based Organic Solar Cells. *Sustainable Energy and Fuels* **2019**, *3* (3), 723–735.

(177) Brabec, C. J.; Hauch, J. A.; Schilinsky, P.; Waldauf, C. Production Aspects of Organic Photovoltaics and Their Impact on the Commercialization of Devices. *MRS Bulletin* **2005**, *30* (1), 50–52.

(178) Grossiord, N.; Kroon, J. M.; Andriessen, R.; Blom, P. W. M. Degradation Mechanisms in Organic Photovoltaic Devices. *Organic Electronics* **2012**, *13* (3), 432–456.

(179) Jørgensen, M.; Norrman, K.; Krebs, F. C. Stability/Degradation of Polymer Solar Cells. *Solar Energy Materials and Solar Cells* **2008**, *92* (7), 686–714.

(180) Krebs, F. C. Stability and Degradation of Organic and Polymer Solar Cells. In *John Wiley & Sons, Ltd, Chichester, UK*; 2012; Vol. ch. 4, pp 71–108.

(181) Cardinaletti, I.; Kesters, J.; Bertho, S.; Conings, B.; Piersimoni, F.; D'Haen, J.; Lutsen, L.; Nesladek, M.; Van Mele, B.; Van Assche, G.; Vandewal, K.; Salleo, A.; Vanderzande, D.; Maes, W.; Manca, J. V. Toward Bulk Heterojunction Polymer Solar Cells with Thermally Stable Active Layer Morphology. *Journal of Photonics for Energy* **2014**, *4* (1), 040997.

(182) Liu, Q.; Toudert, J.; Liu, F.; Mantilla-Perez, P.; Bajo, M. M.; Russell, T. P.; Martorell, J. Circumventing UV Light Induced Nanomorphology Disorder to Achieve Long Lifetime PTB7-Th:PCBM Based Solar Cells. *Advanced Energy Materials* **2017**, *7* (21), 1–9.

(183) Jagadamma, L. K.; Sajjad, M. T.; Savikhin, V.; Toney, M. F.; Samuel, I. D. W. Correlating Photovoltaic

Properties of a PTB7- Th : PC 71 BM Blend to Photophysics and Microstructure as a Function of Thermal Annealing. *Journal of Materials Chemistry A* **2017**, *5*, 14646–14657.

(184) Planes, E.; Juillard, S.; Matheron, M.; Charvin, N.; Cros, S.; Qian, D.; Zhang, F.; Berson, S.; Flandin, L. Encapsulation Effect on Performance and Stability of Organic Solar Cells. *Advanced Materials Interfaces* **2020**, *7* (15), 1–13.

(185) Ashraf, U.; Baishakhi, U. M.; Haimang, Y.; Leiping, D. Encapsulation of Organic and Perovskite Solar Cells: A Review. *Coatings* **2019**, *9* (2), 65.

(186) Duan, L.; Sang, B.; He, M.; Zhang, Y.; Hossain, M. A.; Rahaman, M. H.; Wei, Q.; Zou, Y.; Uddin, A.; Hoex, B. Interface Modification Enabled by Atomic Layer Deposited Ultra-Thin Titanium Oxide for High-Efficiency and Semitransparent Organic Solar Cells. *Solar RRL* **2020**, *4* (12), 1–12.

(187) Savva, A.; Burgués-Ceballos, I.; Papazoglou, G.; Choulis, S. A. High-Performance Inverted Organic Photovoltaics Without Hole-Selective Contact. *ACS Applied Materials and Interfaces* **2015**, *7* (44), 24608–24615.

(188) Kawano, K.; Pacios, R.; Poplavskyy, D.; Nelson, J.; Bradley, D. D. C.; Durrant, J. R. Degradation of Organic Solar Cells Due to Air Exposure. *Solar Energy Materials and Solar Cells* **2006**, *90* (20), 3520–3530.

(189) Liu, P.; Gao, P.; Liu, X.; Wang, H.; He, J.; Yang, X.; Zeng, Y.; Yan, B.; Fang, J.; Ye, J. High-Performance Organic-Silicon Heterojunction Solar Cells by Using Al-Doped ZnO as Cathode Interlayer. *Solar RRL* **2018**, *2* (3), 1–8.

(190) Kim, Y. H.; Kim, D. G.; Maduwu, R. D.; Jin, H. C.; Moon, D. K.; Kim, J. H. Organic Electrolytes Doped ZnO Layer as the Electron Transport Layer for Bulk Heterojunction Polymer Solar Cells. *Solar RRL* **2018**, *2* (8), 2–8.

(191) Perednis, D.; Gauckler, L. J. Thin Film Deposition Using Spray Pyrolysis. *Journal of Electroceramics* **2005**, *14* (2), 103–111.

(192) Mooney, J. B.; Radding, S. B. Spray Pyrolysis Processing. *Annual Review of Materials Science* **1982**, *12*, 81–101.

(193) Cheng, J.; Hu, R.; Wang, Q.; Zhang, C.; Xie, Z.; Long, Z.; Yang, X.; Li, L. Substrate Temperature Effect on Charge Transport Performance of ZnO Electron Transport Layer Prepared by a Facile Ultrasonic Spray Pyrolysis in Polymer Solar Cells. *International Journal of Photoenergy* **2015**, *2015*.

(194) Prasada Rao, T.; Santhoshkumar, M. C. Effect of Thickness on Structural, Optical and Electrical Properties of Nanostructured ZnO Thin Films by Spray Pyrolysis. *Applied Surface Science* **2009**, *255* (8), 4579–4584. https://doi.org/10.1016/j.apsusc.2008.11.079.

(195) Pallarès, J.; Cabré, R.; Marsal, L. F.; Schropp, R. E. I. A Compact Equivalent Circuit for the Dark Current-Voltage Characteristics of Nonideal Solar Cells. *Journal of Applied Physics* **2006**, *100* (8), 084513–084515.

(196) Nolasco, J. C.; Cabré, R.; Ferré-Borrull, J.; Marsal, L. F.; Estrada, M.; Pallarès, J. Extraction of Poly (3-Hexylthiophene) (P3HT) Properties from Dark Current Voltage Characteristics in a P3HT/ n -Crystalline-Silicon Solar Cell. *Journal of Applied Physics* **2010**, *107* (4), 044505.

(197) Samiee, M.; Joshi, P.; Aidarkhanov, D.; Dalal, V. Measurement of Defect Densities and Urbach Energies of Tail States in PTB7 Solar Cells. *Applied Physics Letters* **2014**, *105* (13), 7–12.

(198) Peiró, A. M.; Ravirajan, P.; Govender, K.; Boyle, D. S.; O'Brien, P.; Bradley, D. D. C.; Nelson, J.; Durrant, J. R. The Effect of Zinc Oxide Nanostructure on the Performance of Hybrid Polymer/Zinc Oxide Solar Cells. In *Organic Photovoltaics VI*; 2005; Vol. 5938, p 593819.

(199) Müller, J.; Rech, B.; Springer, J.; Vanecek, M. TCO and Light Trapping in Silicon Thin Film Solar Cells. *Solar Energy* **2004**, *77* (6), 917–930.

(200) Scholtz, L.; Ladanyi, L.; Mullerova, J. Influence of Surface Roughness on Optical Characteristics of Multilayer

Solar Cells. *Advances in Electrical and Electronic Engineering* **2014**, *12* (6), 631–638.

(201) Krč, J.; Zeman, M.; Kluth, O.; Smole, F.; Topič, M. Effect of Surface Roughness of ZnO:Al Films on Light Scattering in Hydrogenated Amorphous Silicon Solar Cells. *Thin Solid Films* **2003**, *426* (1–2), 296–304.

(202) Sheng, X.; Broderick, L. Z.; Kimerling, L. C. Photonic Crystal Structures for Light Trapping in Thin-Film Si Solar Cells: Modeling, Process and Optimizations. *Optics Communications* **2014**, *314*, 41–47. https://doi.org/10.1016/j.optcom.2013.07.085.

(203) Reese, M. O.; Gevorgyan, S. A.; Jørgensen, M.; Bundgaard, E.; Kurtz, S. R.; Ginley, D. S.; Olson, D. C.; Lloyd, M. T.; Morvillo, P.; Katz, E. A.; Elschner, A.; Haillant, O.; Currier, T. R.; Shrotriya, V.; Hermenau, M.; Riede, M.; Kirov, K. R.; Trimmel, G.; Rath, T.; Inganäs, O.; Zhang, F.; Andersson, M.; Tvingstedt, K.; Lira-Cantu, M.; Laird, D.; McGuiness, C.; Gowrisanker, S.; Pannone, M.; Xiao, M.; Hauch, J.; Steim, R.; Delongchamp, D. M.; Rösch, R.; Hoppe, H.; Espinosa, N.; Urbina, A.; Yaman-Uzunoglu, G.; Bonekamp, J. B.; Van Breemen, A. J. J. M.; Girotto, C.; Voroshazi, E.; Krebs, F. C. Consensus Stability Testing Protocols for Organic Photovoltaic Materials and Devices. *Solar Energy Materials and Solar Cells* **2011**, *95* (5), 1253–1267.

(204) Guerrero, A.; Marchesi, L. F.; Boix, P. P.; Bisquert, J.; Garcia-Belmonte, G. Recombination in Organic Bulk Heterojunction Solar Cells: Small Dependence of Interfacial Charge Transfer Kinetics on Fullerene Affinity. *Journal of Physical Chemistry Letters* **2012**, *3* (10), 1386–1392.

(205) Hailegnaw, B.; Sariciftci, N. S.; Scharber, M. C. Impedance Spectroscopy of Perovskite Solar Cells: Studying the Dynamics of Charge Carriers Before and After Continuous Operation. *Physica Status Solidi (A) Applications and Materials Science* **2020**, *217* (22), 1–8.

(206) Arredondo, B.; Martín-López, M. B.; Romero, B.; Vergaz, R.; Romero-Gomez, P.; Martorell, J. Monitoring Degradation Mechanisms in PTB7:PC71BM Photovoltaic Cells by Means of Impedance Spectroscopy. *Solar Energy Materials and Solar Cells* **2016**, *144*, 422–428.

(207) He, Z.; Huang, K.; Guo, C.; Jin, Z.; Hou, C. A Debye Dispersion Model of a Two-Layered Material. *AIP Advances* **2019**, *9* (4), 045321.

(208) Schroeder, H. Poole-Frenkel-Effect as Dominating Current Mechanism in Thin Oxide Films - An Illusion?! *Journal of Applied Physics* **2015**, *117* (21), 215103.

(209) Mullenbach, T. K.; Zou, Y.; Holst, J.; Holmes, R. J. Interpreting Impedance Spectra of Organic Photovoltaic Cells - Extracting Charge Transit and Recombination Rates. *Journal of Applied Physics* **2014**, *116* (12), 124513.

(210) Ondo-Ndong, R.; Essone-Obame, H.; Moussambi, Z. H.; Koumba, N. Capacitive Properties of Zinc Oxide Thin Films by Radiofrequency Magnetron Sputtering. *Journal of Theoretical and Applied Physics* **2018**, *12* (4), 309–317.

(211) Torabi, S.; Jahani, F.; Van Severen, I.; Kanimozhi, C.; Patil, S.; Havenith, R. W. A.; Chiechi, R. C.; Lutsen, L.; Vanderzande, D. J. M.; Cleij, T. J.; Hummelen, J. C.; Koster, L. J. A. Strategy for Enhancing the Dielectric Constant of Organic Semiconductors without Sacrificing Charge Carrier Mobility and Solubility. *Advanced Functional Materials* **2015**, *25* (1), 150–157.

(212) Sánchez, J. G.; Balderrama, V. S.; Estrada, M.; Osorio, E.; Ferré-Borrull, J.; Marsal, L. F.; Pallarès, J. Stability Study of High Efficiency Polymer Solar Cells Using TiOx as Electron Transport Layer. *Solar Energy* **2017**, *150*, 147–155.

(213) Li, Y.; Lin, Y. Planar Heterojunctions for Reduced Non-Radiative Open-Circuit Voltage Loss and Enhanced Stability of Organic Solar Cells. *materials chemistry C* **2021**, *9*, 11715–11721.

(214) Lenes, M.; Morana, M.; Brabec, C. J.; Blom, P. W. M. Recombination-Limited Photocurrents in Low Bandgap Polymer/Fullerene Solar Cells. *Advanced Functional Materials* **2009**, *19* (7), 1106–1111.

(215) Xu, W.; Xia, R.; Ye, T.; Zhao, L.; Kan, Z.; Mei, Y.; Yan, C.; Zhang, X. W.; Lai, W. Y.; Keivanidis, P. E.; Huang, W. Understanding the Light Soaking Effects in Inverted Organic Solar Cells Functionalized with Conjugated Macroelectrolyte Electron-Collecting Interlayers. *Advanced Science* **2015**, *3* (2), 1–7.

References

(216) Kuwabara, T.; Yano, K.; Yamaguchi, T.; Taima, T.; Takahashi, K.; Son, D.; Marumoto, K. Mechanistic Investigation into the Light Soaking Effect Observed in Inverted Polymer Solar Cells Containing Chemical Bath Deposited Titanium Oxide. *Journal of Physical Chemistry C* **2015**, *119* (10), 5274–5280.

(217) Barreiro-Argüelles, D.; Ramos-Ortiz, G.; Maldonado, J. L.; Pérez-Gutiérrez, E.; Romero-Borja, D.; Meneses-Nava, M. A.; Nolasco, J. C. Stability Study in Organic Solar Cells Based on PTB7:PC71BM and the Scaling Effect of the Active Layer. *Solar Energy* **2018**, *163*, 510–518.

(218) Romero-Gomez, P.; Betancur, R.; Martinez-Otero, A.; Elias, X.; Mariano, M.; Romero, B.; Arredondo, B.; Vergaz, R.; Martorell, J. Enhanced Stability in Semi-Transparent PTB7/PC71BM Photovoltaic Cells. *Solar Energy Materials and Solar Cells* **2015**, *137*, 44–49.

(219) Ko, E. Y.; Park, G. E.; Lee, J. H.; Kim, H. J.; Lee, D. H.; Ahn, H.; Uddin, M. A.; Woo, H. Y.; Cho, M. J.; Choi, D. H. Excellent Long-Term Stability of Power Conversion Efficiency in Non-Fullerene-Based Polymer Solar Cells Bearing Tricyanovinylene-Functionalized n-Type Small Molecules. *ACS Applied Materials and Interfaces* **2017**, *9* (10), 8838–8847.

(220) Duan, L.; Uddin, A. Progress in Stability of Organic Solar Cells. *Advanced Science* **2020**, *7* (11), 1903259.

(221) Liu, B.; Wang, Y.; Chen, P.; Zhang, X.; Sun, H.; Tang, Y.; Liao, Q.; Huang, J.; Wang, H.; Meng, H.; Guo, X. Boosting E Ffi Ciency and Stability of Organic Solar Cells Using Ultralow-Cost BiOCl Nanoplates as Hole Transporting Layers. *ACS Applied Materials & Interfaces* **2019**, *11*, 33505–33514.

(222) Huai, Z.; Wang, L.; Sun, Y.; Fan, R.; Huang, S.; Zhao, X.; Li, X.; Fu, G.; Yang, S. High-E Ffi Ciency and Stable Organic Solar Cells Enabled by Dual Cathode Bu Ff Er Layers. *ACS Applied Materials & Interfaces* **2018**, *10*, 5682–5692.

(223) Page, Z. A.; Liu, Y.; Duzhko, V. V. Fulleropyrrolidine Interlayers: Tailoring Electrodes to Raise Organic Solar Cell Efficiency. *Science* **2014**, *346* (6208), 441–444.

(224) Lee, J. A Highly Robust and Stable Graphene-Encapsulated Cu-Grid Hybrid Transparent Electrode. *materials chemistry A* **2018**, *6*, 24805–24813.

(225) Wu, J.; Luke, J.; Lee, H. K. H.; Shakya Tuladhar, P.; Cha, H.; Jang, S. Y.; Tsoi, W. C.; Heeney, M.; Kang, H.; Lee, K.; Kirchartz, T.; Kim, J. S.; Durrant, J. R. Tail State Limited Photocurrent Collection of Thick Photoactive Layers in Organic Solar Cells. *Nature Communications* **2019**, *10* (1), 5159.

(226) Cheng, H. W.; Raghunath, P.; Wang, K. L.; Cheng, P.; Haung, T.; Wu, Q.; Yuan, J.; Lin, Y. C.; Wang, H. C.; Zou, Y.; Wang, Z. K.; Lin, M. C.; Wei, K. H.; Yang, Y. Potassium-Presenting Zinc Oxide Surfaces Induce Vertical Phase Separation in Fullerene-Free Organic Photovoltaics. *Nano Letters* **2020**, *20* (1), 715–721.

(227) Cui, Y.; Yao, H.; Hong, L.; Zhang, T.; Tang, Y.; Lin, B.; Xian, K.; Gao, B.; An, C.; Bi, P.; Ma, W.; Hou, J. Organic Photovoltaic Cell with 17% Efficiency and Superior Processability. *National Science Review* **2020**, *7* (7), 1239–1246.

(228) Ye, W.; Yang, Y.; Zhang, Z.; Zhu, Y.; Ye, L.; Miao, C.; Lin, Y.; Zhang, S. Nonfullerene All-Small-Molecule Organic Solar Cells: Prospect and Limitation. *Solar RRL* **2020**, *4*, 2000258.

(229) Zhu, T.; Zheng, L.; Xiao, Z.; Meng, X.; Liu, L.; Ding, L.; Gong, X. Functionality of Non-Fullerene Electron Acceptors in Ternary Organic Solar Cells. *Solar RRL* **2019**, *3* (12), 1–8.

(230) Tong, Y.; Xiao, Z.; Du, X.; Zuo, C.; Li, Y.; Lv, M.; Yuan, Y.; Yi, C.; Hao, F.; Hua, Y.; Lei, T.; Lin, Q.; Sun, K.; Zhao, D.; Duan, C.; Shao, X.; Li, W.; Yip, H. L.; Xiao, Z.; Zhang, B.; Bian, Q.; Cheng, Y.; Liu, S.; Cheng, M.; Jin, Z.; Yang, S.; Ding, L. Progress of the Key Materials for Organic Solar Cells. *Science China Chemistry* **2020**, *63* (6), 758–765.

(231) Wu, J.; Lee, J.; Chin, Y. C.; Yao, H.; Cha, H.; Luke, J.; Hou, J.; Kim, J. S.; Durrant, J. R. Exceptionally Low Charge Trapping Enables Highly Efficient Organic Bulk Heterojunction Solar Cells. *Energy and Environmental Science* **2020**, *13* (8), 2422–2430.

(232) Cheng, H.-W.; Mohapatra, A.; Chang, Y.-M.; Liao, C.-Y.; Hsiao, Y.-T.; Chen, C.-H.; Lin, Y.-C.; Huang, S.-

Y.; Chang, B.; Yang, Y.; Chu, C.-W.; Wei, K.-H. High-Performance Organic Solar Cells Featuring Double Bulk Heterojunction Structures with Vertical-Gradient Selenium Heterocyclic Nonfullerene Acceptor Concentrations. *ACS Applied Materials & Interfaces* **2021**, *13* (23), 27227–27236.

(233) Cheng, H. W.; Juan, C. Y.; Mohapatra, A.; Chen, C. H.; Lin, Y. C.; Chang, B.; Cheng, P.; Wang, H. C.; Chu, C. W.; Yang, Y.; Wei, K. H. High-Performance Organic Photovoltaics Incorporating an Active Layer with a Few Nanometer-Thick Third-Component Layer on a Binary Blend Layer. *Nano Letters* **2021**, *21* (5), 2207–2215.

(234) Xue, P.; Dai, S.; Lau, T. K.; Yu, J.; Zhou, J.; Xiao, Y.; Meng, K.; Xie, Z.; Lu, G.; Lu, X.; Han, R. P. S.; Zhan, X. High-Performance Nonfullerene Organic Solar Cells with Unusual Inverted Structure. *Solar RRL* **2020**, *4* (7), 1–8.

(235) Yao, J.; Qiu, B.; Zhang, Z. G.; Xue, L.; Wang, R.; Zhang, C.; Chen, S.; Zhou, Q.; Sun, C.; Yang, C.; Xiao, M.; Meng, L.; Li, Y. Cathode Engineering with Perylene-Diimide Interlayer Enabling over 17% Efficiency Single-Junction Organic Solar Cells. *Nature Communications* **2020**, *11* (1), 2726.

(236) Wang, X.; Zhang, L.; Hu, L.; Xie, Z.; Mao, H.; Tan, L.; Zhang, Y.; Chen, Y. High-Efficiency (16.93%) Pseudo-Planar Heterojunction Organic Solar Cells Enabled by Binary Additives Strategy. *Advanced Functional Materials* **2021**, 2102291.

(237) Zhan, L.; Li, S.; Lau, T. K.; Cui, Y.; Lu, X.; Shi, M.; Li, C. Z.; Li, H.; Hou, J.; Chen, H. Over 17% Efficiency Ternary Organic Solar Cells Enabled by Two Non-Fullerene Acceptors Working in an Alloy-like Model. *Energy and Environmental Science* **2020**, *13* (2), 635–645.

(238) Ismail, Y. A. M.; Soga, T.; Jimbo, T. Features in Optical Absorption and Photocurrent Spectra of Organic Solar Cells Due to Organic/Organic Interface. *Journal of Applied Physics* **2011**, *109* (10), 1–8.

(239) Xiong, C.; Sun, J.; Yang, H.; Jiang, H. Real Reason for High Ideality Factor in Organic Solar Cells: Energy Disorder. *Solar Energy* **2019**, *178* (November 2018), 193–200.

(240) Fu, H.; Gao, W.; Li, Y.; Lin, F.; Wu, X.; Son, J. H.; Luo, J.; Woo, H. Y.; Zhu, Z.; Jen, A. K. Y. A Generally Applicable Approach Using Sequential Deposition to Enable Highly Efficient Organic Solar Cells. *Small Methods* **2020**, *4* (12).

(241) Wang, R.; Jiang, Y.; Gruber, W.; He, Y.; Wu, M.; Weitz, P.; Zhang, K.; Lüer, L.; Forberich, K.; Unruh, T.; Spiecker, E.; Deibel, C.; Li, N.; Brabec, C. J. Tailoring the Nature of Interface States in Efficient and Stable Bilayer Organic Solar Cells by a Transfer-Printing Technique. *Advanced Materials Interfaces* **2022**, *9* (15), 2200342.

(242) Gagorik, A. G.; Mohin, J. W.; Kowalewski, T.; Hutchison, G. R. Effects of Delocalized Charge Carriers in Organic Solar Cells: Predicting Nanoscale Device Performance from Morphology. *Advanced Functional Materials* **2015**, *25* (13), 1996–2003.

(243) Zhang, G.; Chen, X. K.; Xiao, J.; Chow, P. C. Y.; Ren, M.; Kupgan, G.; Jiao, X.; Chan, C. C. S.; Du, X.; Xia, R.; Chen, Z.; Yuan, J.; Zhang, Y.; Zhang, S.; Liu, Y.; Zou, Y.; Yan, H.; Wong, K. S.; Coropceanu, V.; Li, N.; Brabec, C. J.; Bredas, J. L.; Yip, H. L.; Cao, Y. Delocalization of Exciton and Electron Wavefunction in Non-Fullerene Acceptor Molecules Enables Efficient Organic Solar Cells. *Nature Communications* **2020**, *11* (1).

(244) Kim, T.; Kim, J. H.; Kang, T. E.; Lee, C.; Kang, H.; Shin, M.; Wang, C.; Ma, B.; Jeong, U.; Kim, T. S.; Kim, B. J. Flexible, Highly Efficient All-Polymer Solar Cells. *Nature Communications* **2015**, *6* (May), 1–7.

(245) Bhattacharya, J.; Joshi, P. H.; Biswas, R.; Dalal, V. L. Pathway for Recovery of Photo-Degraded Polymer Solar Cells by Post Degradation Thermal Anneal. *Solar Energy Materials and Solar Cells* **2017**, *164*, 70–79.

(246) Duan, L.; Elumalai, N. K.; Zhang, Y.; Uddin, A. Progress in Non-Fullerene Acceptor Based Organic Solar Cells. *Solar Energy Materials and Solar Cells* **2019**, *193* (December 2018), 22–65.

(247) Yao, H.; Wang, J.; Xu, Y.; Zhang, S.; Hou, J. Recent Progress in Chlorinated Organic Photovoltaic Materials. *Accounts of Chemical Research* **2020**, *53*, 822.

(248) Gao, J.; Li, Y.; Li, S.; Xia, X.; Lu, X.; Shi, M.; Chen, H. Non-Fullerene Acceptors with Nitrogen-Containing Six-Membered Heterocycle Cores for the Applications in Organic Solar Cells. *Solar Energy Materials and Solar Cells* **2021**, *225* (March), 111046.

(249) Cui, M.; Li, D.; Du, X.; Li, N.; Rong, Q.; Li, N.; Shui, L.; Zhou, G.; Wang, X.; Brabec, C. J.; Nian, L. A Cost-Effective, Aqueous-Solution-Processed Cathode Interlayer Based on Organosilica Nanodots for Highly Efficient and Stable Organic Solar Cells. *Advanced Materials* **2020**, *32* (38), 1–8.

(250) Holliday, S.; Ashraf, R. S.; Wadsworth, A.; Baran, D.; Yousaf, S. A.; Nielsen, C. B.; Tan, C. H.; Dimitrov, S. D.; Shang, Z.; Gasparini, N.; Alamoudi, M.; Laquai, F.; Brabec, C. J.; Salleo, A.; Durrant, J. R.; McCulloch, I. High-Efficiency and Air-Stable P3HT-Based Polymer Solar Cells with a New Non-Fullerene Acceptor. *Nature Communications* **2016**, *7*, 1–11.

(251) Hu, L.; Jiang, Y.; Sun, L.; Xie, C.; Qin, F.; Wang, W.; Zhou, Y. Significant Enhancement of Illumination Stability of Nonfullerene Organic Solar Cells via an Aqueous Polyethylenimine Modification. *Journal of Physical Chemistry Letters* **2021**, *12* (10), 2607–2614.

(252) Günther, M.; Blätte, D.; Oechsle, A. L.; Rivas, S. S.; Yousefi Amin, A. A.; Müller-Buschbaum, P.; Bein, T.; Ameri, T. Increasing Photostability of Inverted Nonfullerene Organic Solar Cells by Using Fullerene Derivative Additives. *ACS Applied Materials and Interfaces* **2021**, *13* (16), 19072–19084.

(253) Du, X.; Heumueller, T.; Gruber, W.; Almora, O.; Classen, A.; Qu, J.; He, F.; Unruh, T.; Li, N.; Brabec, C. J. Unraveling the Microstructure-Related Device Stability for Polymer Solar Cells Based on Nonfullerene Small-Molecular Acceptors. *Advanced Materials* **2020**, *32* (16), 1908305.

(254) Yang, W.; Luo, Z.; Sun, R.; Guo, J.; Wang, T.; Wu, Y.; Wang, W.; Guo, J.; Wu, Q.; Shi, M.; Li, H.; Yang, C.; Min, J. Acceptor Additive. *Nature Communications* **2020**, *11* (2020), 1–10.

(255) Li, S.; Zhan, L.; Liu, F.; Ren, J.; Shi, M.; Li, C. Z.; Russell, T. P.; Chen, H. An Unfused-Core-Based Nonfullerene Acceptor Enables High-Efficiency Organic Solar Cells with Excellent Morphological Stability at High Temperatures. *Advanced Materials* **2018**, *30* (6), 1705208.

(256) Xiao, J.; Ren, M.; Zhang, G.; Wang, J.; Zhang, D.; Liu, L.; Li, N.; Brabec, C. J.; Yip, H.; Cao, Y. An Operando Study on the Photostability of Nonfullerene Organic Solar Cells. *Solar RRL* **2019**, *3*, 1900077.

(257) Huang, S.; Kang, B.; Duan, L.; Zhang, D. Highly Efficient Inverted Polymer Solar Cells by Using Solution Processed MgO/ZnO Composite Interfacial Layers. *Journal of Colloid and Interface Science* **2021**, *583*, 178–187.

(258) Naz, H.; Ali, R. N.; Liu, Q.; Yang, S.; Xiang, B. Niobium Doped Zinc Oxide Nanorods as an Electron Transport Layer for High-Performance Inverted Polymer Solar Cells. *Journal of Colloid and Interface Science* **2018**, *512*, 548–554.

(259) Ke, J. C.; Wang, Y. H.; Chen, K. L.; Huang, C. J. Effect of Organic Solar Cells Using Various Power O2 Plasma Treatments on the Indium Tin Oxide Substrate. *Journal of Colloid and Interface Science* **2016**, *465*, 311–315.

(260) Ibrahem, M. A.; Wei, H. Y.; Tsai, M. H.; Ho, K. C.; Shyue, J. J.; Chu, C. W. Solution-Processed Zinc Oxide Nanoparticles as Interlayer Materials for Inverted Organic Solar Cells. *Solar Energy Materials and Solar Cells* **2013**, *108*, 156–163.

(261) Ong, C. B.; Ng, L. Y.; Mohammad, A. W. A Review of ZnO Nanoparticles as Solar Photocatalysts: Synthesis, Mechanisms and Applications. *Renewable and Sustainable Energy Reviews* **2018**, *81* (July 2016), 536–551.

(262) Manor, A.; Katz, E. A.; Tromholt, T.; Krebs, F. C.; Tromholt, T.; Krebs, F. C. Electrical and Photo-Induced Degradation of ZnO Layers in Organic Photovoltaics. *Advanced Energy Materials* **2011**, *1*, 836–843.

(263) Zhao, F.; Dai, S.; Wu, Y.; Zhang, Q.; Wang, J.; Jiang, L.; Ling, Q.; Wei, Z.; Ma, W.; You, W.; Wang, C.; Zhan, X. Single-Junction Binary-Blend Nonfullerene Polymer Solar Cells with 12.1% Efficiency. *Advanced Materials* **2017**, *29* (18), 1700144.

(264) Gasparini, N.; Salvador, M.; Strohm, S.; Heumueller, T.; Levchuk, I.; Wadsworth, A.; Bannock, J. H.; de Mello,

J. C.; Egelhaaf, H. J.; Baran, D.; McCulloch, I.; Brabec, C. J. Burn-in Free Nonfullerene-Based Organic Solar Cells. *Advanced Energy Materials* **2017**, *7* (19), 1700770.

(265) Zhang, X.; Cai, J.; Guo, C.; Li, D.; Du, B.; Zhuang, Y.; Cheng, S.; Wang, L.; Liu, D.; Wang, T. Simultaneously Enhanced Efficiency and Operational Stability of Nonfullerene Organic Solar Cells via Solid-Additive-Mediated Aggregation Control. *Small* **2021**, *17* (35), 1–10.

(266) Duan, L.; Meng, X.; Zhang, Y.; Yi, H.; Jin, K.; Haque, F.; Xu, C.; Xiao, Z.; Ding, L.; Uddin, A. Comparative Analysis of Burn-in Photo-Degradation in Non-Fullerene COi8DFIC Acceptor Based High-Efficiency Ternary Organic Solar Cells. *Materials Chemistry Frontiers* **2019**, *3* (6), 1085–1096.

(267) Roesch, R.; Faber, T.; Von Hauff, E.; Brown, T. M.; Lira-Cantu, M.; Hoppe, H. Procedures and Practices for Evaluating Thin-Film Solar Cell Stability. *Advanced Energy Materials* **2015**, *5* (20), 1–24.

(268) Mateker, W. R.; McGehee, M. D. Progress in Understanding Degradation Mechanisms and Improving Stability in Organic Photovoltaics. *Advanced Materials* **2017**, *29* (10), 1603940.

(269) Gasparini, N.; Paleti, S. H. K.; Bertrandie, J.; Cai, G.; Zhang, G.; Wadsworth, A.; Lu, X.; Yip, H.-L.; McCulloch, I.; Baran, D. Exploiting Ternary Blends for Improved Photostability in High-Efficiency Organic Solar Cells. *ACS Energy Letters* **2020**, *5* (5), 1371–1379.

(270) Jiang, Y.; Sun, L.; Jiang, F.; Xie, C.; Hu, L.; Dong, X.; Qin, F.; Liu, T.; Hu, L.; Jiang, X.; Zhou, Y. Photocatalytic Effect of ZnO on the Stability of Nonfullerene Acceptors and Its Mitigation by SnO2 for Nonfullerene Organic Solar Cells. *Materials Horizons* **2019**, *6* (7), 1438–1443.

(271) Kusumi, T.; Kuwabara, T.; Fujimori, K.; Minami, T.; Yamaguchi, T.; Taima, T.; Takahashi, K.; Murakami, T.; Rachmat, V. A. S. A.; Marumoto, K. Mechanism of Light-Soaking Effect in Inverted Polymer Solar Cells with Open-Circuit Voltage Increase. *ACS Omega* **2017**, *2* (4), 1617–1624.

(272) Trost, S.; Zilberberg, K.; Behrendt, A.; Polywka, A.; Görrn, P.; Reckers, P.; Maibach, J.; Mayer, T.; Riedl, T. Overcoming the "Light-Soaking" Issue in Inverted Organic Solar Cells by the Use of Al:Zno Electron Extraction Layers. *Advanced Energy Materials* **2013**, *3* (11), 1437–1444.

(273) Ecker, B.; Egelhaaf, H. J.; Steim, R.; Parisi, J.; Von Hauff, E. Understanding S-Shaped Current-Voltage Characteristics in Organic Solar Cells Containing a TiO x Interlayer with Impedance Spectroscopy and Equivalent Circuit Analysis. *Journal of Physical Chemistry C* **2012**, *116* (31), 16333–16337.

(274) Sundqvist, A.; Sandberg, O. J.; Nyman, M.; Smått, J. H.; Österbacka, R. Origin of the S-Shaped JV Curve and the Light-Soaking Issue in Inverted Organic Solar Cells. *Advanced Energy Materials* **2016**, *6* (6), 1–7.

(275) Dusza, M.; Strek, W.; Granek, F. Significance of Light-Soaking Effect in Proper Analysis of Degradation Dynamics of Organic Solar Cells. *Journal of Photonics for Energy* **2016**, *6* (3), 035503.

(276) Lim, F. J.; Set, Y. T.; Krishnamoorthy, A.; Ouyang, J.; Luther, J.; Ho, G. W. Addressing the Light-Soaking Issue in Inverted Organic Solar Cells Using Chemical Bath Deposited Fluorinated TiOx Electron Transport Layer. *Journal of Materials Chemistry A* **2015**, *3* (1), 314–322.

(277) Jeon, I. I.; Matsuo, Y. Vertical Phase Separation and Light-Soaking Effect Improvements by Photoactive Layer Spin Coating Initiation Time Control in Air-Processed Inverted Organic Solar Cells. *Solar Energy Materials and Solar Cells* **2015**, *140*, 335–343.

(278) Schilinsky, P.; Waldauf, C.; Hauch, J.; Brabec, C. J. Simulation of Light Intensity Dependent Current Characteristics of Polymer Solar Cells. *Journal of Applied Physics* **2004**, *95* (5), 2816–2819.

(279) Van Mensfoort, S. L. M.; Coehoorn, R. Determination of Injection Barriers in Organic Semiconductor Devices from Capacitance Measurements. *Physical Review Letters* **2008**, *100* (8), 1–4.

(280) Cowan, S. R.; Street, R. A.; Cho, S.; Heeger, A. J. Transient Photoconductivity in Polymer Bulk Heterojunction Solar Cells: Competition between Sweep-out and Recombination. *Physical Review B - Condensed Matter and Materials Physics* **2011**, *83* (3), 1–8.

(281) Cowan, S. R.; Roy, A.; Heeger, A. J. Recombination in Polymer-Fullerene Bulk Heterojunction Solar Cells. *Physical Review B - Condensed Matter and Materials Physics* **2010**, *82* (24), 10.

(282) Oh, J.; Jung, S.; Jeong, M.; Lee, B.; Lee, J.; Cho, Y.; Lee, S. M.; Chen, S.; Zhang, Z. G.; Li, Y.; Yang, C. Ring-Perfluorinated Non-Volatile Additives with a High Dielectric Constant Lead to Highly Efficient and Stable Organic Solar Cells. *Journal of Materials Chemistry C* **2019**, *7* (16), 4716–4724.

(283) Kong, X.; Lin, H.; Du, X.; Li, L.; Li, X.; Chen, X.; Zheng, C.; Wang, D.; Tao, S. Hydrogen Bond Induced High Performance Ternary Fullerene-Free Organic Solar Cells with Increased Current Density and Enhanced Stability. *Journal of Materials Chemistry C* **2018**, *6* (36), 9691–9702.

(284) Jain, N.; Chandrasekaran, N.; Sadhanala, A.; Friend, R. H.; McNeill, C. R.; Kabra, D. Interfacial Disorder in Efficient Polymer Solar Cells: The Impact of Donor Molecular Structure and Solvent Additives. *Journal of Materials Chemistry A* **2017**, *5* (47), 24749–24757.

(285) He, Z.; Xiao, B.; Liu, F.; Wu, H.; Yang, Y.; Xiao, S.; Wang, C.; Russell, T. P.; Cao, Y. Single-Junction Polymer Solar Cells with High Efficiency and Photovoltage. *Nature Photonics* **2015**, *9* (3), 174–179.

(286) Peters, C. H.; Sachs-Quintana, I. T.; Mateker, W. R.; Heumueller, T.; Rivnay, J.; Noriega, R.; Beiley, Z. M.; Hoke, E. T.; Salleo, A.; McGehee, M. D. The Mechanism of Burn-in Loss in a High Efficiency Polymer Solar Cell. *Advanced Materials* **2012**, *24* (5), 663–668.

(287) Hawks, S. A.; Deledalle, F.; Yao, J.; Rebois, D. G.; Li, G.; Nelson, J.; Yang, Y.; Kirchartz, T.; Durrant, J. R. Relating Recombination, Density of States, and Device Performance in an Effi Cient Polymer:Fullerene Organic Solar Cell Blend. *Advanced Energy Materials* **2013**, *3* (9), 1201–1209.

(288) Mackenzie, R. C. I.; Shuttle, C. G.; Dibb, G. F.; Treat, N.; Von Hauff, E.; Robb, M. J.; Hawker, C. J.; Chabinyc, M. L.; Nelson, J. Interpreting the Density of States Extracted from Organic Solar Cells Using Transient Photocurrent Measurements. *Journal of Physical Chemistry C* **2013**, *117* (24), 12407–12414.

(289) Credgington, D.; Durrant, J. R. Insights from Transient Optoelectronic Analyses on the Open-Circuit Voltage of Organic Solar Cells. *Journal of Physical Chemistry Letters* **2012**, *3* (11), 1465–1478.

(290) Wan, J.; Xu, X.; Zhang, G.; Li, Y.; Feng, K.; Peng, Q. Highly Efficient Halogen-Free Solvent Processed Small-Molecule Organic Solar Cells Enabled by Material Design and Device Engineering. *Energy and Environmental Science* **2017**, *10* (8), 1739–1745.

(291) An, Q.; Zhang, F.; Li, L.; Wang, J.; Zhang, J.; Zhou, L.; Tang, W. Improved Efficiency of Bulk Heterojunction Polymer Solar Cells by Doping Low-Bandgap Small Molecules. *ACS Applied Materials and Interfaces* **2014**, *6* (9), 6537–6544.

(292) Li, Y.; Guo, Y.; Chen, Z.; Zhan, L.; Zuo, L.; He, C.; Bi, Z.; Yao, N.; Li, S.; Zhou, G.; Yi, Y.; Yang, Y. M.; Zhu, H.; Ma, W.; Gao, F.; Zhang, F.; Chen, H. Mechanism Study on Organic Ternary Photovoltaics with 18.3% Certified Efficiency: From Molecule to Device. *Energy & Environmental Science* **2022**, *15*, 855–865.

(293) Lin, Y.; Adilbekova, B.; Firdaus, Y.; Yengel, E.; Faber, H.; Sajjad, M.; Zheng, X.; Yarali, E.; Seitkhan, A.; Bakr, O. M.; El-Labban, A.; Schwingenschlögl, U.; Tung, V.; McCulloch, I.; Laquai, F.; Anthopoulos, T. D. 17% Efficient Organic Solar Cells Based on Liquid Exfoliated WS2 as a Replacement for PEDOT:PSS. *Advanced Materials* **2019**, *31* (46), 1902965.

(294) Lee, J.; Sin, D. H.; Moon, B.; Shin, J.; Kim, H. G.; Kim, M.; Cho, K. Highly Crystalline Low-Bandgap Polymer Nanowires towards High-Performance Thick-Film Organic Solar Cells Exceeding 10% Power Conversion Efficiency. *Energy and Environmental Science* **2017**, *10* (1), 247–257.

(295) Riede, M.; Spoltore, D.; Leo, K. Organic Solar Cells—The Path to Commercial Success. *Advanced Energy Materials* **2021**, *11* (1), 2002653.

(296) Zhao, W.; Qian, D.; Zhang, S.; Li, S.; Inganäs, O.; Gao, F.; Hou, J. Fullerene-Free Polymer Solar Cells with over 11% Efficiency and Excellent Thermal Stability. *Advanced Materials* **2016**, *28* (23), 4734–4739.

(297) Qian, D.; Zheng, Z.; Yao, H.; Tress, W.; Hopper, T. R.; Chen, S.; Li, S.; Liu, J.; Chen, S.; Zhang, J.; Liu, X. K.;

Gao, B.; Ouyang, L.; Jin, Y.; Pozina, G.; Buyanova, I. A.; Chen, W. M.; Inganäs, O.; Coropceanu, V.; Bredas, J. L.; Yan, H.; Hou, J.; Zhang, F.; Bakulin, A. A.; Gao, F. Design Rules for Minimizing Voltage Losses in High-Efficiency Organic Solar Cells. *Nature Materials* **2018**, *17* (8), 703–709.

(298) Sonar, P.; Lim, J. P. F.; Chan, K. L. Organic Non-Fullerene Acceptors for Organic Photovoltaics. *Energy and Environmental Science* **2011**, *4* (5), 1558–1574.

(299) Liu, W.; Xu, X.; Yuan, J.; Leclerc, M.; Zou, Y.; Li, Y. Low-Bandgap Non-Fullerene Acceptors Enabling High-Performance Organic Solar Cells. *ACS Energy Letters* **2021**, *6* (2), 598–608.

(300) Ran, N. A.; Roland, S.; Love, J. A.; Savikhin, V.; Takacs, C. J.; Fu, Y. T.; Li, H.; Coropceanu, V.; Liu, X.; Brédas, J. L.; Bazan, G. C.; Toney, M. F.; Neher, Di.; Nguyen, T. Q. Impact of Interfacial Molecular Orientation on Radiative Recombination and Charge Generation Efficiency. *Nature Communications* **2017**, *8* (1), 1–9.

(301) Liu, J.; Chen, S.; Qian, D.; Gautam, B.; Yang, G.; Zhao, J.; Bergqvist, J.; Zhang, F.; Ma, W.; Ade, H.; Inganäs, O.; Gundogdu, K.; Gao, F.; Yan, H. Fast Charge Separation in a Non-Fullerene Organic Solar Cell with a Small Driving Force. *Nature Energy* **2016**, *1* (7), 1–7.

(302) Baran, D.; Kirchartz, T.; Wheeler, S.; Dimitrov, S.; Abdelsamie, M.; Gorman, J.; Ashraf, R. S.; Holliday, S.; Wadsworth, A.; Gasparini, N.; Kaienburg, P.; Yan, H.; Amassian, A.; Brabec, C. J.; Durrant, J. R.; McCulloch, I. Reduced Voltage Losses Yield 10% Efficient Fullerene Free Organic Solar Cells with >1 V Open Circuit Voltages. *Energy and Environmental Science* **2016**, *9* (12), 3783–3793.

(303) Zhang, G.; Zhang, K.; Yin, Q.; Jiang, X. F.; Wang, Z.; Xin, J.; Ma, W.; Yan, H.; Huang, F.; Cao, Y. High-Performance Ternary Organic Solar Cell Enabled by a Thick Active Layer Containing a Liquid Crystalline Small Molecule Donor. *Journal of the American Chemical Society* **2017**, *139* (6), 2387–2395.

(304) Upama, M. B.; Elumalai, N. K.; Mahmud, M. A.; Wright, M.; Wang, D.; Xu, C.; Uddin, A. Effect of Annealing Dependent Blend Morphology and Dielectric Properties on the Performance and Stability of Non-Fullerene Organic Solar Cells. *Solar Energy Materials and Solar Cells* **2018**, *176* (August 2017), 109–118.

(305) Gasparini, N.; Salvador, M.; Strohm, S.; Heumueller, T.; Levchuk, I.; Wadsworth, A.; Bannock, J. H.; de Mello, J. C.; Egelhaaf, H. J.; Baran, D.; McCulloch, I.; Brabec, C. J. Burn-in Free Nonfullerene-Based Organic Solar Cells. *Advanced Energy Materials* **2017**, *7* (19), 1–7.

(306) O'Hara, K. A.; Ostrowski, D. P.; Koldemir, U.; Takacs, C. J.; Shaheen, S. E.; Sellinger, A.; Chabinyc, M. L. Role of Crystallization in the Morphology of Polymer:Non-Fullerene Acceptor Bulk Heterojunctions. *ACS Applied Materials and Interfaces* **2017**, *9* (22), 19021–19029.

(307) Weng, K.; Ye, L.; Zhu, L.; Xu, J.; Zhou, J.; Feng, X.; Lu, G.; Tan, S.; Liu, F.; Sun, Y. Optimized Active Layer Morphology toward Efficient and Polymer Batch Insensitive Organic Solar Cells. *Nature Communications* **2020**, *11* (1), 2855.

(308) Fukuda, K.; Yu, K.; Someya, T. The Future of Flexible Organic Solar Cells. *Advanced Energy Materials* **2020**, *10* (25), 1–10.

(309) Zhao, F.; Wang, C.; Zhan, X. Morphology Control in Organic Solar Cells. *Advanced Energy Materials* **2018**, *8* (28), 1703147.

(310) Du, B.; Geng, R.; Tan, W.; Mao, Y.; Li, D.; Zhang, X.; Liu, D.; Tang, W.; Huang, W.; Wang, T. Heating Induced Aggregation in Non-Fullerene Organic Solar Cells towards High Performance. *Journal of Energy Chemistry* **2021**, *54*, 131–137.

(311) Li, Y.; Wang, M.; Zhang, Q.; Wu, Z.; Lim, H.; Wang, Y.; Qin, H.; Yang, J.; Gao, C.; Young Woo, H.; Yuan, J. Fine-Tuned Crystallinity of Polymerized Non-Fullerene Acceptor via Molecular Engineering towards Efficient All-Polymer Solar Cell. *Chemical Engineering Journal* **2022**, *428* (May 2021), 131232.

(312) Li, X.; Zhang, W.; Usman, K.; Fang, J. Small Molecule Interlayers in Organic Solar Cells. *Advanced Energy Materials* **2018**, *8* (28), 1702730.

(313) Peiro, A. M.; Ravirajan, P.; Govender, K.; Boyle, D. S.; O'Brien, P.; Bradley, D. D. C.; Nelson, J.; Durrant, J.

R. Hybrid Polymer/Metal Oxide Solar Cells Based on ZnO Columnar Structures. *Journal of Materials Chemistry* **2006**, *16* (21), 2088.

(314) Wetzelaer, G. A. H.; Kuik, M.; Lenes, M.; Blom, P. W. M. Origin of the Dark-Current Ideality Factor in Polymer:Fullerene Bulk Heterojunction Solar Cells. *Applied Physics Letters* **2011**, *99* (15), 2011–2014.

(315) Kim, G. M.; Oh, I. S.; Lee, A. N.; Oh, S. Y. Applications of Ytterbium in Inverted Organic Photovoltaic Cells as High-Performance and Stable Electron Transport Layers. *Journal of Materials Chemistry A* **2014**, *2* (26), 10131–10136.

(316) Armin, A.; Kassal, I.; Shaw, P. E.; Hambsch, M.; Stolterfoht, M.; Lyons, D. M.; Li, J.; Shi, Z.; Burn, P. L.; Meredith, P. Spectral Dependence of the Internal Quantum Efficiency of Organic Solar Cells: Effect of Charge Generation Pathways. *Journal of the American Chemical Society* **2014**, *136* (32), 11465–11472.

(317) Tang, H.; Chen, H.; Yan, C.; Huang, J.; Fong, P. W. K.; Lv, J.; Hu, D.; Singh, R.; Kumar, M.; Xiao, Z.; Kan, Z.; Lu, S.; Li, G. Delicate Morphology Control Triggers 14.7% Efficiency All-Small-Molecule Organic Solar Cells. *Advanced Energy Materials* **2020**, *10* (27), 2001076.

(318) Markov, D. E.; Amsterdam, E.; Blom, P. W. M.; Sieval, A. B.; Hummelen, J. C. Exciton Diffusion and Dissociation in Conjugated Polymer/Fullerene Heterostructures. *Organic Optoelectronics and Photonics* **2004**, *5464* (23), 449.

(319) Liu, T.; Luo, Z.; Fan, Q.; Zhang, G.; Zhang, L.; Gao, W.; Guo, X.; Ma, W.; Zhang, M.; Yang, C.; Li, Y.; Yan, H. Use of Two Structurally Similar Small Molecular Acceptors Enabling Ternary Organic Solar Cells with High Efficiencies and Fill Factors. *Energy and Environmental Science* **2018**, *11* (11), 3275–3282.

(320) Elumalai, N. K.; Uddin, A. Open Circuit Voltage of Organic Solar Cells: An in-Depth Review. *Energy and Environmental Science* **2016**, *9* (2), 391–410.

(321) Gelmetti, I.; Montcada, N. F.; Pérez-Rodríguez, A.; Barrena, E.; Ocal, C.; García-Benito, I.; Molina-Ontoria, A.; Martín, N.; Vidal-Ferran, A.; Palomares, E. Energy Alignment and Recombination in Perovskite Solar Cells: Weighted Influence on the Open Circuit Voltage. *Energy and Environmental Science* **2019**, *12* (4), 1309–1316.

(322) Garcia-Belmonte, G.; Boix, P. P.; Bisquert, J.; Sessolo, M.; Bolink, H. J. Simultaneous Determination of Carrier Lifetime and Electron Density-of-States in P3HT:PCBM Organic Solar Cells under Illumination by Impedance Spectroscopy. *Solar Energy Materials and Solar Cells* **2010**, *94* (2), 366–375.

(323) Foster, J. M.; Kirkpatrick, J.; Richardson, G. Asymptotic and Numerical Prediction of Current-Voltage Curves for an Organic Bilayer Solar Cell under Varying Illumination and Comparison to the Shockley Equivalent Circuit. *Journal of Applied Physics* **2013**, *114* (10), 1–15.

(324) Tvingstedt, K.; Deibel, C. Temperature Dependence of Ideality Factors in Organic Solar Cells and the Relation to Radiative Efficiency. *Advanced Energy Materials* **2016**, *6* (9), 1–13.

(325) Tang, Y.; Sun, H.; Wu, Z.; Zhang, Y.; Zhang, G.; Su, M.; Zhou, X.; Wu, X.; Sun, W.; Zhang, X.; Liu, B.; Chen, W.; Liao, Q.; Woo, H. Y.; Guo, X. A New Wide Bandgap Donor Polymer for Efficient Nonfullerene Organic Solar Cells with a Large Open-Circuit Voltage. *Advanced Science* **2019**, *6* (21), 1901773.

(326) Ma, L.; Zhang, S.; Yao, H.; Xu, Y.; Wang, J.; Zu, Y.; Hou, J. High-Efficiency Nonfullerene Organic Solar Cells Enabled by 1000 Nm Thick Active Layers with a Low Trap-State Density. *ACS Applied Materials and Interfaces* **2020**, *12* (16), 18777–18784.

(327) Choi, H.; Lee, J.; Oh, C. M.; Jang, S.; Kim, H.; Jeong, M. S.; Park, S. H.; Hwang, I. W. Efficiency Enhancements in Non-Fullerene Acceptor-Based Organic Solar Cells by Post-Additive Soaking. *Journal of Materials Chemistry A* **2019**, *7* (15), 8805–8810.

(328) Bristow, H.; Thorley, K. J.; White, A. J. P.; Wadsworth, A.; Babics, M.; Hamid, Z.; Zhang, W.; Paterson, A. F.; Kosco, J.; Panidi, J.; Anthopoulos, T. D.; McCulloch, I. Impact of Nonfullerene Acceptor Side Chain Variation on Transistor Mobility. *Advanced Electronic Materials* **2019**, *5* (10), 1–11.

(329) Mica, N. A.; Thomson, S. A. J.; Samuel, I. D. W. Electron Mobility of Non-Fullerene Acceptors Using a Time

of Flight Method. *Organic Electronics* **2018**, *63* (August), 415–420.

(330) Wang, F.; Yang, M.; Zhang, Y.; Du, J.; Yang, S.; Yang, L.; Fan, L.; Sui, Y.; Sun, Y.; Yang, J. Full-Scale Chemical and Field-Effect Passivation: 21.52% Efficiency of Stable MAPbI3 Solar Cells via Benzenamine Modification. **2021**, *14* (8), 2783–2789.

(331) Lin, B.; Zhou, X.; Zhao, H.; Yuan, J.; Zhou, K.; Chen, K.; Wu, H.; Guo, R.; Scheel, M. A.; Chumakov, A.; Roth, S. V.; Mao, Y.; Wang, L.; Tang, Z.; Müller-Buschbaum, P.; Ma, W. Balancing the Pre-Aggregation and Crystallization Kinetics Enables High Efficiency Slot-Die Coated Organic Solar Cells with Reduced Non-Radiative Recombination Losses. *Energy and Environmental Science* **2020**, *13* (8), 2467–2479.

(332) Mikie, T.; Saeki, A.; Masuda, H.; Ikuma, N.; Kokubo, K.; Seki, S. New Efficient (Thio)Acetalized Fullerene Monoadducts for Organic Solar Cells: Characterization Based on Solubility, Mobility Balance, and Dark Current. *Journal of Materials Chemistry A* **2014**, *3* (3), 1152–1157.

(333) Jiang, K.; Zhang, J.; Peng, Z.; Lin, F.; Wu, S.; Li, Z.; Chen, Y.; Yan, H.; Ade, H.; Zhu, Z.; Jen, A. K. Y. Pseudo-Bilayer Architecture Enables High-Performance Organic Solar Cells with Enhanced Exciton Diffusion Length. *Nature Communications* **2021**, *12* (1), 468.

(334) Zhang, L.; Xu, X.; Lin, B.; Zhao, H.; Li, T.; Xin, J.; Bi, Z.; Qiu, G.; Guo, S.; Zhou, K.; Zhan, X.; Ma, W. Achieving Balanced Crystallinity of Donor and Acceptor by Combining Blade-Coating and Ternary Strategies in Organic Solar Cells. *Advanced Materials* **2018**, *30* (51), 1805041.

(335) Athanasopoulos, S.; Schauer, F.; Nádaždy, V.; Weiß, M.; Kahle, F. J.; Scherf, U.; Bässler, H.; Köhler, A. What Is the Binding Energy of a Charge Transfer State in an Organic Solar Cell? *Advanced Energy Materials* **2019**, *9* (24), 1900814.

(336) Wilken, S.; Sandberg, O. J.; Scheunemann, D.; Österbacka, R. Watching Space Charge Build Up in an Organic Solar Cell. *Solar RRL* **2020**, *4* (3), 1900505.

(337) Moustafa, E.; Méndez, M.; Pallarès, J.; Marsal, L. F. Low Temperature Based PDINO Cathode Interlayer for High Operational Photostable Inverted Non-Fullerene Organic Solar Cells. *Solar Energy Materials and Solar Cells* **2022**, *248*, 111985.

(338) Nolasco, J. C.; Sánchez-Díaz, A.; Cabŕ, R.; Ferŕ-Borrull, J.; Marsal, L. F.; Palomares, E.; Pallaŕs, J. Relation between the Barrier Interface and the Built-in Potential in Pentacene/C60 Solar Cell. *Applied Physics Letters* **2010**, *97* (1), 013305.

(339) Seemann, A.; Egelhaaf, H. J.; Brabec, C. J.; Hauch, J. A. Influence of Oxygen on Semi-Transparent Organic Solar Cells with Gas Permeable Electrodes. *Organic Electronics* **2009**, *10* (8), 1424–1428.

(340) Zhang, H.; Yao, H.; Hou, J.; Zhu, J.; Zhang, J.; Li, W.; Yu, R.; Gao, B.; Zhang, S.; Hou, J. Over 14% Efficiency in Organic Solar Cells Enabled by Chlorinated Nonfullerene Small-Molecule Acceptors. *Advanced Materials* **2018**, *30* (28), 1800613.

(341) Guo, C.; Li, D.; Wang, L.; Du, B.; Liu, Z. X.; Shen, Z.; Wang, P.; Zhang, X.; Cai, J.; Cheng, S.; Yu, C.; Wang, H.; Liu, D.; Li, C. Z.; Wang, T. Cold-Aging and Solvent Vapor Mediated Aggregation Control toward 18% Efficiency Binary Organic Solar Cells. *Advanced Energy Materials* **2021**, *11* (39), 2102000.

(342) Wang, T.; Bredas, J. L. Organic Photovoltaics: Understanding the Preaggregation of Polymer Donors in Solution and Its Morphological Impact. *Journal of the American Chemical Society* **2021**, *143* (4), 1822–1835.

(343) Gao, M.; Wang, W.; Hou, J.; Ye, L. Control of Aggregated Structure of Photovoltaic Polymers for High-efficiency Solar Cells. *Aggregate* **2021**, *2* (5), 1–38.

(344) Wadsworth, A.; Hamid, Z.; Kosco, J.; Gasparini, N.; McCulloch, I. The Bulk Heterojunction in Organic Photovoltaic, Photodetector, and Photocatalytic Applications. *Advanced Materials* **2020**, *32* (38), 1–27.

(345) Jiang, K.; Zhang, J.; Zhong, C.; Lin, F. R. Suppressed Recombination Loss in Organic Photovoltaics Adopting a Planar – Mixed Heterojunction Architecture. *Nature Energy* **2022**, *7* (November), 1076–1086.

References

(346) Yong Cui, Ye Xu, Huifeng Yao, Pengqing Bi, Ling Hong, Jianqi Zhang, Yunfei Zu, Tao Zhang, Jinzhao Qin, Junzhen Ren, Zhihao Chen, Chang He, Xiaotao Hao, Zhixiang Wei, and J. H. Single-Junction Organic Photovoltaic Cell with 19 % Efficiency. *Advanced Materials* **2021**, *33*, 2102420.

(347) Mikhnenko, O. V.; Blom, P. W. M.; Nguyen, T. Q. Exciton Diffusion in Organic Semiconductors. *Energy and Environmental Science* **2015**, *8* (7), 1867–1888.

(348) Petritsch, K.; Arias, A. C.; Granstro, M.; Friend, R. H. Laminated Fabricationof Polymericphotovoltaic Diodes. *Nature* **1998**, *395*, 1532–1535.

(349) Zhang, J.; Kan, B.; Pearson, A. J.; Parnell, A. J.; Cooper, J. F. K.; Liu, X. K.; Conaghan, P. J.; Hopper, T. R.; Wu, Y.; Wan, X.; Gao, F.; Greenham, N. C.; Bakulin, A. A.; Chen, Y.; Friend, R. H. Efficient Non-Fullerene Organic Solar Cells Employing Sequentially Deposited Donor-Acceptor Layers. *Journal of Materials Chemistry A* **2018**, *6* (37), 18225–18233. https://doi.org/10.1039/c8ta06860g.

(350) Zhang, J.; Pearson, A. J.; Liu, X. K.; Conaghan, P. J.; Greenham, N. C.; Friend, R. H.; Hopper, T. R.; Wu, Y.; Bakulin, A. A.; Kan, B.; Wan, X.; Chen, Y.; Parnell, A. J.; Cooper, J. F. K.; Gao, F. Efficient Non-Fullerene Organic Solar Cells Employing Sequentially Deposited Donor-Acceptor Layers. *Journal of Materials Chemistry A* **2018**, 1–18.

(351) Sun, R.; Guo, J.; Sun, C.; Wang, T.; Luo, Z.; Zhang, Z.; Jiao, X.; Tang, W.; Yang, C.; Li, Y.; Min, J. A Universal Layer-by-Layer Solution-Processing Approach for Efficient Non-Fullerene Organic Solar Cells. *Energy and Environmental Science* **2019**, *12* (1), 384–395.

(352) Wang, Y.; Zhan, X. Layer-by-Layer Processed Organic Solar Cells. *Advanced Energy Materials* **2016**, *6* (17), 1–18. https://doi.org/10.1002/aenm.201600414.

(353) MouÍ, A. J.; Bonekamp, J. B.; Meerholz, K. The Effect of Active Layer Thickness and Composition on the Performance of Bulk-Heterojunction Solar Cells. *Journal of Applied Physics* **2006**, *100* (9), 094503.

(354) Nelson, J. Diffusion-Limited Recombination in Polymer-Fullerene Blends and Its Influence on Photocurrent Collection. *Physical Review, American Physical Society* **2003**, *67* (15), 1–10.

(355) Zhu, W.; Spencer, A. P.; Mukherjee, S.; Alzola, J. M.; Sangwan, V. K.; Amsterdam, S. H.; Swick, S. M.; Jones, L. O.; Heiber, M. C.; Herzing, A. A.; Li, G.; Stern, C. L.; DeLongchamp, D. M.; Kohlstedt, K. L.; Hersam, M. C.; Schatz, G. C.; Wasielewski, M. R.; Chen, L. X.; Facchetti, A.; Marks, T. J. Crystallography, Morphology, Electronic Structure, and Transport in Non-Fullerene/Non-Indacenodithienothiophene Polymer:Y6 Solar Cells. *Journal of the American Chemical Society* **2020**, *142* (34), 14532–14547.

(356) Layer-by-Layer Processed PM6 Y6-Based Stable Ternary Polymer Solar Cells with ImprovedEfficiency over 18% by Incorporating an Asymmetric Thieno[3,2-b]Indole-Based Acceptor Jinglong. *Advanced Functional Materials* **2022**, *32* (25), 2200629.

(357) Sun, R.; Wu, Q.; Guo, J.; Wang, T.; Wu, Y.; Qiu, B.; Luo, Z.; Yang, W.; Hu, Z.; Guo, J.; Shi, M.; Yang, C.; Huang, F.; Li, Y.; Min, J. A Layer-by-Layer Architecture for Printable Organic Solar Cells Overcoming the Scaling Lag of Module Efficiency. *Joule* **2020**, *4* (2), 407–419.

(358) Azzouzi, M.; Kirchartz, T.; Nelson, J. Factors Controlling Open-Circuit Voltage Losses in Organic Solar Cells. *Trends in Chemistry*. 2019, pp 49–62.

(359) Liu, L.; Najar, A.; Wang, K.; Du, M.; Liu, S. Perovskite Quantum Dots in Solar Cells. *Advanced Science* **2022**, *9* (7), 1–20.

(360) Pan, J.; Shang, Y.; Yin, J.; De Bastiani, M.; Peng, W.; Dursun, I.; Sinatra, L.; El-Zohry, A. M.; Hedhili, M. N.; Emwas, A. H.; Mohammed, O. F.; Ning, Z.; Bakr, O. M. Bidentate Ligand-Passivated CsPbI 3 Perovskite Nanocrystals for Stable Near-Unity Photoluminescence Quantum Yield and Efficient Red Light-Emitting Diodes. *Journal of the American Chemical Society* **2018**, *140* (2), 562–565.

(361) Khan, J.; Ullah, I.; Yuan, J. CsPbI3perovskite Quantum Dot Solar Cells: Opportunities, Progress and Challenges. *Materials Advances* **2022**, *3* (4), 1931–1952.

(362) Keqiang Chen, Qiaohui Zhong, Wen Chen, Binghua Sang, Yingwei Wang, Tingqiang Yang, Yueli Liu,Yupeng Zhang, and H. Z. Short-Chain Ligand-Passivated Stable -CsPbI3 Quantum Dot for All-Inorganic Perovskite. *Advanced Functional Materials* **2019**, *29*, 1900991.

(363) Yuan, J.; Zhang, X.; Sun, J.; Patterson, R.; Yao, H.; Xue, D.; Wang, Y.; Ji, K.; Hu, L.; Huang, S.; Chu, D.; Wu, T.; Hou, J.; Yuan, J. Hybrid Perovskite Quantum Dot/Non-Fullerene Molecule Solar Cells with Efficiency Over 15%. *Advanced Functional Materials* **2021**, *31* (27), 2101272.

(364) Bai, Y.; Hao, M.; Ding, S.; Chen, P.; Wang, L. Surface Chemistry Engineering of Perovskite Quantum Dots: Strategies, Applications, and Perspectives. *Advanced Materials* **2022**, *34* (4), 2105958.

Appendices

Supporting Figures and Tables

Appendix 1. Supporting Figures

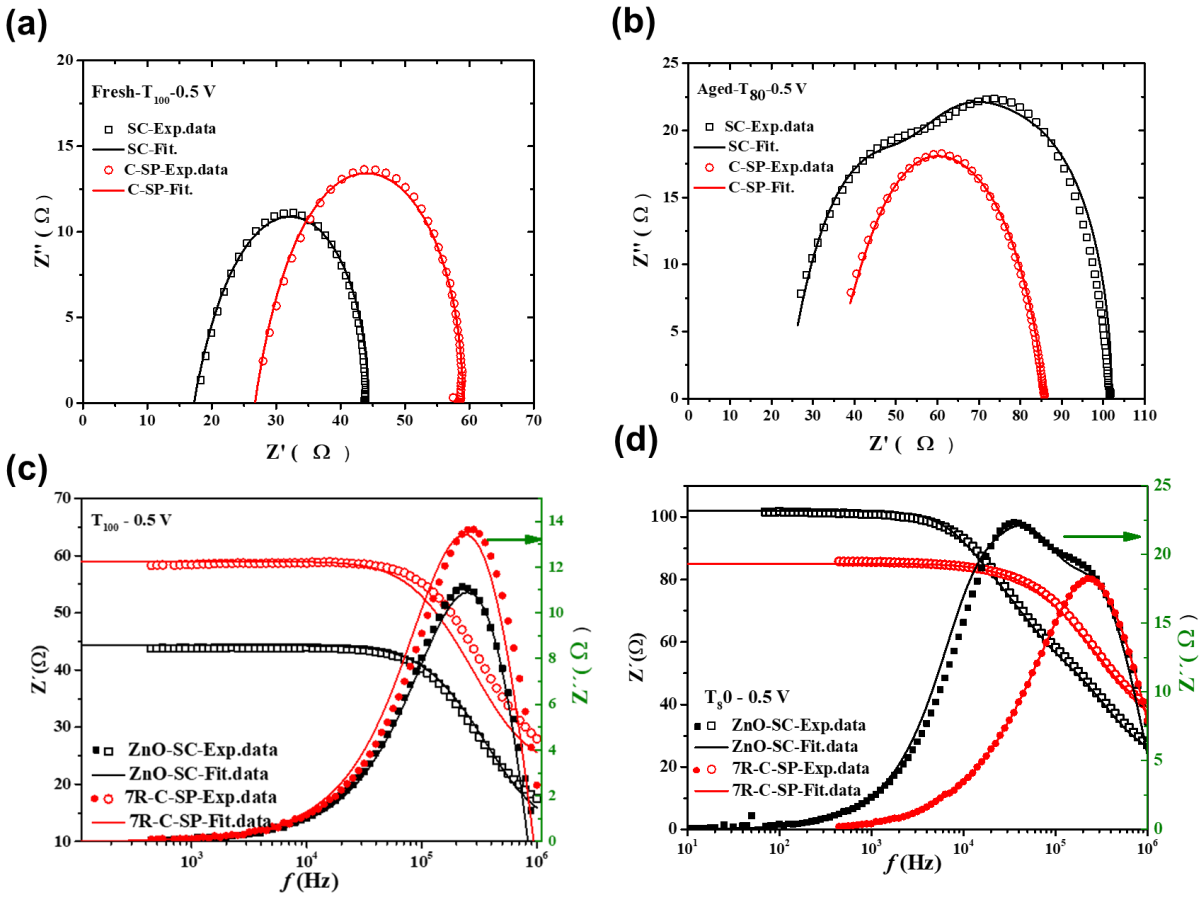

Figure A.1 Impedance spectra measured under illumination (IS- AM1.5) for ZnO-SC and C-7R-SP iF-OPVs at V_{MPP} (a) for the T_{100} freshly prepared devices, (b) for the degraded devices after 5000 h (T_{80}) and the corresponding Bode plots of (c) the T_{100} Fresh devices, and (d) T_{80} aged devices. Using symbols for the experimental data and the fitting results in solid lines by applying the equivalent circuit model in Figure 3.11e 3RC solid black lines for the freshly prepared iF-OPVs and the added dashed red lines for the T_{80} degraded ones following Debye model.

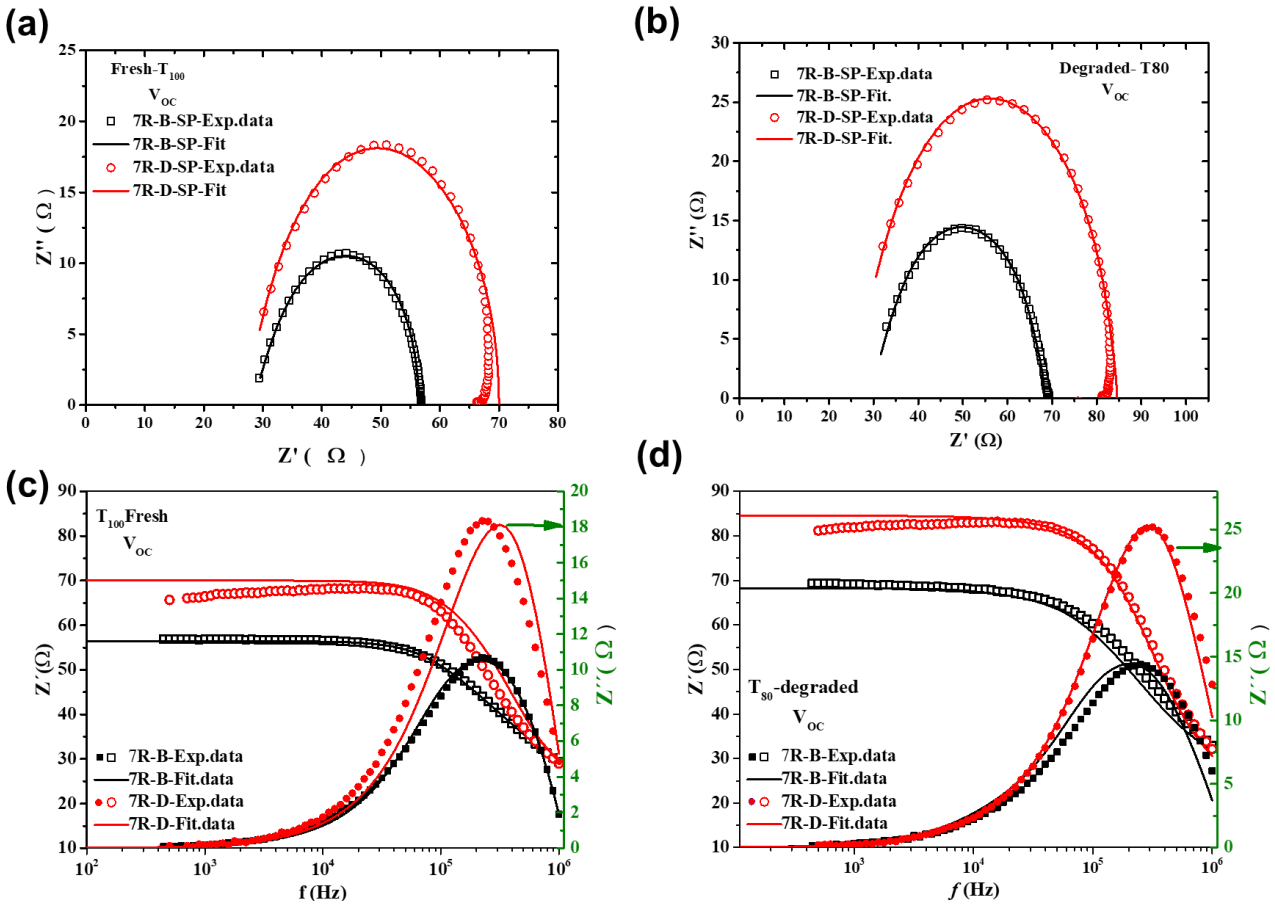

Figure A.2 The IS at V_{OC} under 1.5 AM illumination of the B-7R-SP and D-7R-SP iPSCs a) Cole-Cole plot of T_{100} fresh prepared iPSCs using the 3RC equivalent circuit, b) Cole-Cole plot of ~T_{80} degraded iPSCs using Debye model. The Bode plot for the real and imaginary parts of the (c) T_{100} fresh iPSCs and (d) ~T_{80} degraded iPSCs. The symbols for the experimental data and the line for using the fitted values summarized in **Table S8.**

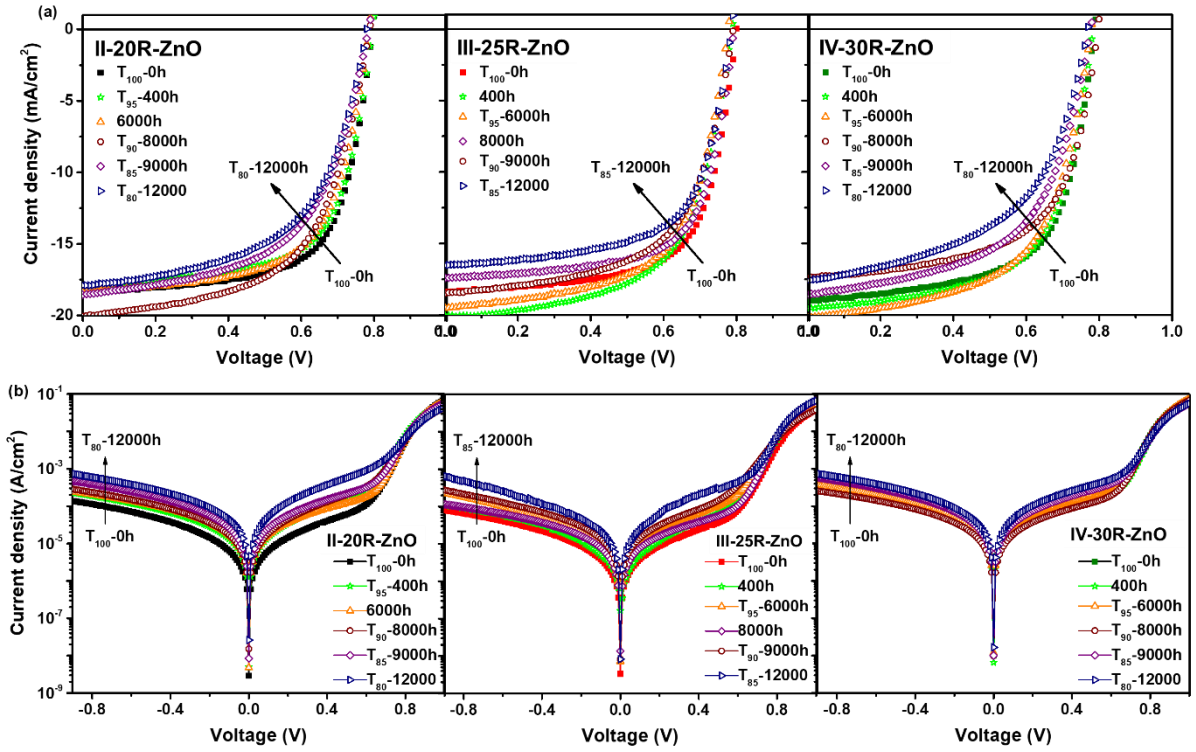

Figure A.3 (a) Current density- voltage (J-V) characteristic curves under AM 1.5 G illumination, (b) at dark of the degraded iF-OPVs with respect to the aging time (12000 h)- devices stability study in Chapter 3-Part II.

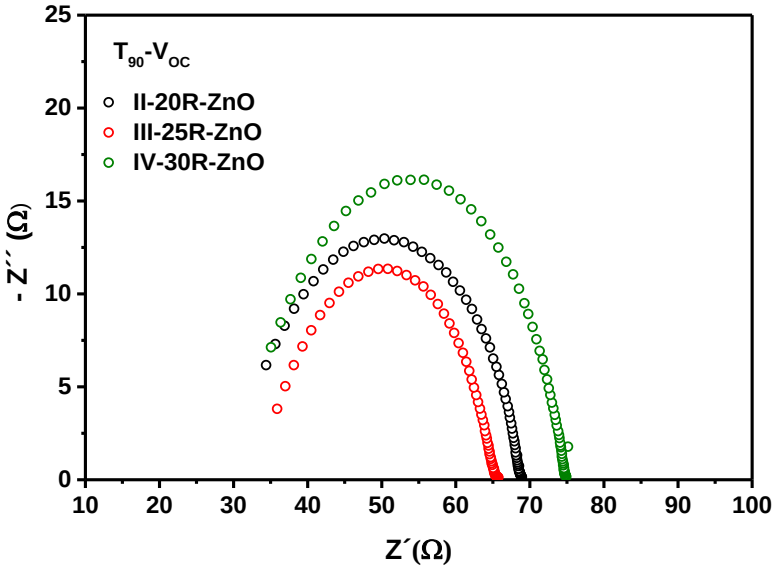

Figure A.4 Cole-cole plots at V_{OC} under AM 1.5G illumination of the T_{90} aged iF-OPVs.

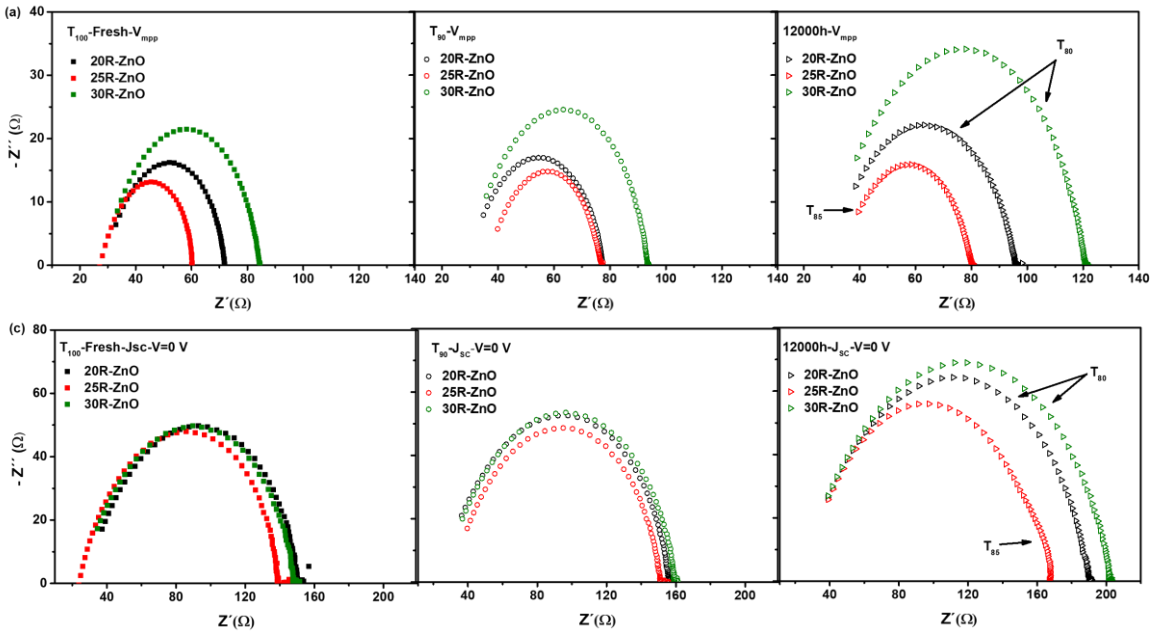

Figure A.5 Cole-cole plots under AM 1.5G illumination of the T_{100}-fresh, T_{90} and 12000 h degraded devices at (a) maximum power point voltage, V_{MPP} (b) Short circuit current condition at voltage = 0 V.

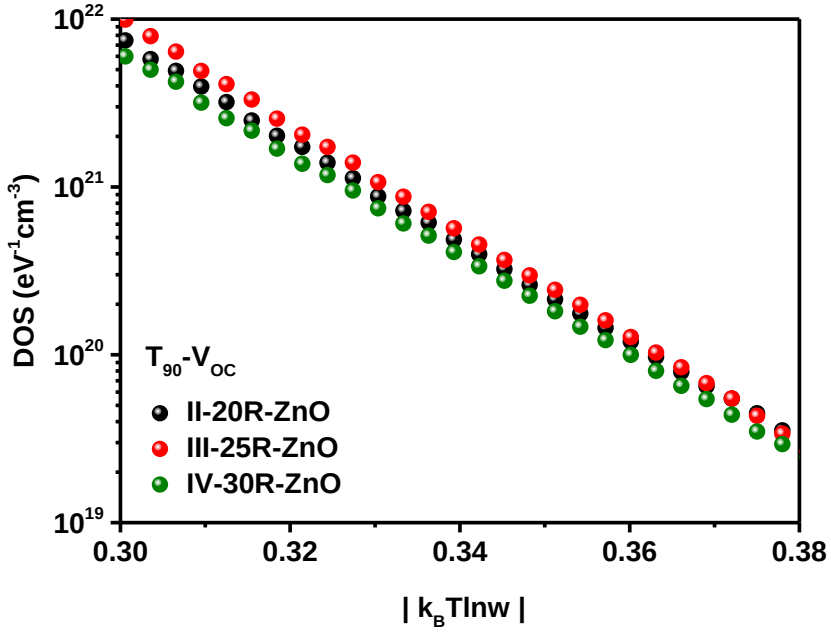

Figure A.6 DOS as function of $\left|k_BTln\omega\right|$ at V_{OC} under AM 1.5G illumination of the T_{90} degraded iF-OPVs.

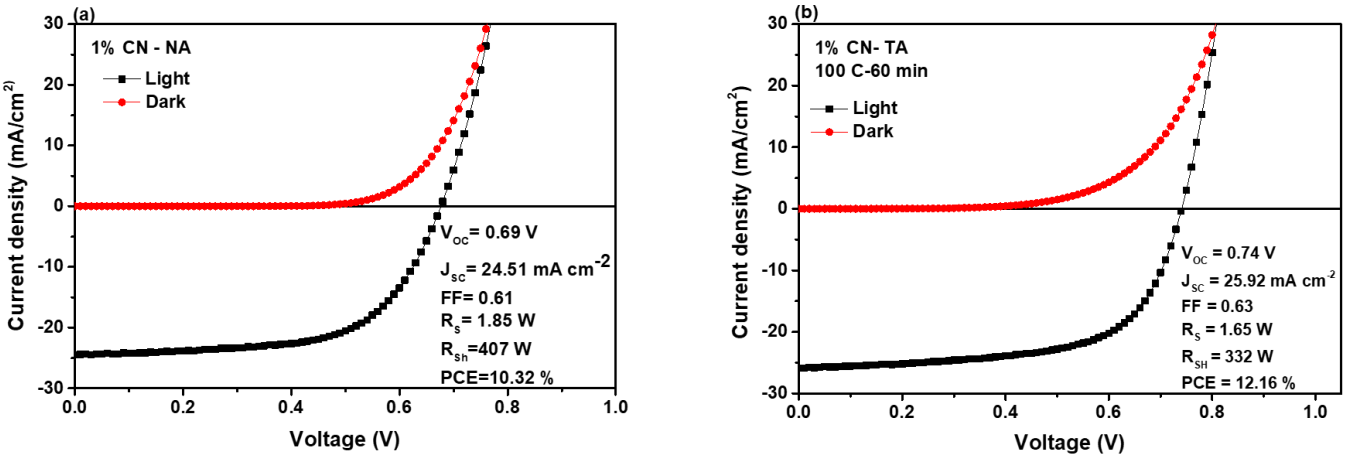

Figure A.7 Current density-voltage (J-V) characteristic curves under Illumination (AM 1.5 G) of the binary iNF-OPVs treated with 1 % CN additives (a) non-annealed (NA) and (b) thermally annealed (TA) at 100 ℃ for 60 min.

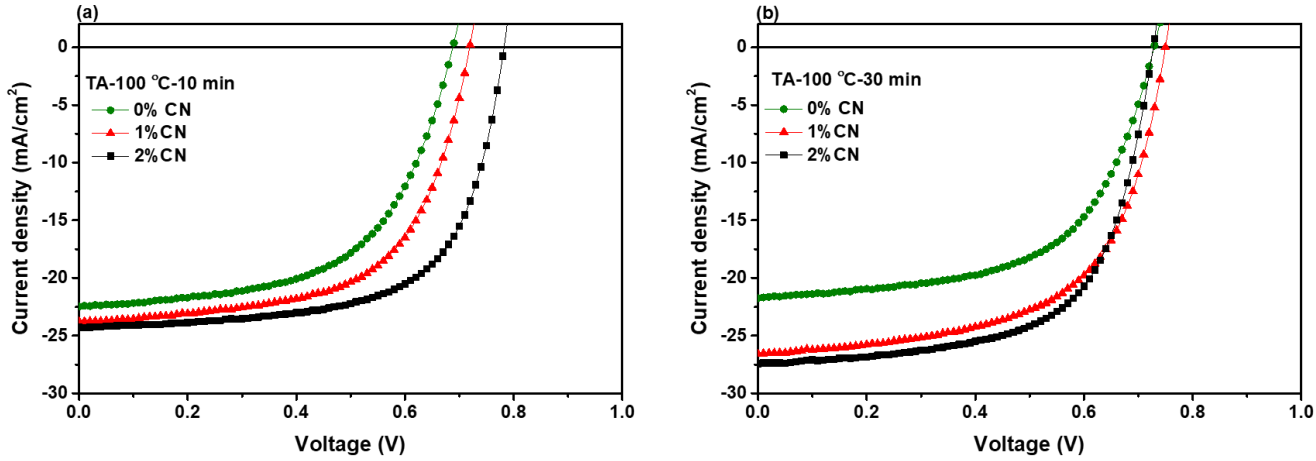

Figure A.8 Current density-voltage (J-V) characteristic curves under Illumination (AM 1.5 G) of the binary iNF-OPVs treated with different percentage of CN additives and thermally annealed at 100 ℃ for (a) for 10 min and (b) 30 min.

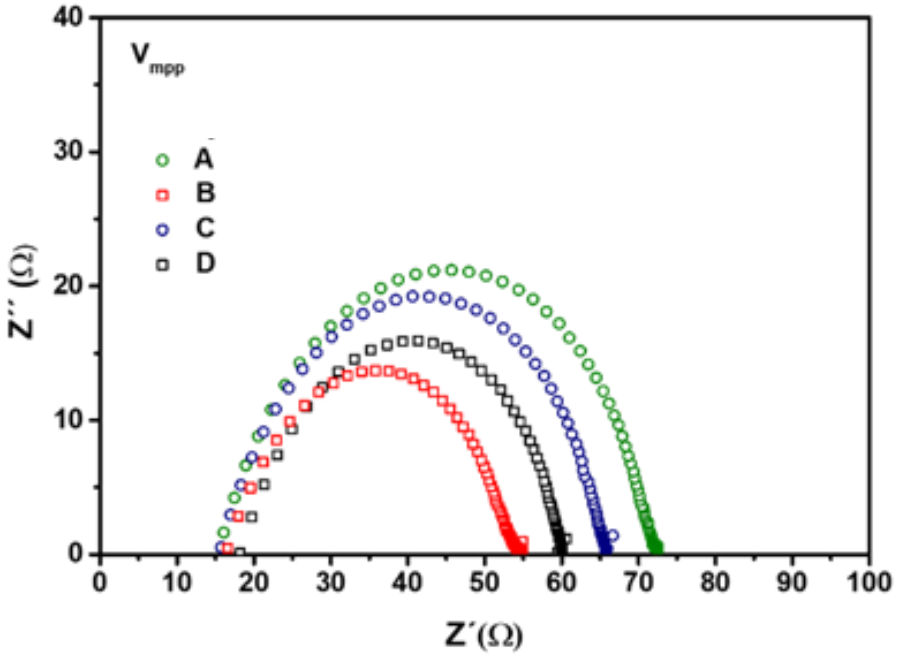

Figure A.9 Nyquist Plots of the pristine and treated iNF-OPVs devices under AM 1.5G illumination and an oscillation amplitude of 50 mV at V_{MPP} bias voltage.

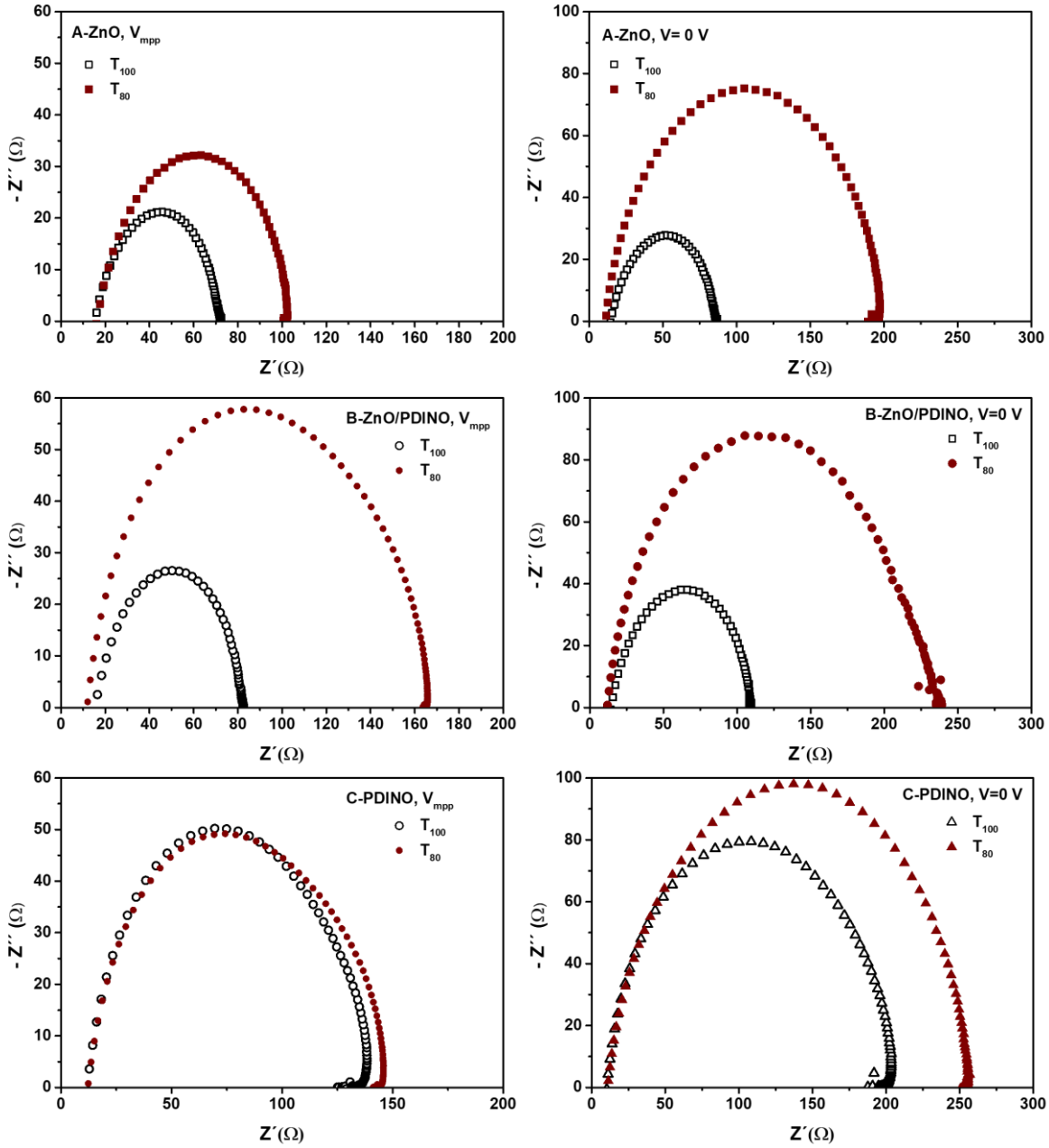

Figure A.10 Nyquist plots under AM 1.5G illumination of the T_{100}-fresh, T_{80} photo- degraded devices at maximum power point voltage, V_{mpp} and short circuit current condition at voltage = 0 V.

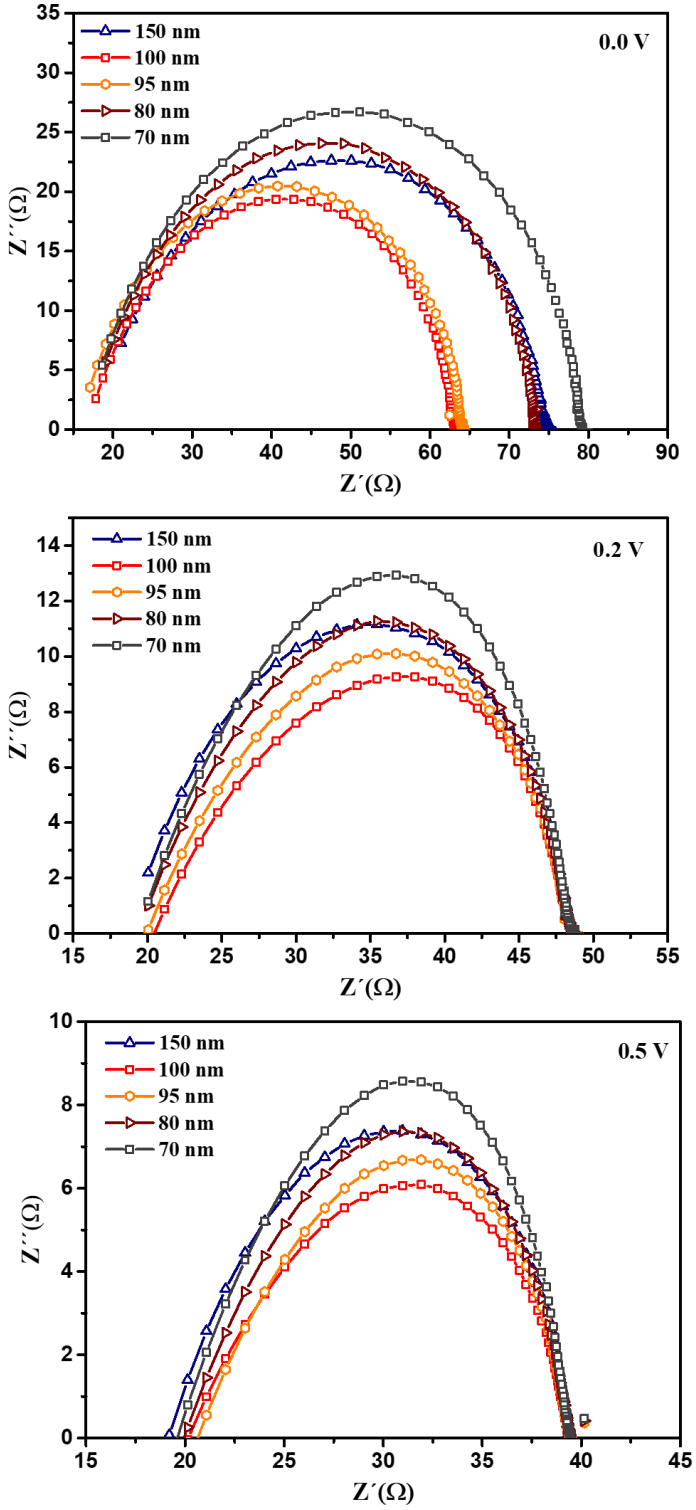

Figure A.11 Cole-Cole plots under AM1.5 G illumination at 0.0, 0.2, and 0.5 V applied bias voltages of various PM6:Y7 photoactive layer thicknesses.

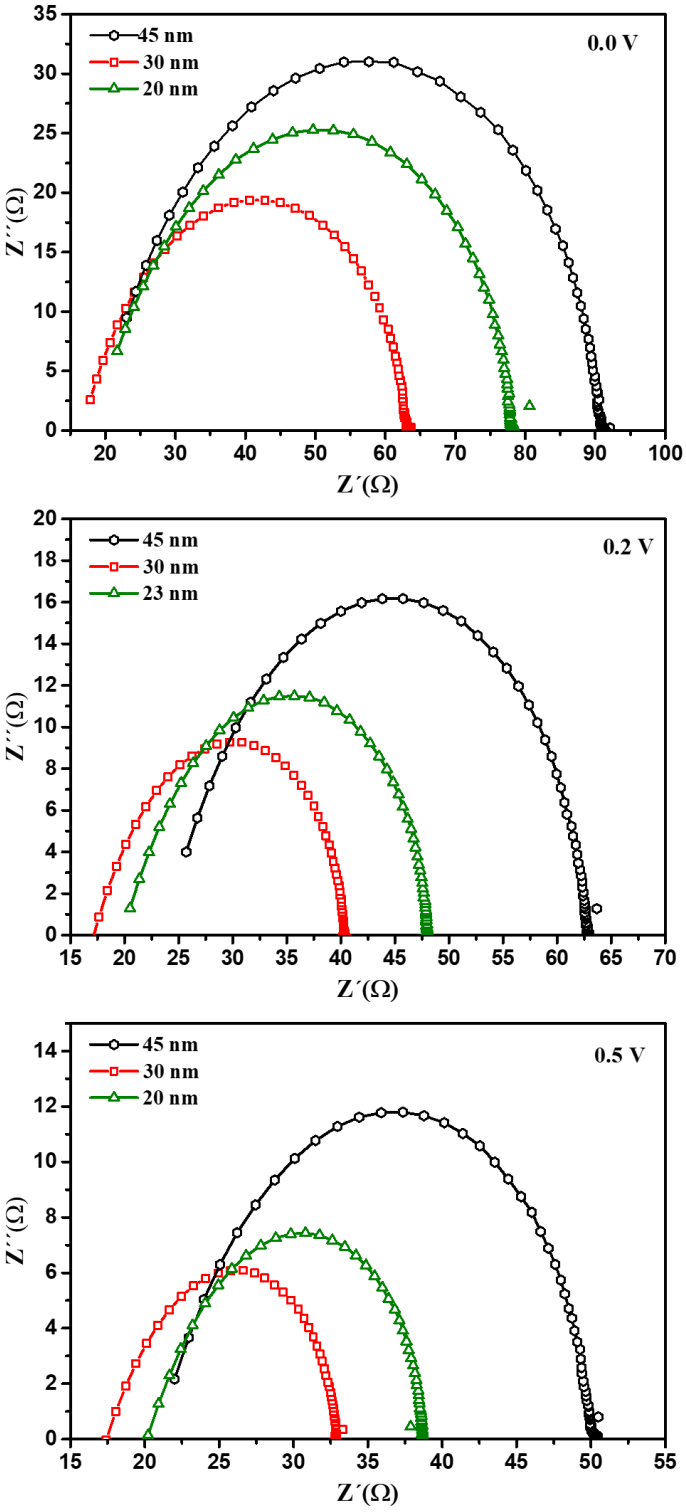

Figure A.12 Cole-Cole plots under AM1.5 G illumination at 0.0, 0.2, and 0.5 V applied bias voltages of various PEDOT:PSS layer thicknesses.

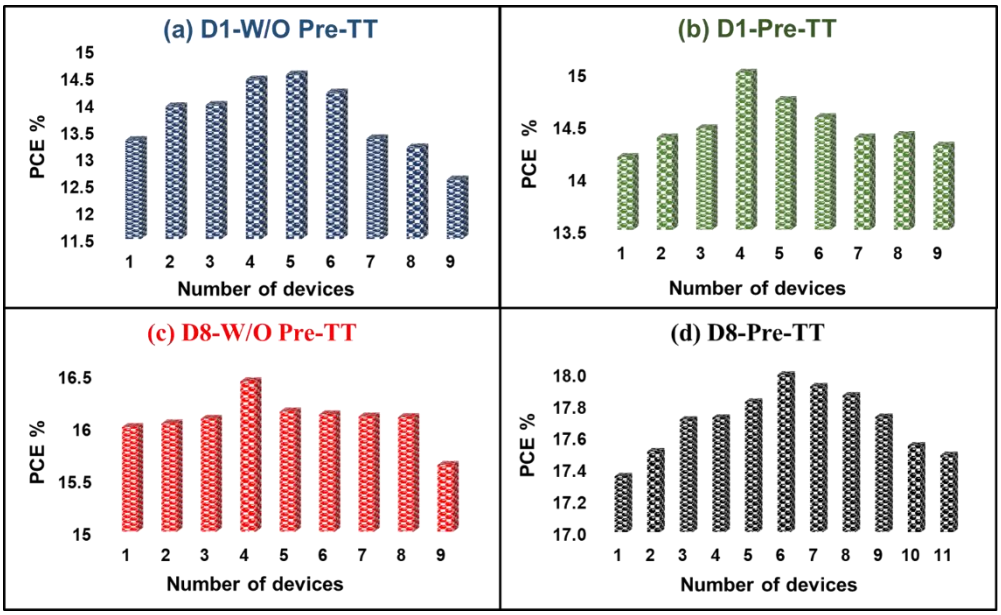

Figure A.13 The PCE % statistics diagrams for the fabricated (a) D1-W/O Pre-TT, (b) D1- Pre-TT, (c) D8-W/O Pre-TT, and (d) D8-Pre-TT NF-OPVs devices.

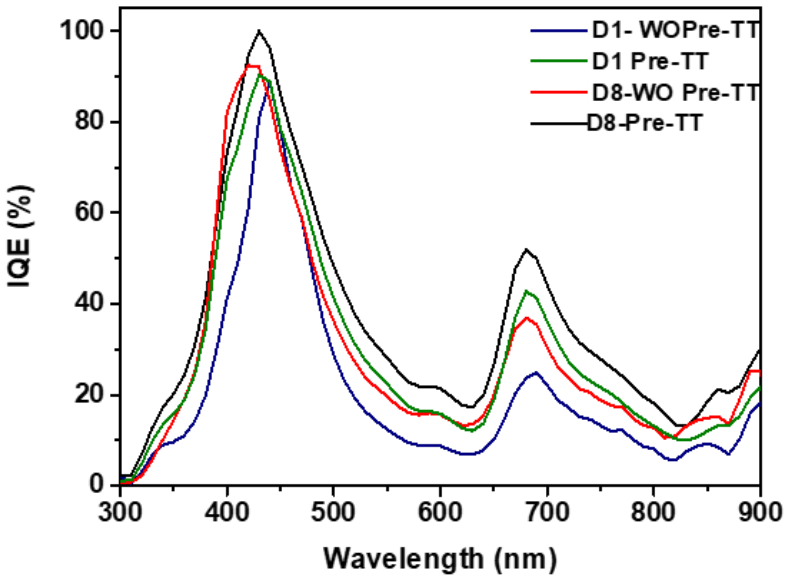

Figure A.14 IQE spectral response of the pristine and Pre-TT D1 and D8 based devices.

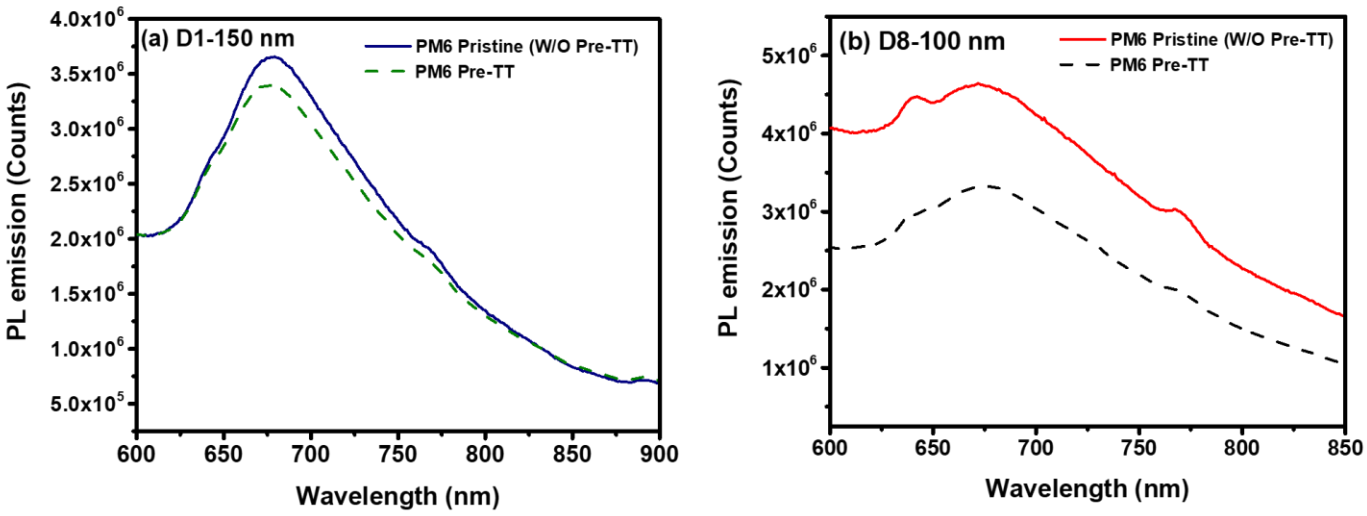

Figure A.15 Photoluminescence characteristics of the PM6 reference of pristine and Pre-TT films for (a) Device 1 with 150 nm thickness and (b) Device 8 with 100 nm

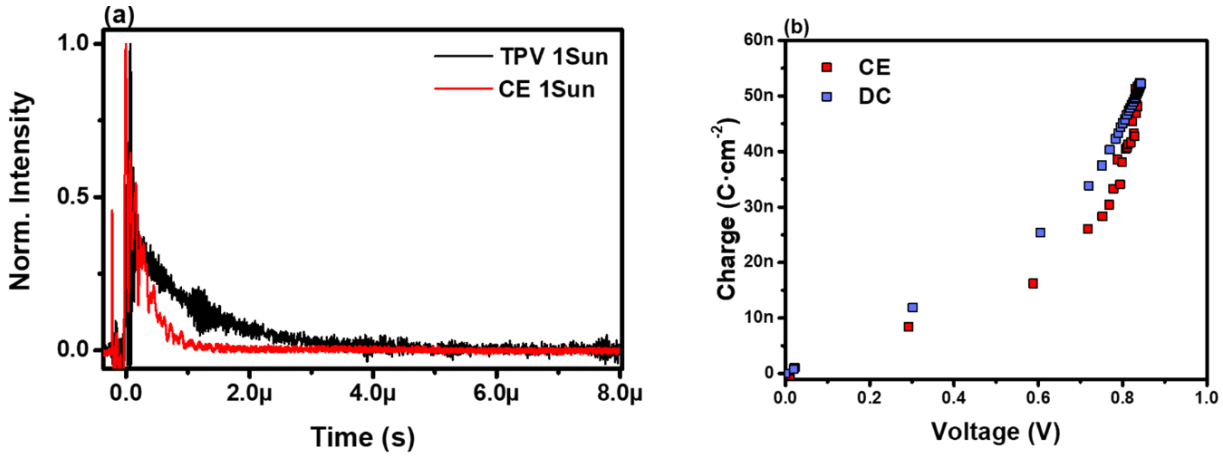

Figure A.16 (a) Comparison of CE and TPV decays at 1 Sun illumination and (b) charge vs voltage obtained by using CE and the combination of TPV/TPC (DC) techniques for D8-Pre-TT devices.

We analyzed the carrier dynamics by using charge extraction (CE) and optoelectronic transient techniques –transient photovoltage and transient photocurrent (TPV, TPC) measurements that were carried out using a white LED controlled by a programmable power supply and a control box that switches from open to short-circuit states. All the signals are recorded in an oscilloscope Yokogawa DLM2052 registering drops in voltage. Light perturbations pulses for TPV and TPC were provided by a nanosecond PTI GL-3300 nitrogen laser and using a 580 nm laser pulse wavelength. We started to analyze the devices under operando conditions

using CE technique, a simple tool to quantify all the charges present at a given light bias. The carrier recombination is usually faster than CE, so in order to validate CE technique for these kind of devices, we need to compare the decays from CE and TPV at 1 Sun conditions[321]. This allows us to extract the charges before they recombine in all devices (see **Figure A.16** as an example). However, differential capacitance (DC), as a combination of TPV and TPC techniques, exists as an alternative to determine the charge density, which as well ensures that the measured charge is proper and both CE and DC results must be alike (see **Figure A.16b** for comparison).

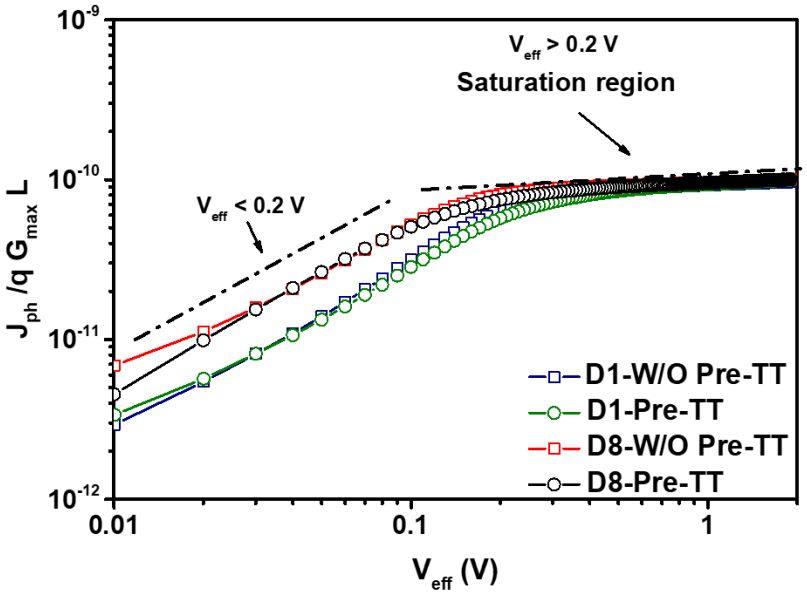

Figure A.17 The plot of the photocurrent to its saturation value ($qG_{max}L$) as a function of V_{eff} for the pristine and the Pre-TT NF-OPVs. The dashed line for guiding the eye.

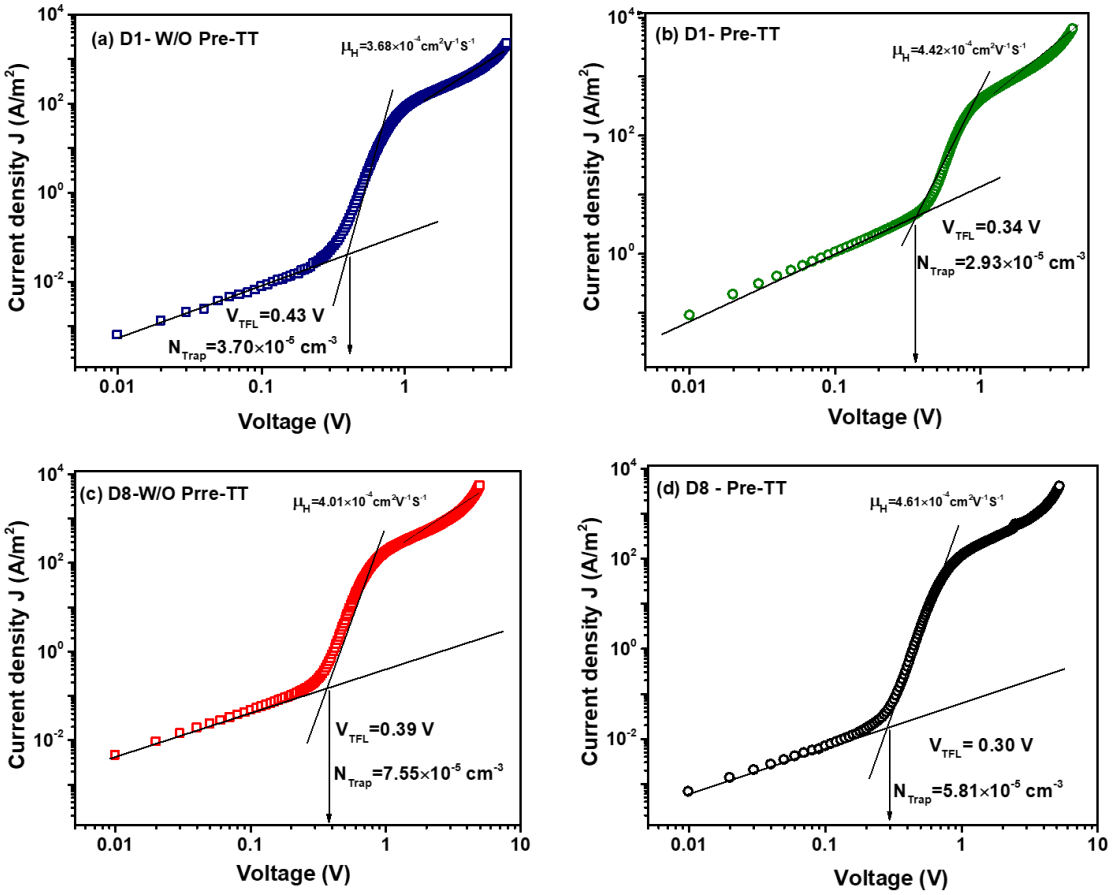

Figure A.18 The SCLC curves of hole only devices based on (a) D1-W/O Pre-TT, (b) D1-Pre-TT, (c) D8-W/O Pre-TT, and (d) D8-Pre-TT.

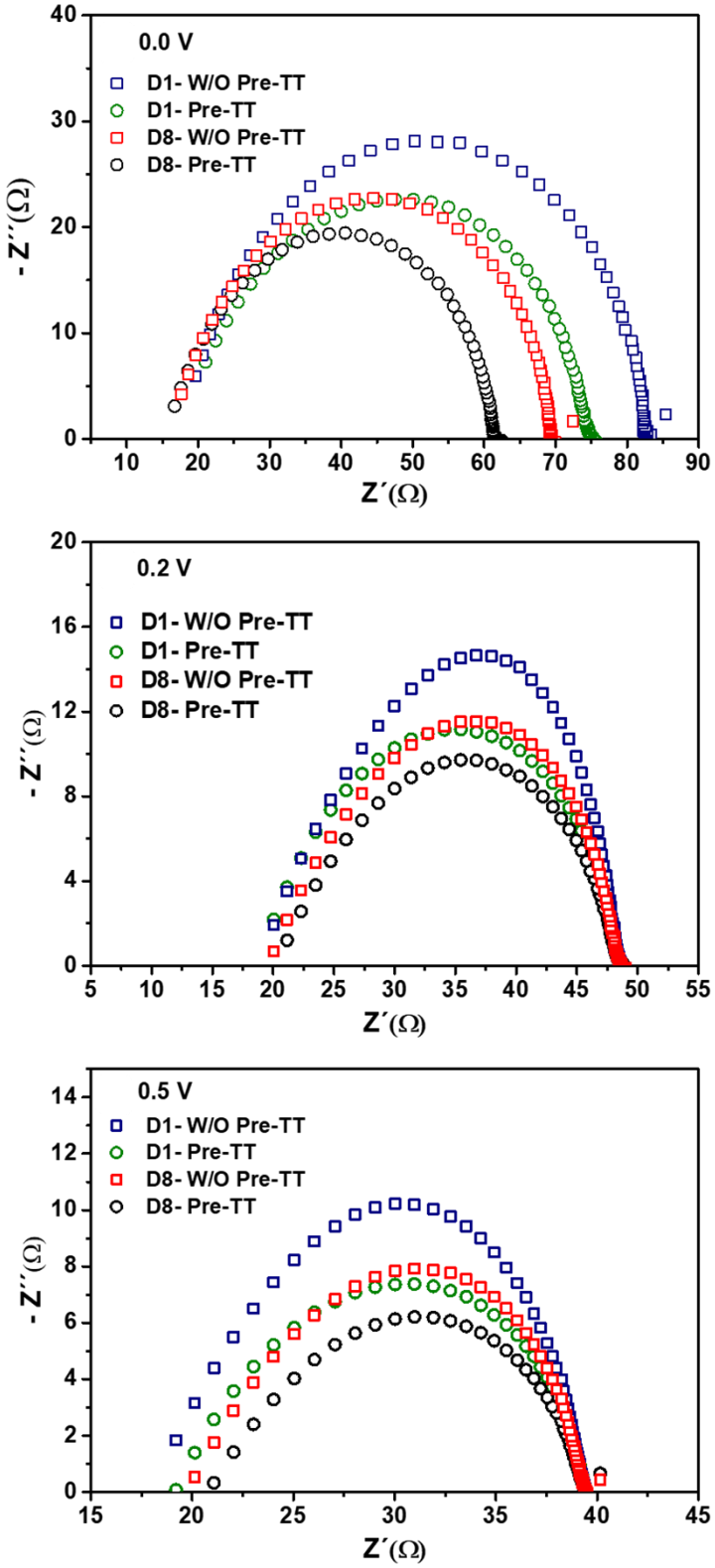

Figure A.19 Cole-Cole plot with various DC applied bias voltages of J_{SC} at 0.0 V, near V_{mpp} of 0.2 V, and V_{mpp} of 0.5 V with frequency range of 1 Hz- 5 MHz under 1.5 AM G illumination and an oscillation amplitude of 50 mV for D1 and D8 Pristine and Pre-TT devices.

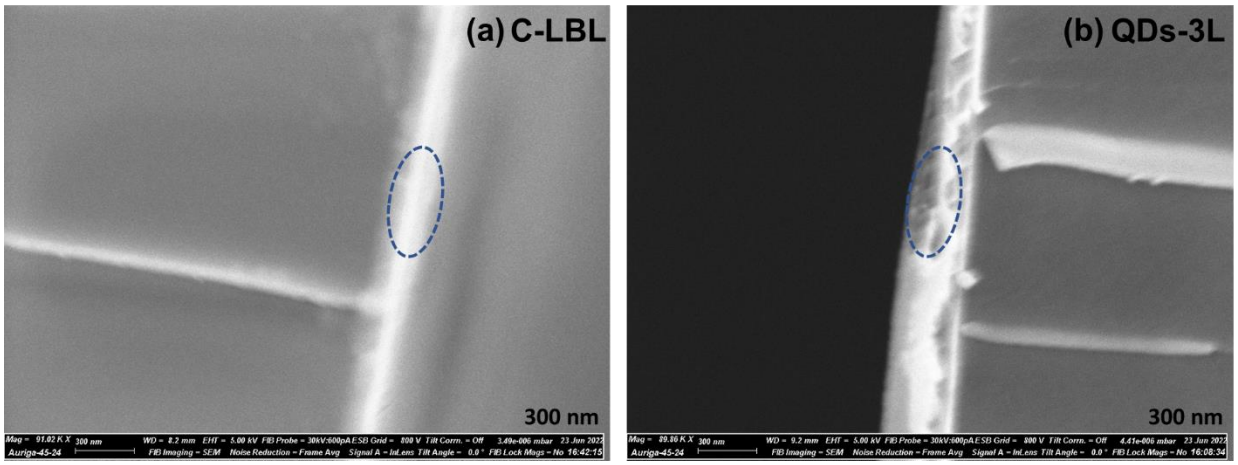

Figure A.20 FE-SEM cross-section image of (a) C-LBL binary based device (D18/Y6), and (b) LBL QDs-3L based device (D18/QDs-3L/Y6).

Appendix 2. Supporting Tables

Table A.1 The evaluated RC circuits fitting parameters of B-7R-SP and D-7R-SP iF-OPVs by the 3RC equivalent circuit model for the fresh samples (T_{100}) and Debye model for the degraded iF-OPVs after 5000 h (~T_{80}), For the V_2O_5 layer of the degraded devices, the parameter $\tau = R_4 \times C_4$ where R_4 parameter were demonstrated in Figure 3.11e.

Parameters of Fresh ZnO-B-7R-SP-iPSCs	**0.8 V (V_{OC})**		
V_2O_5	R_S = 10.2 Ω L = 1.7E-6 H	R_1= 12.5 Ω	C_1= 99.0nF
ZnO		R_2= 15.2 Ω	C_2= 24.0nF
The Blend		R_3= 18.5 Ω	C_3= 2.8 nF
Parameters of degraded ZnO-B-7R-SP-iPSCs-Debye model	**0.77 V (V_{OC})**		
V_2O_5	R_S =11.0 Ω L = 1.7E-6 H	R_1= 16.2 Ω τ = 9.0E-6 s	C_1= 99.0 nF C_4=51.0 nF
ZnO		R_2= 20.0 Ω	C_2= 24.0 nF
The Blend		R_3= 21.0 Ω	C_3= 2.8 nF
Parameters of Fresh ZnO-D-7R-SP iPSCs	**0.76 V (V_{OC})**		
V_2O_5	R_S = 15.5 Ω L = 1.7E-6 H	R_1= 10.5 Ω	C_1= 99.0 nF
ZnO		R_2= 36.0 Ω	C_2= 10.0 nF
The Blend		R_3= 8.0 Ω	C_3= 2.8 nF
Parameters of degraded ZnO-D-7R-SP iPSCs--Debye model	**0.72 V (V_{OC})**		
V_2O_5	R_S = 9.0 Ω L =1.7 E-6 H	R_1= 12.0 Ω τ = 9.0E-6 s	C_1= 99.0 nF C_4= 61.0 nF
ZnO		R_2= 45.5 Ω	C_2= 10.0 nF
The Blend		R_3= 18.0 Ω	C_3= 2.8 nF

Table A.2 Photovoltaic performance parameters statistics of the fabricated binary devices at 100 ℃ thermal annealing.

Device	Voltage (V)	Jsc (A/cm^2)	Fill Factor	Efficiency (%)	R Series	R Parallel
TA-100 ℃,10 min						
0% CN	0.69 ± 0.02	22.47 ± 0.45	0.58 ± 0.02	8.92 ± 0.86	2.04 ± 0.25	350 ± 21
1 % CN	0.72 ± 0.03	23.77 ± 2.05	0.61 ± 0.04	10.41 ± 0.54	1.63 ± 0.17	328 ± 18
2% CN	0.78 ± 0.05	24.27 ± 0.86	0.65 ± 0.02	12.36 ± 0.33	1.17 ± 0.44	441 ± 61
TA-100 ℃,30 min						
0% CN	0.73 ± 0.02	21.75 ± 0.22	0.59 ± 0.03	9.31 ± 0.11	2.42 ± 0.41	347 ± 31
1 % CN	0.75 ± 0.01	25.59 ± 0.49	0.62 ± 0.01	11.94 ± 0.43	1.54 ± 0.18	318 ± 16
2% CN	0.73 ± 0.01	27.43 ± 0.36	0.63 ± 0.04	12.65 ± 0.27	1.44 ± 0.22	448 ± 22

Table A.3 Dielectric constants and calculated capacitances for each layer of the fabricated iNF-OSCs.

Layer	ε_{Layer}	**Capacitance (nF)**	**Thickness (nm) d_{Layer}**
ZnO	6 [121,210]	16	30
		24	20
PDINO	5 [88]	19.92	20
		39.84	10
Blend	3.5 [58,211,212]	2.79	100
V_2O_5	5 [166]	79.7	5

Table A.4 The calculated values of V_{TFL}, N_t and N_f for the pristine and Pre-TT hole only devices

Hole only devices	**V_{TFL} (V)**	**N_t (× 10^{15} cm^{-3})**	**N_f (× 10^{13} cm^{-3})**
D1-W/O Pre-TT	0.43	3.70	1.00
D1-Pre-TT	0.34	2.93	1.06
D8-W/O Pre-TT	0.39	7.55	1.66
D8-Pre-TT	0.30	5.81	2.21

UNIVERSITAT
ROVIRA i VIRGILI

Imperial College
London

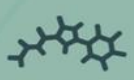

ICIQ Institute of Chemical Research of Catalonia